博士論文

Search for astrophysical antineutrinos with deep neural-network-based event identification in the full KamLAND dataset

（深層ニューラルネットワークでの事象識別を用いた
KamLAND全データ期間における天体起源反ニュートリノ探索）

永塚穂里

令和 7 年

Abstract

On 23 February 1987, the observation of neutrinos from SN1987A in the Large Magellanic Cloud marked the beginning of neutrino astronomy. Various sources have since been proposed for astrophysical neutrinos, including supernovae, the Sun, and dark matter, each providing physics motivation spanning a broad range of areas. KamLAND, a 1-kiloton liquid scintillator detector, is well suited for astrophysical neutrino searches owing to its large exposure and high sensitivity below 10 MeV. Electron antineutrinos in KamLAND are detected via the inverse beta-decay reaction, in which the delayed coincidence between the prompt positron signal and the delayed neutron-capture signal allows a substantial suppression of background events. However, with conventional analysis techniques, it has not been possible to sufficiently distinguish astrophysical neutrino signal from backgrounds such as atmospheric neutrinos and fast neutrons, which has limited the achievable sensitivity.

In this thesis, electron-type astrophysical antineutrinos are searched for using the full KamLAND data set accumulated over more than 6000 days. To enhance the rejection power against background events, a deep neural network-based event identification method has been developed. A total of seven astrophysical neutrino candidates are observed, consistent with an expected background of 16.2 ± 9.4 events. By exploiting both the energy spectrum and radial distribution of the events, fits to various signal models yield upper limits on the diffuse supernova neutrino background fluxes that are improved by a factor of two from the previous KamLAND results. From a dedicated search for neutrinos from primordial black holes, a new constraint is obtained on the fraction of primordial black holes in the dark matter energy density. In addition, one of the most stringent limits are set on the model-independent electron antineutrino flux. Limits are also obtained on the ^{8}B solar neutrino conversion probability and on the dark matter self-annihilation cross section.

These results provide complementary information to those from other detectors such as Super-Kamiokande, and they serve as a pioneering step toward future large liquid scintillator detectors, including KamLAND2 and JUNO.

Acknowledgements

First and foremost, I would like to express my deepest gratitude to Associate Professor Koji Ishidoshiro, who has supervised me since my fourth undergraduate year. Through not only regular meetings but also frequent and lively discussions on a daily basis, he helped me significantly improve the quality of this research. His guidance, ranging from astrophysical insight to detailed analysis techniques, has been essential to the completion of this thesis.

I am also deeply grateful to Professor Kunio Inoue, the spokesperson of the KamLAND collaboration, for his incisive comments and advice at many critical stages of this study, which greatly contributed to refining the content of this thesis. I would furthermore like to thank Associate Professor Hiroko Watababe for many helpful suggestions throughout all aspects of the antineutrino analysis.

I am indebted to Professor Christopher Grant and Assistant Professor Aobo Li for their expert advice on the analysis using deep neural networks. I sincerely appreciate their willingness to engage in discussions despite the time difference with Japan. I also thank Dr. Nanami Kawada for many insightful comments provided during our weekly meetings. I am especially grateful to Ryo Nakamura, a former member of the group, whose prior work on the primordial black hole analysis and on the development of the shower likelihood cut formed an important foundation for this study.

Finally, I would like to express my sincere appreciation to all members of the laboratory and all staff involved in the Kamioka facility, as well as to my family for their constant support.

Contents

List of Figures

List of Tables

Chapter 1

Introduction

The observation of supernova neutrinos from SN1987A in the Large Magellanic Cloud on 23 February 1987 marked the beginning of neutrino astronomy. Various sources of astrophysical neutrinos have since been considered, and the motivations for neutrino observations are correspondingly diverse. Among low-energy astrophysical neutrinos in the few to few tens of MeV range, the Diffuse Supernova Neutrino Background (DSNB) has recently attracted particular attention. The DSNB is the superposition of supernova neutrinos emitted throughout the past history of the Universe. It depends on several astrophysical inputs such as the star formation rate, the supernova neutrino spectrum, and the fraction of black-hole formation following core collapse. Observations of the DSNB are therefore motivated by the possibility of constraining these astrophysical parameters from the perspective of neutrino measurements.

In addition, for the nearby astrophysical neutrino source represented by the Sun, it has been suggested that electron neutrinos may convert into electron antineutrinos ($\bar{\nu}_e$s). Searches for solar $\bar{\nu}_e$s thus provide a means to test physics beyond the Standard Model. Furthermore, primordial black holes, which are candidates of dark matter, are expected to emit neutrinos via Hawking radiation, making it possible to search for dark matter through neutrino observations.

Searches for low-energy astrophysical neutrinos are being carried out worldwide using neutrino detectors such as KamLAND, Super-Kamiokande, Borexino, and SNO. In this thesis, the 2022 search with the KamLAND detector is updated by extending the analysis to the full data period and by developing a new background rejection method. In KamLAND, the main detection channel is inverse beta decay of $\bar{\nu}_e$s, and the dominant backgrounds arise from atmospheric neutrino neutral-current interactions and fast neutron events. These are exceedingly difficult to separate with current analysis methods. However, in principle, the particle content and spatiotemporal distribution of their interactions differ. I exploit corresponding differences in the photon-hit information used for event reconstruction and develop a deep-neural-network-based event separation technique. The method is then integrated into the existing analysis framework to perform the astrophysical $\bar{\nu}_e$ search.

In this thesis, Chap. 2 describes the source of astrophysical $\bar{\nu}_e$s targeted in this search and summarizes the results of other global experiments conducting similar searches. Chap. 3 introduces the KamLAND experiment, and Chap. 4 explains the event reconstruction procedure employed in KamLAND. Chap. 5 provides a general introduction to machine learning and neural networks, followed by Chap. 6, which presents in detail the deep neural network-based event identification method developed in this study. Chap. 7 describes the selection criteria for astrophysical $\bar{\nu}_e$ candidate events, while Chap. 8 focuses on the estimation of background events in the astrophysical $\bar{\nu}_e$ search. The results of various astrophysical $\bar{\nu}_e$ searches are presented in Chap. 9, and the conclusion is given in Chap. 10.

Chapter 2

Low Energy Astrophysical Neutrino Sources

2.1 Supernova

2.1.1 Stellar Evolution and Supernova

Stars are self-gravitating concentrations of gas, and their shape is maintained by hydrostatic equilibrium between gravity and pressure gradients. Assuming that the constituent gases are ideal gases, pressure and temperature are proportional, and the smaller the radius and the greater the mass, the higher the central temperature. A newly born star cannot produce energy by hydrogen fusion reaction because its central temperature is not so high. However, they lose energy by emitting light because energy must flow from the interior to the exterior to create the pressure gradient needed to maintain hydrostatic equilibrium. Since this energy is carried by the release of gravitational energy, the star contracts and the internal temperature increases. When the internal temperature is high enough for hydrogen fusion reactions, the rate of energy generation from the hydrogen-helium synthesis reaction is balanced by the energy release from the surface, and the star evolves into a main-sequence star. This hydrogen-burning process will occupy the majority of the star's lifetime.

Here the stellar evolution process and its end depends on the mass, as shown in Fig. 2.1, which is summarized below (M denotes the stellar mass and $M_\odot$ denotes the solar mass).

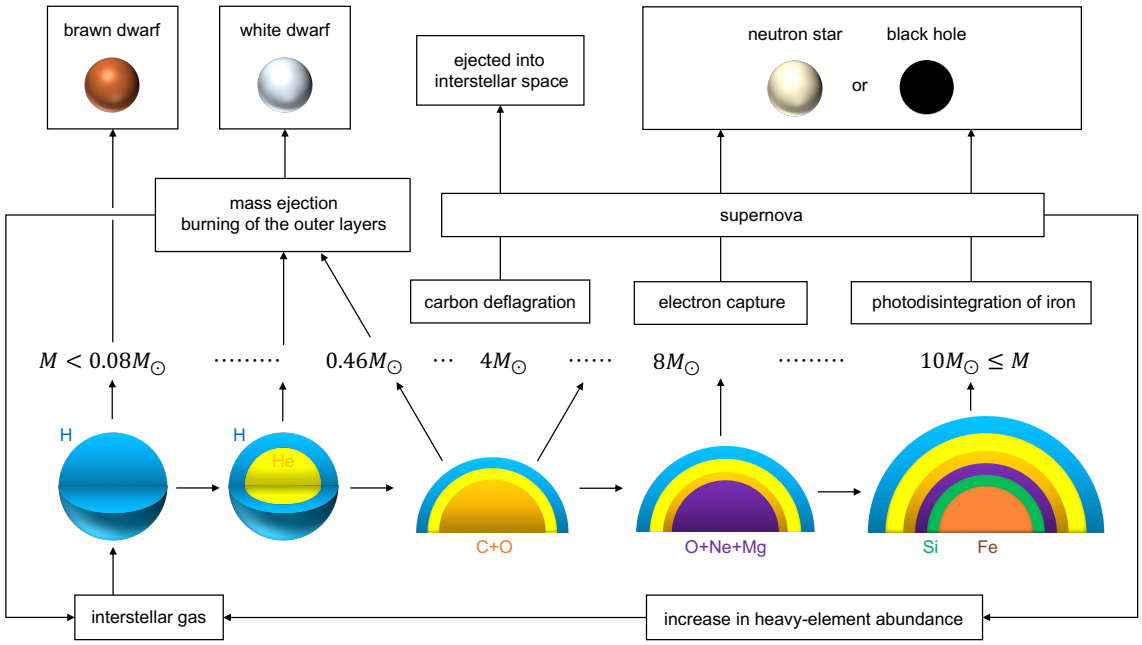

Figure 2.1: Stellar mass and evolution. This figure is based on [1].

- $M < 0.08\,M_\odot$
  Because their masses are too small to reach a central temperature sufficient for hydrogen fusion, they cannot become main-sequence stars. Such stars become brown dwarfs.

- $0.08\,M_\odot < M < 0.46\,M_\odot$
  The nuclear fusion reaction of hydrogen creates a helium core in a star. In such a light star, the electrons in the core are degenerate due to the extremely high density in the center. Since electron degeneracy is independent of temperature, the core becomes nearly isothermal and can be supported by the density-dependent pressure gradient and gravitational equilibrium (the mass of the core at the limit supported by the degeneracy pressure is called the Chandrasekhar mass). Because gravitational contraction ceases, the temperature required for helium fusion is not reached, and the star cools by releasing energy and eventually becomes a white dwarf.

- $0.46\,M_\odot < M < 4\,M_\odot$
  The helium core mass exceeds the Chandrasekhar mass, and the density gradient alone is no longer sufficient to support the star. In order to support the star, a temperature gradient must be created, and thermal energy begins to be emitted outward from the core. The core then loses energy and gravitationally contracts, and the temperature rises. For $M < 2\,M_\odot$, the core becomes dense and degenerate, resulting in an explosive helium burn called a helium flash. On the other hand, for $M > 2\,M_\odot$, the core does not become dense enough to be degenerate, and normal helium burning occurs. In both cases, the outer hydrogen-burning shell expands with increasing temperature, and the star as a whole evolves into a red giant. The core, which is composed of carbon and oxygen, does not undergo a fusion reaction due to insufficient temperature, and the star loses energy and becomes a white dwarf. The expanded outer layers are scattered into interstellar space due to weak gravitational constraints.

- $4\,M_\odot < M < 8\,M_\odot$
  Explosive carbon burning occurs in the degenerate carbon-oxygen core. The reaction raises the temperature of the core, but the star cannot expand due to its mass, resulting in a positive feedback that further raises the temperature. The core burns out in less than 0.1 second, and the burning wavefront, called the "explosive combustion wave," propagates outward at subsonic speed and explodes. The end of such a star is called a thermonuclear (carbon detonation) supernova.

- $8\,M_\odot < M < 10\,M_\odot$
  As the core mass exceeds the Chandrasekhar mass, it gravitationally contracts. The center of the core is weakly degenerate, so the temperature dependence of pressure is small, and the carbon in the periphery begins to burn first. A core composed of oxygen, neon, and magnesium is formed, but the temperature is not high enough for neon to burn, and electrons become degenerate in the core. Because of the high density, electron capture reaction ($p + e^- \to n + \nu_e$) by protons inside and outside the nucleus occurs, and gravitational collapse occurs due to the decrease of degeneracy pressure. The shock wave generated by the core recoil then propagates outward, causing a core-collapse supernova, leaving a neutron star at the center.

- $M > 10\,M_{\odot}$
  Unlike above, the carbon core begins to burn from the center. In the core, synthesis of heavier elements is repeated, and once iron, which has the maximum binding energy per nucleon, is synthesized, the reaction proceeds no further. As the mass of the iron core increases, the temperature rises, and the reaction of the nucleus decomposition by photons
  $$^{56}\mathrm{Fe} \rightarrow 13\,^{4}\mathrm{He} + 4n - 124.4\,\mathrm{MeV} \tag{2.1}$$
  will occur. Since this reaction works in the direction of reducing the temperature gradient supporting gravity, the core undergoes gravitational collapse, leading to a core-collapse supernova. Some massive stars exceeding $30\,M_{\odot}$ are thought to collapse gravitationally and form a black hole.

2.1.2 Supernova Classification

Supernovae are classified according to the combination of their spectra and luminosity curves as shown in Fig. 2.2. The presence or absence of absorption lines of a particular element in the spectrum allows us to estimate how much of the outer layer remained at the time of the explosion.

Type I has absorption lines for silicon, Type Ib and Type Ic do not have absorption lines for helium, and Type Ic has no absorption lines for helium. Type Ib and Ic have no helium absorption lines, while Type Ic has no helium absorption lines. Among Type II, those with a plateau in the luminous intensity curve that does not change with time are called Type IIP, while those with a monotonically decreasing luminous intensity are called Type IIL. Among type II, those with narrow hydrogen absorption lines are called type IIN.

Type Ia corresponds to the thermonuclear-decay supernova explosions mentioned in Sec. 2.1.1. The energy released in such a supernova explosion is about 10^{51} erg due to the nuclear fusion reaction. The other type of supernova explosion is the Type Ib, Ic, and II supernovae. In this case, gravitational energy is released and the energy is about 10^{53} erg.

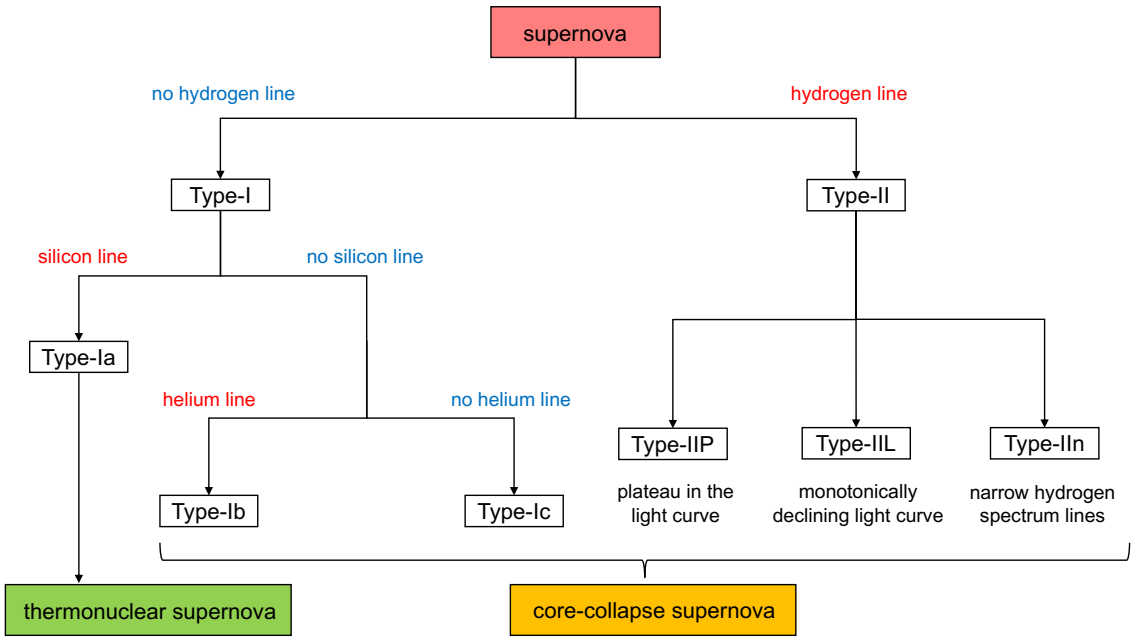

Figure 2.2: Supernova classification

2.1.3 Pre-Supernova Neutrino

After the carbon burning process, the main cause of the core's gravitational collapse is cooling due to neutrino emissions. The timescales of the burning processes for each element in the core are estimated as follows: carbon burning occurs up to a few hundred years before the explosion, oxygen and neon burning up to a few years before, and silicon burning, which leads to the synthesis of stable iron, takes only a few weeks. During this process, neutrinos are thermally produced through the following reactions.

$$e^+ + e^- \to \nu + \bar{\nu} \quad \text{(pair creation)} \tag{2.2}$$

$$\gamma \to \nu + \bar{\nu} \quad \text{(Plasmon decay)} \tag{2.3}$$

$$e^- + \gamma \to e^- + \nu_e + \bar{\nu}_e \quad \text{(photo neutrino)} \tag{2.4}$$

$$e^- + (Z, A) \to e^- + (Z, A) + \nu + \bar{\nu} \quad \text{(bremsstrahlung)} \tag{2.5}$$

The neutrinos emitted before a supernova explosion are called pre-supernova neutrinos. Just before the explosion, neutrinos produced by nuclear reactions dominate over the thermally generated ones. Fig. 2.3 illustrates the luminosity of $\bar{\nu}_e$ expected before and after the explosion. Detecting pre-supernova neutrinos could serve as an alert for the explosion. However, because their average energy is below 2 MeV, detectors only with low energy thresholds, such as the liquid scintillator KamLAND, are considered suitable for observation.

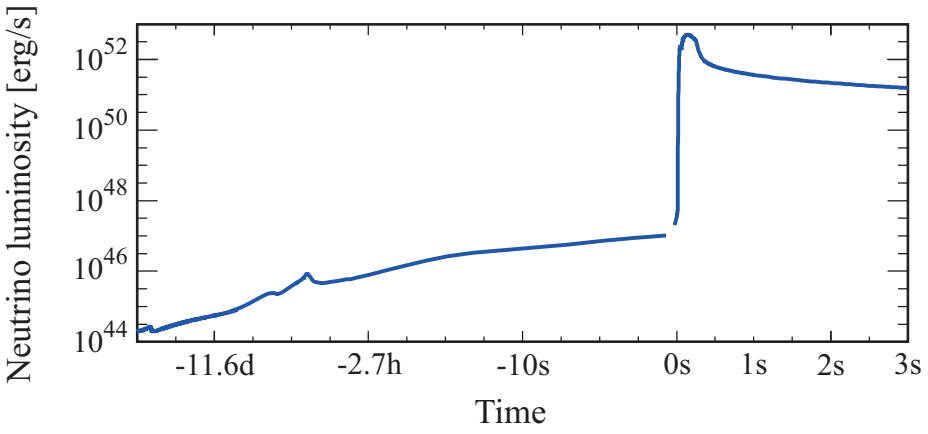

Figure 2.3: The luminosity of $\bar{\nu}_e$ expected before [2] and after [3] the supernova explosion. Note that the time axis is in logarithmic scale before the explosion and linear scale after, with 0 s representing the moment of the explosion.

2.1.4 Supernova Neutrino

Core-Collapse Supernovae (CCSNe)

When electron capture and nuclear photodisintegration in the core occur as described in Sec. 2.1.1, a core-collapse supernova occurs, leaving a neutron star or black hole at the end. Here, neutrinos are ejected through the processes described below.

i) Neutrino Trapping
As the electron capture reaction proceeds in the core, ν_e is produced and the core becomes neutron-rich. This can be regarded as the process of the core becoming a neutron star. Normally, neutrinos only have a weak interaction and its rate is very small, but in the gravitationally collapsing core, the neutrino reaction rate is high

because the density is very high. When the neutrinos and nuclei become coherently scattered, the mean free path of neutrinos in the core is equal to the radius $\sim 10^7$ cm of the core. In addition, the diffusion time of the neutrino at this time is also about the same as the time scale of the core contraction, so the neutrino is effectively confined to the core. This is called neutrino trapping, and in particular, the surface of the region where neutrinos are confined is called the neutrino sphere.

ii) Core Bounce and Shock Wave Creation
When the density of the core reaches the saturation density of nuclei $\sim 10^{14}\,\mathrm{g/cm^3}$ due to gravitational contraction, the core becomes uniform nuclear matter composed of nucleons and becomes very hard due to the repulsion of nuclear forces. The gravitationally contracting core is divided into an inner core contracting at subsonic speeds and an outer core contracting at supersonic speeds. When the core recoils due to repulsion, the information propagates at the speed of sound, thus suppressing the contraction of the inner core. The external core, however, contracts at supersonic speeds, so the recoil information is not transmitted, resulting in the generation of a shock wave at the boundary between the internal and external cores.

iii) Shock Wave Propagation and Neutronization Burst
The shock wave is pushed by the pressure of the downstream material and travels outward from the core. The material through which the shock wave passes is compressed and heated, causing the nucleus to undergo photodisintegration. Since the reaction rate of the electron capture that produces ν_e is greater for the nucleon after the decomposition than for the nucleus, the electron capture reaction occurs rapidly after the shock wave surface. In addition, as the photodisintegration of the nucleus progresses, the coherent scattering of neutrinos becomes ineffective and the neutrino sphere shrinks. Then, when the shock wave reaches the neutrino sphere, the ν_e luminosity increases rapidly. Such a phenomenon is called a neutronization burst, in which ν_e is emitted with a luminosity of $10^{53}\,\mathrm{erg/s}$ in a period of several 10 ms. If we can observe the neutronization burst, we can put a limit on the absolute mass of the neutrino, since the arrival time of neutrinos depends on their energy and mass. It is also expected to observe neutrino oscillations of ν_e.

iv) Neutrino Emission
When the electron degeneracy is lifted due to shock-wave heating, neutrino-antineutrino pairs are produced through electron-positron annihilation, as expressed by Eq. 2.2. In addition to this reaction, neutrinos are also generated through nucleon-nucleon bremsstrahlung, which contributes similarly to the overall production.

$$N + N \to N + N + \nu + \bar{\nu} \tag{2.6}$$

Due to their large masses, muons and tauons are absent in the core of a supernova, and thus, no production of ν_μ or ν_τ occurs through charged current interactions involving them.

v) Shock Wave Stall and Revival
When photodissociation occurs just after the shock wave front, the thermal energy of the shock wave is converted into rest mass energy, causing the shock wave to lose energy. Consequently, the shock wave cannot propagate through the outer core and

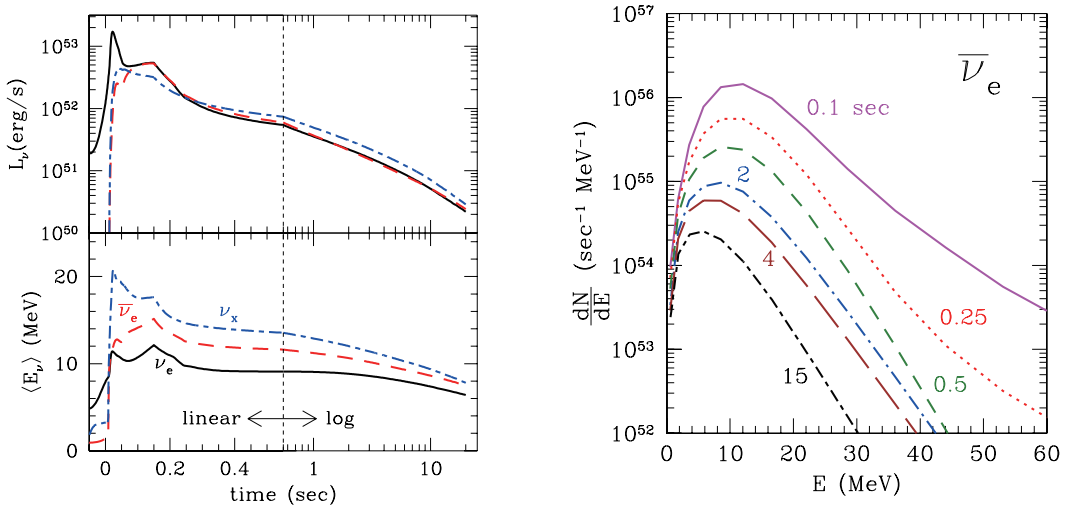

Figure 2.4: The time evolution of the luminosity (left) and energy distribution of emitted number of $\bar{\nu}_e$ (right) [3]. ν_x represents ν_μ, ν_τ, $\bar{\nu}_\mu$, and $\bar{\nu}_\tau$. Additionally, the lines in the right figure indicate the time from the core bounce.

becomes stagnant. In this state, external material cannot gain outward velocity due to the shock wave, leading to accretion onto the central proto-neutron star. If this mass accretion continues, the neutron star undergoes gravitational collapse and becomes a black hole, resulting in what is known as a failed supernova. Several theories have been proposed to explain the revival of the stalled shock wave, with the most compelling being shock heating by neutrinos. The proto-neutron star cools while emitting neutrinos. These neutrinos, although having low interaction rates, are absorbed by nucleons produced by the shock wave via the following reactions:

$$\nu_e + n \rightarrow p + e^- \tag{2.7}$$
$$\bar{\nu}_e + p \rightarrow n + e^+ \tag{2.8}$$

It is believed that this neutrino-induced heating of the shock wave occurs on a time scale of about 100 ms. However, the specific conditions necessary for the revival of the shock wave have yet to be established.

vi) Proto-Neutron Star Cooling
The proto-neutron star still contains a relatively large number of protons and electrons, cooing down while emitting neutrinos as it evolves into a neutron star. During this process, approximately 10^{53} erg or energy is released over a timescale of about 10 s.

The shockwave continues to propagate outward through the star, and once it passes through the photosphere near the surface, an optical supernova explosion is observed. At this point, the outer layers of the star are blown away, leaving behind a proto-neutron star at the center. Fig. 2.4 shows the typical neutrino spectrum from a supernova. Supernova neutrino is searched by neutrino detectors around the world.

Thermonuclear Supernovae

Thermonuclear supernovae have lower temperatures at the sites where neutrinos are produced compared to core-collapse supernovae, and the typical neutrino energies are therefore only at the level of a few MeV. In addition, because no proto-neutron star is formed after

the explosion, there is no long cooling phase accompanied by neutrino emission, and the total neutrino flux is much smaller than in the core-collapse case. For these reasons, this type of supernova is not considered further in this thesis.

2.1.5 Diffuse Supernova Neutrino Background (DSNB)

Neutrinos emitted from past supernovae, known as Diffuse Supernova Neutrino Background (DSNB) or Supernova Relic Neutrinos (SRNs), persist in outer space. The DSNB flux is represented by the integrated supernova neutrino spectrum across cosmic history, weighted by the supernova rate, as shown in the following equation:

$$\frac{dF_\nu}{dE_\nu} = c \int_0^{z_{\max}} R_{\mathrm{SN}}(z) \frac{dN_\nu(E'_\nu)}{dE'_\nu} \left| \frac{dt}{dz} \right| dz \tag{2.9}$$

where c denotes the speed of light, z is the red shift, E_ν represents the neutrino energy, and R_{SN} is the supernova rate as a function of z. The neutrino spectrum from each supernova depends on the neutrino energy affected by the redshift, as given by the relation $E'_\nu = (1+z)E_\nu$. From the Friedmann equation, the relation between redshift z and time t can be expressed as

$$\frac{dz}{dt} = -H_0(1+z)\sqrt{\Omega_m(1+z)^3 + \Omega_\Lambda} \tag{2.10}$$

where H_0 represents the Hubble constant, Ω_m represents the fraction of cosmic energy density, and Ω_Λ denotes the fraction of the dark matter density. The dependence of the supernova rate R_{SN} on the star formation rate R_{SF} is given by

$$R_{\mathrm{SN}}(z) = \frac{\int dm\, \phi_{\mathrm{IMF}}(m)}{\int dm\, m \phi_{\mathrm{IMF}}(m)} R_{\mathrm{SF}}(z) \tag{2.11}$$

where $\phi_{\mathrm{IMF}}(m)$ is the initial mass function (IMF) which depends on the stellar mass m.

The motivation for observing DSNB spans a wide range of physics topics. As shown in Eq. 2.9, the DSNB flux includes contributions from the neutrino spectra of each supernova. This provides crucial insights into supernova physics, whose mechanisms remain incompletely understood. While supernova-burst neutrinos (observed only once in 1987) offer similar information, DSNB provide averaged characteristics of supernova neutrinos. Moreover, neutrino oscillations in stellar matter alter the DSNB spectrum, offering further understanding of neutrino physics. Additionally, the supernova rate term incorporates astronomical data. Current measurements of the cosmic supernova rate have a large uncertainty, and the measured values are approximately half of the predicted values [4]. If dark supernovae or dust-filled regions obscure light from reaching Earth, DSNB observations—due to neutrino's high transparency—may address these uncertainties. As shown in Eq. 2.11, the supernova rate is directly related to the cosmic star formation rate (SFR), which can be inferred from DSNB observations assuming the initial mass function. Since the SFR also has a large uncertainty, DSNB observations provide valuable additional data on the cosmic SFR, particularly within $z \sim 1$. Given the broad range of physics involved (supernova mechanisms, neutrino physics, and astronomy), DSNB searches are highly motivated and should proceed accordingly.

2.1.6 DSNB Models

This section describes various DSNB models employed in this study. The DSNB fluxes predicted by each model are shown in Fig. 2.5.

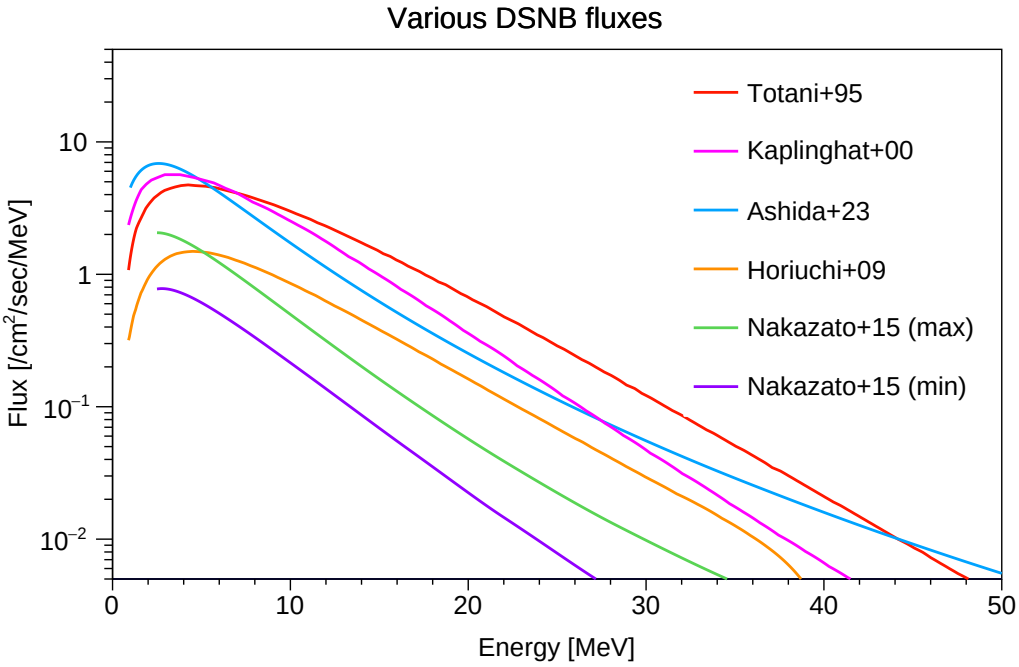

Figure 2.5: Predicted DSNB fluxes from various theoretical models as a function of neutrino energy. The curves represent predictions from Horiuchi [5], Nakazato [6], Kaplinghat [7], Ashida [8], and Totani [9].

Totani Model [9]

This model is one of the earlier DSNB models that incorporate cosmological inputs. The effects of neutrino oscillations are not included in this model. Denoting the neutrino energy by q, the neutrino number spectrum emitted from a supernova is expressed using a Fermi-Dirac distribution as

$$\frac{dN_\nu(q)}{dq} = \frac{c}{4}\frac{4\pi}{(2\pi\hbar c)^3}\frac{q^2}{e^{\beta(q-\mu)}+1}4\pi r_\nu^2 \Delta t_{\rm burst}. \tag{2.12}$$

Here, r_ν and $\Delta t_{\rm burst}$ are the radius of the neutrinosphere and the duration of the explosion, respectively. Using this spectral form, the differential DSNB number flux can be written as

$$\frac{dF_\nu}{dq} = \frac{cn_G(t_0)}{H_0}\int_0^{z_{\rm max}} R_{\rm SN}(t)\frac{dN_\nu\{(1+z)q\}}{dq}\frac{dz}{\sqrt{(1+\Omega_0 z)(1+z)^2-\lambda(2z+z^2)}}. \tag{2.13}$$

In this expression, z is the redshift, $H_0 = 50\,{\rm km\,s^{-1}\,Mpc^{-1}}$ is the Hubble constant, and $n_G(t_0) = 0.02\,h_{50}^3\,{\rm Mpc^{-3}}$ ($h_{50} = H_0/(50\,{\rm km/s/Mpc})$) is the number density of galaxies. $R_{\rm SN}$ denotes the supernova explosion rate; in this study, a *constant model* is adopted in which the rate is assumed to be constant for $z > 5$. The DSNB flux predicted by this model is shown in Fig. 2.6. The parameter λ is the cosmological-constant density parameter.

Kaplinghat Model [7]

This model establishes a conservative upper bound for the DSNB flux. According to Eq. 2.9, the differential DSNB flux at Earth is expressed as

$$j_\nu(\epsilon) = \frac{c}{H_0}\int_0^\infty dz \frac{N_{\rm SN}(z)\langle\mathcal{L}_\nu^S(\epsilon')\rangle}{(1+z)\sqrt{1+\Omega_0 z}}, \tag{2.14}$$

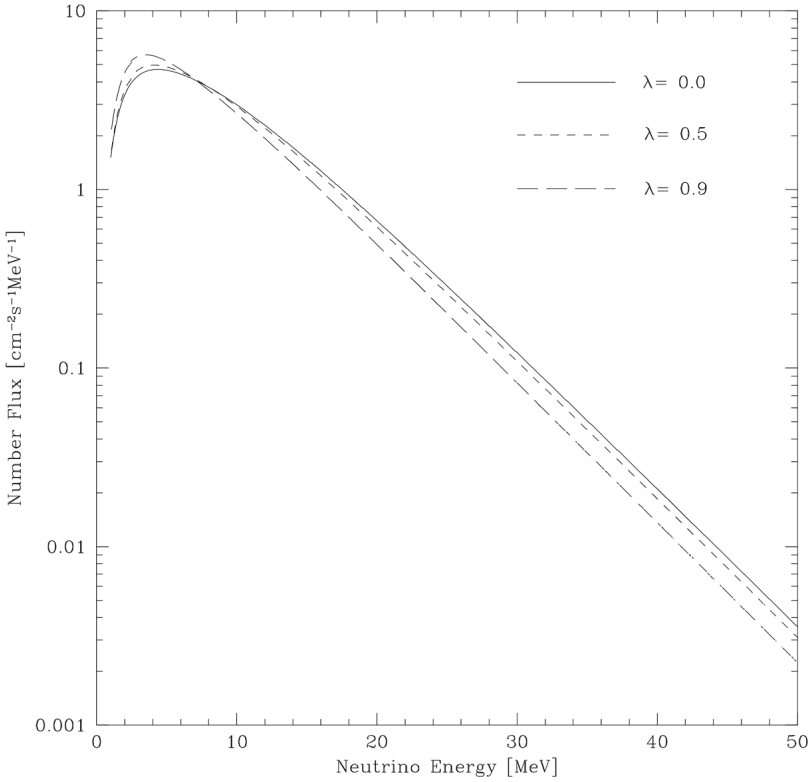

Figure 2.6: DSNB flux predicted by the Totani model for the constant supernova rate scenario [9]. The curves correspond to cosmological-constant density parameters $\lambda = 0.0$, 0.5, and 0.9, respectively.

where $N_{\rm SN}(z)$ represents the supernova rate per unit comoving volume at redshift z, and $\mathcal{L}_\nu^S(\epsilon')$ denotes the neutrino energy distribution at the source. The angular brackets signify that the neutrino flux, which depends on supernova progenitors of different masses, should be averaged across the IMF. The neutrino spectrum originating from a supernova is modeled using a Fermi-Dirac distribution with zero chemical potential, represented as:

$$\mathcal{L}_\nu^S(\epsilon) = E_\nu \frac{120}{7\pi^4}\frac{\epsilon^2}{T_\nu^4}\left[\exp\left(\frac{\epsilon}{T_\nu}\right)+1\right]^{-1}. \tag{2.15}$$

Based on Eq. 2.15, with the adoption of a flat $\Omega_0 = 1$ cosmology and the application of $x \equiv 1+z$, Eq. 2.14 can be approximated as

$$j_\nu(\epsilon) = \mathcal{A}\frac{\langle E_\nu\rangle}{\langle T_\nu\rangle^4}\epsilon^2\int_1^\infty dx N_{\rm SN}(x)\frac{\sqrt{x}}{\exp(\epsilon x/\langle T_\nu\rangle)+1}, \tag{2.16}$$

where $\mathcal{A} = (120/7\pi^4)\,cH_0^{-1} = 1056\,h_{50}^{-1}$. The averaged total neutrino energy, and the averaged effective neutrino temperature are fixed as $\langle E_\nu\rangle = 11\times10^{52}$ ergs and $\langle T_\nu\rangle = 5.3$ MeV, derived from the results of Woosley et al [10]. In addition, $N_{\rm SN}$ is assumed to follow the metal enrichment rate, which is insensitive to the IMF.

Fig. 2.7 shows the conservative predicted flux in this model. The event rates associated with the DSNB detection are also described. In the main model provided by Kaplinghat, neutrino oscillations are not included, but their contribution is discussed as a mechanism that can maximize the DSNB flux. Because muon- and tau- type neutrinos do not undergo charged-current interactions in matter, they decouple from deeper, higher-temperature regions than electron-type neutrinos. Neutrino oscillations can therefore shift the observed $\bar{\nu}_e$

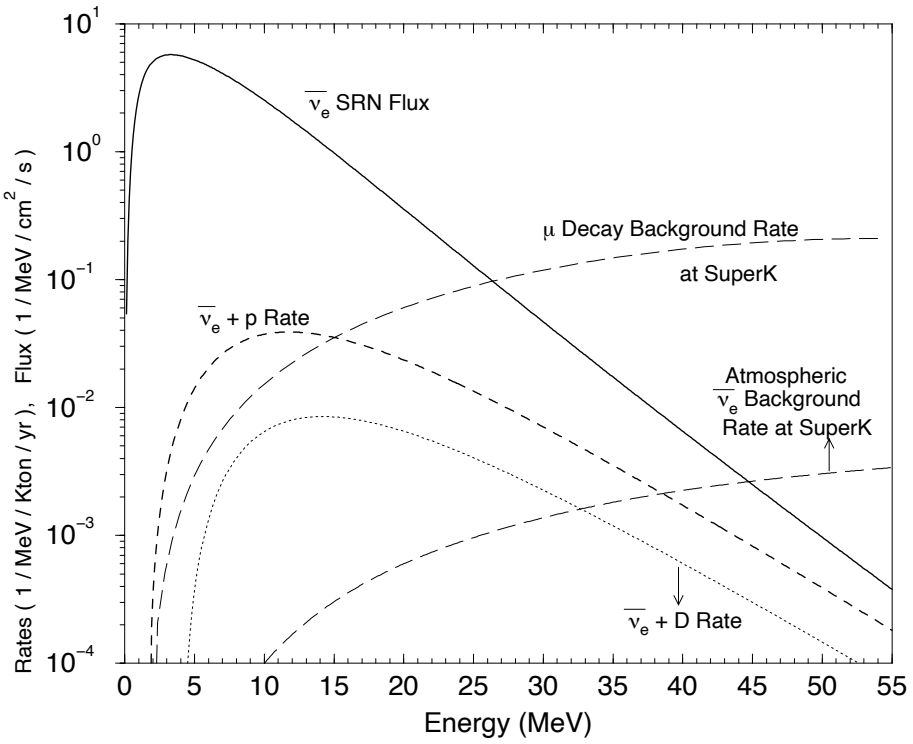

Figure 2.7: The predicted supernova relic neutrino flux in Kaplinghat and relevant event rates for its detection [7]. The $\bar{\nu}_e p$ rate is for detection at Super-Kamiokande, while the $\bar{\nu}_e D$ rate is for detection at SNO. The horizontal axis represents $\bar{\nu}_e$ energy except for the μ decay rate which corresponds to the energy of decay electron.

energy spectrum toward higher energies, increasing the number of events that fall within the observable energy window of the detector.

Horiuchi Model [5]

This model is based on the observations of the cosmic star formation history (CSFH): UV [11, 12, 13, 14], far-infrared (FIR) [15], and high redshift[1][16] measurements in HB06 data set [17], and also Lyman break galaxies (LBG) [18] and Hα emission [19] measurements in other data set. The observed data of the SFR density are analytically fitted by a continuous broken power law,

$$\dot{\rho}_*(z) = \dot{\rho}_0 \left[(1+z)^{\alpha\eta} + \left(\frac{1+z}{B}\right)^{\beta\eta} + \left(\frac{1+z}{C}\right)^{\gamma\eta} \right]^{1/\eta} \tag{2.17}$$

where $\dot{\rho}_0$ is the normalization, η is a transition smoothing parameter, α, β, γ are the slopes of the low. The constants B and C are defined as

$$B = (1+z_1)^{1-\alpha/\beta} \tag{2.18}$$

$$C = (1+z_1)^{(\beta-\alpha)/\gamma}(1+z_2)^{1-\beta/\gamma} \tag{2.19}$$

where z_1 and z_2 are the redshift breaks. The parameters used in this fit are given in Tab. 2.1. Fig. 2.8 shows the SFR density band obtained from the fit taking into account the scatter

[1] measured from the Hubble ultra deep field (UDF)

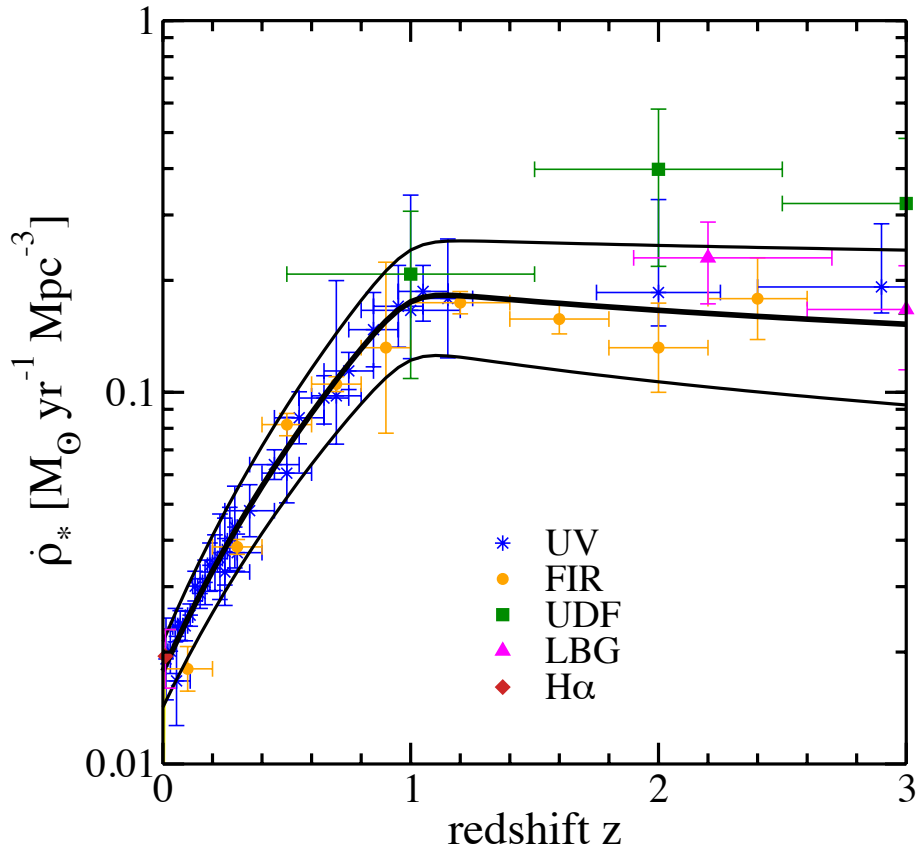

Figure 2.8: Redshift evolution of the comoving SFR density [5]. Colored points are given by HB06 [17], LBG [18], and Hα [19] data set scaled by a Salpeter IMF [20]. The thick solid curve represents fiducial CSFH, and thin solid curves show upper and lower bounds of uncertainty.

of the observed data. In this context, the supernova rate in this model, referred to as the CCSN rate history, is derived from the CSFH and is expressed as

$$R_{\rm SN} = \dot{\rho}_*(z) \frac{\int_8^{50} dm\, \phi_{\rm IMF}(m)}{\int_{0.1}^{100} dm\, m\phi_{\rm IMF}(m)}. \tag{2.20}$$

$R_{\rm SN}$ is largely insensitive to the choice of IMF, since the effect of the IMF is nearly canceled out between $\dot{\rho}_*(z)$ and the integrals in Eq. 2.20.

Table 2.1: Fit parameters of the CSFH data [5]

Fit parameters	$\dot{\rho}_0$	α	β	γ	z_1	z_2
Upper	0.0213	3.6	-0.1	-2.5	1	4
Fiducial	0.0178	3.4	-0.3	-3.5	1	4
Lower	0.0142	3.2	-0.5	-4.5	1	4

The $\bar{\nu}_e$ spectrum term in Eq. 2.9 is assumed to follow the Fermi-Dirac distribution under the zero chemical potential approximation,

$$\frac{dN_{\bar{\nu}_e}}{dE'_{\bar{\nu}_e}}(E'_{\bar{\nu}_e}) = \frac{E_\nu^{\rm tot}}{6} \frac{120}{7\pi^4} \frac{E'^2_{\bar{\nu}_e}}{T^4_{\bar{\nu}_e}} (e^{E'_{\bar{\nu}_e}/T_{\bar{\nu}_e}} + 1)^{-1} \tag{2.21}$$

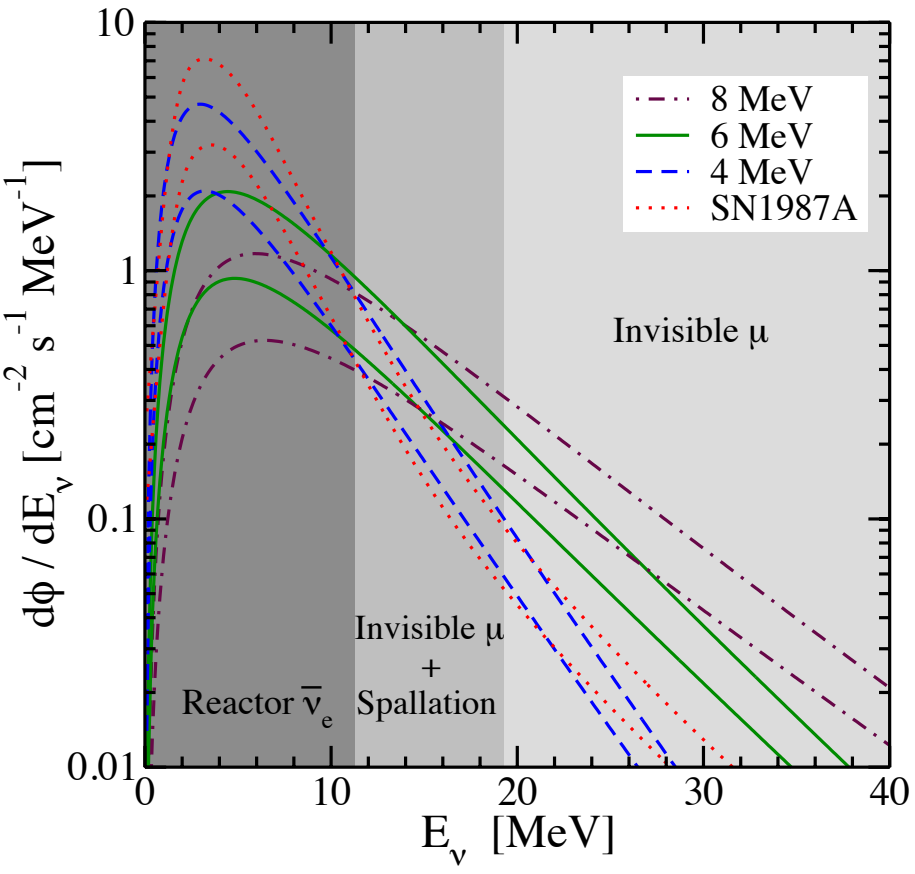

Figure 2.9: DSNB flux spectrum of Horiuchi model [5]. The predicted fluxes at different effective temperatures, along with the reconstructed flux from the SN 1987A data, are shown. For each spectrum, two curves represent the lower and upper bounds of the uncertainties arising from the astrophysical inputs. The shading highlights the dominant background sources in each energy region.

where $E_\nu^{\rm tot}$ represents the total energy in all flavors of neutrinos and $T_{\bar{\nu}_e}$ represents the effective $\bar{\nu}_e$ temperature outside the star after neutrino mixing. The amount of $E_\nu^{\rm tot}$ is determined by the binding energy of the final remnant, $E_{\rm bind}$, as follows:

$$E_\nu^{\rm tot} \simeq E_{\rm bind} = 3 \times 10^{53} \left(\frac{M_{\rm NS}}{1.4\, M_\odot} \right)^2 \left(\frac{R_{\rm NS}}{10\,{\rm km}} \right)^{-1} {\rm erg} \tag{2.22}$$

where $M_{\rm NS}$ and $R_{\rm NS}$ are the neutron star mass and radius.

Fig. 2.9 shows the predicted DSNB flux at various $T_{\bar{\nu}_e}$. These three values of $T_{\bar{\nu}_e}$ are intended to reflect the spread arising from the different initial temperatures of each flavor by various models and from the effects of neutrino mixing. The neutrino spectrum, directly reconstructed from the SN 1987A data [21], is also displayed. In this thesis, $T_{\bar{\nu}_e} = 6\,{\rm MeV}$ case is adopted.

Nakazato Model [6]

This model constructs the DSNB spectra by incorporating cosmic matallicity evolution derived from galaxy evolution models. Since the formulation of the DSNB involves neutrino emissions from various types of progenitors, these progenitors are assumed to be characterized by their initial mass, M, and metallicity, Z. As a variation of Eq. 2.9, this model

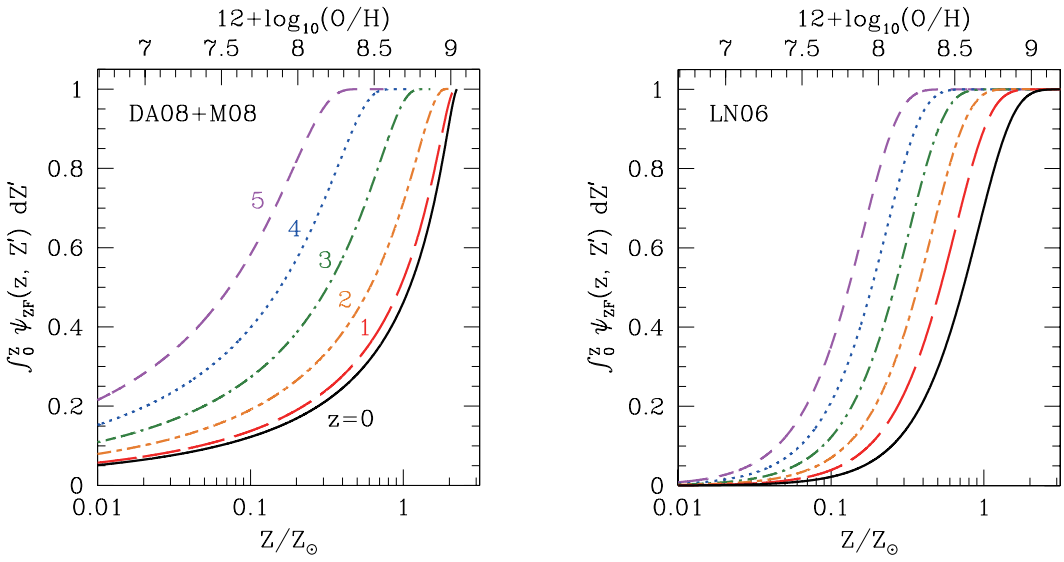

Figure 2.10: Normalized cumulative metallicity distribution function [6]. The left panel shows the model from DA08+M08, and the right panel shows the model from LN06. Both figures show results for various redshifts. The function in these plots indicates the fraction of progenitors with metallicities below Z.

employs the following equation:

$$\frac{dF(E_\nu)}{dE_\nu} = c\int_0^{z_{\max}} \frac{dz}{H_0\sqrt{\Omega_m(1+z)^3+\Omega_\Lambda}} \times \left[R_{\rm SN}(z)\int_0^{Z_{\max}} \psi_{\rm ZF}(z,Z) \times \left[\int_{M_{\min}}^{M_{\max}} \psi_{\rm IMF}(M)\frac{dN(M,Z,E'_\nu)}{dE'_\nu}dM\right]dZ\right], \tag{2.23}$$

where $\psi_{\rm ZF}$ and $\psi_{\rm IMF}$ represent the metallicity distribution function and initial mass function of progenitors normalized as

$$\int_{M_{\min}}^{M_{\max}} \psi_{\rm IMF}(M)dM = \int_0^{Z_{\max}} \psi_{\rm ZF}(z,Z)dZ = 1. \tag{2.24}$$

The supernova neutrino spectrum is adopted from [3], where neutrino oscillations are taken into account. As a model for the metallicity evolution, the work of Drory and Alvarez [22] is combined with that of Maiolino et al [23] (DA08+M08). This model is compared with the model derived from the result of Langer and Norman [24] (LN06), as shown in Fig. 2.10. In this figure, the oxygen abundance is related to the metallicity according to

$$\log_{10}\left(\frac{Z}{Z_\odot}\right) = 12 + \log_{10}\left(\frac{\rm O}{\rm H}\right) - 8.69, \tag{2.25}$$

where the solar metallicity ($Z_\odot = 0.02$) is assumed to correspond to an oxygen abundance of $12+\log_{10}({\rm O/H}) = 8.69$. Stars release synthesized elements through stellar winds or explosions, leading to an increase in metallicity over cosmic time. Consequently, the fraction of high-metallicity stars contributing to the DSNB spectrum becomes larger at lower redshifts.

The differential fluxes of DSNB for the maximum, reference, and minimum cases with the metallicity evolution model of DA08+M08 are shown in Fig. 2.11. The upper and lower bounds account for uncertainties in the SFR, the shock wave revival time in supernova explosions, and the equation of state for black hole formation. The lower panels of Fig. 2.11 present the expected event rate spectra in Super-Kamiokande over 1 yr. This thesis adopts

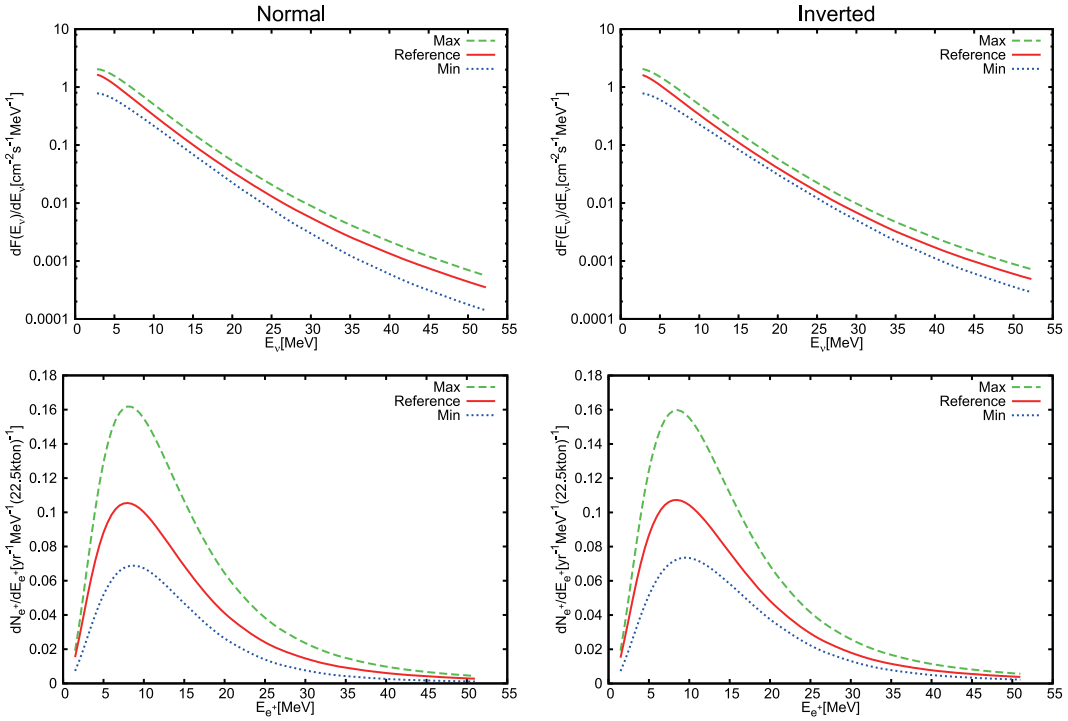

Figure 2.11: Differential fluxes of DSNB in Nakazato model and expected event rate spectra in Super-Kamiokande over 1 yr [6]. The left panels show the normal mass hierarchy, while the right panels show the inverted mass hierarchy. Each panel includes three curves representing the maximum (green dashed), reference (red solid), and minimum (blue dotted) DSNB flux and event rates.

the maximum case in the inverted mass hierarchy for the maximum event scenario and the minimum case in the normal mass hierarchy for the minimum event scenario.

Ashida model [8]

This model accounts for galactic chemical evolution by incorporating variable initial mass functions that depend on the type of galaxy. Additionally, it includes the contribution of failed supernovae, which form black holes, to the neutrino spectrum associated with each progenitor.

In Eq. 2.11, let k_{CCSN} denote the scaling factor between the supernova rate, R_{SN}, and the cosmic SFR, R_{SF}. Since R_{SF} is a composite of the SFRs contributed by various types of galaxies, k_{CCSN} varies depending on the value of z. Therefore, in this model, galaxies are classified into five categories: spheroids (E/S0) and four types of spiral galaxies (Sab, Sbc, Scd, and Sdm). Thus k_{CCSN} is defined as the weighted average of contributions from these galaxy types:

$$k_{\mathrm{CCSN}}(z) = \sum_{j=1}^{5} k_{\mathrm{CCSN},j} \frac{w_j \psi_j(z)}{\sum_{j=1}^{5} w_j \psi_j(z)}, \tag{2.26}$$

where $k_{\mathrm{CCSN},j}$ represents the scaling factor for galaxy type j. The weight, w_j is calculated based on the relative proportion and the mass-to-luminosity ratio [25] and the SFR, ψ_j is adopted from the works by Hopkins & Beacom [17] and Madau & Dickinson [26]. Considering the different types of IMFs, $k_{\mathrm{CCSN},j} = 0.006\, M_{\odot}^{-1}$ is derived for the late-type galaxies (Sbc, Scd, and Sdm), and $k_{\mathrm{CCSN},j} = 0.018\, M_{\odot}^{-1}$ is derived for early-type galaxies (E/S0 and Sab). In the same way, the black hole formation rate, R_{BH}, is deduced by shifting

the mass range of progenitor starts from 8–18 $M_\odot$, corresponding to CCSNe, to 18–100 $M_\odot$, corresponding to failed SNe.

The neutrino spectrum emitted from CCSNe, $dN_{\rm CCSN}/dE'_\nu$, depends on the properties of the remnant object, namely the neutron star (NS). In this context, the total energy of the emitted neutrinos is determined by the mass of the NS. Given that the mass distribution of NSs exhibits a central peak around 1.35 $M_\odot$, $dN_{\rm CCSN}/dE'_\nu$ is modeled by Ashida & Nakazato [27] under the assumption that a NS with a mass of 1.35 $M_\odot$ is formed. In the case of a failed SN that forms a black hole, the neutrino spectrum, $dN_{\rm BH}/dE'_\nu$ is also modeled by Ashida & Nakazato [27]. For both $dN_{\rm CCSN}/dE'_\nu$ and $dN_{\rm BH}/dE'_\nu$, matter-induced neutrino oscillations are taken into account. Neutrinos emitted by failed SNe have higher energies than CCSNe because mass accretion continues until black hole formation, resulting in greater heating of the collapsed core. Then the DSNB flux is described as

$$\begin{aligned}\frac{d\Phi(E_\nu)}{dE_\nu} = c\int_0^{z_{\rm max}} &\frac{dz}{H_0\sqrt{\Omega_m(1+z)^3+\Omega_\Lambda}} \\ &\times\left[R_{\rm CCSN}(z)\frac{dN_{\rm CCSN}(E'_\nu)}{dE'_\nu} + R_{\rm BH}(z)\frac{dN_{\rm BH}(E'_\nu)}{dE'_\nu}\right]\end{aligned} \tag{2.27}$$

where c is the speed of light and the cosmological constants are $\Omega_m = 0.3089$, $\Omega_\Lambda = 0.6911$, and $H_0 = 67.74\,{\rm km\,sec^{-1}\,Mpc^{-1}}$.

Fig. 2.12 shows the predicted DSNB flux in this model along with its associated uncertainties. The shaded band represents variations due to different SFRs and nuclear equations of state. In the neutrino energy region below 30 MeV, the flux predicted by this model lies within the range of variations arising from different model choices. At higher energies, the model predicts an enhanced flux due to the significant contribution of black hole formation. Conversely, the low energy region below 10 MeV also exhibits a higher flux. This is attributed to the larger contribution of early-type galaxies, which results in a higher CCSN rate compared to other models, thereby increasing the number of neutrinos originating from $z > 1$.

2.2 Solar

2.2.1 Solar Neutrino

The term *solar neutrino* refers to electron neutrinos emitted from nuclear fusion reactions occurring in the core of the Sun. There are two primary processes responsible for the production of solar neutrinos: the pp chain and the CNO cycle (Fig. 2.13). In both cases, when considering the initial and final states of the sequential reactions, the overall process can be expressed as follows:

$$4p \rightarrow \alpha + 2e^+ + 2\nu_e + 26.7\,{\rm MeV}. \tag{2.28}$$

Fig. 2.14 shows the spectrum of solar neutrino fluxes. In the neutrino analysis conducted with the KamLAND detector, the primary source of solar neutrinos is the ^{8}B reaction, expressed as

$$^8{\rm B} \rightarrow {}^8{\rm B}^* + e^+ + \nu_e. \tag{2.29}$$

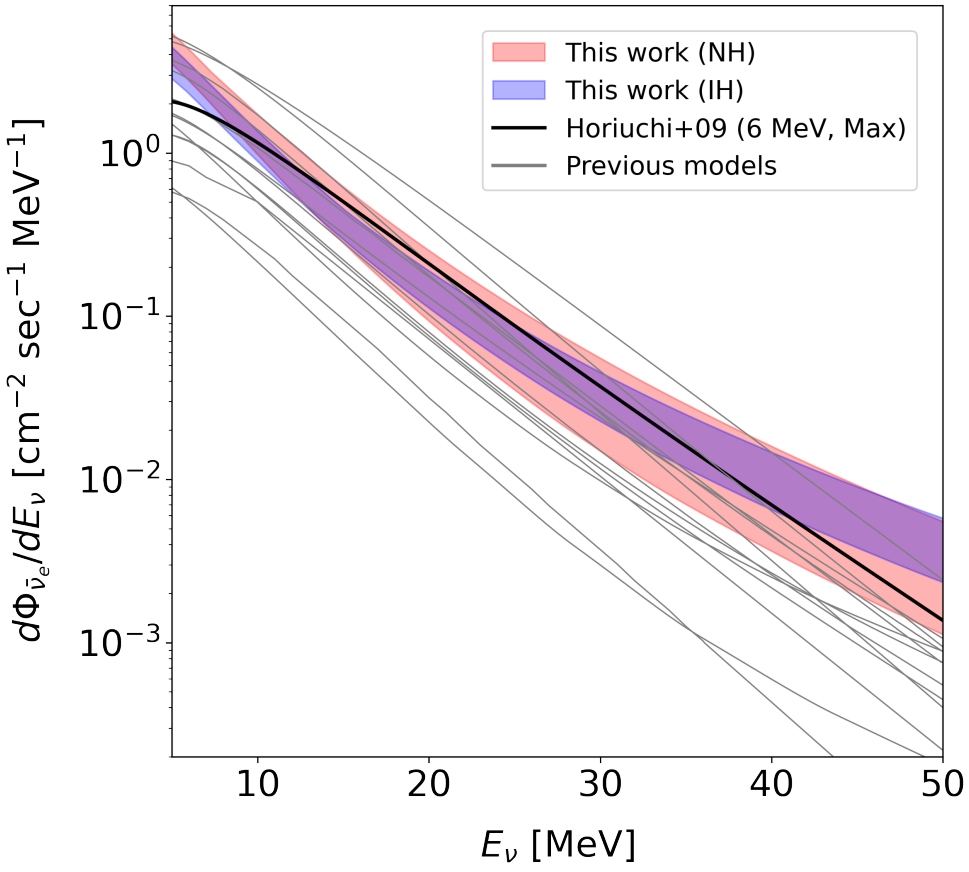

Figure 2.12: Prediction bands of the DSNB $\bar{\nu}_e$ flux in Ashida model [8]. The black curves represent previous DSNB predictions cited in the Super-Kamiokande paper [28], where the highlighted Horiuchi model [5] is used as the reference. The red band corresponds to the prediction assuming the normal mass hierarchy, while the blue band represents the prediction assuming the inverted mass hierarchy. Both bands include uncertainties arising from variations in the SFR and the nuclear equation of state.

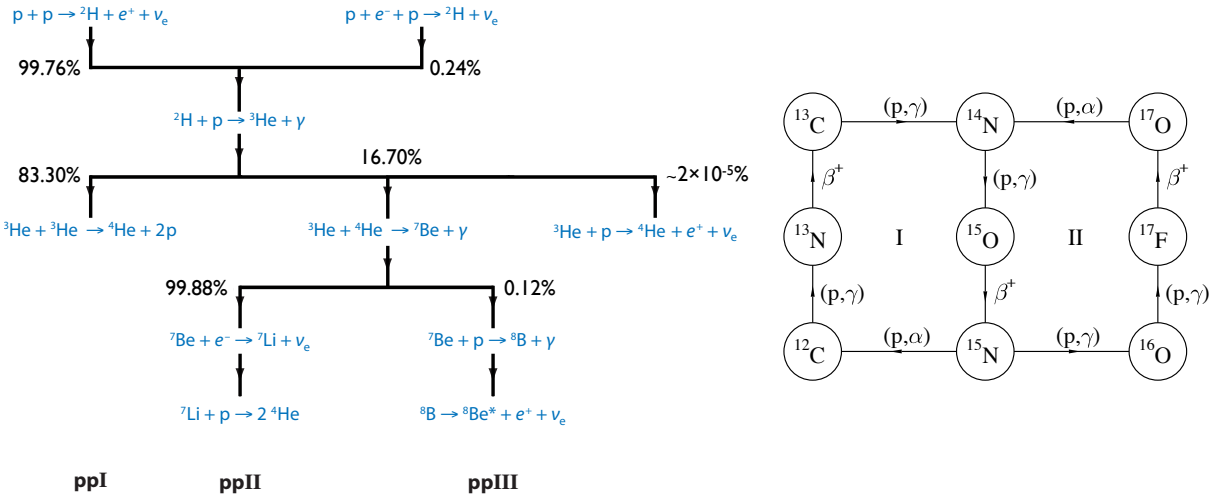

Figure 2.13: Schematic views of pp chain (left) and CNO cycle (right) [29]. The branching percentages are shown in the left figure associated with a unique neutrino. The CN cycle, marked I in the right figure, produces ∼1% of solar energy and has a significant influence on the solar neutrino flux.

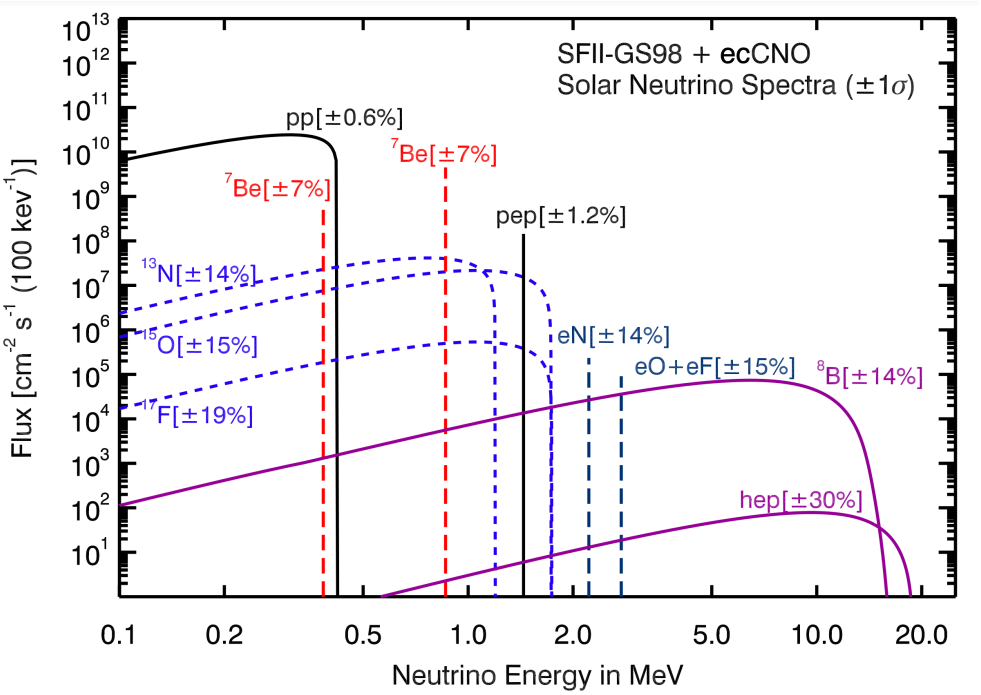

Figure 2.14: Spectrum of solar neutrino fluxes [30].

2.2.2 Solar Neutrino Conversion

If neutrinos have a non-zero mass, their magnetic moment can be expressed within the framework of the standard model as [31]

$$\mu_\nu = \frac{3eG_F m_\nu}{8\pi^2\sqrt{2}} = 3\times 10^{-19}\mu_B \left(\frac{m_\nu}{1\,\mathrm{eV}}\right), \tag{2.30}$$

where m_ν is the neutrino mass, G_F is the Fermi coupling constant, and $\mu_B = e/2m_e$ is the Bohr magneton. If the magnetic moment is measured to exceed the value predicted by Eq. 2.30, it would indicate the existence of new physics, potentially involving interactions that break chirality conservation beyond the standard model.

The interaction between the neutrino magnetic moment and the solar magnetic field induces a phenomenon known as neutrino spin-flavor precession. This precession is resonantly amplified in matter, a process referred to as Resonant Spin-Flavor Precession (RSFP). When considering RSFP in a neutrino of a single flavor, which represents a simplified scenario, the propagation function in the solar magnetic field, $B_\odot$, can be expressed as follows:

$$i\frac{d}{dt}\begin{pmatrix}\nu_L\\ \nu_R\end{pmatrix} = \begin{pmatrix}0 & \mu B_\odot\\ \mu B_\odot & 0\end{pmatrix}\begin{pmatrix}\nu_L\\ \nu_R\end{pmatrix}, \tag{2.31}$$

where μ represents the neutrino magnetic moment. Since RSFP can convert left-handed ν_e into right-handed $\bar{\nu}_\mu$ or $\bar{\nu}_\tau$, it was once considered a potential explanation for the so-called *solar neutrino problem*. However, this scenario requires a large neutrino magnetic moment of $10^{-10}\mu_B$, which has already been ruled out by experimental results [32].

To address the limitations of the simple RSFP scenario, a combined model incorporating both RSFP and the Mikheyev-Smirnov-Wolfenstein (MSW) effect has been proposed:

$$\nu_e \xrightarrow{\text{MSW}} \nu_x \xrightarrow{\text{RSFP}} \bar{\nu}_e \tag{2.32}$$

$$\nu_e \xrightarrow{\text{RSFP}} \bar{\nu}_x \xrightarrow{\text{MSW}} \bar{\nu}_e. \tag{2.33}$$

By combining neutrino oscillation in matter, represented by

$$i\frac{d}{dt}\begin{pmatrix}\nu_e\\ \nu_x\end{pmatrix} = \begin{pmatrix}\frac{\Delta m^2}{2E}\sin^2\theta + V_e & \frac{\Delta m^2}{4E}\sin 2\theta\\ \frac{\Delta m^2}{4E}\sin 2\theta & \frac{\Delta m^2}{2E}\cos^2\theta + V_\mu\end{pmatrix}\begin{pmatrix}\nu_e\\ \nu_x\end{pmatrix}, \tag{2.34}$$

with Eq. 2.31, the propagation of a Dirac neutrino can be described as [33]

$$i\frac{d}{dt}\begin{pmatrix}\nu_{eL}\\ \nu_{xL}\\ \nu_{eR}\\ \nu_{xR}\end{pmatrix} = \begin{pmatrix}\frac{\Delta m^2}{2E}\sin^2\theta + V_e & \frac{\Delta m^2}{4E}\sin 2\theta & \mu^*_{ee}B & \mu^*_{ex}B\\ \frac{\Delta m^2}{4E}\sin 2\theta & \frac{\Delta m^2}{2E}\cos^2\theta + V_\mu & \mu^*_{xe}B & \mu^*_{xx}B\\ \mu_{ee}B & \mu_{ex}B & \frac{\Delta m^2}{2E}\sin^2\theta & \frac{\Delta m^2}{4E}\sin 2\theta\\ \mu_{xe}B & \mu_{xx}B & \frac{\Delta m^2}{4E}\sin 2\theta & \frac{\Delta m^2}{2E}\cos^2\theta\end{pmatrix}\begin{pmatrix}\nu_{eL}\\ \nu_{xL}\\ \nu_{eR}\\ \nu_{xR}\end{pmatrix}. \tag{2.35}$$

In Eq. 2.35, x represents the neutrino flavors of μ and τ. The potentials in matter, V_e and V_x, are given by

$$V_e = \frac{G_F}{\sqrt{2}}(2N_e - N_n) \tag{2.36}$$

$$V_\mu = -\frac{G_F}{\sqrt{2}}N_n, \tag{2.37}$$

where N_e and N_x denote the number densities of electrons and neutrons in matter, respectively. In the case of Majorana neutrinos, they cannot have diagonal magnetic moments, then their propagation is described as

$$i\frac{d}{dt}\begin{pmatrix}\nu_e\\ \nu_x\\ \bar{\nu}_e\\ \bar{\nu}_x\end{pmatrix} = \begin{pmatrix}\frac{\Delta m^2}{2E}\sin^2\theta + V_e & \frac{\Delta m^2}{4E}\sin 2\theta & 0 & \mu^*_{ex}B\\ \frac{\Delta m^2}{4E}\sin 2\theta & \frac{\Delta m^2}{2E}\cos^2\theta + V_\mu & \mu^*_{xe}B & 0\\ 0 & \mu_{ex}B & \frac{\Delta m^2}{2E}\sin^2\theta - V_e & \frac{\Delta m^2}{4E}\sin 2\theta\\ \mu_{xe}B & 0 & \frac{\Delta m^2}{4E}\sin 2\theta & \frac{\Delta m^2}{2E}\cos^2\theta - V_\mu\end{pmatrix}\begin{pmatrix}\nu_e\\ \nu_x\\ \bar{\nu}_e\\ \bar{\nu}_x\end{pmatrix}. \tag{2.38}$$

Therefore, the conversion probability of $\nu_e \to \bar{\nu}_e$ in the RSFP+MSW scenario is described as [34]

$$P(\nu_{eL} \to \bar{\nu}_{eR}) \simeq 1.8 \times 10^{-10}\sin^2 2\theta_{12}\left[\frac{\mu}{10^{-12}\mu_B}\frac{B_T(0.05R_\odot)}{10\,\text{kG}}\right]^2, \tag{2.39}$$

where B_T represents the transverse solar magnetic field in the region of neutrino production, $R_\odot$ represents the solar radius, and μ is the neutrino magnetic moment. The observation results can be expressed in terms of the conversion probability, where a large value indicates a significant neutrino magnetic moment, implying physics beyond the standard model.

2.3 Light Dark Matter Annihilation

Light particles with masses on the MeV scale are considered potential candidates for dark matter (DM). In the mass range below 100 MeV, their annihilation can only produce standard model particles, namely e^-e^+ pairs, photons, and $\nu\bar{\nu}$ pairs. However, except for $\nu\bar{\nu}$ pairs, the annihilation channels into standard model particles are strongly constrained by

observational results, as the observed cross section is significantly smaller than that required to account for the present dark matter abundance in the Universe [35]. In contrast, the interaction between light DM and neutrinos remains poorly constrained and may even be stronger than weak interactions. Therefore, analyzing the annihilation cross section $\chi\chi \to \nu\bar{\nu}$ provides a test of the abundance of MeV-scale DM.

The detection of neutrinos originating from the annihilation of light DM has been investigated by Palomares-Ruiz and Pascoli [36]. Under the assumption that the branching ratio into neutrinos dominates in light DM self-annihilation, a limit on the neutrino flux can provide a conservative upper bound on the total annihilation cross section. For a spherically symmetric matter density with an isotropic velocity dispersion, the DM distribution in the galaxy can be described as

$$\rho(r) = \rho_{\rm sc} \left(\frac{R_{\rm sc}}{r}\right)^{\gamma} \left[\frac{1+(R_{\rm sc}/r_{\rm s})^{\alpha}}{1+(r/r_{\rm s})^{\alpha}}\right]^{(\beta-\gamma)/\alpha}, \tag{2.40}$$

where $R_{\rm sc}$ =8.5 kpc is the solar radius circle, $\rho_{\rm sc}$ is the DM density at $R_{\rm sc}$, $r_{\rm s}$ is the scale radius, and α, β, γ are parameters that define the DM distribution. Since neutrinos produced by DM annihilation in the halo carry little directional information when detected via interactions with nucleon, the focus is on the flux arriving from all directions. Therefore, the DM flux is averaged over the entire galaxy, and the mean number flux is obtained by integrating the square of the DM density (given in Eq. 2.40) as

$$\mathcal{J}_{\rm avg} = \frac{1}{2R_{\rm sc}\rho_0^2} \int_{-1}^{1} \int_{0}^{l_{\rm max}} \rho^2(r) dl d(\cos\psi), \tag{2.41}$$

where $\rho_0 = 0.3\,{\rm GeV\,cm^{-3}}$ is a normalizing DM density. The radius value r and the upper limit of integration $l_{\rm max}$ are defined as follows:

$$r = \sqrt{R_{\rm sc}^2 - 2lR_{\rm sc}\cos\psi + l^2} \tag{2.42}$$

$$l_{\rm max} = \sqrt{(R_{\rm halo}^2 - R_{\rm sc}^2 \sin^2\psi)} + R_{\rm sc}\cos\psi, \tag{2.43}$$

where $R_{\rm halo}$ represents the size of the halo. Consequently, the differential neutrino and antineutrino flux from each flavor produced by light DM annihilation is given by

$$\frac{d\phi}{dE_\nu} = \frac{\langle\sigma_A v\rangle}{2} \mathcal{J}_{\rm avg} \frac{R_{\rm sc}\rho_0^2}{m_\chi^2} \frac{1}{3} \delta(E_\nu - m_\chi), \tag{2.44}$$

where m_χ is the DM mass and $\langle\sigma_A v\rangle$ is the averaged cross section of light DM annihilation. The factor of 1/2 reflects the property of dark matter as its own antiparticle, while the factor of 1/3 arises from the assumption that the annihilation branching ratio is identical for all three neutrino flavors. To incorporate the uncertainties associated with the dark matter profiles parameterized by $\rho_{\rm sc}$, $r_{\rm sc}$, α, β, and γ, Palomares-Ruiz and Pascoli [36] also analyzed these paramter's impact on the averaged number flux, $\mathcal{J}_{\rm avg}$, across three different models. Consequently, in the most conservative scenario, $\mathcal{J}_{\rm avg}$ is found to be 1.3, whereas in the most favorable case, it reaches 104.

2.4 Primordial Black Hole

2.4.1 Formation of Primordial Black Hole and Hawking Radiation

Primordial Black Holes (PBHs) are one of the proposed candidates for DM, hypothesized to form from primordial energy density fluctuations in the early universe. Depending on their

formation time, PBHs can span a wide range of masses and provide an explanation for the DM abundance without requiring physics beyond the Standard Model. In particular, PBHs with masses in the range of 10^{15} to 10^{17} g are expected to emit particles and eventually evaporate. As a result, the observed spectra of these particles set constraints on the PBH contribution to the total DM energy, f_{PBH}, as

$$f_{\mathrm{PBH}} = \frac{\Omega_{\mathrm{PBH}}}{\Omega_{\mathrm{DM}}}, \tag{2.45}$$

where Ω_{PBH} is the energy density of PBH and Ω_{DM} is the energy density of DM.

The mechanism behind such particle emission is understood as a quantum process occurring near the event horizon of a black hole. Due to vacuum fluctuations, particle-antiparticle pairs can be spontaneously generated; one of the pair may escape the horizon while the other is absorbed by the black hole. This results in the emission of radiation analogous to blackbody radiation, a process known as Hawking radiation. In this framework, the black hole behaves like a blackbody with a temperature T_{BH} inversely proportional to its mass M_{BH}, given by:

$$T_{\mathrm{BH}} = \frac{\hbar c^3}{8\pi G M_{\mathrm{BH}} k_B}, \tag{2.46}$$

where $\hbar$ is the Plank constant, c is the speed of light, G is the gravitational constant, and k_B is the Boltzmann constant. The luminosity of particle i emitted through Hawking radiation is expressed as:

$$\frac{d^2 N_i}{dE_i dt} = \frac{g_i}{2\pi} \frac{\Gamma_i(E, M_{\mathrm{BH}})}{e^{E/T_{\mathrm{BH}}} \pm 1}. \tag{2.47}$$

In this expression, Γ is the greybody factor, which accounts for deviations from perfect blackbody radiation (i.e., $\Gamma = 1$ in the ideal case) and g_i denotes the degrees of freedom associated with particle i, which vary depending on the particle species. As the black hole emits particles, it loses energy and gradually evaporates. Notably, lighter black holes have higher temperatures and therefore evaporate more rapidly.

Among the primary components of particles directly emitted via Hawking radiation, quarks and gluons hadronize through strong interactions. The resulting hadrons and leptons may decay into additional particles, which are referred to as the secondary components. The total luminosity of particle j from a PBH, incorporating both primary and secondary contributions, is given by:

$$\frac{d^2 N_j}{dE_j dt} = \int_0^\infty dM \frac{dn}{dM} \int_0^\infty dE' \sum_i \frac{d^2 N_i}{dE' dt} \frac{dN_j^i}{dE_j}. \tag{2.48}$$

Here, $d^2 N_i / dE' dt$ corresponds to the luminosity of the primary particle i as defined in Eq. 2.47, and dN_j^i/dE_j represents the branching ratio for the decay of particle i into particle j. The factor dn/dM describes the PBH mass distribution, which is assumed to be a monochromatic mass distribution ($dn/dM = \delta(M - M_{\mathrm{BH}})$). The emission spectra of both primary and secondary particles from PBHs are computed using BlackHawk [37, 38], and the hadronization and decay process for secondary particles are simulated using PYTHIA [39]. As an illustrative example, Fig. 2.15 shows the emission processes of the primary and secondary components of neutrinos from a PBH due to Hawking radiation.

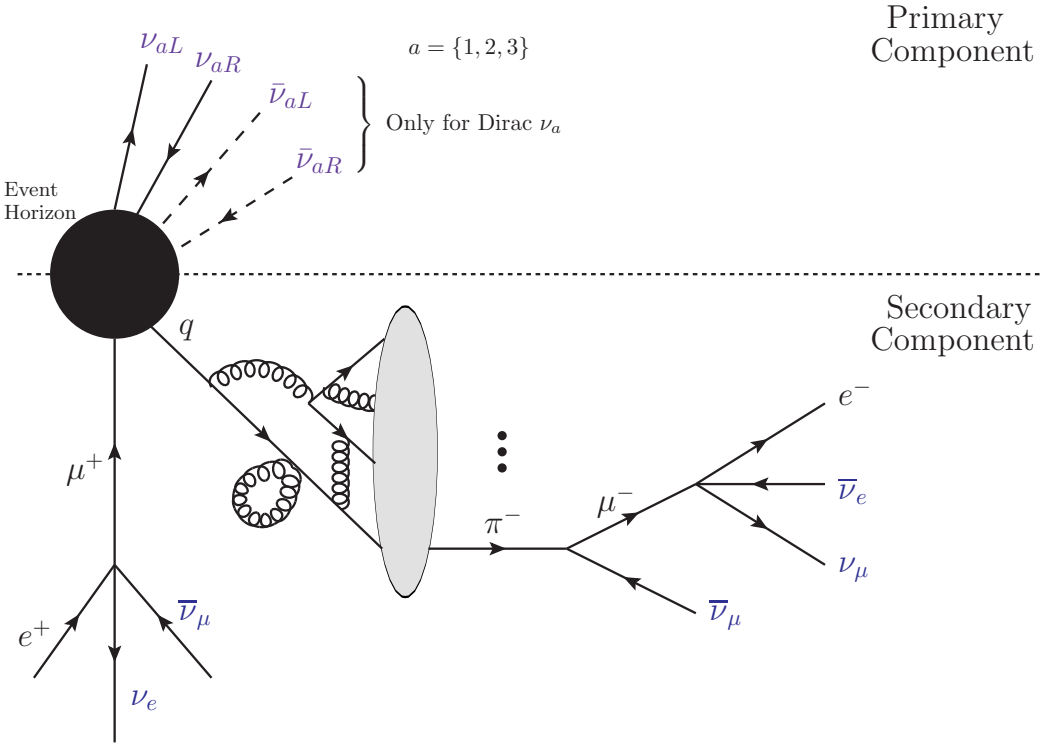

Figure 2.15: Illustration of the neutrino emission from a PBH [40]. There are two types of emission, primary and secondary component.

2.4.2 Neutrino Flux from Primordial Black Hole

In order to set constraints on the PBH contribution to DM via neutrino observations, we discuss the expected neutrino flux from PBHs. The flux of neutrinos originating from extra-Galactic PBHs is affected by redshift and is given by [41]

$$\Phi_{\rm EG} = \int_{t_{\rm min}}^{\tau_{\rm U}} dt[1+z(t)]\, \frac{f_{\rm PBH}\rho_{\rm DM}}{M_{\rm PBH}} \frac{d^2N}{dE'dt}\bigg|_{E'=[1+z(t)]E}, \tag{2.49}$$

where we assume a homogeneous present-day DM energy density $\rho_{\rm DM}$, and adopt an average value of $\rho_{\rm DM} = 2.35 \times 10^{-30}\,{\rm g\cdot cm^{-3}}$[2]. The cosmic time $\tau_{\rm U}$ corresponds to the current age of the Universe, and $z(t)$ denotes the redshift at time t. At large redshifts, PBHs are less evaporated and hence more massive, resulting in lower temperatures (see Eq. 2.46). Consequently, their neutrino luminosity and the typical energy of emitted neutrinos are relatively low. On the other hand, PBHs at low redshift are more evaporated, and thus emit higher luminosity neutrinos with greater average energies. Given this, contributions from epochs earlier than $t_{\rm min} = 10^{11}\,{\rm s}$ is neglected, where the flux is expected to be negligible.

In contrast, for the Galactic neutrino flux, the effect of redshift is negligible. The Galactic PBH population is assumed to follow the DM distribution within the Milky Way, therefore the Navarro-Frenk-White (NFW) profile [43] is adopted. The corresponding PBH energy density is given by

$$\rho_{\rm NFW} = 0.4 \times \left(\frac{8.5}{r}\right)\left(\frac{1+8.5/20}{1+r/20}\right)^2. \tag{2.50}$$

[2]calculated using $\rho_{\rm DM} = (3H_0^2/(8\pi G)) \times \Omega_{\rm DM}$ where each parameter is adopted from Planck 2018 results [42]

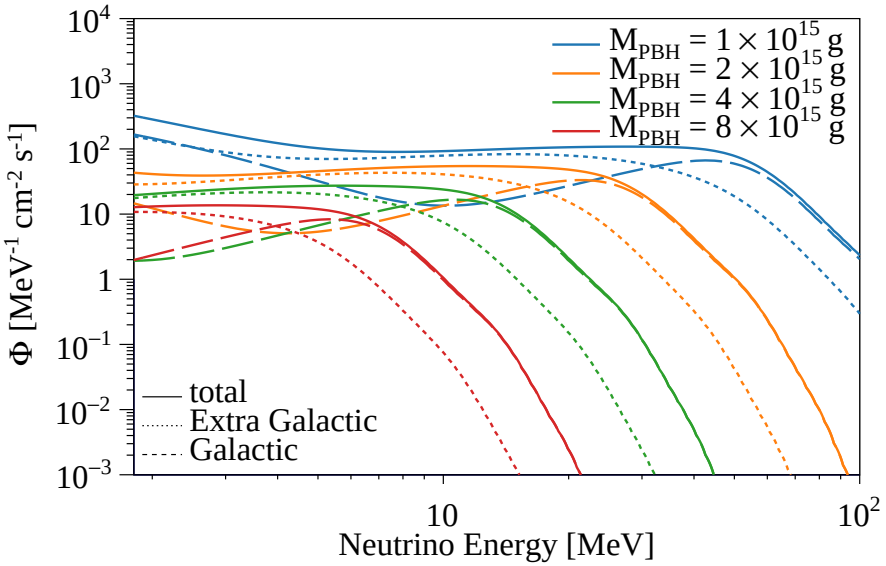

Figure 2.16: Neutrino flux from a PBH. Dashed curves show the Galactic component and dotted curves show the extra Galactic component. Each colors show different PBH masses.

Here, r is the radial distance from the Galactic center, calculated from the solar position $r_\odot = 8.5\,\mathrm{kpc}$ and the line-of-sight coordinate l via

$$r(l,\psi) = \sqrt{r_\odot^2 - 2lr_\odot \cos\psi + l^2}. \tag{2.51}$$

Using the density distribution following MFW profile, the neutrino flux from Galactic PBHs is obtained as [41]

$$\Phi_{\mathrm{Gal}} = \int \frac{d\Omega}{4\pi} \int_0^{l_{\max}} dl \frac{d^2N}{dEdt} \frac{f_{\mathrm{PBH}}\rho_{\mathrm{NFW}}[r(l,\psi)]}{M_{\mathrm{PBH}}}. \tag{2.52}$$

The total Galactic flux is obtained by integrating over the solid angle Ω, which corresponds to a full-sky integration over both the azimuthal and zenith angles. The upper limit of l is determined from the halo radius $r_h = 200\,\mathrm{kpc}$ and solar position $r_\odot$ as

$$l_{\max} = \sqrt{r_h^2 - r_\odot^2 \sin^2\psi} + r_\odot \cos\psi. \tag{2.53}$$

The total neutrino flux from PBHs is obtained by summing the extra-Galactic and Galactic components, and is expressed as

$$\Phi(f_{\mathrm{PBH}}, M_{\mathrm{PBH}}) = \Phi_{\mathrm{EG}} + \Phi_{\mathrm{Gal}} \propto f_{\mathrm{PBH}}. \tag{2.54}$$

Fig. 2.16 shows the neutrino flux from PBHs for each M_{PBH}. The resulting neutrino energy lies in the MeV range, making it suitable for detection by world neutrino detectors.

2.5 Astrophysical Neutrino Search Experiments

2.5.1 Recent Detectors

KamLAND [44, 45]

The Kamioka Liquid Scintillator Anti-Neutrino Detector (KamLAND) is a 1-kiloton liquid scintillator detector located 1000 meters underground in the Kamioka mine. KamLAND detects electron antineutrinos via the inverse beta decay (IBD) reaction, which produces a characteristic time- and space-correlated event pair: a prompt event from the kinetic energy of the emitted positron and its subsequent annihilation gamma rays, followed by a delayed event from the gamma ray emitted upon neutron capture on a proton or carbon nucleus. This detection technique is referred to as the delayed coincidence method.

In the most recent search for astrophysical electron antineutrinos using KamLAND, data collected from March 2002 to July 2020, corresponding to a total exposure of 6.72 kiloton-years, were analyzed. Eighteen candidate events were observed, compared to an expected background of 31.4±9.7 events. A spectral fit over energy and radial distributions was performed to extract the contribution from DSNB, using several flux models (Horiuchi [5], Nakazato [6], and Kaplinghat [7]). The best fit result and 90% upper limit of DSNB signal are shown in Fig. 2.17. In all cases, the best-fit number of DSNB events was zero.

In addition to the DSNB search, a fit was performed under the hypothesis of electron antineutrinos originating from flavor conversion of solar ^{8}B neutrinos. No significant excess was found, and a 90% confidence level upper limit of 3.5×10^{-5} was set on the conversion probability. This result was further interpreted as an upper limit on the neutrino magnetic moment of $4.9 \times 10^{-10}\mu_B$ assuming the transverse solar magnetic field of 10 kG.

KamLAND also placed constraints on the dark matter self-annihilation cross section into neutrinos. For dark matter masses below 15 MeV, the resulting limits are currently the most stringent. Furthermore, model-independent upper limits on the astrophysical electron antineutrino flux in the energy range 8.3–30.8 MeV was derived. Below 13.3 MeV, KamLAND provides the world's most stringent constraint on the $\bar{\nu}_e$ flux, although the limit remains approximately one order of magnitude above the predictions of standard DSNB models.

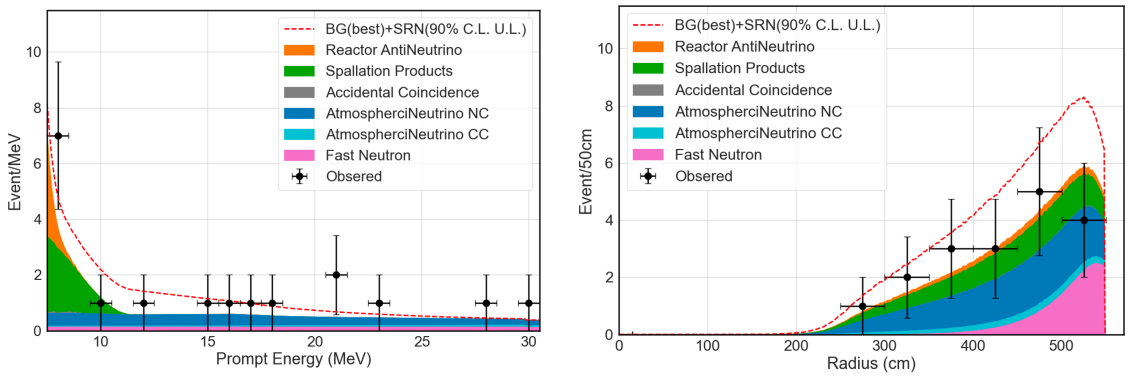

(a) Energy (b) Radius

Figure 2.17: Best fit result and 90% upper limit of DSNB signal of (a) energy spectrum and (b) radial distribution in KamLAND [44]. The black points represents observed data, the red dashed line corresponds to the DSNB upper limit with 90% confidence level assuming Nakazato model [6], and stacked spectra filled by colors are the best fit backgrounds.

Super-Kamiokande / SK-Gd [28, 46]

The Super-Kamiokande (SK) detector is a 50-kiloton water-Cherenkov detector located 1000 m underground in the Kamioka mine. A schematic view of the SK detector is shown in Fig. 2.18. SK began operation in 1996 and completed the pure-water phases SK-I through SK-V in 2020. Thereafter, the SK-Gd program commenced with SK-VI, introducing gadolinium into the water to enhance neutron-capture efficiency; the experiment is currently operating in the SK-VIII period. In SK, astrophysical $\bar{\nu}_e$ are searched for by reconstructing IBD candidates within the 22.5-kiloton fiducial volume using Cherenkov light from the prompt and delayed signals and identifying them via delayed-coincidence selection.

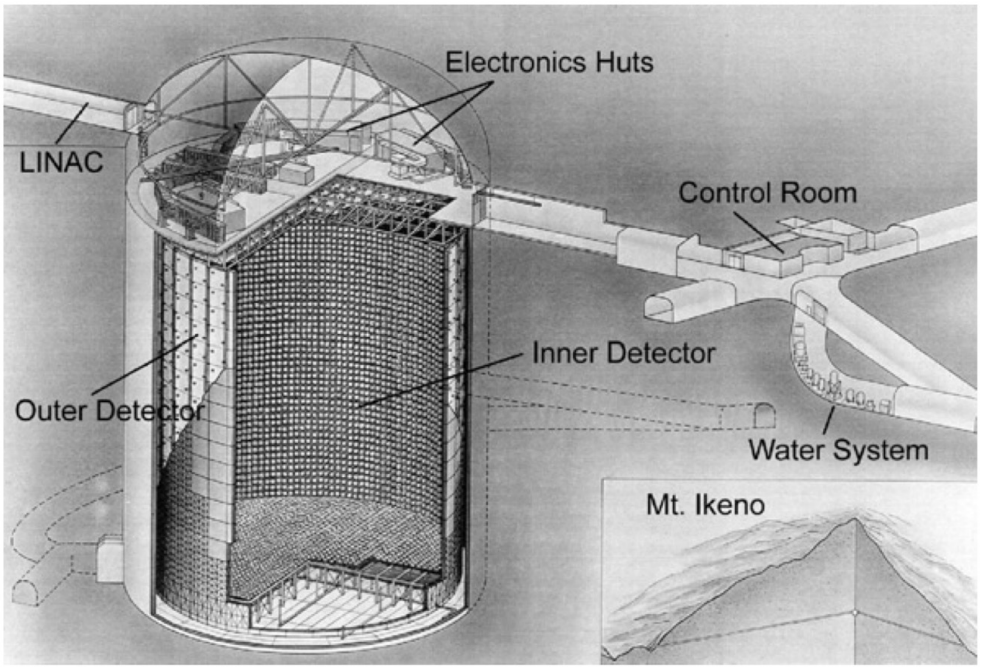

Figure 2.18: Schematic view of the Super-Kamiokande detector [47].

The DSNB search using the SK-I through SK-IV periods is reported in [28]. The total livetime of this search is 5823 days, and neutrino energies $E_\nu \geq 17.3\,\text{MeV}$ are used. A spectral fit reveals an excess at the level of $\sim 1.5\sigma$ across various DSNB models. Fig. 2.19 shows the 90% C.L. upper limits, best-fit values, and expected sensitivities for the DSNB fluxes from the SK-I-IV combined analysis. These results exclude high-flux models such as the Totani +95 model and the most optimistic variants of the Kaplinghat model.

Astrophysical $\bar{\nu}_e$ searches have continued in the Gd-loaded phases starting with SK-VI, and the SK-VI-only results are reported in [46]. That analysis uses a data set with 0.01% gadolinium mass concentration and a livetime of 552.2 days. Although no significant signal excess is observed in the bin-by-bin energy analysis, a model-independent upper limit on the $\bar{\nu}_e$ flux is obtained with a sensitivity comparable to that of SK-IV, which was based on 2970 days of livetime.

Borexino [48, 49]

The Borexino detector is a 278-ton liquid scintillator detector located at the Laboratori Nazionali del Gran Sasso in Italy. Fig. 2.20 shows the schematic view of the Borexino detector. In its search for astrophysical electron antineutrinos, Borexino analyzed data collected between December 2007 and October 2017, corresponding to an effective exposure of 1494 ton-years. Electron antineutrinos were detected via the IBD reaction, and 101

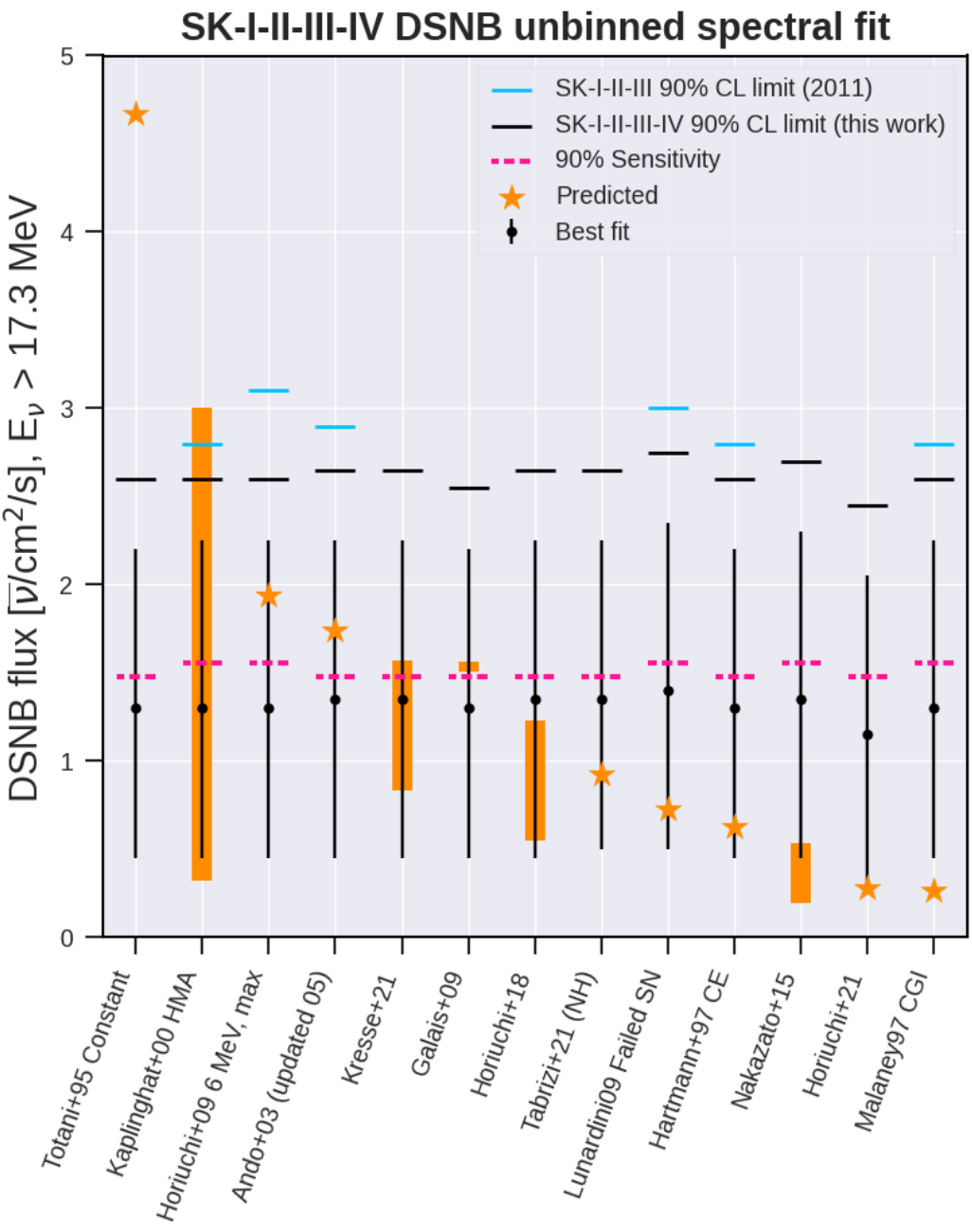

Figure 2.19: The 90% CL upper limits, best-fit values, and expected sensitivities for the DSNB fluxes [28].

candidate events were identified, compared to an expected background of 85.9±4.2 events. The observed energy spectrum with the expected background is shown in Fig. 2.21. An excess observed in the lowest energy bin (1.8–2.8 MeV) is interpreted as a result of the conservative assumption of the minimal geo-neutrino model. Above 2.8 MeV, the number of observed events (62) is consistent with the expected background of 63±2 events.

A search for solar $\bar{\nu}_e$ originating from spin-flavor precession (SFP) of ^{8}B neutrinos yielded an upper limit on the $\nu_e \to \bar{\nu}_e$ conversion probability of 7.2×10^{-5} at 90% C.L. This corresponds to an upper limit on the neutrino magnetic moment in the range 1.1×10^{-8} to $1.1 \times 10^{-12}\,\mu_B$, depending on the assumed strength of the solar magnetic field. In parallel, an independent study based on electron scattering of solar pp and ^{7}Be neutrinos using Borexino Phase-II data (1291.5 days) reported a model-independent upper limit of $\mu_\nu^{\text{eff}} < 2.8 \times 10^{-11}\,\mu_B$ (90% C.L.), derived from distortions in the electron recoil spectrum. These two approaches are complementary, constraining the neutrino magnetic moment through both appearance and scattering channels.

In addition, the data were interpreted using two DSNB flux models, yielding 90% C.L. upper limits on the $\bar{\nu}_e$ flux of $< 112.3\,\text{cm}^{-2}\,\text{s}^{-1}$ (Nakazato [3]) and $< 106.0\,\text{cm}^{-2}\,\text{s}^{-1}$ (Hüdepohl [50]) in the 7.8–16.8 MeV range. Lastly, model-independent upper limits on the $\bar{\nu}_e$ flux were set in 1 MeV-wide bins across the 1.8–16.8 MeV neutrino energy range, with Borexino setting the world's strongest constraints in the sub-8 MeV region.

SNO [52]

The Sudbury Neutrino Observatory (SNO) was a 1-kiloton heavy water Cherenkov detector located in the Creighton mine in Sudbury, Canada. Fig. 2.22 shows a schematic view of the SNO detector. In a search for astrophysical electron antineutrinos, SNO analyzed data taken during its first phase between November 2, 1999 and May 28, 2001, corresponding to a total livetime of 305.9 days. Electron antineutrinos were detected via the charged-current interaction on deuterons, producing a positron and two neutrons. Candidate events were selected based on the time and spatial coincidence of the prompt Cherenkov light from the positron and delayed signals from neutron captures. A total of one two-fold coincidence event was observed in the analysis window. Assuming this single candidate as signal and no background contribution, a model-independent 90% C.L. upper limit on the $\bar{\nu}_e$ flux was derived in 1-MeV energy bins from 4 to 14.8 MeV.

2.5.2 Next-Generation Detectors

JUNO [54]

The Jiangmen Underground Neutrino Observatory (JUNO) is a 20-kton liquid scintillator detector located 700 m underground in Jiangmen, Guangdong, China. It is situated at an equal distance from the Taishan and Yangjiang reactor complexes. The primary goals of JUNO are to determine the neutrino mass hierarchy and to precisely measure oscillation parameters through reactor antineutrino observations. Fig. 2.23 shows a schematic view of the JUNO detector.

Detector construction has been completed in 2025, with data acquisition commencing thereafter. JUNO observes antineutrinos primarily via the IBD channel, identified through delayed coincidence between the prompt positron signal and the delayed neutron capture signal. In addition to the reactor antineutrino observation, the detector is also anticipated to achieve high sensitivity in astrophysical neutrino searches.

In the search for the DSNB at JUNO, the dominant background arises from atmospheric neutrinos, which outnumber the expected DSNB events by roughly an order of magnitude. However, by employing pulse-shape discrimination and triple-coincidence techniques, this

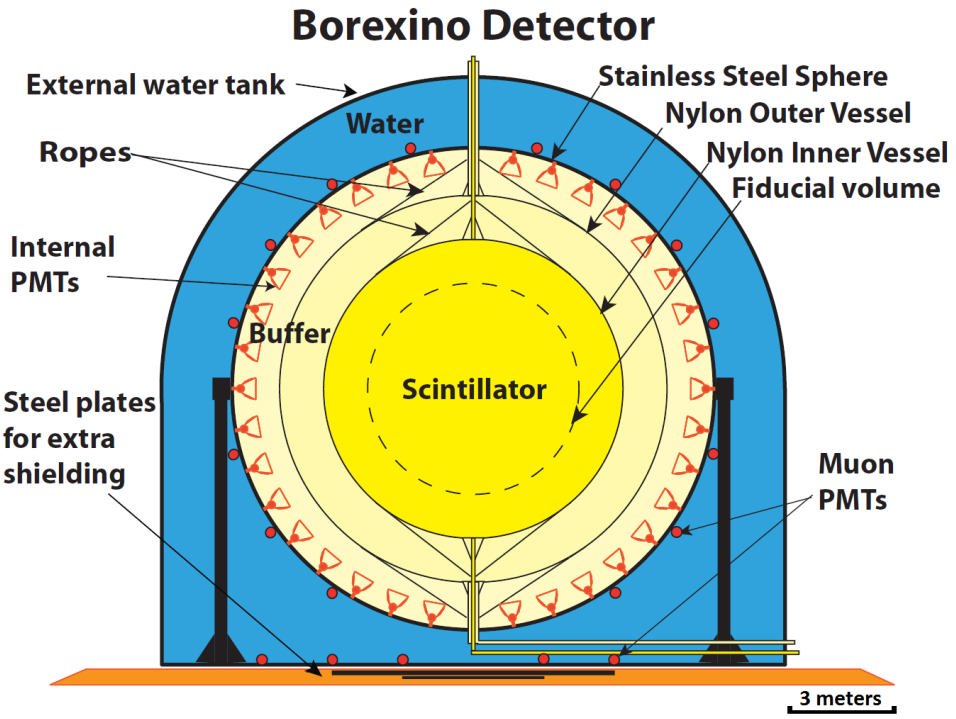

Figure 2.20: Schematic view of the Borexino detector [51].

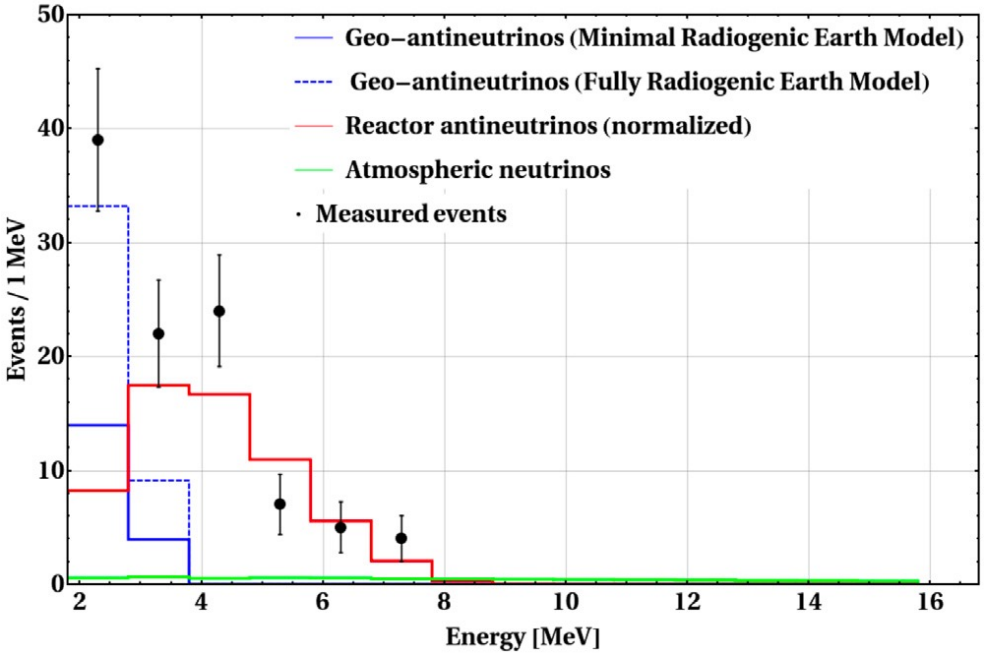

Figure 2.21: The number of observed events compared with the expected backgrounds in the Borexino astrophysical neutrino search [48].

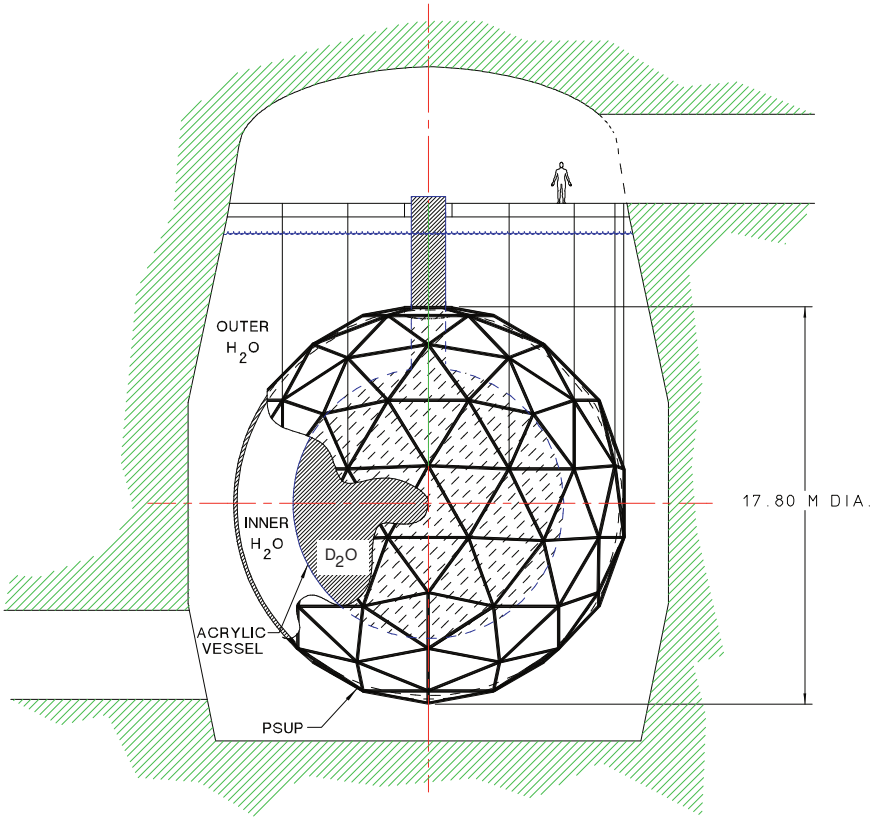

Figure 2.22: Schematic view of the SNO detector [53].

background can be substantially suppressed, making DSNB detection promising. The analysis focuses on the energy window of 12–30 MeV, where the DSNB signal is most accessible. Fig. 2.24 shows the prompt energy spectra of the DSNB signal and backgrounds. Based on calculations using reference DSNB models cited in the study, JUNO is expected to achieve a detection significance of 3σ after three years of data taking and 5σ after ten years.

Hyper-Kamiokande [55]

The Hyper-Kamiokande detector (HK) is a water Cherenkov detector designed as the successor to SK. HK aims to begin data taking in 2028, and as of August 2025, the excavation of the main cavern, located 600 meters underground in the Kamioka mine, has been completed. Fig. 2.25 shows a schematic view of the HK detector. The fiducial volume of HK is expected to be 0.19 million tons, approximately eight times larger than that of SK. The primary physics goals of HK are the discovery of CP violation in the lepton sector and the determination of the neutrino mass hierarchy, while contributing to the advancement of neutrino astronomy is also one of its important objectives. In particular, for the DSNB search, HK is projected to surpass the sensitivity of SK owing to its large statistics, and 4 to 7 DSNB events per year are expected to be observed in the energy range of 16–30 MeV.

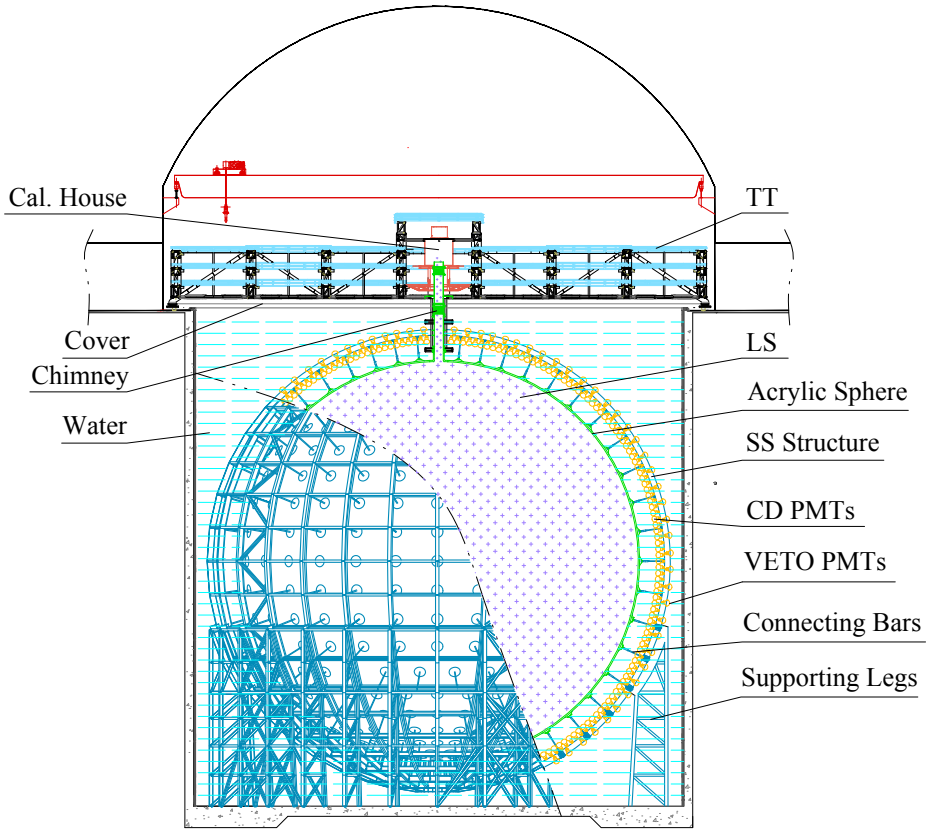

Figure 2.23: Schematic view of the JUNO detector [54].

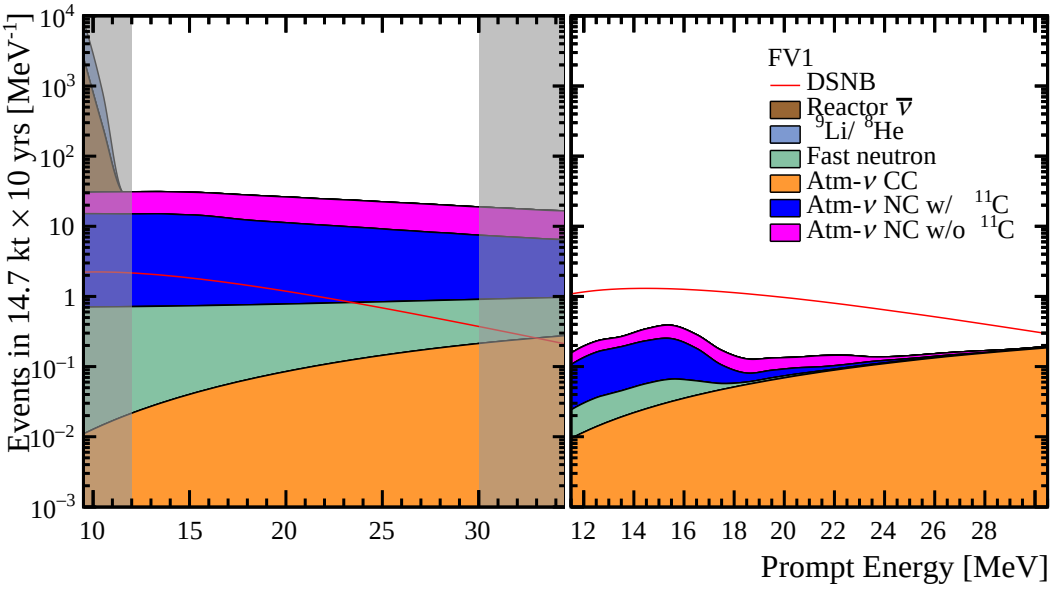

Figure 2.24: Prompt energy spectra of the reference DSNB signal versus all the backgrounds [54]. The left (right) panel shows the spectra before (after) the background reduction techniques.

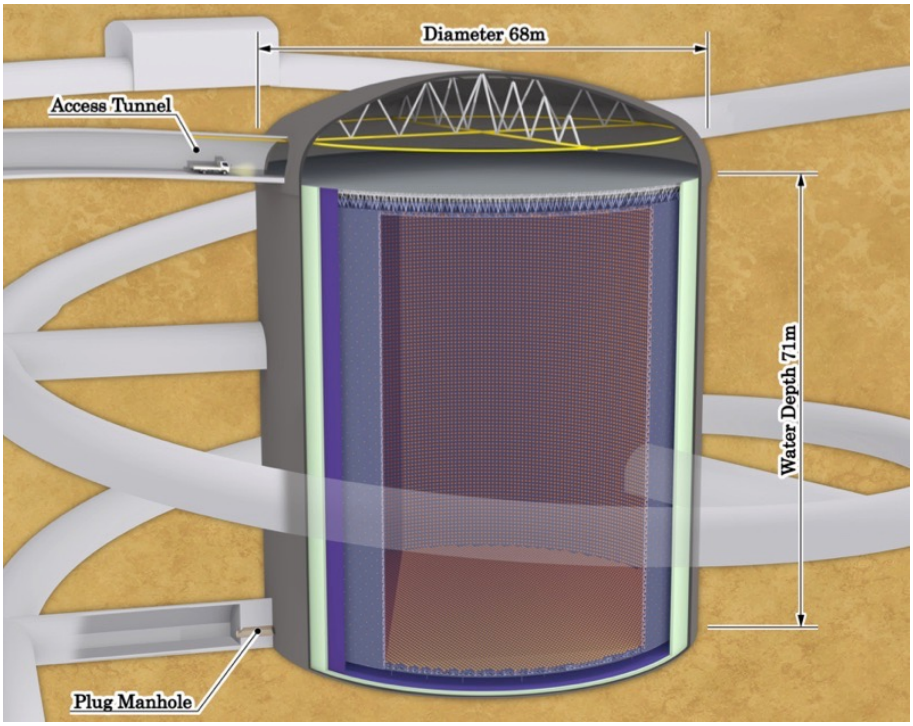

Figure 2.25: Schematic view of the Hyper-Kamiokande detector [56].

2.5.3 Model Independent Flux Upper Limits

In searches for astrophysical $\bar{\nu}_e$s, detectors worldwide have reported model-independent upper limits on the 90% C.L. $\bar{\nu}_e$ flux. These limits are obtained in each neutrino-energy bin by assuming a flat spectrum within the bin and using the number of observed events together with the number of background events. Fig. 2.26 summarizes the model-independent $\bar{\nu}_e$ flux limits reported by recent detectors—KamLAND [45], Super-Kamiokande [28, 46], and Borexino [48]—as well as the expected sensitivities from next-generation detectors such as JUNO [54] and Hyper-Kamiokande [55].

For neutrino energies above 13.3 MeV, JUNO and HK are expected, with ten years of exposure, to approach the theoretical predictions for the DSNB flux. In this energy range, the most stringent current constraint is set by Super-Kamiokande; the pure-water SK-IV phase and the gadolinium-loaded SK-VI phase provide comparable limits. In contrast, the 8.3–13.3 MeV region, KamLAND achieves the most stringent limit.

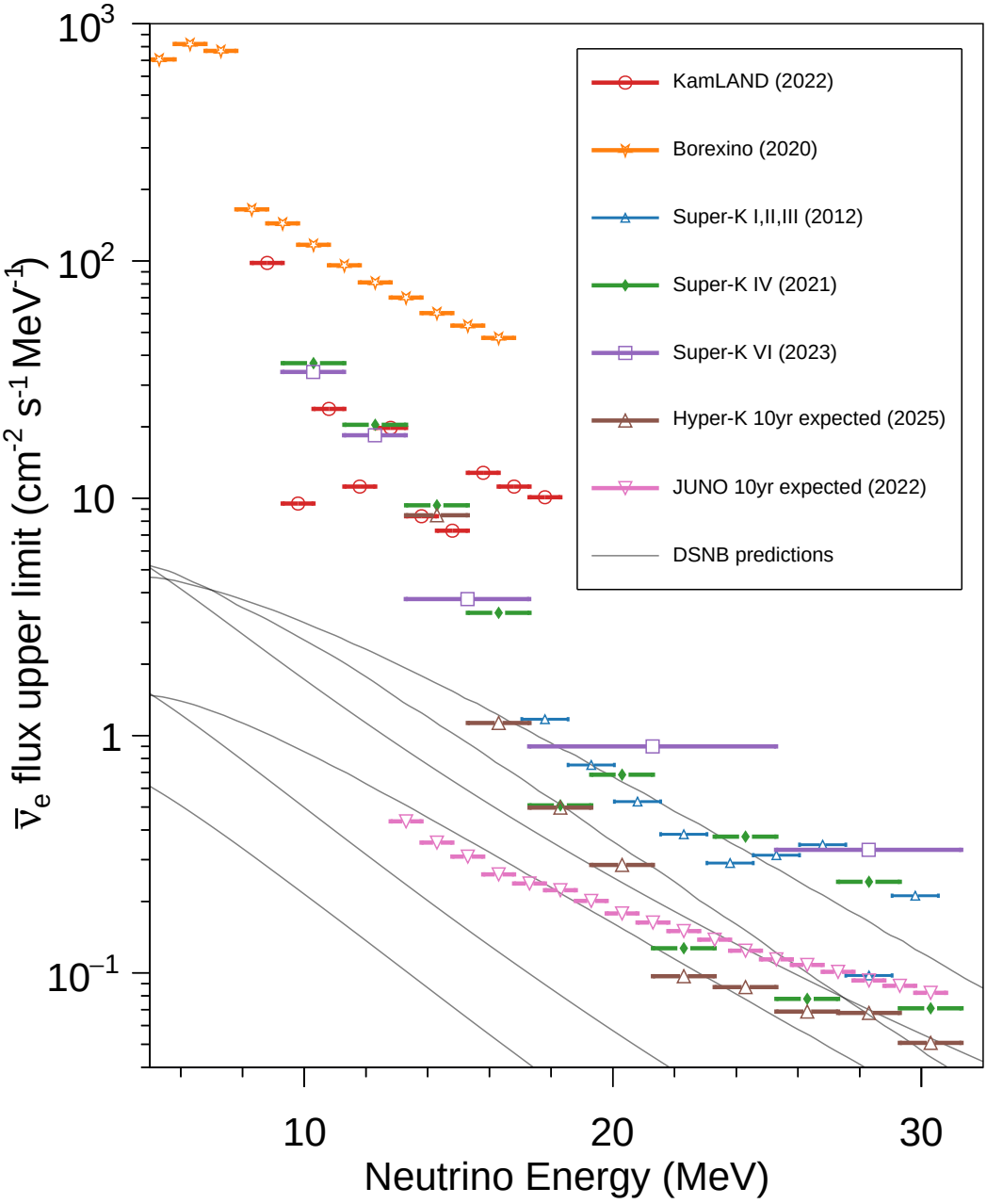

Figure 2.26: Observed (expected) model-independent $\bar{\nu}_e$ flux limits from recent (next-generation) detectors. Black lines represent various DSNB prediction models.

2.6 Advantage of Astrophysical $\bar{\nu}_e$ Search in KamLAND

In this thesis, a search for low-energy astrophysical neutrinos is conducted using the KamLAND detector. KamLAND is a 1-kt liquid scintillator detector that has been taking data for more than 20 years, and therefore has an advantage in exposure compared to other liquid scintillator detectors. In comparison with JUNO, a 20-kt liquid scintillator detector that started data taking in 2025, KamLAND has a smaller fiducial volume but benefits from the longer observation period. In addition, KamLAND has a lower energy threshold than water Cherenkov detectors such as Super-Kamiokande, and thus has sensitivity in a lower energy region. The current status of searches for each type of astrophysical neutrino source and the advantages of KamLAND are summarized below.

For the DSNB, models in which the contribution from supernova explosions in the early Universe is particularly large predict an enhanced flux at low energies of order a few MeV. KamLAND can probe such models with higher sensitivity than other detectors. In the present situation, where Super-Kamiokande reports a 1.5σ excess of events consistent with a DSNB signal, KamLAND can provide complementary information by exploring a different energy range.

KamLAND currently provides the most stringent limits worldwide on both the conversion probability of ^{8}B solar neutrinos ($\nu_e \to \bar{\nu}_e$) and the dark-matter annihilation cross section for $m_\chi < 15\,\mathrm{MeV}$, and the aim of this work is to update these results.

For searches for neutrinos from PBHs, existing constraints on f_{PBH} in the mass range relevant to this analysis ($M_{\mathrm{PBH}} = 10^{15}$–$10^{16}\,\mathrm{g}$) are dominated by gamma-ray observations [57]. In this thesis, the goal is to set new constraints from the perspective of neutrino observations. In particular, more massive PBHs emit neutrinos at lower energies via Hawking radiation, which makes KamLAND especially advantageous for this search.

Chapter 3

KamLAND

KamLAND (**Kam**ioka **L**iquid-scintillator **A**nti-**N**eutrino **D**etector) is a large liquid scintillator detector locates 1000 m underground from the top of Mt. Ikenoyama. The thickness of the rock is equivalent to 2700 m of water, significantly reducing the flux of cosmic muons to about 10^{-5} at ground level, which greatly reduces the background events from cosmic muons. As shown in Fig. 3.1, in the same tunnel, there are not only the KamLAND detector itself but also the high-voltage room for photomultiplier tubes (PMT), control room, electronics hut, as well as the pure water production facility and the first and second purification systems for liquid scintillator.

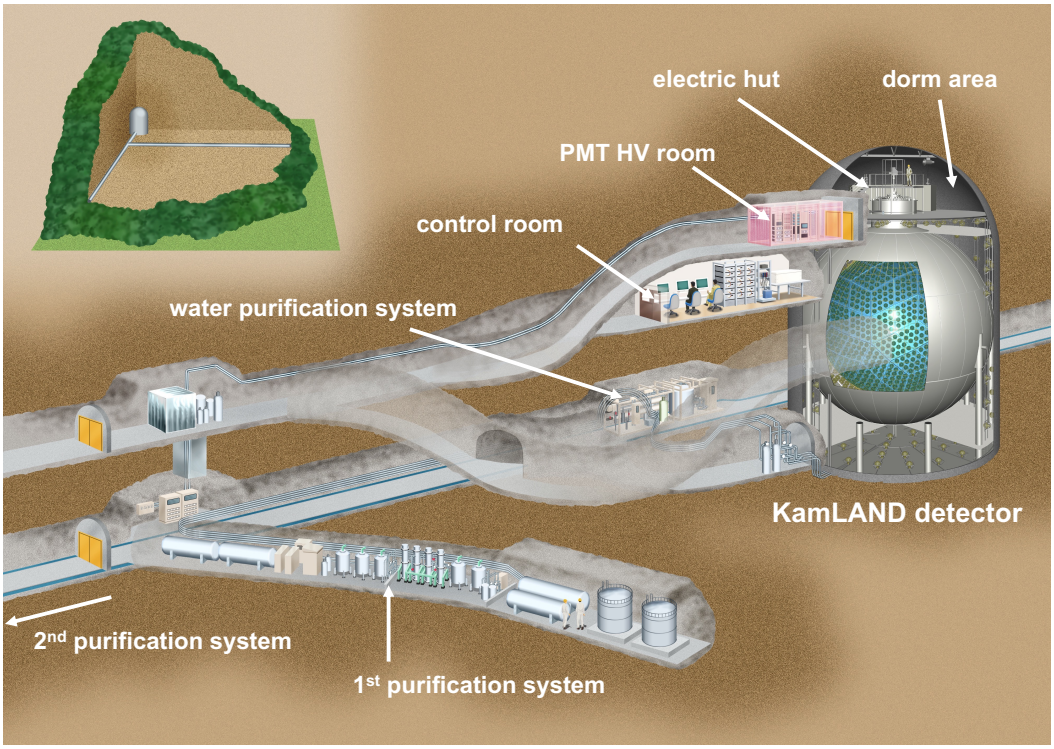

Figure 3.1: KamLAND detector and its surroundings.

3.1 Detector Components

The KamLAND detector, as shown in Fig. 3.2, is divided into two main parts: the Inner Detector (ID) and the Outer Detector (OD), each equipped with PMTs. The ID is located within a stainless steel tank with an 18-meter diameter, where it detects scintillation light for physical observations. The OD, situated outside the ID, is used to observe Cherenkov light, which serves to veto cosmic muons.

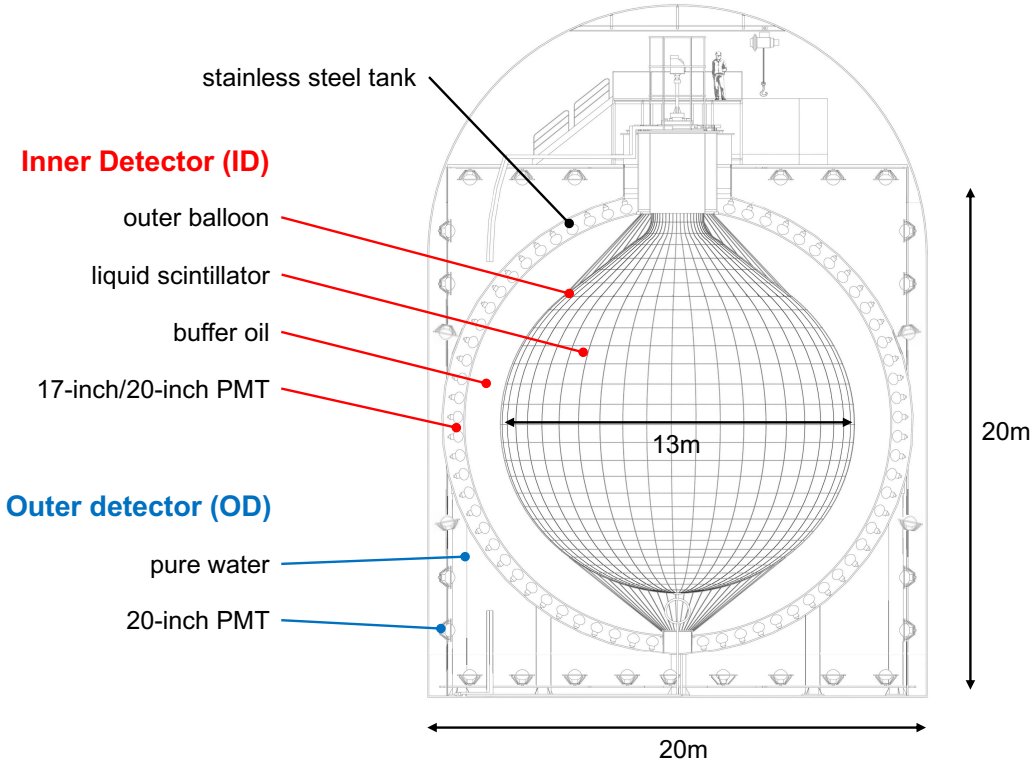

Figure 3.2: Schematic view of the KamLAND detector.

3.1.1 Inner Detector (ID)

ID refers to the inner region of a spherical stainless steel tank with a diameter of 18 meters, inside which a 13-meter diameter balloon is suspended. This balloon is filled with 1 kiloton of liquid scintillator (LS), while the space outside it is filled with non-luminous buffer oil. When charged particles pass through the LS, isotropic scintillation light is emitted and detected by PMTs mounted on the inner wall of the tank. Additionally, during the period when the search for $0\nu\beta\beta$ decay is being conducted, an inner balloon is suspended, as explained in Sec. 3.6.

KamLAND Liquid Scintillator (KamLS)

When a charged particle loses energy in the scintillator, the material becomes excited, and then scintillation light is emitted isotropically as it de-excites. In the KamLAND experiment, a liquid organic scintillator is used due to its ease of purification and scalability. Approximately 1 kt of LS fills the balloon, consisting of pseudocumene as the solvent, 2,5-diphenyloxazole (PPO) as the fluor, and dodecane for density adjustment and preventing optical degradation. Tab. 3.1 summarizes the components of KamLS.

Outer Balloon and Buffer Oil

The balloon is made from a five-layer film composed of nylon and ethylene-vinyl alcohol copolymer, with a total thickness of 135 μm. It is supported by 44 Kevlar ropes. The non-luminous buffer oil surrounding the balloon is designed to have a density similar to that of KamLS, providing structural support for the balloon. The buffer oil also serves to shield

Table 3.1: KamLS components

Material		Density	Volume Ratio
Dodecane	$C_{12}H_{26}$	$0.749\,g/cm^3$	80%
Pseudocumene	C_9H_{12}	$0.875\,g/cm^3$	20%
2,5-diphenyloxazole	$C_{15}H_{11}NO$	–	1.36 g/l
KamLS	-	$0.77721\,g/cm^3$	-

ID from γ-rays originating from the stainless steel tank and PMTs. Additionally, a 3 mm acrylic plate separates the inner and outer regions of the buffer oil, preventing damage from potential PMT breakage. Tab. 3.2 summarizes the buffer oil components.

Table 3.2: Buffer oil components

Material		Density	Volume Ratio
Dodecane	$C_{12}H_{26}$	$0.749\,g/cm^3$	53%
Isoparafin	C_nH_{2n+2}	$0.795\,g/cm^3$	47%
Buffer Oil	-	$0.77690\,g/cm^3$	-

3.1.2 Outer Detector (OD)

The outer detector (OD) is a cylindrical cavity about 20 m high and 10 m in radius, filled with approximately 3.2 kt of pure water. This water provides shielding from high-energy neutrons and radiation from the surrounding rock. From January to April 2016, refurbishment work was carried out on the OD, as the number of functioning PMTs had decreased. After the refurbishment, the number of 20-inch PMTs was changed from 225 to 140, with their positions and orientations adjusted for better performance.

3.1.3 Photo Multiplier Tubes (PMT)

A Photomultiplier Tube (PMT) is a type of optical sensor with high time resolution, capable of detecting weak light signals on the order of a single photon. When a photon strikes the photocathode of a PMT, a photoelectron is emitted via the photoelectric effect. This photoelectron is accelerated by focusing electrodes and guided towards a dynode. Upon striking the dynode, the photoelectron causes the release of secondary electrons. This process is repeated multiple times, resulting in a total amplification of around 10^7 times. The secondary electron cascade is finally collected at the anode and converted into an electrical signal. Fig. 3.3 shows the PMT used in the KamLAND detector. At KamLAND, scintillation and Cherenkov light are observed using multiple types of PMTs.

ID PMT

The ID is equipped with 1325 17-inch PMTs (R7250) and 554 20-inch PMTs (R3600) mounted on the inner wall of the stainless steel tank, providing a coverage of approximately 34%. The 20-inch PMTs, originally used in the KamiokaNDE detector, have been modified with oil-resistant coatings and feature a venetian blind-type dynode. The 17-inch PMTs, developed as an improvement over the 20-inch model, have masked edges to enhance time resolution and incorporate box- and line-focused dynodes for superior time

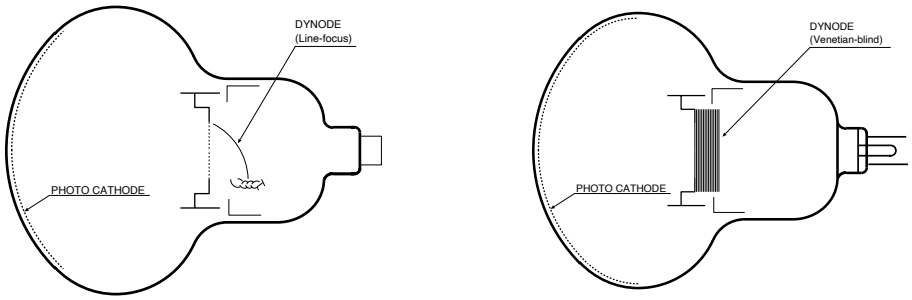

(a)17-inch PMT (b)20-inch PMT

Figure 3.3: Schematic view of (a) 17-inch PMT and (b) 20-inch PMT

performance. Additionally, the peak-to-valley (PV) ratio[1] of the 17-inch PMTs is higher, improving single-photoelectron (p.e.) signal discrimination. Tab. 3.3 summarizes the performance characteristics of the 17-inch and 20-inch PMTs used in the ID.

Table 3.3: Performance of 17-inch PMT and 20-inch PMT. λ represents the wavelength of the incident light.

Parameter	17-inch PMT	20-inch PMT
Effective photocathode (ϕ [mm])	430	460
Dynode	box and line focus (10 steps)	venetian blind (13 steps)
Quantum efficiency ($\lambda = 390$ nm)	22%	23%
Transit time	110 ns	90 ns
Transit time spread	3.5 ns	7.7 ns
PV ratio	3	1.5
Dark rate	22 kHz	40 kHz

OD PMT

Before the 2016 OD refurbishment, 225 units of 20-inch PMTs (R3600) from the former KamiokaNDE experiment were repurposed as OD PMTs. Following the refurbishment, these were replaced by 140 new 20-inch PMTs (R3600-06MOD), which remain in use today. Fig. 3.4 provides an overview of this new PMT model. Although this PMT type was also employed in Super-Kamiokande, KamLAND utilizes a version with higher quantum efficiency. Specifically, some PMTs with High Quantum Efficiency (HQE) are positioned in the equatorial region and detector base for enhanced sensitivity. Additionally, 16 eight-inch PMTs and six five-inch PMTs are installed to detect muons passing through the upper detector region. Tab. 3.4 summarizes the specifications of PMTs used in the OD.

3.2 Data Acquisition System

KamLAND operates two parallel data acquisition systems (DAQs). One is KamDAQ, which utilizes KamLAND Front-End Electronics (KamFEE)[2] and has been in use since the start

[1] the ratio between the peak representing single-photoelectron events and the valley between this peak and the pedestal

[2] KamFEE is also referred to as Front-end Berkeley Electronics (FBE).

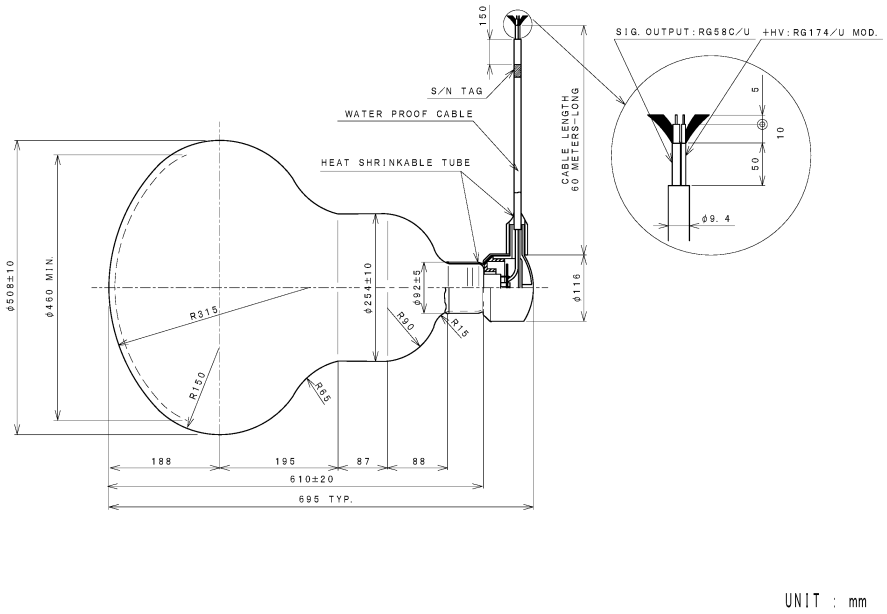

Figure 3.4: Schematic view of R3600-06MOD.

Table 3.4: Performance of OD 20-inch PMT. λ represents the wavelength of the incident light.

Parameter	OD PMT	OD HQE PMT
Effective photocathode (ϕ [mm])	460	
Dynode	venetian blind (11 step)	
Quantum efficiency ($\lambda = 390$ nm)	20−21%	32%
Transit time	95 ns	
Transit time spread	5.9 ns	
PV ratio	1.6	
Dark rate	17 kHz	25 kHz

of KamLAND observations. The other, MogDAQ, is based on the Module for General-Use Rapid Application (MoGURA) and was introduced at the start of the KamLAND-Zen experiment to reduce dead time after cosmic-ray muons. As shown in Fig. 3.5, analog signals from PMTs are digitized in the electronics hut atop the KamLAND detector and then split for transmission to each DAQ system.

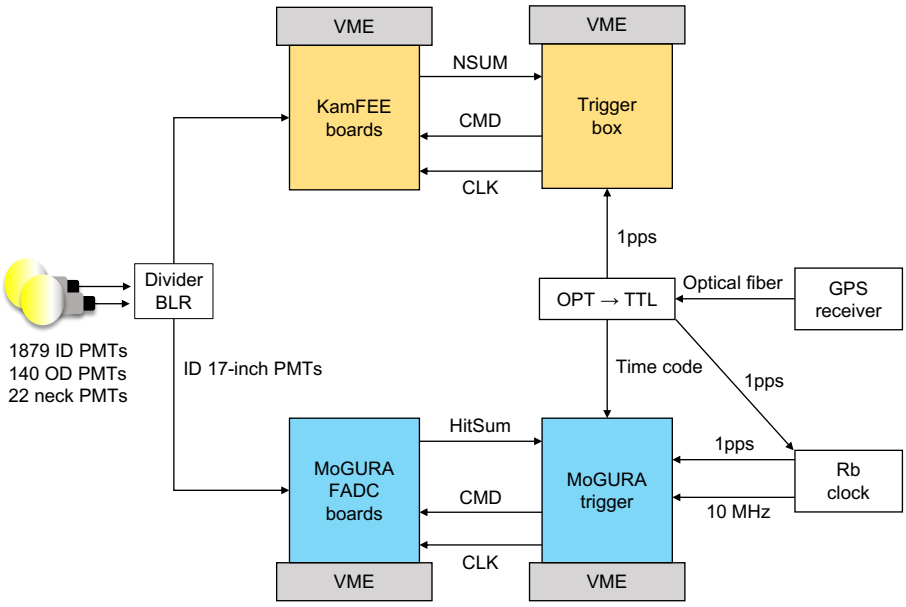

Figure 3.5: Overview of KamLAND DAQ.

3.2.1 KamDAQ

KamDAQ is a data acquisition system composed of KamFEE, a trigger circuit, a GPS receiver, and other components. The data acquisition process in KamDAQ operates as follows. First, PMT hit information is sent from KamFEE to the trigger circuit, which then issues a data acquisition trigger back to KamFEE. This trigger initiates the digitization of the acquired signal, which is subsequently transferred to the DAQ computer. This section describes the main components of KamDAQ in detail.

KamFEE

KamFEE is a custom-developed data acquisition circuit for the KamLAND detector, to which all PMTs in KamLAND are connected. Each KamFEE board can accommodate up to 12 PMTs, with approximately 200 such boards employed throughout the detector.

A schematic diagram of KamFEE is shown in Fig. 3.6. The analog signal waveform from each PMT input to KamFEE is split into two paths. One path is sent to a discriminator, which determines a *hit* if the signal exceeds a threshold set to approximately one-sixth of the single-photoelectron amplitude. This hit information is then transmitted to the trigger circuit. The other path is delayed and amplified before being sent to an Analog Transient Waveform Digitizer (ATWD). The amplifier has three gain settings (0.5x, 4x, and 20x), and if the signal exceeds the dynamic range of the ATWD, a lower-gain signal is digitized instead. This mechanism ensures that PMT signals across a wide output range are accurately recorded.

The digitization process in the ATWD takes approximately 25 μs, during which time the ATWD cannot acquire new signals. To address this limitation, KamFEE employs two ATWDs per channel, which alternate operation. However, following signals from cosmic

ray muons, the combined effects of waveform overshoot and afterpulses can prevent both ATWDs from completing data acquisition in time, resulting in dead time. MogDAQ, discussed in a later section, was developed to mitigate this dead time.

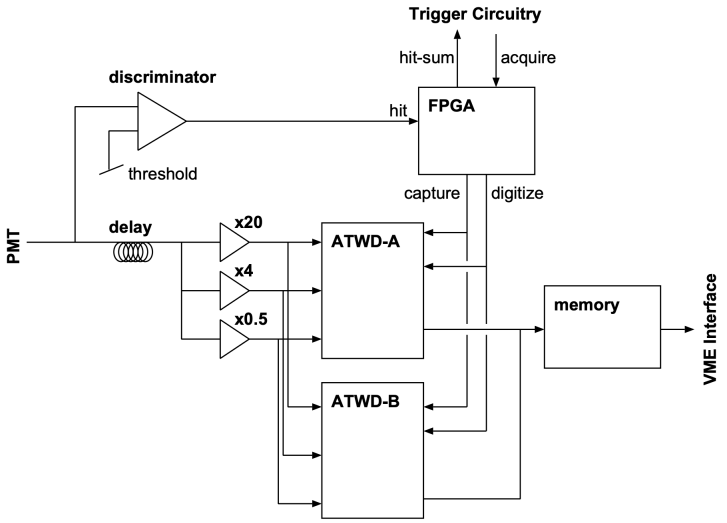

Figure 3.6: Schematic diagram of KamFEE [58]

Trigger Circuit

The hit information from 200 KamFEE boards is aggregated in the trigger circuit, where the total number of hits, Nsum, is calculated. The trigger circuit determines whether Nsum in the Inner Detector (ID) and Outer Detector (OD) channels exceeds preset thresholds, in which case a trigger is issued and sent back to KamFEE. In addition to threshold-based triggers, other triggers are generated independently of Nsum, including those issued in response to external command requests.

The trigger circuit also distributes a 40 MHz system clock to KamFEE boards, synchronized with a GPS receiver installed at the Kamioka mine entrance. This clock provides precise time information to the data recorded by KamFEE.

3.2.2 MogDAQ

MogDAQ is a data acquisition system consisting primarily of a Baseline Restorer (BLR), MoGURA, and MoGURA trigger. It was developed to reduce dead time caused by afterpulses and overshoot following cosmic ray muon events, as shown in Fig. 3.7. This system is particularly effective in suppressing background events in the KamLAND-Zen experiment by removing ^{10}C decay events produced through ^{12}C spallation induced by cosmic ray muons.

The data acquisition process in MogDAQ is generally similar to that in KamDAQ; however, MoGURA is connected only to the 17-inch PMTs in the ID.

BaseLine Restorer (BLR)

Cosmic ray muons incident on the KamLAND detector emit a large amount of Cherenkov and scintillation light within the detector. This results in a phenomenon known as *overshoot,* where the baseline of the PMT signal waveform fluctuates, as shown in Fig. 3.7. When overshoot occurs, the signal amplitude may fall below the discriminator threshold, causing a period during which no triggers are issued. This dead time due to overshoot can last up

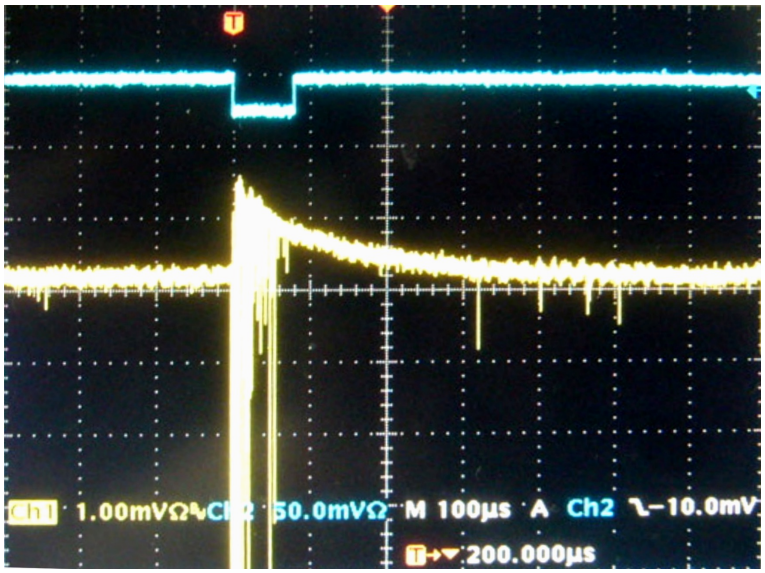

Figure 3.7: Overshoot and afterpulses following muon events [59]. The grid is set to 100 μs horizontally and 1 mV vertically.

to approximately 2 ms, which poses a significant issue for detecting neutron capture events with a mean capture lifetime of about 207 μs. The Baseline Restorer (BLR) circuit was developed to mitigate overshoot in the signal waveform, allowing the detection of events immediately following cosmic ray muons.

The input signal to the BLR is split into two paths: one path passes through a low-pass filter to extract the baseline component of the overshoot. By subtracting this baseline component from the other signal, baseline fluctuations can be reduced to around 1.4 μs. This reduction enables the undetected neutron capture events caused by overshoot to be kept below 1%.

MoGURA

As previously mentioned, MoGURA was developed to suppress ^{10}C decay events, which are a primary background in the KamLAND-Zen experiment. Like KamFEE, each MoGURA board is connected to 12 PMTs; however, the system clock supplied by the MoGURA trigger operates at 50 MHz. Additionally, a crystal clock is implemented on the board to enable standalone operation, with a switchable configuration between clocks. Fig. 3.8 shows a photograph and schematic of the MoGURA board. The MoGURA board emphasizes scalability, employing a Field Programmable Gate Array (FPGA) to allow flexible circuit configurations.

The data flow within MoGURA proceeds as follows. Signals input to MoGURA pass through amplifiers with four gain settings: L (0.24x), M (2.4x), M (24x), and P (20x). These signals are then sent to a Flash Analog-to-Digital Converter (FADC), which addresses the dead time limitations in signal digitization encountered with the ATWD in KamFEE, enabling rapid signal digitization. Subsequently, in the Front End FPGA (FEF), digital signals are recorded, and waveforms are converted into rectangular pulses to generate hit information. The System FPGA (sFPGA) then calculates the total hit count (HitSum) on the board, which is transmitted to the MoGURA trigger. The issued trigger is sent back to the MoGURA board, and data is transferred from the sFPGA to the VME system.

The P-gain setting enables the acquisition of single-photoelectron-equivalent signals at high voltage and time resolutions, with sampling at 1 GHz. The remaining gain settings are sampled at 200 MHz, allowing the detection of signals across a wide voltage range. A wide

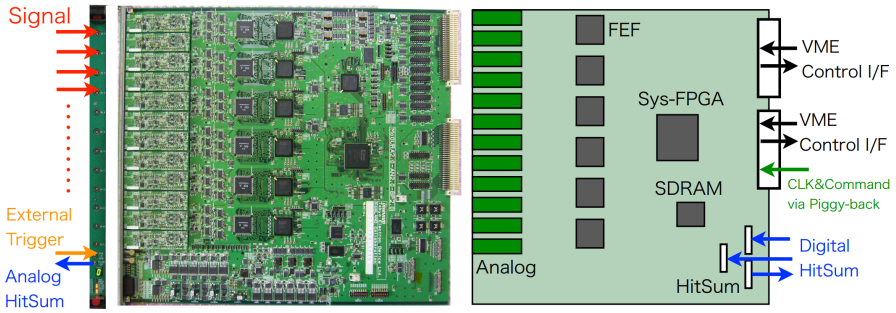

Figure 3.8: Photograph (left) and schematic (right) of the MoGURA board [60]

dynamic range and low dead time of MoGURA result in a substantial amount of recorded data. Therefore, a feature known as zero suppression is implemented to reduce unnecessary waveform data.

MoGURA Trigger

As shown in Fig. 3.7, false signals known as afterpulses are observed tens to hundreds of μs after cosmic ray muon signals. These afterpulses are caused by ionization of residual gases in the PMT following high-light-yield events, which generate photoelectrons at the photocathode and dynodes. Since afterpulses are indistinguishable from physical event waveforms, they interfere with the tagging of cosmic ray muons and subsequent neutron capture events. To mitigate the effect of afterpulses, MoGURA employs a trigger known as the Adaptive Trigger.

The HitSum information transmitted from the MoGURA board is summed within a predefined time window, known as the Hit Window, in the MoGURA trigger circuit. This sum is defined as NHit, and when NHit exceeds a certain threshold, various triggers are issued. Specifically, for high-light-yield events such as cosmic ray muons, a Launch Trigger is issued once the high NHit threshold is crossed, activating the Adaptive Trigger for the following 1 ms. The Adaptive Trigger differentiates the PMT hit distribution, enabling the extraction of neutron capture events from afterpulses. Additionally, the MoGURA trigger is synchronized with GPS, similar to the KamDAQ trigger circuit, and supplies the MoGURA board with a 50 MHz system clock.

3.3 Purification System

A low-background environment is one of the key features of the KamLAND detector, particularly important for detecting low-rate signals such as solar and geo-neutrinos. To achieve the target background rate of less than 0.1 events per day—necessary to observe approximately one inverse beta decay event per day—strict control of radioactive impurities in the LS is required. Specifically, the concentrations of ^{238}U, ^{232}Th, and ^{40}K had to be reduced to less than 10^{-14} g/g, 10^{-14} g/g, and 10^{-15} g/g, respectively.

1st purification system

During the construction of KamLAND in 2002, the LS and buffer oil were purified using the so-called 1st purification system, which consisted of a liquid-liquid (water) extraction stage and a nitrogen purge tower as shown in Fig. 3.9. In the water extraction process, heavy metal ions such as uranium, thorium, potassium, and radium were effectively transferred from the non-polar LS and buffer oil to purified water. The subsequent nitrogen purge

process removed residual water, oxygen (which quenches scintillation light), and radioactive noble gasses such as ^{222}Rn, ^{85}Kr, and ^{39}Ar. Measurements before and after this purification process, using ICP-MS for raw materials and in-situ KamLAND data for purified LS, confirmed that radioactivity was reduced by approximately five orders of magnitude as shown in Tab. 3.5. However, for low-energy solar neutrino detection, further reduction of background was necessary. Notably, the 1st purification system could not sufficiently remove isotopes like ^{85}Kr and ^{210}Pb, which are major background sources both for solar neutrinos and for anti-neutrino analysis via the $^{13}\mathrm{C}(\alpha, n)^{16*}\mathrm{O}$ reaction, driven by α-decays from ^{210}Po (a daughter of ^{210}Pb).

Table 3.5: Radioactivity of the LS components and the final mixture after 1st purification. The LS components were measured by ICP-MS, while the final mixture was measured in-situ by KamLAND [61].

Material	^{238}U [g/g]	^{232}Th [g/g]	^{40}K [g/g]
- before purification -			
Isoparaffin	3×10^{-13}	$\leq 6 \times 10^{-12}$	-
Dodecane	$\leq 10^{-13}$	$\leq 6 \times 10^{-12}$	$\leq 1.2 \times 10^{-12}$
Pseudocumene	$\leq 10^{-13}$	-	-
PPO	1.2×10^{-13}	$\leq 5 \times 10^{-11}$	$\leq 5.3 \times 10^{-11}$
- after purification -			
LS	$(3.4 \pm 0.4) \times 10^{-18}$	$(5.7 \pm 0.8) \times 10^{-17}$	2.7×10^{-16}
- target level -			
LS	$< 10^{-14}$	$< 10^{-14}$	$< 10^{-15}$

2nd purification system

To reduce ^{85}Kr and ^{210}Pb, the 2nd purification system was developed and implemented between 2007 and 2009 in two major campaigns. The core of this system was distillation, a highly effective technique that removes volatile radioactive impurities based on differences in boiling points. More than 5000 m^3 of LS, which is equivalent to three full volume exchanges, were processed during these campaigns.

Fig. 3.10 illustrates the schematic view of the 2nd purification system. This system consists of multiple towers operating under tightly controlled temperature and pressure. After distillation, the components were remixed to maintain the correct LS density (within a precision of 10^{-3} g/cm^3), followed by nitrogen purging to remove residual noble gasses. Before reintroduction into the detector, key quality parameters such as PPO concentration, transparency and the concentrations of ^{222}Rn and ^{85}Kr were evaluated.

These two purification system together enabled KamLAND to maintain an ultra-low background environment, essential for its success in detecting reactor, geo, and solar neutrinos.

3.4 Source Calibration Equipment

KamLAND data quality is verified and corrected using various sealed radioactive sources, as illustrated in Tab. 3.6. Periodic source calibrations were performed before the start of KamLAND-Zen. However, during the KamLAND-Zen 400 phase, these calibrations could not be conducted due to the presence of the inner balloon suspended at the center of the

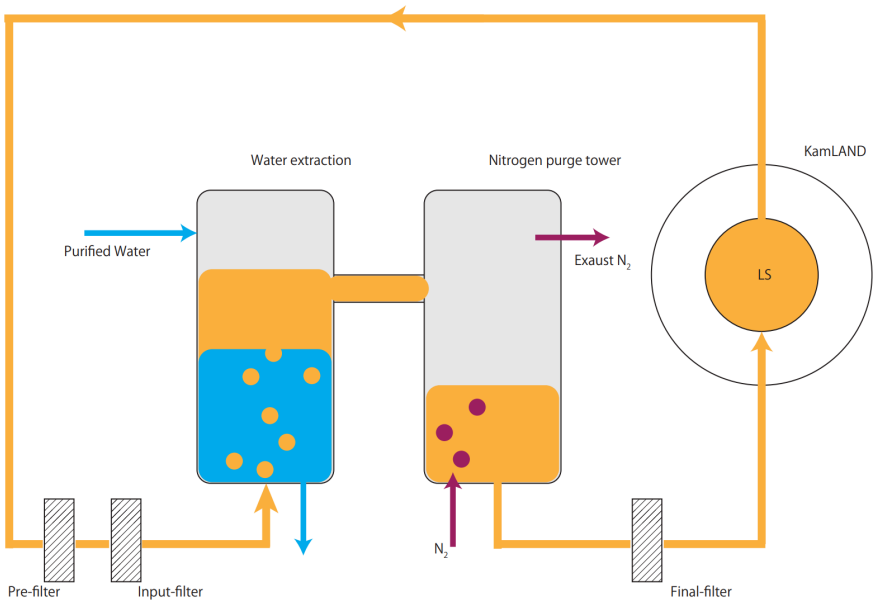

Figure 3.9: Schematic view of the 1st purification system [62]

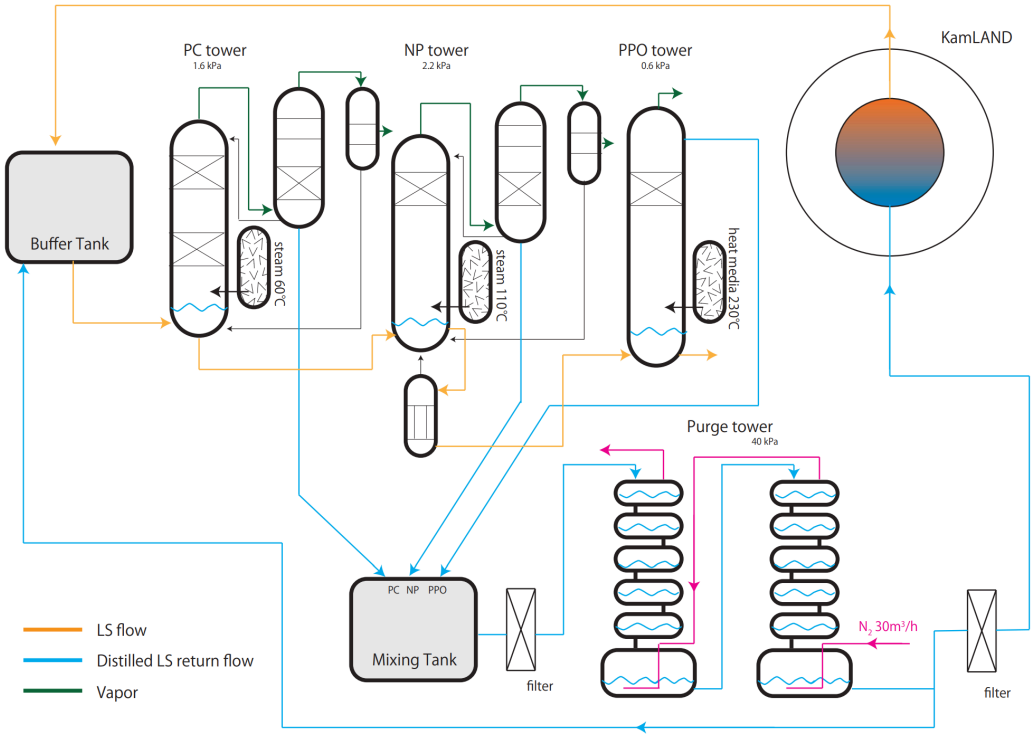

Figure 3.10: Schematic view of the 2nd purification system [62]

detector. In this period, spallation products and delayed neutron capture events following muons were instead utilized to monitor detector stability.

For precise estimation of the fiducial volume uncertainties, a full-volume calibration called 4π-calibration was conducted in 2006 and 2007. In this method, calibration sources mounted on a segmented pole are maneuvered within the detector by two control cables, allowing source deployment at various positions throughout the detector. A schematic diagram of this system is illustrated in Fig. 3.11.

Table 3.6: KamLAND calibration sources

Source	Particle type	Energy [MeV]	Half life
^{208}Hg	γ	0.2792	46.612 d
^{137}Cs	γ	0.6616	30.07 y
^{65}Zn	γ	1.1116	244.3 d
^{68}Ge	γ	0.511×2	270.8 d
^{60}Co	γ	1.732, 1.3325	5.271 y
^{241}Am^{9}Be	γ, n	γ; 4.4, n; <10	432 y
^{210}Po^{13}C	γ, n	γ; 6.13, n; <7.5	22 y

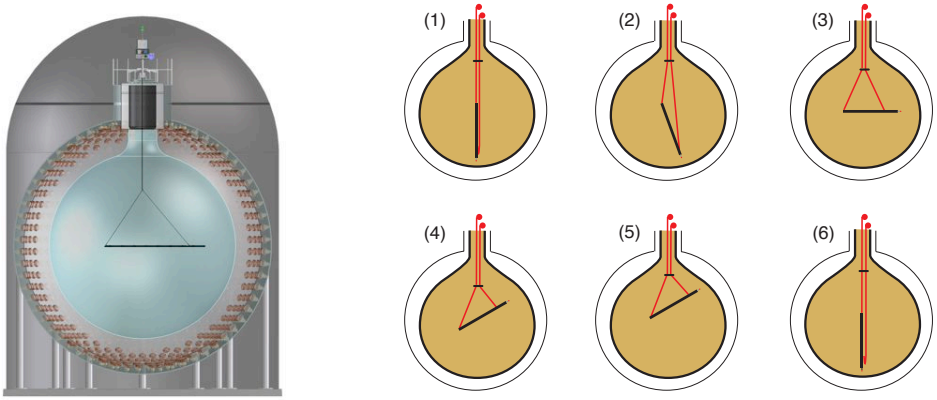

Figure 3.11: Illustration of the 4-π calibration system and typical deployment sequence for 4-π calibration [63].

3.5 Neutrino Detection Channel

3.5.1 Inverse Beta Decay

Inverse beta decay (IBD) is the primary detection channel for electron antineutrinos ($\bar{\nu}_e$) in KamLAND due to its large interaction cross section. This reaction can be efficiently identified using a technique known as delayed coincidence, which significantly suppresses background contamination (detailed selection criteria are described in Sec. 7.4).

An incoming $\bar{\nu}_e$ interacts with a free proton in the LS via the IBD interaction:

$$\bar{\nu}_e + p \rightarrow n + e^+ \tag{3.1}$$

The resulting positron loses its kinetic energy in the LS, producing scintillation light, and eventually annihilates with an electron, emitting two 511 keV gamma rays. These signals

collectively constitute the prompt event. Meanwhile, the neutron produced in the same reaction thermalizes through scattering with protons in the LS and is subsequently captured, predominantly on a proton, after an average capture time of about 207 μs. This neutron capture process releases a 2.2 MeV gamma ray corresponding to the binding energy of the deuteron:

$$n + p \rightarrow d + \gamma\,(2.2\,\mathrm{MeV}) \tag{3.2}$$

The 2.2 MeV gamma ray undergoes multiple Compton scatterings in the LS, producing additional scintillation light. As this signal appears after the prompt event, it is referred to as the delayed event. Delayed coincidence refers to the technique of identifying correlated prompt and delayed events in both time and space, allowing for effective rejection of uncorrelated background events.

An additional advantage of the IBD interaction is that the energy of the incident $\bar{\nu}_e$ can be reconstructed from the observed energy of the prompt event. Denoting the $\bar{\nu}_e$ energy as E_ν, and the kinetic energies of the positron and neutron as T_e and T_n, energy conservation is written as

$$E_\nu + m_p = T_e + m_e + T_n + m_n, \tag{3.3}$$

where m_p, m_e, and m_n are the masses of the proton, electron, and neutron, respectively. The observed prompt energy E_p, which includes the positron's kinetic energy and the energy from annihilation, is given by

$$\begin{aligned} E_p &= T_e + 2m_e \\ &= E_\nu + m_p + m_e - T_n - m_n \\ &= E_\nu - T_n - 0.783\,[\mathrm{MeV}]. \end{aligned} \tag{3.4}$$

Therefore, the relationship between the $\bar{\nu}_e$ energy and the observed prompt energy can be written as

$$E_\nu = E_p + T_n + 0.783\,[\mathrm{MeV}]. \tag{3.5}$$

At energies on the order of a few MeV, the neutron kinetic energy after thermalization is negligible, and thus $T_n \simeq 0$ can be assumed above equation.

The IBD interaction also has a threshold energy, below which the interaction cannot occur. When the kinetic energies of the final-state positron and neutron are zero, the threshold is derived from the invariant mass relation:

$$(m_p + E_\nu^{\mathrm{th}})^2 - (E_\nu^{\mathrm{th}})^2 = (m_n + m_e)^2 \tag{3.6}$$

and the energy threshold of IBD is derived as

$$E_\nu^{\mathrm{th}} = \frac{(m_n + m_e)^2 - m_p^2}{2m_p} \simeq 1.806\,[\mathrm{MeV}]. \tag{3.7}$$

The IBD cross section as a function of neutrino energy is shown in Fig. 3.12.

3.5.2 Electron Scattering

In KamLAND, electron scattering is also used for neutrino detection:

$$\nu_x + e^- \rightarrow \nu_x + e^- \qquad (x = e, \mu, \tau) \tag{3.8}$$

In this reaction, unlike IBD, only a single scintillation signal is produced by the recoil electron. As a result, background rejection based on delayed-coincidence tagging is not available, and the signal is estimated by subtracting the expected background contribution

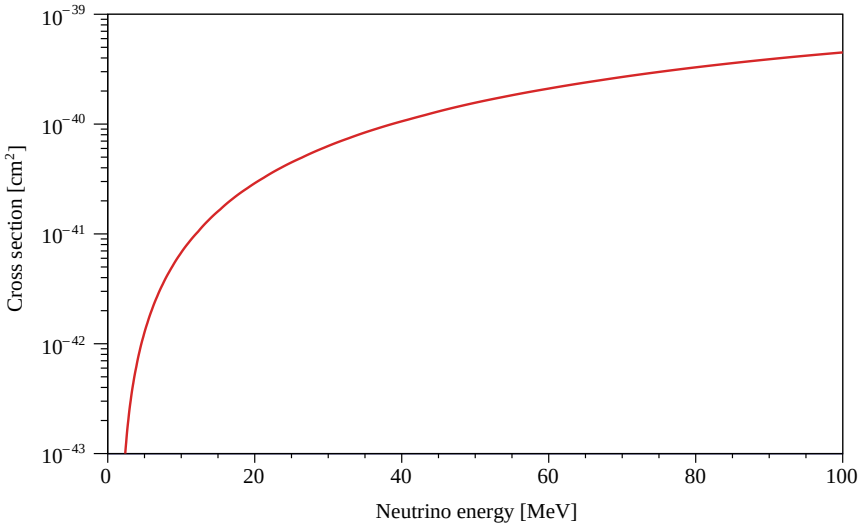

Figure 3.12: Cross section of inverse beta decay

from the observed event sample. This channel is sensitive to all neutrino flavors and has energy threshold. At KamLAND, electron scattering is primarily used in observations of solar neutrinos.

3.6 KamLAND-Zen Experiment

KamLAND Zero-Neutrino double beta decay search (KamLAND-Zen) is an extension of the KamLAND experiment designed to search for neutrinoless double beta decay ($0\nu\beta\beta$) using ^{136}Xe. In 2011, a 1.54-meter-radius inner balloon filled with xenon-loaded liquid scintillator was installed at the center of the KamLAND detector, initiating the KamLAND-Zen 400 phase. This was later upgraded to KamLAND-Zen 800 by doubling the xenon mass to enhance the sensitivity. KamLAND-Zen experiment altered the detector configuration and event selection, particularly for anti-neutrino analysis. Further technical details of the experiment are described in the subsequent sections.

3.6.1 Motivation of $0\nu\beta\beta$ Search

Majorana neutrino

In the standard model, only left-handed neutrinos and right-handed anti-neutrinos have been observed. The extremely small neutrino masses inferred from oscillation experiments raise the possibility that neutrinos are not Dirac particles but rather Majorana particles, meaning they are their own antiparticles. If neutrinos are Majorana particles, the so-called seesaw mechanism naturally explains their small masses by introducing heavy right-handed neutrinos that exist at a high mass scale.

Furthermore, the existence of heavy right-handed Majorana neutrinos enables a mechanism called *leptogenesis,* in which the decay of these particles in the early universe violates lepton number conservation and generates a lepton asymmetry. This asymmetry can then be partially converted in to a baryon asymmetry through sphaleron processes, potentially explaining why the present universe is dominated by matter over antimatter.

Understanding whether neutrinos are Majorana particles is therefore not only important for explaining the origin of neutrino mass but also has profound implications for understanding the fundamental properties of the universe, including the origin of its matter-antimatter asymmetry.

$0\nu\beta\beta$ search

The most practical way to test whether neutrinos are Majorana particles is to search for $0\nu\beta\beta$. This rare nuclear process, which violates lepton number conservation, can occur only if neutrinos are Majorana particles. In contrast to the standard two-neutrino double beta decay ($2\nu\beta\beta$), which emits two anti-neutrinos along with two electrons, $0\nu\beta\beta$ emits only two electrons, allowing the entire Q-value of the decay to be shared between them. The detection of such a signal would provide unambiguous evidence of the Majorana nature of neutrinos.

Moreover, the half-life of $0\nu\beta\beta$ decay is related to the effective Majorana neutrino mass $\langle m_{\beta\beta}\rangle$ as follows

$$\left(T_{1/2}^{0\nu\beta\beta}\right)^{-1} = G^{0\nu\beta\beta}\left|M^{0\nu\beta\beta}\right|^2 \langle m_{\beta\beta}\rangle^2 , \tag{3.9}$$

where $G^{0\nu\beta\beta}$ is the phase space factor, $\left|M^{0\nu\beta\beta}\right|$ is the nuclear matrix element, and $\langle m_{\beta\beta}\rangle$ is given by

$$\langle m_{\beta\beta}\rangle = \left|\left|U_{e1}^L\right|^2 m_1 + \left|U_{e2}^L\right|^2 m_2 e^{i\phi_2} + \left|U_{e3}^L\right|^2 m_3 e^{i\phi_3}\right| . \tag{3.10}$$

Here, U_{ei}^L $(i = 1, 2, 3)$ are elements of the mixing matrix elements, m_i are the mass eigenvalues, and ϕ_2, ϕ_3 are Majorana CP-violating phases. Measuring or constraining $\langle m_{\beta\beta}\rangle$ through $0\nu\beta\beta$ experiments thus provides unique information about the absolute neutrino mass scale and the mass hierarchy.

3.6.2 KamLAND-Zen

In the KamLAND-Zen experiment, which uses a detector modified from the original KamLAND detector, employs ^{136}Xe as the isotope for $0\nu\beta\beta$ searches. ^{136}Xe has a Q-value of 2.458 MeV and a relatively high natural abundance. The advantages of using ^{136}Xe include its chemical stability, high solubility in LS, and its ability to maintain high optical transparency after dissolution. In the KamLAND-Zen experiment, xenon is enriched such that the ^{136}Xe content reaches approximately 91%, and this enriched xenon is dissolved in to the LS to produce xenon-loaded liquid scintillator. Its composition is summarized in Tab. 3.7. Xenon-loaded liquid scintillator is referred to as XeLS to distinguish it from the original KamLAND LS, often called KamLS. The reduction in light yield due to quenching caused by the dissolved xenon is compensated by adding a higher concentration of PPO than that used in KamLS. Additionally, to reduce the pressure exerted on the inner balloon, the density of XeLS is adjusted to match that of KamLS.

The XeLS is contained within a inner balloon (miniballoon) made by several 25 μm-thick nylon film (See Fig. 3.13). To reduce background events induced by external gamma rays entering from outside the detector, the inner balloon is suspended at the center of the KamLAND detector. A schematic view of the KamLAND-Zen detector is shown in Fig. 3.14.

KamLAND-Zen 400

The first phase of the KamLAND-Zen experiment (KamLAND-Zen 400) began in October 2011 with 320 kg of xenon loaded into the liquid scintillator. This initial observation period, called phase1, continued until June 2012. During this phase, an unexpected background

Table 3.7: Composition of xenon-loaded liquid scintillator. The values for Zen400 are taken from [64] and [65], while those for Zen800 are from [66]. Two values in the Xe concentration of Zen400 phase1 were measured at different times. The density of decane and PC is 0.731 g/cm^3 and 0.875 g/cm^3, respectively.

	Decane	PC	PPO	Xe
Zen400 phase1	82.3%	17.7%	2.7 g/L	2.44/2.48 wt%
Zen400 phase2	80.7%	19.3%	2.29±0.03 g/L	2.91 wt%
Zen800	82.4%	17.6%	2.38±0.02 g/L	3.13 wt%

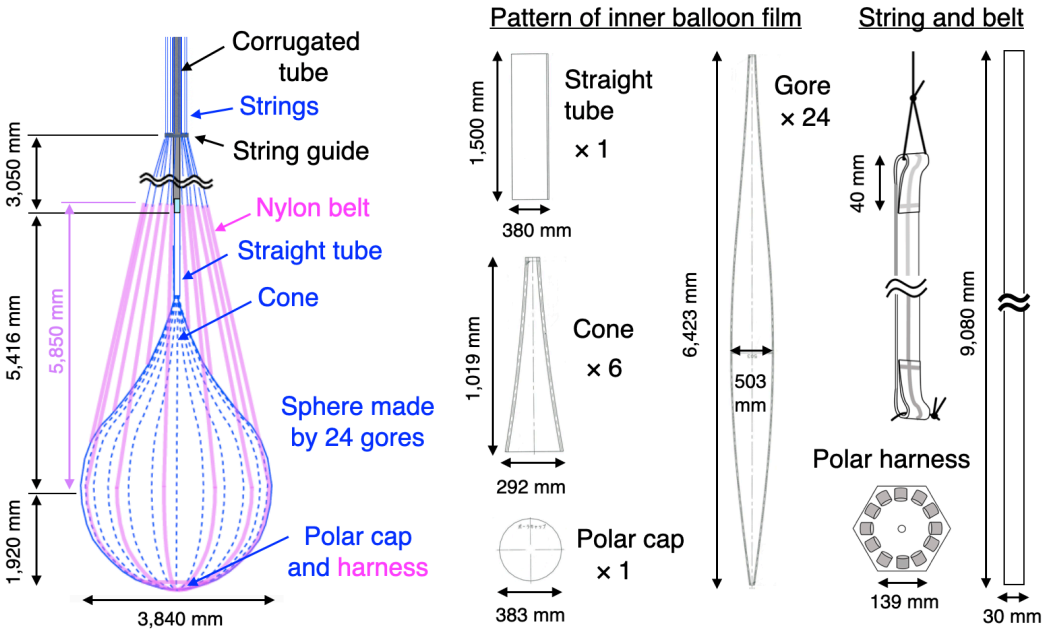

Figure 3.13: Schematic view of inner balloon for KamLAND-Zen 800 [67]

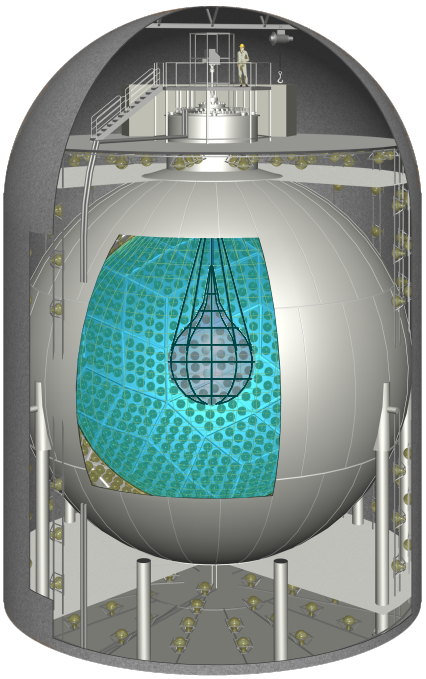

Figure 3.14: Schematic view of the KamLAND-Zen detector

from ^{110m}Ag (β^- decay, $\tau = 360\,\text{days}$, $Q = 3.01\,\text{MeV}$) was found near the ^{136}Xe $0\nu\beta\beta$ Q-value of 2.458 MeV (See Fig. 3.15).

To mitigate this background, the XeLS was replaced and purified using distillation and liquid-liquid extraction techniques. After the purification, the experiment entered phase2, which began in December 2013 with an increased xenon mass of 383 kg. By this time, ^{110m}Ag background had almost completely disappeared. The observation of KamLAND-Zen 400 was completed in October 2015. The combined analysis of data from both phase1 and phase2 yielded the most stringent upper limit at the time [68] on the half life of ^{136}Xe $0\nu\beta\beta$ decay:

$$T_{1/2}^{0\nu\beta\beta} > 1.07 \times 10^{26}\,\text{yr (90\% C.L.)}$$

This corresponds to a constraint on the effective Majorana neutrino mass of

$$\langle m_{\beta\beta} \rangle < 61\text{–}165\,\text{meV}.$$

KamLAND-Zen 800

To improve the sensitivity to the $0\nu\beta\beta$ search, the KamLAND-Zen 800 experiment was conducted with a total xenon amount of 745 kg from 5 February 2019 to 12 January 2024. During this period, amplifiers were introduced for the low-gain PMTs, as described in Sec. 3.8, which suppressed the degradation of the energy resolution and thereby reduced $2\nu\beta\beta$ events in the energy ROI. Furthermore, high-background periods caused by radioactive impurities were excluded using a machine-learning technique. A detailed estimation of long-lived Xe spallation products was also performed. As shown in Fig. 3.16, the data set was fitted by separating it into single data (SD) and long-lived data (LD).

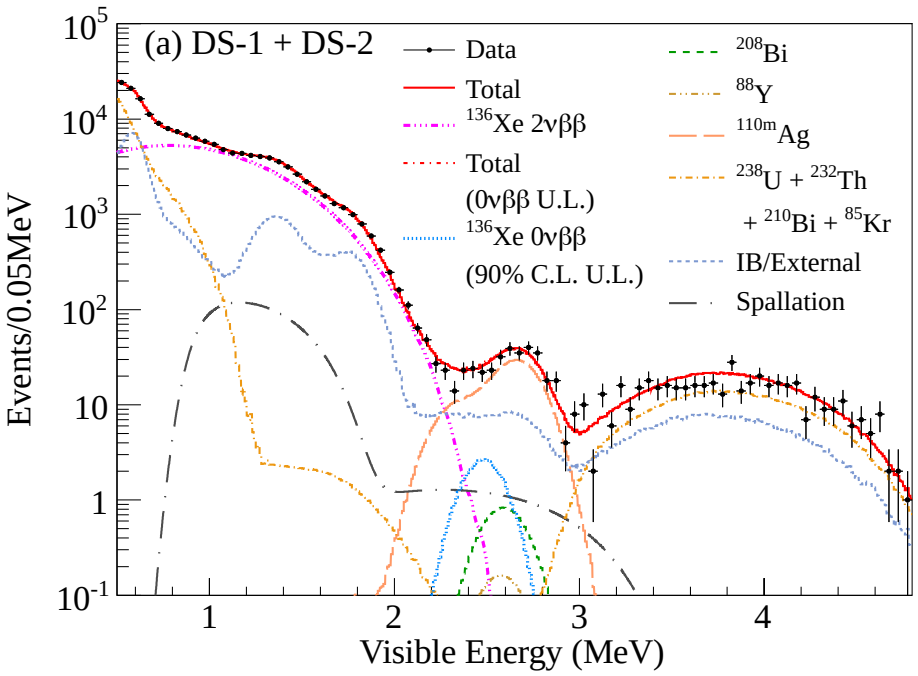

Figure 3.15: Observed energy spectrum in KamLAND-Zen400 phase1 [69]

Using the full KamLAND-Zen 800 data set, the analysis placed the world's most stringent limit on the $0\nu\beta\beta$ decay half-life of ^{136}Xe, given by

$$T_{1/2}^{0\nu\beta\beta} > 3.8 \times 10^{26}\,\mathrm{yr}\ (90\%\ \mathrm{C.L.})$$

This corresponds to a constraint on the effective Majorana neutrino mass of

$$\langle m_{\beta\beta} \rangle < 28\text{–}122\,\mathrm{meV}.$$

The periods related to the KamLAND-Zen experiment are summarized in Tab. 3.8.

Table 3.8: Summary of KamLAND-Zen phases

Phase	Date	Amount of Xe	Size of inner balloon radius
Zen400 phase1	2011/10/12–2012/06/14	320 kg	1.54 m
Zen400 phase2	2013/12/11–2015/10/27	383 kg	1.54 m
Failed Zen800	2016/08/08–2016/11/26	-	1.92 m
Zen800	2019/02/05–2024/1/12	745 kg	1.92 m

3.7 OD Refurbishment

In the OD, PMTs reused from the former KamiokaNDE detector had gradually degraded, leading to an increase in the number of bad PMTs with few detected hits. Consequently, the OD showed a tendency toward reduced detection efficiency for muons, which in turn resulted in an increased rate of muon-induced background events. To address these issues, a refurbishment of the OD was carried out from January to April 2016. Fig. 3.17 summarizes the changes made before and after the refurbishment. The main modifications are as follows. First, based on simulation studies, the optimal number of PMTs for achieving the highest muon detection efficiency was determined to be 140. In addition, to increase the number

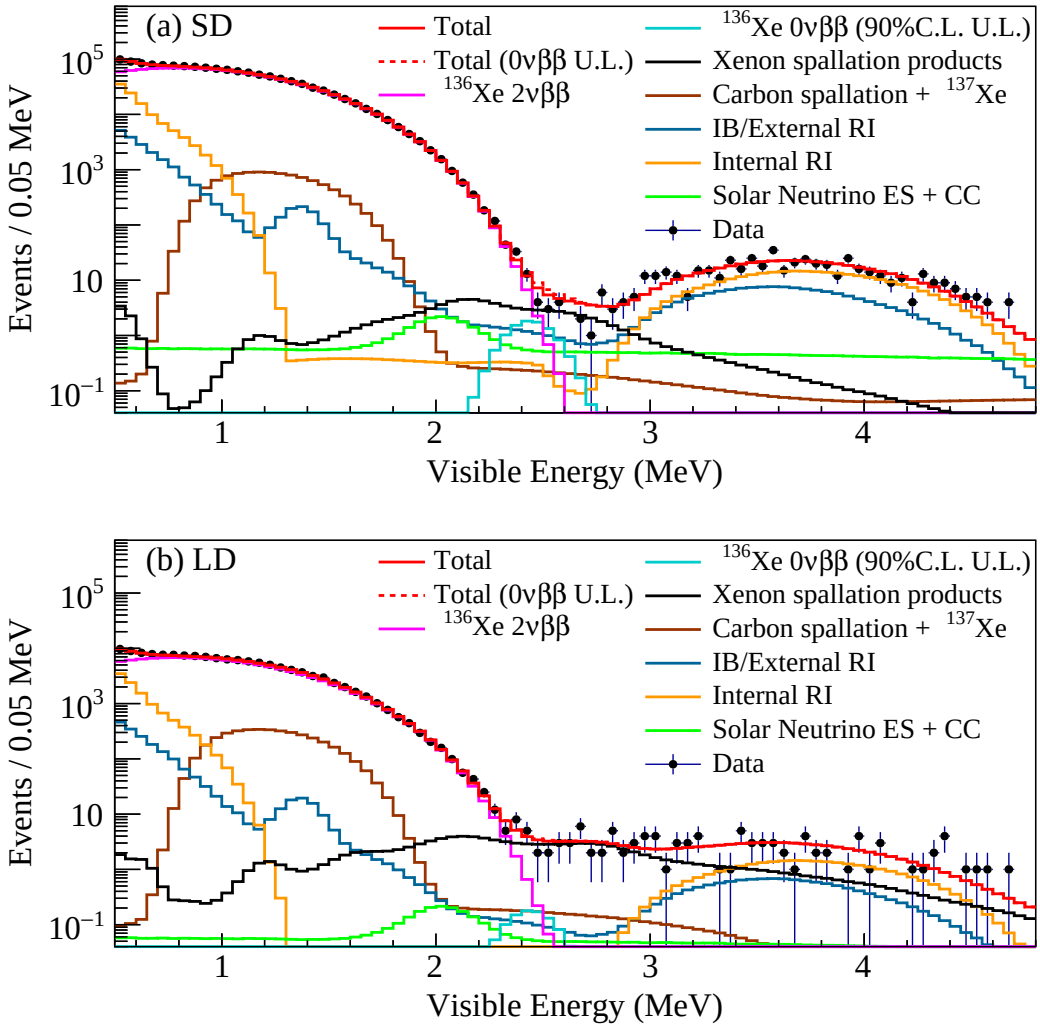

Figure 3.16: Observed energy spectrum in KamLAND-Zen800 [70]. The upper panel shows the single data (SD) and the lower panel corresponds to the long-lived data (LD).

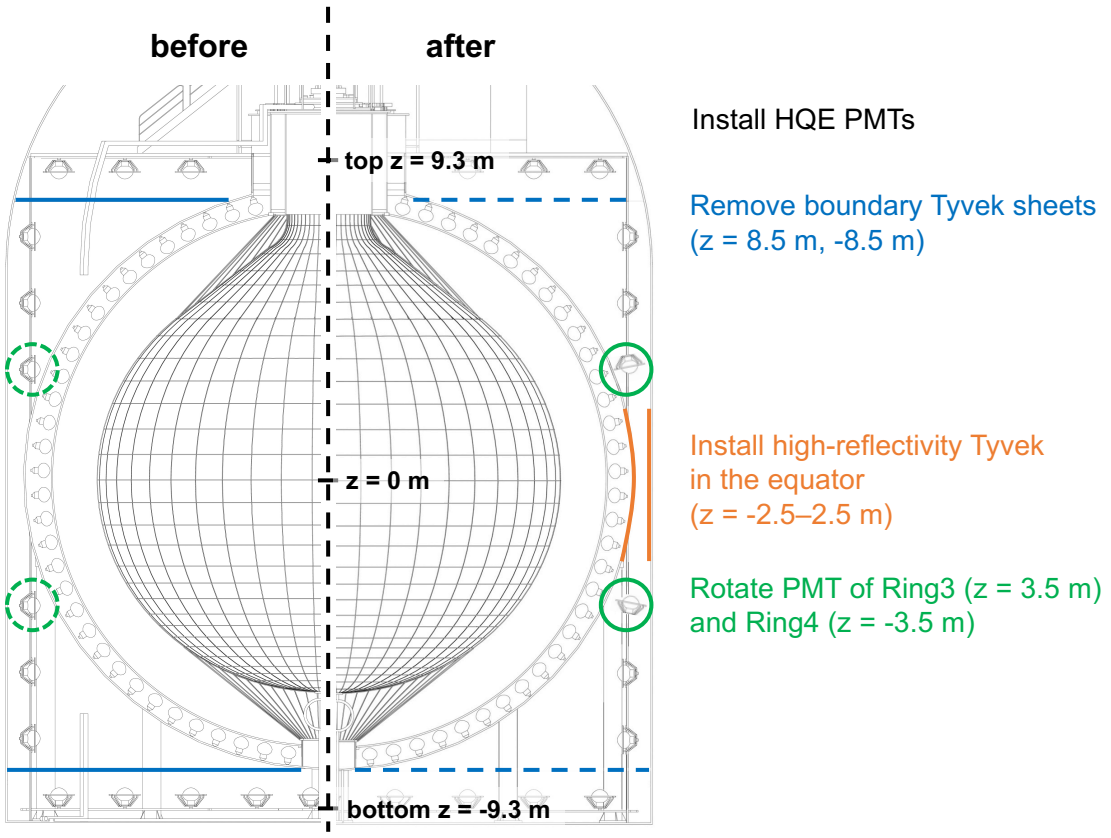

Figure 3.17: Changes before and after the OD refurbishment

of PMTs hit by photons and thereby improve the detection efficiency, the boundary Tyvek was removed. Furthermore, in the equatorial region, a high-reflectivity Tyvek sheet was introduced to enhance the detection efficiency, and the installation angle of the HQE PMTs was adjusted so that their photocathode surfaces were tilted outward by 11 degrees from the vertical direction.

3.8 HV Reduction and Amplifier Installation

As the KamLAND data-taking progressed, a phenomenon in which the impedance of PMTs suddenly drops, referred to as *low-imp*, began to be observed. PMTs affected by low-imp do not produce signals from physical events, but only noise similar to dark hits. The low-imp phenomenon occurs almost exclusively in the 17-inch PMTs, and the detailed mechanism responsible for this issue is not yet understood. However, once it was found that reducing the applied high voltage (HV) on the PMTs alleviates the load and suppresses the occurrence of low-imp, HV reductions have been performed more than 200 times. Because PMTs that have undergone HV reduction exhibit reduced gain, this leads to a deterioration of photon statistics and a decrease in the number of usable PMTs.

To mitigate this issue, the installation of signal amplifiers on the KamFEE boards was initiated in March 2020 and subsequently carried out repeatedly in 64 times. These hardware modifications introduce effects on the PMT hit information that are difficult to reproduce in the simulation. Consequently, this limits the period of data for which the deep-neural-network-based event selection can be reliably applied (see Chap. 6).

Chapter 4

Event Reconstruction and Detector Calibration

The KamLAND's ID uses 1879 PMTs, and event reconstruction is performed by observing scintillation and Cherenkov radiation. Cosmic-ray muon events with GeV-scale energies are reconstructed as trajectories and used to remove background events due to muons. On the other hand, events by $\bar{\nu}_e$ and spallation products with MeV-scale energies are reconstructed as point events. The process of event reconstruction is as follows:

1. Waveform analysis
   Event hit timing and observed charge for each PMT are calculated from the waveform data.

2. Time and charge correction
   Since the hit timing of each PMT varies depending on factors such as the observed charge and cable length, it is necessary to apply corrections for these effects.

3. Gain correction
   Each PMT records a different ADC value for the same amount of photon. Moreover, this response varies over time, so it is normalized to a predefined scale.

4. Data quality check for each PMT
   Some PMTs fail to record hit information correctly or exhibit much noise due to malfunctions or electronics issues. These PMTs are excluded from event reconstruction.

4. Muon track reconstruction
   To reduce muon-induced backgrounds, muon events are reconstructed under the assumption of track-like topology.

5. Point-like event reconstruction

4.1 Waveform Analysis

In the waveform analysis, hit time and charge are estimated from the analog signal waveform of each PMT; the signal waveform acquired by DAQ consists of 128 ADC samples with a sampling rate of approximately 1.49 ns.

The signal waveform has an offset, called a pedestal, the magnitude of which varies with each PMT. The offset is estimated from the 50 signal waveforms that are acquired at the beginning of each run[1]. The signal waveforms, from which offsets are subtracted, are smoothed to remove high-frequency noise. Even after smoothing, the baseline of the signal waveform may vary from 0 due to the influence of the previous event, so the baseline is set

[1] Observations in KamLAND are separated by a day, which are referred to as runs.

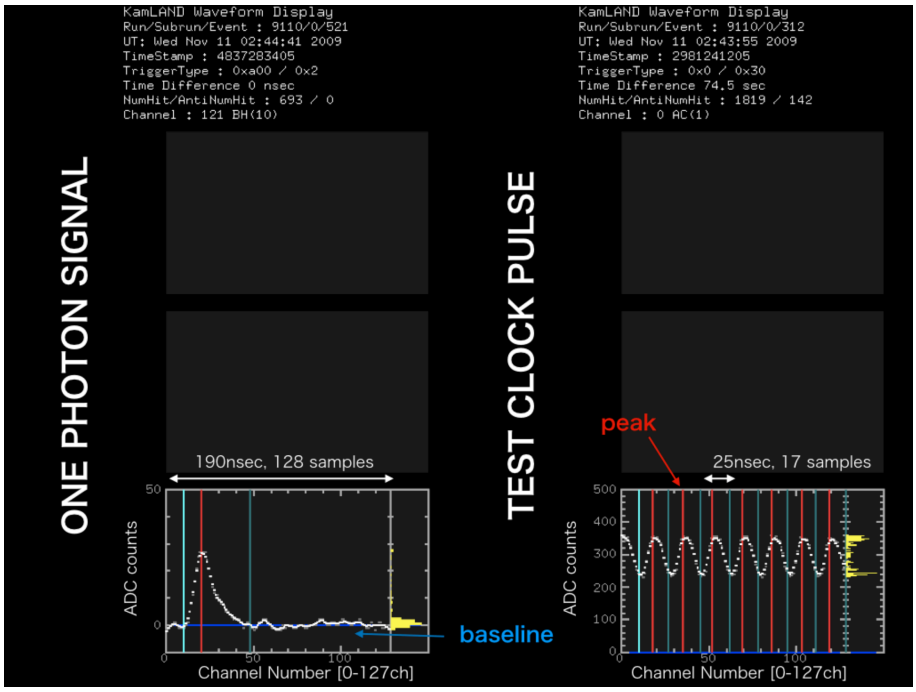

Figure 4.1: Typical 1 p.e. signal waveform (left) and clock pulse waveform (right) [62]. In the signal waveforms, the red vertical lines represent the peak positions, the light blue vertical lines represent the rising and ending positions, and the blue horizontal lines represent the recalculated baseline. In the clock pulse waveform, the spacing is 25 ns.

to 0 again here. The derivative of the waveform is then taken to determine the positions of the rise, peak, and end of the waveform, respectively. The signal time is defined as the rise time of the waveform, and the signal charge is defined as the area of the waveform from rise to end. The time width of each ADC sample is calibrated with a clock of 40 MHz for FBE. In this calibration, the time information for each PMT is corrected and used later in timing correction as T_{trigger}. A typical 1 p.e. signal waveform and 40 MHz clock pulse waveform are shown in Fig. 4.1.

4.2 Time and Charge (TQ) Correction

The time-charge correlations for each PMT differ due to variations in their quantum efficiency, gain, and noise characteristics, as well as differences in the connected electronics. To account for these effects, corrections to the timing response of each PMT are applied using calibration data from a dye-laser. Subsequently, run-dependent variations in time-charge correlations are further corrected using ^{60}Co source calibration events and ^{40}K evens which originates from materials of the miniballoon.

4.2.1 Laser Timing Calibration

Time and charge corrections for each PMT are performed using pulsed dye-laser calibration. Fig. 4.2 shows the schematic view of dye-laser calibration. The laser, which emits green light at a wavelength of 500 nm—longer than the absorption edge of the liquid scintillator (∼400 nm)—is located in the KamLAND control room to avoid inducing electrical noise near the detector. The light is delivered to the detector via an optical fiber and diffused isotropically by a diffuser ball placed at the detector center. A dedicated 2-inch PMT is

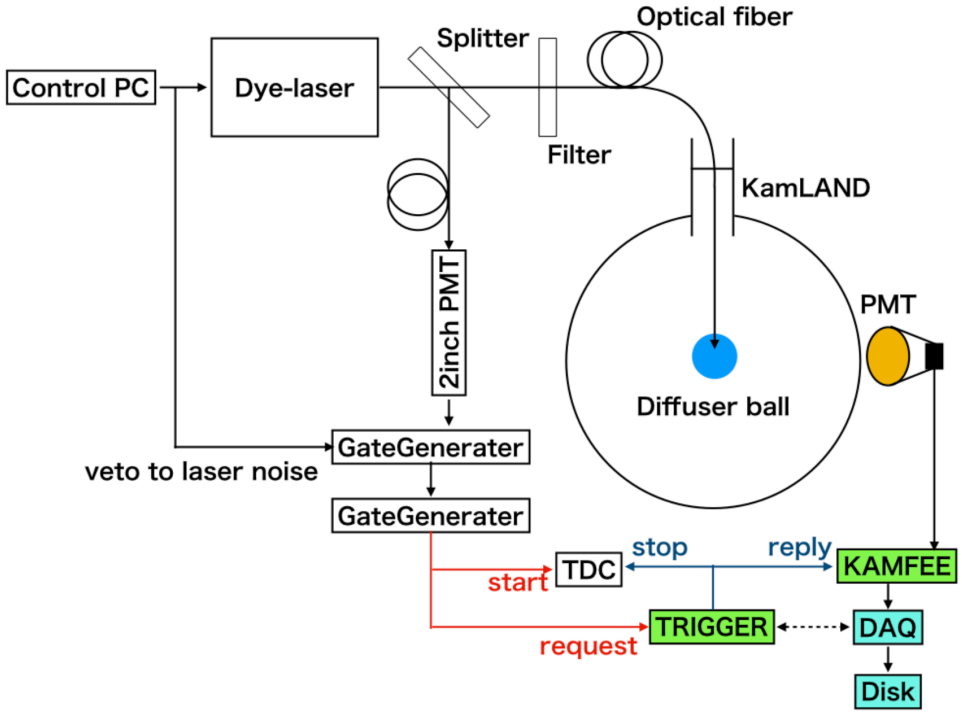

Figure 4.2: Schematic view of dye-laser calibration [62]

.

used to monitor the laser intensity and provide timing triggers to KamFEE. Measurements are carried out at various light intensities to study the timing response over a wide charge range. The PMT timing response as a function of observed charge Q is modeled as

$$T(Q)_{\text{laser}} = P_0 + P_1 \times (\log_{10} Q) + P_2 \times (\log_{10} Q)^2, \tag{4.1}$$

where P_0, P_1, and P_2 are fit parameters determined by comparing photon arrival times across PMTs. Fig. 4.3 shows the time-charge correlation in the dye-laser timing calibration data.

4.2.2 Cable Delay by BLR Installation

In 2009, BaseLine Restorer (BLR) was installed between the PMTs and FBEs, resulting in the extension of signal cables. This modification introduced additional timing delayed, summarized in Tab. 4.1. This correction is referred to as the cable delay offset T_{cable}. The delay depends on the PMT type and the physical location of the VME crate, and is categorized into four values accordingly. These delays were measured using an oscilloscope at the time of installation. Note that the signal cables for the 20-inch OD PMTs were not extended, and thus no timing offset is introduced for them.

4.2.3 Timing Calibration with ^{60}Co Source Run

Before the start of the KamLAND-Zen 400 experiment, the time variation of PMT latency after laser calibration was monitored using regular calibration runs with a ^{60}Co source. The source, which emits 1173 keV and 1333 keV gamma rays isotropically, was placed at the center of the detector approximately every two weeks. Since the photon arrival times at all PMTs are expected to be identical, deviations in the measured hit times reflect variations in the PMT transit time. This timing offset is defined as $T_{\text{run}}^{\text{Co}}$.

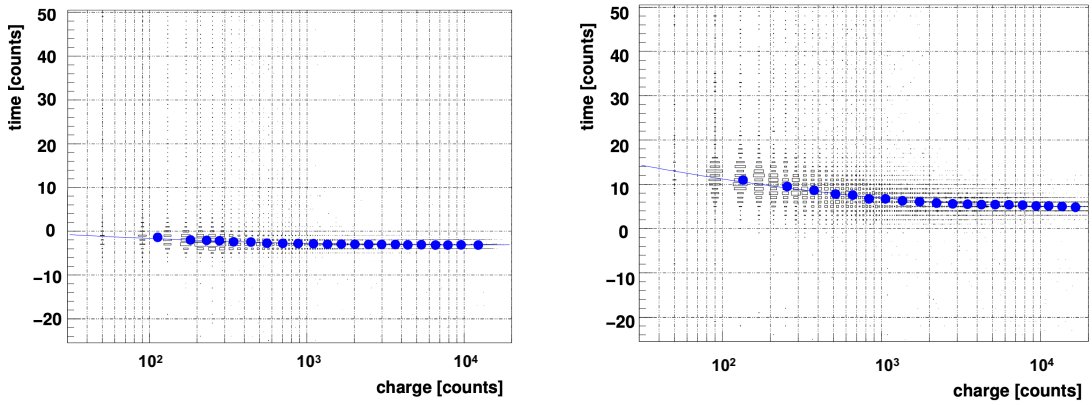

(a) 17-inch PMT (b) 20-inch PMT

Figure 4.3: Time-charge correlation in the dye-laser timing calibration data for (a)17-inch PMT and (b)20-inch PMT [71]. The blue curve represents the fitting function given in Eq. 4.1.

Table 4.1: Cable length and delay for BLR installation

Channel	Cable length [m]	Delay [nsec]
ID 17-inch in the upper VME crates	1.92	8.4
ID 17-inch in the lower VME crates	4.43	23.4
ID 20-inch in the upper VME crates	0.44	2.4
ID 20-inch in the upper VME crates	1.50	9.9

4.2.4 Timing Calibration with ^{40}K on PEEK Material

During the KamLAND-Zen 400 and 800 periods, calibration using a ^{60}Co source was no longer possible, as the inner balloon was installed at the detector center. Instead, a Poly Ether Ether Ketone (PEEK) pipe—serving as the connection between the inner balloon and the corrugated tube at the top of the detector—was utilized as an alternative timing calibration source. This PEEK tube contains ^{40}K, which emits sufficiency gamma rays for run-by-run timing calibration. The tube is located at approximately $(x, y, z) = (0, 0, 4.3\,\mathrm{m})$ for KamLAND-Zen 400 and $(x, y, z) = (0, 0, 5.5\,\mathrm{m})$ for KamLAND-Zen 800.

Modeling of reference function

To construct the reference timing function, data from the initial runs of the KamLAND-Zen 400 and 800 periods are used, during which the time jitter was minimal. Selected ^{40}K events are required to satisfy the following criteria:

- Muon and 2 ms after muon events are vetoed
- Radius selection: $\sqrt{x^2 + y^2} < 0.8\,\mathrm{m}$
- Vertical position: $4.2 < z\,[\mathrm{m}] < 4.8$ (Zen400), $5.3 < z\,[\mathrm{m}] < 6.5$ (Zen800)
- Number of KamFEE channel which detect PMT hit, NsumMax
  - Zen400: NsumMax > 210
  - Zen800: NsumMax > 160

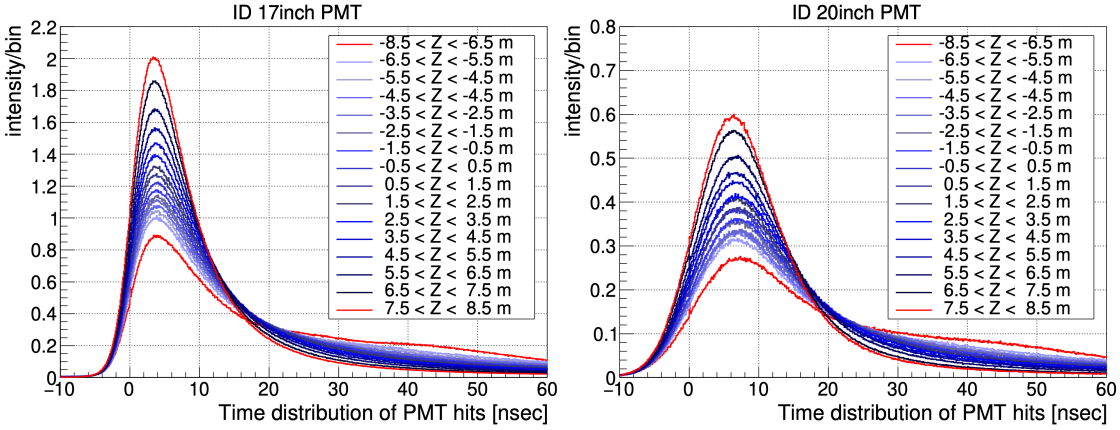

Figure 4.4: Reference functions of hit timing fitting for Zen400. The left panel shows the functions for 17-inch PMTs and the right panel shows for 20-inch PMTs. Reference hit functions are created for each z range.

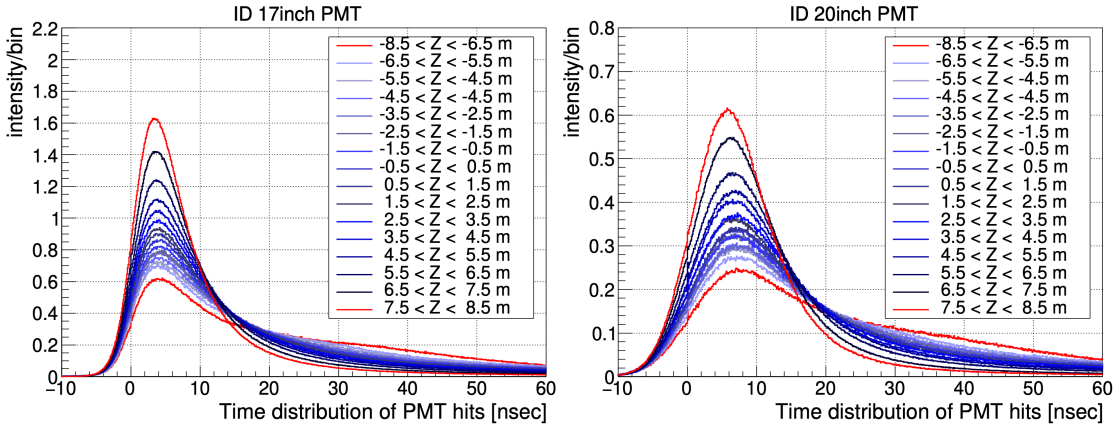

Figure 4.5: Reference functions of hit timing fitting for Zen800. The left panel shows the functions for 17-inch PMTs and the right panel shows for 20-inch PMTs. Reference hit functions are created for each z range.

PMTs are grouped into 16 categories based on their z-positions, with each group spanning 1 m. The lowest region, however, spans 2 m due to limited statistics. For each group, hit timing distributions (after time-of-flight subtraction) are aligned by their half-maximum point, and averaged after removing outlier shapes to form reference templates. This classification helps account for the dependence of photon travel time on PMT z-position. The normalized reference functions for KamLAND-Zen 400 and 800 are shown in Fig. 4.4 and Fig. 4.5, respectively.

Run-by-run fitting

For run-by-run timing calibration, the shift from the reference timing function is estimated by fitting observed timing distributions over a time window of −50-130 ns. Fig. 4.6 shows examples of hit timing distribution with the best-fit reference function. The timing offset for each run is defined as

$$T_{\mathrm{run}}^{\mathrm{PEEK}} = T_{\mathrm{fit}}^{\mathrm{PEEK}} - T_{\mathrm{ref}}^{\mathrm{PEEK}}, \tag{4.2}$$

where $T_{\mathrm{fit}}^{\mathrm{PEEK}}$ is the fitted timing value for the current run, and $T_{\mathrm{ref}}^{\mathrm{PEEK}}$ is the reference value. If a PMT was excluded from the reference due to bad status but later becomes usable (e.g.,

after amplifier replacement), its reference value is inferred from neighboring PMTs.

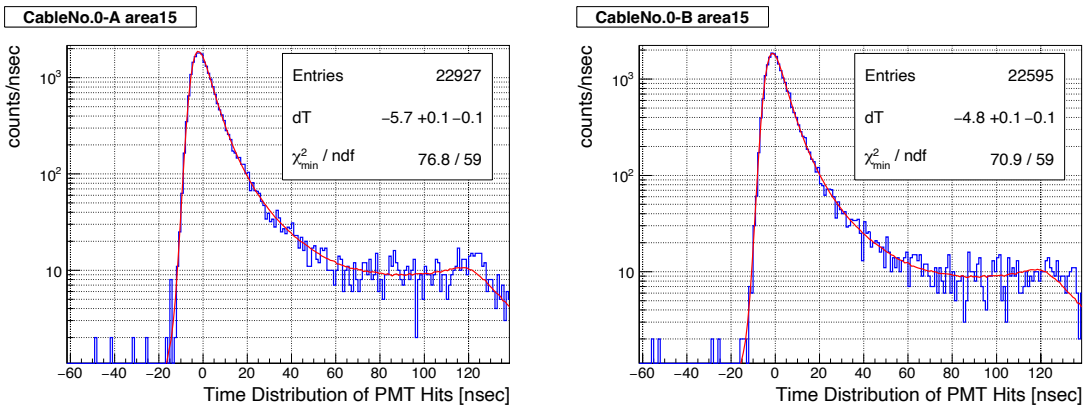

Figure 4.6: Examples of hit timing distribution with the best-fit reference function. The left panel shows the fitting result for ATWD A and the right panel shows for ATWD B.

4.2.5 Summary of Time Correction

The total timing correction factor is expressed as follows:

$$T_{\text{correction}} = T_{\text{trigger}} + T_{\text{laser}} + T_{\text{cable}} + T_{\text{run}}, \tag{4.3}$$

where T_{trigger} is the trigger timing offset described in Sec. 4.1; T_{laser} is the charge dependent timing offset from laser calibration, as described in Sec. 4.2.1; T_{cable} is the timing offset due to cable delays discussed in Sec. 4.2.2; and T_{run} is the run-dependent time correction, described in Sec. 4.2.3 for the period before KamLAND-Zen 400 and in Sec. 4.2.4 for the period after.

4.3 Gain Correction

In KamLAND analysis, the gain of each PMT is defined as the ADC value corresponding to a 1 p.e. signal. This value is normalized to the reference value of 700 ADC counts per p.e., which was set at the beginning of the experiment. This gain varies from run to run due to changes in PMT characteristics and electronics conditions over time. Therefore, gain calibration is performed for each run using low-energy events that are expected to contain 1 p.e. signal. The gain calibration procedure differs between the 17-inch and 20-inch PMTs due to their different charge resolutions.

17-inch gain correction

The 17-inch PMTs, which have good charge resolution, exhibit a clear 1 p.e. peak and are calibrated using the average charge of this peak obtained via Gaussian fitting. Events used for this correction are selected based on the following criteria:

- Muon and noise event veto
- 2 ms veto after muon to avoid afterpulses and overshoots
- 100 μs veto after any preceding event to avoid digitizer dead time

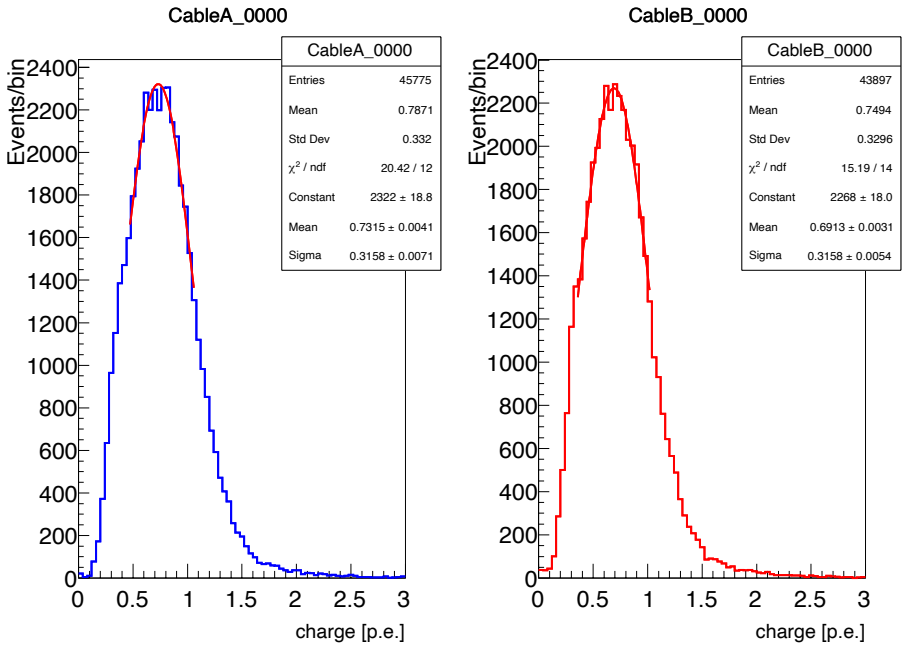

Figure 4.7: Examples of 1 p.e. charge distributions for a 17-inch PMT. Red curves show the Gaussian fit function.

- Selection for the number of hit 17-inch PMTs, N_{hit}, assuming low-energy event
  - before purification: $120 < N_{\text{hit}} < 180$
  - after purification: $120 < N_{\text{hit}} < 230$
- Distance between the event and each PMT $> 5.6\,\text{m}$
- Single peak in the waveform

Fig. 4.7 shows examples of the 1 p.e. charge distribution and Gaussian fit. The fitted mean is used to derive the gain correction factor for each channel. The goal of the calibration is to align the fitted mean to 1 p.e.

20-inch gain correction

The 20-inch PMTs, originally developed for the Kamoikande experiment over 40 years ago, suffer from poor charge resolution and do not exhibit a distinct 1 p.e. peak. As a result, direct gain calibration using low-energy events is not feasible. Instead, their gain is inferred by comparing the charge observed in each 20-inch PMT to the average charge in neighboring 17-inch PMTs. The gain ratio for the j-th 20-inch PMT is defined as

$$\text{ratio}_j = \frac{Q_{20}^j}{\langle Q_{17} \rangle_{\text{neighbor}}} \times \left(\frac{17}{20}\right)^2, \tag{4.4}$$

where $\langle Q_{17} \rangle_{\text{neighbor}}$ is the average charge of 5–8 surrounding gain-corrected 17-inch PMTs. This ratio is determined using high-charge muon events, which provide better signal statistics and reduce the impact of timing and charge resolution limitations. The event selection criteria for high-charge muon events include:

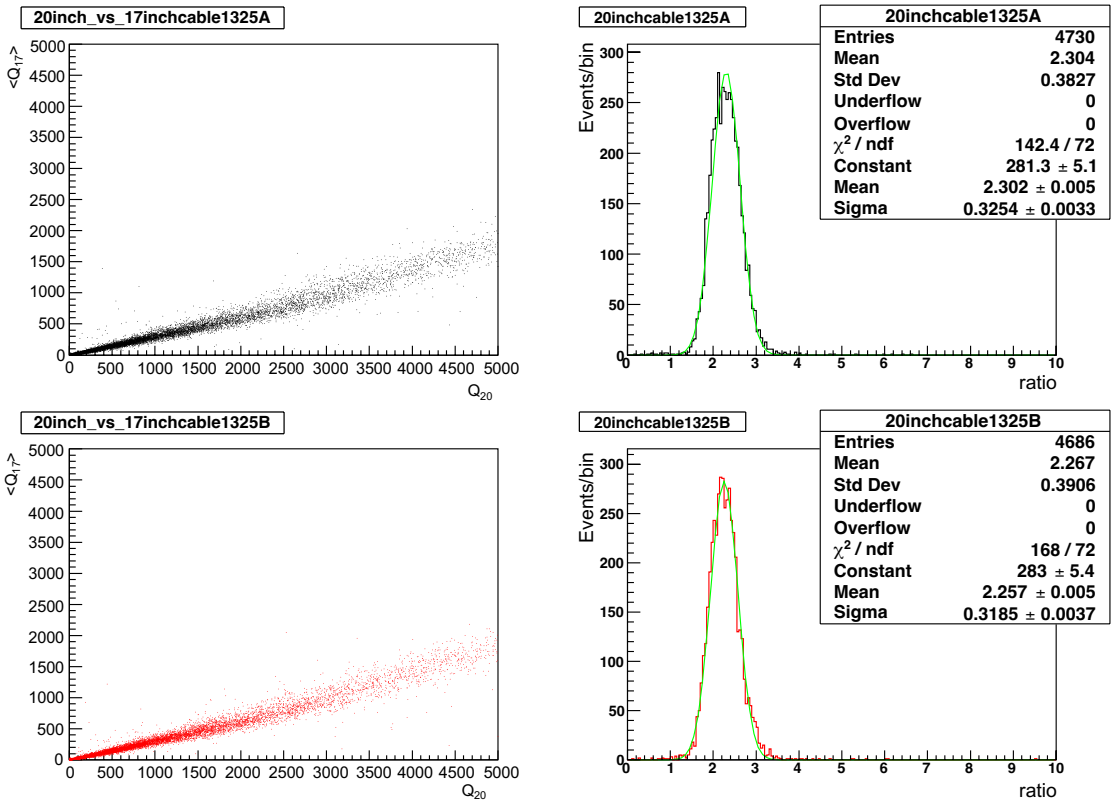

Figure 4.8: Examples of charge ratio for a 20-inch PMT and its correlation with neighboring 17-inch PMTs. Light green curves show the Gaussian fit function to decide mean charge ratio.

- Noise and non-muon event veto
- NsumMax ≥ 1000
- Observed charge in ID, $Q_{\mathrm{ID}} \geq 10000$

For selecting reference 17-inch PMTs, the following conditions are applied:

- Bad channel veto
- Low statistics channel veto ($N_{\mathrm{hit}} < 100$)
- Charge selection for each 17-inch PMT: $1.0 < Q_{17}^{i}$ [p.e.] < 10000
- Average charge selection for neighboring 17-inch PMTs: $300 < Q_{17}^{\mathrm{average}}$ [p.e.] < 5000

Fig. 4.8 shows examples of charge ratio for a 20-inch PMT and its correlation with neighboring 17-inch PMTs.

Fig. 4.9 and Fig. 4.10 show time variation of average 17-inch and 20-inch PMT gain, respectively.

4.4 Bad Channel Selection

Although many PMTs are installed in KamLAND, not all of them operate properly throughout the experiment. Some PMTs exhibit abnormal behavior such as low hit rates, unusual

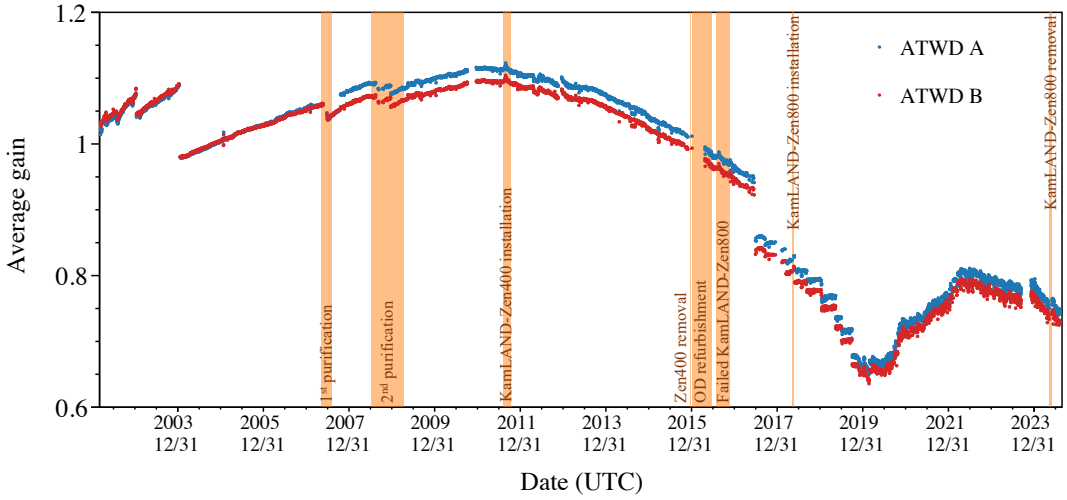

Figure 4.9: Time variation of average 17-inch PMT gain. Blue points represent gain for ATWD A and red points represent gain for ATWD B. The orange-shaded regions correspond to periods with on-site work. Gaps outside these regions indicate periods excluded from the analysis due to DAQ malfunctions or degraded data quality.

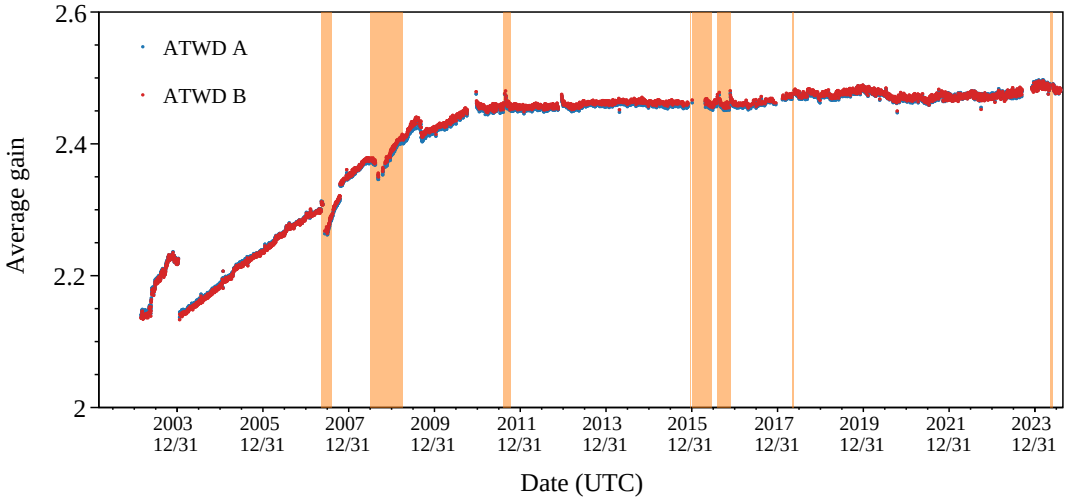

Figure 4.10: Time variation of average 20-inch PMT gain

charge distributions, or unstable gains. These issues are often caused by malfunctions, high-voltage instabilities, or failures in the signal readout electronics. These PMTs are classified as *bad channels* and are excluded from the analysis to prevent systematic bias. The list of bad channels is maintained as a table data and updated on a run-by-run bias, reflecting the time-dependent characteristics of the detector status. The selection criteria for selecting bad channels among ID PMTs are as follows:

- Low hit rate in the first 10000 event of a run
  Channels with reduced response due to electronic failure are identified.
  - PMT hit < 1000 (until purification end)
  - PMT hit < 800 (for one year after purification)
  - PMT hit < 1000 (until the end of data taking)
- Missing waveform events > 1000 in the first 10000 events
  Channels affected by high-voltage or readout issues are selected.
- Hit rate < 80 in 100 high-charge muon events
  Extremely low gain PMTs independent of gain correction are excluded.
- Low hit rate in 10000 events excluding muon events
  Low-response channels at lower energy are detected.
  - PMT hit < 800 (before KamLAND-Zen 400)
  - PMT hit < 480 (after KamLAND-Zen 400)
- Large hit rate rate difference between ATWD-A and B channels
  This criteria is used to identify electronic failures.
  - diff > 0.22 (until April 2015)
  - diff > 0.25 (April 2015–January 2021)
  - diff > 0.18 (after January 2021)
- Significant charge deviation from neighboring PMTs
  PMTs with charge response significantly different from adjacent PMTs, excluding known low/high-gain neighbors, are assigned as bad channels as follows:

$$\frac{1}{N_i}\sum_{j=1}^{N_i}\frac{(Q_i-\bar{Q}_{\text{neighbor}})^2}{\bar{Q}_{\text{neighbor}}} > 1000\,[\text{p.e.}], \tag{4.5}$$

  where N_i is the number of event used for i-th PMT's bad channel selection, Q_i is the charge observed by the i-th PMT, which is being evaluated for classification as a bad channel, and $\bar{Q}_{\text{neighbor}}$ is average charge of neighbor 17-inch PMTs.
- Abnormal gain values
  - 17-inch PMTs: gain ≤ 0.4 or ≥ 4.0
  - 20-inch PMTs: gain ≤ 0.4 or ≥ 6.0

For OD PMTs, the criterion is:

- Hit rate < 5 in energetic muon events

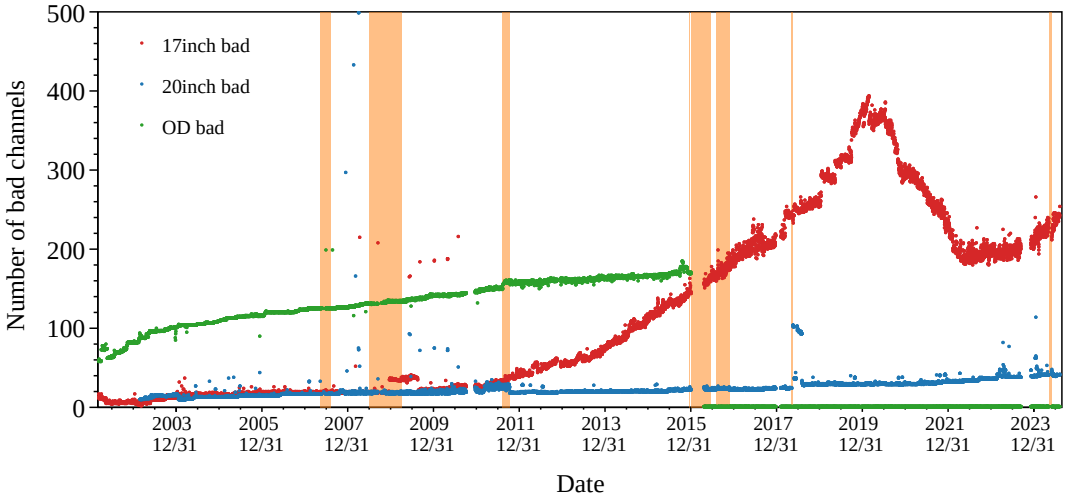

Figure 4.11: Time variation of the number of bad channels. Red, blue, and green points correspond to 17-inch, 20-inch, and OD PMT respectively. After OD refurbishment, the number of OD PMTs was reduced to one. The 20-inch PMTs were turned on after March 2003.

Fig. 4.11 shows the time variation of the number of bad channels identified by the above criteria. In particular, the number of OD bad channels increased over time due to waterproofing failures until the OD refurbishment in 2016. During the refurbishment, all OD PMTs were replaced; however, one PMT failed shortly after replacement. The increase in 17-inch bad channels is primarily attributed to the rise in low-gain PMTs. In this analysis, the impact of these increasing bad channels is treated as a quenching effect.

4.5 Dark Charge Estimation

PMTs may occasionally record *dark charge* even when no photoelectron is incident on the photocathode. Such signals originate from thermal electron emissions from the photocathode or noise from the electronics. Because dark charge is not correlated with physical scintillation events, it can be estimated using an offtime window of 50 ns, while energy and vertex reconstructions use an ontime window (see Fig. 4.12).

The dark charge is defined as the average charge per hit PMT in the offtime window, and is calculated using the following equation:

$$\text{dark charge} = \frac{\text{total charge of hit PMTs in the offtime window}}{\text{number of hit PMTs in the offtime window}} \tag{4.6}$$

This estimation is performed for each run, and the resulting value is subtracted from the observed charge during event reconstruction to reduce systematic uncertainties caused by dark charge. Since dark charge is affected by various detector and environmental conditions—such as LS convection or temperature—higher values are observed during or after the LS purification periods and other on-site works as shown in Fig. 4.13.

4.6 Muon Track Reconstruction

Because KamLAND is located 1000 m underground, the flux of cosmic ray muons is suppressed to about 10^{-5} compared to the ground level. However, cosmic-ray muons still arrive

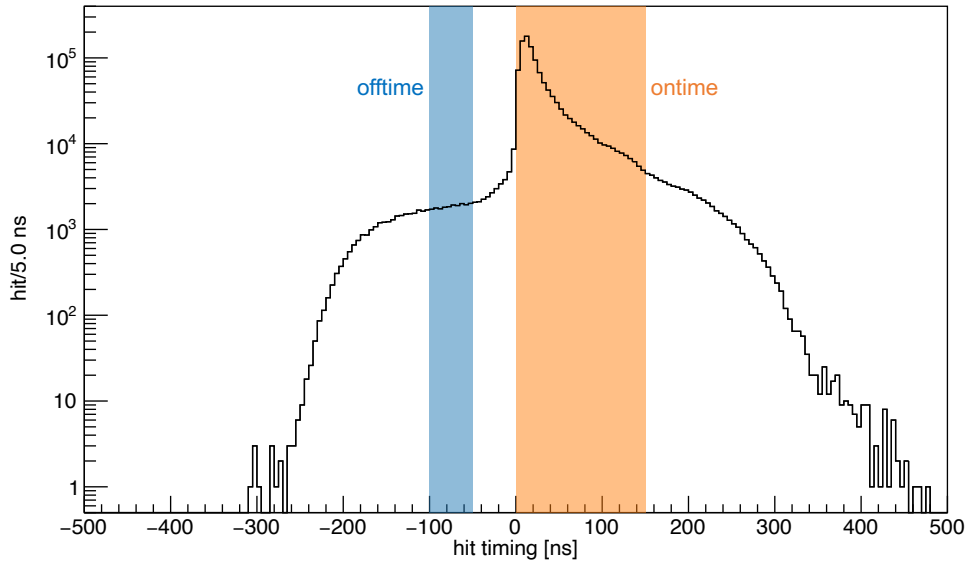

Figure 4.12: Hit timing distribution. The blue shaded time window corresponds to the offtime window, which is used for dark charge estimation. On the other hand, the orange shaded region corresponds to the ontime window, which is used for the energy and vertex reconstruction.

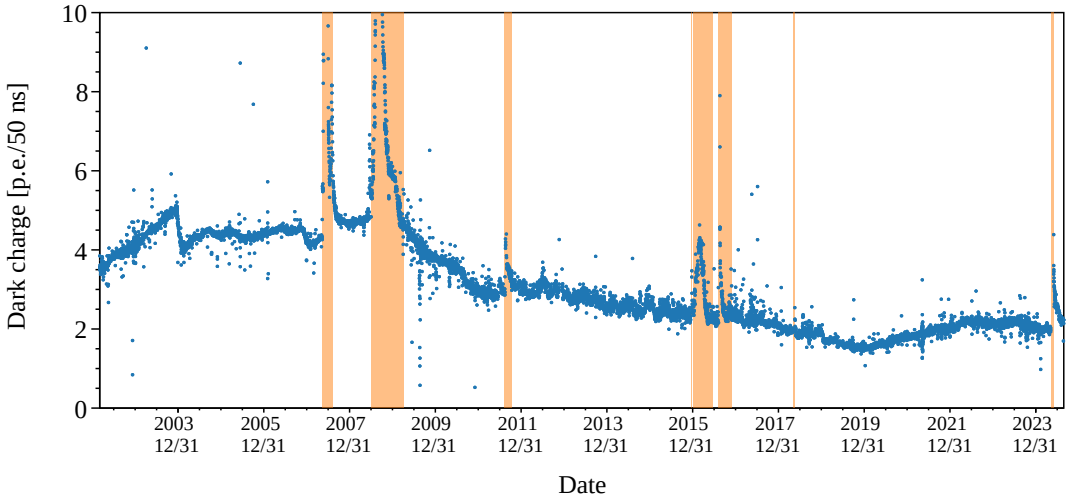

Figure 4.13: Time variation of dark charge

at the KamLAND detector with a frequency of about 0.3 Hz. Such muons interact with materials around the detector to produce high-energy neutrons or shatter carbon nuclei in the detector to form unstable nuclei. The events originating from such reactions are used to evaluate the accuracy of event reconstruction or serve as background events in observations. Therefore, event reconstruction of cosmic-ray muons is very important for the KamLAND experiment. In this section, the trajectory reconstruction algorithm for cosmic-ray muons is described.

4.6.1 Selection Criteria for Cosmic Muon Events

When a muon flies into the detector, Cherenkov light is detected by multiple PMTs at the OD and a large amount of scintillation light is detected by the ID PMT. Therefore, the muon event is determined by tagging the ID and OD detection results as follows.

- Through going muon (scintillation muon): $Q_{17} \geq 8500$ p.e.
  muons that pass through the LS while emitting scintillation and Cherenkov light
- Clipping muon (Cherenkov muon):
  $Q_{17} \geq 500$ p.e. and $N_{200\mathrm{OD}} \geq 5$ (before OD refurbishment), 9 (after OD refurbishment)
  muons that snatched the buffer oil while emitting Cherenkov light

where Q_{17} is the amount of charge detected in 17-inch PMTs and $N_{200\mathrm{OD}}$ is the maximum number of OD PMTs hit during 200 ns. Because the number of OD PMT dark hits increased after the OD refurbishment work, The selection criteria for clipping muon has changed. Fig. 4.14 illustrates the muon selection criteria drawn on 2D plane of Q_{17} and $N_{200\mathrm{OD}}$. In addition, through going muon is further classified into two types based on the following conditions.

- Showering muon ($\Delta Q > 7.5 \times 10^5$ p.e.)
- Non-showering muon ($\Delta Q < 7.5 \times 10^5$ p.e.)

ΔQ is called the residual charge and referred in Sec. 4.6.3.

Of these muons, approximately 90% of the muons observed in KamLAND are non-showering muons. Muon events for which sufficient light intensity was not observed in the trajectory reconstruction described below are called *miss reconstructed muons*. The 17-inch PMT charge distribution of the muon events classified in this way is shown in Fig. 4.15.

As illustrated in Fig. 4.16, the muon rate in KamLAND is estimated from the distribution of time intervals between successive muon events, yielding a value of approximately 0.31 Hz. Fig. 4.17 presents the time variation of the muon rate, indicating that muons are observed at nearly uniform intervals.

4.6.2 Algorithm of Muon Track Reconstruction

Muons entering the KamLAND detector emit Cherenkov light, which is radiated at a fixed Cherenkov angle θ_C. In addition, through-going muons also produce isotropic scintillation light. To determine the incident position of such muons using the scintillation light, the timing information from the first photons detected by the PMTs is utilized.

Let θ be the angle between the muon track and the trajectory of the scintillation photon that first reaches a PMT. If t_0 denoted the time when the muon enters the ID, t the time when the scintillation photon reaches the PMT, and n the refractive index of the LS, then their relationship can be expressed as follows:

$$t = t_0 + \frac{l}{c} + \frac{(z-l)/\cos\theta}{c/n} = t_0 + \frac{z - \rho/\tan\theta}{c} + \frac{\rho/\sin\theta}{c/n}, \tag{4.7}$$

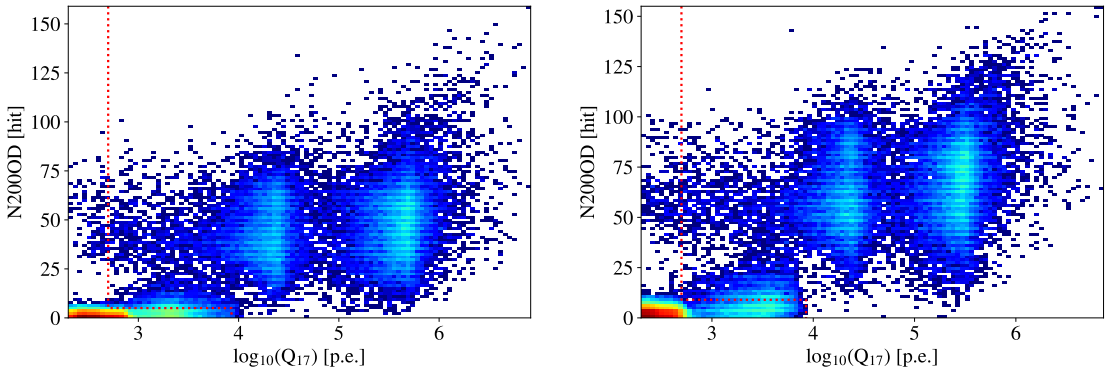

Figure 4.14: Muon selection criteria. The left panel shows data taken before OD refurbishment, while the right panel corresponds to data after OD refurbishment. The red dotted lines indicate the selection criteria: through going muons are identified by $Q_{17} > 8500$ p.e., and clipping muons by $Q_{17} > 500$ p.e. and $N_{200\mathrm{OD}} \geq 5$ or ≥ 9, depending on the period (before or after OD refurbishment, respectively).

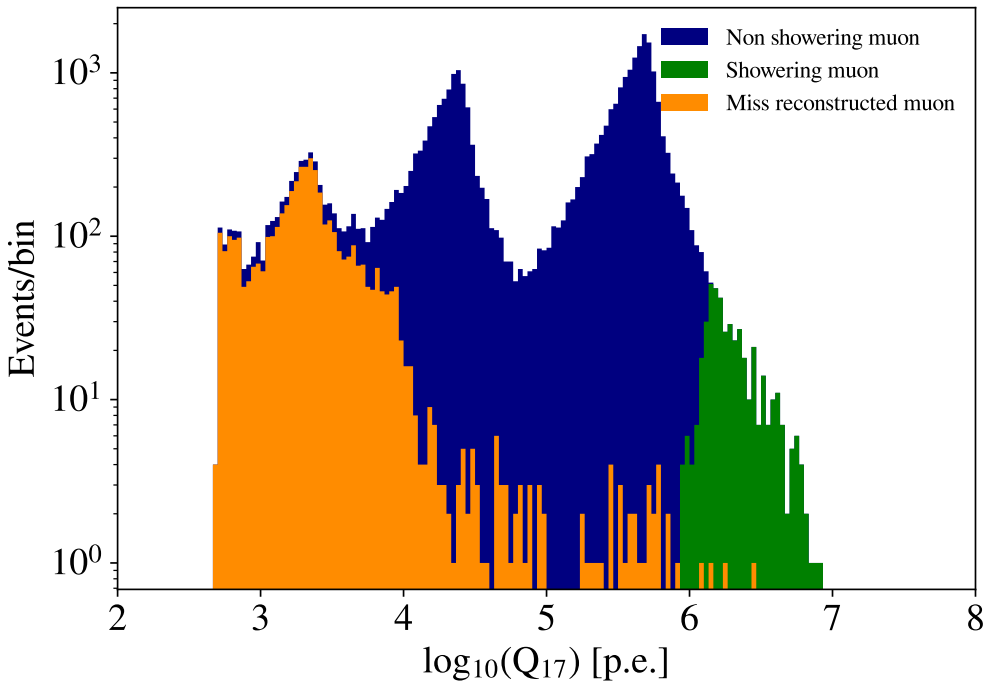

Figure 4.15: Charge distribution of muon events observed on 17-inch PMT

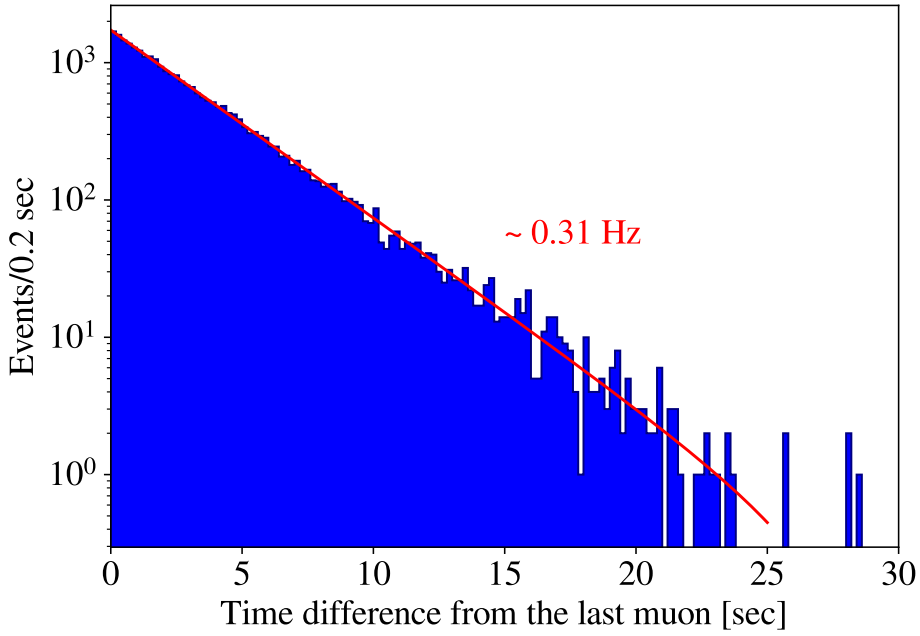

Figure 4.16: Distribution of time difference between muon events

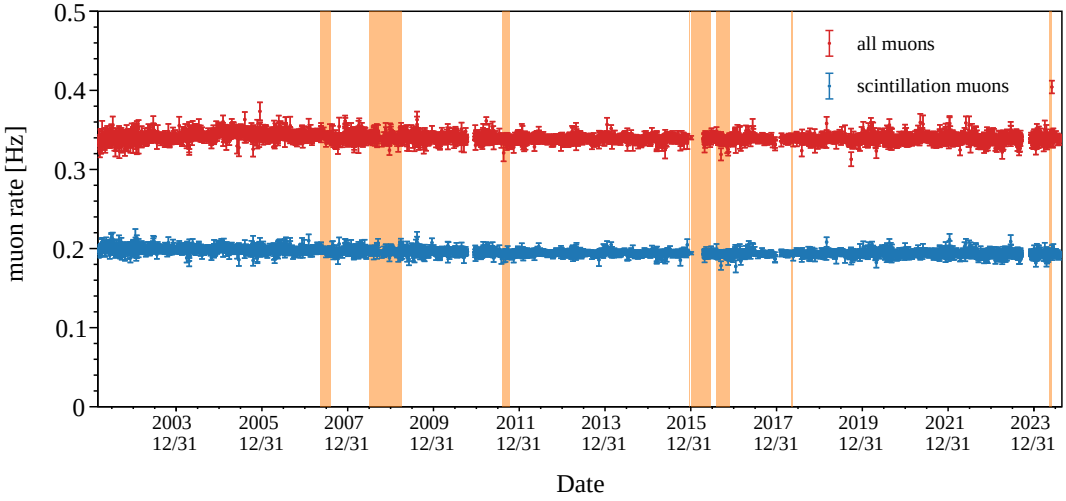

Figure 4.17: Time variation of muon events

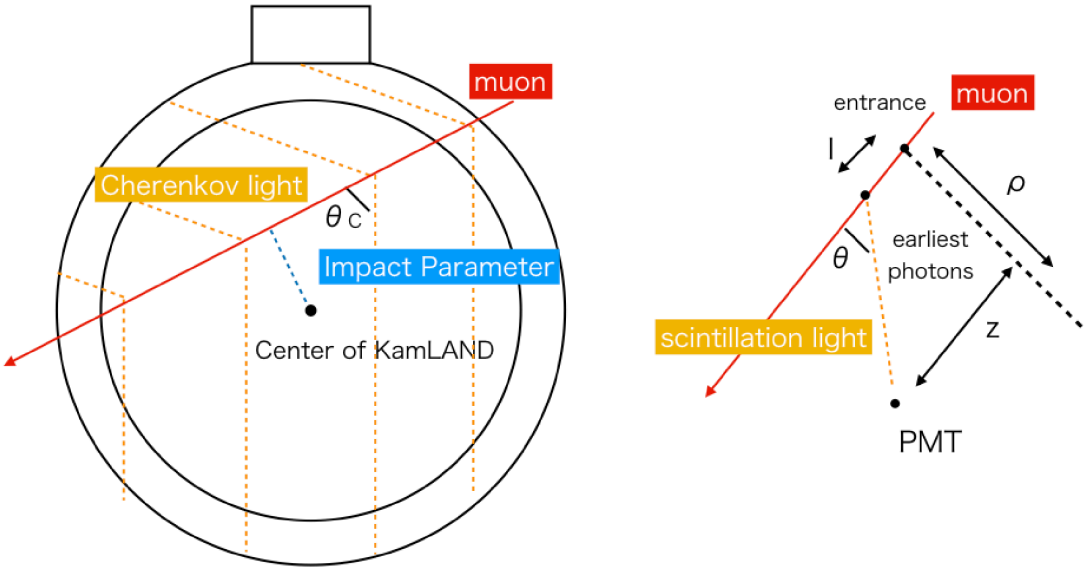

Figure 4.18: Schematic view of muon track reconstruction [62]. As shown in the left panel, muons emit Cherenkov light at a fixed angle θ_C. In addition, as illustrated in the right panel, they emit isotropic scintillation light while traversing the LS. In this context, the point where the muon enters the ID is referred to as the *entrance*. The distance from the entrance to the light emission point is denoted as l, the distance from the muon track to the PMT as ρ, and the projection of the distance from the entrance to the PMT along the muon trajectory as z.

where l, θ, and z are defined as illustrated in Fig. 4.18. By minimizing t with respect to θ (solving $dt/d\theta = 0$), the condition for the minimum θ is found to be

$$\cos\theta = \frac{1}{n}. \tag{4.8}$$

This condition is identical to that of the Cherenkov angle θ_C. Therefore, the determination of the muon incident position does not distinguish between scintillation and Cherenkov light, and relies solely on the first photon arrival time at each PMT. The refractive indices of the LS and buffer oil are wavelength-dependent and have been measured to range from approximately 1.44–1.47.

After the first photon is detected by the PMTs, the PMT with the highest detected charge plays a crucial role in track reconstruction. This is because the point at which the muon exits the LS is defined as the intersection between he detector center-PMT line and the balloon surface. Additionally, to avoid complications in the PMT timing analysis, PMTs located outside the Cherenkov angle are excluded from the track reconstruction.

4.6.3 Tracking Performance

The residual charge, ΔQ, is defined as the difference between the observed charge and the estimated contributions from Cherenkov and scintillation light, based on the reconstructed track length in the LS and buffer oil. The expression of ΔQ is as follows

$$\Delta Q \equiv Q_{17} - (L_{\mathrm{LS}} + L_{\mathrm{BO}}) \left\langle \frac{dQ}{dX} \right\rangle_{\mathrm{Cherenkov}} - L_{\mathrm{LS}} \left\langle \frac{dQ}{dX} \right\rangle_{\mathrm{scintillator}}, \tag{4.9}$$

where Q_{17} is the total charge observed by the 17-inch PMTs, L_{LS} and L_{BO} are the lengths of the muon tracks in LS and buffer oil. The average charge per unit length of Cherenkov

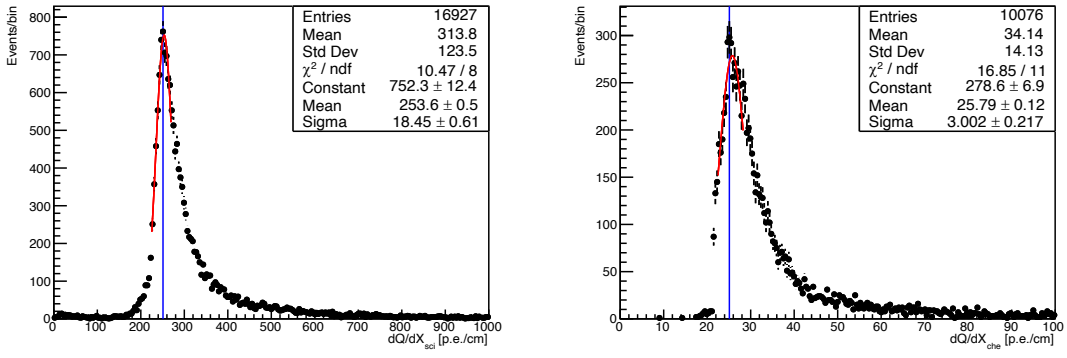

Figure 4.19: Muon charge per track length. The left panel shows the distribution for scintillation muons and the right panel shows for Cherenkov muons.

and scintillation light is expressed as

$$\left\langle \frac{dQ}{dX} \right\rangle_{\text{Cherenkov}} \equiv \frac{Q_{17}}{L_{\text{BO}}} \tag{4.10}$$

$$\left\langle \frac{dQ}{dX} \right\rangle_{\text{scintillator}} \equiv \frac{Q_{17} - L_{\text{BO}} \left\langle \frac{dQ}{dX} \right\rangle_{\text{Cherenkov}}}{L_{\text{LS}} + L_{\text{BO}}} \tag{4.11}$$

and these are obtained by fitting as shown Fig. 4.19 for each run. As described in Sec. 4.6.1, muon are classified based on their residual charge. Those with $\Delta Q > 7.5 \times 10^5$ p.e. are categorized as *showering muons,*, indicating excess light yield relative to the expected value based on the track length. On the other hand, muon with residual charge below this threshold are considered *non-showering muons*. A small subset of muons exhibit total charge significantly smaller than expected from the reconstructed track length. These are labeled *miss reconstructed muons* and are typically due to track fitting errors. Their occurrence rate among through-going muons is about 0.2%. Fig. 4.20 and Fig. 4.21 shows the time variation of scintillation/Cherenkov light charge per track length, respectively. Run-by-run monitoring of dQ/dX is essential to account for changes in detector response over time. Time variation plots reveal that the scintillation light yield has decreased, likely due to an increasing number of bad channels.

As shown in Fig. 4.22, the correlation between Q_{17} and the impact parameter, which is the shortest distance between the reconstructed muon track and the detector center, further validates the tracking algorithm. A distinct discontinuity at 650 cm corresponds to the boundary between the LS and buffer oil regions, consistent with the expected difference in light charge per unit length in each medium.

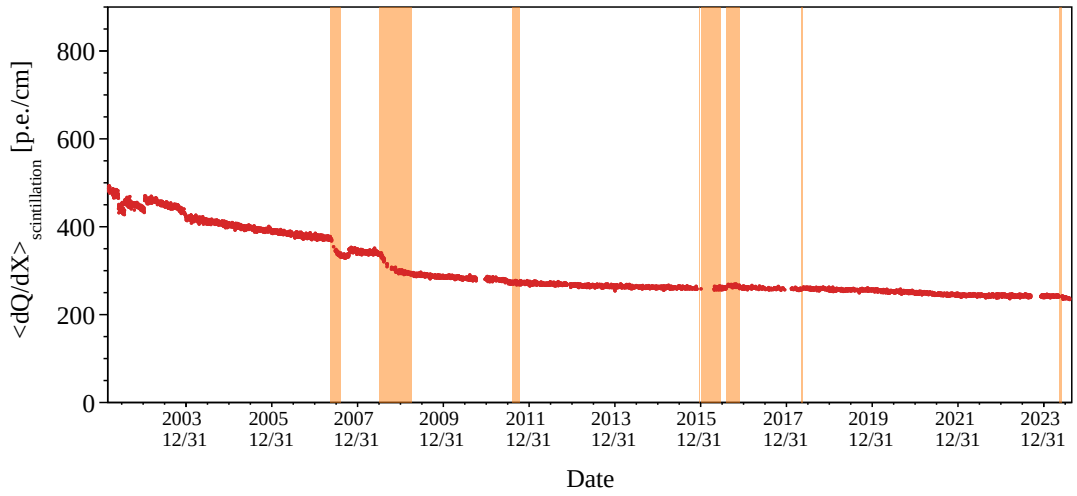

Figure 4.20: Time variation of scintillation light charge per track length

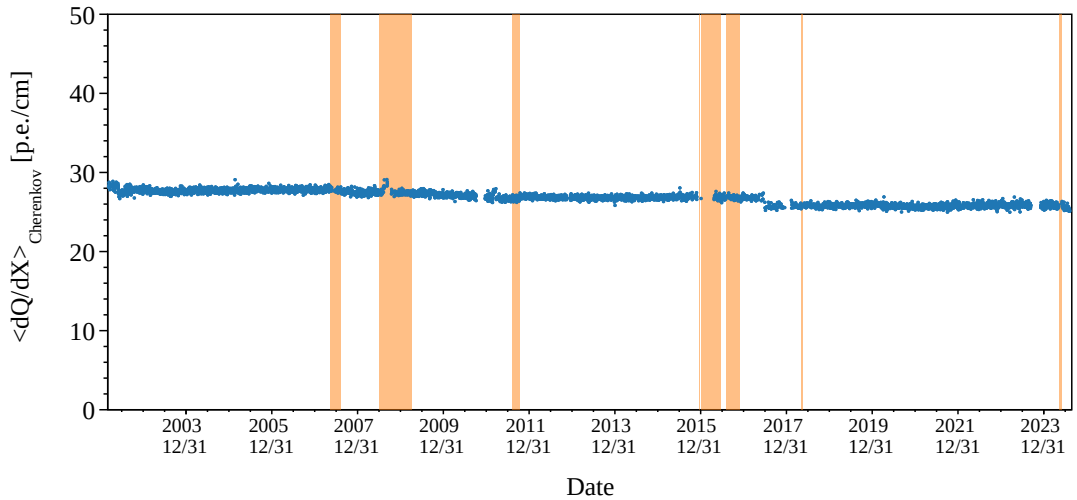

Figure 4.21: Time variation of Cherenkov light charge per track length

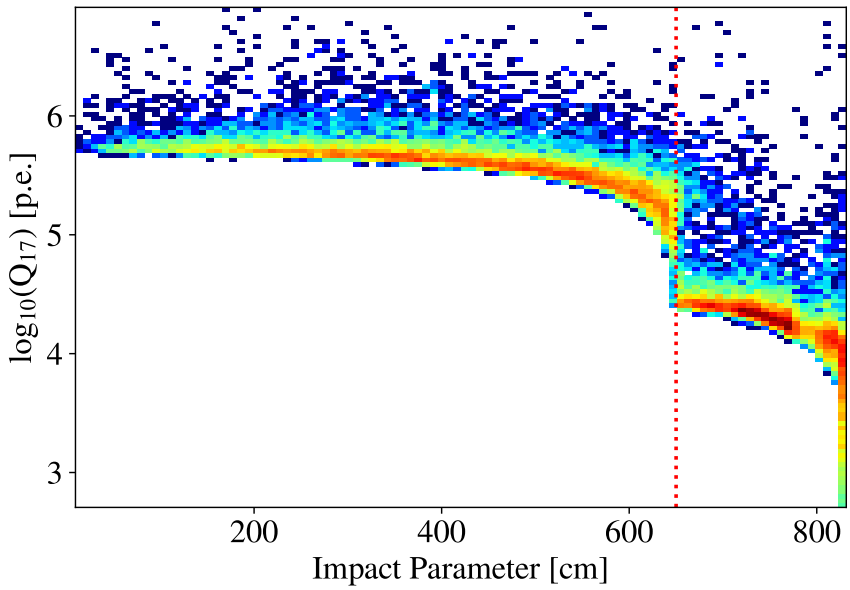

Figure 4.22: Correlation between the total charge of 17-inch PMTs and impact parameter. The red line represents impact parameter = 650 cm, which corresponds the boundary between LS and buffer oil.

4.7 Event Reconstruction

4.7.1 Energy Reconstruction Algorithm

In KamLAND, the visible energy—defined as the scintillation light yield observed by the PMTs—is different from the real energy deposited by charged particles in the LS. This is due to non-linear effects such as quenching, dark hits, and the detection efficiency of single photo-electron (p.e.).

Basic corrections

To suppress time-dependent variations in detector response, PMT charges are calibrated prior to energy reconstruction as follows:

- Gain calibration
  Each PMT has a different single p.e. charge and time variation due to degradation or high voltage tuning. Therefore, the charge is normalized channel by channel and run by run using 1 p.e. peak as described in Sec. 4.3.

- Bad channel selection
  Channels with abnormal behavior, such as too many hits, or unusual charge output, are considered to be bad channels and masked before energy reconstruction (Sec. 4.4).

- Software discriminator threshold
  To reduce accidental dark hits from PMT noise, a software threshold of 0.3 p.e. is applied to each PMT charge.

- Dark hit subtraction
  PMT charge includes contributions from dark hits, which depend on detector conditions such as temperature. The dark charge is estimated using an off-time window and subtracted from the total charge (Sec. 4.5).

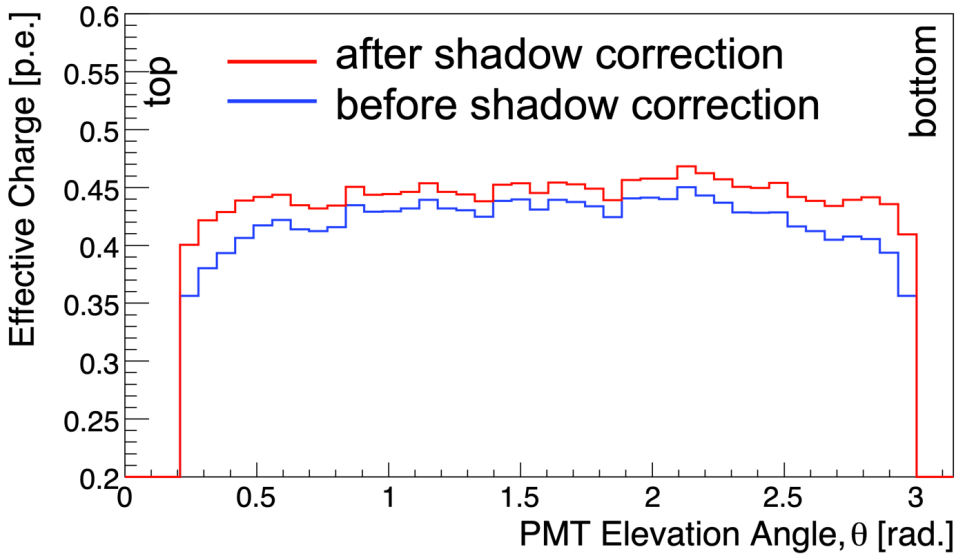

Figure 4.23: Shadow effect correction from the balloon and kevlar ropes [72].

Photon yield correction

In the energy reconstruction process, the shadow effect and attenuation length affect the photon yield; therefore, they must be corrected. Their descriptions are as follows:

- Shadow effect
  The observed charge in the bottom and chimney regions is reduced due to the shadowing of scintillation light by the balloon film and kevlar ropes. This effect is calibrated using a ^{60}Co source calibration run. As shown in Fig. 4.23, the small asymmetry in the charge distribution as a function polar angle is suppressed after the correction.

- Attenuation length
  The attenuation length is one of the important parameters in the characterization of LS. In KamLAND, a significant fraction of scintillation photons are absorbed by the LS, and some are subsequently re-emitted. Since the composition of the KamLAND LS changes with each purification campaign, the effective attenuation length must be evaluated separately for three periods: before the 1st purification, between the 1st and 2nd purification, and after the 2nd purification. The attenuation length is estimated using the charge observed at the i-th PMT and the distance from the reconstructed event vertex, as illustrated in Fig. 4.24. Spallation neutron capture events are used for this evaluation. To avoid the influence of solid angle effects on the collected charge, the photon collection region is defined as a right-angle cylinder with a diameter of 42.9 cm centered on each 17-inch PMT. The resulting attenuation lengths for the three periods are summarized in Fig. 4.25.

Photoelectron detection efficiency

A photon detection inefficiency arises due to the 0.3 p.e. software threshold described above. Its non-linear impact on the total observed charge is parametrized and calibrated as follows.

Assuming a scintillation event occurs at a vertex $\vec{X}$, and M photons are emitted, the expected number of photoelectrons produced at the photocathode of the i-th PMT, N_i, is given by

$$N_i = \mathfrak{q} b_i(\vec{X}) M, \tag{4.12}$$

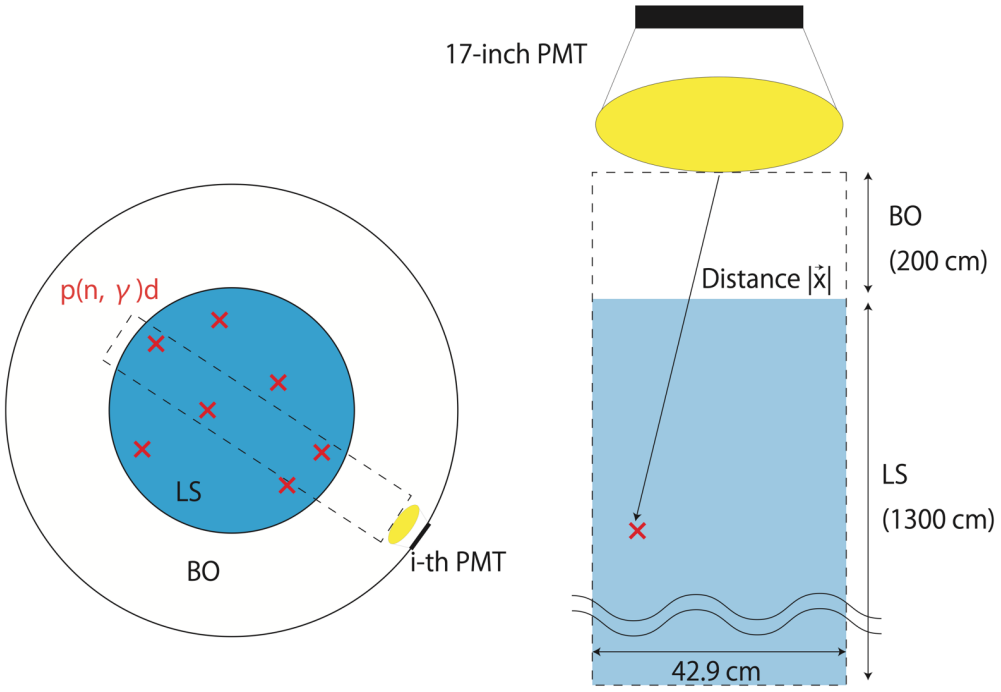

Figure 4.24: Schematic view of attenuation length estimation [62].

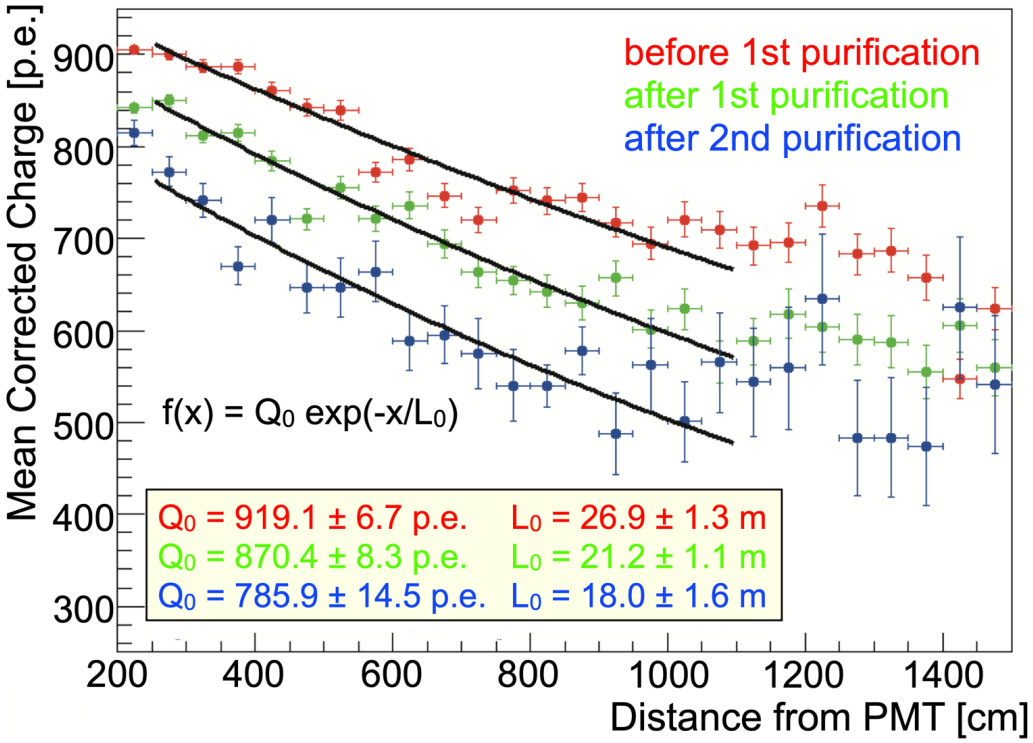

Figure 4.25: Effective attenuation length in LS with using spallation neutron events [72]. The black curves represents the exponential fitting function with the initial charge Q_0 and the attenuation length L_0.

where $\mathfrak{q}$ is the quantum efficiency of the PMT, and $b_i(\vec{X})$ represents the fraction of photons that reach the i-th PMT. This fraction accounts for the solid angle subtended by the PMT's photocathode as viewed from the vertex, shadow effects, and the effective attenuation length described previously. A normalization constant is omitted here, as it will be absorbed into subsequent calculations. The number of photoelectrons detected by the i-th PMT, denoted as n, follows a Poisson distribution with a mean value of N_i. That is,

$$P(n; N_i) = \frac{N_i^n e^{-N_i}}{n!}. \tag{4.13}$$

The expected charge detected by the i-th PMT without applying the software threshold is given by

$$Q_i^{\text{exp-no-th.}} \equiv q_1 N_i = \sum_{n\geq 1} q_n P(n; N_i), \tag{4.14}$$

where q_n denotes the average observed charge when the PMT detect n photoelectrons. Let ϵ denote the efficiency of the software threshold. the effective probability distribution that the number of detected photoelectrons n follows, $P_{\text{eff}}(n; N_i)$, is modified from the original Poisson distribution as:

$$\begin{aligned}
P_{\text{eff}}(0; N_i) &= P(0; N_i) + (1-\epsilon)P(1; N_i) && (4.15)\\
P_{\text{eff}}(1; N_i) &= \epsilon P(1; N_i) && (4.16)\\
P_{\text{eff}}(n; N_i) &\simeq P(1; N_i) \qquad (n \geq 2) && (4.17)
\end{aligned}$$

The expected charge detected by the i-th PMT, taking into account the software threshold, is given by:

$$\begin{aligned}
Q_i^{\text{exp}} &= q_{1,\text{residual}} P_{\text{eff}}(1; N_i) + \sum_{n\geq 2} q_n P_{\text{eff}}(n; N_i)\\
&= \sum_{n\geq 1} q_n P(n; N_i) - q_1 P(1; N_i) + q_{1,\text{residucal}} P_{\text{eff}}(1; N_i)\\
&= Q_i^{\text{exp-no-th.}} - q_1 N_i e^{-N_i} + \epsilon q_{q,\text{residual}} N_i e^{-N_i}\\
&= Q_i^{\text{exp-no-th.}}(1 - e^{-N_i}\delta) \qquad (4.18)
\end{aligned}$$

Here, $q_{1,\text{residual}}$ denotes the average observed charge for a single photoelectron after applying the 0.3 p.e. threshold. The factor δ, which quantifies the software threshold effect, is defined as

$$\delta = 1 - \frac{q_{1,\text{residual}}}{q_1}\epsilon. \tag{4.19}$$

The value of δ is estimated to be 0.03 based on calibration data from ^{60}Co (2γ: 1.173 MeV and 1.333 MeV) and ^{65}Zn (γ: 1.116 MeV) sources.

The expected number of detected photoelectrons in the i-th PMT, μ_i^{signal}, is calculated by distributing the total observed charge among the good PMTs as follows:

$$\mu_i^{\text{signal}} = \sum_j Q_j^{\text{obs}} \times \frac{Q_i^{\text{exp}}/q_1}{\Sigma_j Q_j^{\text{exp}}} \tag{4.20}$$

This expected value μ_i^{signal}, expressed as a function of the total number of emitted photons M, constitutes one of the essential components in the likelihood function used to estimate the visible energy of the event.

Energy reconstruction algorithm

The likelihood function for energy reconstruction, $\mathcal{L}$, is defined as:

$$\mathcal{L} \equiv \prod_{i\in\text{no-hit}} P^{\text{hit}}(0|\mu_i) \times \prod_{i\in\text{hit}} \left[\sum_{j=1}^{\infty} P^{\text{hit}}(j|\mu_i)\,\text{PDF}^{\text{charge}}(q_i, j|\mu_i)\right] \text{PDF}^{\text{time}}(t_i|\mu_i) \quad (4.21)$$

Here, "hit" and "no-hit" denote the sets of PMTs that record and do not record hits, respectively. For the i-th PMT, j is the number of detected photoelectrons, q_i is the observed charge associated with the j photoelectrons, and t_i is the arrival time of the first detected photon.

The expected number of detected photoelectrons, μ_i, is given by the sum of the signal and dark contributions as

$$\mu_i = \mu_i^{\text{signal}} + \mu_i^{\text{dark}}, \quad (4.22)$$

where μ_i^{signal} is calculated from the visible energy as described in Eq. 4.20, and μ_i^{dark} is estimated from the dark charge as described in Sec. 4.5. The probability for a PMT to register zero photoelectrons, $P^{\text{hit}}(0|\mu_i)$, and the complementary probability to register one or more photoelectrons, $P^{\text{hit}}(1 \le |\mu_i)$, are given by:

$$P^{\text{hit}}(0|\mu_i) = e^{-\mu_i} + (1-\epsilon)\mu_i e^{-\mu_i} \quad (4.23)$$

$$P^{\text{hit}}(1 \le |\mu_i) = 1 - P^{\text{hit}}(0|\mu_i) \quad (4.24)$$

$P^{\text{hit}}(n;\mu_i)$ is Poisson distribution, and the probability density function of the observed charge, $\text{PDF}^{\text{charge}}(q_i, j|\mu_i)$ is modeled as a Gaussian distribution. Therefore, their combination is written as follows

$$\sum_{j=1}^{\infty} P^{\text{hit}}(j|\mu_i)\,\text{PDF}^{\text{charge}}(q_i, j|\mu_i) = \sum_{j=1}^{\infty} \left[\frac{\mu_i^j}{j!} e^{-\mu_i} \times \frac{1}{\sqrt{2\pi j\sigma^2}} e^{-\frac{(q_i-j)^2}{2j\sigma^2}}\right], \quad (4.25)$$

where σ is the standard deviation of the 1 p.e. charge distribution obtained from source calibration data. The timing PDF, $\text{PDF}^{\text{time}}(t_i|\mu_i)$, is constructed using the hit-time distribution $\phi_i(t_i)$ derived from source calibration, and the dark rate d_i as follows

$$\text{PDF}^{\text{time}}(t_i|\mu_i) = \frac{(a_i\mu_i^{\text{signal}})\phi_i(t_i) + d_i}{\mu_i}, \quad (4.26)$$

where a_i is a normalization factor for each PMT.

The visible energy E_{vis} is reconstructed by maximizing the likelihood function $\mathcal{L}$, i.e., by solving

$$\frac{\partial \log \mathcal{L}}{\partial E_{\text{vis}}} = 0 \quad (4.27)$$

This optimization is performed using the Newton-Raphson method [73].

Combination of 20-inch PMTs

The 20-inch PMTs have been in use since February 2003. Due to the absence of a clear 1 p.e. peak and their differing charge-to-energy linearity compared to the 17-inch PMTs, the energy reconstruction procedure described above is applied separately to the 17-inch and 20-inch PMTs. The final visible energy, E_{vis}, is then obtained by linearly combining

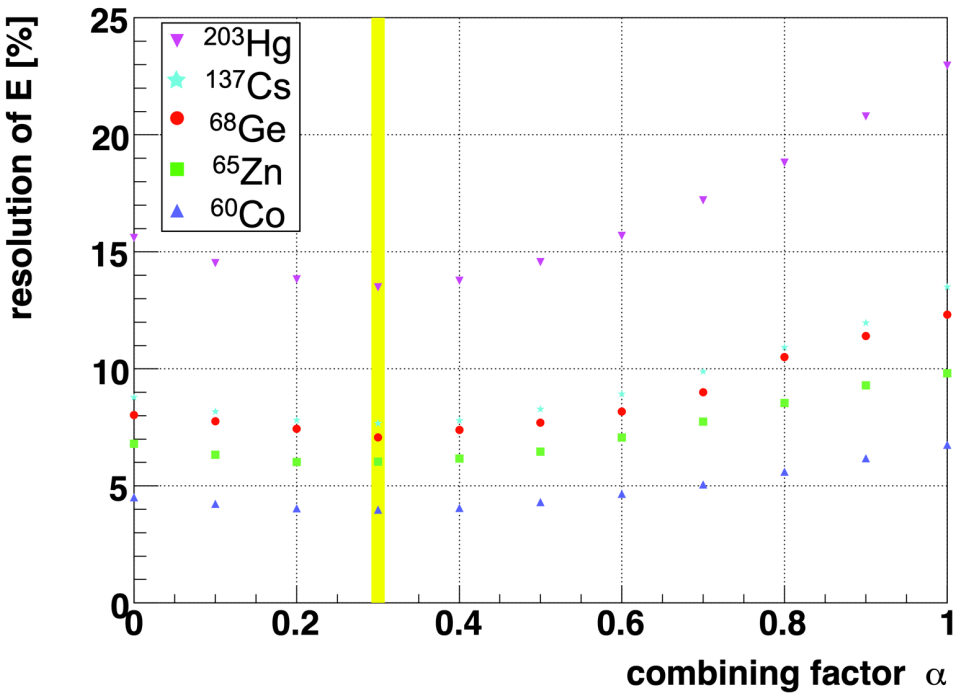

Figure 4.26: The combined energy resolution as a function of the combining factor [72]. The yellow band shows the best parameter $\alpha = 0.3$.

the two reconstructed energies using a weighting factor α, as follows:

$$E_{\text{vis}} = (1-\alpha)E_{\text{vis}}^{\text{17-inch}} + \alpha E_{\text{vis}}^{\text{20-inch}} \tag{4.28}$$

The parameter α is optimized to achieve the best energy resolution, based on various calibration data, as shown in Fig. 4.26. A value of $\alpha = 0.3$ is adopted. The deviation of the combined visible energy from that reconstructed using only the 17-inch PMTs is evaluated using source calibration data in the low-energy region and spallation product data in the high-energy region, as shown in Fig. 4.27. The deviation is confirmed to be less than 0.6%.

4.7.2 Energy Reconstruction Quality

The quality of energy reconstruction—such as its position and time dependence or resolution—is evaluated using source calibration data. Fig. 4.28 shows the visible energy spectra for each source calibration data.

Energy deviation

The Z dependence of the deviation from the energy reconstructed at the detector center is shown in Fig. 4.29, and its magnitude is about a few percent. The time variation of the reconstructed energy is evaluated using calibration data with the source placed at the detector center, and is found to be within 1.5%. In addition, this time dependence is also estimated using spallation products, as described in Sec. 4.8.

Energy resolution

The energy resolution is evaluated by fitting the calibration data as a function of visible energy. As shown in Fig. 4.30, the resolutions before and after purification are obtained as follows:

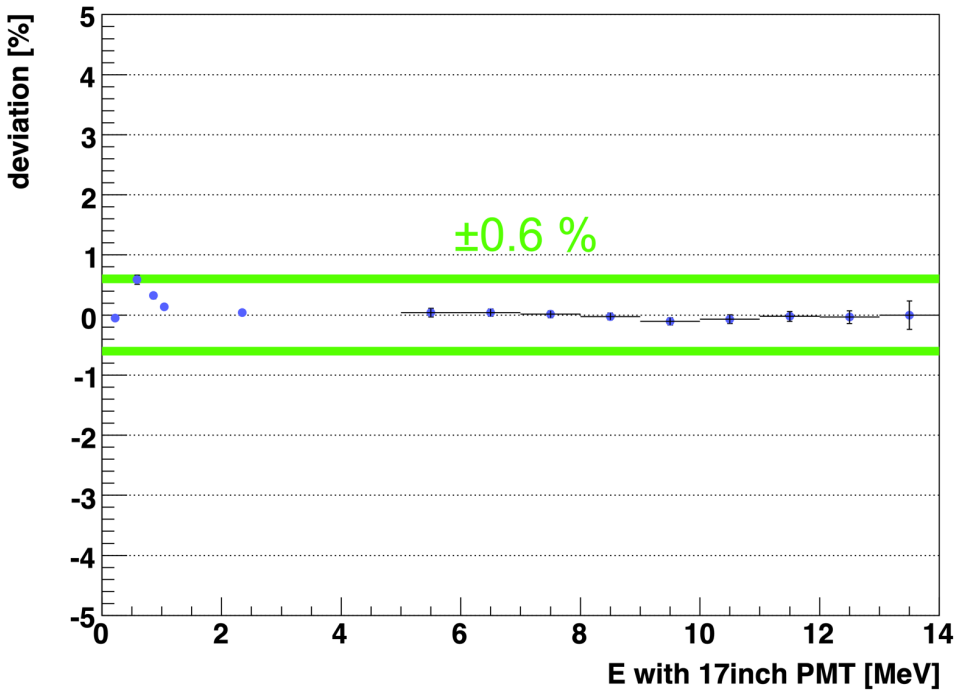

Figure 4.27: Deviations between combined energy and 17-inch PMT energy [72]. The linearity is verified by calibration sources (^{203}Hg, ^{137}Cs, ^{68}Ge, ^{65}Zn and ^{60}Co) for low energy region, and by spallation ^{12}B for high energy region.

- Before purification (17-inch PMT): $7.0 \pm 0.1\,\% \times \sqrt{E\,[\mathrm{MeV}]}$
- Before purification (17-inch+20-inch PMT): $6.1 \pm 0.1\,\% \times \sqrt{E\,[\mathrm{MeV}]}$
- After purification (17-inch PMT): $8.2 \pm 0.1\,\% \times \sqrt{E\,[\mathrm{MeV}]}$
- After purification (17-inch+20-inch PMT): $7.0 \pm 0.1\,\% \times \sqrt{E\,[\mathrm{MeV}]}$

Following the purification of KamLS, the scintillation light yield decreased, leading to a deterioration in resolution. After the start of KamLAND-Zen 400, energy resolution can no longer be estimated using source calibration. Instead, it is assessed using a *quenching factor* that accounts for effects such as the increased number of bad channels as $\sqrt{E} \rightarrow \sqrt{E} \times (\text{quenching factor})$. Fig. 4.31 shows the time variation of the relative quench factor with respect to the calibration data taken before purification. A larger quench factor corresponds to a lower effective light yield and thus a worse energy resolution.

4.7.3 Vertex Reconstruction Algorithm

In this section, the vertex reconstruction method for *point-like* events such as $\bar{\nu}_e$ interaction is described. The vertex position (x, y, z) and time t are determined using a maximum likelihood approach based on the photon arrival time distribution observed by the 17-inch PMTs in the ID. Assuming a scintillation event occurs at (t, x, y, z), the the delay of the photon detection time of the i-th PMT relative to the expected time t_i can be expressed as

$$\tau_i(t, x, y, z) = t_i - (t + TOF_i(t, x, y, z)) \tag{4.29}$$

where TOF_i is the time of flight from the vertex to the i-th PMT, calculated using the distance and the light speed in the LS. This delay arises from factors such as the time

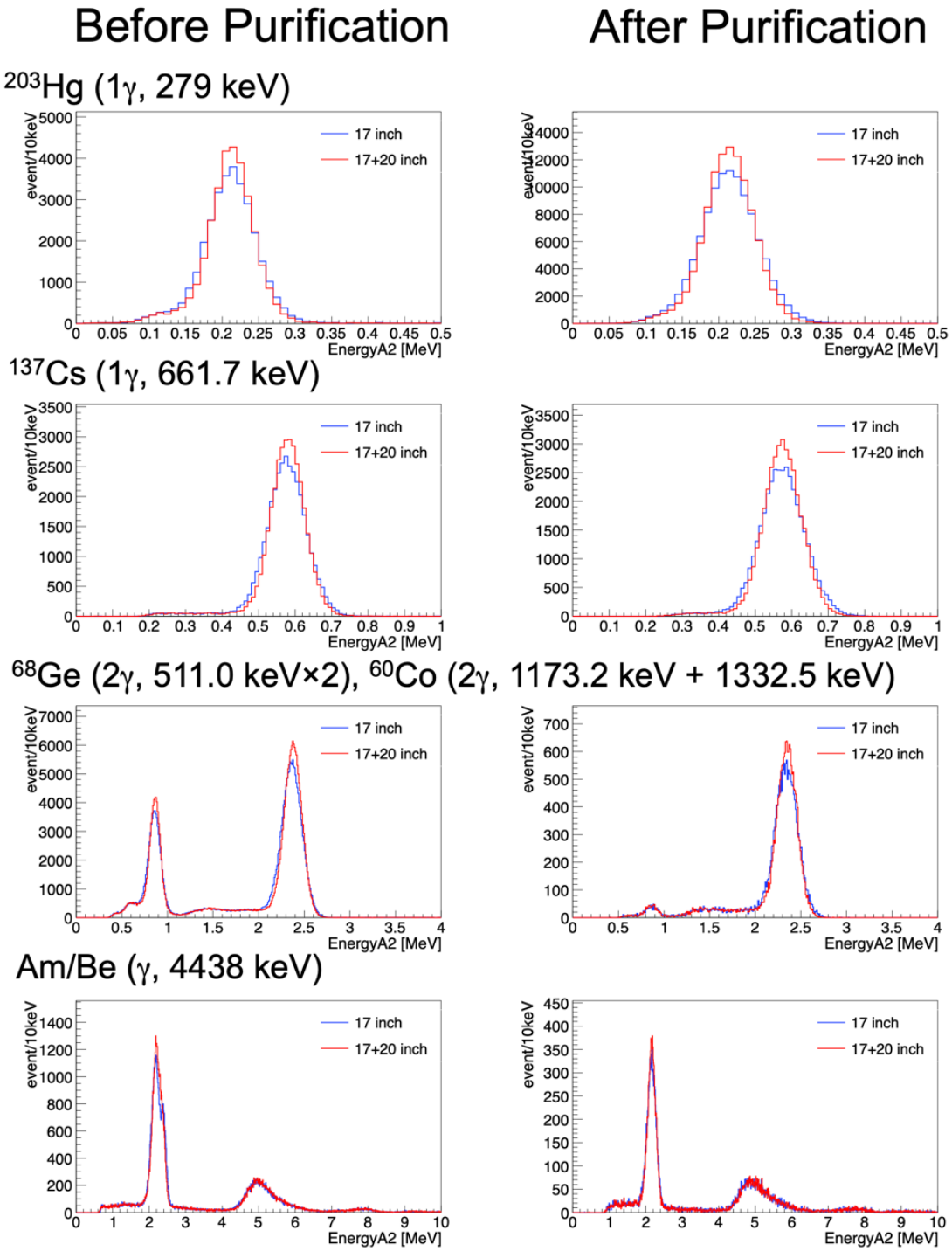

Figure 4.28: Visible energy spectrum for various source calibration data before/after purification [72].

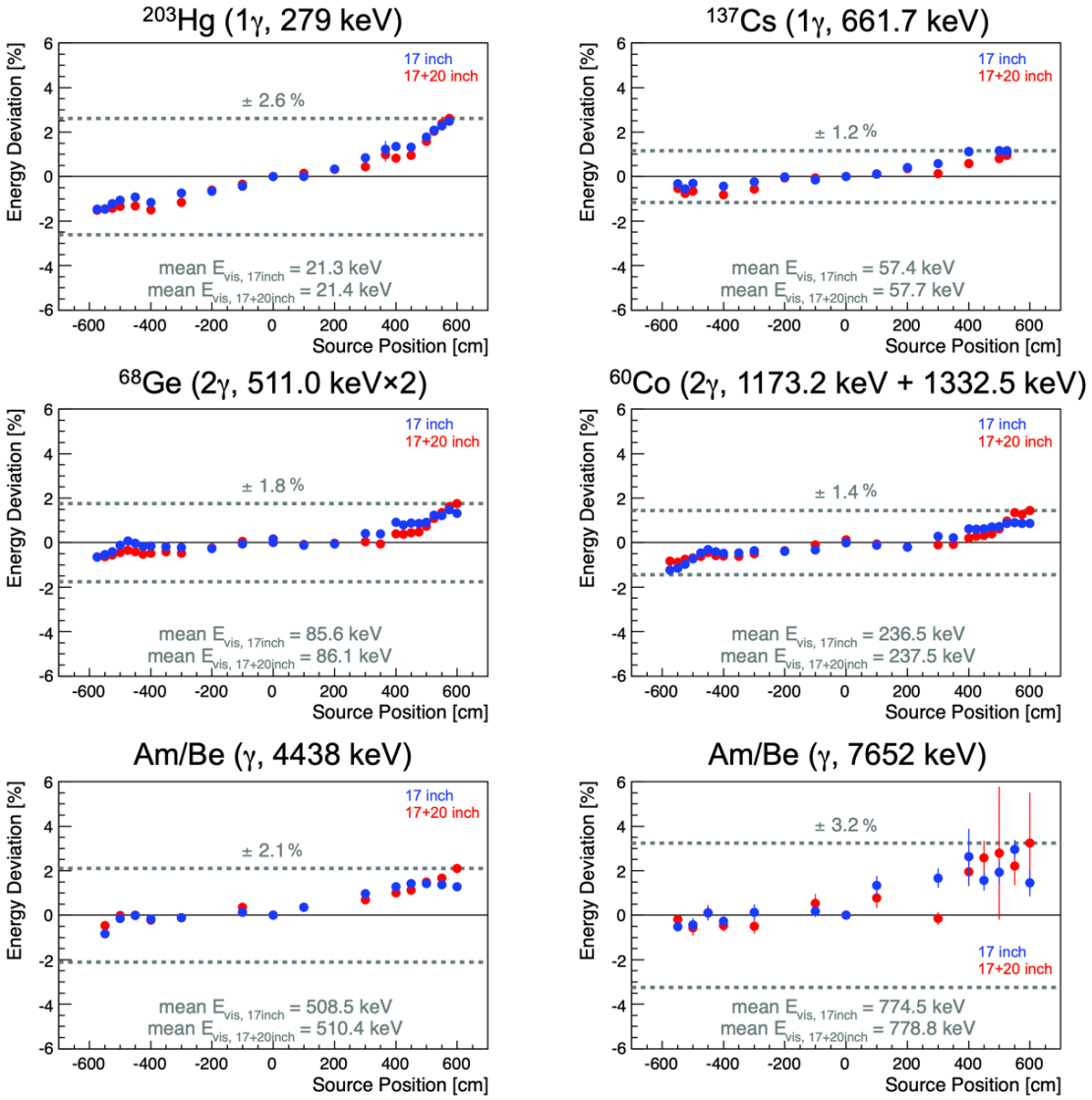

Figure 4.29: Z dependence of the deviation from the energy reconstructed at the detector center [72]. This figure is the example of before purification.

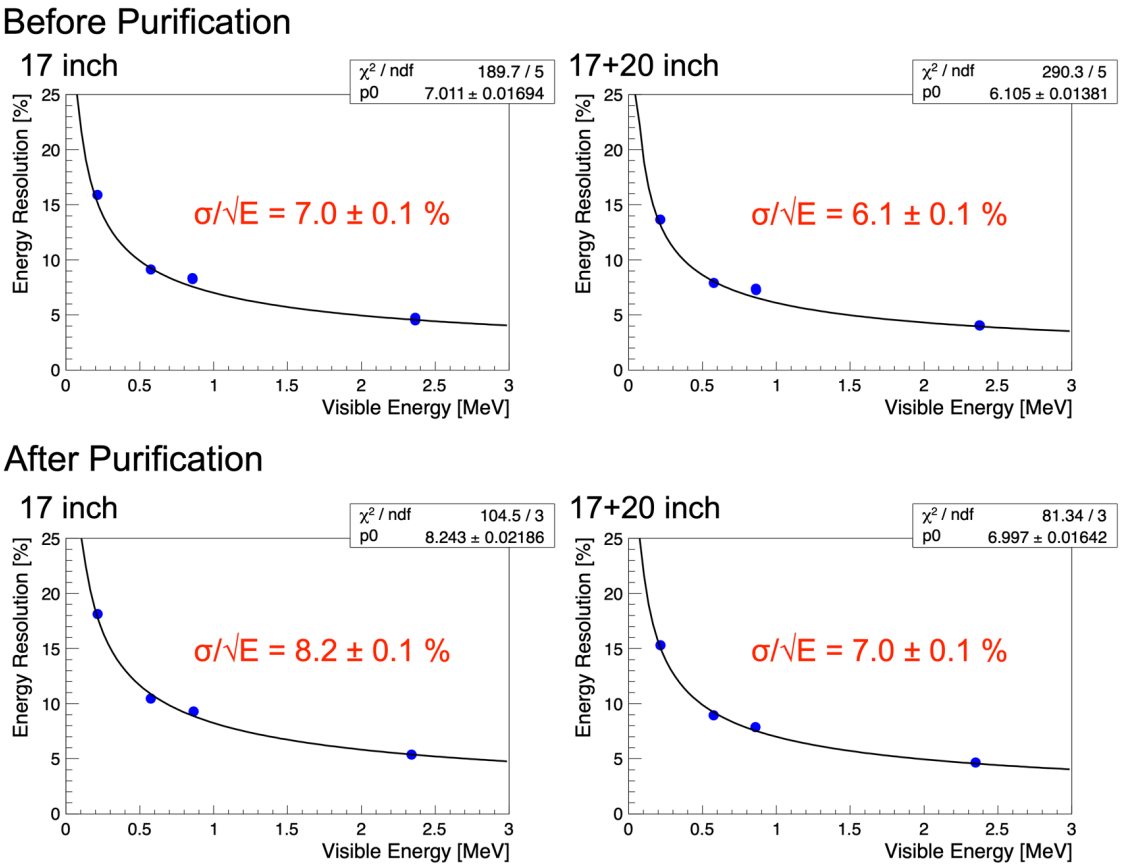

Figure 4.30: Energy resolution for various source calibration as a function of visible energy [72].

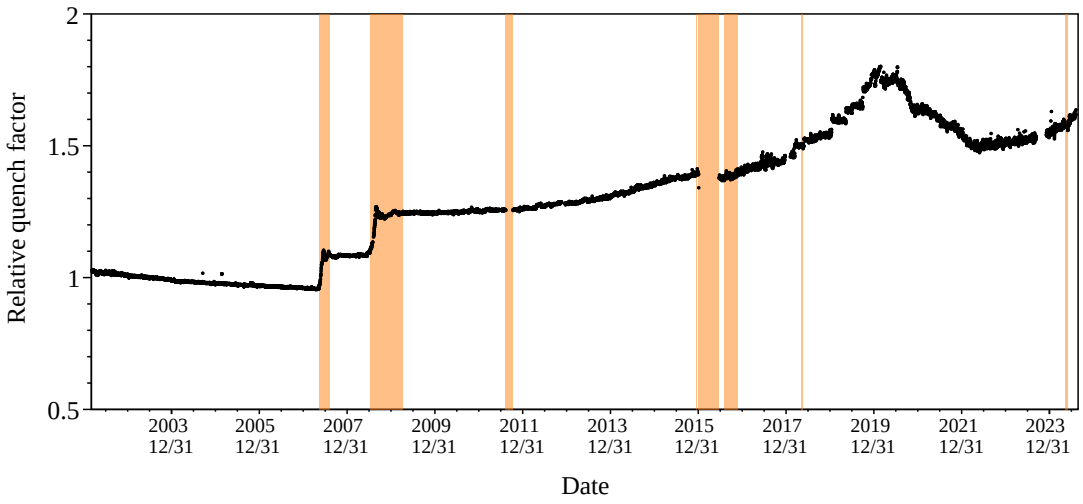

Figure 4.31: Time variation of the relative quench factor.

spread of scintillation photon emission (typically 10 ns to a few hundred ns), as well as absorption and re-emission processes within the LS.

The distribution of τ_i, denoted as $\phi(\tau_i)$, is constructed constructed using source calibration data. This pulse shape is treated as invariant at each vertex and include effects such as multiple photon hits and re-emission components. The likelihood function for the vertex reconstruction is then defined as

$$\begin{aligned} \mathcal{L} &= \prod_{i}^{N_{\mathrm{hit}}} \phi(\tau_i(t,x,y,z)) \\ \iff \log\mathcal{L} &= \sum_{i}^{N_{\mathrm{hit}}} \phi(\tau_i(t,x,y,z)), \end{aligned} \tag{4.30}$$

where N_{hit} is the number of PMTs that recorded hits. The event vertex and time are reconstructed by finding the set of parameters (t,x,y,z) that maximizes the likelihood function as follows:

$$\frac{\partial(\log\mathcal{L})}{\partial t} = \sum_{i}^{N_{\mathrm{hit}}} \frac{d(\log\mathcal{L})}{d\tau_i}\frac{\partial\tau_i}{\partial t} = 0 \tag{4.31}$$

$$\frac{\partial(\log\mathcal{L})}{\partial x} = \sum_{i}^{N_{\mathrm{hit}}} \frac{d(\log\mathcal{L})}{d\tau_i}\frac{\partial\tau_i}{\partial x} = 0 \tag{4.32}$$

$$\frac{\partial(\log\mathcal{L})}{\partial y} = \sum_{i}^{N_{\mathrm{hit}}} \frac{d(\log\mathcal{L})}{d\tau_i}\frac{\partial\tau_i}{\partial y} = 0 \tag{4.33}$$

$$\frac{\partial(\log\mathcal{L})}{\partial z} = \sum_{i}^{N_{\mathrm{hit}}} \frac{d(\log\mathcal{L})}{d\tau_i}\frac{\partial\tau_i}{\partial z} = 0 \tag{4.34}$$

4.7.4 Vertex Reconstruction Quality

The quality of the vertex reconstruction is verified using various source calibration data, including both z-axis and off-axis calibrations. In this section, the results from z-axis calibrations are presented, while off-axis calibrations are used to evaluate the fiducial volume uncertainty, as discussed in Sec. 4.8.3. The performance of vertex reconstruction is assessed in terms of vertex bias, resolution, and miss-reconstruction probability.

Vertex bias

The vertex bias is evaluated using z-axis source calibration data. The deviations between the reconstructed z position and the the true source positions are shown in Fig. 4.32. The bias confirmed to be within ±3.0 cm before purification and ±5.0 cm after purification. Consistent results are obtained in both the 17-inch PMT and the combined 17-inch+20-inch PMT analysis. After the start of KamLAND-Zen 400, the long-term stability of the vertex reconstruction is monitored using spallation products, as discussed in Sec. 4.8.3.

Vertex resolution

The vertex resolution is estimated by comparing the reconstructed vertex distributions from calibration data with those from Geant4-based simulations [74]. Fig. 4.33 shows the comparison of distance between reconstructed vertex and the true source position for calibration

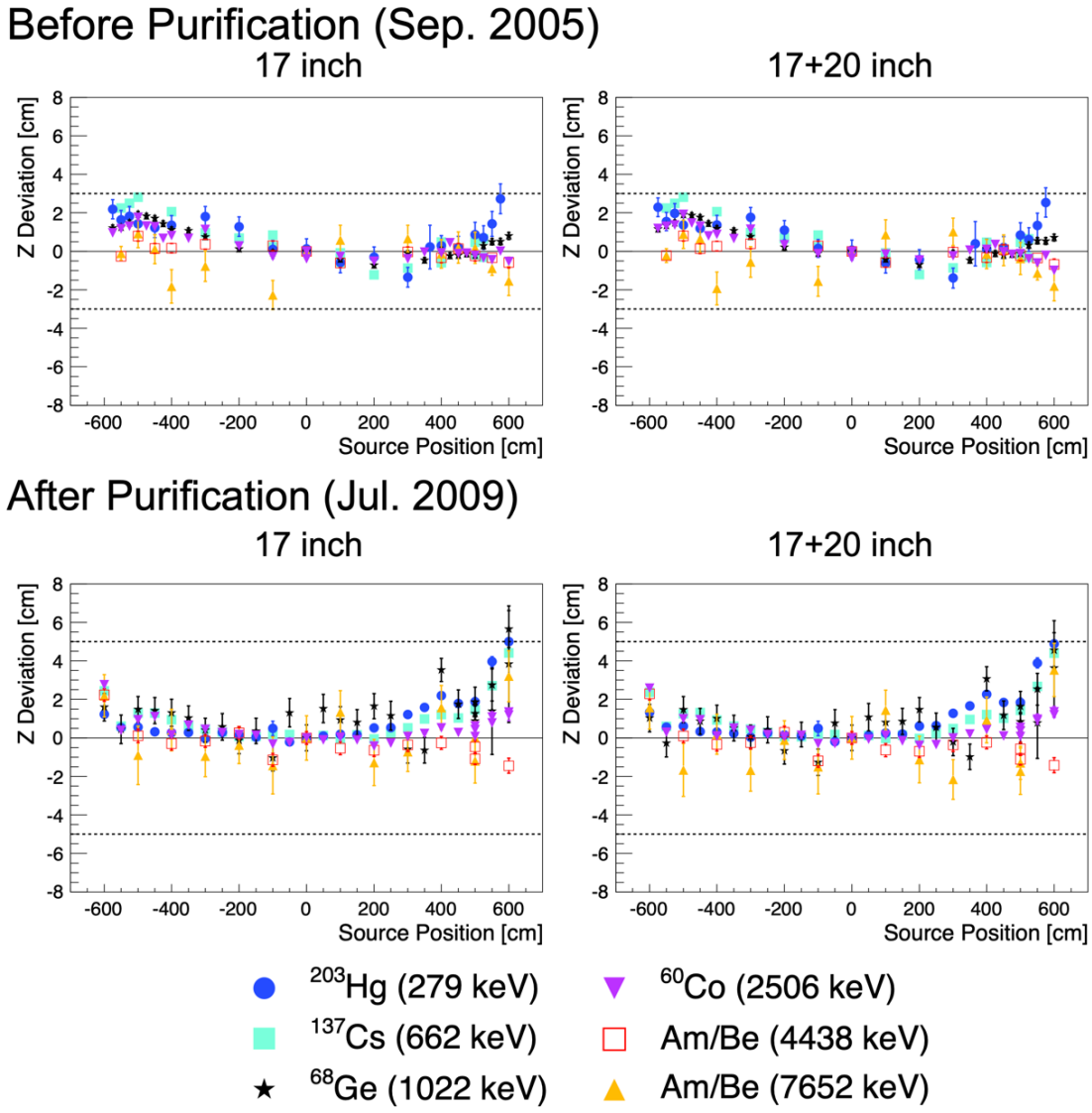

Figure 4.32: Vertex deviations between reconstructed z position and expected source position before/after purification [72].

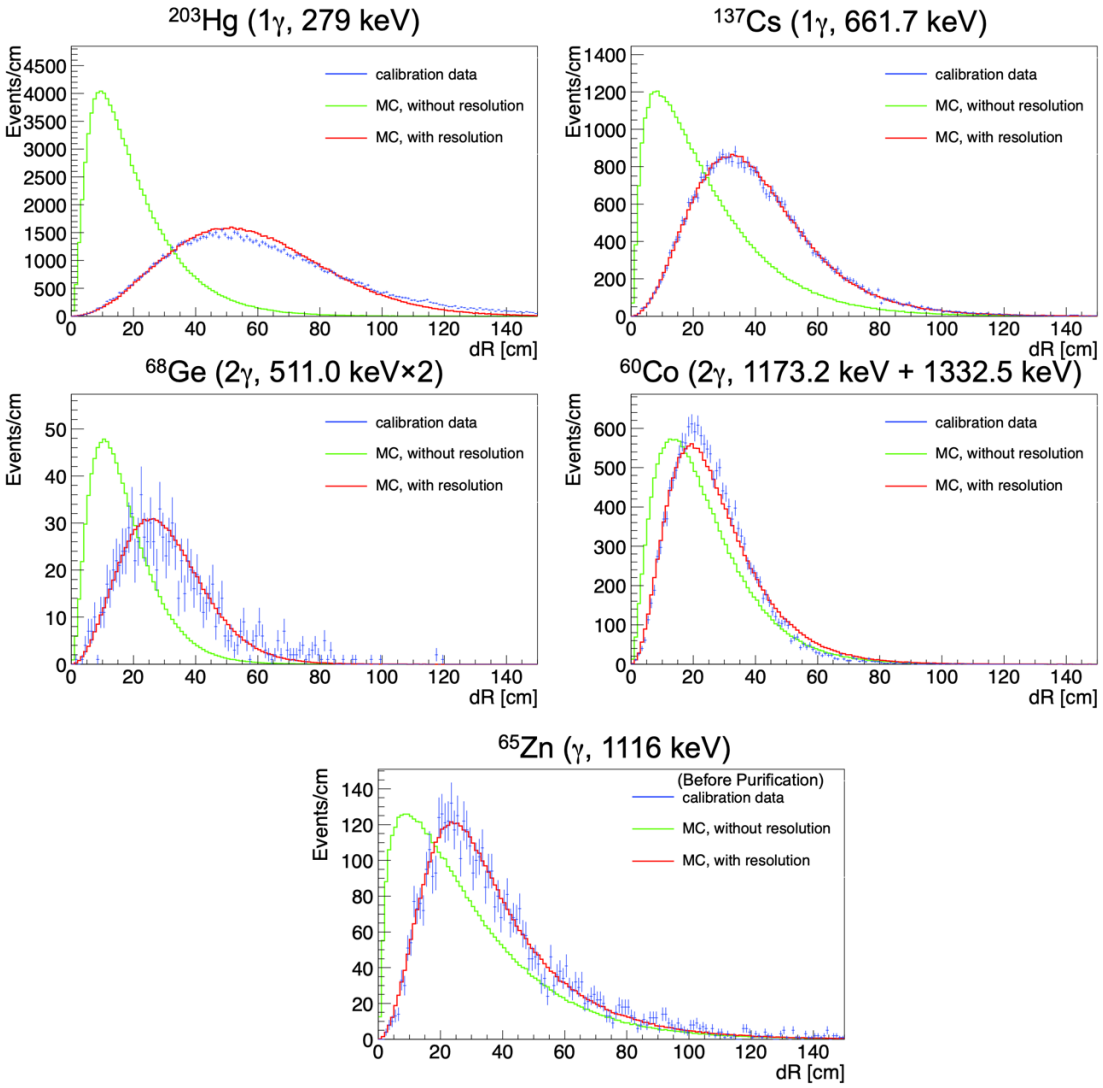

Figure 4.33: Comparison of distance between reconstructed vertex and the true source position [72]. Blue points represent the observed data. The green and red curves represent the distance without and with the vertex resolution, respectively.

data and simulation data, respectively. As the reconstructed vertex distribution is influenced by physical effects such as particle dispersion, the distribution of simulated distance is modified before compared to calibration data. Fig. 4.34 summarizes the estimated vertex resolution as a function of visible energy and the results are as follows:

- Before purification (17-inch PMT): $13.1 \pm 2.1\,\mathrm{cm}/\sqrt{E\,[\mathrm{MeV}]}$
- Before purification (17-inch+20-inch PMT): $11.7 \pm 2.2\,\mathrm{cm}/\sqrt{E\,[\mathrm{MeV}]}$
- After purification (17-inch PMT): $15.3 \pm 2.5\,\mathrm{cm}/\sqrt{E\,[\mathrm{MeV}]}$
- After purification (17-inch+20-inch PMT): $13.8 \pm 2.3\,\mathrm{cm}/\sqrt{E\,[\mathrm{MeV}]}$

Due to the purification campaigns , which altered the composition of the LS and reduced its light yield, the vertex resolution after purification is degraded compared to that before purification.

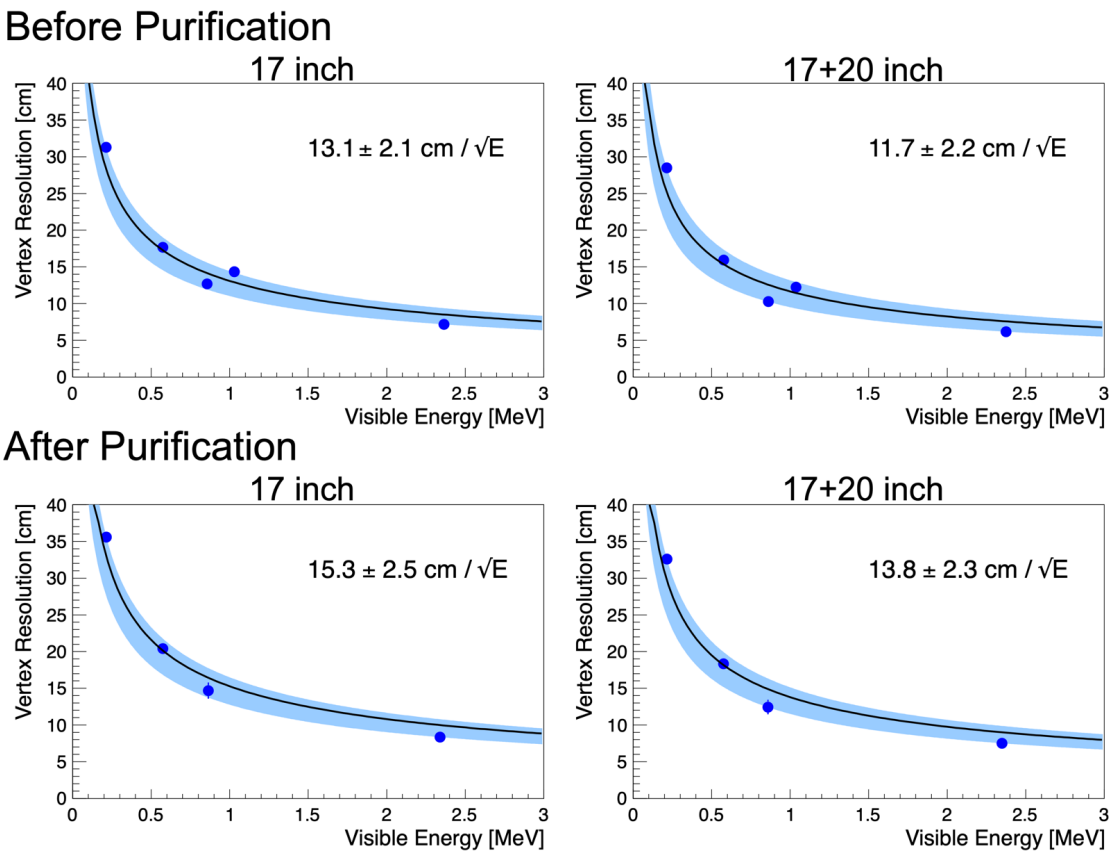

Figure 4.34: Vertex resolution for various source calibration as a function of visible energy [72]. Black curves represent the best fit resolution curve and blue bands show their error range.

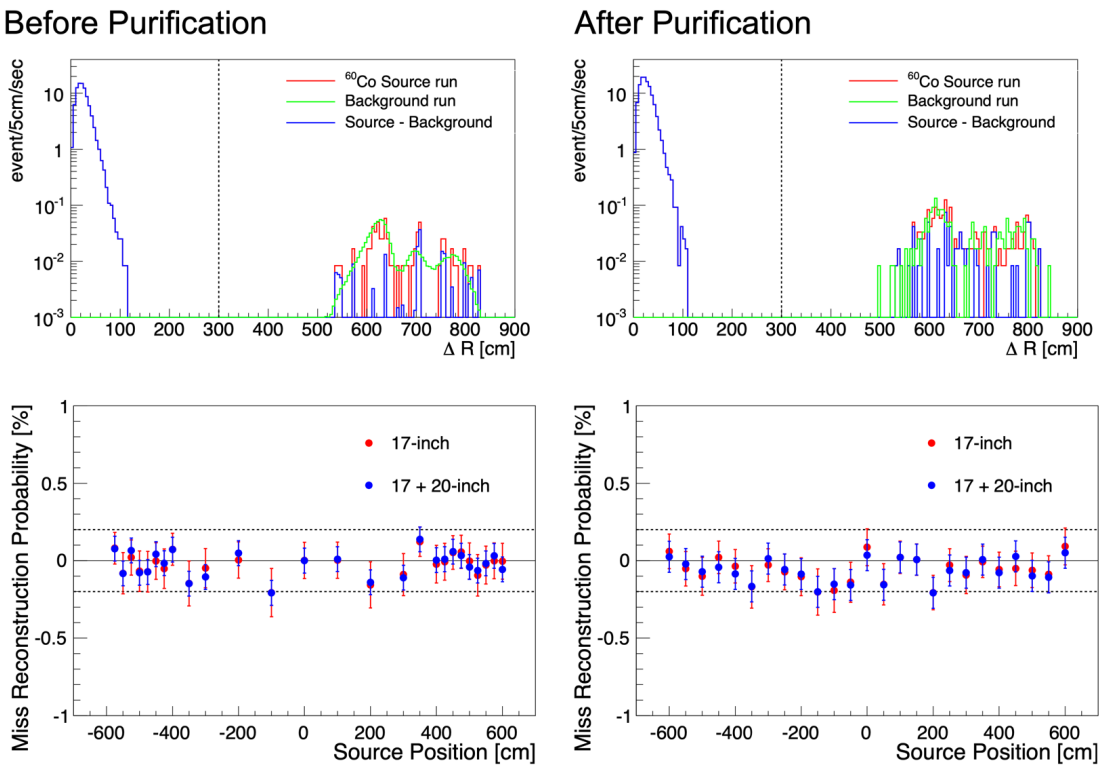

Figure 4.35: Miss reconstruction probability with ^{60}Co events of before/after purification [72]. Upper figures are the distance distribution and lower figures are miss reconstruction probabilities.

Miss reconstruction

The miss-reconstruction probability is evaluated using calibration data from a ^{60}Co source, which emits two γ rays at 1173.2 keV and 1332.5 keV. It is defined based on the distance ΔR between the known source position and the reconstructed vertex, subtracting the background contribution. Therefore, the miss-reconstruction probability is given by

$$P = \frac{N_{^{60}\mathrm{Co}}(\Delta R > R_{\mathrm{cut}}) - N_{\mathrm{BG}}(\Delta R > R_{\mathrm{cut}})}{N_{^{60}\mathrm{Co}} - N_{\mathrm{BG}}}, \tag{4.35}$$

where R_{cut} is a threshold value set sufficiently larger than the attenuation length of ^{60}Co γ rays to isolate significantly miss reconstructed events. $N_{^{60}\mathrm{Co}}$ and N_{BG} denote the number of events from the source data and background, respectively. Fig. 4.35 shows the distance distribution between the reconstructed vertices and the true source position before and after purification. The miss-reconstruction probability is confirmed to be suppressed below 0.2% in all periods.

4.8 Energy and Vertex Uncertainty

Uncertainties in the reconstructed energy and vertex arise from position-dependent effects within the detector and from long-term variations in the detector response. These uncertainties are evaluated using various spallation events, which are expected to be uniformly distributed in both time and space.

4.8.1 Selection Criteria of Spallation Products

Spallation neutron

Muons entering KamLAND induce hadronic reactions, producing numerous spallation products and neutrons. The resulting spallation neutrons are captured on protons, emitting a 2.211 MeV gamma ray. Because this event produces a single, well-defined energy, it is commonly used for detector calibration. In this analysis, events occurring more than 1200 μs after a muon are used. This selection reduces the fraction of missing waveform events to about 1%, allowing us to use a high-quality dataset. The selection criteria for spallation neutrons in this analysis are summarized as follows:

- Not a flasher event (described in Sec. 7.2.2)
- Nhit17 $\leq$ NsumMax:

  Nhit17 is the number of recorded waveforms in the 17-inch PMTs, while NsumMax is the number of triggered PMTs. This criterion is applied to remove missing waveform events.
- Fiducial volume cut: $r \leq 550\,\mathrm{cm}$
- Zen volume veto: exclude events with $r \leq 250\,\mathrm{cm}$ and $\rho \leq 250\,\mathrm{cm}$ in the upper sphere (described in Sec. 7.4)
- Time difference from muon:
  - 1200–1600 μs as the ontime window
  - 2800–4000 μs as the offtime window

Fig 4.36 shows the profile of the spallation neutron events selected using the above criteria.

Spallation ^{8}He and ^{9}Li

Among the isotopes produced by spallation, ^{8}He ($Q = 10.7\,\mathrm{MeV}$, $\tau = 171.7\,\mathrm{ms}$) and ^{9}Li ($Q = 13.6\,\mathrm{MeV}$, $\tau = 257.2\,\mathrm{ms}$) emit neutrons following beta decay. Therefore, these events can be collected by applying the delayed-coincidence method after muon events. Since spallation ^{8}He/^{9}Li events consist of two correlated signals with different energies (prompt and delayed), they are useful for evaluating the energy-dependent vertex bias. The selection criteria for spallation ^{8}He/^{9}Li events are as follows:

- Not a flasher event
- Fiducial volume cut: $r \leq 550\,\mathrm{cm}$
- Zen volume veto
- Delayed coincidence selection after muon event

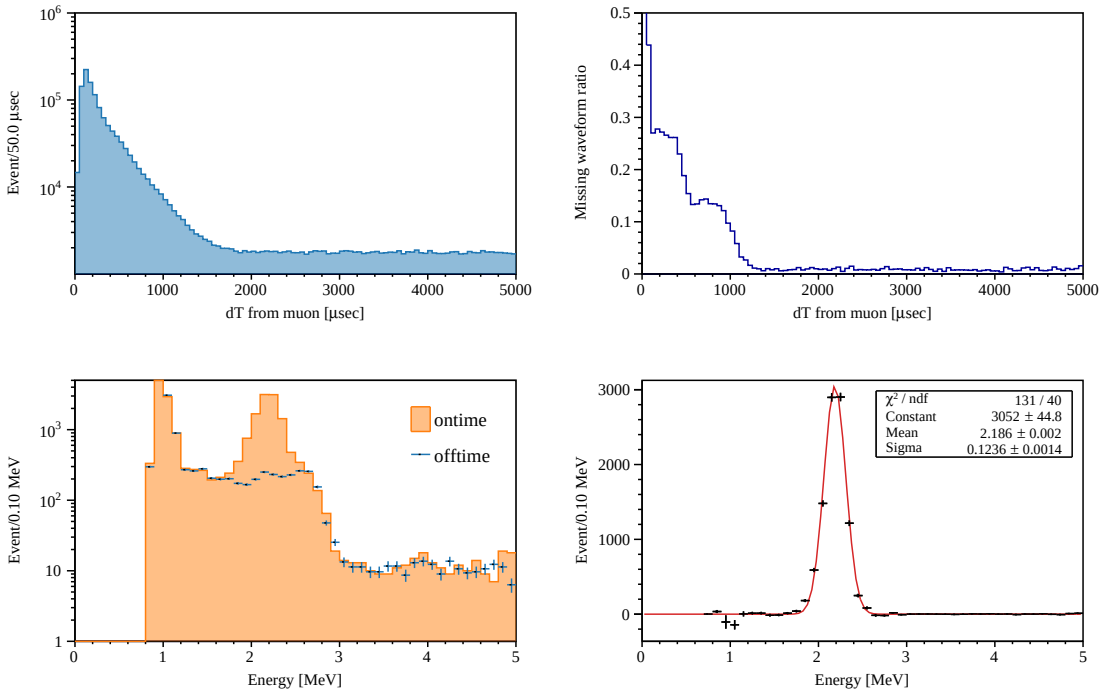

Figure 4.36: Profile of spallation neutron events. (Upper left) Distribution of time differences from preceding muons. (Upper right) Missing waveform ratio for each time difference bin from muons. (Lower left) Ontime and offtime energy spectra after the time window scaling. (Lower right) Energy spectrum of the subtracted events. All plots correspond to the before purification.

Spallation ^{12}B and ^{12}N

Spallation ^{12}B ($Q = 13.4\,\mathrm{MeV}$, $\tau = 29.1\,\mathrm{ms}$) and ^{12}N ($Q = 17.3\,\mathrm{MeV}$, $\tau = 15.9\,\mathrm{ms}$) are also used to evaluate detector-related uncertainties. Owing to their high Q-values, these events are particularly useful for assessing the energy scale around 10 MeV. This analysis employs a dataset obtained by subtracting the contribution in the offtime window from that in the ontime window, based on the time difference from preceding muons. The selection criteria for spallation ^{12}B/^{12}N events are as follows:

- Energy selection: $E_{\mathrm{vis}} \geq 4\,\mathrm{MeV}$
- Not a flasher event
- Fiducial volume cut: $r \leq 550\,\mathrm{cm}$
- Zen volume veto
- Time difference from muon:
  - 2–60 ms as the ontime window
  - 502–560 ms as the offtime window

4.8.2 Energy Scale Uncertainty

In this section, the long-term stability and position dependent of the energy scale are evaluated using spallation products.

Time variation of energy scale

The time variation of the energy scale in KamLAND was discussed in Sec. 4.7.2 using source calibration data. However, since the installation of the miniballoon at the detector center for the KamLAND-Zen experiment, such calibrations have no longer been feasible. Therefore, the long-term stability of the energy scale is evaluated using spallation products.

For spallation neutrons, the time variation is examined based on the deviation between the reconstructed energy and the known gamma-ray energy (2.211 MeV) from neutron capture on protons. The energy deviation is defined as follows:

$$\text{Energy deviation} = \frac{(\text{Mean reconstructed energy [MeV]}) - 2.211}{2.211}. \tag{4.36}$$

For spallation ^{12}B and ^{12}N, the subtracted energy spectrum obtained from data is fitted with Monte Carlo-generated beta-spectrum models, and the time variation of the energy shift is evaluated. The energy shift is defined in the fitting function, f, as follows:

$$f(E) = C_{12B} \times f_{12B}\left(E - \frac{(\text{Energy shift})}{100}\right) + C_{12N} \times f_{12N}\left(E - \frac{(\text{Energy shift})}{100}\right), \tag{4.37}$$

where C_{12B} and C_{12N} represents the scaling constants of ^{12}B and ^{12}N spectrum models, and f_{12B} and f_{12N} represents the spectrum functions of ^{12}B and ^{12}N. Fig. 4.37 shows an example of the fitting of the ^{12}B and ^{12}N energy spectra.

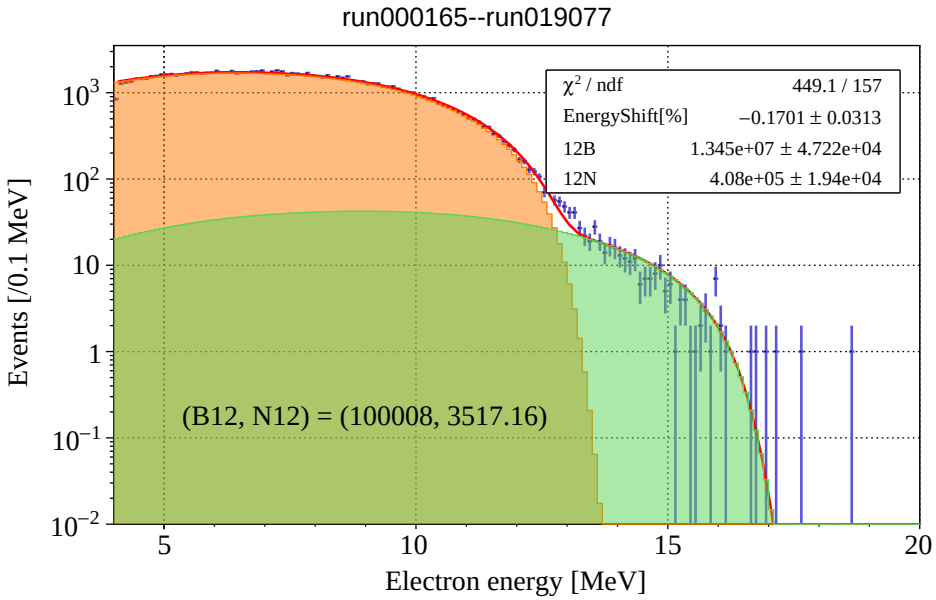

Figure 4.37: An example of the energy spectrum fitting with spallation ^{12}B and ^{12}N. Blue points represent the observed events obtained from the ontime/offtime subtraction. The orange and green histograms show the MC-generated beta spectrum models of ^{12}B and ^{12}N, respectively. The red line indicates the total spectrum model composed of both ^{12}B and ^{12}N. This figure corresponds to the entire data taking period.

While the energy-scale study using spallation neutrons reflects detector response around 2 MeV, that based on spallation ^{12}B/^{12}N is sensitive to the energy scale around 10 MeV. Fig. 4.38 shows the time variation of the energy scale evaluated using these spallation products. The data period is divided into six phases: (i) before purification, (ii) after purification, (iii) KamLAND-Zen 400 phase, (iv) after OD refurbishment works, (v) KamLAND-Zen 800 phase, and (vi) after Zen800. The periods after OD refurbishment and after Zen800 have relatively large statistical uncertainties, resulting in larger error bars. Based on these results, a conservative 2% uncertainty is assigned to account for the time variation of the energy scale.

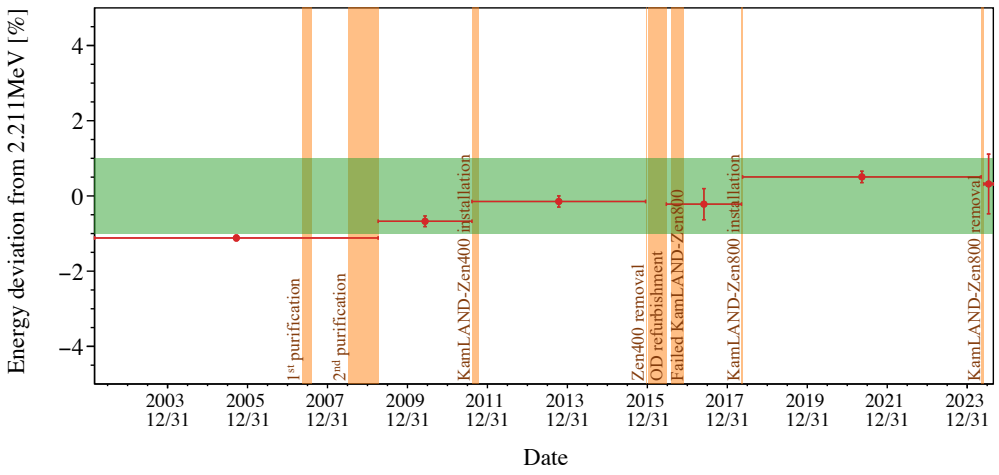

(a) Spallation neutron capture

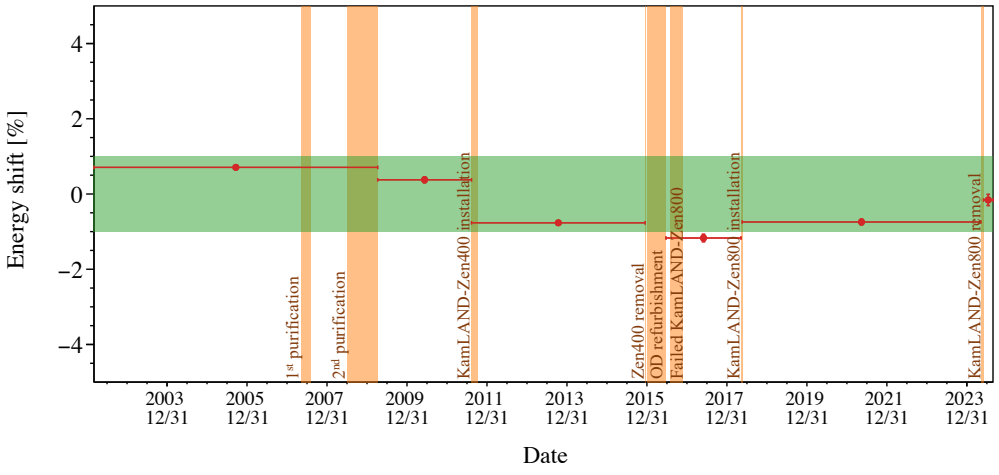

(b) Spallation ^{12}B/^{12}N beta spectrum

Figure 4.38: Time variation of the energy scale evaluated using various spallation products. (a) Deviation of the reconstructed energy of spallation neutron captures on protons from 2.211 MeV. (b) Energy shift of spallation ^{12}B/^{12}N events relative to the model. The orange shaded vertical regions indicate the periods of onsite work, while the green shaded horizontal band represents the ±1% range of energy deviation (shift).

Position dependence of energy scale

The position dependence of the reconstructed energy has been precisely measured through the 4π calibration. Here, the time variation of this position dependence is evaluated using spallation neutrons. Fig. 4.39 shows the radial dependence of the energy deviation for each period. for the periods without the miniballoon, the relative difference is evaluated with respect to the deviation in the central region (radius bin of 0–200 cm). During the KamLAND-Zen experimental periods, when the miniballoon was installed and events near the detector center were excluded from the fiducial volume, the 400-450 cm radius bin is used as the reference for the deviation. From this analysis, the position-dependent energy-scale uncertainty within the 550 cm fiducial volume is estimated to be 1%.

Summary of energy scale uncertainty

The total energy-scale uncertainty is obtained by combining the 2% contribution from time variation and the 1% contribution from position dependence as

$$\text{Energy scale uncertainty} = \sqrt{2\%^2 + 1\%^2} = 2.24\%. \tag{4.38}$$

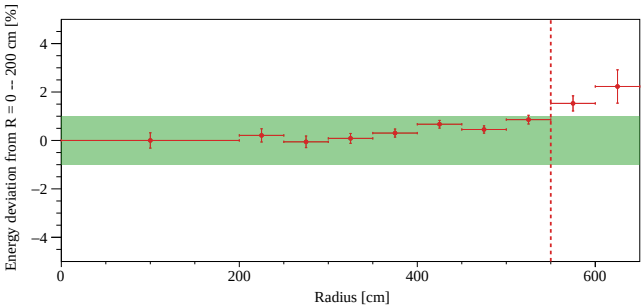

(a) Before purification

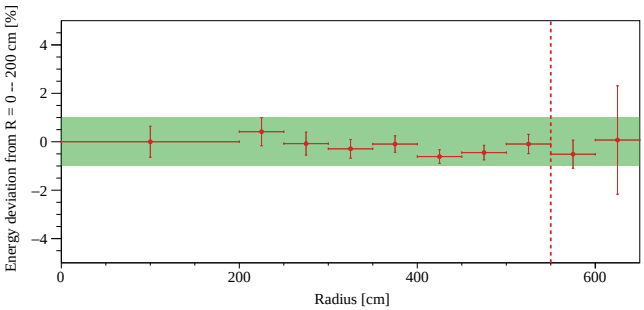

(b) After purification

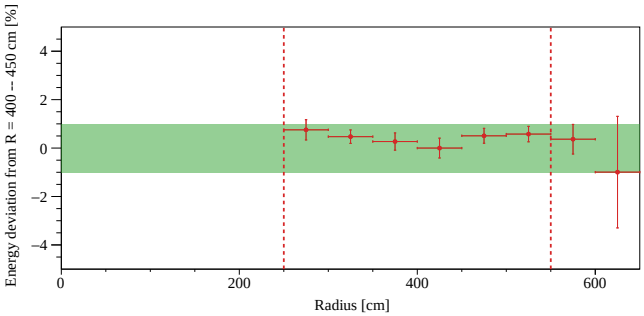

(c) Zen400

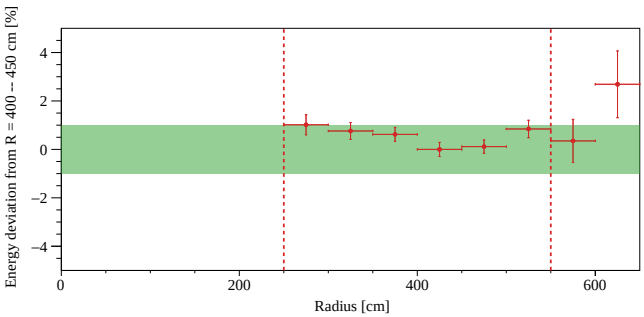

(d) Zen800

Figure 4.39: Radial dependence of the energy deviation evaluated using spallation neutron capture events for each period. The red dotted lines indicate radii of 250 cm and 550 cm, while the green shaded horizontal band represents the ±1% range of energy deviation. During the KamLAND-Zen experimental periods, the miniballoon region (< 250 cm) was not available; therefore, the energy deviation was evaluated based on the value in the 400–450 cm bin.

4.8.3 Fiducial Volume Uncertainty

The uncertainty of the fiducial volume was evaluated by the 4π calibration performed in 2006 and 2011; however, to assess its long-term stability, spallation products must be used. In addition, contributions from energy-dependent vertex bias and vertex correction are also taken into account as sources of uncertainty.

Uncertainty from 4π calibration and spallation events

For the before purification period, the uncertainty of the fiducial volume within a radius of 550 cm was estimated by the 4π calibration conducted in 2006, yielding a value of 1.6%. Defining P_{bef} as the number of protons contained with a 550 cm radius in the before purification period, this gives

$$\frac{\Delta P_{\mathrm{bef}}}{P_{\mathrm{bef}}} = 0.016. \tag{4.39}$$

Similarly, the uncertainty of the fiducial volume for the after purification period was estimated to be 3.3% from the 4π calibration performed in 2011:

$$\frac{\Delta P_{\mathrm{aft}}}{P_{\mathrm{aft}}} = 0.033. \tag{4.40}$$

After the start of the KamLAND-Zen 400 experiment, a miniballoon was installed at the detector center, making it impossible to perform fiducial volume calibration using deployed radioactive sources. Therefore, the fiducial volume after the purification period is evaluated using the time variation of spallation $^{12}\mathrm{B}/^{12}\mathrm{N}$ events. Fig. 4.40 shows the time variation of the ratio of $^{12}\mathrm{B}/^{12}\mathrm{N}$ events within a 550 cm radius to those in the full detector volume. The ratios of $^{12}\mathrm{B}$ event are estimated as follows for the after purification and after the start of KamLAND-Zen 400 periods:

$$\left(\frac{N_{550}}{N_{\mathrm{total}}}\right)_{\mathrm{aft}} = 0.6185 \pm 0.003518, \tag{4.41}$$

$$\left(\frac{N_{550}}{N_{\mathrm{total}}}\right)_{\mathrm{Zen}} = 0.5906 \pm 0.001765. \tag{4.42}$$

Let β denote the fiducial-volume scaling factor between the two periods. Then

$$P_{\mathrm{Zen}} = \beta P_{\mathrm{aft}}. \tag{4.43}$$

Assuming the $^{12}\mathrm{B}$ count ratio is proportional to the number of protons, β is obtained as

$$\beta = \frac{0.5906}{0.6185} = 0.9548. \tag{4.44}$$

Ideally $\beta = 1$; the deviation from 1 is taken as a contribution to the fiducial volume uncertainty, and the statistical uncertainty on β is also included. Accordingly, the relative uncertainty due to time variation, estimated from spallation $^{12}\mathrm{B}/^{12}\mathrm{N}$, is defined as

$$\begin{aligned}\frac{\Delta\beta}{\beta} &\equiv (1-\beta) + \sqrt{\left(\frac{P_{\mathrm{Zen}}\Delta P_{\mathrm{aft}}}{P_{\mathrm{aft}}^2}\right)^2 + \left(\frac{\Delta P_{\mathrm{Zen}}}{P_{\mathrm{aft}}}\right)^2} \\ &= (1-0.9541) + \sqrt{\left(\frac{0.5906 \times 0.003518}{0.6185^2}\right)^2 + \left(\frac{0.001765}{0.6185}\right)^2} = 0.051.\end{aligned} \tag{4.45}$$

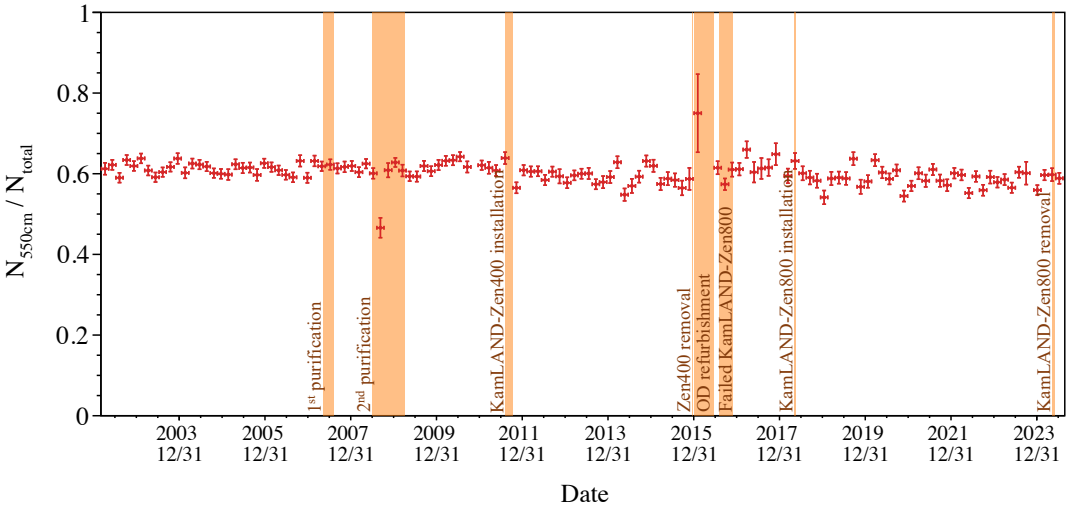

Figure 4.40: Time variation of the ratio of the number of ^{12}B/^{12}N events within a 550 cm radius to that within the full detector volume.

Thus, the fiducial volume uncertainty for the period following the start of the KamLAND-Zen 400 experiment is evaluated as follows:

$$\Delta P_{\mathrm{Zen}} = \sqrt{(P_{\mathrm{aft}}\Delta\beta)^2 + (\beta\Delta P_{\mathrm{Zen}})^2} \tag{4.46}$$

$$\frac{\Delta P_{\mathrm{Zen}}}{P_{\mathrm{Zen}}} = \sqrt{\left(\frac{\Delta\beta}{\beta}\right)^2 + \left(\frac{\Delta P_{\mathrm{Zen}}}{P_{\mathrm{Zen}}}\right)^2} = \sqrt{0.051^2 + 0.033^2} = 0.061. \tag{4.47}$$

Energy dependent vertex bias

Possible energy-dependent bias in the reconstructed vertex is assessed using delayed-coincidence-tagged prompt-delayed pairs spanning different energies. Since spallation ^{8}He/^{9}Li undergo β decay accompanied by a neutron, these isotopes provide a suitable sample for assessing the energy-dependent vertex bias. Fig. 4.41 shows the energy-dependent vertex bias evaluated with spallation ^{8}He/^{9}Li. In the absence of any energy-dependent bias between the prompt and delayed vertices, one expects $R_{\mathrm{neutron}} - R_{\mathrm{average}} = 0$. From this analysis, the vertex bias is found to be within 3 cm. When translated to a fractional uncertainty for a fiducial radius of 550 cm, this corresponds to $3/550 = 0.545\%$.

Uncertainties related to purification

Systematic uncertainties arising from the purification of the LS should also be taken into account. The LS volume measured by the flow meter is estimated to have decreased by 16 m^3 after purification. This corresponds to 1.4% of the total volume and is treated as an uncertainty on the fiducial volume. In addition, the LS light yield decreased after purification, introducing a 0.7% uncertainty at the energy threshold used for the ^{12}B/^{12}N selection ($E_{\mathrm{vis}} \geq 4$ MeV).

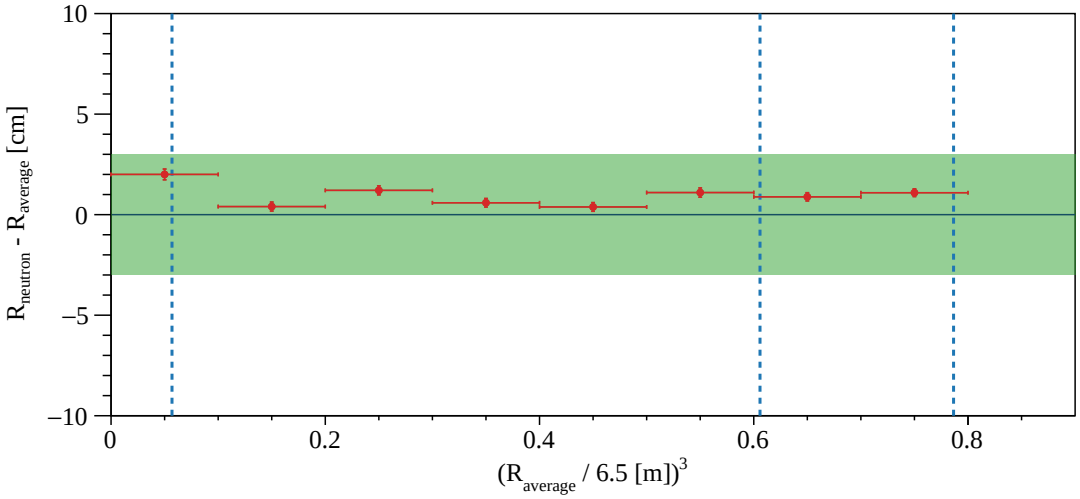

Figure 4.41: Energy dependent vertex bias evaluated using ^{8}He/^{9}Li delayed coincidence events. R_{neutron} is the vertex of delayed neutron captured event, and R_{average} is the mean vertex of prompt-delayed events. The blue dotted lines indicate radii of 250 cm, 550 cm, and 600 cm, while the green shaded horizontal band represents the ±3 cm difference.

Summary of fiducial volume uncertainty

The fiducial-volume uncertainties from the 4π calibrations and from the spallation product study, each of which includes time variation, are first evaluated. The total fiducial-volume uncertainty is then obtained by adding these in quadrature with the contribution from the energy-dependent vertex bias and the purification effect; the results are summarized in Tab. 4.2.

Table 4.2: Summary of fiducial volume uncertainty

Period	Uncertainty
before purification	1.7%
after purification	3.7%
post Zen400 start	6.3%

Chapter 5

Neural Network Models

In the search for astrophysical neutrinos in KamLAND, the dominant background around 10 MeV in the observed energy region arises from atmospheric neutrinos (and fast neutrons). Both electron antineutrino-induced inverse beta decay signals and background events by atmospheric neutrinos create time- and space-correlated events, leading conventional delayed coincidence discrimination (Sec. 7.4) challenging. However, differences in hit characteristics—such as charge, timing, and position—arise due to variations in their interactions and final-state particles. KamNet, a deep neural network developed by the KamLAND group, utilizes this hit information to effectively distinguish between these event types. This chapter presents an introduction of machine learning and neural networks in Sec. 5.1 and Sec. 5.2, respectively. After that, an overview of KamNet is described in Sec. 5.3 , with details on its unique features provided in Sec. 5.3.2, 5.3.3, and 5.3.4. Applications of KamNet to the astrophysical neutrino search are discussed in the following chapter.

5.1 Machine Learning

Machine learning, which has developed as a subfield of artificial intelligence (AI), is a methodology that enables computers to autonomously learn models capable of analyzing data, identifying patterns, and making decisions. Machine learning is generally categorized into supervised learning, unsupervised learning, and reinforcement learning. Among these, supervised learning comprises two principal problem settings: classification and regression. Classification is the task of learning from data labeled with discrete class values in order to predict the class label of new data. In contrast, regression is the task of constructing a model that predicts a continuous target variable from the relationship between input features and the target. The separation of signal and background events addressed in this study corresponds to a classification task within supervised learning.

Representative methods for addressing classification tasks include decision trees, logistic regression, and support vector machines. These approaches can achieve sufficiency classification performance for relatively small- to medium-scale datasets; however, their performance often degrades when applied to large datasets or to data with high dimensionality and complex structures, owing to limitations in expressive power and computational cost. One approach to overcoming these limitations is to apply neural networks to classification problems, as described in the following section. It should be noted, however, that neural networks also require substantial training data and computational resources, and they are subject to the risk of overfitting.

5.2 Neural Network

5.2.1 Fully Connected Neural Network (FCNN)

Basic concept of neural network

In the field of AI, the concept of an artificial neuron was inspired by the function of biological nerve cells. It was proposed as a gate that *receives multiple signals and generates an output signal when the accumulated input exceeds a threshold.* An algorithm constructed by combining such artificial neurons is called a neural network. In supervised learning classification tasks, neural networks are utilized to predict the class label to which the input signal belongs.

If the input data of the neural network are denoted by x_i $(i = 1, 2, .., n)$, the weights by w_i, and the bias by b, then the net input z can be expressed as follows:

$$z = w_1 x_1 + ... + w_n x_n + b = \boldsymbol{w}^{\boldsymbol{T}} \boldsymbol{x} + b. \tag{5.1}$$

The net input is passed through the activation function σ, introducing non-linearity, and in some cases it is further processed by a threshold function to compute the predicted class label. By comparing this predicted value with the true class label, a loss function is computed. The values of the weights and the bias are then updated by feeding back from the loss function, allowing the learning process to proceed toward achieving more accurate predictions. Fig. 5.1 shows the schematic view of an example of a single-layer neural network composed only of an input layer and an output layer[1]. In such a structure, each output unit is expressed as a linear combination of all input input units with associated weights and a bias; a neural network with this property is referred to as a fully connected neural network (FCNN).

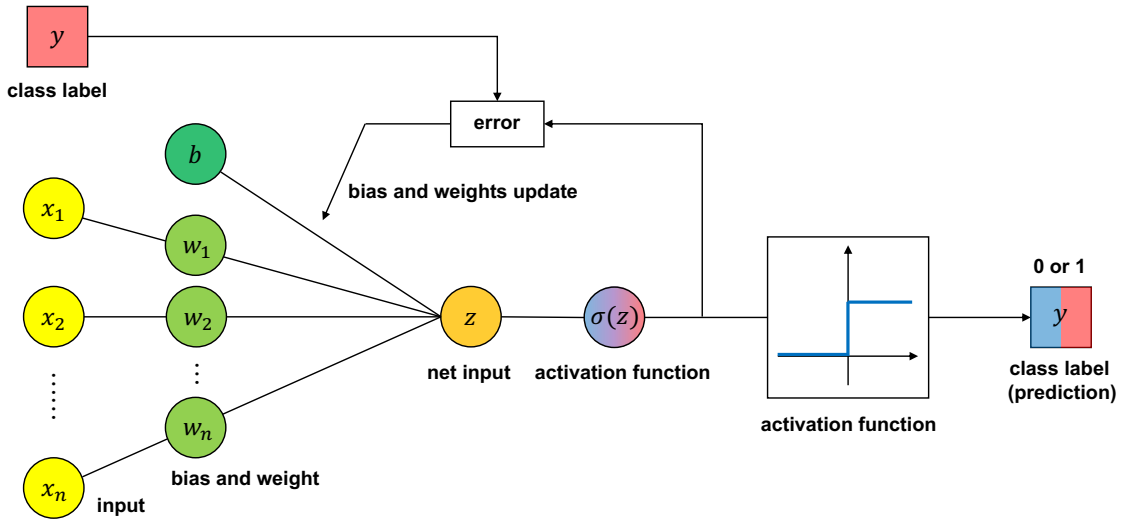

Figure 5.1: Example of a single-layer neural network. In binary classification tasks, the output value obtained after passing through the activation function is converted into a class label of 0 or 1 by applying a threshold function. When the activation function is a sigmoid, its output can be interpreted as a continuous probability value between 0 and 1.

A neural network obtained by inserting a hidden layer between the input and output layers of the single-layer network shown above is referred to as a deep neural network.

[1]Although it may appear counterintuitive, a neural network consisting solely of an input layer and an output layer is referred to as a 'single-layer' neural network.

Introducing hidden layers increases the nonlinearity of the model, thereby enabling it to handle more complex tasks. Fig. 5.2 illustrates a schematic view of a neural network with one hidden layer. The output of each layer can be described as follows:

- Output of the hidden layer j $(j = 1, 2, ..., m)$

$$a_j^{(h)} = \sigma\left(z_j^{(h)}\right) = \sigma\left(\sum_{i=1}^{n} w_{j,i}^{(h)} x_i + b^{(h)}\right) \tag{5.2}$$

- Output of the output layer k $(k = 1, 2, ..., l)$

$$a_k^{(o)} = \sigma\left(z_k^{(o)}\right) = \sigma\left(\sum_{j=1}^{m} w_{k,j}^{(o)} a_j^{(h)} + b^{(o)}\right) \tag{5.3}$$

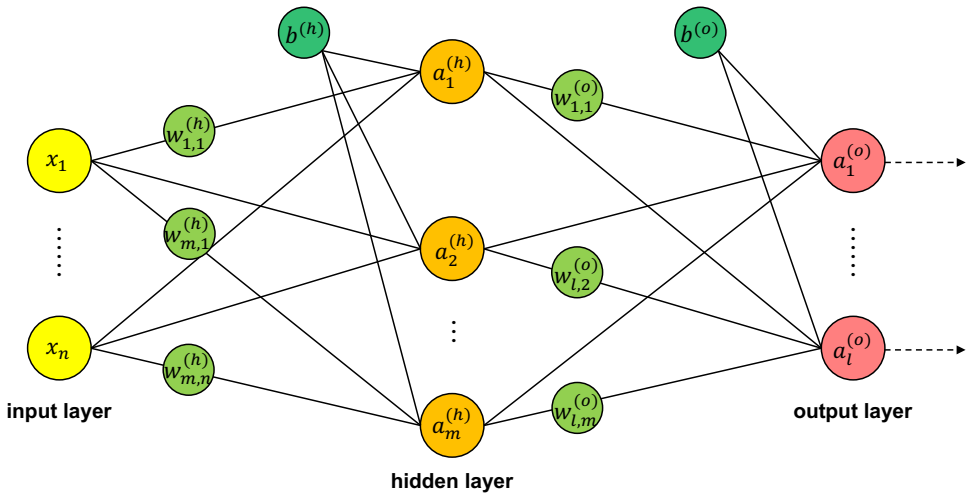

Figure 5.2: Neural network with one hidden layer. The numbers of units in the input, hidden, and output layers are denoted by n, m, and l, respectively.

Activation function

In the original perceptron, which served as a prototype of neural networks, the activation function was a step function. Subsequently, ADALINE was proposed with the identity function as its activation function, allowing the loss function to be defined in terms of continuous values. However, in order to address more complex tasks, it was necessary to introduce nonlinearity into the network. For this purpose, nonlinear functions such as the sigmoid function and the hyperbolic tangent function were introduced, and in recent years the Rectified Linear Unit (ReLU) has become widely used. Tab. 5.1 summarizes examples of activation functions and their primary applications.

Loss function and backpropagation

In supervised learning, the loss function is computed at each training step, and the weights and biases are updated so as to minimize the value of the loss function. This function serves as an objective function to be optimized, quantitatively evaluating the discrepancy between the predicted and true outputs. Representative loss functions include the following:

Table 5.1: Examples of the activation functions

Activation function	Expression	Major applications
Heaviside step function	$\sigma(z) = \begin{cases} 0 & z < 0 \\ 0.5 & z = 0 \\ 1 & z > 0 \end{cases}$	perceptron
Linear function	$\sigma(z) = z$	ADALINE, linear regression
Logistic (sigmoid) function	$\sigma(z) = \dfrac{1}{1+e^{-z}}$	logistic regression, FCNN
Hyperbolic tangent function	$\sigma(z) = \dfrac{e^{z}-e^{-z}}{e^{z}+e^{-z}}$	FCNN, RNN
Rectified Linear Unit (ReLU)	$\sigma(z) = \begin{cases} 0 & z \leq 0 \\ z & z > 0 \end{cases}$	FCNN, CNN

- Cross Entropy (CE)

$$L(\boldsymbol{w}, b) = -\sum_{i=1}^{n} \sigma\left(z^{(i)}\right) \log y^{(i)} \tag{5.4}$$

  This function is well suited for classification tasks in which the predicted probabilities are compared with discrete class labels.

- Mean Square Error (MSE)

$$L(\boldsymbol{w}, b) = \frac{1}{n} \sum_{i=1}^{n} \left(y^{(i)} - \sigma\left(z^{(i)}\right)\right)^2 \tag{5.5}$$

  This function is appropriate for regression tasks under the assumption that the outputs follow a Gaussian distribution. Although MSE can also be used for classification, CE is generally preferred in practice owing to its efficiency and probabilistic foundation.

The update of parameters is based on the gradient of the loss function and can be written as

$$\boldsymbol{w} := \boldsymbol{w} + \Delta\boldsymbol{w} = \boldsymbol{w} - \eta \nabla_w L(\boldsymbol{w}, b) \tag{5.6}$$

$$b := b + \Delta b = b - \eta \nabla_b L(\boldsymbol{w}, b). \tag{5.7}$$

Here, η denotes the learning rate, a hyperparameter that requires tuning to achieve both efficient convergence and satisfactory performance of the trained network.

In deep neural networks, parameter updates are carried out using the backpropagation algorithm. This method propagates the partial derivatives of the loss function from the output layer back to the input layer based on the chain rule, thereby enabling efficient computation of the gradients for parameters. For instance, the partial derivative required

to update an output-layer weight $w_{1,1}^{(o)}$ can be expressed as:

$$\frac{\partial L}{\partial w_{1,1}^{(o)}} = \frac{\partial L}{\partial a_1^{(o)}} \cdot \frac{\partial a_1^{(o)}}{\partial z_1^{(o)}} \cdot \frac{\partial z_1^{(o)}}{\partial w_{1,1}^{(o)}}. \tag{5.8}$$

Such calculations are performed for all parameters in every layer, after which their values are updated and the training proceeds to the next step.

5.2.2 Convolutional Neural Network (CNN)

Convolutional Neural Networks (CNNs) are models inspired by the functioning of the human visual cortex and have demonstrated high discriminative performance in image classification tasks. In CNNs, low-level features such as edges and and blobs[2] are extracted in the layers close to the input image, and these features are combined in deeper layers to form higher-level representations such as object contours and shapes. CNNs are generally composed of multiple convolutional layers and pooling layers, although in recent architectures pooling is often replaced by strided convolutions. In the following, a CNN for two-dimensional image classification is described as an example.

Fig. 5.3 illustrates an example of convolution and pooling. In a convolutional layer, a convolution operation is performed between the input tensor and a filter, where each element of the filter represents a trainable weight. In this operation, the element-wise products between the filter and the input are summed to produce an output value (feature map). The filter is then shifted by the stride, and the same computation is repeated. By performing this operation across the entire input image, an output feature map is obtained. To control the output size, padding is applied by adding zero-valued elements around the input. In the example shown in Fig. 5.3, padding ensures that the size of the output vector is identical to that of the input vector. Let the input size be n, the filter size m, the padding p, and the stride s. Then, the output size o is given by

$$o = \frac{n + 2p - m}{s} + 1. \tag{5.9}$$

The pooling layer computes, for each local region of the feature map, either the maximum or the average value, thereby reducing the dimensionality. This not only decreases the computational cost but also provides local translation invariance to the feature representation.

Fig. 5.4 shows an example of a deep convolutional neural network (DCNN) consisting of two convolutional layers and two pooling layers. The feature maps produced by the CNN are multidimensional tensors, which are flattened into one-dimensional vectors before being connected to fully connected layers. This process transforms features that depend on the position and shape in the image into a simple vector form suitable for classification. The flattened vector is then passed to a fully connected neural network, and finally, the output layer with a softmax function provides the probability distribution over the class labels.

5.2.3 Recurrent Neural Network (RNN)

In the neural networks introduced earlier, the input data are assumed to be independent. However, in the case of sequential data, the inputs are not independent, and their order carries essential information. Recurrent Neural Networks (RNNs) were developed to exploit

[2] A blob refers to a local patch in an image characterized by a region of relatively uniform intensity or a spot-like structure, serving as one of the basic elements for feature extraction.

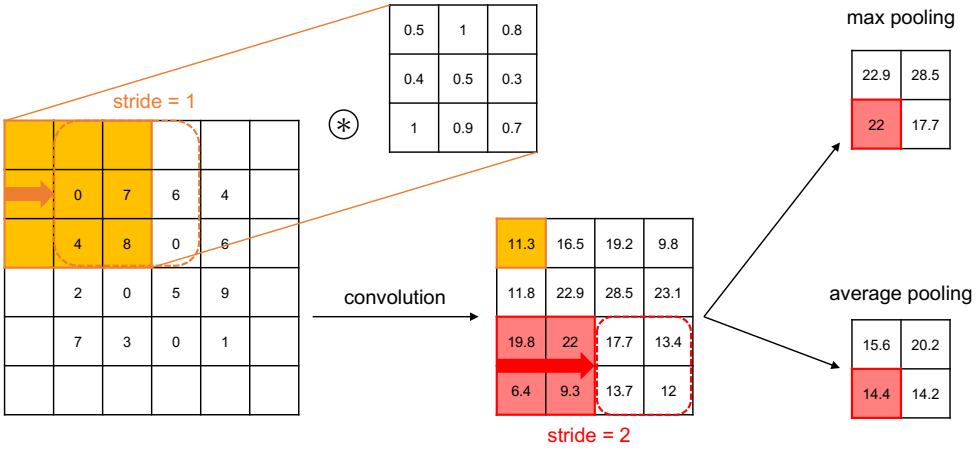

Figure 5.3: Example of convolution and pooling. A 4×4 input tensor is padded with zeros around its boundary, and a 3×3 filter is applied through convolution. With a stride of 1, the resulting output feature map has a size of 4×4. When pooling is performed over 2×2 regions with a stride of 2, the output feature map is reduced to 2×2.

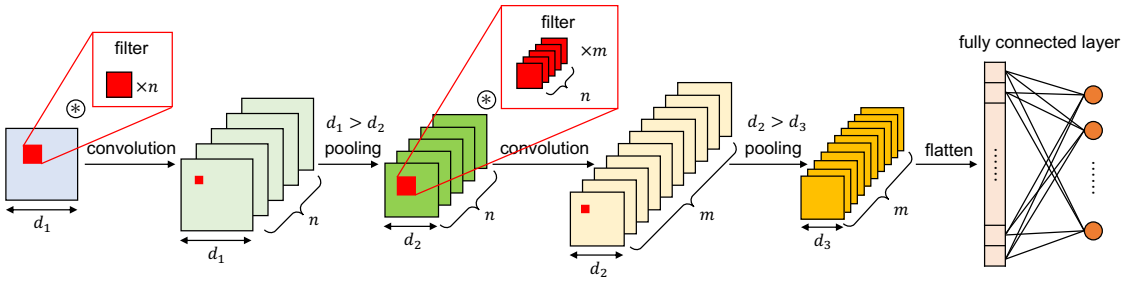

Figure 5.4: Example of a deep convolutional neural network.

such order information. Here, we take time series data as a representative example of sequential data and describe the structure of RNNs[3].

Fig. 5.5 illustrates an example of an RNN with a single hidden layer. Let the input at time step t be denoted as $\boldsymbol{x}^{(t)}$ $(t = 0, 1, ..., T)$, and the output as $\boldsymbol{o}^{(t)}$. At each time step, there exists a hidden state $\boldsymbol{h}^{(t)}$. The net input of the hidden state, $z_h^{(t)}$, is computed from the input $\boldsymbol{x}^{(t)}$ at the same time step and the hidden state $\boldsymbol{h}^{(t-1)}$ from the previous time step as follows:

$$z_h^{(t)} = \boldsymbol{W}_{xh}\boldsymbol{x}^{(t)} + \boldsymbol{W}_{hh}\boldsymbol{h}^{(t-1)} + b_h \tag{5.10}$$

Here, $\boldsymbol{W}_{xh}$ is the weight matrix between the input and hidden layers, $\boldsymbol{W}_{hh}$ is the recurrent weight matrix between hidden states, and b_h is the bias parameter of the hidden layer. The hidden state is then updated using the activation function σ_h as:

$$\boldsymbol{h}^{(t)} = \sigma_h\left(z_h^{(t)}\right) = \sigma_h\left(\boldsymbol{W}_{xh}\boldsymbol{x}^{(t)} + \boldsymbol{W}_{hh}\boldsymbol{h}^{(t-1)} + b_h\right) \tag{5.11}$$

The activation of the output layer is expressed by applying the weight matrix $\boldsymbol{W}_{ho}$ and bias parameter b_o to the hidden state:

$$\boldsymbol{o}^{(t)} = \sigma_o\left(\boldsymbol{W}_{ho}\boldsymbol{h}^{(t)} + b_o\right) \tag{5.12}$$

In this way, information flows across hidden states over time, allowing the network to retain past information and exploit the order structure inherent in sequential data. Another characteristic of RNNs is that the same set of parameters is shared across all time steps. However, standard RNNs have difficulty in capturing long-term dependencies due to issues such as vanishing and exploding gradients. To overcome these limitations, extended models such as long short-term memory (LSTM) has been developed.

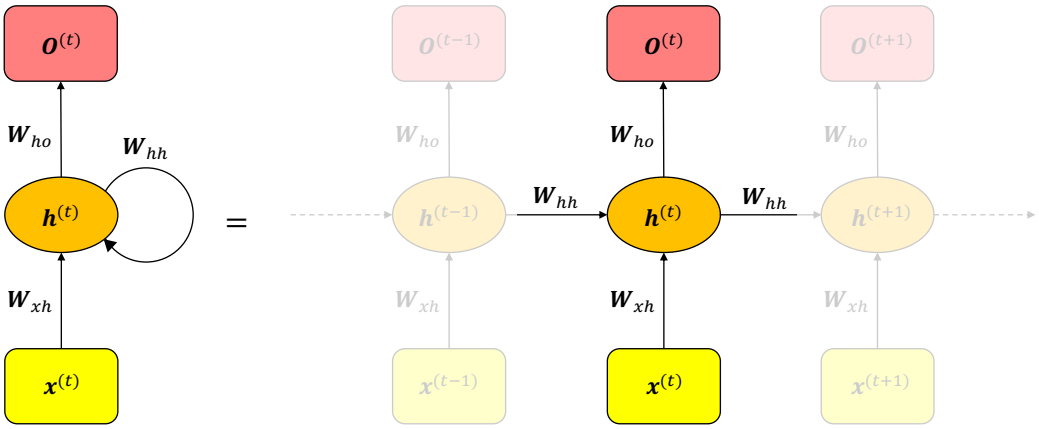

Figure 5.5: Example of a recurrent neural network.

[3]Other examples of sequential data include natural language, speech, and video.

5.3 KamNet

5.3.1 Overview of KamNet

KamNet is a deep neural network initially developed for the analysis of neutrinoless double beta decay ($0\nu\beta\beta$) in the KamLAND-Zen experiment. The $0\nu\beta\beta$ signal comprises two electrons, while a typical background source is ^{214}Bi $\beta+\gamma$ decay. Electrons deposit their energy locally in LS, resulting in highly isotropic scintillation light. In contrast, γ rays undergo multiple Compton scatters, producing slightly less isotropic scintillation light. KamNet is designed to leverage these differences in PMT hit information to discriminate between signal and background events.

The input of KamNet is a time sequence of a spherical PMT hit map. Fig. 5.6 illustrates an example input for KamNet in the $0\nu\beta\beta$ analysis. Here, the proper hit time τ is calculated by the following equation:

$$\tau = T_{\text{raw}} - \text{TOF} - T_0 \tag{5.13}$$

where T_{raw} represents the PMT hit time by a photon, TOF is the time-of-flight of photons from the event vertex to the PMT location, and T_0 is the proper start time. Time window for KamNet input ranges from -20 to +24 ns around $\tau = 0$, with a bin width of 1.5 ns per time interval. A spherical hit map is labeled by the azimuthal angle ϕ and polar angle θ axis, with each axis divided into 38 bins. Consequently, the time sequence of the spherical PMT hit map, which forms the overall input for KamNet, has dimensions of $28 \times 38 \times 38$, corresponding to the t, θ and ϕ axes.

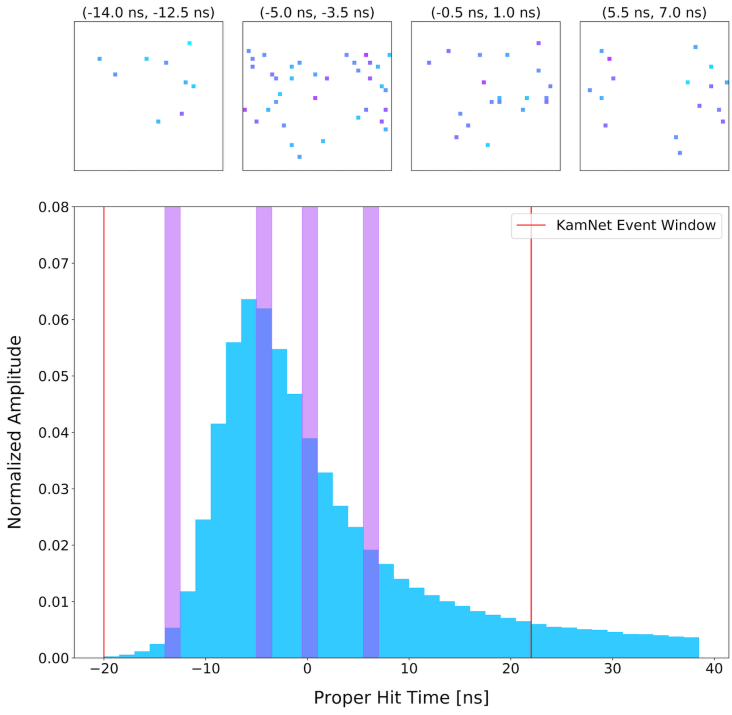

Figure 5.6: Input example of KamNet [75]. The lower figure shows PMT hit time distribution. Upper figures show spherical hit distributions of the PMT hit times highlighted in violet bands.

Fig. 5.7 illustrates the schematic diagram of KamNet. The initial layer represents the input images as outlined above. These images pass through Convolutional Long Short Term Memory (ConvLSTM, referred in Sec. 5.3.2) layers, converting them into images with dimensions $22 \times 38 \times 38$ along the c (context), θ, and ϕ dimensions. Next, an S^2

convolution transforms the 2D spherical surface images into 3D rotational images, followed by convolutions based on the special orthogonal group across four KamNet layers. This approach, using S^2 and SO(3) convolutions to retain spherical symmetry, is known as the Spherical Convolutional Neural Network (Spherical CNN), detailed in Sec. 5.3.3. Between each Spherical CNN layer, values undergo activation via the Rectified Linear Unit (ReLU) function. ReLU is a standard activation method in which the output is linear ($f(x) = x$) for positive inputs and zero for negative ones. To mitigate overfitting, where neurons become overly dependent on specific other neurons, dropout layers (Drop) are applied; certain neurons have their input set to zero with a set probability, promoting generalization. Both ReLU activations and dropout mechanisms are incorporated into the Spherical CNN layers.

After the final layer of the Spherical CNN, the input images are condensed into a 128-dimensional feature vector. This vector is then classified by a fully connected (FC) network with ReLU activation and dropout layers. The input feature values are scaled and shifted so that their distribution has a mean of zero and a standard deviation of one—a process known as Batch Normalization (Norm). Ultimately, KamNet generates a score for each event, with higher scores indicating a greater likelihood of signal-like characteristics in the input event.

5.3.2 Convolutional Long Short Term Memory

The Long Short Term Memory (LSTM) network was developed as a specialized architecture of recurrent neural networks (RNNs), exhibiting stable and robust performance in processing sequential data with long-range dependencies. A distinctive feature of the LSTM architectures is its memory cell, denoted as c_t, which serves as a state information accumulator. The memory cell comprises several gates that regulate its functionality. The advantage of using such memory cells and gates to handle sequential information is that the gradient does not vanish too quickly, which is a major problem seen in ordinal RNNs. When the input gate, denoted i_t, is activated, the incoming information is accumulated in the cell. In contrast, the forget gate, f_t, determines the extent to which the previous cell state, c_{t-1}, is retained or discarded, with this operation being governed by a sigmoid activation function. The updated cell state, c_t, is then propagated to the final cell output, denoted h_t. Finally, the output of the memory cell is modulated by the output gate, o_t. To summarize, the key equations of LSTM are expressed as follows:

$$
\begin{aligned}
i_t &= \sigma(W_{xi}x_t + W_{hi}h_{t-1} + W_{ci} \circ c_{t-1} + b_i) && (5.14)\\
f_t &= \sigma(W_{xf}x_t + W_{hf}h_{t-1} + W_{cf} \circ c_{t-1} + b_f) && (5.15)\\
c_t &= f_t \circ c_{t-1} + i_t \circ \tanh\left(W_{xc}x_t + W_{hc}h_{t-1} + b_c\right) && (5.16)\\
o_t &= \sigma(W_{xo}x_t + W_{ho}h_{t-1} + W_{co} \circ c_t + b_o) && (5.17)\\
h_t &= o_t \circ \tanh\left(c_t\right) && (5.18)
\end{aligned}
$$

where Ws denote the weights of each values, bs denote the biases, and $\circ$ denotes the Hadamard product.

When the information is 1D vectors, Fully Connected LSTM (FC-LSTM) would be a good choice as an extended version of LSTM. However, in this context, KamNet deals with 2D images with temporal correlation. To reduce much of the redundancy seen in FC-LSTM, convolutional operators are incorporated into the LSTM architecture (ConvLSTM [76]). In ConvLSTM, the future state of a given memory cell is determined by the input state and the past states of its local neighbors. The equations of each ConvLSTM state are shown

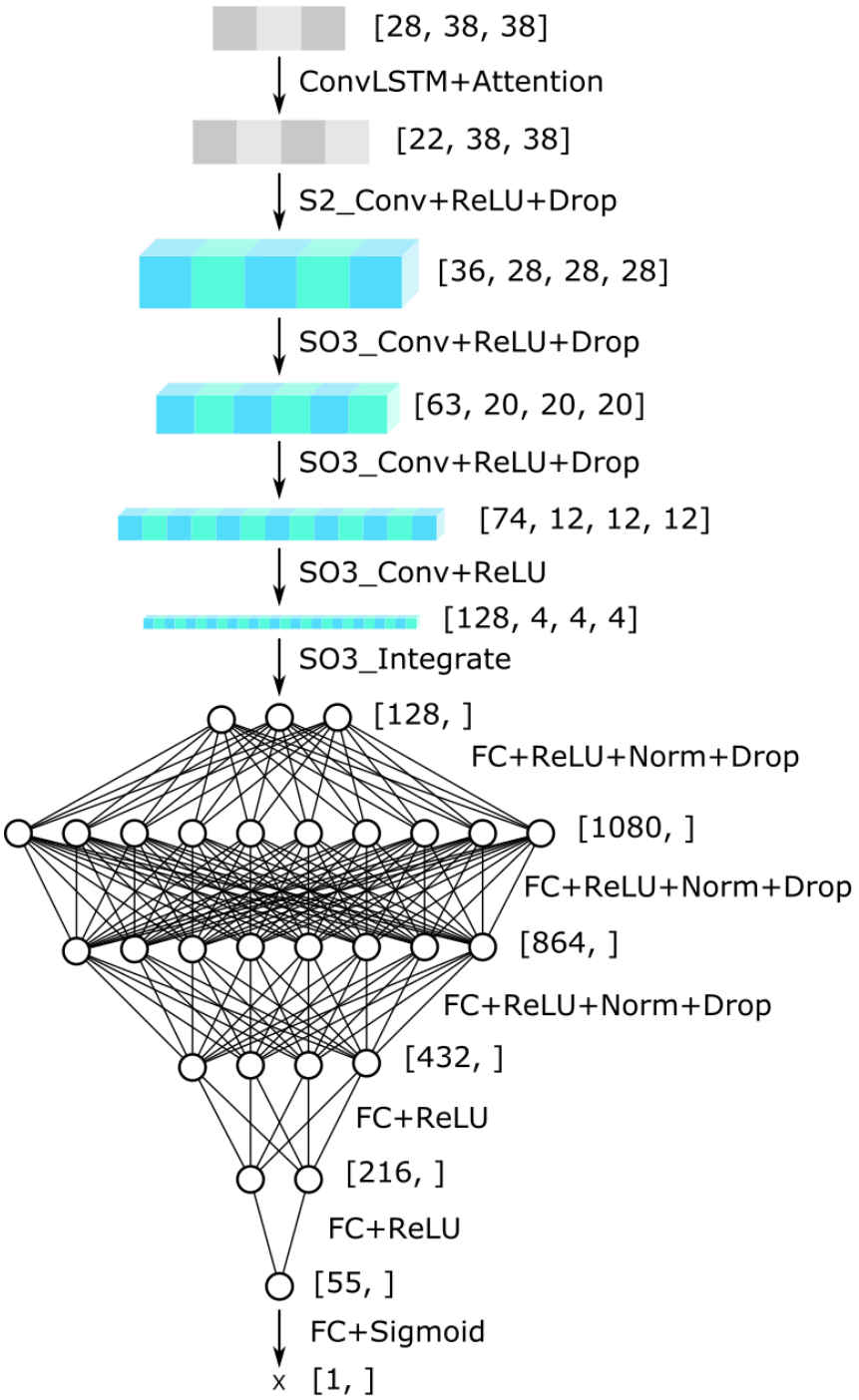

Figure 5.7: Schematic diagram of KamNet [75].

below:

$$
\begin{aligned}
i_t &= \sigma(W_{xi} * \mathcal{X}_t + W_{hi} * \mathcal{H}_{t-1} + W_{ci} \circ \mathcal{C}_{t-1} + b_i) && (5.19)\\
f_t &= \sigma(W_{xf} * \mathcal{X}_t + W_{hf} * \mathcal{H}_{t-1} + W_{cf} \circ \mathcal{C}_{t-1} + b_f) && (5.20)\\
\mathcal{C}_t &= f_t \circ \mathcal{C}_{t-1} + i_t \circ \tanh\left(W_{xc} * \mathcal{X}_t + W_{hc} * \mathcal{H}_{t-1} + b_c\right) && (5.21)\\
o_t &= \sigma(W_{xo} * \mathcal{X}_t + W_{ho} * \mathcal{H}_{t-1} + W_{co} \circ \mathcal{C}_t + b_o) && (5.22)\\
\mathcal{H}_t &= o_t \circ \tanh\left(\mathcal{C}_t\right) && (5.23)
\end{aligned}
$$

where $*$ represents the convolution operator and $\circ$ represents the Hadmard product. Fig. 5.8 shows the schematic diagram of the ConvLSTM layer in KamNet. It consists of two ConvLSTM layers and incorporates an attention mechanism.

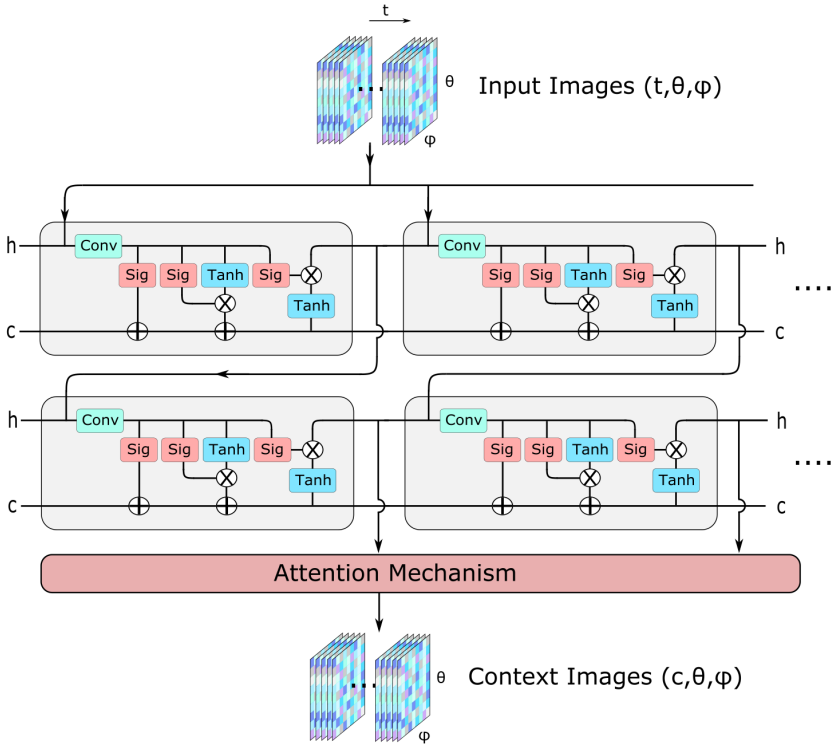

Figure 5.8: Schematic diagram of the ConvLSTM layer [75]. This diagram includes two ConvLSTM layers and the attention mechanism.

ConvLSTM, like conventional RNNs, is capable of capturing local dependencies in sequential data, while the convolutional operations additionally enable it to model local spatial structures. However, this alone is insufficient for incorporating more global information across the sequence. To address this limitation, an attention mechanism is introduced into ConvLSTM, which assigns a score to each time step of the sequence. This score represents how strongly each temporal unit contributes to the classification task—that is, its relative importance—and thereby helps to improve classification performance.

Let the hidden state output of the ConvLSTM be denoted as $I_{\text{hidden}}(c, t, \theta, \phi)$, and the integrated output over the temporal dimension be denoted as $I_{\text{output}}(c, \theta, \phi)$. The attention score at time step t, $S(t)$, is defined as follows:

$$
S(t) = \text{Softmax}\left[I_{\text{hidden}}(c, t, \theta, \phi) \circ W(c, t, \theta, \phi) \circ I_{\text{output}}(c, \theta, \phi)\right] \qquad (5.24)
$$

Here, $W(c, t, \theta, \phi)$ represents a set of trainable weight parameters updated during learning.

The final output of the convLSTM, $I_{\text{context}}(c, \theta, \phi)$, is obtained by weighting the hidden states with the corresponding attention scores, as expressed by the following equation:

$$I_{\text{context}}(c, \theta, \phi) = \sum_t S(t) I_{\text{hidden}}(c, t, \theta, \phi). \tag{5.25}$$

The attention score can be visualized and thus serves as an interpretable indicator of which temporal information the network emphasizes as being important.

5.3.3 Spherical Convolutional Neural Network

Due to the geometry of the KamLAND's inner detector, the input images to KamNet exhibit spherical symmetry. While CNNs are widely employed for the feature extraction in 2D images, directly applying a naive planar projection of spherical signals introduces significant spatial distortions. The discrepancy in invariance between planar and spherical images gives rise to this issue. Specifically, while the motion space in a two-dimensional plane is isomorphic to the plane itself, the motion space on a sphere corresponds to the three-dimensional manifold known as SO(3). As a result, convolution operations on a plane can be implemented using sliding filters that preserve translational symmetry; however, implementing convolution operations on a sphere requires special techniques to preserve rotational symmetry.

In the KamNet architecture, the Spherical Convolutional Neural Network (Spherical CNN) [77] is introduced to solve this problem. Fig. 5.9 shows the processing of spherical correlations by the Spherical CNN. As described in Sec. 5.3, the input signals of KamNet possess two spatial dimensions: the azimuth angle $\theta \in [0, 2\pi]$ and the zenith angle $\phi \in [0, \pi]$. In order to consider the spherical correlation between signal f and filter ψ, the generalized Fourier transform (GFT) is employed. Given Y_m^l as the spherical harmonics, the GFT of signals f on the sphere S^2 can be expressed as follows:

$$\hat{f}_m^l = \int_{S^2} f(x) \bar{Y}_m^l dx \tag{5.26}$$

where x represents points on the sphere. As in Eq. 5.26, local filters ψ are also Fourier-transformed. The multiplication of signals and filters is based on the indices l and m, resulting in the creation of block-wise tensors. These tensors are labeled by the indices l, m, and n, and they are summed up over channels. To generate correlation maps in the SO(3) space, the inverse Fourier transform of the spherical correlation $\hat{f}_{mn}^l$ is applied as follows:

$$f(R) = \sum_{l=0}^{b} (2l+1) \sum_{m=-l}^{l} \sum_{n=-l}^{l} \hat{f}_{mn}^l D_{mn}^l(R) \tag{5.27}$$

where D_{mn}^l represents the Wigner D-function and R represents rotations on SO(3). Here, the 3D correlation map $f(R)$ is described using ZYZ-Euler angles α, β, and γ. SO(3) convolution is performed by 3D filters, which have Euler angle axes.

5.3.4 Additional Structures

After the spherical CNN, the extracted features are flattened and integrated through fully connected (FC) layers. The activation function employed in KamNet is ReLU, as it is particularly well suited for CNNs. Compared with sigmoid or tanh functions, ReLU alleviates the vanishing gradient problem, provides computational efficiency. It also introduces sparsity in the feature maps, which collectively contribute to stable learning in deep CNNs. As the loss

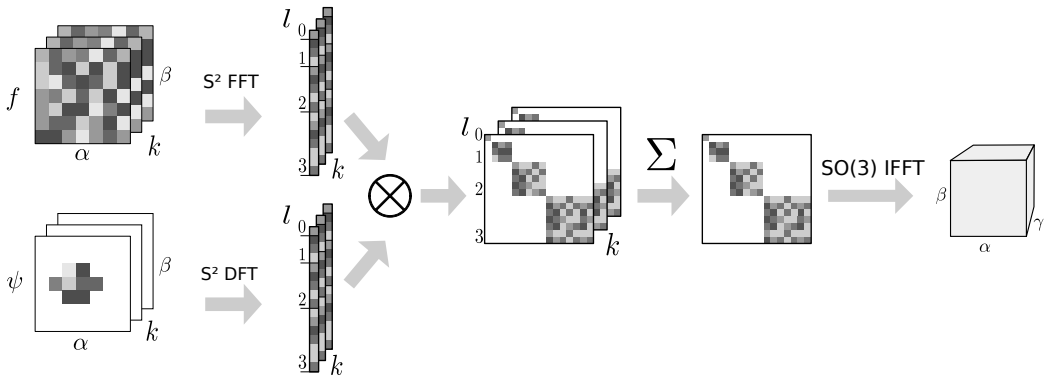

Figure 5.9: Processing of spherical correlations by the Spherical CNN [77]. The signal f and the filter ψ with k channels are Fourier transformed. The spherical correlation is calculated by the multiplication of signals and filters, then they are summed over channels. As a result of the inverse Fourier transform, feature maps are generated with ZYZ-Euler angles α, β, and γ

function, binary cross entropy is adopted, which is commonly used for binary classification tasks.

Chapter 6

Application of KamNet for the Astrophysical Antineutrino Search

In the search for astrophysical neutrinos with KamLAND, electron antineutrinos ($\bar{\nu}_e$s) are detected via the inverse beta decay (IBD) interaction, identified through the delayed coincidence method (detailed in Sec.7.4). To improve the sensitivity of this search, it is crucial to suppress other backgrounds that can also produce delayed coincidence events. In this study, we focus on the differences in hit-pattern information arising from the distinct interaction process of signal and background events, and develop an event classification method to distinguish them. The classification technique employed in this work is based on KamNet, a deep neural network (DNN) introduced in Chap. 5. The event identification method developed in this chapter is used for the selection of $\bar{\nu}_e$ candidates in Chap. 7. Furthermore, the rejection efficiencies estimated here are applied to the background estimation described in Chap. 8.

6.1 Overview of This Study

In the IBD interaction, an $\bar{\nu}_e$ interacts with a proton to produce a positron and a neutron. The generated positron annihilates with an electron, emitting gamma rays that form the prompt event. Meanwhile, the neutron becomes thermalized and is subsequently captured by a proton, releasing a 2.2 MeV gamma ray that is observed as the delayed event. These prompt and delayed events are detected as delayed-coincidence events by exploiting their temporal and spatial correlations (Fig. 6.1 (a)). A major background for such delayed-coincidence events arises from neutral-current (NC) interactions induced by atmospheric neutrinos. In KamLAND, NC interactions primarily produce an excited ^{11}C nucleus and a neutron. The de-excitation of ^{11}C and proton recoils caused by neutron scattering are observed as the prompt event, while neutron capture on a proton produces the delayed event in a manner same as IBD (Fig. 6.1 (b)). Consequently, IBD signals and atmospheric neutrino background events exhibit no significant differences in *downstream* observables such as visible energy or reconstructed event position, making it difficult to distinguish them using conventional analysis methods.

On the other hand, the two types of events differ in the species of interacting particles, their ranges, and the characteristics of their energy deposition. As a representative example, Fig. 6.2 presents the track information of the positron and annihilation gamma rays produced in IBD, while Fig. 6.3 shows the track information of neutrons produced in atmospheric neutrino NC interactions. For the IBD sample, histograms are filled using track information from 100 events generated at the detecter center with a visible energy of ∼10 MeV. For the NC sample, histograms are filled using track information from 100 neutrons with an

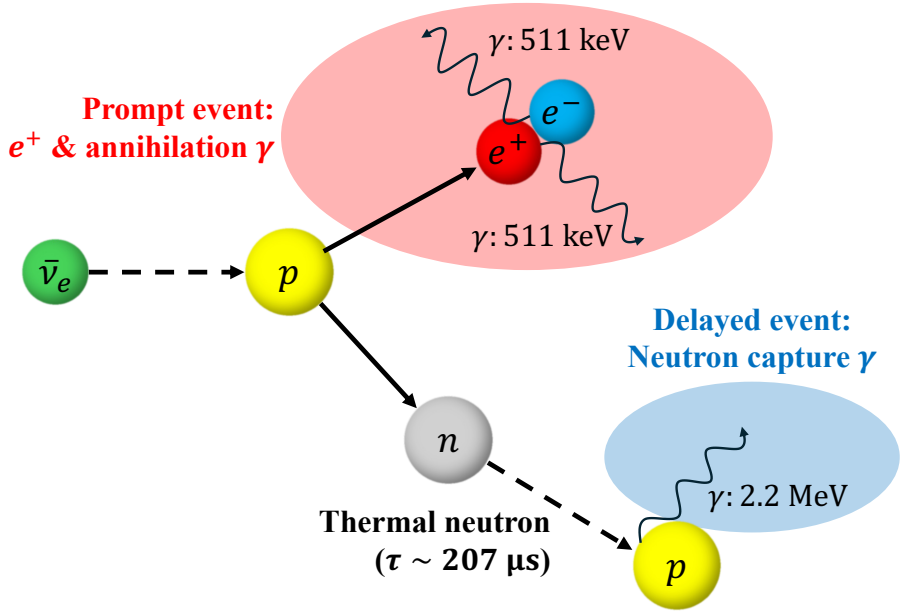

(a) Inverse Beta Decay interaction (signal)

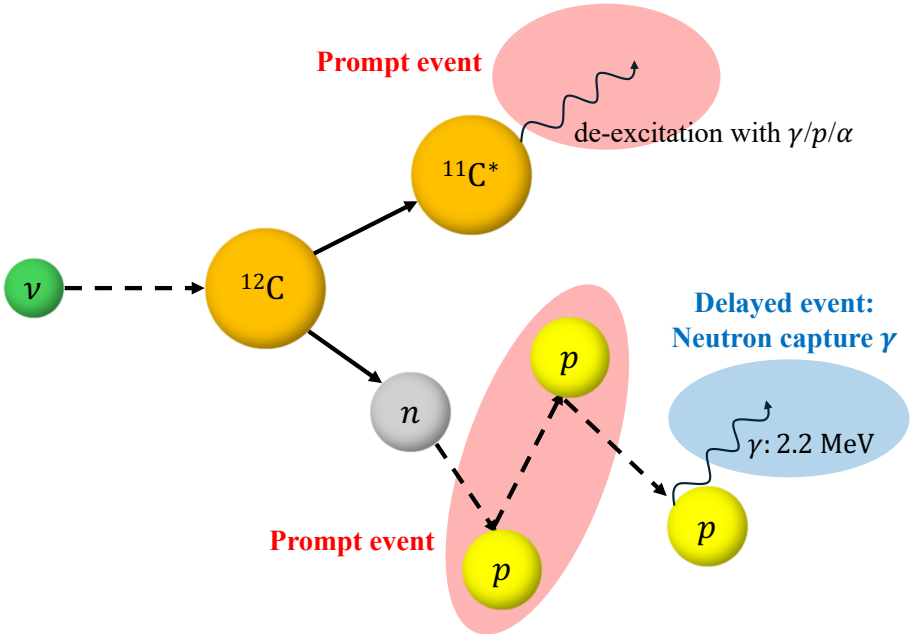

(b) Atmospheric neutrino NC interaction (background)

Figure 6.1: Schematic images of the (a) IBD interaction and the (b) atmospheric neutrino NC interaction.

initial kinetic energy of 200 MeV generated at the detector center[1]. These track information indicate that the spatial extent of the IBD prompt signal is at the level of a few tens of cm, and its temporal spread is of order a few ns. In contrast, a neutron produced in a NC interaction typically travels ∼1 m for ∼20 ns before its first scatter on a proton. The neutron then undergoes on average about five proton scatters while slowing down to a kinetic energy below 1 MeV, and consequently migrates to a point roughly 3 m away from its production vertex, as illustrated in Fig. 6.3. The corresponding neutron flight-time distribution exhibits a tail extending to ∼50 ns. In NC interactions, a 2 MeV gamma ray is also emitted predominantly from de-excitation of ^{11}C; its propagation length is about 1 m and its flight time is approximately 5 ns.

The difference between IBD and atmospheric neutrino NC can also be discussed in terms of the temporal and spatial extent of the energy-deposition points. Fig. 6.4 and Fig. 6.5 show representative examples of the time-space distributions of energy-deposition points from prompt particles for IBD and NC events, respectively. While the positron and gamma rays in IBD deposit their energy locally within a short time window of a few ns, the neutron produced in a NC event can be seen to propagate through the detector and scatter on protons over several tens of ns. Such differences lead to distinct time-space distributions of scintillation-light emission points in the LS, which ultimately appear as differences in the PMT hit patterns. Therefore, discrimination between IBD signals and atmospheric neutrino NC events is expected to be feasible.

The discrimination between IBD and atmospheric neutrino NC events in the liquid scintillator detector has been investigated through simulation studies for the next-generation detector JUNO, where a background rejection efficiency of approximately 98% has been reported [54]. This suggests that a similar event classification approach can be effectively applied to KamLAND as well. In addition, fast neutrons originating from outside the detector can also produce delayed-coincidence events; however, since these involve proton recoils similar to atmospheric neutrino NC interactions, they are likewise expected to be distinguishable by the same method.

Based on these considerations, this study aims to develop an event classification method that fully exploits the spatial and temporal distributions of PMT hits, using KamNet, a DNN optimized for the KamLAND data structure.

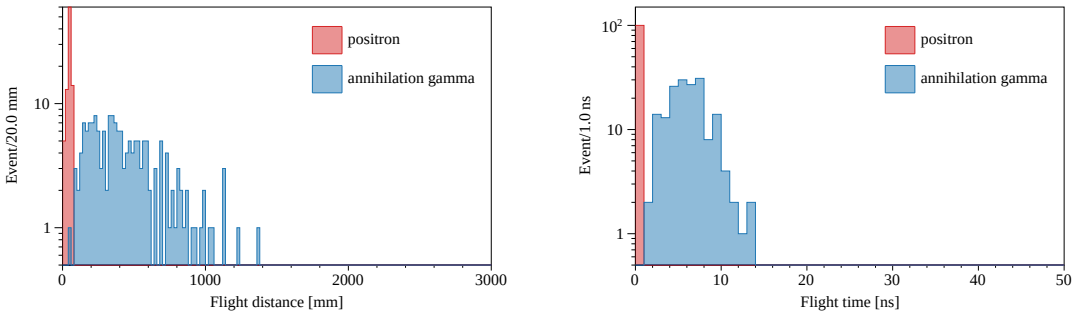

Figure 6.2: Track information for particles produced in the inverse beta decay reaction. The left panel shows the flight distances of the positron and the annihilation gamma rays, while the right panel shows the corresponding flight times.

[1] A typical neutron produced in atmospheric neutrino NC interactions has a kinetic energy of about 200 MeV.

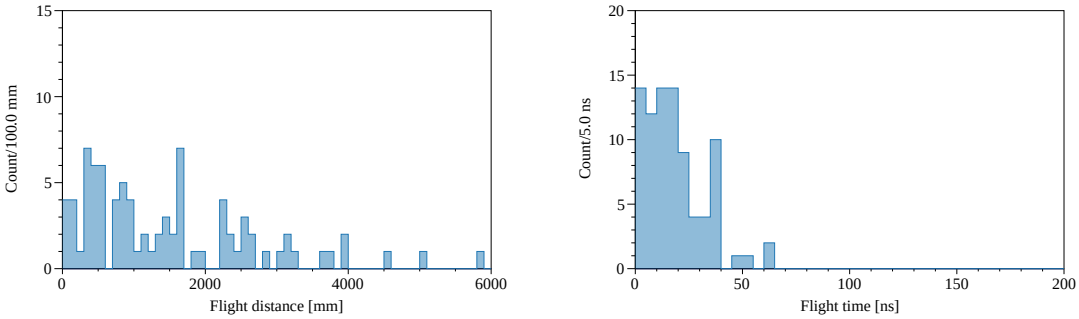

Figure 6.3: Track information for neutrons produced by atmospheric neutrino NC interactions. The left panel shows the distance from the neutron production point to the point where its kinetic energy falls below 1 MeV, while the right panel shows the corresponding neutron flight time.

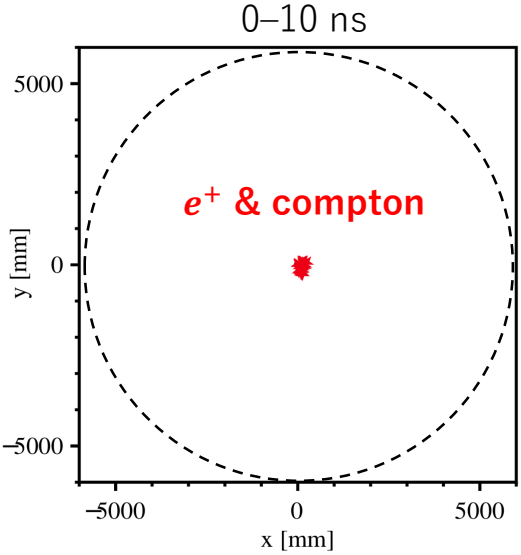

Figure 6.4: Spatial and temporal distribution of energy-deposition points from prompt particles in IBD. Energy-deposition points from particle production up to 10 ns are shown. The black dashed line indicates the boundary at a radius of 600 cm from the detector center.

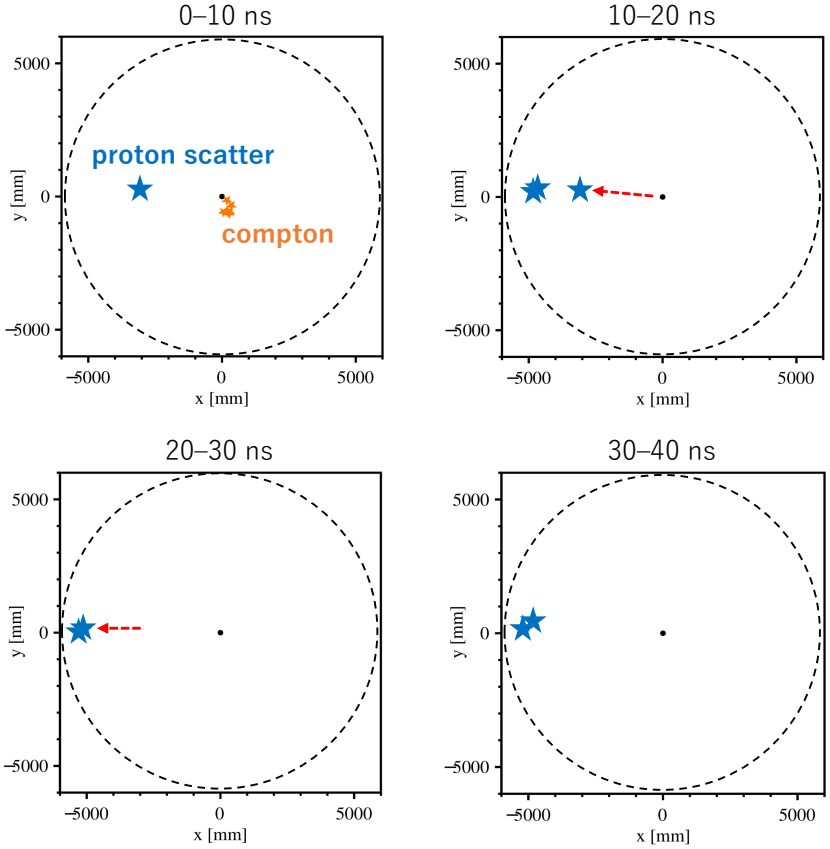

(a) Energy-deposition points

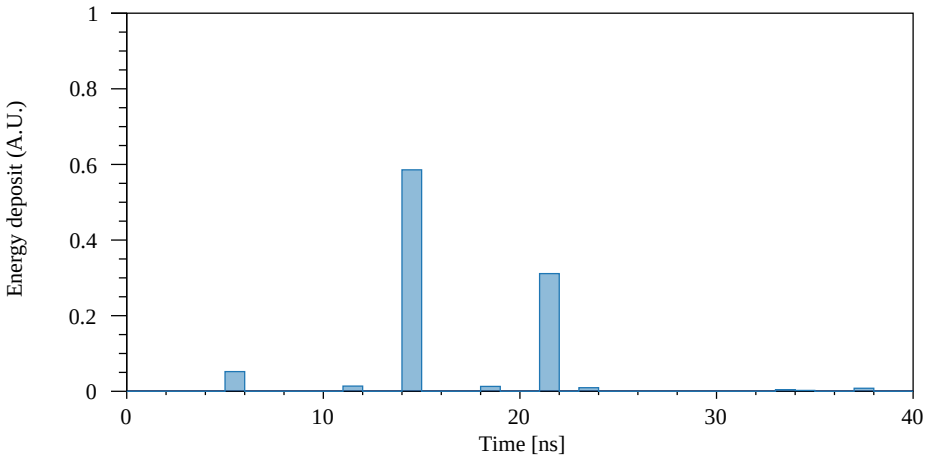

(b) Relative energy deposition

Figure 6.5: Spatial and temporal distribution of energy-deposition points from prompt particles in atmospheric-neutrino NC interactions. Top: energy-deposition points from particle production up to 40 ns, shown in 10-ns intervals. Orange points indicate gamma rays from ^{11}C de-excitation, and blue points indicate protons recoiled by neutron scattering. The red arrows illustrate the shift of the centroid of the light-emission points. Bottom: relative energy deposition by the recoil protons.

Data periods for KamNet

Tab. 6.1 summarizes the definitions of the data periods used in this analysis. The data are divided because the scintillation properties of the LS changed before and after the purification. In addition, during the KamLAND-Zen experimental periods, a miniballoon filled with Xe-loaded LS was installed at the detector center, resulting in a reduction of the fiducial volume. Therefore, the data are further separated depending on the presence or absence of the miniballoon. Furthermore, in the middle of the Zen800 period, amplifier installation to the KamFEE was initiated to recover the low-gain PMTs (described in Sec. 3.8). Since this installation was performed more than sixty times, the PMT gains changed each time, making it extremely difficult to reproduce the real data accurately in the simulation. To mitigate the resulting degradation in discrimination performance and systematic uncertainties discussed later, the dataset are divided into period before and after the amplifier installation.

Table 6.1: Definition of data periods for KamNet

KamNet-period	Date	Run	Detector status
KamNet-1	Mar. 9th, 2002– Apr. 7th, 2009	run000220– run008501	before purification and during purification
KamNet-2	Apr. 7th, 2009– Oct. 12th, 2011	run008502– run010773	after purification
KamNet-3	Oct. 12th, 2011– Dec. 15th, 2015	run011000– run013414	Zen400
KamNet-4	Dec. 15th, 2015– Aug. 2nd, 2016 Nov. 22nd, 2016– May 9th, 2018	run013415– run013785 run013963– run014990	after OD refurbishment and after failed Zen800
KamNet-5	Aug. 3rd, 2016– Nov. 22nd, 2016 May 19th, 2018– Mar. 18th, 2020	run013786– run013962 run014991– run016092	failed Zen800 and Zen800 before amp installation
KamNet-6	Mar. 19th, 2020– May 7th, 2024	run016093– run018927	Zen800 after amp installation
KamNet-7	May 31st, 2024– Aug. 8th, 2024	run018928– run019046	after Zen800

Event categorization and analysis flow

Fig. 6.6 shows the categorization of event samples used in this analysis. The signal samples consist of simulated e^++ annihilation γ (prompt signal of IBD), simulated ^{12}B β^- decay, and real data spallation ^{12}B β^- decay events. Ideally, IBD events should be used as the signal sample in real data; however, in the astrophysical antineutrino search, the number of IBD events above 7.5 MeV is extremely limited. Therefore, spallation ^{12}B events, which have relatively high statistics and are expected to exhibit hit-pattern characteristics similar to those of IBD events, are used instead. When comparing the simulated ^{12}B decay with the real-data ^{12}B decay, it is first necessary to demonstrate within the simulation framework that $e^+ + \gamma$ and ^{12}B decay events share similar features.

For the background samples, simulated atmospheric neutrino NC, simulated neutrinos from the surrounding rock, and real data fast neutron events are used. In real data, it is difficult to collect a large number of atmospheric neutrino events with high purity. Therefore, fast neutron events collected via delayed-coincidence selection—which contain a small fraction of atmospheric neutrino events—are used as substitutes. Similarly to the signal sample, before comparing simulated atmospheric neutrino NC events with real fast neutron events, the similarity between NC and high-energy neutron events must be demonstrated within the simulation.

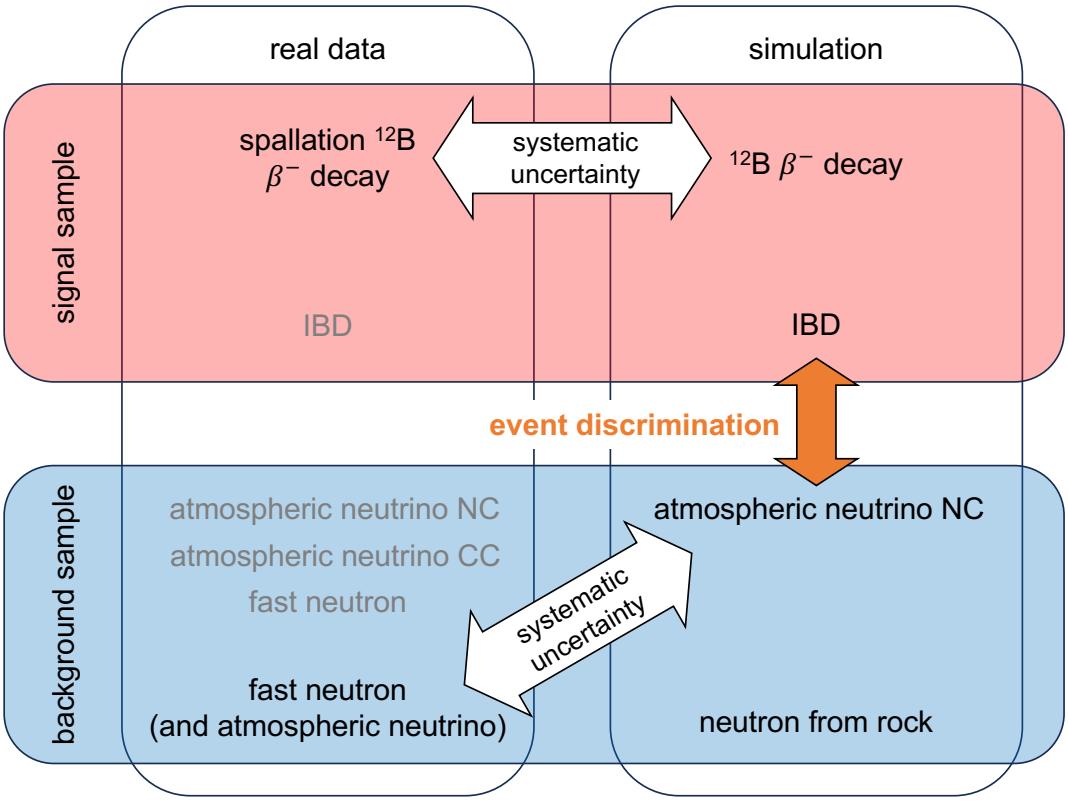

Figure 6.6: Categorization of event samples used in this analysis. Signal samples consist of light particles, whereas background samples involve heavy particles that induce proton scattering. The difference between data and simulation is treated as a systematic uncertainty; however, before evaluating it, the similarity between $e^+ + \gamma$ from IBD prompt signal (atmospheric neutrino NC) and spallation ^{12}B β^- decay (neutron) must be validated within the simulation framework.

The ultimate goal of this study is to distinguish $e^+ + \gamma$ (IBD) signals from atmospheric neutrino (and fast neutron) backgrounds in real data. To achieve this, the analysis proceeds according to the following flow:

1. Verification of hit information
   Before developing the classification method using KamNet, the similarities and differences among the events shown in Fig. 6.6 are examined and evaluated in terms of their hit information.

2. Training of KamNet, determination of cut threshold, and estimation of efficiencies (Fig. 6.7 (a))
   KamNet is trained using large simulation samples of $e^+ + \gamma$ (signal) and atmospheric

neutrino NC (background) events. Although fast neutrons are expected to share similar characteristics with atmospheric neutrino NC events, generating sufficient statistics for them in simulation would be computationally expensive. Therefore, after confirming that the hit information (KamNet input features) of atmospheric neutrino NC and neutrons from rock are similar, only NC events are used for training. After training, the score distributions for signal and background are used to calculate the Figure of Merit (FoM) and determine the optimal cut threshold. The signal efficiency and background rejection efficiency are then estimated at this threshold.

3. Performance evaluation of KamNet and estimation of systematic uncertainties using real data (Fig. 6.7 (b))
   The trained KamNet model is applied to the hit information of signal and background samples in real data and simulation, respectively, and the resulting score distributions are compared. The differences in signal and background efficiencies are evaluated as systematic uncertainties.

4. Application of KamNet cuts to $\bar{\nu}_e$ candidate events (Fig. 6.7 (c))
   As the final step in the $\bar{\nu}_e$ selection described in Chap. 7, the hit information of candidate events is input to the trained KamNet model, and the predetermined cut threshold is applied to perform additional event selection.

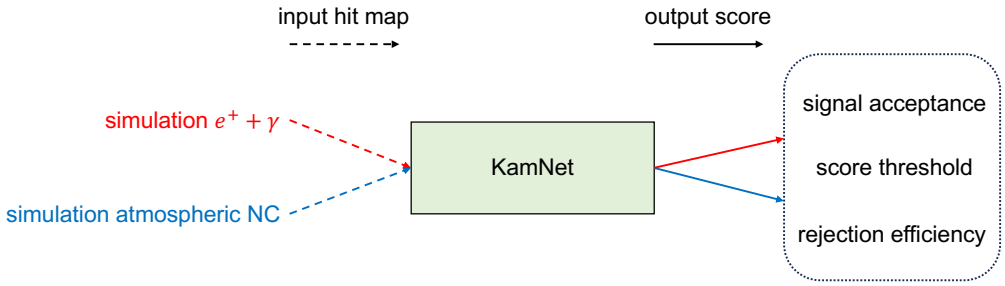

(a) KamNet training using simulated events

(b) KamNet evaluation using real data

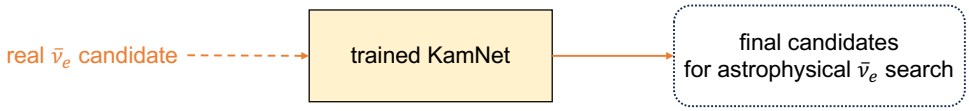

(c) KamNet application to the antineutrino candidates

Figure 6.7: Analysis flow of KamNet (a) training, (b) evaluation, and (c) application.

6.2 Event Selection and Verification of Hit Information

In this section, the generation and selection conditions of the event samples used in this analysis are first described. Subsequently, the hit information of each event sample is compared, and their similarities and differences are discussed.

6.2.1 Event Selection

The generation conditions for the simulated events and the selection criteria for the real data used in the analysis are summarized below.

- Signal samples (Fig. 6.8)
  - Simulated e^++ annihilation γ
    Events are generated with a constant energy spectrum and uniform spatial distribution.
  - Simulated ^{12}B β^- decay
    ^{12}B decay events are simulated with Geant4 and generated with a uniform spatial distribution.
  - Real spallation ^{12}B β^- decay
    Events are collected using the time correlation from preceding muons:
    dT_μ =5–105 ms
- Background samples (Fig. 6.9)
  - Simulated atmospheric neutrino NC
    The atmospheric neutrino simulation is based on [78]. Only events with delayed signals tagged by neutron capture are used.
  - Simulated neutron
    Neutrons injected from the surrounding rock along the x-axis. Original kinetic energy of neutrons set to 1000 MeV.
  - Real fast neutron
    Delayed coincidence selection is applied, and muon veto is removed for the prompt event. Due to the limited statistics of the fast neutron event, events collected over the entire data-taking period are used for the analysis in each period.

As common conditions for all samples, events with visible energies of 7.5–30 MeV and reconstructed vertices within a 600 cm radius from the detector center are selected. During the KamLAND-Zen experimental periods, the miniballoon region is excluded from the fiducial volume.

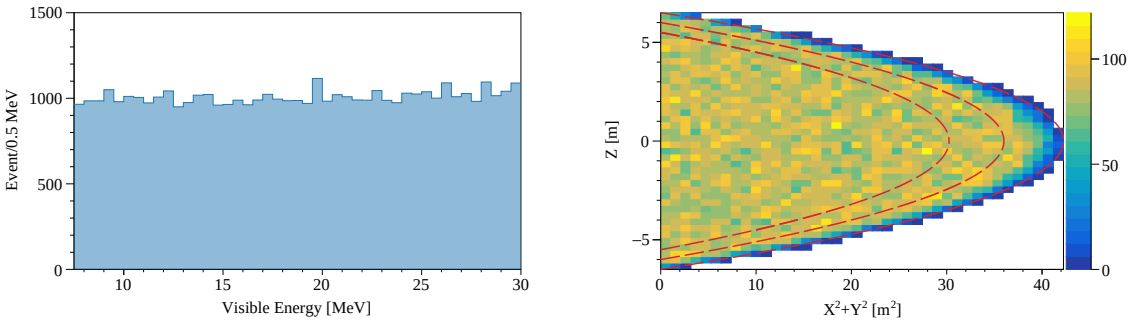

(a) Simulated e^++ annihilation γ events

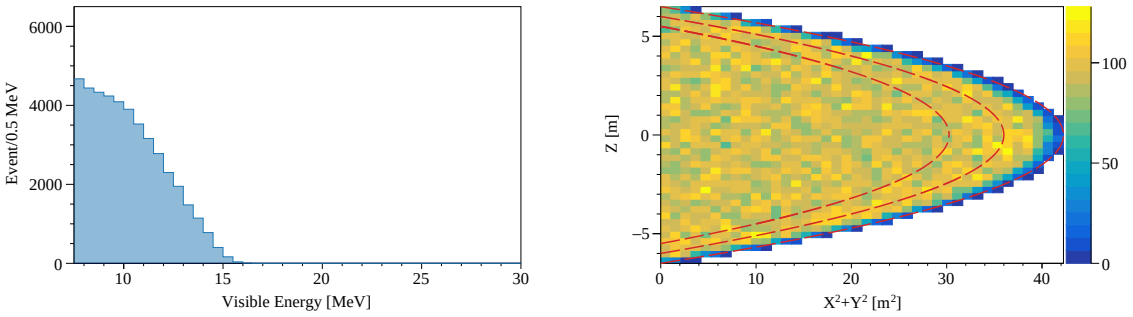

(b) Simulated ^{12}B β^- decay events

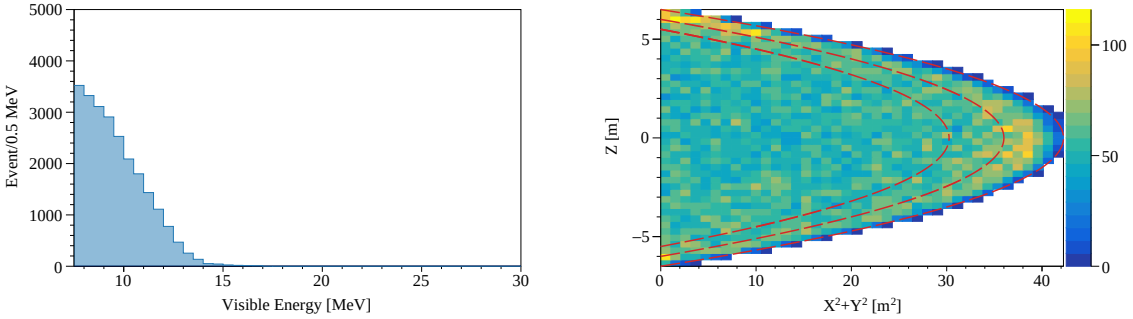

(c) Real spallation ^{12}B β^- decay events

Figure 6.8: Visible energy spectra and vertex distributions of signal samples. Events within a 600 cm radius are plotted in the energy spectra. The red curves represent radii of 650 cm, 600 cm, and 550 cm, respectively. Simulated e^++ annihilation γ events are generated with a constant energy spectrum and a uniform vertex distribution. For real spallation ^{12}B β^- decay events, only ontime events are included in the energy spectra.

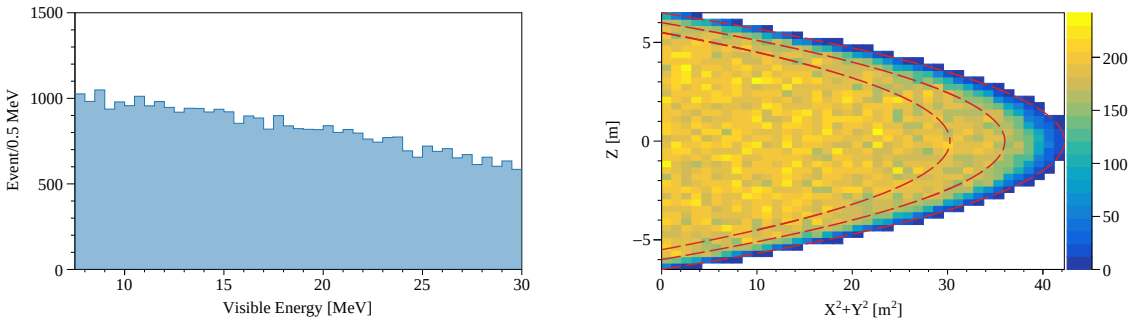

(a) Simulated atmospheric neutrino NC events

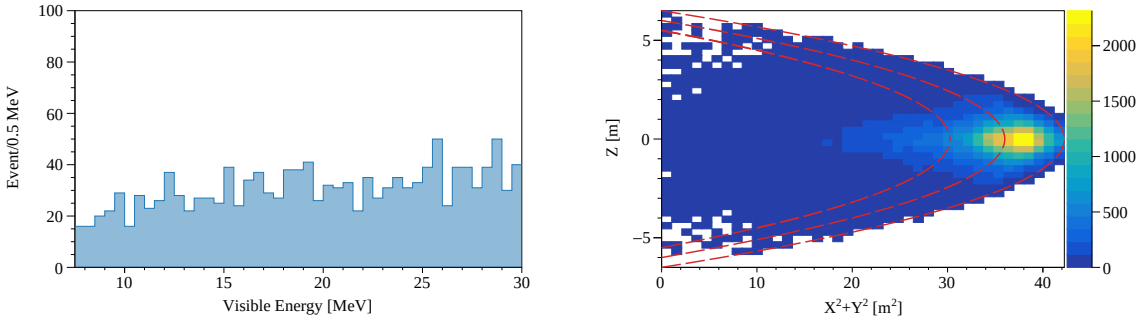

(b) Simulated neutron events

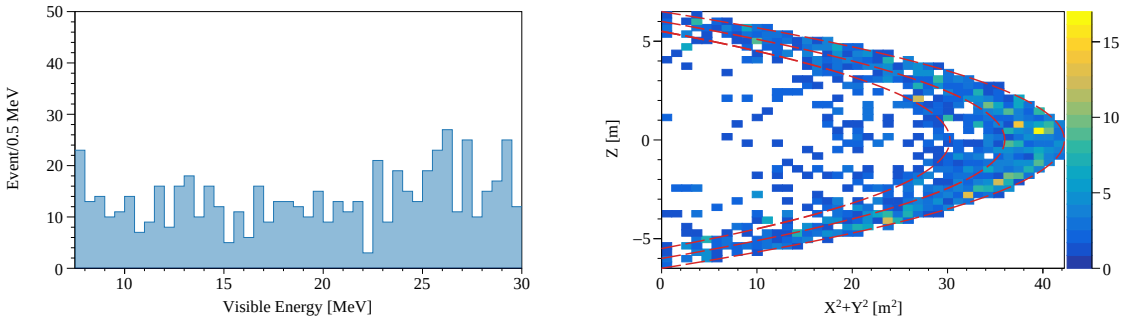

(c) Real fast neutron events

Figure 6.9: Visible energy spectra and vertex distributions of background samples. Events within a 600 cm radius are plotted in the energy spectra. The red curves represent radii of 650 cm, 600 cm, and 550 cm, respectively. Simulated neutrons are generated in the outer rock region and injected into the detector along the x-axis direction. Real fast neutron events are collected by applying a delayed-coincidence selection, and their energy spectra and vertex distributions correspond to the prompt events.

6.2.2 Verification of Hit Information

Verification of the hit information is performed using the hit-time distribution. This distribution is constructed by first subtracting, for every PMT and for every hit, the Time of Flight (ToF) from the photon hit time (see Eq. 4.29); the resulting ToF-subtracted times are then aggregated over all PMTs and all hits to form a hit-time distribution. Ideally, this distribution exhibits a sharp peak at $t = 0$. In practice, differences in energy deposition and ionization density in the LS lead to variations in the scintillation time profile. In addition, the spatial spread of interaction vertices broadens the distribution of emission points, which appears as variations in the width of the ToF-subtracted hit-time distribution. The hit-time distribution therefore reflects the temporal and spatial extent of scintillation-light production. It is also an experimentally accessible observable, making it well suited for this study. The 20-inch PMTs are excluded from the KamNet-related studies below because their timing resolution and timing stability are poor.

For the comparison of hit information, the observed energy range is divided into two intervals: 7.5–13 MeV and 13–30 MeV. This choice is motivated by the spallation ^{12}B decay (real signal sample), whose Q value is 13.4 MeV; therefore, discussions based on this sample are limited to $\leq$ 13 MeV. The hit-time window of interest for the comparison—also used later as input to KamNet—is set to -10 to $+50$ ns. This choice reflects that, outside this window, the number of hits decreases and the available discriminating features diminish. In addition, enlarging the window would lengthen KamNet training time without a commensurate gain in performance. As a quantitative metric, the bin-by-bin deviation between two hit-time distributions $f(t)$ and $g(t)$ is used. It is defined as

$$\text{Deviation} = \frac{f(t) - g(t)}{f(t)}. \tag{6.1}$$

This quantity is evaluated in 5 ns bins, and the corresponding statistical uncertainties are reported.

- Similarities among signal samples

  Fig. 6.10 compares the hit-time distributions among signal samples during the KamNet-1 period (before purification). Panel (a) shows a comparison between simulated $e^+ + \gamma$ and ^{12}B β^- decay events. The deviation between the two distributions remains within 5% (green band) inside the time window (orange region), indicating good agreement. This confirms that the hit information for particles categorized as light particles in this study is very similar. It also demonstrates that the ^{12}B decay sample can serve as a proxy for IBD events, which cannot be accumulated in sufficient numbers in real data. Panel (b) compares simulated ^{12}B decay events with spallation ^{12}B decay events from real data. Although the deviation increases near the leading edge of the hit-time distribution, it remains within 5% thereafter. The larger deviation observed around the leading edge arises because the distribution rises steeply there; even a slight offset in time produces a highly sensitive change in the apparent height of the distribution. Therefore, it is concluded that the two hit-time distributions are similar and that the simulation reproduces the hit information observed in real data.

- Similarities among background samples

  Fig. 6.11 compares the hit-time distributions among background samples, using the KamNet-1 period as an example. Panel (a) compares simulated atmospheric neutrino NC with neutrons entering from the surrounding rock. The two distributions agree well within the time window (deviation $\leq$ 5%). This indicates that the hit information of atmospheric neutrino NC events is similar to that of high-energy neutrons arriving

from the detector periphery. This, in turn, demonstrates that fast neutron events in real data can serve as a dataset with background-like hit information characteristic of heavy particles. Panel (b) compares the simulated atmospheric neutrino NC with fast neutron events in real data. This reveals a larger deviation near the leading edge, but deviations remain within about 5% after the peak. Assuming the two event classes share the same hit-information features, the simulation reproduces the real data well.

- Differences between signal samples and background samples

  Fig. 6.12 compares the hit-time distributions between the signal and background samples. Panel (a) shows the comparison for simulated events. Unlike comparisons between samples with same characteristics, a deviation of about 20% is observed on the falling edge of the peak (0–20 ns). Moreover, the deviation remains persistently negative at later times. These results indicate that the background sample exhibits a qualitatively broader timing distribution, which is consistent with the event-classification principle employed in this study. Because KamNet is trained on the simulated events shown here, if it learns these differences as discriminating features, KamNet-based event classification is expected to be effective. Panel (b) presents the comparison for real data. A deviation of roughly 20% is likewise observed around the falling edge of the peak, demonstrating that differences between the signal and background hit information are also present in the KamLAND real data.

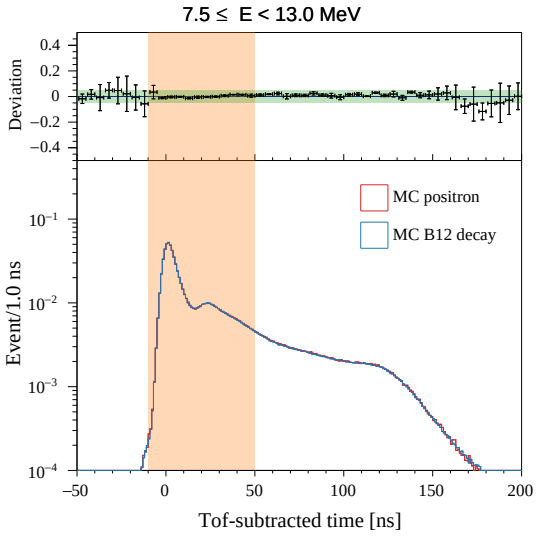

(a) Comparison between simulated e^++ annihilation γ and simulated ^{12}B β^- decay events

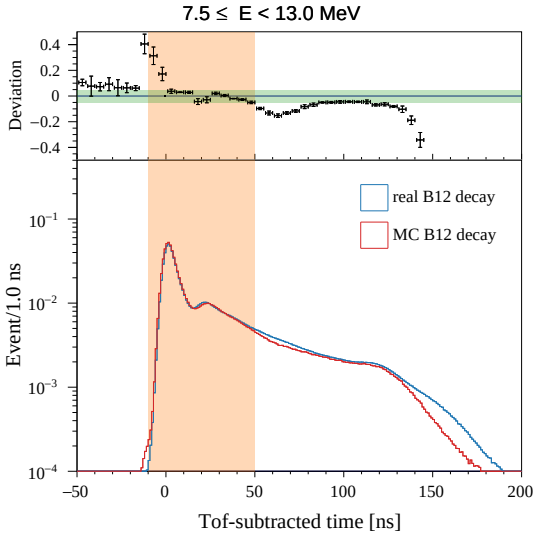

(b) Comparison between simulated ^{12}B β^- decay and real spallation ^{12}B β^- decay events

Figure 6.10: Comparison of hit timing distributions among signal samples. Both figures correspond to the before purification period. The orange band indicates the time window used as KamNet input, while the green band represents the deviation range of ±5%. The error bars in the deviation plot represent the statistical uncertainty within each 5 ns time bin.

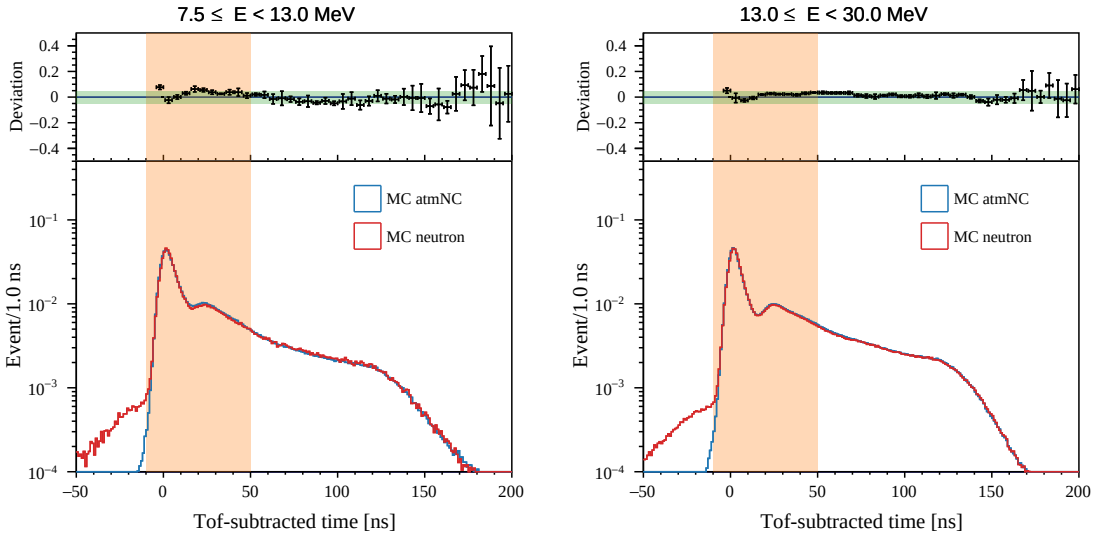

(a) Comparison between simulated atmospheric neutrino NC and simulated neutron events

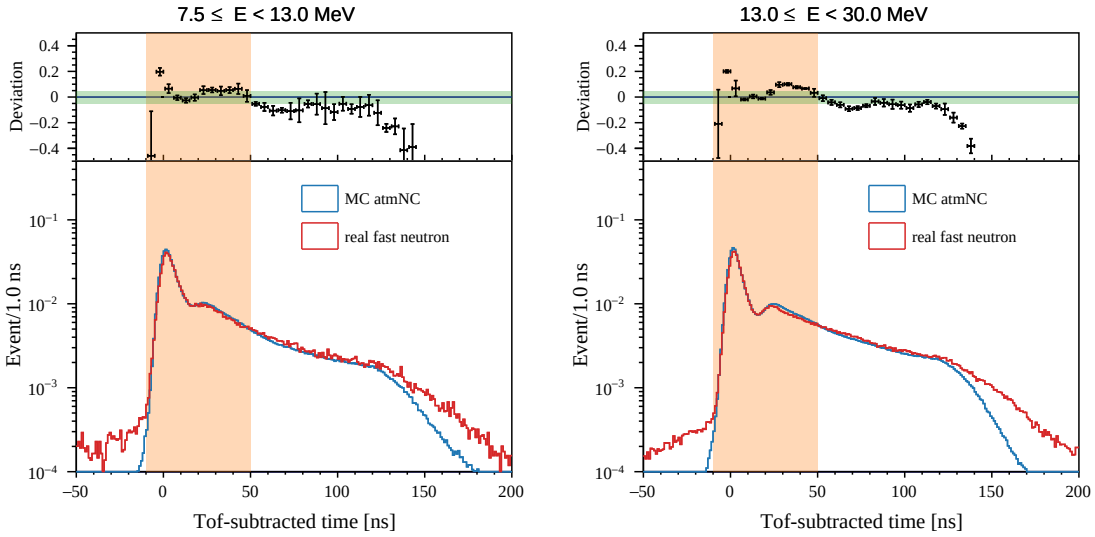

(b) Comparison between simulated atmospheric neutrino NC and real fast neutron events

Figure 6.11: Comparison of hit timing distributions among background samples. Both figures correspond to the before purification period.

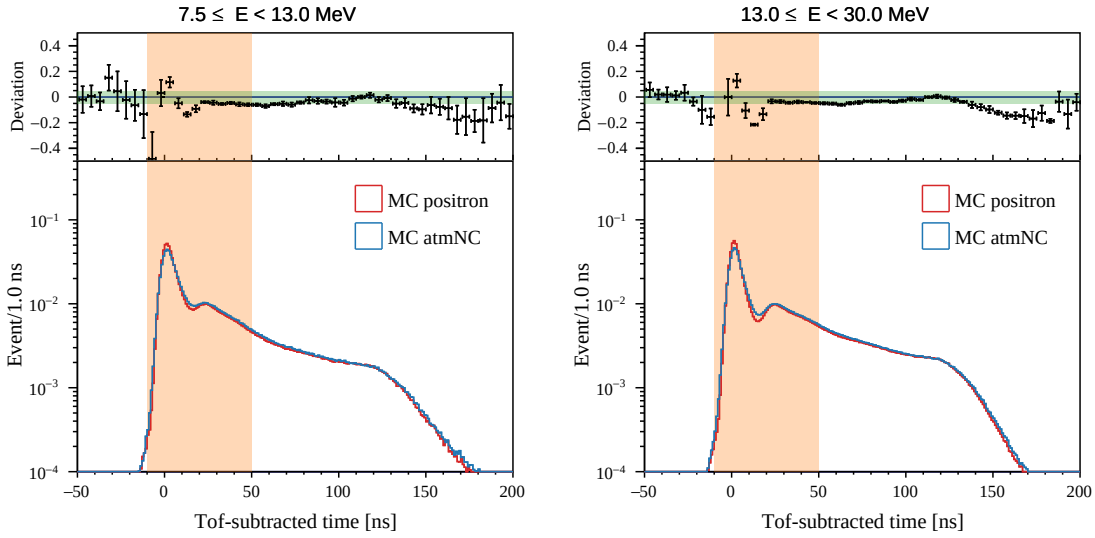

(a) Comparison between simulated signal ($e^+ + \gamma$) and simulated background (atmospheric neutrino NC) events

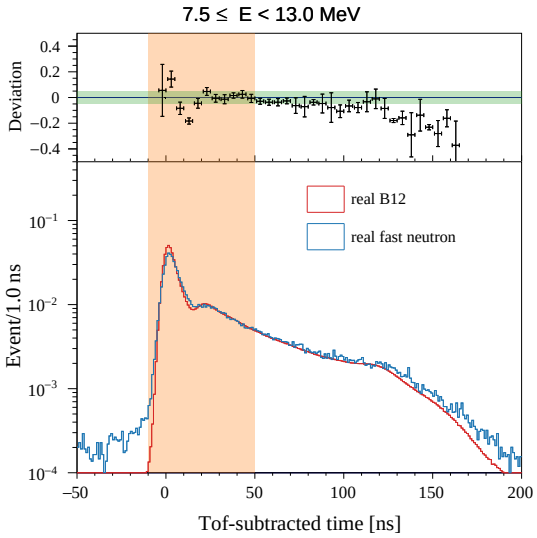

(b) Comparison between real signal (spallation ^{12}B) and real background (fast neutron) events

Figure 6.12: Comparison of hit timing distributions between signal and background events. Both figures correspond to the before purification period.

Comparisons for the other KamNet periods are summarized as follows:

- Fig. 6.13: Simulated ^{12}B β^- decay vs. real spallation ^{12}B events, to assess the similarity among signal samples.
- Fig. 6.14, Fig. 6.15: Simulated atmospheric neutrino NC events vs. real fast neutron events, to assess the similarity among background samples.
- Fig. 6.16, Fig. 6.17: Simulated $e^+ + \gamma$ vs. simulated atmospheric neutrino NC events, to quantify signal-background differences in simulation.
- Fig. 6.18: Real spallation ^{12}B vs. real fast neutron events, to quantify signal-background differences in real data.

As discussed in the *Data periods for KamNet* subsection, inspection of the hit-time distributions in the periods after the KamFEE amplifier installation (i.e., the Zen800 after amp installation and after Zen800 periods) shows that the hit information in real data is difficult to reproduce with the simulation. As described in the next section, the deep neural network is trained using simulated events, and it is therefore not appropriate to apply it to periods in which the simulation fails to reproduce the hit information reliably. In order to obtain a simulation that accurately reproduces the data in these periods, separate simulations corresponding to each of the 64 distinct amplifier-installation stages would be required, which is not practically feasible. To avoid an unacceptably large systematic uncertainty, the deep-neural-network-based event selection is therefore not applied to the periods after the amplifier installation.

Because the analysis exploits PMT *multi-hit* information, a single PMT can be assigned multiple photon hits. The dip that appears after the peak in the hit-time distributions (10–20 ns) is a consequence of the waveform-analysis algorithm. The algorithm first locates the peak due to the first photon and extracts the time-charge information. It then refrains from searching for the next peak for a fixed sampling interval. This enforced gap creates an interval with few recorded hits between successive photons, which in turn produces the dip observed in the hit-time distributions.

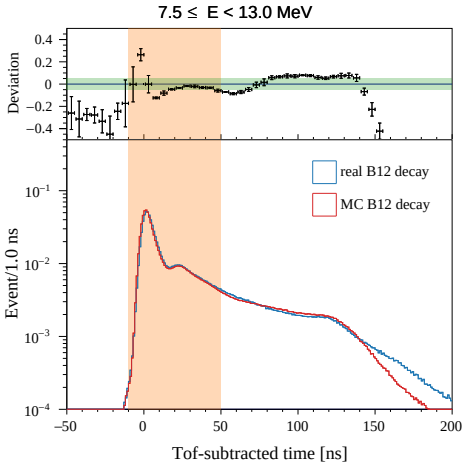

(a) After purification

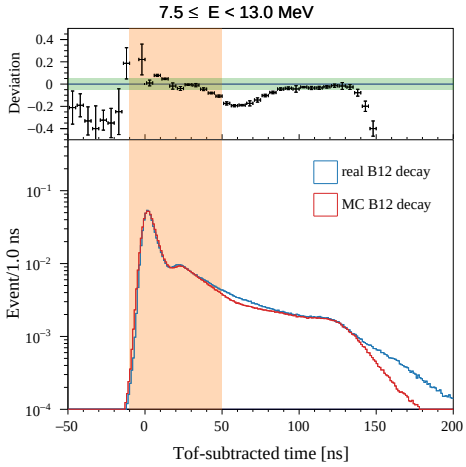

(b) Zen400

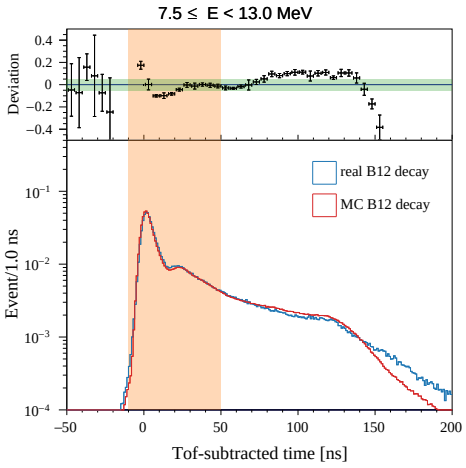

(c) After OD refurbishment

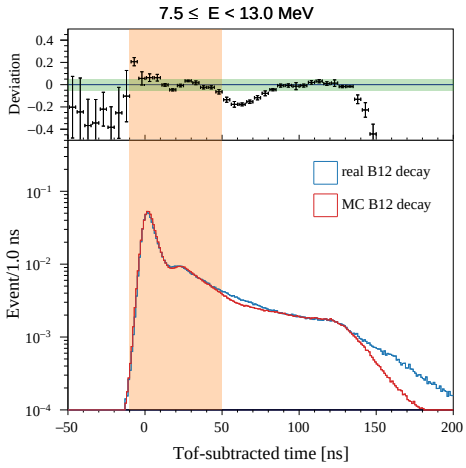

(d) Zen800 before amp installation

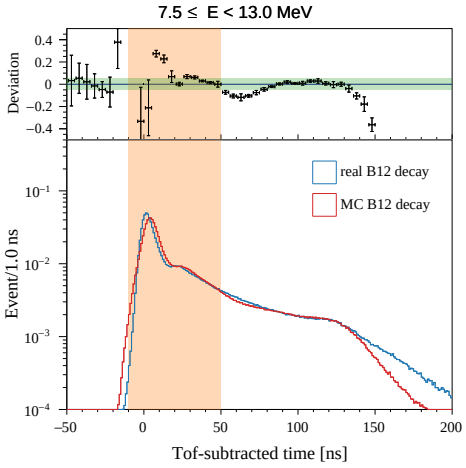

(e) Zen800 after amp installation

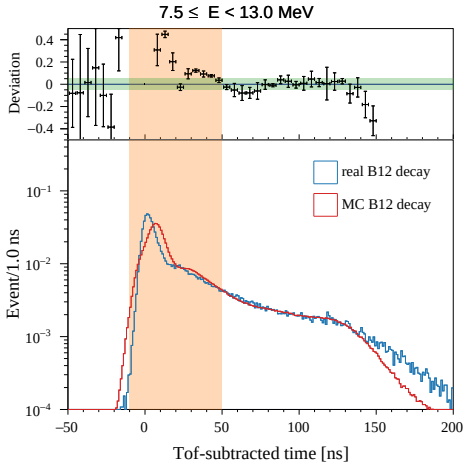

(f) After Zen800

Figure 6.13: Comparison of hit timing distributions between simulated ^{12}B β^- decay and real spallation ^{12}B β^- decay events.

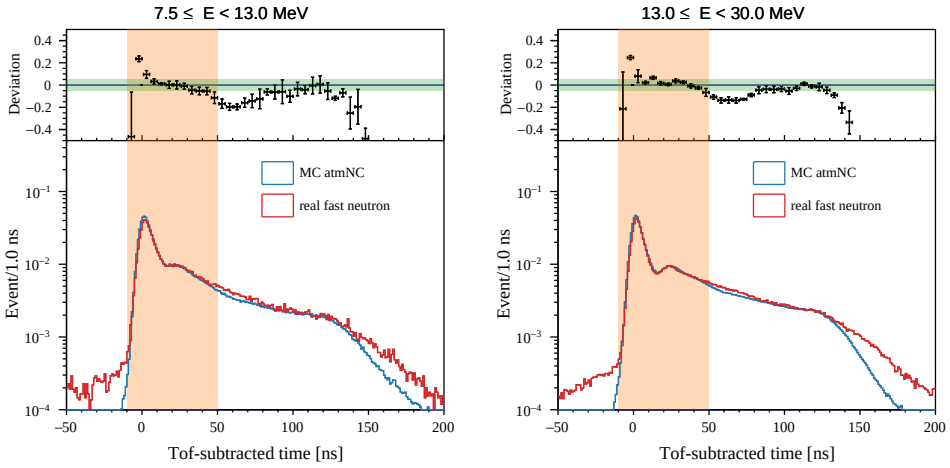

(a) After purification

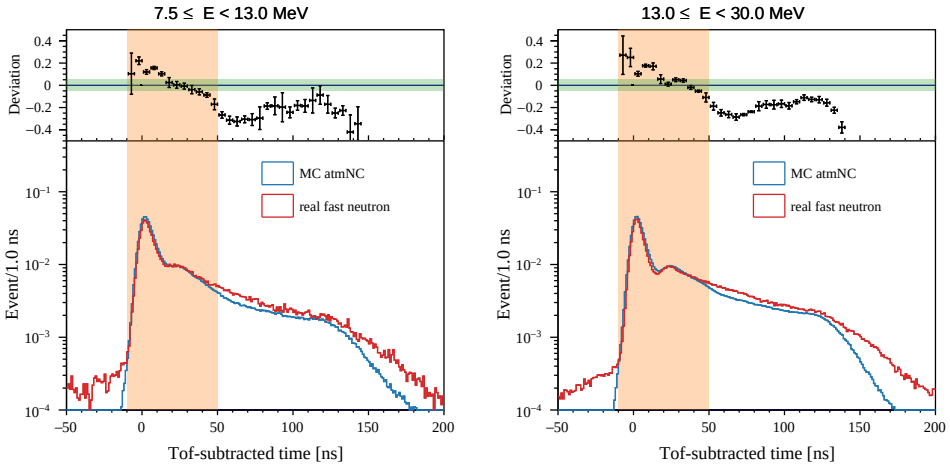

(b) Zen400

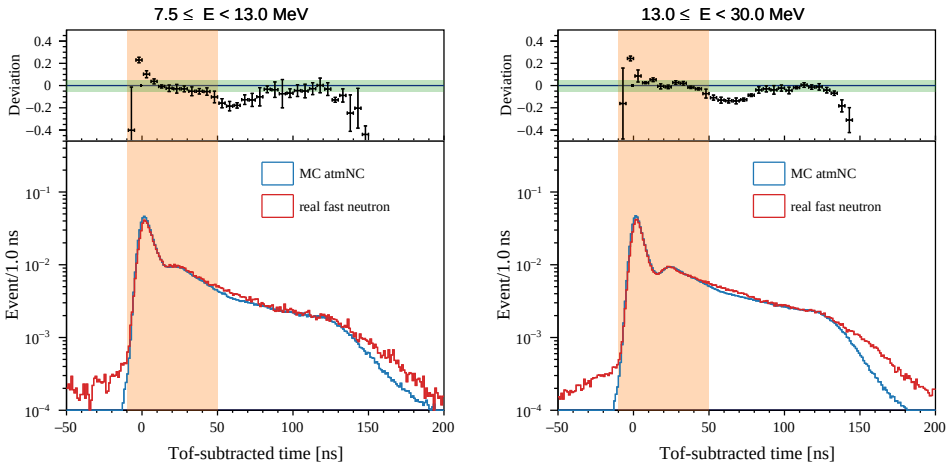

(c) After OD refurbishment

Figure 6.14: Comparison of hit timing distributions between simulated atmospheric neutrino NC and real fast neutron events (1).

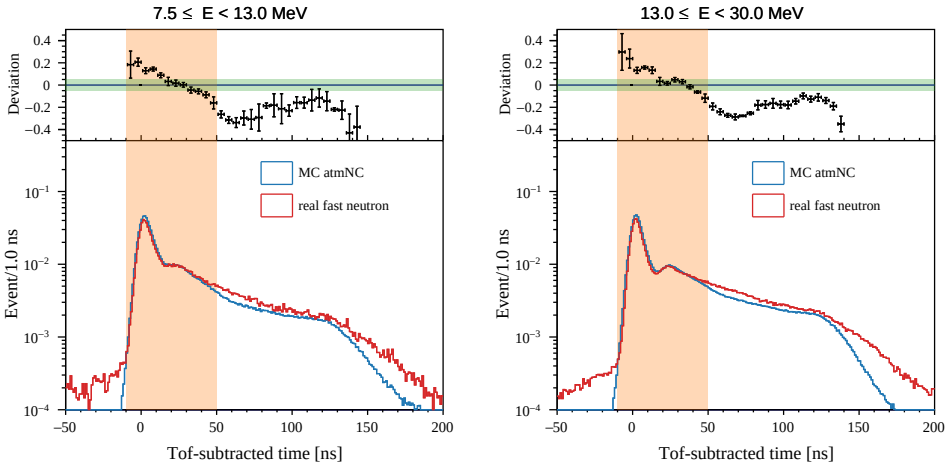

(d) Zen800 before amp installation

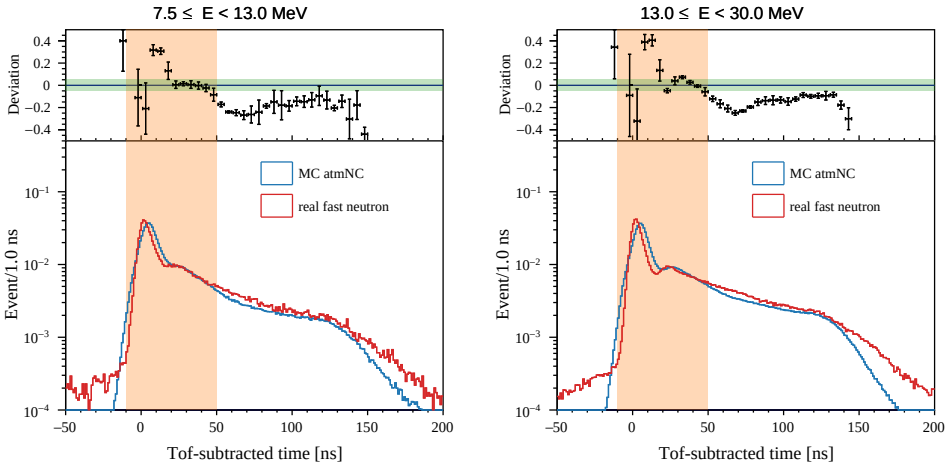

(e) Zen800 after amp installation

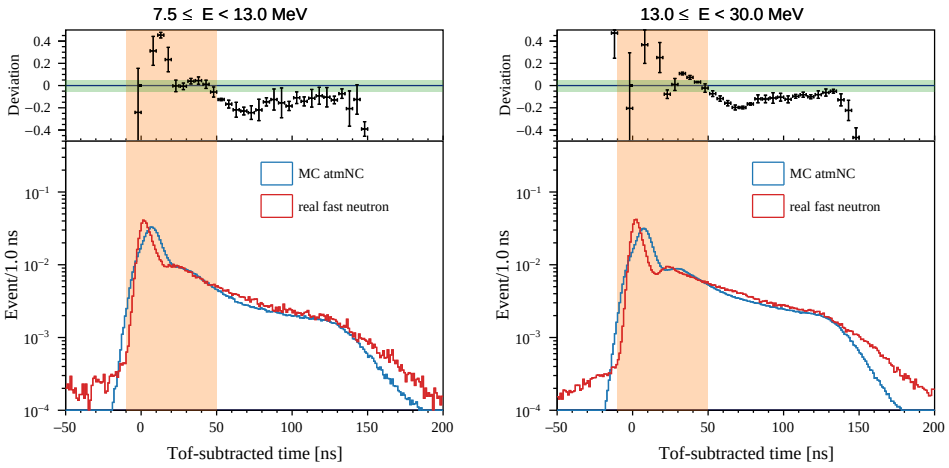

(f) After Zen800

Figure 6.15: Comparison of hit timing distributions between simulated atmospheric neutrino NC and real fast neutron events (2).

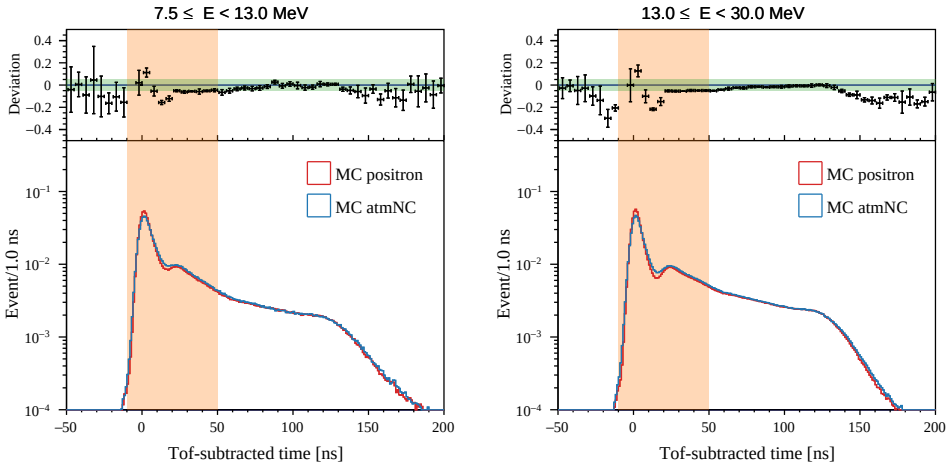

(a) After purification

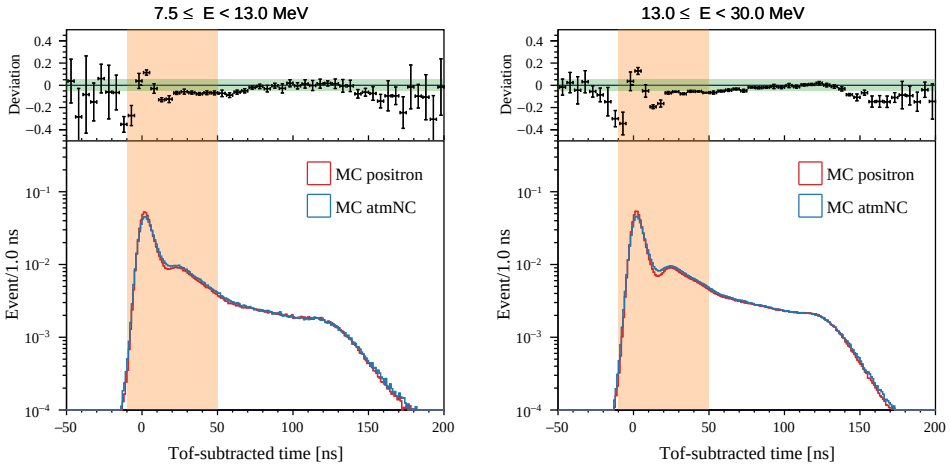

(b) Zen400

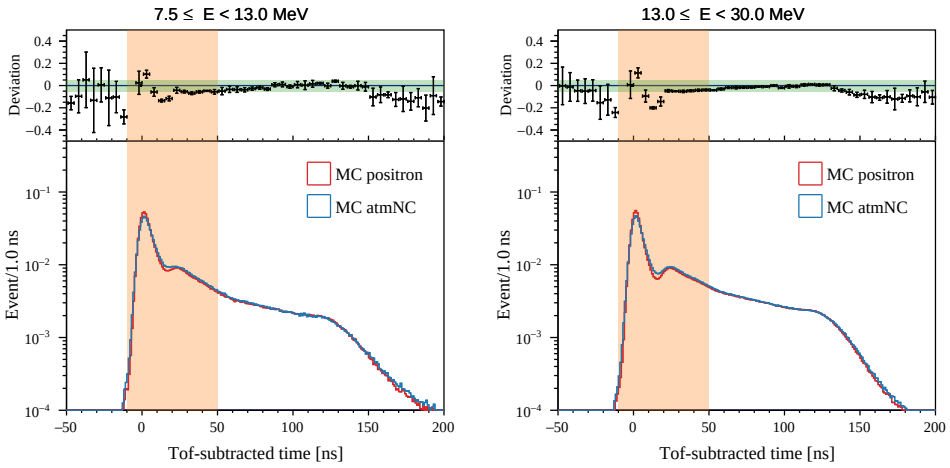

(c) After OD refurbishment

Figure 6.16: Comparison of hit timing distributions between simulated e^++ annihilation γ and simulated atmospheric neutrino NC events (1).

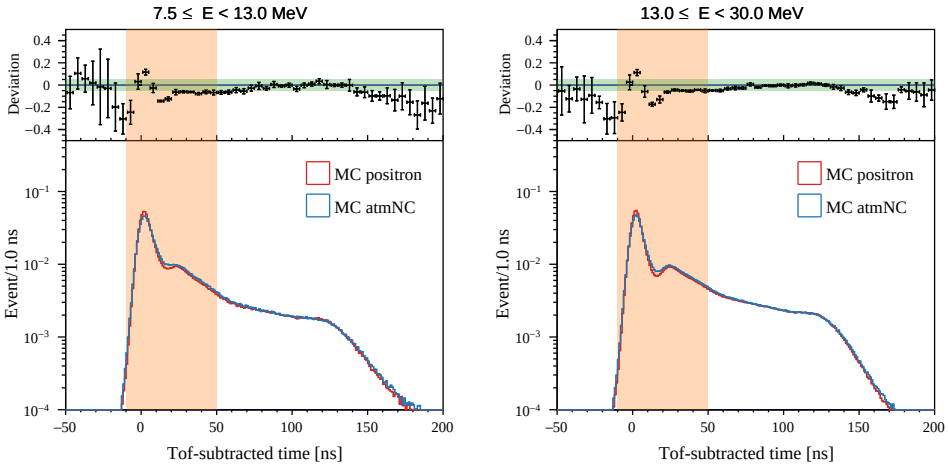

(d) Zen800 before amp installation

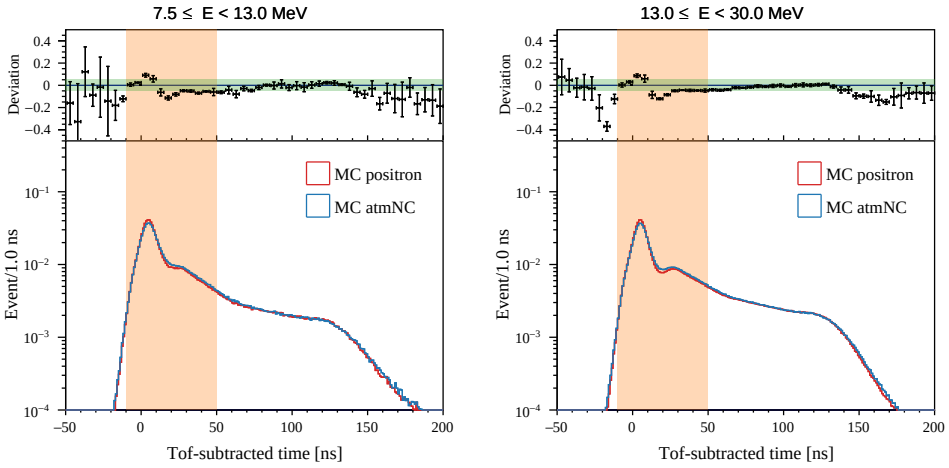

(e) Zen800 after amp installation

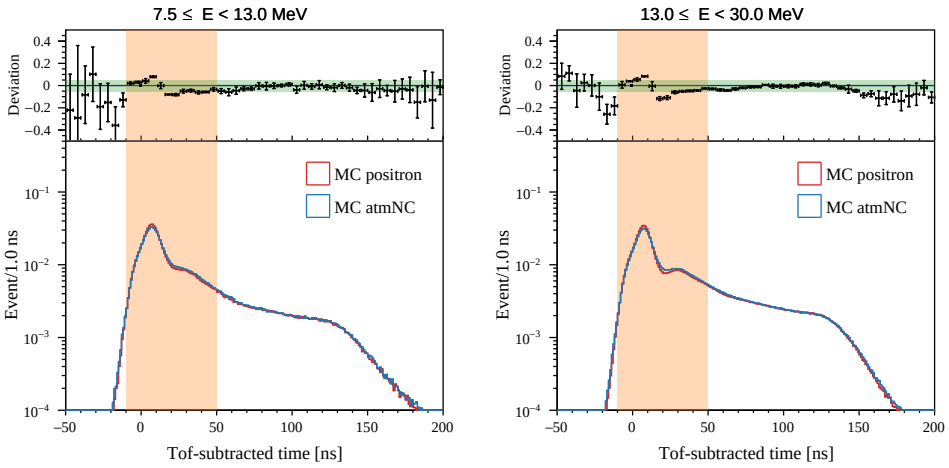

(f) After Zen800

Figure 6.17: Comparison of hit timing distributions between simulated e^++ annihilation γ and simulated atmospheric neutrino NC events (2).

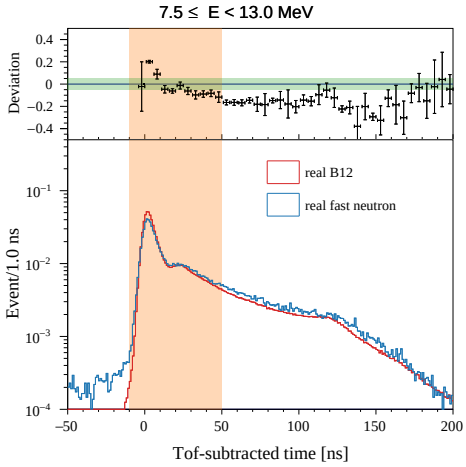

(a) After purification

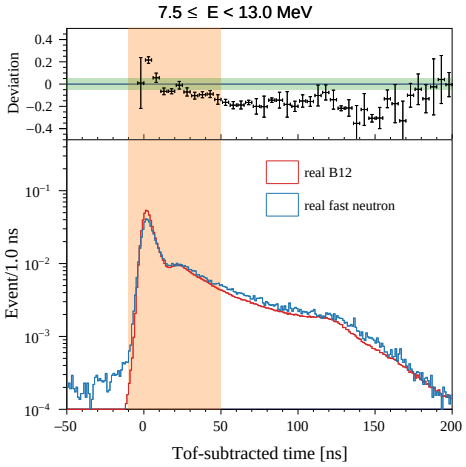

(b) Zen400

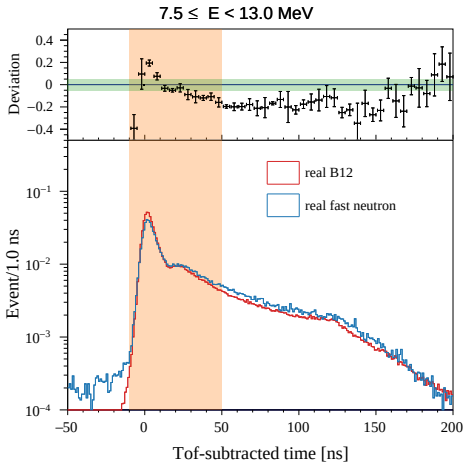

(c) After OD refurbishment

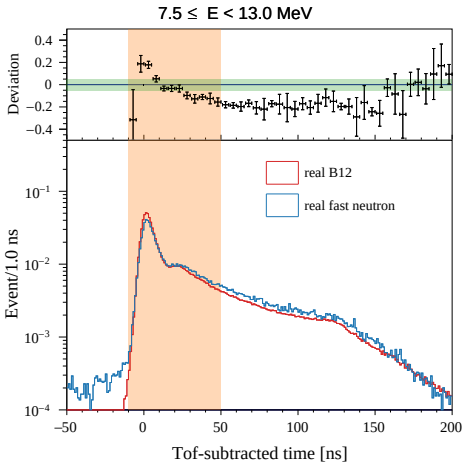

(d) Zen800 before amp installation

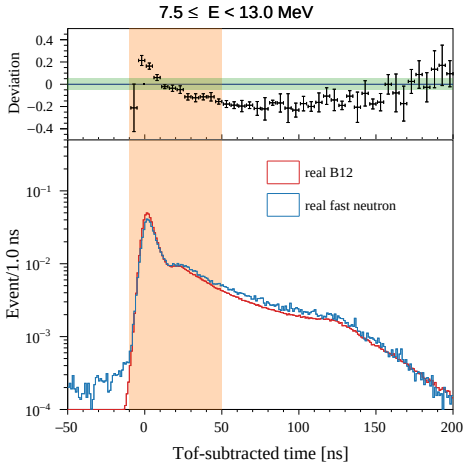

(e) Zen800 after amp installation

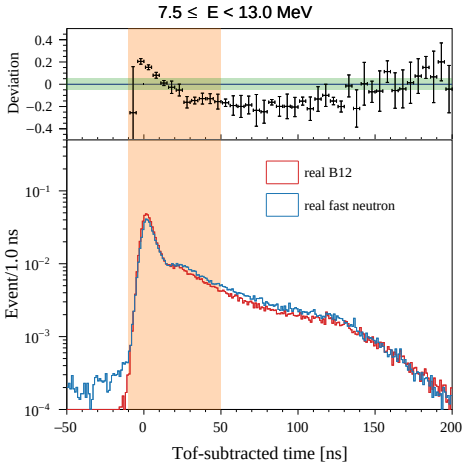

(f) After Zen800

Figure 6.18: Comparison of hit timing distributions between real spallation ^{12}B β^- decay and real fast neutron events.

6.3 KamNet Training and Model Construction

This chapter describes the training of a deep neural network (DNN) for event classification, as illustrated in Fig. 6.7 (a). As the DNN architecture, KamNet (see Sec. 5.3)—which is optimized for the KamLAND event-data structure—is employed. KamNet takes PMT hit information as input and outputs a KamNet score interpreted as signal-likeness. Because KamNet is designed to extract temporal and spatial features from hit information, it is expected to exploit efficiently the signal-background differences established in the previous chapter.

To secure large statistics for training, simulated events are used. The dataset is divided into a signal sample ($e^+ + \gamma$) and a background sample (atmospheric neutrino NC). Each sample is split into training data (10,000 events) and validation data (3,000 events) and then fed to KamNet. Class labels are assigned as 1 for signal and 0 for background; the loss is computed on the training data and used to update the network parameters. The validation data do not contribute to parameter updates and are used sorely to monitor training. Inputs are processed in mini-batches of 50 events; once all mini-batches have been used to update the parameters, one *training epoch* is completed. For efficiency and to control overtraining (overfitting), the number of epochs is set to 30. The input format is a three-dimensional tensor: a spherical hit map represented on azimuth ($-\pi$, π) with 38 bins and zenith (0, π) with 38 bins, combined with a hit-time window of -10 to $+50$ ns with 40 bins. Hit information earlier than -10 ns is integrated into the first time bin, and hit information later than 50 ns is integrated into the last time bin. Fig. 6.19 shows an example of the hit time distribution and hit maps for an event used as input to KamNet. In what follows, a KamNet trained to distinguish signal from background is referred to as the KamNet *model*.

Fig. 6.20 shows the evolution of the loss over training epoch. Because this is a binary classification, binary cross-entropy is used as the loss function. As training proceeds, the losses for both the training and validation sets decrease.

Fig. 6.21 shows the evolution of the background-rejection efficiency versus epoch. Here, the rejection efficiency is defined at a score threshold chosen to yield a signal acceptance of 90%. As the epochs progress, the training-set rejection efficiency continues to improve, whereas the validation-set rejection efficiency tends to saturate. When the rejection efficiencies for the two sets are similar, the trained model is considered *general*. In contrast, if only the training-set rejection efficiency becomes high, the model is considered *specific*, i.e., indicative of overtraining. The number of epochs is therefore chosen to avoid pronounced overtraining.

Fig. 6.22 presents the score distribution for the validation data at the end of training. The signal and background distributions are separated, demonstrating discriminating power.

In summary, KamNet is trained separately for each KamNet period using simulated events, and the loss and rejection-efficiency trends confirm stable convergence. The analyses in the subsequent chapter are based on the KamNet models produced here.

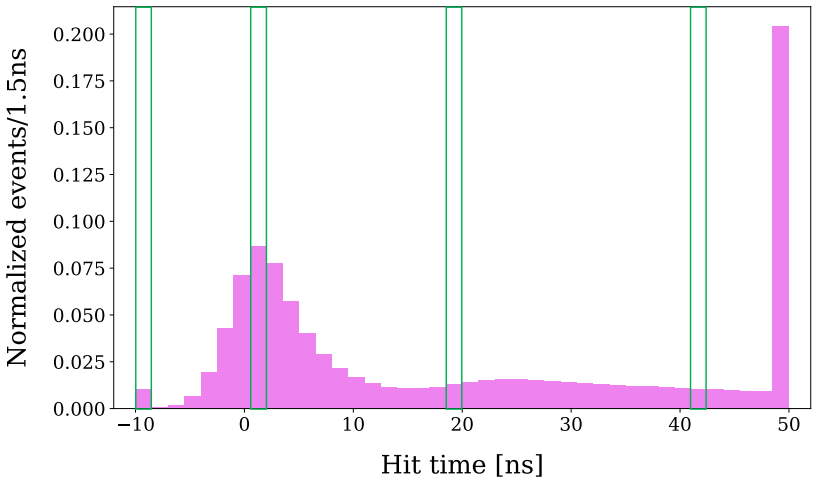

(a) Hit timing distribution

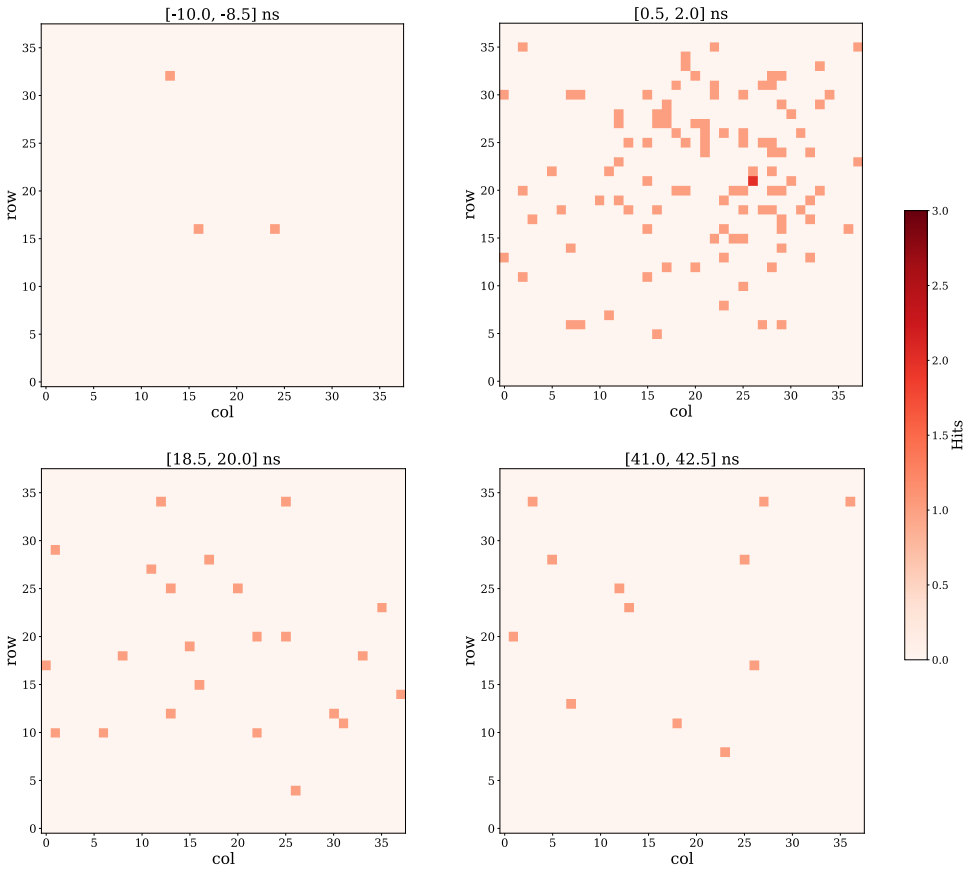

(b) Hit maps

Figure 6.19: Example of (a) hit timing distribution and (b) hit maps for events input to KamNet. The hit timing distribution corresponds to simulated signal events in KamNet-period 1, and the hit maps show an example event from this sample. The green regions in the hit time distribution indicate the time bins used to plot each hit map. In the hit maps, the horizontal axis is the azimuthal angle $(-\pi, \pi)$ divided into 38 bins, and the vertical axis is the zenith angle $(0, \pi)$ divided into 38 bins.

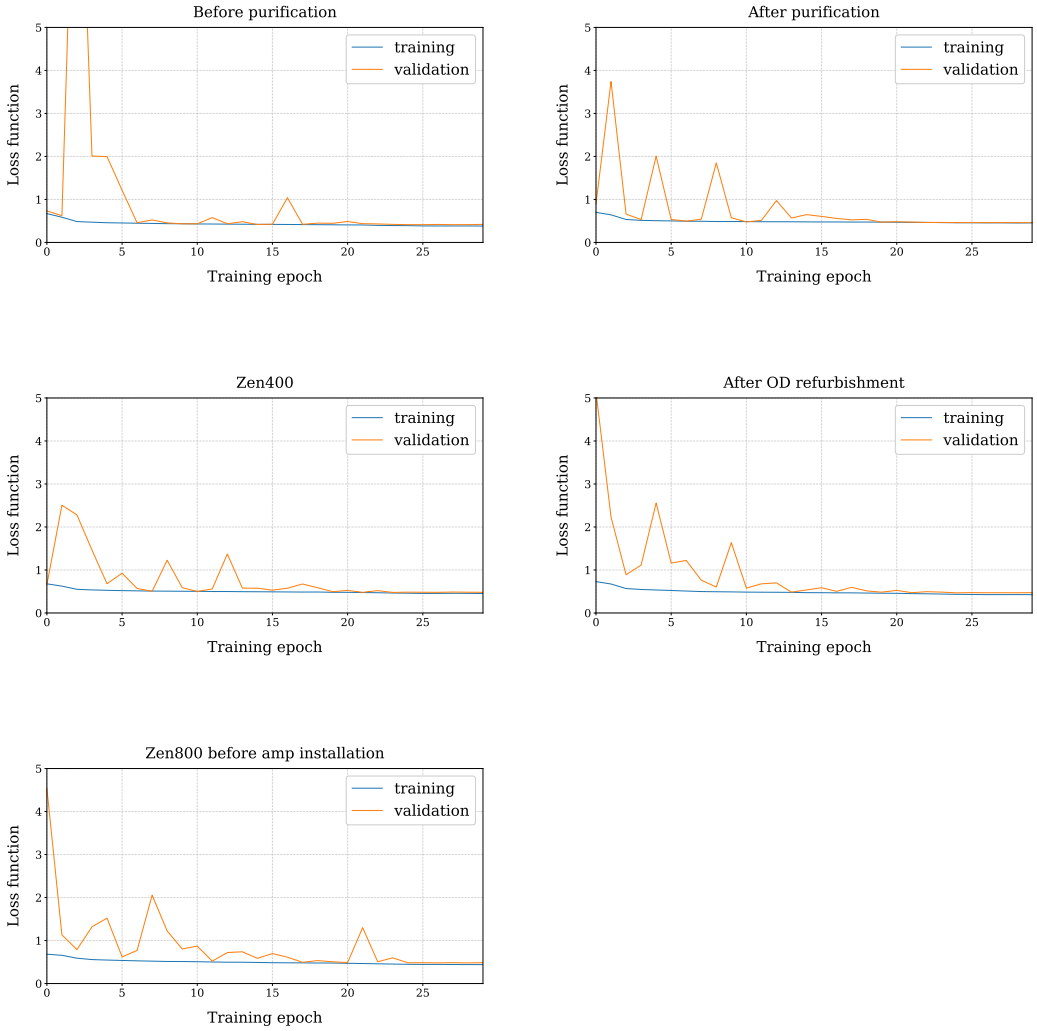

Figure 6.20: Loss function over training. Each panel corresponds to a different KamNet period. The losses for both the training and validation sets decrease, indicating convergence of the training.

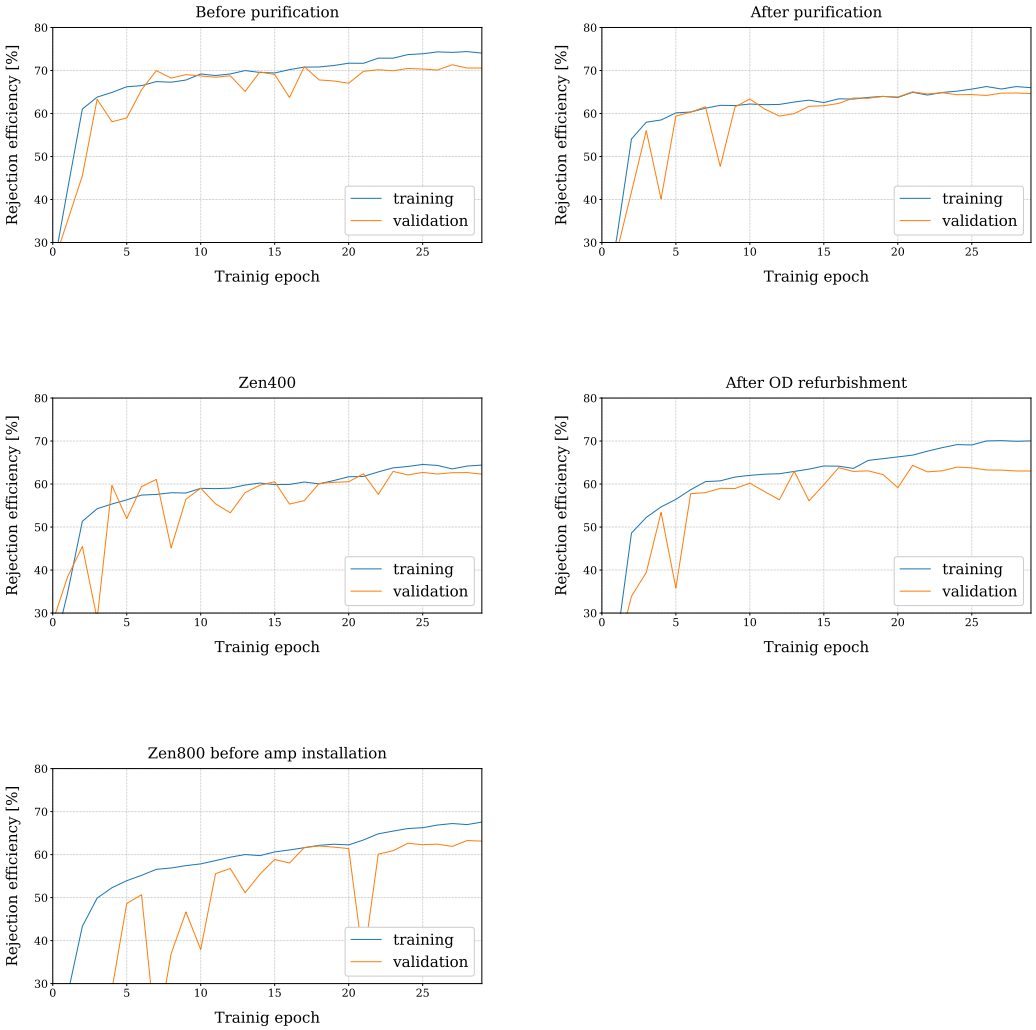

Figure 6.21: Background rejection efficiency with 90% signal acceptance. The rejection efficiency for the validation set saturates toward the end of training, whereas that for the training set continues to increase. To mitigate overtraining, the number of epochs is limited to 30.

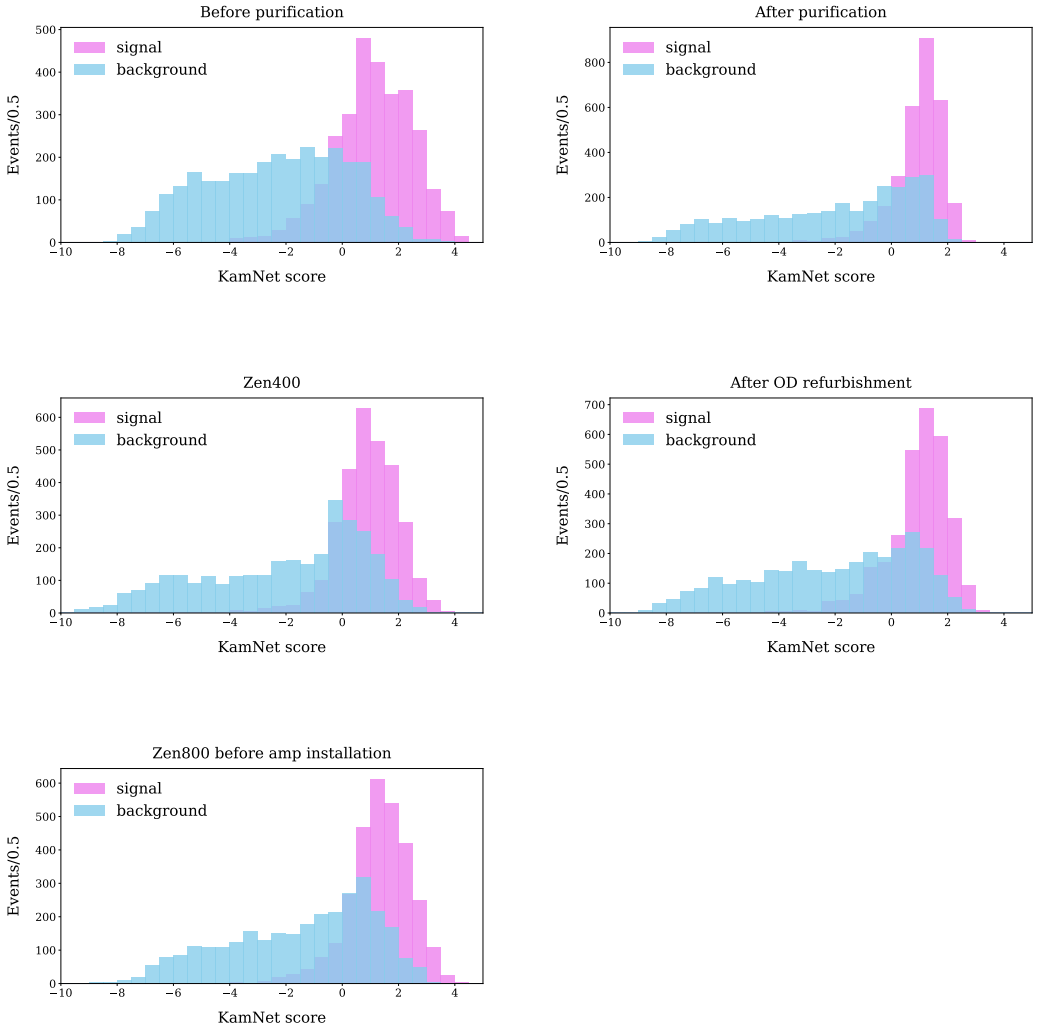

Figure 6.22: KamNet score distribution of the validation data set at the end of training. All validation data in the visible-energy range of 7.5–30 MeV and within a volume of 600 cm radius are plotted.

6.4 KamNet Score Threshold and Efficiencies

In the classification of signal and background using KamNet, we apply a cut by the KamNet score. The score threshold is determined from the output score distribution of the model constructed in the previous section using simulated events.

To determine the score threshold, a Figure of Merit (FoM) that accounts for the expected numbers of signal and background events is calculated. In this analysis, the signal components are the IBD events induced by reactor antineutrinos and astrophysical antineutrinos. As the reference model for the astrophysical antineutrino source, the Horiuchi model [5] of the DSNB is adopted. For the background-like components, atmospheric neutrino NC and fast neutron events are considered. The FoM used in this work is therefore defined as

$$\mathrm{FoM} = \frac{N_{\mathrm{DSNB}}}{\sqrt{N_{\mathrm{DSNB}} + N_{\mathrm{reactor}} + N_{\mathrm{atmNC}} + N_{\mathrm{fastn}}}}, \tag{6.2}$$

where N_{xxx} denotes the expected number of events for component "xxx". Because the target of this search is astrophysical antineutrinos, reactor neutrinos—although observed via the same IBD channel—do not appear in the numerator. Owing to the characteristic shape of the reactor-neutrino energy spectrum, the expected number of event changes markedly around 8.5 MeV. Therefore, the KamNet score threshold is determined separately for each energy region and for each KamNet period.

As noted above, Fig. 6.22 presents the KamNet score distribution for 7.5–30 MeV. The distribution is subsequently partitioned at 8.5 MeV, and the two resulting distributions are analyzed separately. The signal and background distributions are normalized to the expected event numbers, and for each score value the cumulative number of events with scores below that value is computed; this quantity is referred to as the number of remaining events. Using these remaining events, the FoM in Eq. 6.2 is evaluated as a function of the score, and the score that maximizes the FoM is taken as the threshold. Fig. 6.23 and Fig. 6.24 show, for 7.5–8.5 MeV, the number of remaining events and the FoM as functions of the KamNet score, respectively. The corresponding plots for 8.5–30 MeV are presented in Fig. 6.25 and Fig. 6.26. the resulting KamNet score thresholds for each energy region and each KamNet period are summarized in Tab. 6.2.

Table 6.2: KamNet score threshold

KamNet-period	Threshold (7.5–8.5 MeV)	Threshold (8.5–30 MeV)
KamNet-1	-0.66	0.73
KamNet-2	0.01	0.40
KamNet-3	0.23	0.23
KamNet-4	0.29	0.54
KamNet-5	0.57	0.81

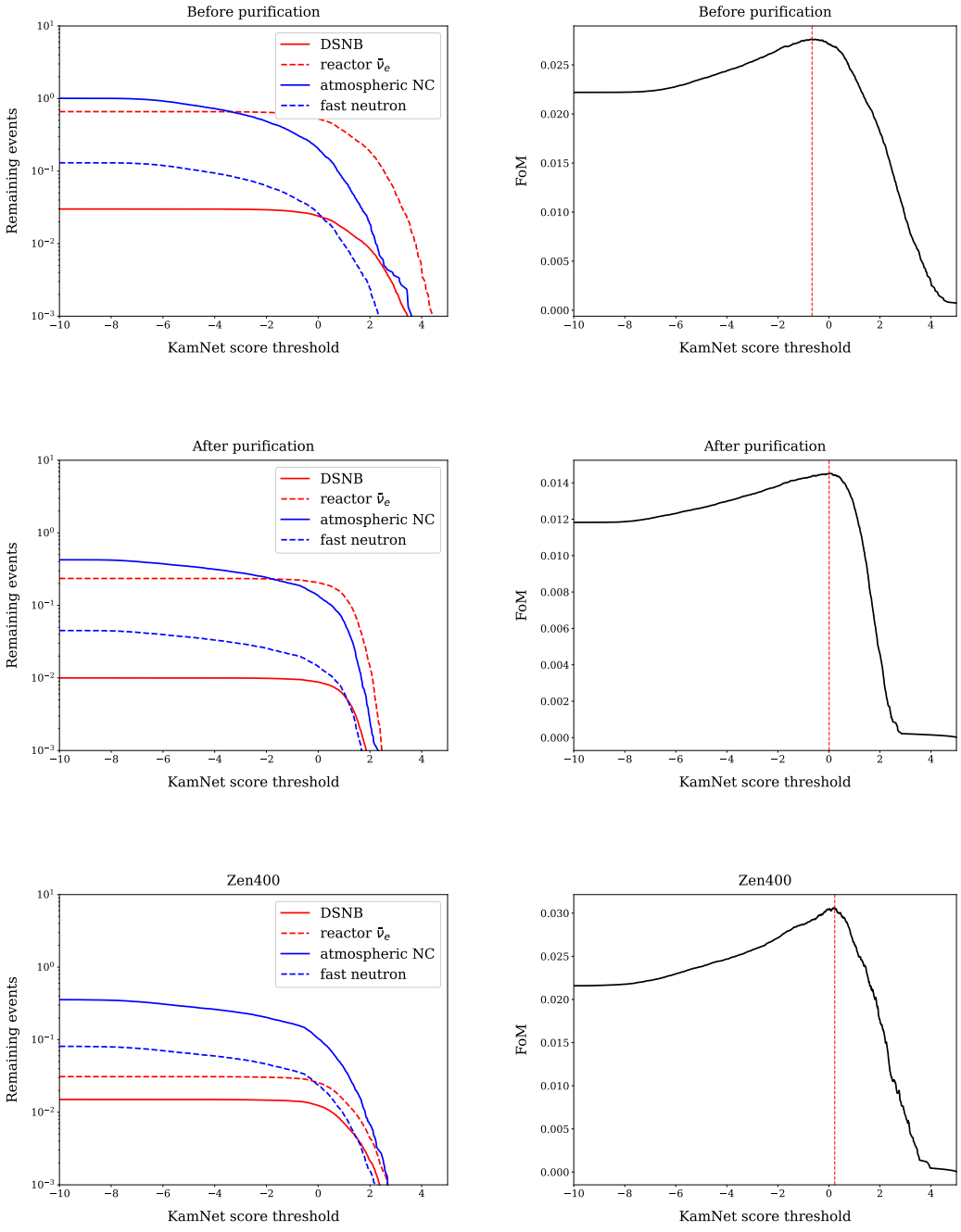

Figure 6.23: Number of remaining events and Figure of Merit (FoM) as a function of the KamNet score threshold (7.5–8.5 MeV) (1). The red line in the FoM plot indicates the optimized KamNet score threshold corresponding to the maximum FoM value.

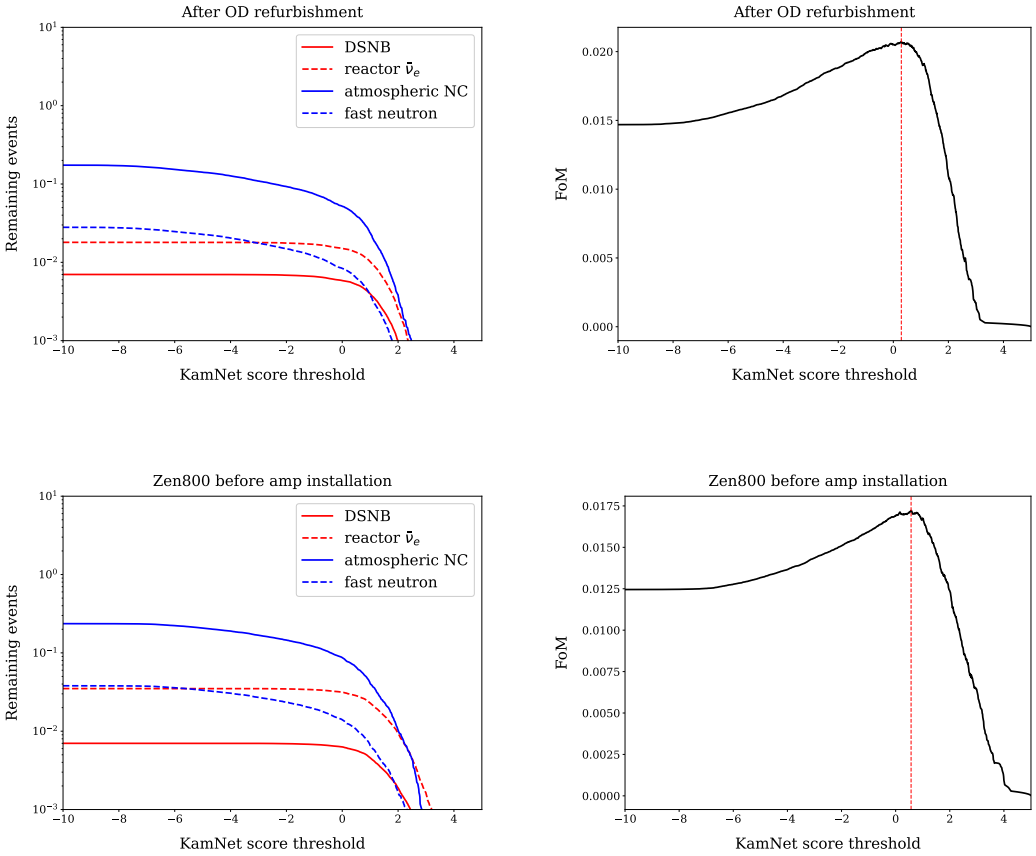

Figure 6.24: Number of remaining events and Figure of Merit (FoM) as a function of the KamNet score threshold (7.5–8.5 MeV) (2).

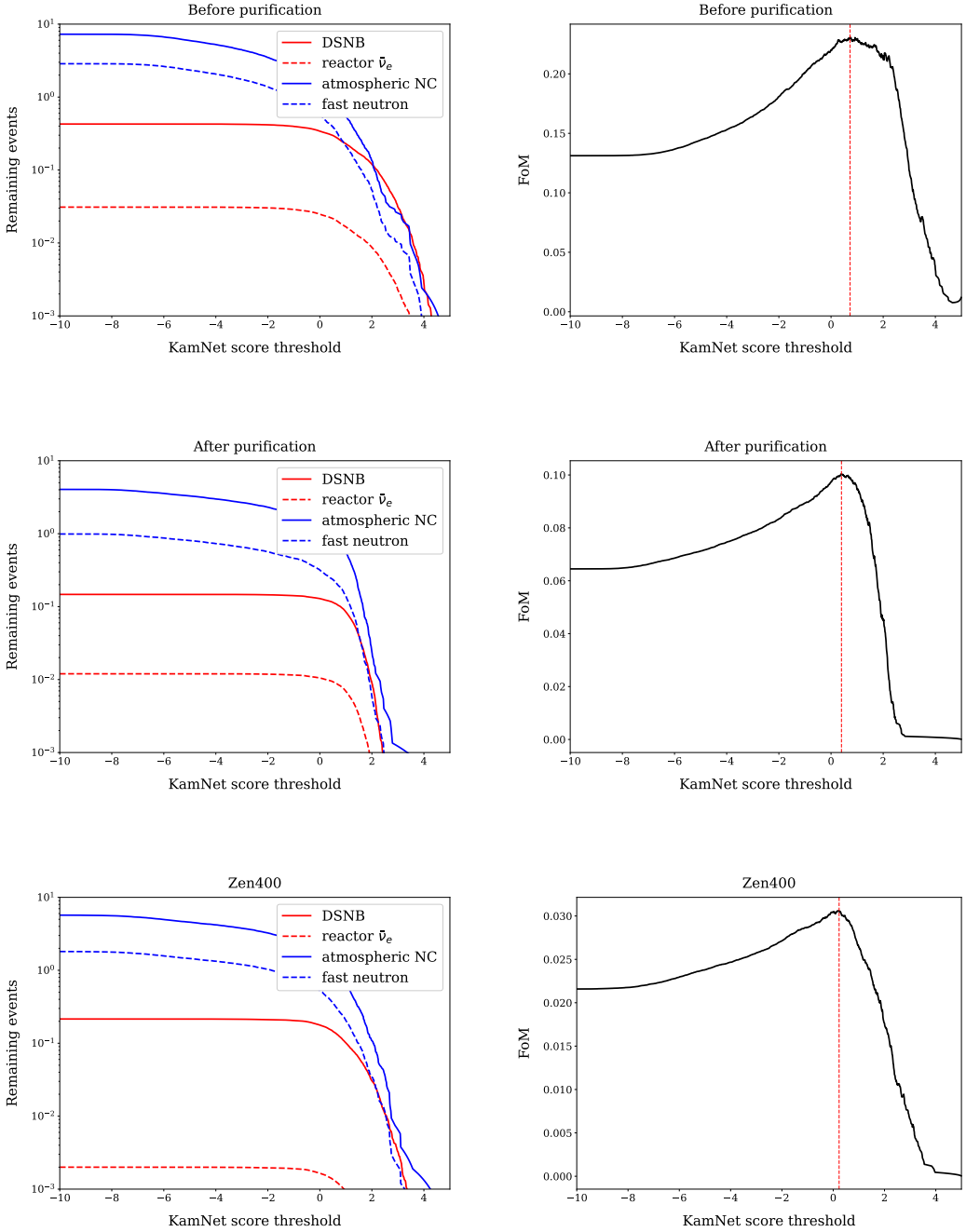

Figure 6.25: Number of remaining events and Figure of Merit (FoM) as a function of the KamNet score threshold (8.5–30 MeV) (1).

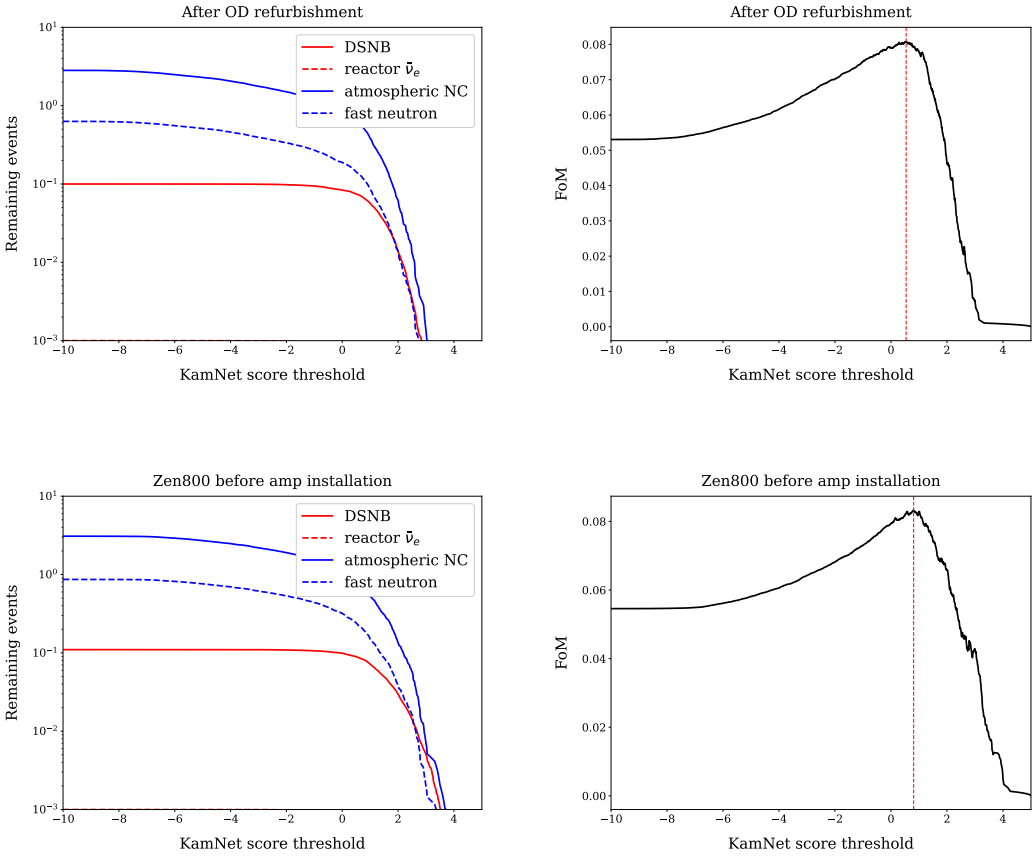

Figure 6.26: Number of remaining events and Figure of Merit (FoM) as a function of the KamNet score threshold (8.5–30 MeV) (2).

Applying the optimized score threshold to the simulated score distributions allows the efficiencies for IBD events and atmospheric neutrino NC events to be estimated[2]. Fig. 6.27 and Fig. 6.28 show the simulated score distributions and the score threshold for 7.5–8.5 MeV and 8.5–30 MeV, respectively. For the normalized score distributions, the IBD acceptance (atmospheric neutrino NC rejection efficiency) is defined as the integral over the region with scores above (below) the threshold. The estimated acceptances and rejection efficiencies are summarized in Tab. 6.3.

Table 6.3: Summary of IBD acceptance and atmospheric neutrino NC rejection efficiencies obtained by the KamNet selection

	IBD acceptance		atmNC rejection efficiency	
KamNet-period	7.5–8.5 MeV	8.5–30 MeV	7.5–8.5 MeV	8.5–30 MeV
KamNet-1	85.4%	62.9%	69.0%	91.3%
KamNet-2	78.4%	81.1%	72.7%	74.4%
KamNet-3	74.5%	77.4%	74.5%	74.8%
KamNet-4	71.5%	74.3%	76.8%	80.8%
KamNet-5	68.8%	75.7%	74.3%	78.3%

[2]Efficiencies for the other event components are evaluated in a later chapter.

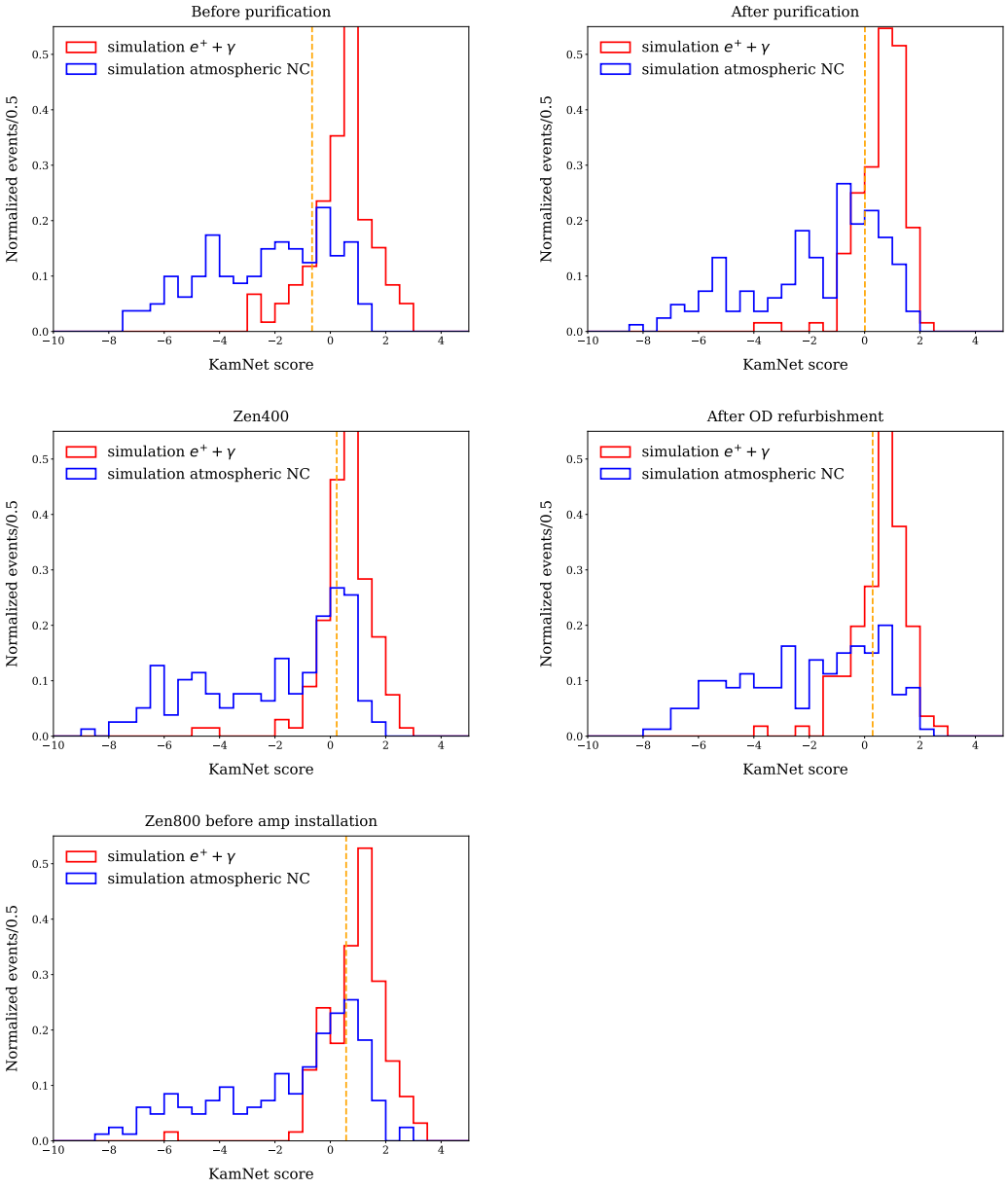

Figure 6.27: KamNet score distributions of simulated e^++ annihilation γ and simulated atmospheric neutrino NC events (7.5–8.5 MeV). The orange line in indicates the optimized KamNet score threshold.

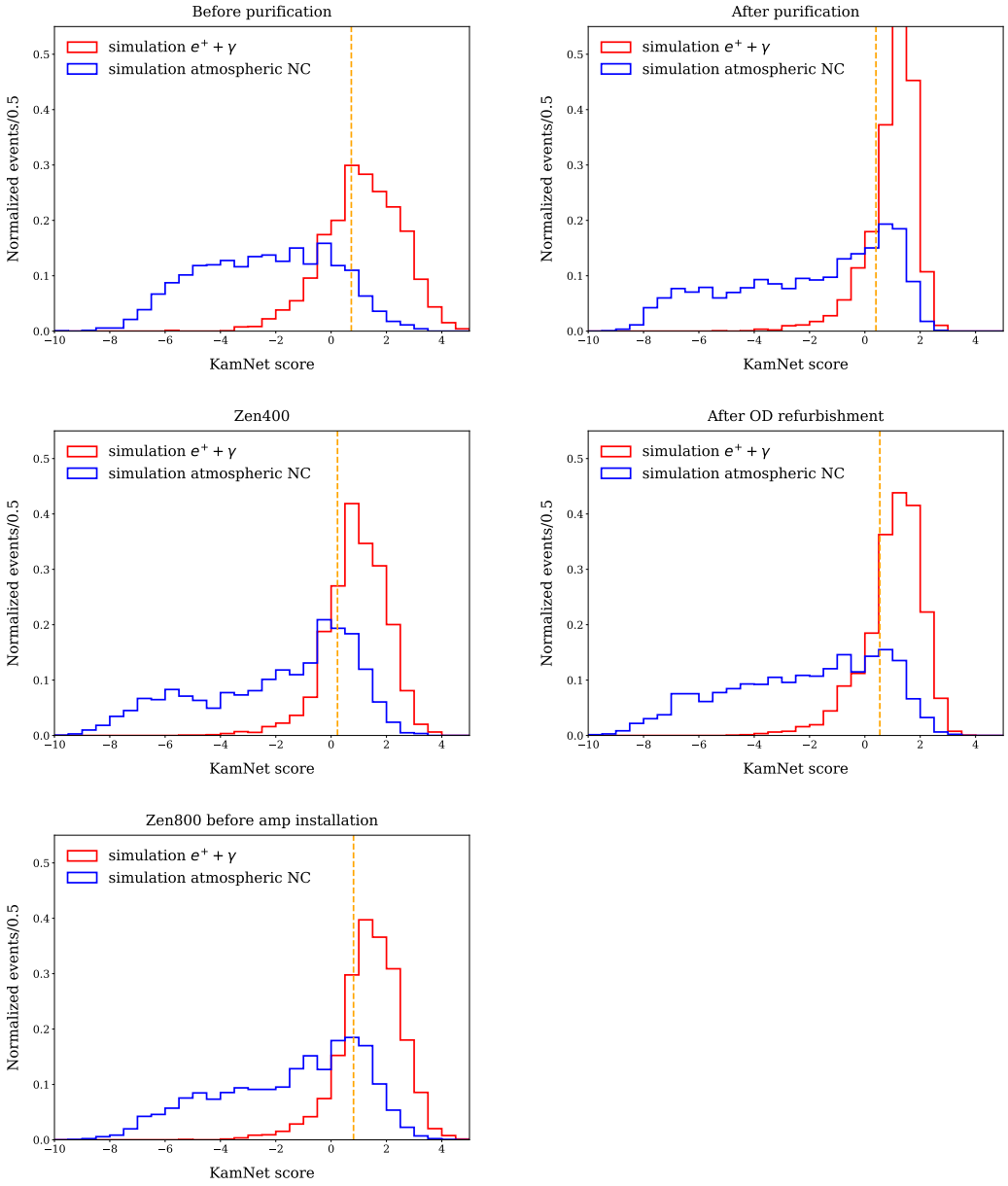

Figure 6.28: KamNet score distributions of simulated e^++ annihilation γ and simulated atmospheric neutrino NC events (8.5–30 MeV).

6.5 Systematic Uncertainties in the Application of KamNet

This section evaluates the systematic uncertainties newly introduced by the application of KamNet. The estimated uncertainties are propagated in Chap. 8 as contributions to the uncertainties on the expected number of events for each event component.

6.5.1 Difference between Particles

In the analysis using KamNet, the discrepancies between simulation and real data are treated as systematic uncertainties as shown in Fig. 6.6. To justify this approach, it is necessary to demonstrate that $e^+ + \gamma$ and $^{12}\mathrm{B}$ β^- decay, as well as atmospheric neutrino NC and neutron events, exhibit similar characteristics within the simulation framework. The similarities among these event types have been quantitatively discussed in terms of hit information in Sec. 6.2.2, while in this section, they are examined from the perspective of the KamNet model output.

Fig. 6.29 shows comparisons of the KamNet scores and efficiencies among different particle types. The score distributions indicate that, within each category (signal or background samples), the distributions are generally consistent. When the efficiency differences are quantified as relative variations in the number of remaining events after the KamNet selection, they are found to be less than $\sim 4\%$ below 8.5 MeV and less than $\sim 11\%$ above 8.5 MeV. In other words, even within the same sample category, efficiency differences of this magnitude may arise depending on the particle type.

In conclusion, $e^+ + \gamma$ and $^{12}\mathrm{B}$ β^- decay can be classified as signal samples from the viewpoint of KamNet score distributions, and likewise, atmospheric neutrino NC and neutron events can be regarded as background samples.

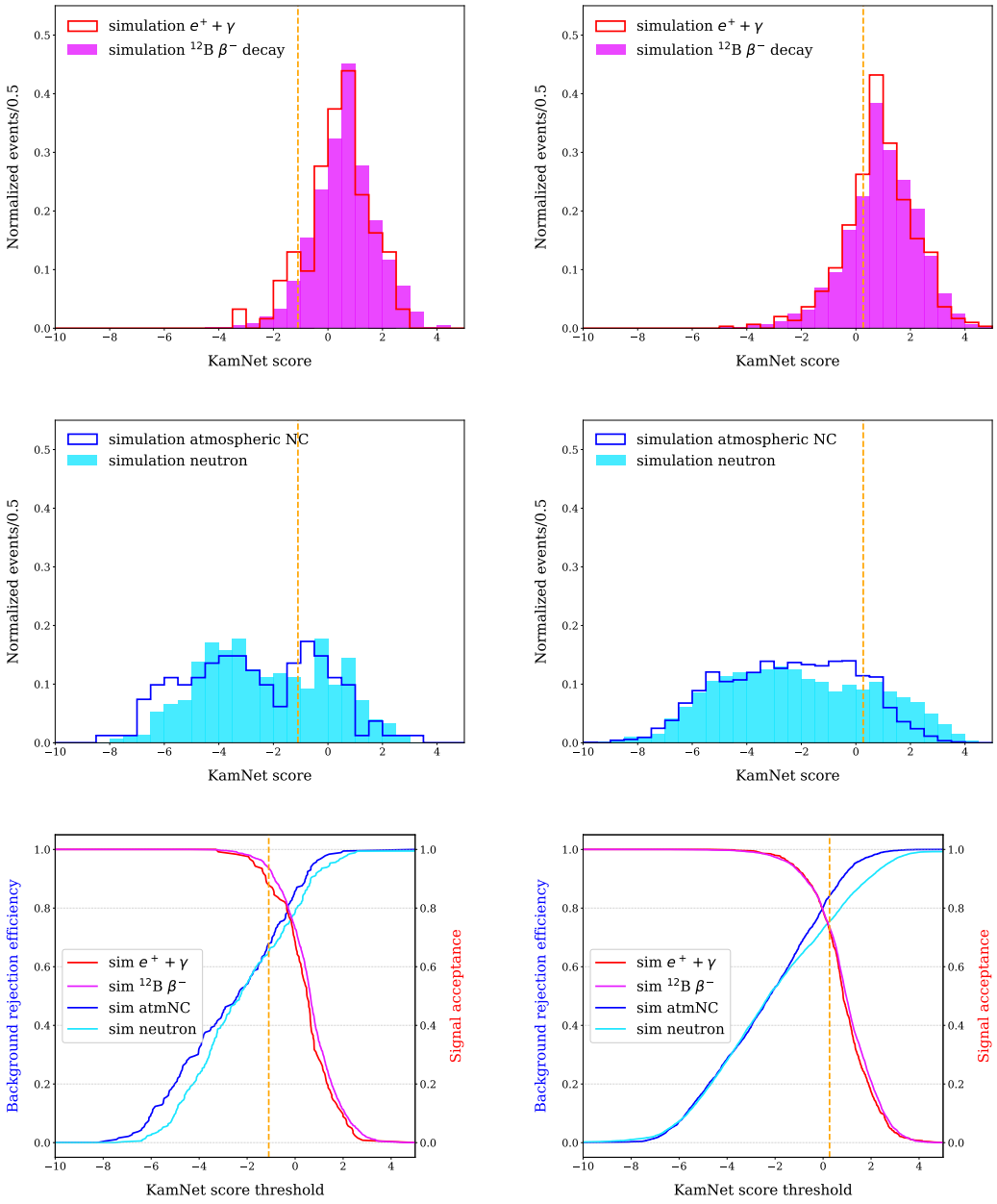

Figure 6.29: Comparison of KamNet scores and efficiencies among different particles. The left panels correspond to the visible energy range of 7.5–8.5 MeV, and the right panels to 8.5–30 MeV. The upper panels show the KamNet score distributions for simulated $e^+ + \gamma$ and ^{12}B β^- decay events, both treated as signal samples. The middle panels show those for simulated atmospheric NC and neutron events, categorized as background samples. The lower panels present the signal acceptances and background rejection efficiencies for each sample. The orange line indicates the optimized KamNet score threshold. These figures show examples of KamNet-1 period.

6.5.2 Difference between Simulation and Real Data

This study trains the KamNet model on simulation. In the actual astrophysical antineutrino search, however, the KamNet model is applied to data. As shown in Sec. 6.2.2, within the hit-time window the differences between simulation and data are contained within deviations of approximately 5%. From the perspective of the KamNet model, it is nevertheless not clear how well the simulation reproduces the data. It is therefore necessary to quantify potential performance differences of the KamNet model between simulation and data.

The evaluation uses differences in efficiency between signal samples or between background samples. These efficiency differences are interpreted as systematic uncertainties arising from the limited fidelity of the simulation relative to data. Comparisons of score distributions and efficiencies between samples are summarized in the following figures:

- Fig. 6.30 and Fig. 6.31: comparison between signal samples in 7.5–8.5 MeV (simulated ^{12}B vs. real spallation ^{12}B events)
- Fig. 6.32 and Fig. 6.33: comparison between signal samples in 8.5–13 MeV (simulated ^{12}B vs. real spallation ^{12}B events)
- Fig. 6.34 and Fig. 6.35: comparison between background samples in 7.5–8.5 MeV (simulated atmospheric neutrino NC vs. real fast neutron events)
- Fig. 6.36 and Fig. 6.37: comparison between background samples in 8.5–30 MeV (simulated atmospheric neutrino NC vs. real fast neutron events)

Because the energy spectrum of spallation ^{12}B in real data extends only up to around 13 MeV, the comparison of the score and efficiency is restricted to 13 MeV. In addition, the fast neutron statistics in real data are limited; consequently, in the 7.5–8.5 MeV bin—whose width is only 1 MeV—the efficiency curves become less smooth.

The systematic uncertainty discussed in this section is defined as the relative error with respect to the signal acceptance and the remaining background ratio (= 1−background rejection efficiency), as follows:

$$\text{signal sys.unc.} = \frac{\text{(signal acceptance diff. between simulation and real data)}}{\text{(signal acceptance in simulation)}} \tag{6.3}$$

$$\text{background sys.unc.} = \frac{\text{(rejection efficiency diff. between simulation and real data)}}{1 - \text{(rejection efficiency in simulation)}} \tag{6.4}$$

This uncertainty also includes the statistic error associated with each sample. The systematic uncertainties estimated for the signal and background samples are summarized in Tab. 6.4.

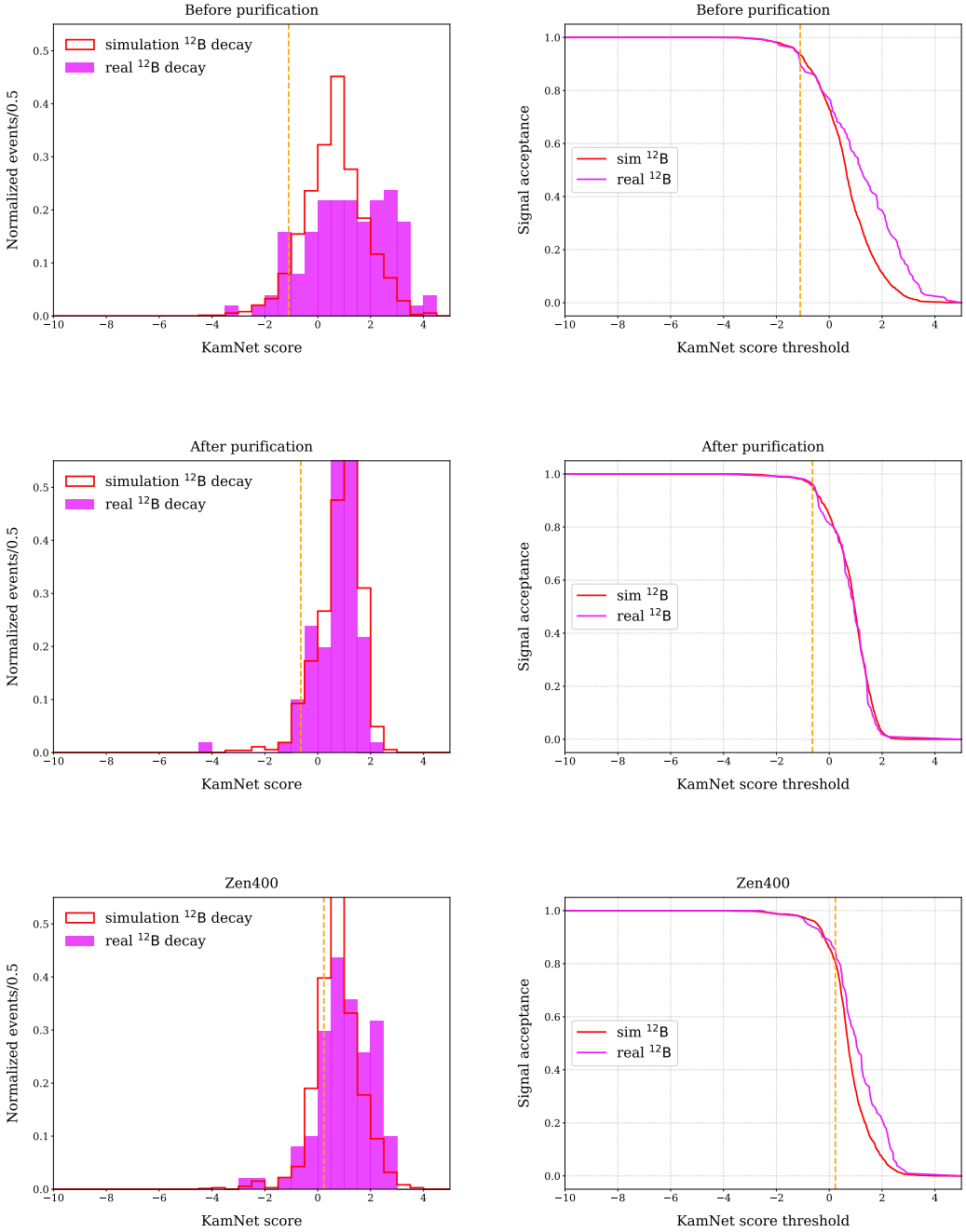

Figure 6.30: Comparisons of the KamNet score distributions and acceptances between simulated ^{12}B β^- decay and real spallation ^{12}B β^- decay events (7.5–8.5 MeV) (1). The orange line indicates the optimized KamNet score threshold.

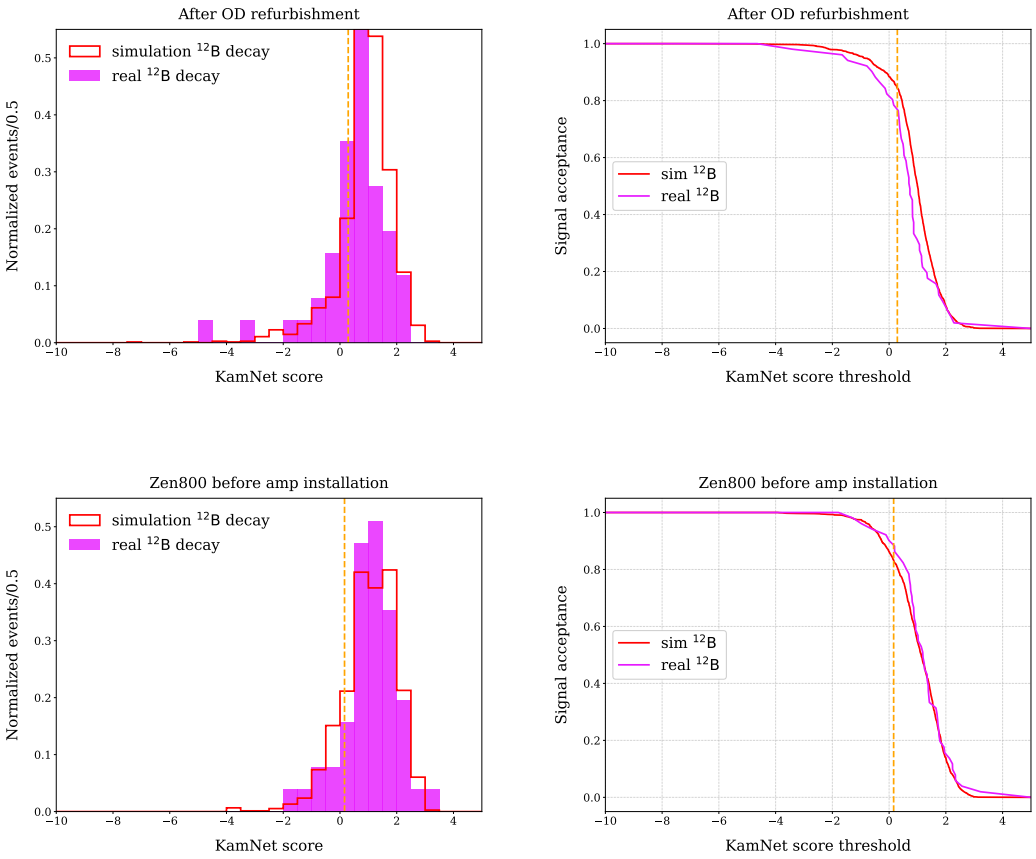

Figure 6.31: Comparisons of the KamNet score distributions and acceptances between simulated ^{12}B β^- decay and real spallation ^{12}B β^- decay events (7.5–8.5 MeV) (2).

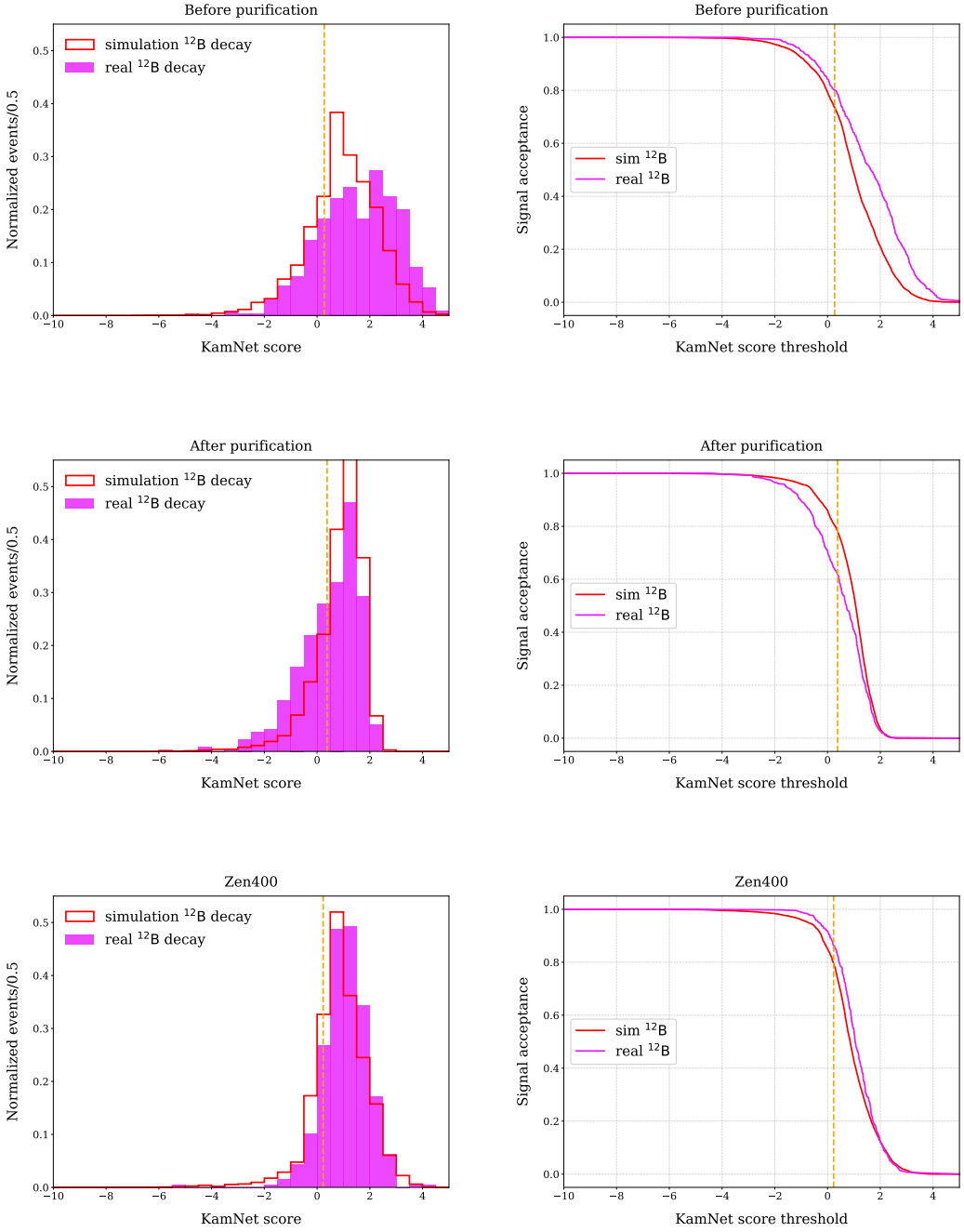

Figure 6.32: Comparisons of the KamNet score distributions and acceptances between simulated ^{12}B β^- decay and real spallation ^{12}B β^- decay events (8.5–13 MeV) (1).

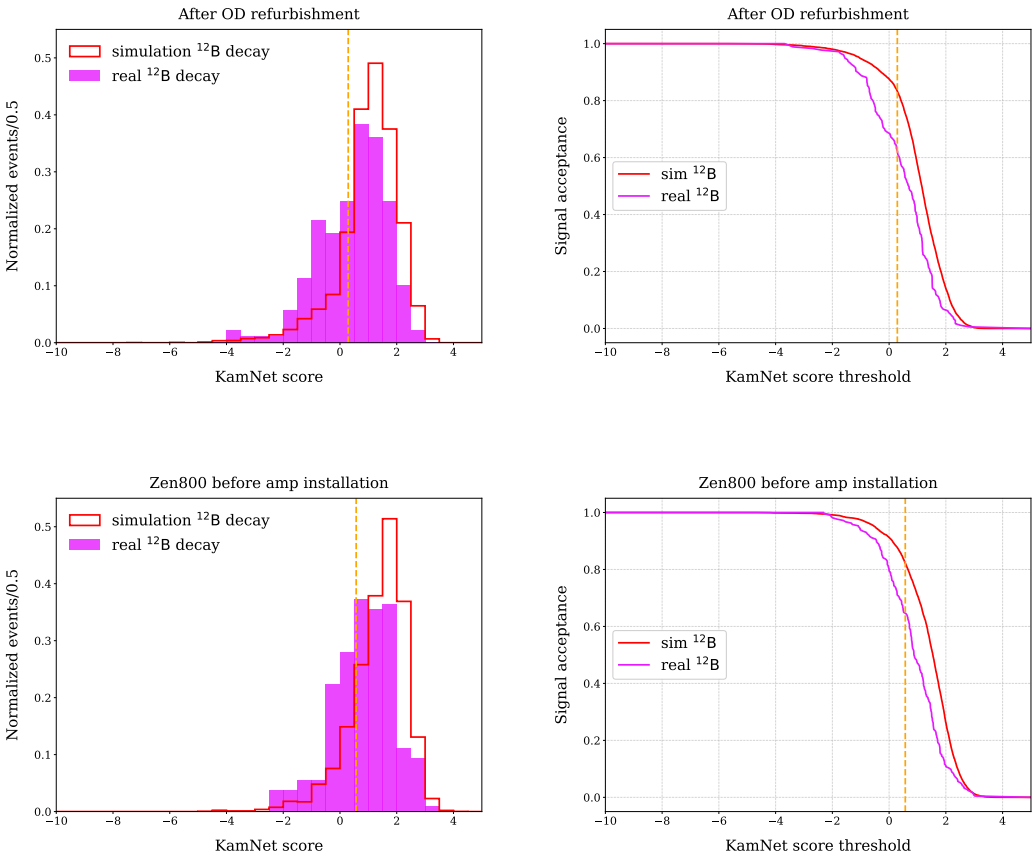

Figure 6.33: Comparisons of the KamNet score distributions and acceptances between simulated ^{12}B β^- decay and real spallation ^{12}B β^- decay events (8.5–13 MeV) (2).

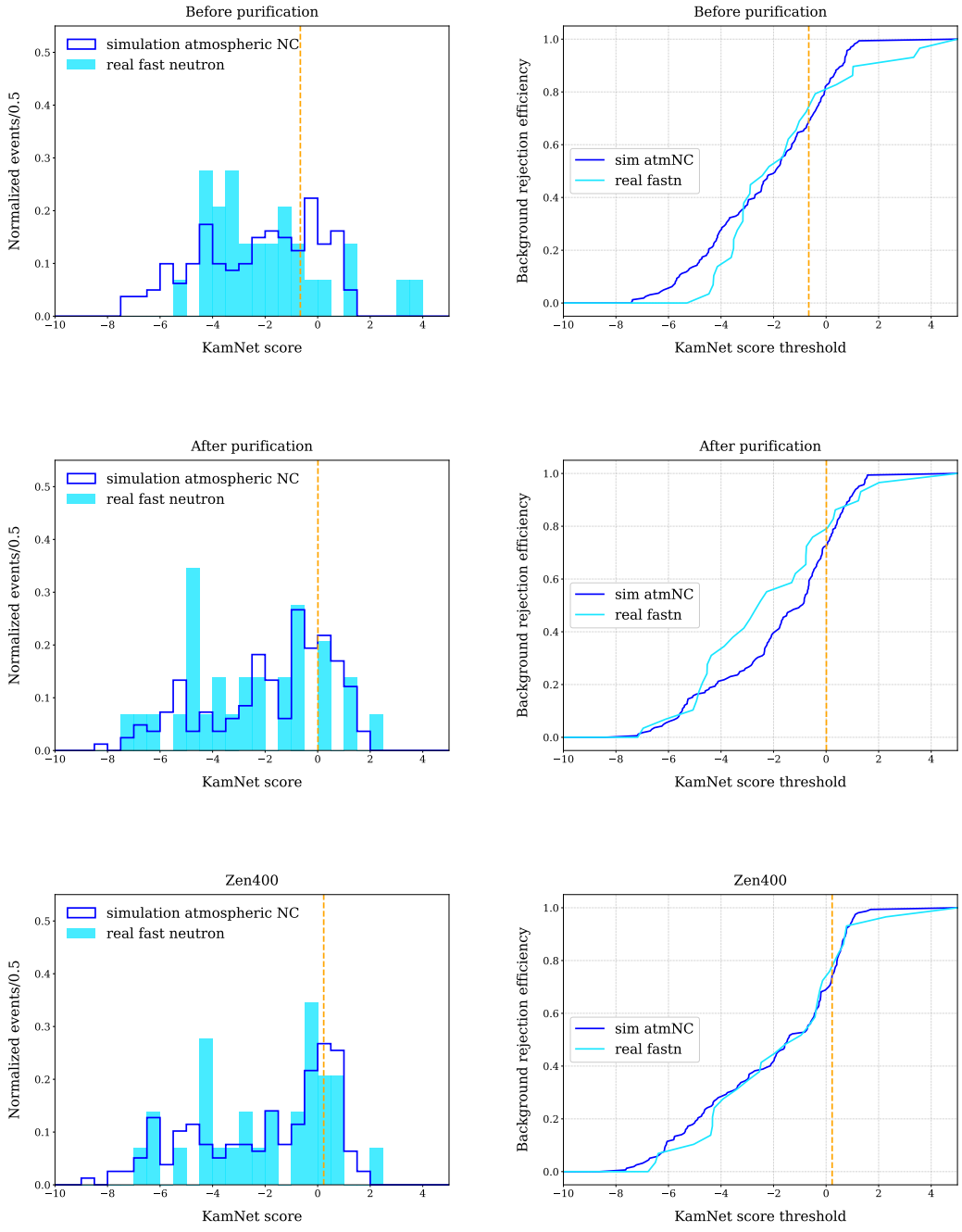

Figure 6.34: Comparisons of the KamNet score distributions and rejection efficiencies between simulated atmospheric neutrino NC events and real fast neutron events (7.5–8.5 MeV) (1). The orange line indicates the optimized KamNet score threshold.

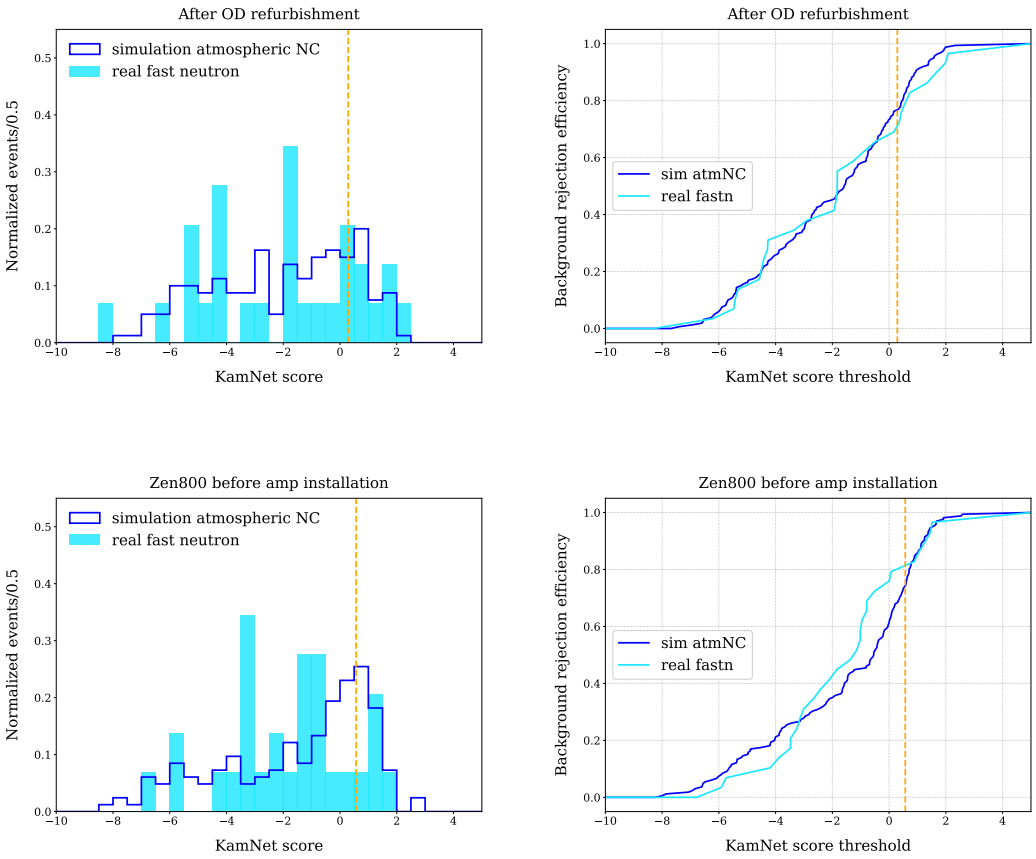

Figure 6.35: Comparisons of the KamNet score distributions and rejection efficiencies between simulated atmospheric neutrino NC events and real fast neutron events (7.5–8.5 MeV) (2).

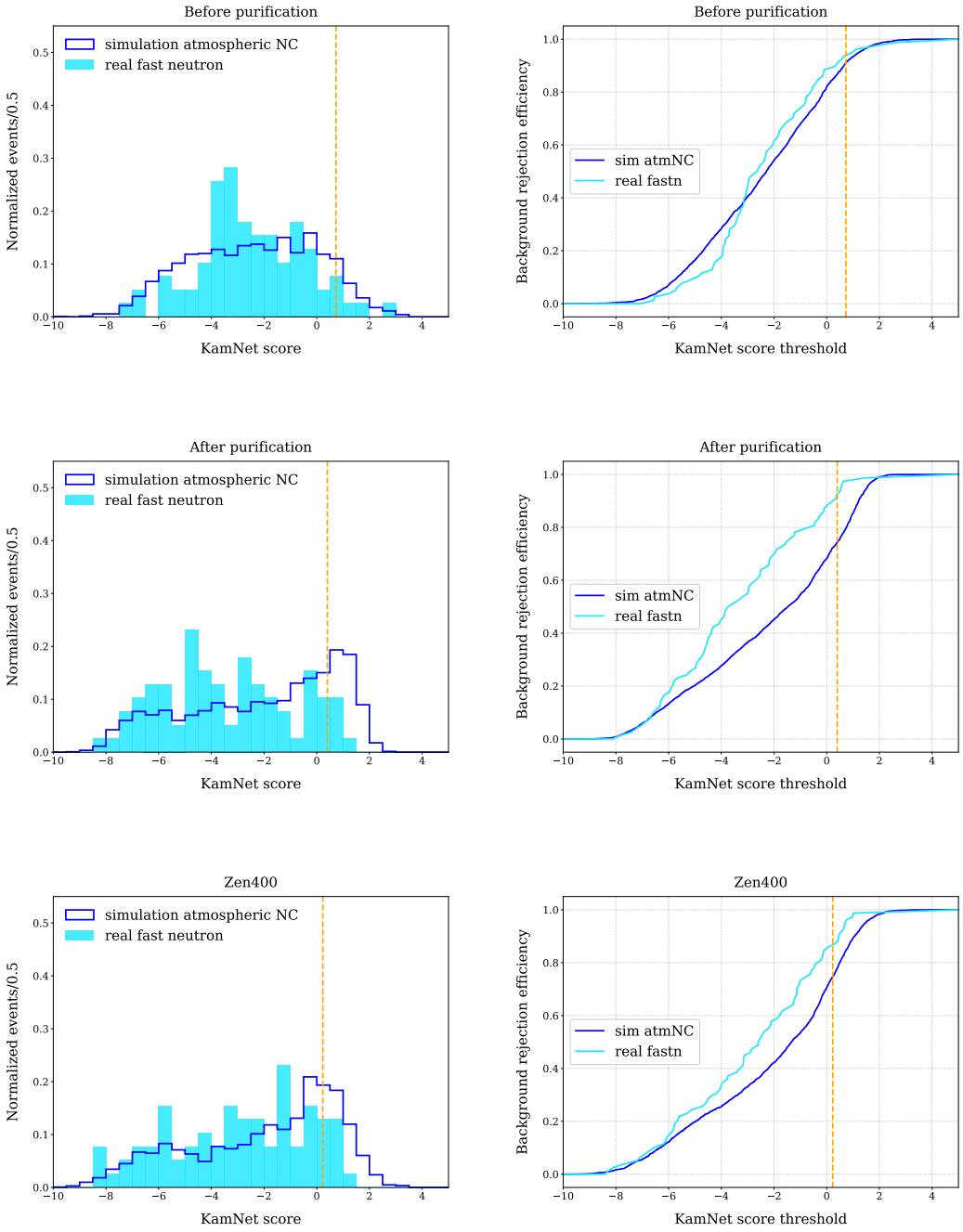

Figure 6.36: Comparisons of the KamNet score distributions and rejection efficiencies between simulated atmospheric neutrino NC events and real fast neutron events (8.5–30 MeV) (1).

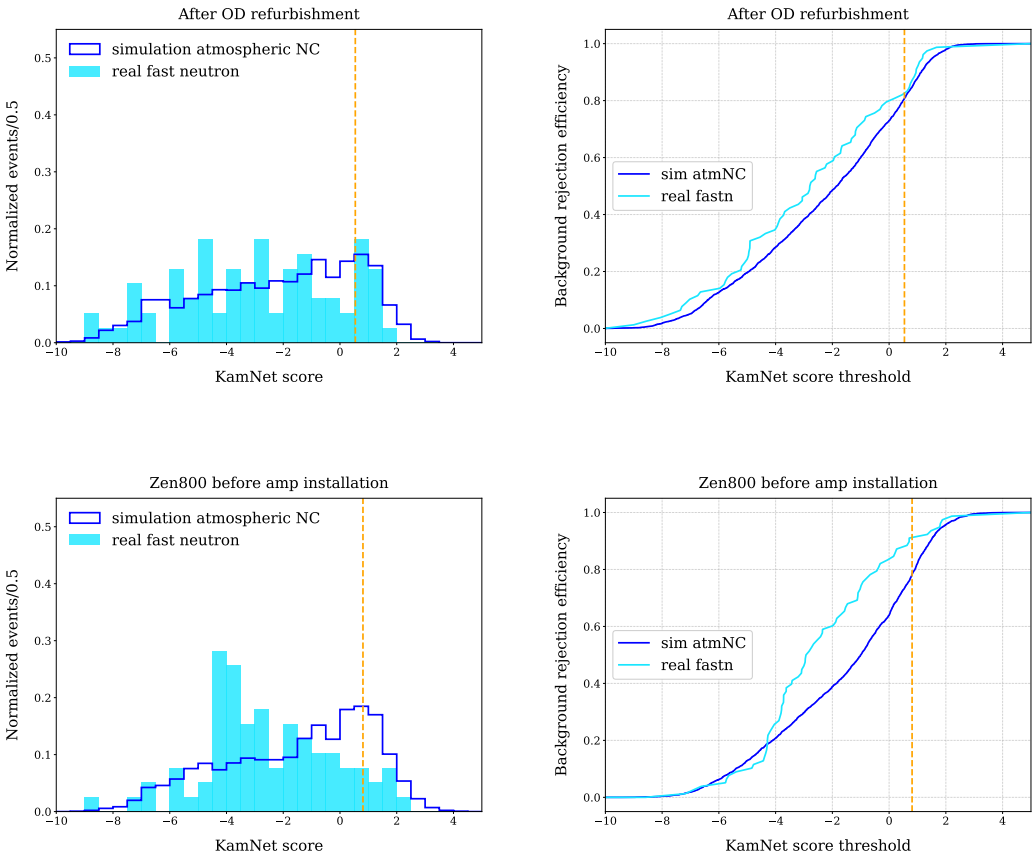

Figure 6.37: Comparisons of the KamNet score distributions and rejection efficiencies between simulated atmospheric neutrino NC events and real fast neutron events (8.5–30 MeV) (2).

Table 6.4: Summary of systematic uncertainties for signal and background arising from differences between simulation and real data

	Signal		Background	
KamNet-period	7.5–8.5 MeV	8.5–30 MeV	7.5–8.5 MeV	8.5–30 MeV
KamNet-1	5.6%	11.0%	33.6%	43.6%
KamNet-2	2.7%	20.3%	38.4%	72.0%
KamNet-3	7.4%	9.0%	35.7%	49.9%
KamNet-4	13.5%	28.7%	45.8%	24.6%
KamNet-5	10.1%	23.6%	32.8%	58.9%

6.5.3 KamNet Performance Fluctuation

In training KamNet, events are randomly selected from a large pool of simulated events. Because of this random selection, the classification performance of the trained KamNet model varies across independent training. To quantify this fluctuation, the signal acceptance and the background rejection efficiency—both defined by the score threshold—are used as performance indicators.

As the evaluation method, a so-called bootstrap procedure is employed. Specifically, the following is repeated 100 times: random training samples are selected from the full pool of simulated events, a KamNet model is trained on each sample, and the signal acceptance and the rejection efficiency are computed for all 100 models. The resulting efficiency distributions are fitted with a Gaussian function, and the fitted standard deviation is used to estimate the systematic uncertainty. An example of the distributions of the signal acceptance and background rejection efficiency obtained from the 100 trainings is shown in Fig. 6.38. The systematic uncertainties associated with KamNet performance fluctuations are defined as follows:

$$\text{signal sys.unc.} = \frac{\text{(signal acceptance standard deviation)}}{\text{(signal acceptance in simulation)}} \tag{6.5}$$

$$\text{background sys.unc.} = \frac{\text{(rejection efficiency standard deviation)}}{1 - \text{(rejection efficiency in simulation)}}, \tag{6.6}$$

and the estimated uncertainties are summarized in Tab. 6.5.

Table 6.5: Summary of systematic uncertainties for signal and background arising from the fluctuation in the KamNet performance

	Signal		Background	
KamNet-period	7.5–8.5 MeV	8.5–30 MeV	7.5–8.5 MeV	8.5–30 MeV
KamNet-1	2.0%	7.5%	10.7%	28.6%
KamNet-2	4.3%	6.5%	13.0%	13.9%
KamNet-3	6.0%	5.8%	14.9%	15.1%
KamNet-4	7.2%	7.9%	16.9%	19.8%
KamNet-5	9.5%	9.5%	14.8%	15.8%

6.5.4 Radial Dependence of KamNet

In this analysis, the events used for training were those reconstructed within a fiducial radius of 6 m. This radius was chosen to secure sufficient statistics in real data when

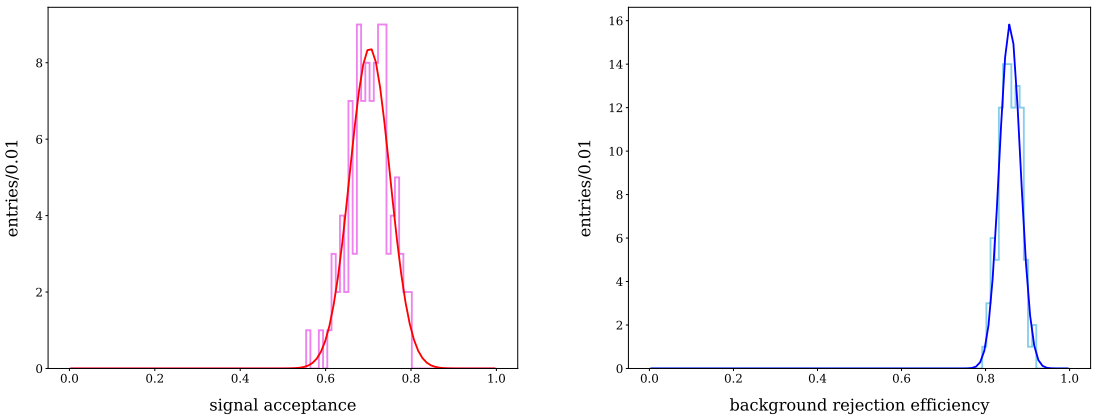

Figure 6.38: Fluctuations in KamNet performance evaluated through efficiencies. Left: signal acceptance, right: background rejection efficiency. These figures show the example for the 8.5–30 MeV in the KamNet-1 period.

discussing the performance differences between simulated and real events for the trained model in Sec. 6.5.2. However, as described in Chap. 7, the fiducial radius is set to 5.5 m in the astrophysical antineutrino search in order to avoid background events that are more abundant near the outer region of the detector. Therefore, if the performance of KamNet exhibits a dependence on the event radius, this effect must be taken into account as a systematic uncertainty.

The radial dependence of the KamNet performance is evaluated by comparing the efficiencies in regions with different distances from the detector center. First, the signal acceptance and background rejection efficiency are estimated in three volume regions ($r = 0$–450 cm, 450–550 cm, and 550–600 cm). Then, for both the simulated and real data samples, the differences between the efficiencies in the outer region ($r = 550$–600 cm) and those in the inner regions ($r = 0$–450 cm and 450–550 cm) are calculated. The largest efficiency difference among these is conservatively adopted as the relative uncertainty on the signal acceptance and background remaining ratio[3]:

$$\text{signal sys.unc.} = \frac{(\text{largest signal acceptance diff. from } r = 550\text{–}600\,\text{cm})}{(\text{signal acceptance in simulation})} \tag{6.7}$$

$$\text{background sys.unc.} = \frac{(\text{largest rejection efficiency diff. from } r = 550\text{–}600\,\text{cm})}{1 - (\text{rejection efficiency in simulation})}, \tag{6.8}$$

Fig. 6.39 shows the radial dependence of the signal acceptance for the simulated signal samples ($e^+ + \gamma$). Likewise, Fig. 6.40 presents the radial dependence of the background rejection efficiency. The systematic uncertainties associated with the radial dependence of the KamNet performance are summarized in Tab. 6.6.

[3]For the background sample, the number of real-data events in the region $r = 0$–450 cm is extremely limited; therefore, only the difference between the $r = 550$–600 cm and $r = 450$–550 cm regions is considered in the evaluation.

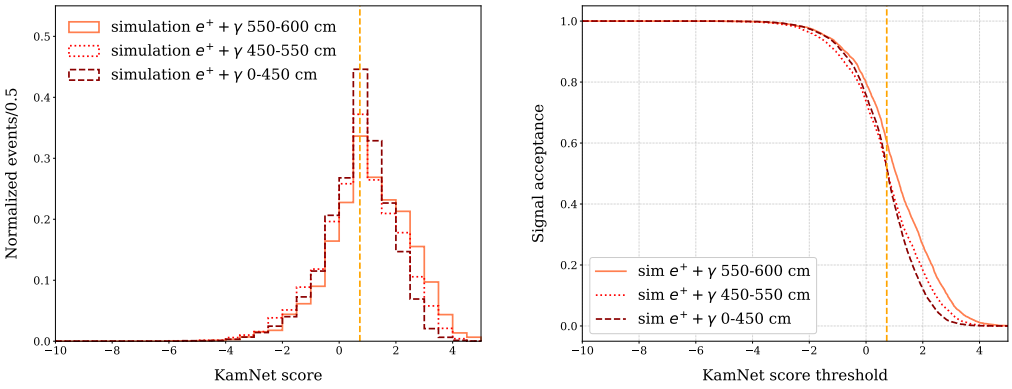

Figure 6.39: Example of the radial dependence of KamNet score distributions and acceptances among simulated $e^+ + \gamma$ events. The figures show examples in the 8.5–13 MeV range during the KamNet-1 period.

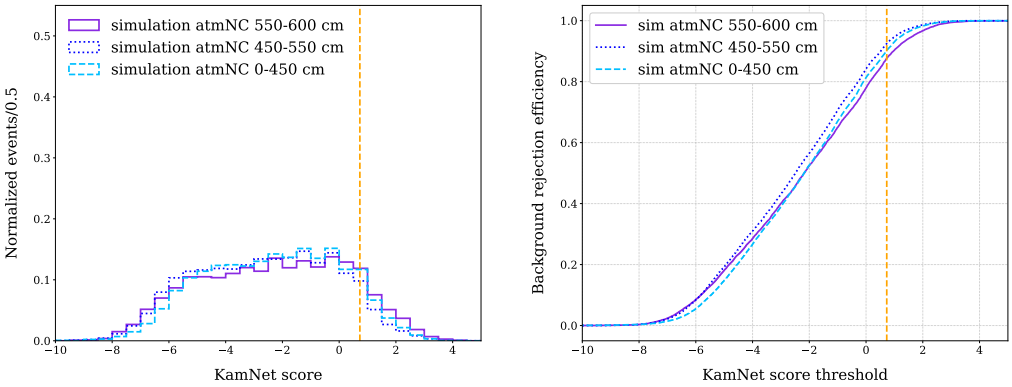

Figure 6.40: Example of the radial dependence of KamNet score distributions and rejection efficiencies among simulated atmospheric NC events. The figures show examples in the 8.5–30 MeV range during the KamNet-1 period.

Table 6.6: Summary of systematic uncertainties from the radial dependence of KamNet

	Signal		Background	
KamNet-period	7.5–8.5 MeV	8.5–30 MeV	7.5–8.5 MeV	8.5–30 MeV
KamNet-1	34.7%	32.8%	9.7%	55.3%
KamNet-2	22.6%	32.8%	22.3%	21.0%
KamNet-3	12.2%	10.5%	18.1%	25.4%
KamNet-4	30.0%	20.1%	18.6%	27.5%
KamNet-5	35.4%	15.3%	40.7%	23.5%

6.5.5 Summary of KamNet-Related Systematic Uncertainties

Tab. 6.7 summarizes the KamNet-related systematic uncertainties, combining the three components discussed above.

Table 6.7: Summary of KamNet-related systematic uncertainties

	Signal		Background	
KamNet-period	7.5–8.5 MeV	8.5–30 MeV	7.5–8.5 MeV	8.5–30 MeV
KamNet-1	35.2%	35.4%	36.6%	76.0%
KamNet-2	23.2%	39.1%	46.3%	76.3%
KamNet-3	15.5%	15.0%	42.8%	57.9%
KamNet-4	33.6%	35.9%	52.2%	41.9%
KamNet-5	38.0%	29.7%	54.3%	65.4%

6.6 KamNet Efficiencies for Other Event Components

Fast neutron

The rejection efficiency for fast neutron events has already been estimated in a data-driven manner, as described in Sec. 6.5.2. The resulting fast-neutron rejection efficiencies are summarized in Tab. 6.8.

Table 6.8: Summary of fast neutron rejection efficiencies obtained by the KamNet selection

KamNet-period	7.5–8.5 MeV	8.5–30 MeV
KamNet-1	74.4%	93.9%
KamNet-2	79.1%	92.6%
KamNet-3	77.9%	86.7%
KamNet-4	71.2%	82.6%
KamNet-5	81.4%	91.2%

Spallation ^{9}Li

When muons traversing the detector cause carbon spallation in the LS, unstable isotopes are produced. Among these spallation products, ^{9}Li and ^{8}He undergo β decay accompanied by a neutron; such events appear as delayed coincidences and constitute a background to the astrophysical antineutrino search (see Sec. 8.3). To estimate the rejection efficiency of the KamNet cut for spallation ^{9}Li (with the negligible contribution from ^{8}He), events are selected using a delayed-coincidence method. Furthermore, by restricting to events tagged as spallation by the *shower likelihood cut*[4], a dataset enriched in spallation events is obtained. The resulting data-driven score distributions for spallation events are shown in Fig. 6.41 and Fig. 6.42. Because the prompt hit information is generated by an e^{-}, the distributions resemble those of $e^{+} + \gamma$ and spallation ^{12}B. The rejection efficiencies for spallation ^{9}Li events are summarized in Tab. 6.9.

Table 6.9: Summary of spallation ^{9}Li rejection efficiencies obtained by the KamNet selection

KamNet-period	7.5–8.5 MeV	8.5–30 MeV
KamNet-1	23.5%	53.0%
KamNet-2	32.1%	27.8%
KamNet-3	10.3%	15.8%
KamNet-4	38.4%	45.4%
KamNet-5	25.2%	51.1%

[4] Spallation ^{9}Li/^{8}He is removed using the shower likelihood cut; see Sec. 7.5.

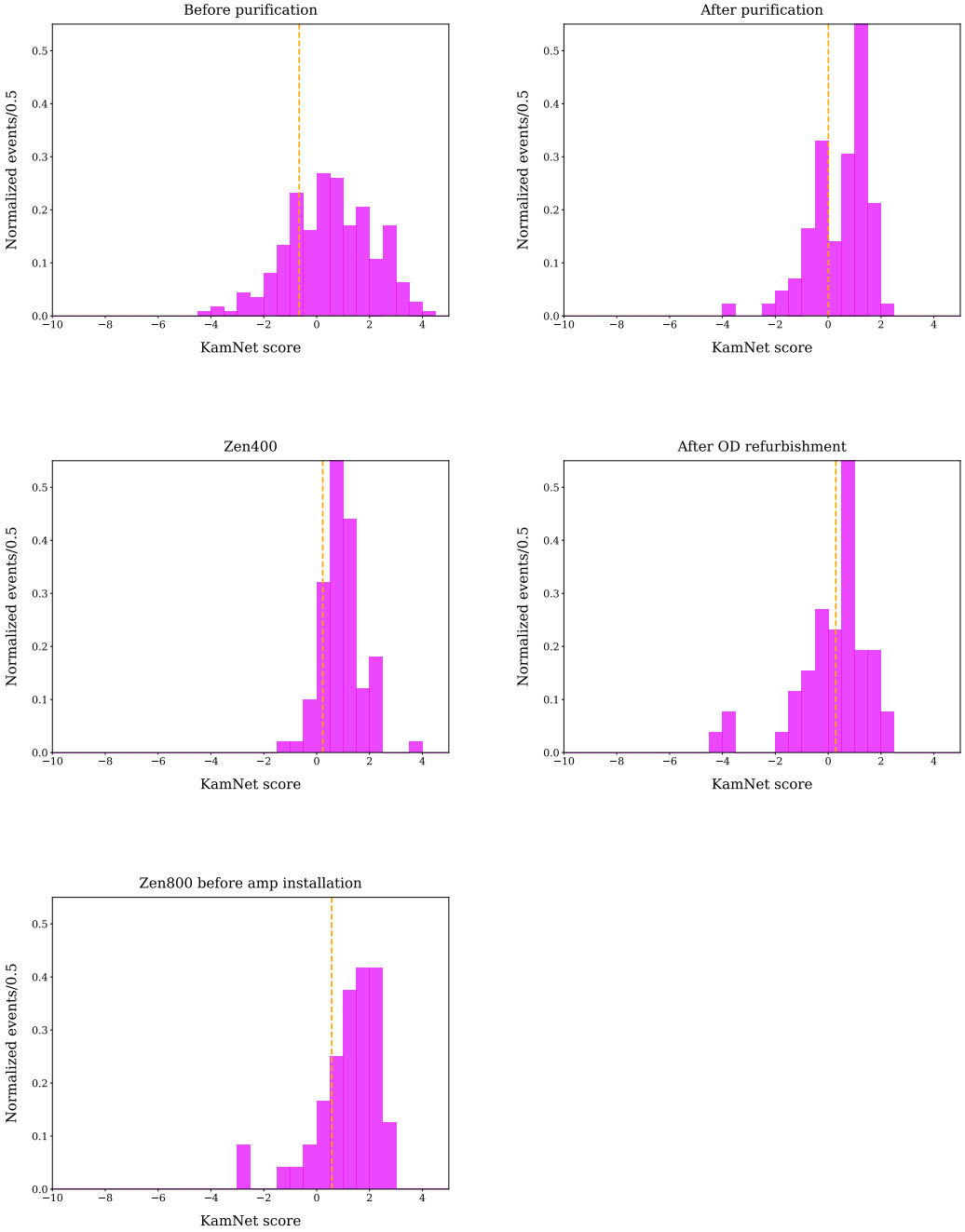

Figure 6.41: KamNet score distributions of real spallation ^{9}Li $\beta^{-}+n$ decay events (7.5–8.5 MeV).

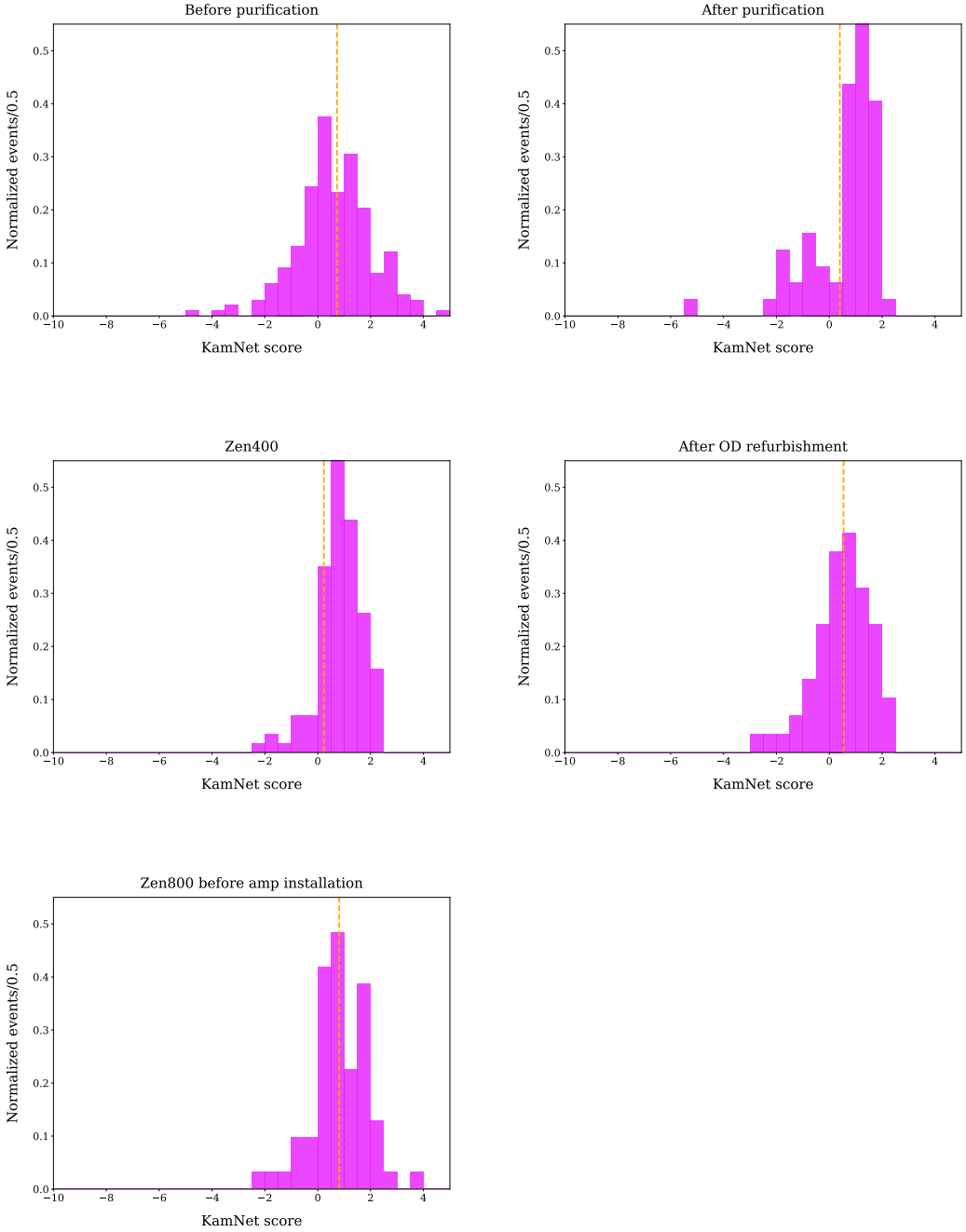

Figure 6.42: KamNet score distributions of real spallation ^{9}Li $\beta^{-}+n$ decay events (8.5–30 MeV).

Atmospheric neutrino CC

When a neutron is knocked out from a carbon nucleus by an atmospheric neutrino charged-current (CC) interaction, it produces a background event observable through delayed coincidence, similar to atmospheric neutrino NC interactions. In the case of atmospheric CC events, neutron-induced proton recoils are also included in the prompt signal; therefore, their hit information and KamNet outputs are expected to resemble those of background samples. Fig. 6.43 shows a comparison of the hit timing distributions between simulated atmospheric NC and CC events. As discussed in Sec. 6.2.2, the deviation among background samples in the hit timing distributions is within 5% (green band in Fig. 6.43). Taking this into account, it can be concluded that atmospheric CC events are sufficiently similar to background samples from the viewpoint of hit information.

Next, to investigate the similarity between atmospheric NC and CC events in terms of KamNet output, a comparison of the KamNet scores and efficiencies was performed using simulated events. The results are shown in Fig. 6.44. As expected, the score distributions of the two event types are generally consistent. However, a slight shift toward more signal-like values is observed for CC events. This is considered to originate from the higher fraction of light particles contributing to the prompt hit information in CC events compared to NC events.

Ideally, the KamNet rejection efficiency for atmospheric CC events should be estimated based on simulation over the entire data-taking period. However, since atmospheric CC events tend to have higher reconstructed visible energies than NC events, generating a comparable number of CC events is computationally demanding. Moreover, even if the rejection efficiency were evaluated purely from simulation, it would not be possible to validate its performance using real data, as no pure atmospheric CC sample can be extracted from the data. Therefore, in this analysis, both the KamNet rejection efficiency and the associated systematic uncertainty for atmospheric CC events are approximated to be the same as those for NC events.

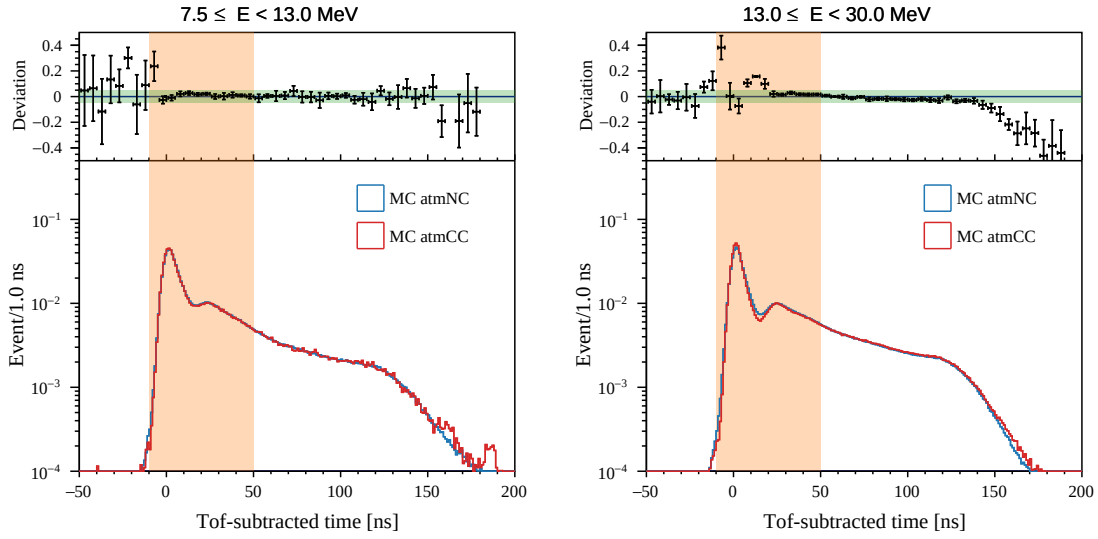

Figure 6.43: Comparison of hit timing distributions between simulated atmospheric neutrino NC and CC events. Both figures correspond to the KamNet-1 period.

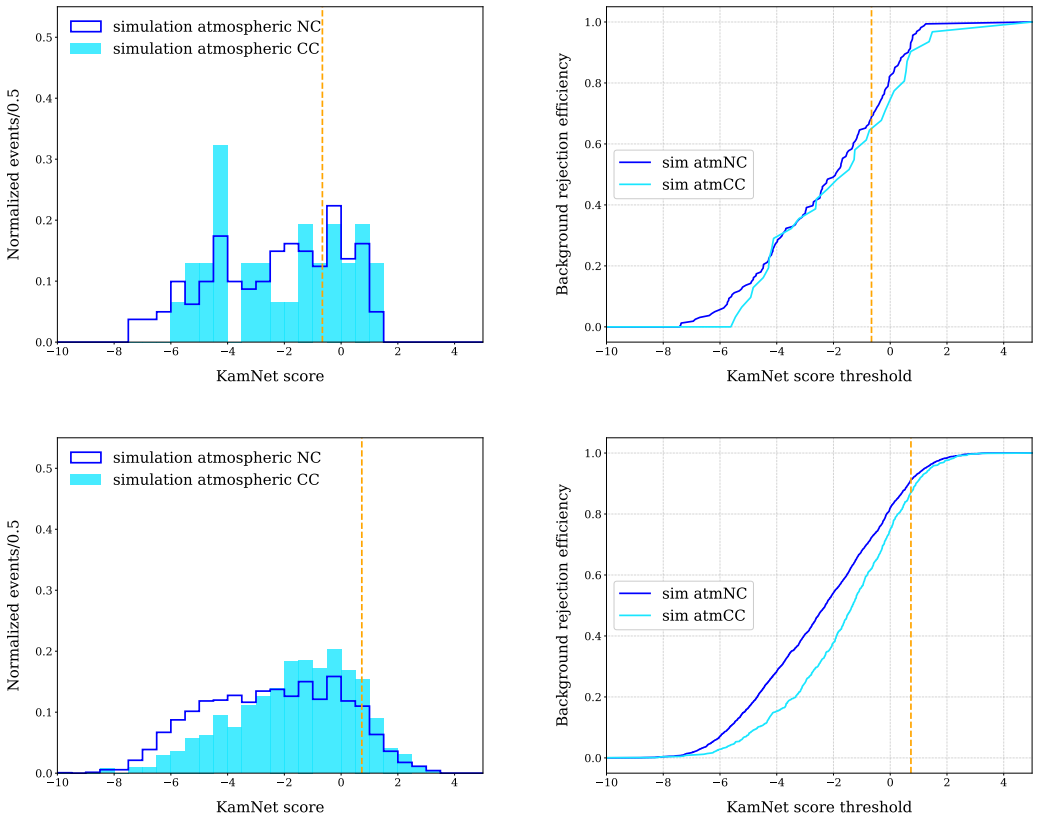

Figure 6.44: Comparisons of the KamNet score distributions and rejection efficiencies between simulated atmospheric neutrino NC and CC events. The upper panels correspond to the visible energy range of 7.5–8.5 MeV, while the lower panels correspond to that of 8.5–30 MeV. The relative efficiency differences with respect to the remaining events are 12.5% in the 7.5–8.5 MeV region and 4.6% in the 8.5–30 MeV region. The results correspond to the KamNet-1 period.

Accidental background

An accidental background refers to a pair of two uncorrelated events that are observed as a delayed-coincidence pair by chance (see Sec. 8.6). In the region with visible energy above 7.5 MeV, the prompt component of the accidental background originates from the decay of high-Q spallation events. Since these events are simple e^- or e^+-like topologies, the rejection efficiency (= 1 − signal acceptance) and its associated systematic uncertainty estimated using the signal sample can be directly applied.

6.7 Validation of the KamNet Performance

This section discusses the information used by KamNet for event classification. Throughout this section, the quantities shown represent only a subset of the information that is internally combined in a highly non-trivial way inside KamNet.

KamNet attention score

As described in Sec. 5.3.2, KamNet implements a convolutional LSTM in order to incorporate temporal correlations. An attention mechanism is integrated into the LSTM, and a weight parameter is learned for each time bin (see Eq. 5.24). This weight parameter is referred to as the *attention score*, and provides a quantity that can be visualized when discussing the separation performance of KamNet. Fig. 6.45 shows the KamNet attention score as a color scale overlaid on the hit-time distribution.

In the upper panel of Fig. 6.45, the last time bin—into which hit information after 50 ns is aggregated—exhibits a high attention score. As discussed in Sec. 6.1, the time scale of proton scattering induced by neutrons in background events shows a tail extending beyond 50 ns, suggesting that differences between signal and background should persist even at such late times. Motivated by this, an additional training is performed with the time window extended to 170 ns, as shown in the lower panel of Fig. 6.45, and the attention scores for each time bin are examined[5]. The results indicate that time bins after 50 ns are assigned attention scores comparable to those in the 10–50 ns range. This implies that there is no specific time region after 50 ns that provides uniquely strong discriminating power; rather, time bins with a similar level of importance continue. Therefore, the high attention score in the last time bin of the upper panel can be interpreted as an apparent effect caused by the aggregation of all hits after 50 ns into a single bin.

Focusing on the time bins other than the last one, the attention score is enhanced immediately after the peak of the hit-time distribution. This time range is consistent with the characteristic timescale for the propagation of particles produced in the IBD prompt signal and the associated scintillation-light emission. It is also consistent with the time at which the deviation of the hit-time distributions between signal and background changes sign from positive to negative. These facts suggest that this region corresponds to a time interval where differences in event topology and hit information between signal and background become pronounced. The high attention score in this region therefore supports the interpretation that KamNet exploits this information for event classification.

KamNet score and neutron energy

In this study, proton scattering induced by neutrons is identified as a key mechanism that produces features distinct from IBD and thereby enables event discrimination. To demonstrate whether KamNet actually exploits this feature, the relationship between the kinetic energy of the neutron produced in each atmospheric neutrino NC event and the KamNet score of that event is investigated. As shown in the upper panel of Fig. 6.46, a correlation between the neutron kinetic energy and the KamNet score is obtained. To visualize the dependence of the score distribution on the neutron energy more clearly, events are divided into two samples using 150 MeV as a boundary, and the corresponding score distributions are plotted in the lower panel of Fig.6.46. The results indicate that the KamNet score tends to decrease as the neutron kinetic energy increases. This trend can be interpreted as follows: a higher-energy neutron transfers more energy to the scattered protons and typically

[5]There is little difference in the event-discrimination performance.

undergoes more proton scatters, making the differences in hit information relative to IBD more pronounced and thus shifting the classification toward smaller scores.

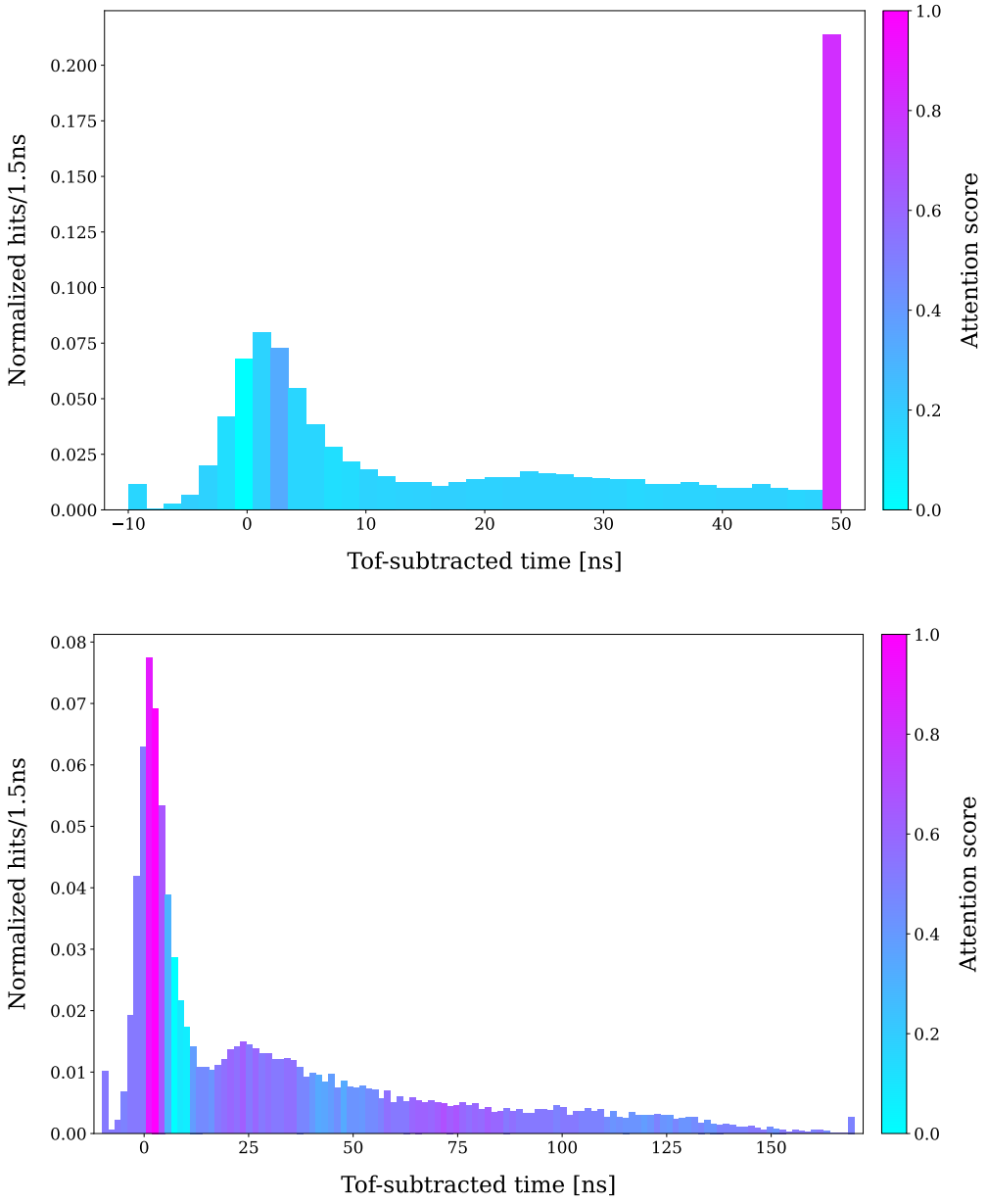

Figure 6.45: KamNet attention scores. The upper panel shows the attention scores for the hit-time distribution from −10 ns to 50 ns; hit information after 50 ns is aggregated into the last time bin. The lower panel shows the attention scores for the hit-time distribution from −10 ns to 170 ns obtained with a separate training. These plots correspond to the KamNet-period 1 model.

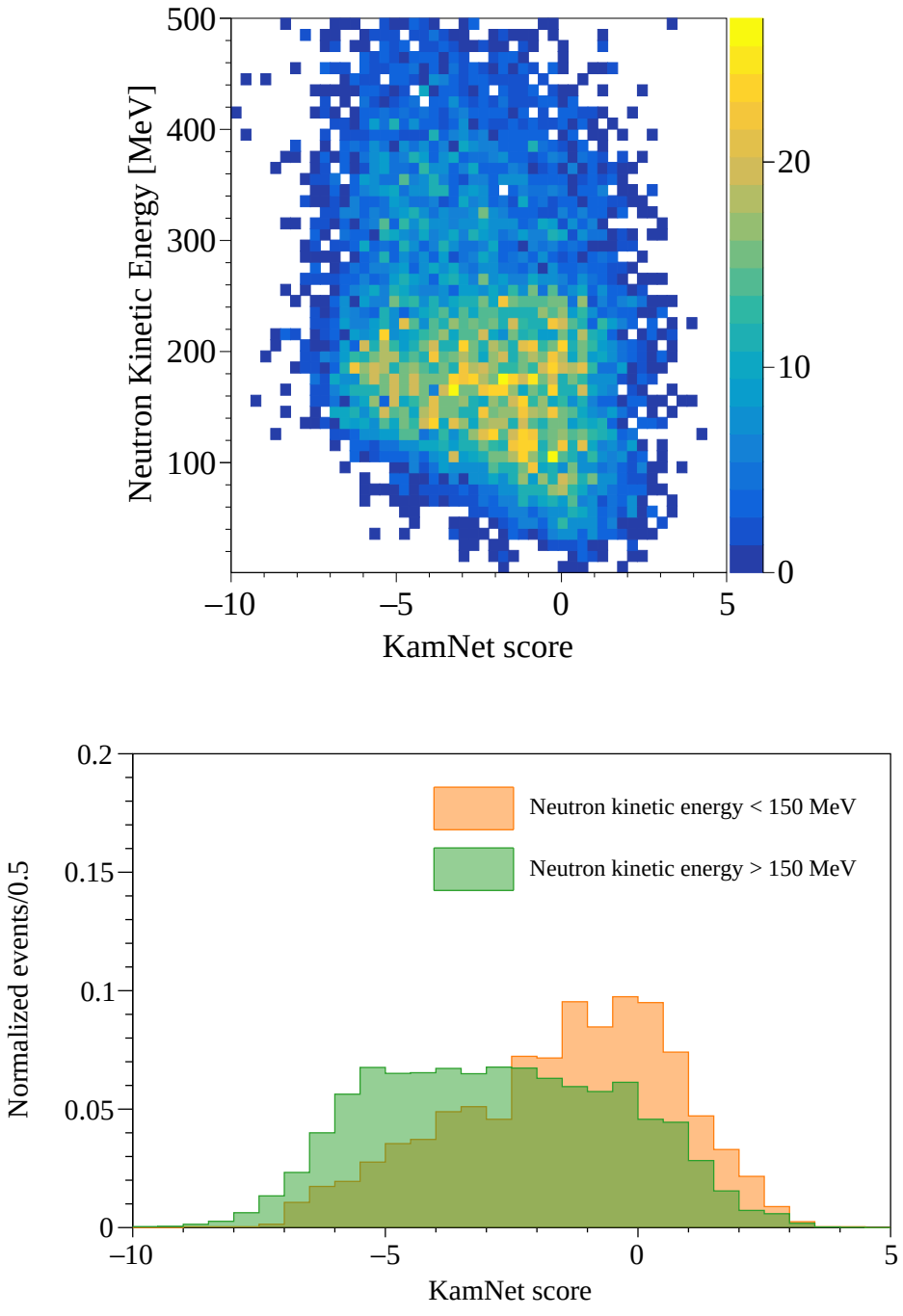

Figure 6.46: Correlation between the kinetic energy of neutrons produced in atmospheric neutrino NC interactions and the KamNet score. Upper: neutron kinetic energy versus KamNet score for individual atmospheric neutrino NC events. Lower: comparison of the KamNet-score distributions for events with neutron kinetic energy below and above 150 MeV.

Chapter 7

Antineutrino Candidates

This chapter describes the selection criteria for inverse beta decay (IBD) candidates induced by electron antineutrinos. The dataset acquired by KamLAND is divided into several subsets depending on the operational status of the KamLAND detector, and further separated into smaller periods referred to as *runs*. For each event, selection begins with basic cuts to isolate physics events, followed by cuts to remove muons and associated spallation-induced backgrounds. Subsequently, the so-called delayed coincidence techniques are applied to identify IBD events, and finally additional event selection is performed using hit information from KamNet.

7.1 Dataset for Astrophysical Antineutrino Search

7.1.1 Data Period and Run Selection

In the search for astrophysical antineutrinos, data collected during the full KamLAND operation period are used. This period spans March 9, 2002–August 8, 2024.

The data acquired by the KamLAND detector are typically separated into units called *runs,* which are defined by changes in the DAQ system and usually correspond to 24-hour periods. These runs are also terminated or restarted due to DAQ malfunctions or on-site operations at the Kamioka mine, where the detector is located. As a result, each run is categorized as follows:

- Good run
  A run during which no problems occurred. These runs are used for analysis.
- Half bad run
  A run in which problems occurred during a portion of the data-taking period. Possible causes include an increase in bad channels, an unstable high voltage applied to the PMTs, or DAQ failures in data collection. The affected periods are treated as dead time and excluded from analysis, while the remaining valid data are used.
- Bad run
  A run with an extremely short duration or one that experienced severe issues. These runs are excluded from the analysis.

7.1.2 Livetime Calculation

The livetime, which is the effective active period for antineutrino detection, is calculated by subtracting both the dead time and the veto time from run time. Dead time refers to periods during which data were either not properly recorded or are considered invalid, and is categorized as follows:

- Bad run (ref: Sec. 7.1.1)
  The data quality of this run is bad. Whole time of this run is treated as dead time.

- Half-bad run (ref: Sec. 7.1.1)
  This run partly includes bad periods, and such periods are treated as dead time.

- Trigger disable period
  During periods when the KamFEE trigger module is busy or fails to issue trigger correctly, a trigger disable flag is issued. The period which this flag is active is treated as dead time.

- Trigger dead period
  Network problems can occasionally corrupt the data packets being recorded. Such problems are identified by searching for periods in which the time difference between consecutive history trigger events exceeds 100 μs. These periods are treated as dead time.

On the other hand, veto time refers to the periods imposed by the muon veto to suppress backgrounds following muon events. The signal inefficiency induced by the shower likelihood cut (Sec. 7.5) is also treated as an effective veto time. In addition, the pedestal-collection period at the beginning of each run is classified as veto time.

The uncertainty in the dead time is evaluated using the count of 1PPS-triggered time. The 1PPS trigger is a forced trigger generated once per second in synchronization with GPS signals; therefore, the total number of such events should ideally match the run time after the veto time. The unknown dead time ratio is defined as

$$R \equiv \left| 1 - \frac{(\text{Number of 1 PPS trigger})}{(\text{run time}) - (\text{veto time})} \right|. \tag{7.1}$$

The mean value of the unknown dead time ratio is estimated to be approximately 0.012% [62].

The livetime for each run is calculated from the run time by subtracting the dead time and veto time. To accurately account for overlaps among different veto periods, a pseudo dataset consisting of uniformly distributed events in time and vertex position, which is generated via Monte Carlo simulation, is used. The livetime is defined as:

$$\text{livetime} \equiv \frac{(\text{number of events after applying all cuts})}{(\text{number of events})} \cdot (\text{run time}). \tag{7.2}$$

The cumulative livetime as a function of calendar time is shown in Fig. 7.1, while the livetime-to-runtime ratio is plotted in Fig. 7.2 and Fig. 7.3. In this work, two livetime tables are prepared: one for the prompt energy region 7.5–8.5 MeV and one for 8.5–30 MeV. This separation is adopted because the shower likelihood cut is optimized separately in the two energy regions, resulting in different signal inefficiencies. Due to the increasing number of bad channels and half bad runs in recent KamLAND data, frequent trigger disable led to an increase in dead time.

Consequently, the total livetime is calculated to be 6082.42 days and 6351.80 days for 7.5–8.5 MeV and 8.5–30 MeV, respectively.

7.2 Physics Event Selection

7.2.1 Noise Event Cut

In genuine physics events, PMT hit times are typically concentrated within a short time window. In contrast, noise originating from PMTs or electronics does not exhibit such time structure. Therefore, these noise-like events can be identified using the correlation between

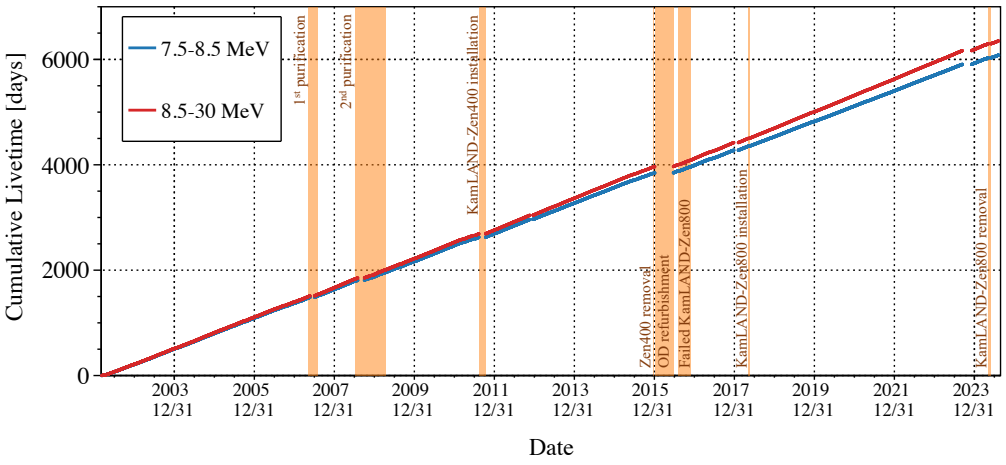

Figure 7.1: Cumulative livetime over the data-taking period. The orange-shaded regions correspond to periods with on-site work. Gaps outside these regions indicate periods excluded from the analysis due to DAQ malfunctions or degraded data quality.

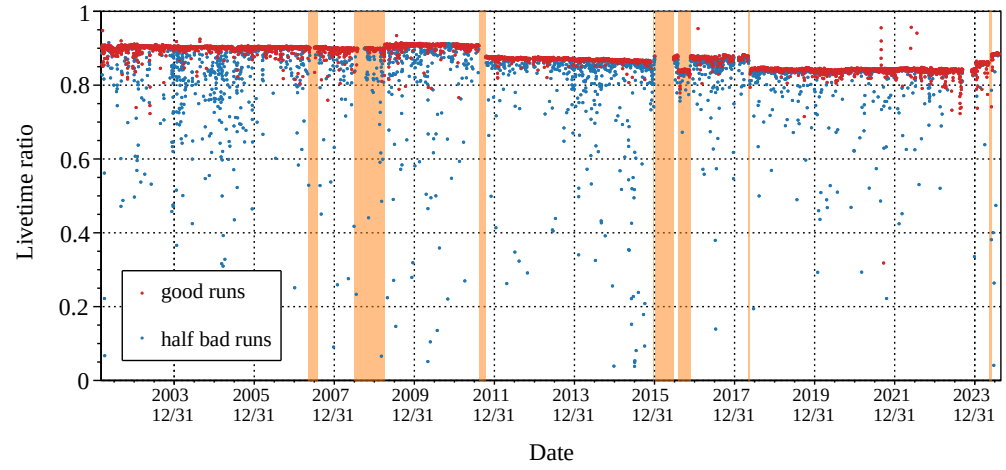

Figure 7.2: Livetime ratio to run time for 7.5–8.5 MeV

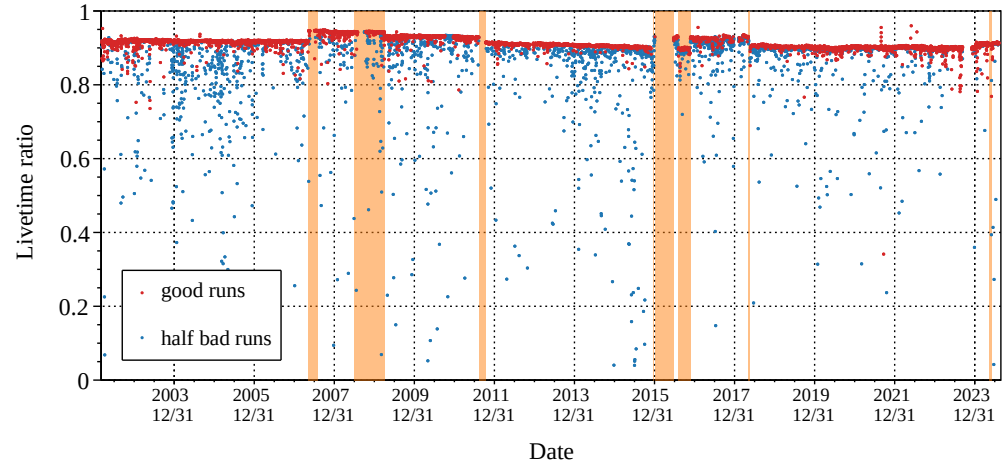

Figure 7.3: Livetime ratio to run time for 8.5–30 MeV

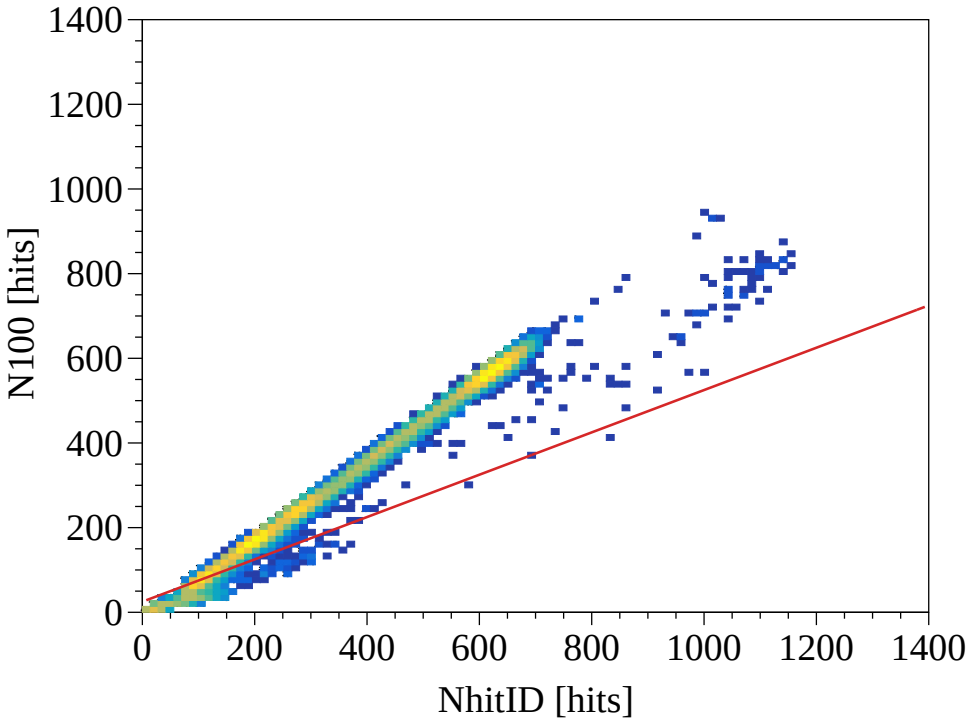

Figure 7.4: Noise event cut. The red line represents noise cut criteria shown in Eq. 7.3.

the number of PMT hits and their timing, as defined by the following criteria.

$$N_{100} \leq \frac{N_{\text{hit}} + 50}{2} \tag{7.3}$$

where N_{100} represents the number of PMT hits within the 100 ns window that contains the highest concentration of hits, while N_{hit} denotes the total number of hits recorded by the 17-inch PMTs and the 20-inch PMTs in the event. Fig. 7.4 illustrates the selection of noise events based on Eq. 7.3.

The inefficiency of the noise event cut is evaluated using calibration data from Co-Ge and Co-Ge-Cs composite sources, and is estimated to be less than $\mathcal{O}(10^{-2})\%$. In this analysis, such inefficiency for low-energy events is considered negligible.

7.2.2 Flasher Event Cut

Flasher events are caused by light emission from a PMT due to discharge in its own dynode. these events are misidentified as high-energy events, typically around 20 MeV. Since the light is predominantly observed near the PMT that caused the discharge, the presence of a single PMT with an unusually large charge is used as a key discriminant. The selection criteria for flasher events are as follows:

- (Total charge observed in the inner detector, Q_{ID}) $\geq$ 2500 p.e.
- (Maximum charge recorded by a single PMT)/$Q_{\text{ID}} \geq 0.6$
- (Average charge among PMTs neighboring the flasher PMT) $\geq$ 20 p.e.
- The event is neither a noise event nor a muon event

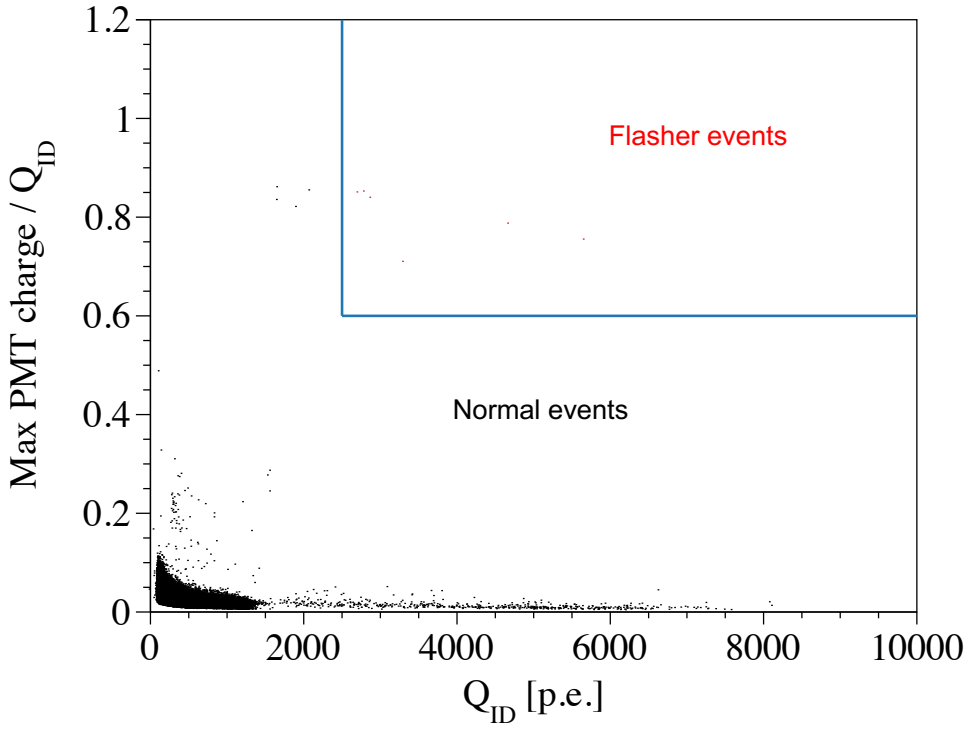

Figure 7.5: Flasher event profile. Blue lines represent selection criteria of flasher events.

Fig. 7.5 shows the example of flasher event profile with the above criteria. The flasher event rate is estimated to be 2.9×10^{-3} Hz before purification and 1.2×10^{-3} Hz after purification. These correspond to approximately 8×10^{-3}% and 9×10^{-3}% of the total low-energy events, respectively. These are well below other sources of systematic uncertainty and thus considered negligible.

7.2.3 Ringing Event Cut

After the KamFEE upgrade in 2003, spurious muon-like events began to appear following true muon events. These events are referred to as *ringing events*, and are believed to result from baseline fluctuations in KamFEE induced by muons. Ringing events are removed based on the time difference from the preceding muon event (ΔT_{muon}) and the total number of PMT hits in the ID (N_{hit}), using the following selection criteria: $\Delta T_{\mathrm{muon}} < 1\,[\mu\mathrm{s}]$ and $N_{\mathrm{hit}} > 600$.

7.3 Muon and Spallation Event Veto

When cosmic-ray muons induce spallation of carbon nuclei in the LS, unstable isotopes are produced, and their subsequent decays can mimic IBD events. Tab 7.1 shows the major carbon spallation isotopes in KamLAND. After muon events with high light yield, signal waveforms is distorted, making accurate event detection difficult. Therefore, before applying energy, timing, and spatial cuts to select IBD events, muon events (described in Sec. 4.6) and associated spallation events described below must be removed.

The veto conditions following muon events are determined based on the charge observed by the 17-inch PMTs (Q_{17}), the residual charge (ΔQ), and the muon track reconstruction quality. Events with large residual charge are likely to be accompanied by many spallation products, and thus the entire detector volume is excluded from analysis. For well-reconstructed muons, a *shower likelihood cut* (see Sec. 7.5) based on spatiotemporal correlation between the muon and spallation products is applied. The muon-related veto criteria are as follows:

- Low-energy muon events ($Q_{17} < 40,000$ p.e.)
  Whole volume veto for 2 ms
- High-energy muon events ($Q_{17} > 40,0000$ p.e.)
  - Bad reconstructed muons
    Whole volume veto for 2 ms
  - Well-reconstructed muons with small residual charge ($\Delta Q < 7.5 \times 10^5$ p.e.)
    Shower likelihood cut
  - Muons with large residual charge ($\Delta Q \geq 7.5 \times 10^5$ p.e.)
    Whole volume veto for 2 s

Table 7.1: Spallation products in KamLAND. Production rates are taken from [79], while those for ^{6}He and ^{7}Be are based on [80].

Isotope	Lifetime	Q value [MeV]	Mode	Production rate [event/day/kt]
^{12}B	29.1 ms	13.4	β^-	58.7±2.5
^{12}N	15.9 ms	17.3	β^+	2.1±0.4
^{8}Li	1.21 s	16.0	$\beta^-\alpha$	27.3±0.8
^{8}B	1.11 s	18.0	$\beta^+\alpha$	<4.7
^{9}C	182.5 ms	16.5	β^+	7.4±2.9
^{8}He/^{9}Li	171.7/257.2 ms	10.7/13.6	$\beta^-\gamma\, n$	2.7±0.8
^{11}C	29.4 ms	1.98	β^+	1093±176
^{10}C	27.8 s	3.65	$\beta^+\gamma$	21.6±2.7
^{11}Be	19.9 s	11.5	β^-	<2.2
^{6}He	1.16 s	3.51	β^-	19
^{7}Be	76.9 d	0.478	EC, γ	231

7.4 Delayed Coincidence Selection

IBD events are identified using the delayed coincidence method. This section provides a detailed description of the selection criteria for the prompt and delayed events, as well as the selections applied to their time and spatial correlations.

Prompt event selection

The prompt event consists of the kinetic energy of the positron and the two annihilation gamma rays. In this study, the energy range of the prompt event is set to

$$7.5 \leq E_p\,[\mathrm{MeV}] \leq 30,$$

which is suitable for the DSNB search, and covers the so-called *golden window*—the energy region between the dominant fluxes of reactor and atmospheric neutrinos. This energy window is also useful for detecting other astrophysical antineutrinos.

In KamLAND, the event rate increases near the 650 cm-radius balloon. This is primarily due to gamma rays from radioactive isotopes such as ^{40}K and ^{208}Tl, originating from materials such as the balloon film, its supporting ropes, the glass of the PMTs, and the surrounding rock. To suppress these external radiation backgrounds, the fiducial radius for prompt events is defined as

$$R_p \leq 550\,[\mathrm{cm}]$$

from the detector center in this analysis.

Delayed event selection

The selection criteria for the delayed event energy are defined as follows:

$$1.8 \leq E_d\,[\mathrm{MeV}] \leq 2.6$$

$$4.4 \leq E_d\,[\mathrm{MeV}] \leq 5.6$$

Delayed events originate from gamma rays emitted by neutron captures on protons or carbon nuclei. The majority of these captures occur on protons, producing a 2.2 MeV gamma ray. Captures on carbon nuclei occur at a rate of approximately 0.5%, emitting a 4.9 MeV gamma ray.

The selection windows for E_d are determined by taking into account the energy resolution of the detector. The selection efficiencies for each window, $\epsilon_{E_d,\,\mathrm{proton}}$ and $\epsilon_{E_d,\,\mathrm{carbon}}$, are estimated from the following formulas:

$$\epsilon_{E_d,\,\mathrm{proton}} = \int_{1.8\,\mathrm{MeV}}^{2.6\,\mathrm{MeV}} \frac{1}{\sqrt{2\pi}\sigma} \exp\left(-\frac{(x-2.211)^2}{2\sigma^2}\right) dx \tag{7.4}$$

$$\epsilon_{E_d,\,\mathrm{carbon}} = \int_{4.4\,\mathrm{MeV}}^{5.6\,\mathrm{MeV}} \frac{1}{\sqrt{2\pi}\sigma} \exp\left(-\frac{(x-5.061)^2}{2\sigma^2}\right) dx, \tag{7.5}$$

where, σ represents the energy resolution of the detector. The constants 2.211 and 5.061 (in units of MeV) correspond to the observed energies of the 2.2 MeV and 4.9 MeV gamma rays from neutron capture on protons and carbon, respectively. Tab. 7.2 summarizes the energy resolution values before and after purification, along with the selection efficiencies in the E_d windows estimated using Eq. 7.4 and Eq. 7.5.

Table 7.2: Delayed energy selection efficiency

Period	Parameter	17-inch	20-inch
before purification	$\sigma\,[\%/\sqrt{E\,[\mathrm{MeV}]}]$	7.0±0.1	6.1±0.1
	$\epsilon_{E_d,\,\mathrm{proton}}$	99.99%	100%
	$\epsilon_{E_d,\,\mathrm{carbon}}$	100%	100%
after purification	$\sigma\,[\%/\sqrt{E\,[\mathrm{MeV}]}]$	8.2±0.1	7.0±0.1
	$\epsilon_{E_d,\,\mathrm{proton}}$	99.98%	99.99%
	$\epsilon_{E_d,\,\mathrm{carbon}}$	99.99%	100%

As with prompt events, the fiducial radius for delayed events is set as

$$R_d \leq 550\,[\mathrm{cm}]$$

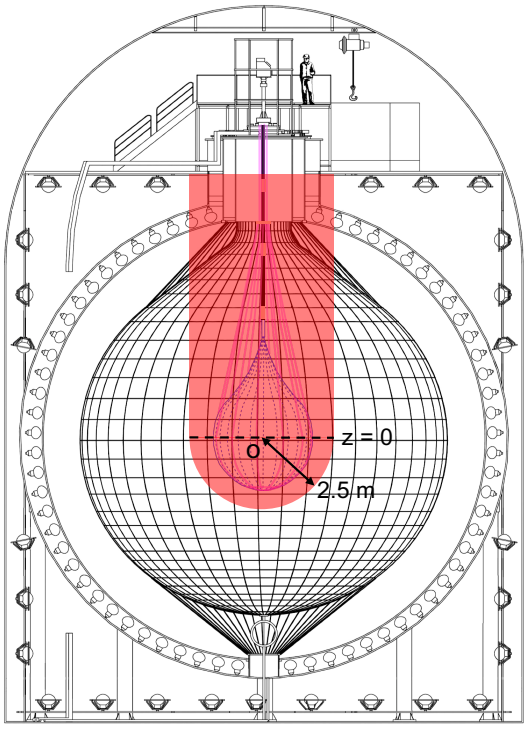

Figure 7.6: Schematic view of Zen volume cut. The red shaded region is excluded from this analysis.

from the detector center to reduce background events originating from external sources. During the KamLAND-Zen experiment, a miniballoon is suspended at the detector center, introducing additional background events associated with the balloon material. To suppress this contribution, the following regions are further excluded from the analysis during periods when the miniballoon is installed:

- $R_d < 250\,\mathrm{cm}$
- $\rho_d < 250\,\mathrm{cm}$ for $Z_d > 0$

Here, ρ_d is defined as $\sqrt{X_d^2 + Y_d^2}$, where $(X_d,\ Y_d,\ Z_d)$ are the coordinates of the delayed event vertex with respect to the detector center. A schematic illustration of the miniballoon cut is shown in Fig. 7.6.

Space correlation

The distance between the prompt and delayed events depends on the diffusion and capture processes of thermalized neutrons, as well as the vertex resolution. To sufficiently follow these characteristics, a cut for spacial correlation is applied as:

$$\Delta R \leq 160\,[\mathrm{cm}]$$

The selection efficiency for this cut is estimated using calibration data by AmBe composite source, which emits both a 4.4 MeV gamma ray and a neutron—allowing for clear identification via delayed coincidence. Fig. 7.7 shows delayed coincidence events obtained during a source calibration performed in August 2003, with the AmBe source placed at the center of the detector. The selection conditions applied in this analysis are: $E_p = 4{-}6\,\mathrm{MeV}$,

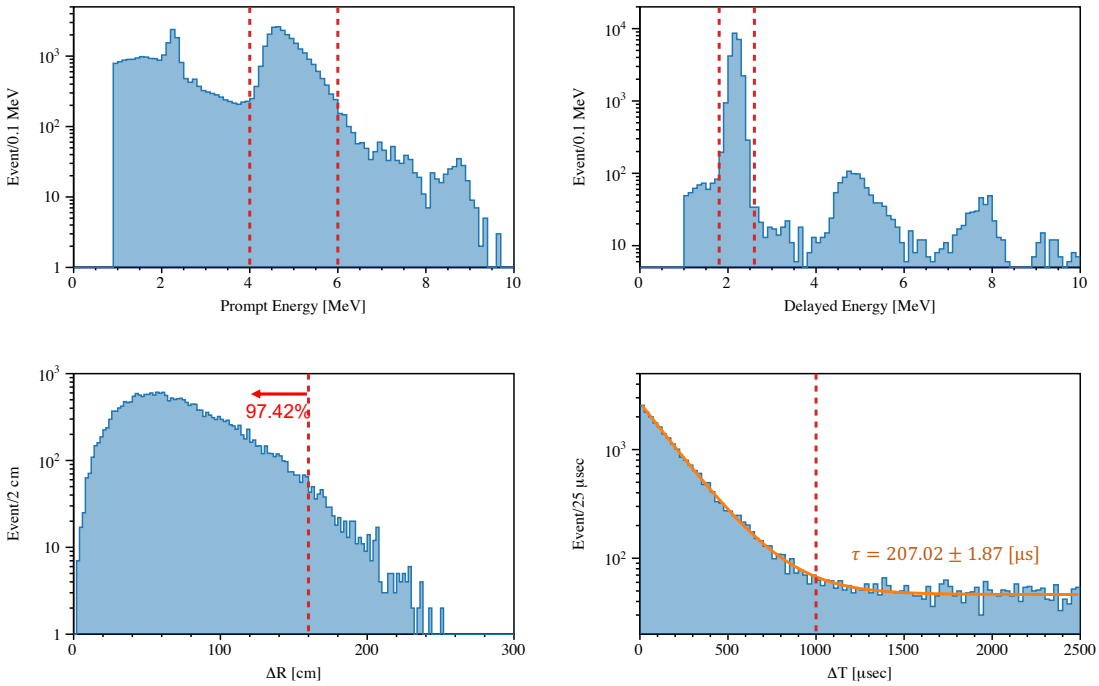

Figure 7.7: Delayed coincidence event of AmBe source calibration run. The source is placed at the center of the KamLAND detector. Each panel shows the following distributions: prompt energy spectrum (upper left), delayed energy spectrum (upper right), space correlation (lower left), and time correlation (lower right). Vertical red dashed lines indicate the applied cut conditions. The two peaks observed in the prompt energy spectrum correspond to neutron capture on proton (2.2 MeV) and γ-ray emission form excited ^{12}C (4.4 MeV), characteristic of the AmBe source. Some of the peaks in the delayed energy spectrum arise from accidental coincidences between the 4.4 MeV γ-ray and γ-rays from neutron capture on ^{12}C.

$E_d = 1.8{-}2.6\,\mathrm{MeV}$, and a time difference between prompt event and delayed event $\Delta T < 1000\,\mu\mathrm{s}$. Fitting the ΔT distribution gives a mean neutron capture time of $207\,\mu\mathrm{s}$, consistent with the expected value. Based on this dataset, the selection efficiency within a spatial correlation of $\Delta R < 160\,\mathrm{cm}$ is estimated to be 97.42%.

Time correlation

The selection criteria based on the time correlation between the prompt and delayed events are set to span a significantly longer time window than the mean neutron capture time. Additionally, to avoid contamination from electronics noise immediately following the prompt event, delayed events occurring within this short time window ($0.5\,\mu\mathrm{s}$) are excluded from the analysis. The time difference between prompt and delayed events is required to satisfy

$$0.5 < \Delta T\,[\mu\mathrm{s}] < 1000$$

The selection efficiency for delayed coincidence events under this condition, $\epsilon_{\Delta T}$, is estimated by fitting the ΔT distribution between muon events and subsequent spallation-induced neutron capture events, as shown in Fig. 7.8, for both before and after purification. Neutron capture events are selected based on NsumMax, which is the number of KamFEE channel which detects PMT hit, using the following criteria:

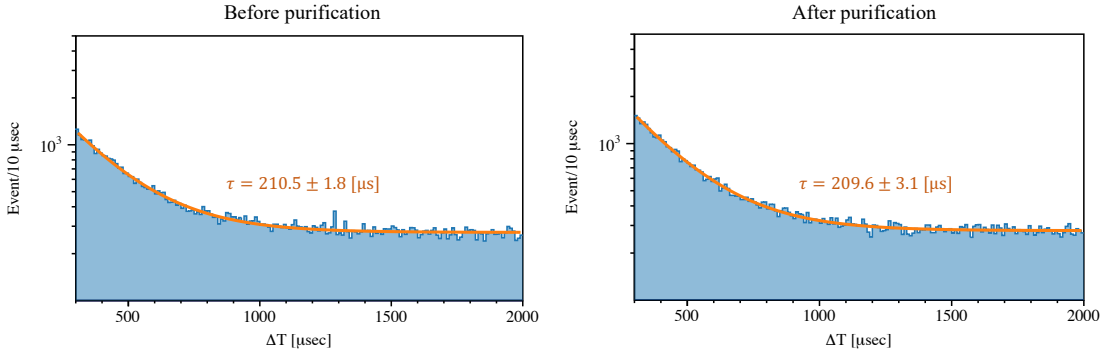

Figure 7.8: Time difference between a muon event and a subsequent neutron capture event induced by spallation. The left panel shows time differences before purification, and the right panel corresponds to those after purification. The orange curves represent the fit functions.

- before purification: $350 < \text{NsumMax} < 550$
- after purification: $300 < \text{NsumMax} < 450$

The mean neutron capture times obtained from the fits are $210.5 \pm 1.8\,\mu$s (before purification) and $209.6 \pm 3.1\mu$s (after purification). Using these values, the selection efficiency for the ΔT cut is calculated as

$$\begin{aligned} \epsilon_{\Delta T} &= \frac{1}{\tau}\int_{0.5\,\mu\text{s}}^{1000\,\mu\text{s}} \exp\left(-\frac{t}{\tau}\right) dt \\ &= 98.90 \pm 0.03\% \quad \text{(before purification)} \\ &= 98.91 \pm 0.06\% \quad \text{(after purification).} \end{aligned} \tag{7.6}$$

Multiple coincidence cut

In IBD events, one prompt event is expected to be associated with one delayed event. However, in rare cases, delayed coincidence selects events in which multiple delayed (or prompt) events correspond to a single prompt (or delayed) event.

For example, multiple delayed events may occur when a muon produced by an atmospheric neutrino interaction serves as the prompt event, and both a neutron capture event and a Michel electron (from muon decay with a mean lifetime of $2.2\,\mu$s) are detected as delayed events. Conversely, multiple prompt events may arise when a fast neutron undergoes multiple scatterings with protons before thermalizing and being captured. Such non-one-to-one coincidence are not considered to be true $\bar{\nu}_e$-induced IBD events and are excluded from this analysis.

7.5 Likelihood Cut for Spallation Events

When a cosmic-ray muon induces nuclear spallation, a correlation with the spallation products can be established for well-reconstructed muon events. This correlation can be quantified using the muon's energy loss along its track dE/dx, the distance dL between the muon track and the spallation event, and the time difference dT_μ between the muon and the spallation event. By combining the probability density functions (PDFs) of these parameters, we construct a likelihood for identifying spallation events; in this work, the corresponding rejection technique is referred to as the *shower likelihood cut*. The data periods used to construct the shower likelihood are categorized according to the scintillation properties of the LS and the detector's fiducial volume, as summarized in Tab. 7.3.

In the observation of $\bar{\nu}_e$s, the dominant spallation background arises from the $\beta + n$ decay of ^{9}Li. In this study, we assume that dE/dx and dL exhibit common features independent of the specific spallation isotope, and we construct a ^{9}Li-specific PDF only for dT_μ. By combining these components, we develop a shower likelihood cut to reject ^{9}Li events originating from muon-induced spallation.

Table 7.3: Definition of data periods for shower likelihood cut

Shower-period	Date	Run	Detector status
Shower-1	Mar. 9th, 2002– May 12th, 2007	run000220– run006801	before purification
Shower-2	May 12th, 2007– Apr. 7th, 2009	run006802– run008501	during purification
Shower-3	Apr. 7th, 2009– Oct. 12th, 2011	run008502– run010773	after purification
Shower-4	Oct. 12th, 2011– Dec. 15th, 2015	run011000– run013414	KamLAND-Zen 400
Shower-5	Dec. 15th, 2015– Aug. 2nd, 2016	run013415– run013785	after OD refurbishment
	Nov. 22nd, 2016– May 9th, 2018	run013963– run014990	after failed Zen400
	May 31st, 2024– Aug. 8th, 2024	run018928– run019046	after Zen800
Shower-6	Aug. 3rd, 2016– Nov. 22nd, 2016	run013786– run013962	failed Zen800
	May 19th, 2018– may 7th, 2024	run014991– run018927	KamLAND-Zen 800

7.5.1 Construction of the Shower Likelihood Function

Likelihood function for dE/dx and dL

Under the assumption that the correlations between muons and spallation products in dE/dx and dL do not depend on the isotope, the likelihood function is constructed using spallation ^{12}B β-decay events, which have the largest statistics in KamLAND. The selection criteria for ^{12}B events are as follows:

- Fiducial volume: $r < 600\,\mathrm{cm}$

During the KamLAND-Zen experimental periods, events in the miniballoon region are excluded.

- Visible energy: $E_{\mathrm{vis}} = 4$–$20\,\mathrm{MeV}$
- Time difference from the preceding muon

  ontime: $dT_\mu = 5$–$7\tau_{^{12}\mathrm{B}}$ ($\tau_{^{12}\mathrm{B}} = 29.1\,\mathrm{ms}$)

  offtime: $dT_\mu = 200$–$1000\,\mathrm{s}$

In the ontime selection, the time window is set to approximately seven times the mean lifetime of ^{12}B to ensure sufficient statistics of ^{12}B events. This condition allows for the collection of about 82% of all ^{12}B spallation events [81].

Fig. 7.9 (a) and (b) show the two-dimensional PDFs of dE/dx and dL constructed using the selected ^{12}B events. The ontime PDF contains a large fraction of spallation events, showing that dE/dx tends to be larger when the distance dL from the muon track is smaller. In contrast, the offtime PDF includes mainly accidental events, exhibiting no spatial correlation with the muon track. Furthermore, the overall dE/dx values are higher for spallation events than for accidental ones.

In this analysis, the likelihood function for spallation events is defined as the ratio of the spallation PDF, $f_{\mathrm{spallation}}(\vec{x})$, to the accidental PDF, $f_{\mathrm{accidental}}(\vec{x})$, as given in the following equation:

$$\mathcal{L}(\vec{x}) = \frac{f_{\mathrm{spallation}}(\vec{x})}{f_{\mathrm{accidental}}(\vec{x})}, \tag{7.7}$$

where $\vec{x}$ represents the parameters used in the likelihood function—dE/dx, dL, and dT_μ in this analysis. Using Eq. 7.7, the two-dimensional PDF of dE/dx and dL for spallation events is obtained by subtracting the contribution of the offtime PDF from the ontime PDF as follows:

$$\mathcal{L}_{\mathrm{withoutdT}}\left(\frac{dE}{dx}, dL\right) = \frac{f_{\mathrm{ontime}}(dE/dx, dL) - f_{\mathrm{offtime}}(dE/dx, dL)}{f_{\mathrm{offtime}}(dE/dx, dL)}. \tag{7.8}$$

An example of the resulting two-dimensional spallation likelihood function in dE/dx and dL is shown in Fig. 7.9 (c).

Likelihood function for dT_μ

The likelihood function for the time difference dT_μ between a muon event and a spallation event is defined as the ratio of the spallation PDF, $f_{\mathrm{spallation}}(dT_\mu)$, to the accidental PDF, $f_{\mathrm{accidental}}(dT_\mu)$. The spallation component $f_{\mathrm{spallation}}$ can be expressed based on the decay lifetimes and production fractions of ^{9}Li and ^{8}He, which constitute the spallation background in the $\bar{\nu}_e$ search, as follows:

$$f_{\mathrm{spallation}}(dT_\mu) = \frac{r_{^8\mathrm{He}}}{\tau_{^8\mathrm{He}}} \exp\left(-\frac{dT_\mu}{\tau_{^8\mathrm{He}}}\right) + \frac{r_{^9\mathrm{Li}}}{\tau_{^9\mathrm{Li}}} \exp\left(-\frac{dT_\mu}{\tau_{^9\mathrm{Li}}}\right) \tag{7.9}$$

Here, r_x denote the production fraction ($r_{^9\mathrm{Li}} = 0.935$, $r_{^8\mathrm{He}} = 0.065$), and τ_x represents the decay lifetime ($\tau_{^9\mathrm{Li}} = 257.2\,\mathrm{ms}$, $\tau_{^8\mathrm{He}} = 171.7\,\mathrm{ms}$). On the other hand, since the accidental component $f_{\mathrm{accidental}}$ has no time structure, it is expressed as

$$f_{\mathrm{accidental}}(dT_\mu) = const. \tag{7.10}$$

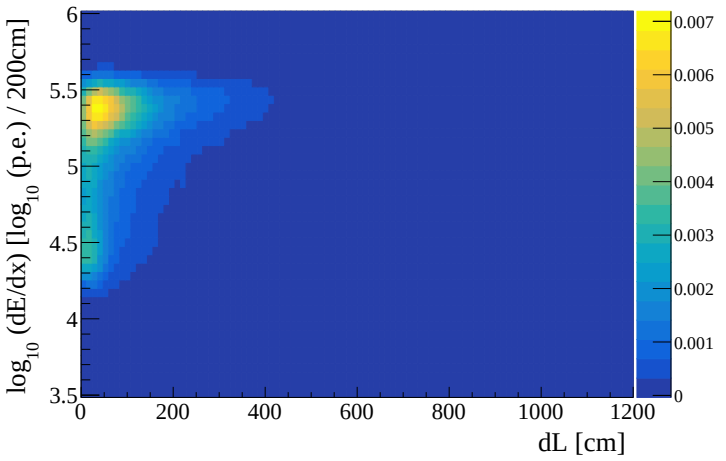

(a) 2D PDF of ontime events

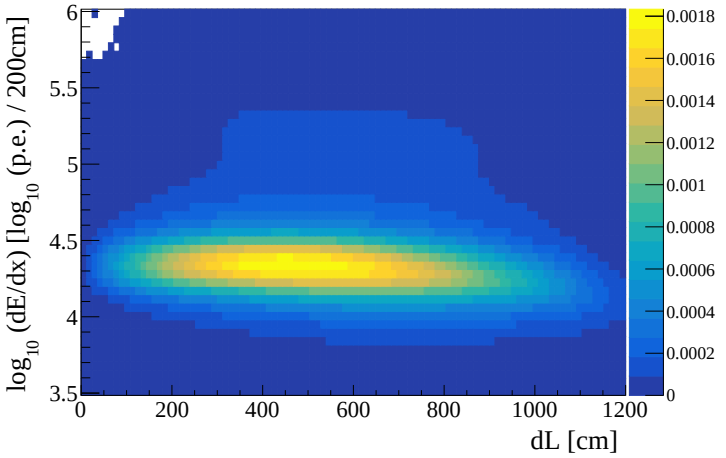

(b) 2D PDF of offtime events

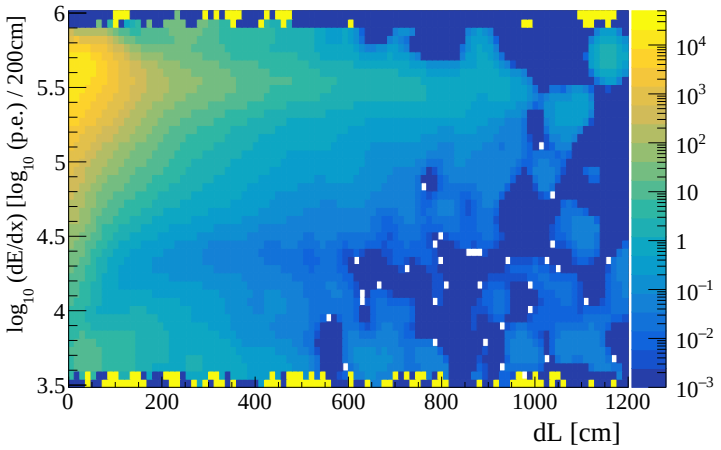

(c) 2D likelihood function of spallation events

Figure 7.9: Probability density functions and likelihood function of spallation events. Figures correspond to the Shower-1 period.

Accordingly, the spallation likelihood as a function of dT_μ can be written using Eq. 7.9 and 7.10 as

$$\mathcal{L}(dT_\mu) = \frac{r_{^8\mathrm{He}}}{\tau_{^8\mathrm{He}}} \exp\left(-\frac{dT_\mu}{\tau_{^8\mathrm{He}}}\right) + \frac{r_{^9\mathrm{Li}}}{\tau_{^9\mathrm{Li}}} \exp\left(-\frac{dT_\mu}{\tau_{^9\mathrm{Li}}}\right). \tag{7.11}$$

Shower likelihood function

By combining $\mathcal{L}_{\mathrm{withoutdT}}(dE/dx, dL)$ and $\mathcal{L}(dT_\mu)$, the likelihood function for spallation events, referred to as the shower likelihood function, can be expressed as follows:

$$\mathcal{L}_{\mathrm{withdT}}\left(\frac{dE}{dx}, dL, dT_\mu\right) = \mathcal{L}_{\mathrm{withoutdT}}\left(\frac{dE}{dx}, dL\right) \mathcal{L}(dT_\mu). \tag{7.12}$$

7.5.2 Cut Threshold and Rejection Efficiency

The threshold of the shower likelihood cut is determined based on the likelihood distribution $\mathcal{L}_{\mathrm{withdT}}$ for spallation events. Therefore, spallation events are first selected, and the shower likelihood is calculated for each events to construct the distribution of $\mathcal{L}_{\mathrm{withdT}}$. The selection criteria for the spallation events used to create this distribution are as follows:

- Fiducial volume: $r < 600\,\mathrm{cm}$

  During the KamLAND-Zen experimental periods, events in the miniballoon region are excluded.

- Visible energy: $E_{\mathrm{vis}} = 4$–$20\,\mathrm{MeV}$

- Rejection of low-energy muon events: $Q_{17} < 40,000\,\mathrm{p.e.}$

- Time difference from the preceding muon

  ontime: $dT_\mu = 5$–$60\,\mathrm{ms}$

  offtime: $dT_\mu = 505$–$560\,\mathrm{ms}$

Fig. 7.10 shows the distribution of the spallation likelihood $\mathcal{L}_{\mathrm{withdT}}$ constructed using the spallation events that satisfy the above selection criteria.

In the energy region of the astrophysical $\bar{\nu}_e$ search (7.5–30 MeV), the contribution from reactor $\bar{\nu}_e$ disappears above 8.5 MeV. Therefore, the shower likelihood cut threshold is determined separately for two energy ranges: 7.5–8.5 MeV, where reactor $\bar{\nu}_e$ are present, and 8.5–15 MeV, which covers the upper range dominated by spallation events. For the 15–30 MeV region, the same threshold as that obtained for 8.5–15 MeV is applied. The thresholds, spallation rejection efficiencies, and signal inefficiencies for each shower period are summarized in Tab. 7.4 and 7.5.

7.5.3 Systematic Uncertainty from the Shower Likelihood Cut

In the antineutrino analysis, the spallation products to be removed are ^{9}Li and ^{8}He. Therefore, a difference is expected between the rejection efficiency estimated using ^{12}B, as described above, and that for ^{9}Li/^{8}He, due to the difference in isotopes. In this section, ^{9}Li/^{8}He events are selected using the delayed coincidence, and the spallation cut inefficiency for these events is compared with that for ^{12}B in order to estimate the systematic uncertainty associated with the shower tag.

The selection criteria for ^{9}Li/^{8}He are as follows:

- Delayed-coincidence selection

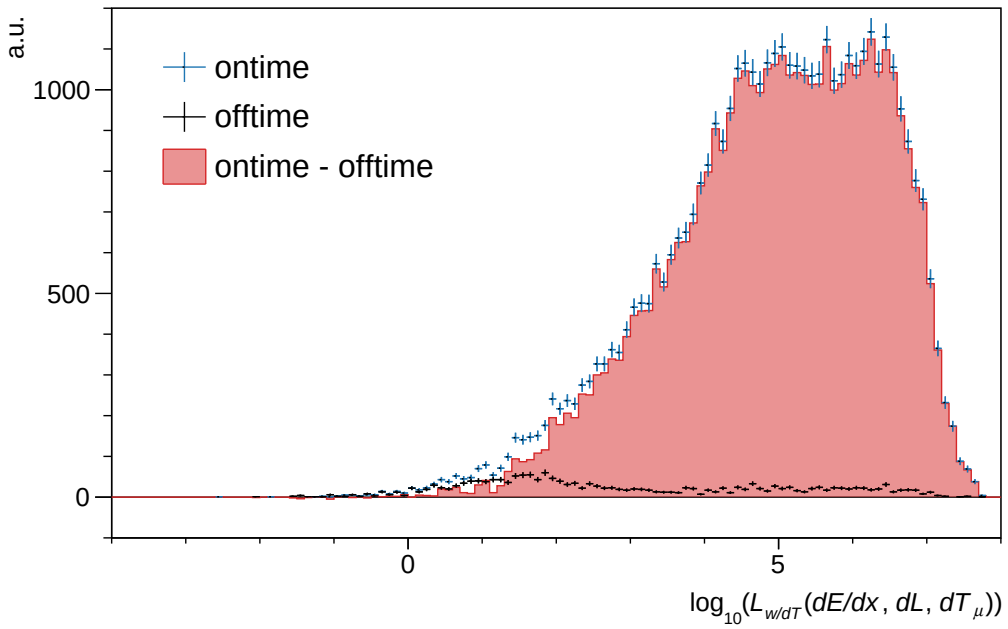

Figure 7.10: Distribution of the shower likelihood function with the dT likelihood. This figure corresponds to the Shower-1 period.

Table 7.4: Summary of the shower likelihood cut ($E_{\rm vis}$ =7.5–8.5 MeV)

Shower-period	Threshold $\mathcal{L}_{\rm th}$	Spallation rejection efficiency	Signal inefficiency
Shower-1	1.2	0.996	0.097
Shower-2	1.3	0.993	0.102
Shower-3	1.4	0.992	0.092
Shower-4	1.0	0.997	0.134
Shower-5	1.2	0.996	0.122
Shower-6	0.9	0.997	0.156

Table 7.5: Summary of the shower likelihood cut ($E_{\rm vis}$ =8.5–15 MeV)

Shower-period	Threshold $\mathcal{L}_{\rm th}$	Spallation rejection efficiency	Signal inefficiency
Shower-1	1.5	0.991	0.075
Shower-2	1.9	0.981	0.060
Shower-3	1.8	0.986	0.066
Shower-4	1.7	0.986	0.085
Shower-5	2.1	0.976	0.073
Shower-6	1.6	0.989	0.097

- Fiducial volume: $R_p < 600\,\mathrm{cm}$ and $R_d < 600\,\mathrm{cm}$

  During the KamLAND-Zen experimental periods, events in the miniballoon region are excluded.

- Prompt energy: $E_p = 4$–$20\,\mathrm{MeV}$

- Rejection of low-energy muon events: $Q_{17} < 40,000\,\mathrm{p.e.}$

- Time difference from the preceding muon

  ontime: $dT_\mu = 0.002$–$1\,\mathrm{s}$

  offtime: $dT_\mu = 10.002$–$11\,\mathrm{s}$

Fig. 7.11 shows the distribution of the shower likelihood function for the ^{9}Li/^{8}He sample. The spallation cut inefficiency for ^{9}Li/^{8}He is evaluated at the threshold $\mathcal{L}_{\mathrm{th}}$ determined from the ^{12}B sample. Fig. 7.12 and Fig. 7.13 compare the spallation cut inefficiencies for ^{12}B and ^{9}Li/^{8}He. The error bars represent the statistical uncertainties arising from the ontime and offtime shower-likelihood distributions. The spallation cut inefficiency for ^{9}Li/^{8}He can become negative because the statistics are limited, and any small imbalance in the offtime component can result in a negative bin content after histogram subtraction.

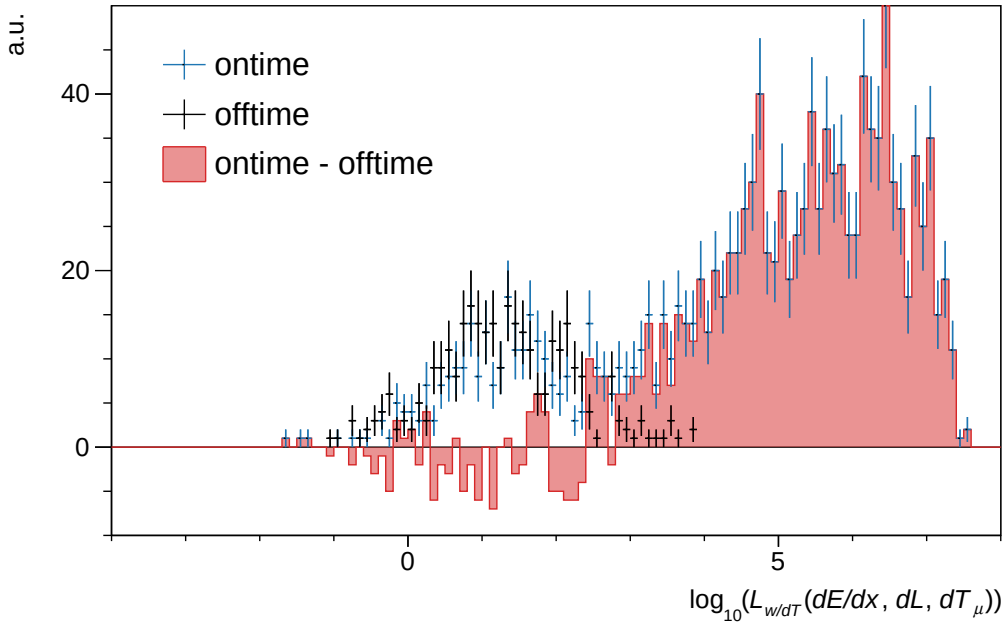

Figure 7.11: Distribution of the shower likelihood function obtained from the delayed coincidence selection. This figure corresponds to the Shower-1 period.

The systematic uncertainty associated with the shower likelihood cut is defined as the relative difference between the ^{12}B and ^{9}Li/^{8}He spallation cut inefficiencies, normalized to the ^{12}B inefficiency. The resulting estimate is summarized in Tab. 7.6 and Tab. 7.7.

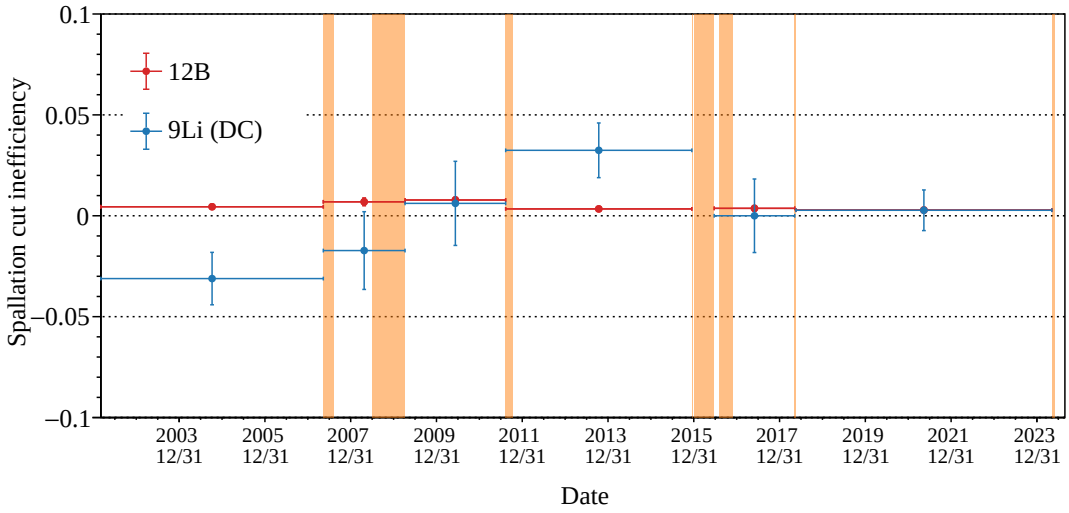

Figure 7.12: Spallation cut inefficiencies for ^{12}B and ^{9}Li (7.5–8.5 MeV). Each point corresponds to the result from an individual shower period. The orange-shaded region indicates periods during which on-site work was conducted.

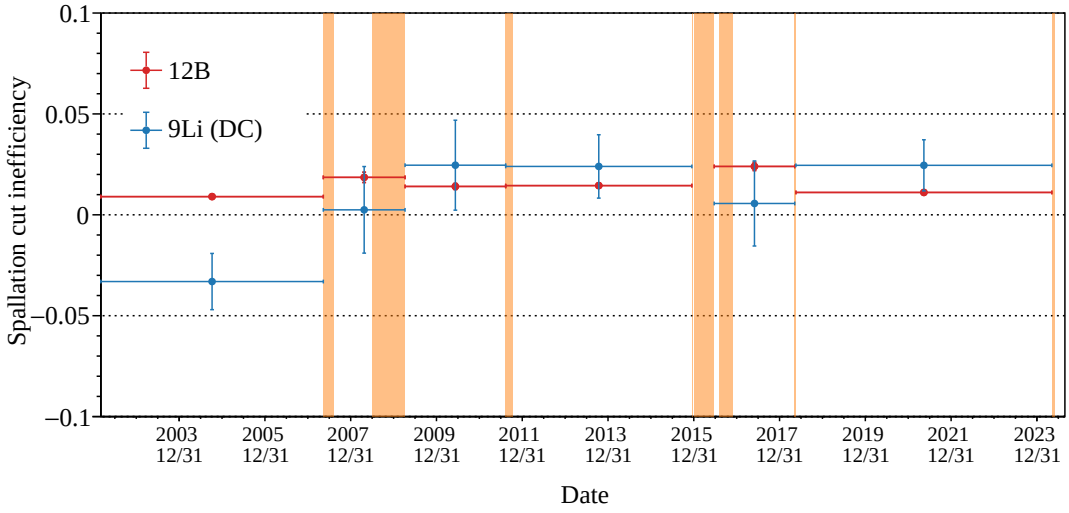

Figure 7.13: Spallation cut inefficiencies for ^{12}B and ^{9}Li (8.5–15 MeV).

Table 7.6: Summary of spallation cut inefficiencies and systematic uncertainties (E_{vis} =7.5–8.5 MeV)

Shower-period	^{12}B inefficiency	^{9}Li inefficiency	Systematic error
Shower-1	$(4.47 \pm 0.75) \times 10^{-3}$	$(-3.11 \pm 1.30) \times 10^{-2}$	847%
Shower-2	$(6.91 \pm 1.87) \times 10^{-3}$	$(-1.72 \pm 1.93) \times 10^{-2}$	447%
Shower-3	$(7.82 \pm 1.29) \times 10^{-3}$	$(0.615 \pm 2.085) \times 10^{-2}$	267%
Shower-4	$(3.40 \pm 0.83) \times 10^{-3}$	$(3.24 \pm 1.35) \times 10^{-2}$	942%
Shower-5	$(3.69 \pm 1.32) \times 10^{-3}$	$(0.00 \pm 1.82) \times 10^{-2}$	504%
Shower-6	$(2.84 \pm 0.61) \times 10^{-3}$	$(2.72 \pm 1.01) \times 10^{-2}$	355%

Table 7.7: Summary of spallation cut inefficiencies and systematic uncertainties (E_{vis} =8.5–15 MeV)

Shower-period	^{12}B inefficiency	^{9}Li inefficiency	Systematic error
Shower-1	$(9.02 \pm 0.88) \times 10^{-3}$	$(-3.31 \pm 1.39) \times 10^{-2}$	492%
Shower-2	$(1.86 \pm 0.26) \times 10^{-2}$	$(0.246 \pm 2.146) \times 10^{-2}$	145%
Shower-3	$(1.41 \pm 0.15) \times 10^{-2}$	$(2.46 \pm 2.23) \times 10^{-2}$	175%
Shower-4	$(1.45 \pm 0.12) \times 10^{-2}$	$(2.40 \pm 1.57) \times 10^{-2}$	127%
Shower-5	$(2.40 \pm 0.20) \times 10^{-2}$	$(0.562 \pm 2.108) \times 10^{-2}$	117%
Shower-6	$(1.11 \pm 0.09) \times 10^{-2}$	$(2.45 \pm 1.27) \times 10^{-2}$	167%

7.6 Antineutrino Selection by KamNet

The antineutrino candidates that pass the shower likelihood cut are subsequently subjected to the KamNet-based event selection developed in Chap. 6. In practice, the hit maps of the antineutrino candidates are input to the trained KamNet model, and event selection is performed by comparing the output score with the predefined score threshold. Candidates with scores above the threshold are regarded as signal-like and retained as the final antineutrino candidates. Fig. 7.14–Fig. 7.18 show the KamNet selection applied to the antineutrino candidates for each KamNet period. In the KamNet-1 and KamNet-2 periods, during which many domestic reactors were in operation, several antineutrino candidates with $E_p \leq 8.5$ MeV remain after the KamNet selection, and these are likely to be reactor neutrinos.

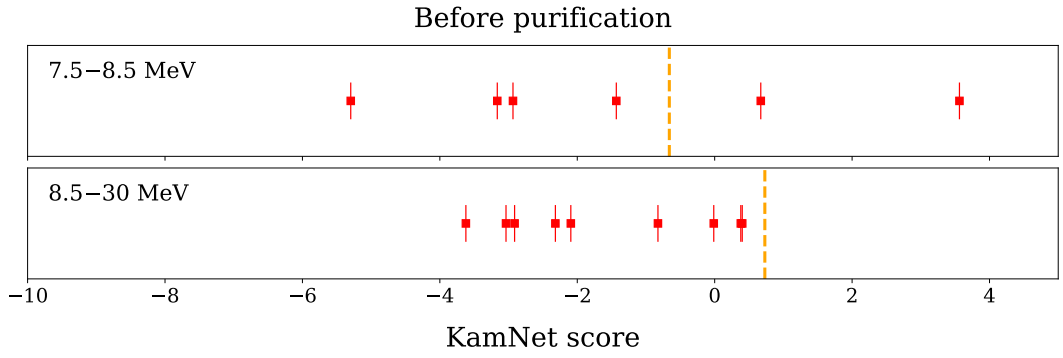

(a) 1D plot of KamNet score

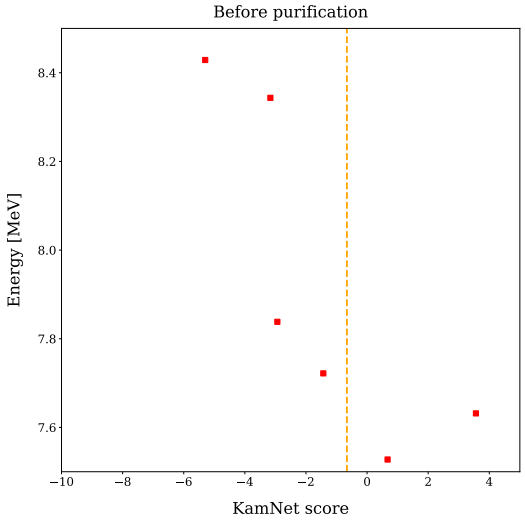

(b) Score vs. energy (7.5–8.5 MeV)

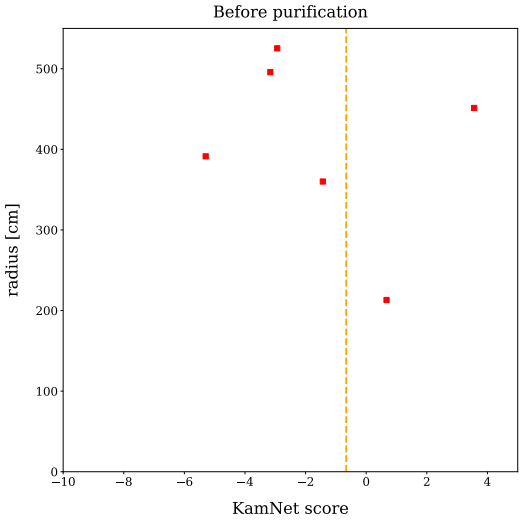

(c) Score vs. radius (7.5–8.5 MeV)

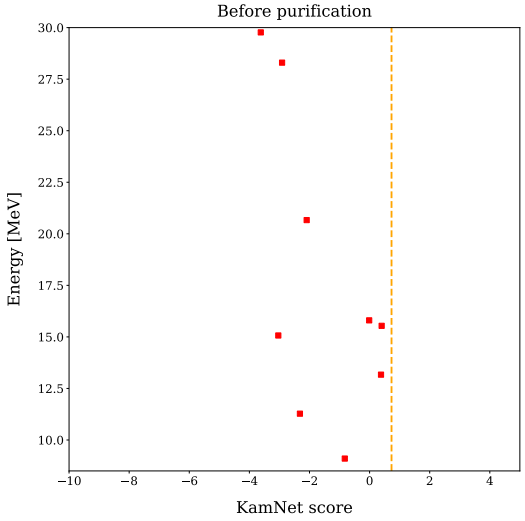

(d) Score vs. energy (8.5–30 MeV)

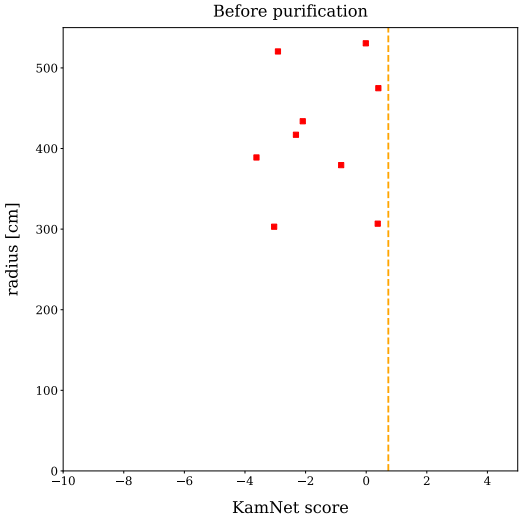

(e) Score vs. radius (8.5–30 MeV)

Figure 7.14: KamNet selection for the antineutrino candidates in KamNet-1 period (before purification). Orange lines indicate the KamNet score threshold.

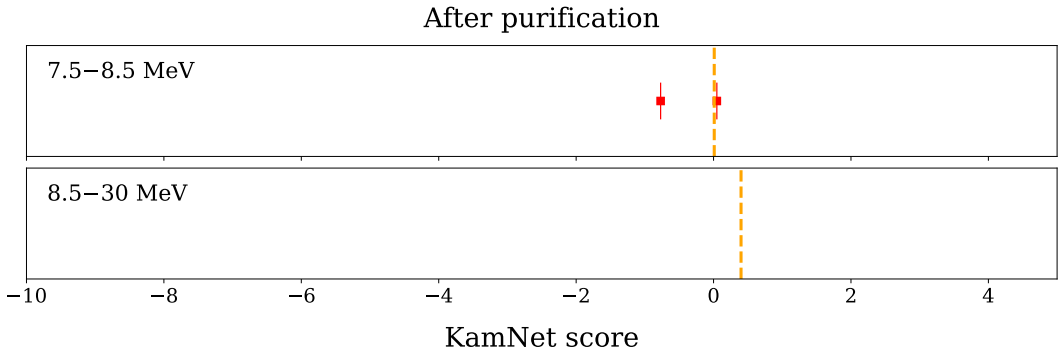

(a) 1D plot of KamNet score

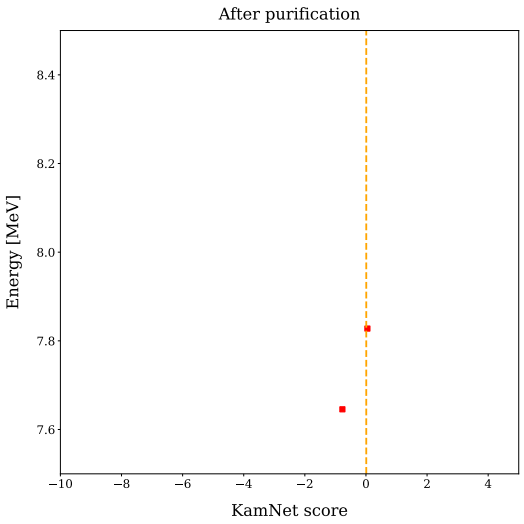

(b) Score vs. energy (7.5–8.5 MeV)

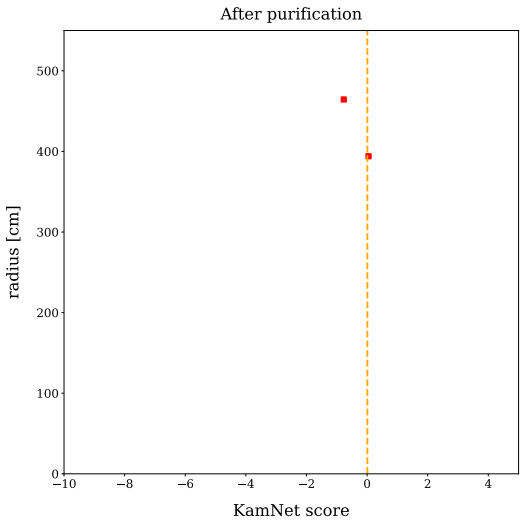

(c) Score vs. radius (7.5–8.5 MeV)

Figure 7.15: KamNet selection for the antineutrino candidates in KamNet-2 period (after purification). No candidates are observed in 8.5–30 MeV.

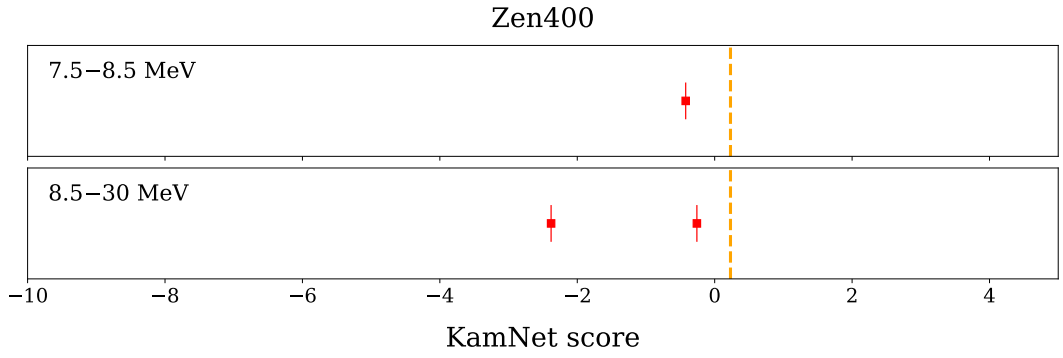

(a) 1D plot of KamNet score

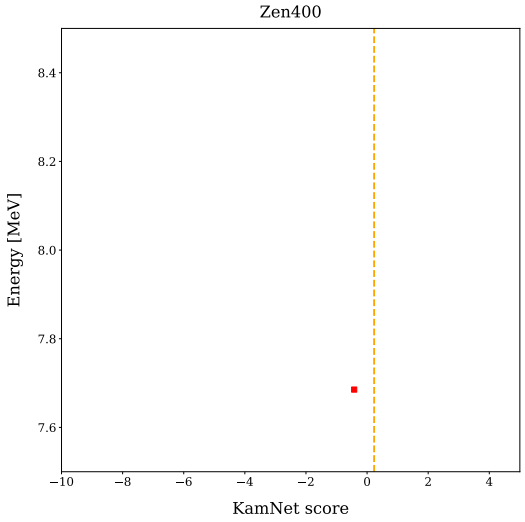

(b) Score vs. energy (7.5–8.5 MeV)

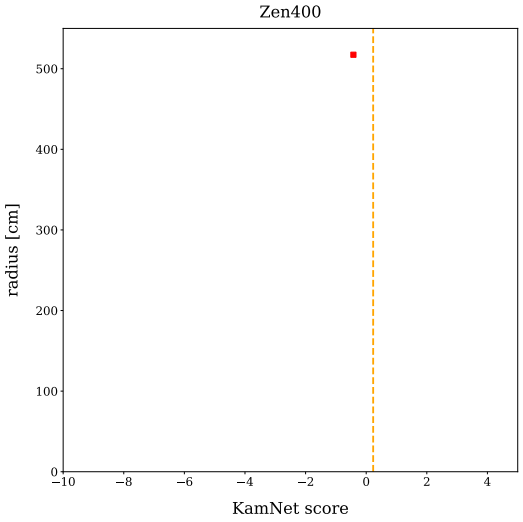

(c) Score vs. radius (7.5–8.5 MeV)

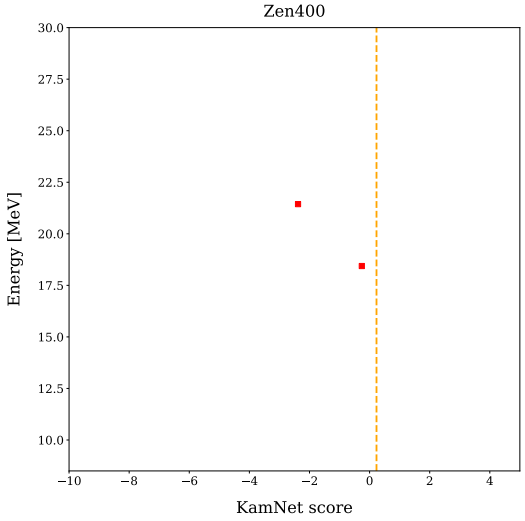

(d) Score vs. energy (8.5–30 MeV)

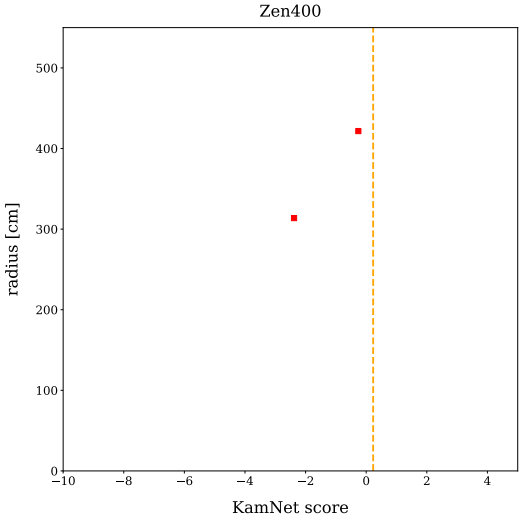

(e) Score vs. radius (8.5–30 MeV)

Figure 7.16: KamNet selection for the antineutrino candidates in KamNet-3 period (Zen400).

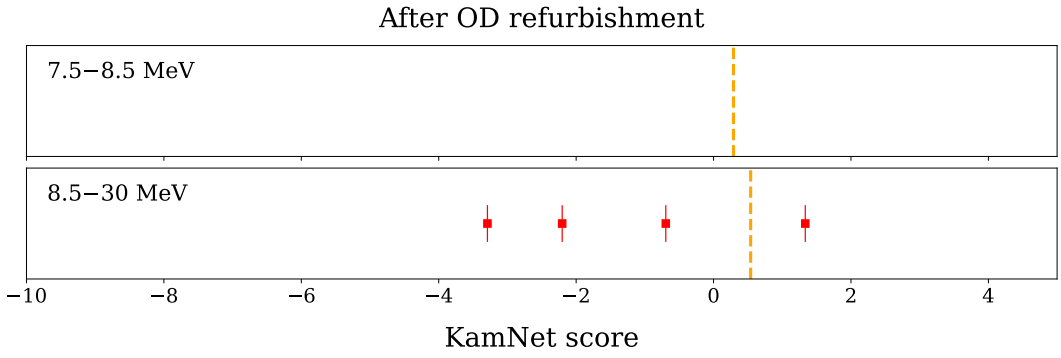

(a) 1D plot of KamNet score

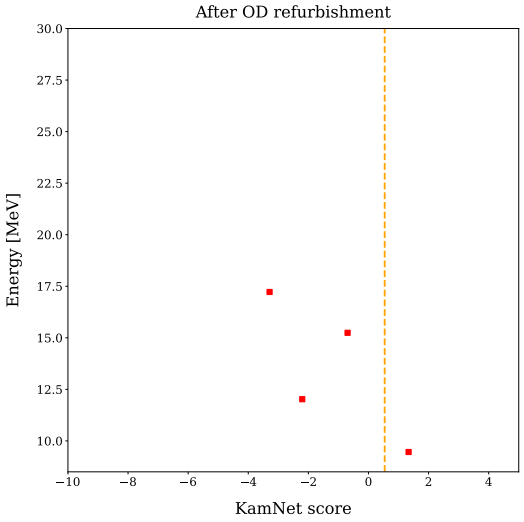

(b) Score vs. energy (8.5–30 MeV)

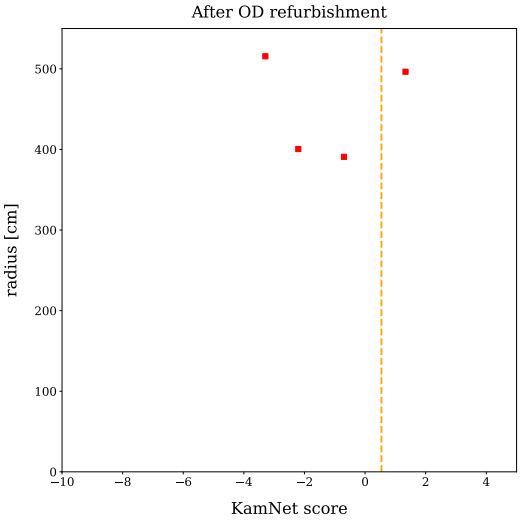

(c) Score vs. radius (8.5–30 MeV)

Figure 7.17: KamNet selection for the antineutrino candidates in KamNet-4 period (after OD refurbishment). No candidates are observed in 7.5–8.5 MeV.

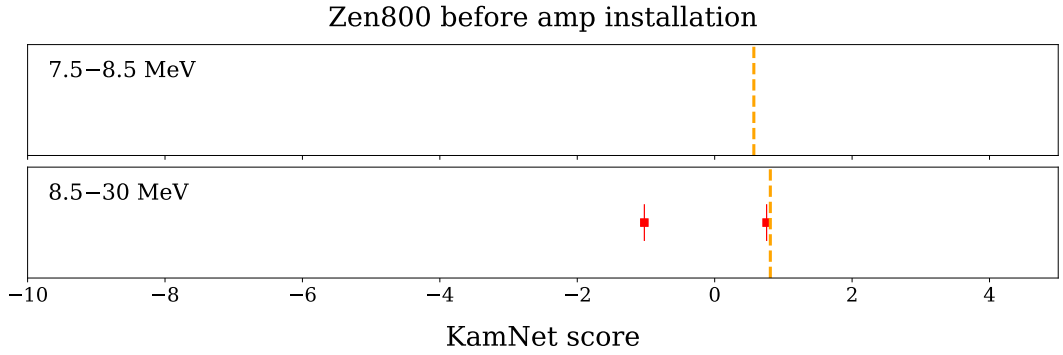

(a) 1D plot of KamNet score

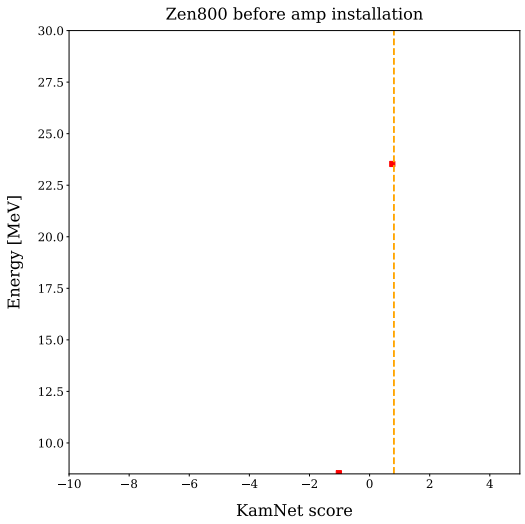

(b) Score vs. energy (8.5–30 MeV)

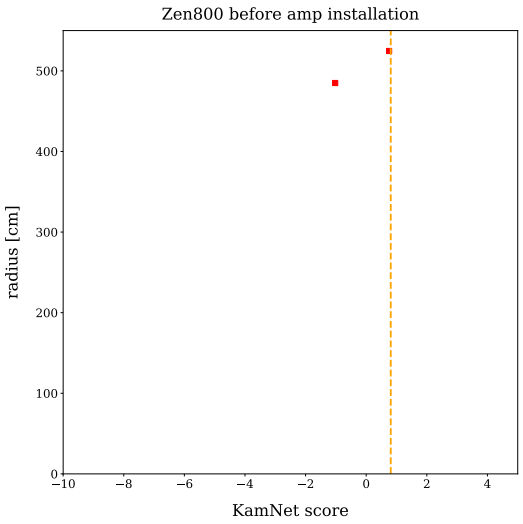

(c) Score vs. radius (8.5–30 MeV)

Figure 7.18: KamNet selection for the antineutrino candidates in KamNet-5 period (Zen800 before amp installation). No candidates are observed in 7.5–8.5 MeV.

7.7 Detector Related Systematic Uncertainties

This section describes the detector-related systematic uncertainties. A summary of these uncertainties is presented in Tab. 7.8. The uncertainty in the livetime calculation is estimated based on the unknown dead time ratio, as described in Sec. 7.1.2, and a value of 0.012% is adopted. The uncertainty associated with the flasher event cut is taken to be than 0.008% before purification and less than 0.009% after purification, as discussed in Sec. 7.2.2. The uncertainties in the energy scale and fiducial volume are taken from the estimates in Sec. 4.8.2 and Sec. 4.8.3, respectively. In addition, the uncertainty due to misreconstruction is evaluated to be 0.2%, as described in Sec. 4.7.4. For the IBD cross section, a 0.2% uncertainty has been used since the KamLAND first result [82], and this value is based on [83] and [84]. Other detector-related systematic uncertainties are discussed below.

OD hit event cut

As described in Sec. 4.6.1, the muon events in the OD are tagged using the maximum number of OD PMT hits within 200 ns for each event ($N_{200\mathrm{OD}}$). However, if accidental OD hits not associated with muons cause $N_{200\mathrm{OD}}$ to exceed the threshold value, the muon veto introduces a dead time in the detector. This *OD miss-tagging probability* is estimated using the 1PPS trigger as follows:

$$P_{\text{OD-miss-tagging}} = \frac{\text{number of 1PPS-triggered event with } N_{200\mathrm{OD}} \geq N_{200\text{OD-th}}}{\text{number of 1PPS-triggered event}}. \tag{7.13}$$

Here, $N_{200\text{OD-th}}$ denotes the threshold for $N_{200\mathrm{OD}}$, which is set to 5 before the OD refurbishment and 9 after it. The OD miss-tagging probability is conservatively estimated to be 0.3%, 0.2%, and 0.2% for the periods before purification, after purification, and after the start of Zen400, respectively. These values are adopted as the systematic uncertainties associated with the event cut based on OD hits.

Number of target proton

Antineutrino events in KamLAND are identified through IBD on protons in the LS. The dominant uncertainty in the estimation of the number of target protons arises from the LS density. The measured density of the KamLAND LS was originally $0.77754 \pm 0.00010\,\mathrm{g/cm^3}$ at 15°C, and the temperature coefficient of the density expansion was determined to be $7.14 \times 10^{-4}\,\mathrm{g/cm^3/K}$. since the LS temperature is controlled at 11.5 ± 1.5°C, the actual density is estimated to be $0.78018\,\mathrm{g/cm^3}$, and the ±1.5°C temperature variation corresponds to a 0.1% uncertainty in the density. This density uncertainty is assigned as the systematic uncertainty on the number of target protons.

The elemental composition of the LS implies H/C, H/N, and H/O to be 1.96908, 17842.0, and 17842.0, respectively. The number of H in the unit mass is therefore given by

$$\begin{aligned} \text{Number of H} &= \frac{N_A}{1.00794 + 12.011/1.96908 + 14.00674/17842.0 + 15.9994/17842.0} \\ &= 8.471 \times 10^{22}\,[/\mathrm{g}] \end{aligned} \tag{7.14}$$

where $N_A = 6.02 \times 10^{23}$ is Avogadro's constant. Using a fiducial volume of 550 cm, the total number of target protons is calculated numerically as

$$\begin{aligned} N_{\text{proton}} &= (8.471 \times 10^{22}\,[/\mathrm{g}]) \times (6.97 \times 10^{8}\,[\mathrm{cm^3}]) \times (0.78013\,[\mathrm{g/cm^3}]) \times (0.99985) \\ &= 4.605 \times 10^{31}, \end{aligned} \tag{7.15}$$

where 0.99985 is the natural abundance of ^{1}H.

Table 7.8: Summary of the detector-related systematic uncertainties

	before purification	after purification	post Zen400 start
– Efficiency –			
Livetime calculation	0.012%	0.012%	0.012%
– Event selection/reconstruction –			
Flasher event cut	0.008%	0.009%	0.009%
OD hit event cut	0.3%	0.2%	0.2%
Fiducial volume cut	1.7%	3.7%	6.3%
Miss-reconstruction	0.2%	0.2%	0.2%
Energy scale	2.24%	2.24%	2.24%
– Target proton/cross section –			
Target proton	0.1%	0.1%	0.1%
IBD cross section	0.2%	0.2%	0.2%
Total	2.84%	4.34%	6.70%

7.8 Antineutrino Candidates

Based on the above selection, the final antineutrino candidates for the astrophysical antineutrino search in this work are determined. The prompt energy spectrum is shown in Fig. 7.19. The other properties of the antineutrino candidates are shown in Fig. 7.20, and Fig. 7.21. The number of final antineutrino candidate is seven.

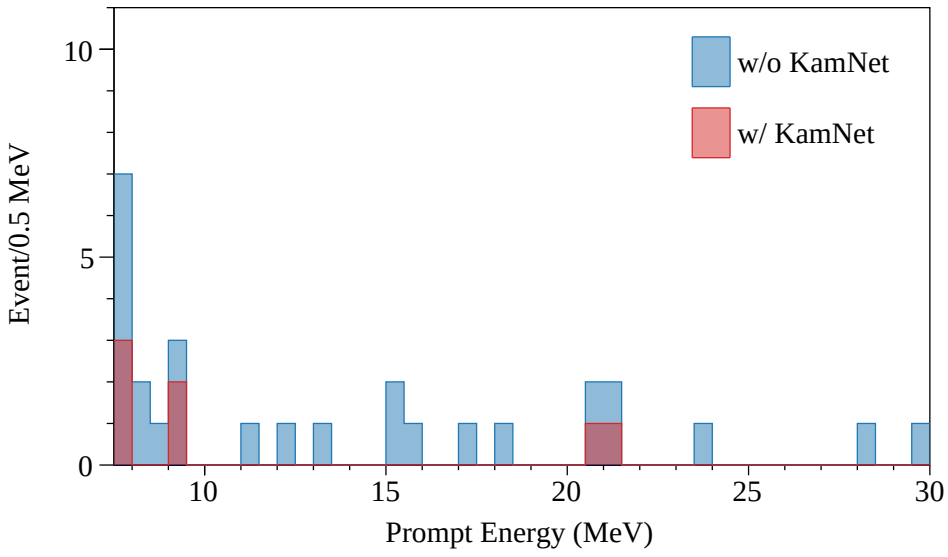

Figure 7.19: Prompt energy spectrum of the final $\bar{\nu}_e$ candidates in the full dataset.

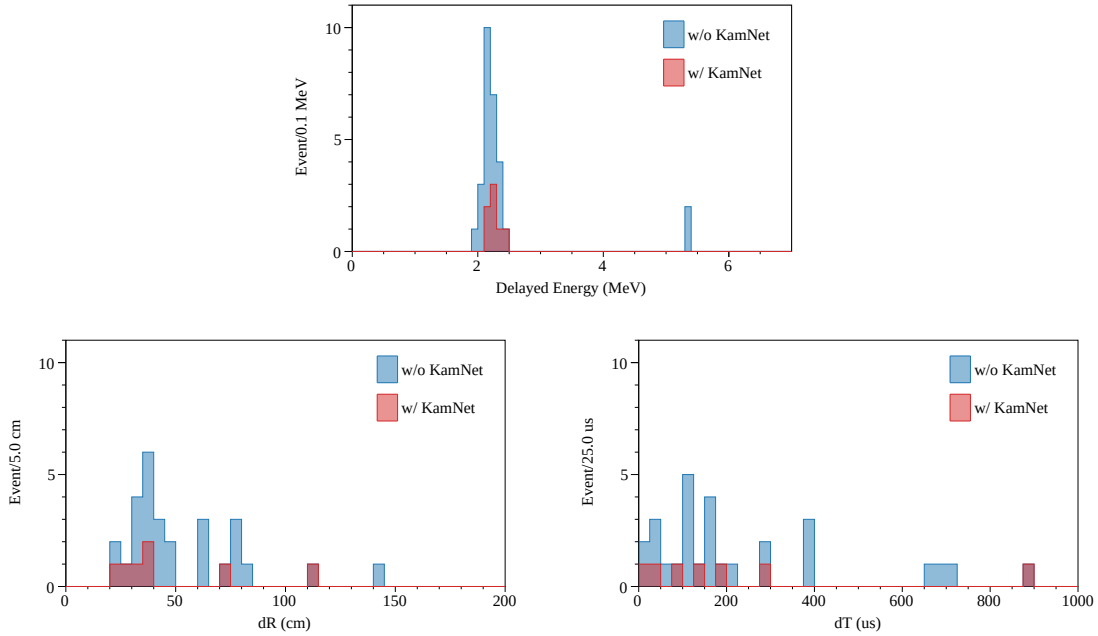

Figure 7.20: Properties of the final antineutrino candidates in the full dataset. Panels: (upper) delayed energy spectrum; (lower left) spatial correlation; (lower right) time correlation. Blue and red histograms correspond to events with and without the KamNet selection, respectively.

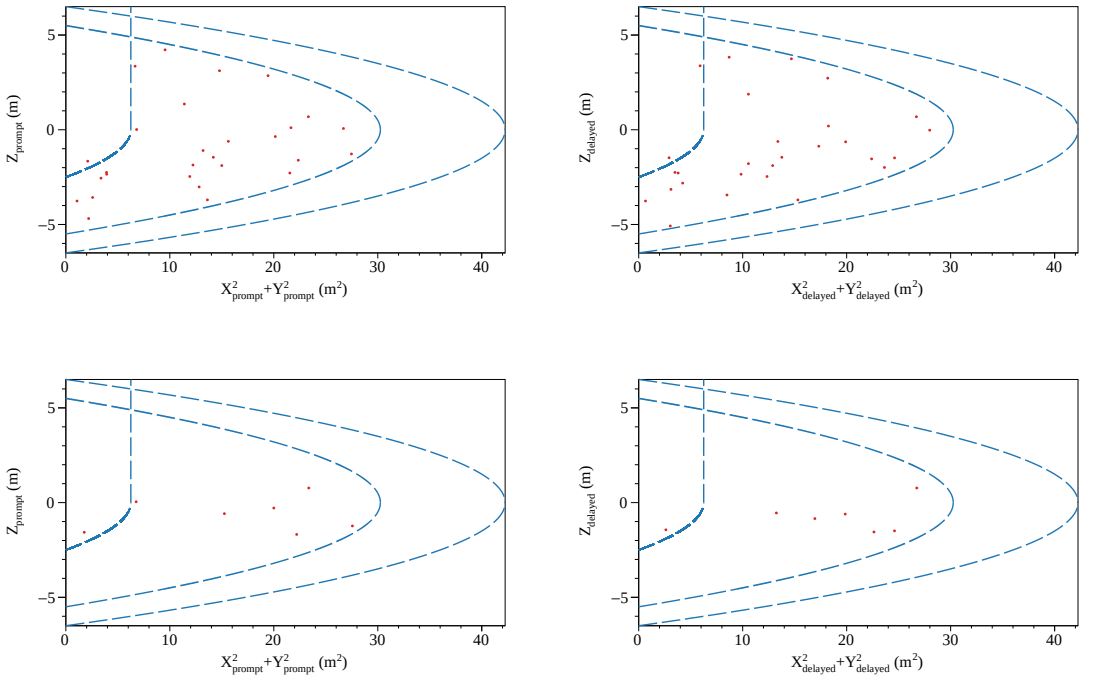

Figure 7.21: Vertex distributions of the final antineutrino candidates in the full dataset. Panels: (upper left) prompt vertex before the KamNet selection; (upper right) delayed vertex before the KamNet selection; (lower left) prompt vertex after the KamNet selection; (lower right) delayed vertex after the KamNet selection. Blue curves indicate, respectively, the Zen volume-cut boundary, the 550 cm radius, and the 650 cm radius.

Chapter 8

Background Estimation

8.1 Overview of Backgrounds

The background events in the search for astrophysical antineutrinos with KamLAND are those observed as delayed-coincidence signals but not originating from IBD of $\bar{\nu}_e$s. In addition, IBD reactions induced by known antineutrino sources must also be considered as background, since they are indistinguishable from astrophysical antineutrinos. The background components treated in this study are listed below.

- Reactor neutrinos (Sec. 8.2)
- Spallation ^{9}Li/^{8}He (Sec. 8.3)
- Atmospheric neutrinos (Sec. 8.4)
- Fast neutrons (Sec. 8.5)
- Accidental background (Sec. 8.6)

Reactor neutrinos are $\bar{\nu}_e$s produced by nuclear fission in reactors. They interact via IBD in the same manner as the target astrophysical $\bar{\nu}_e$s and cannot be distinguished on an event-by-event basis. Their contribution is therefore evaluated through accurate estimates of the number of events and energy spectrum.

Spallation events arise when cosmic-ray muons traverse the detector and produce unstable isotopes such as ^{9}Li and ^{8}He, which undergo $\beta + n$ decays. These events mimic IBD signatures and thus constitute one of the background sources.

Atmospheric neutrinos contribute not only through IBD reactions of their $\bar{\nu}_e$ component but also through other interactions that produce thermal neutrons, which are subsequently observed as delayed-coincidence events. They are therefore an important source of background.

Fast neutrons can enter the detector from outside, scatter on protons, thermalize, and eventually be captured, creating a double signal that closely resembles IBD. Their contribution is suppressed and estimated using the OD and shielding structures.

Accidental coincidences are produced when uncorrelated single events, primarily due to radioactive impurities within detector materials, overlap in time and space to mimic delayed coincidences. Although their contribution is small in this study, they cannot be entirely neglected, particularly in the low-energy region.

In the following, the estimation of the number of events and uncertainties for each of these background components are described.

8.2 Reactor Neutrinos

Reactor neutrinos refer to electron antineutrinos ($\bar{\nu}_e$) produced by the β-decay of fission fragments in nuclear reactors used for power generation. Fig. 8.1 shows the operational status of nuclear reactors in Japan as of December 2023. KamLAND was constructed at an average distance of about 180 km from these reactors in order to observe neutrino oscillations from their flux. Due to their large flux, reactor neutrinos initially dominated the delayed-coincidence events in KamLAND. However, following the Great East Japan Earthquake on March 11, 2011, all domestic reactors were shut down, and their contribution became relatively small compared to other event sources. As of 2026, although some reactors in Japan have resumed operation, the number of delayed-coincidence events from reactor neutrinos remains only a few times larger than those from other sources discussed later.

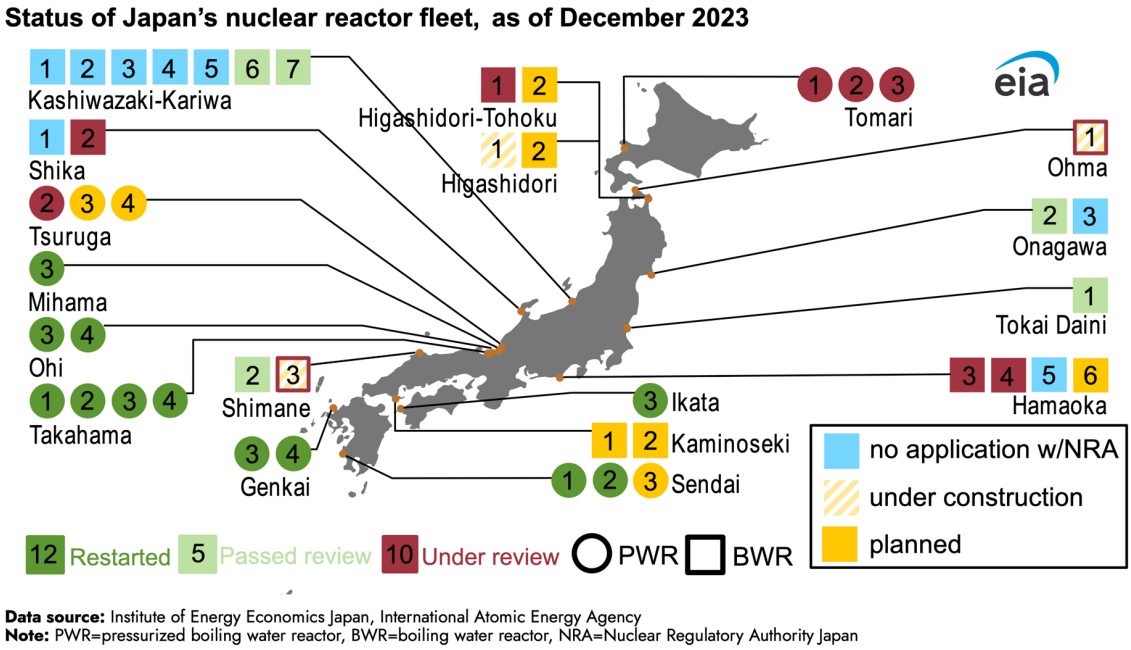

Figure 8.1: Status of Japanese nuclear reactor [85]. This figure is from December 2023.

Fig. 8.2 shows the nuclear power reactors in the world as of May 2025, and Fig. 8.3 shows the time variation of the reactor neutrino flux, including contributions from reactors outside Japan. Information on the operational status of Japanese reactors has been provided through a special collaboration between Tohoku University and the electric power companies operating each reactor. For foreign reactors, the dominant contribution to the flux comes from those in South Korea, estimated using publicly available electric power output data. Information on the operational status of other foreign reactors is obtained from publications of the IAEA [86]. In this chapter, the estimation of the number of event induced by reactor neutrinos is described.

8.2.1 Reactor Antineutrino Energy Spectrum

More than 99.9% of the $\bar{\nu}_e$ emitted from nuclear reactors are produced through the fission of four unstable isotopes, ^{235}U, ^{238}U, ^{239}Pu, ^{241}Pu, followed by the subsequent β-decays of the fission fragments, as summarized below:

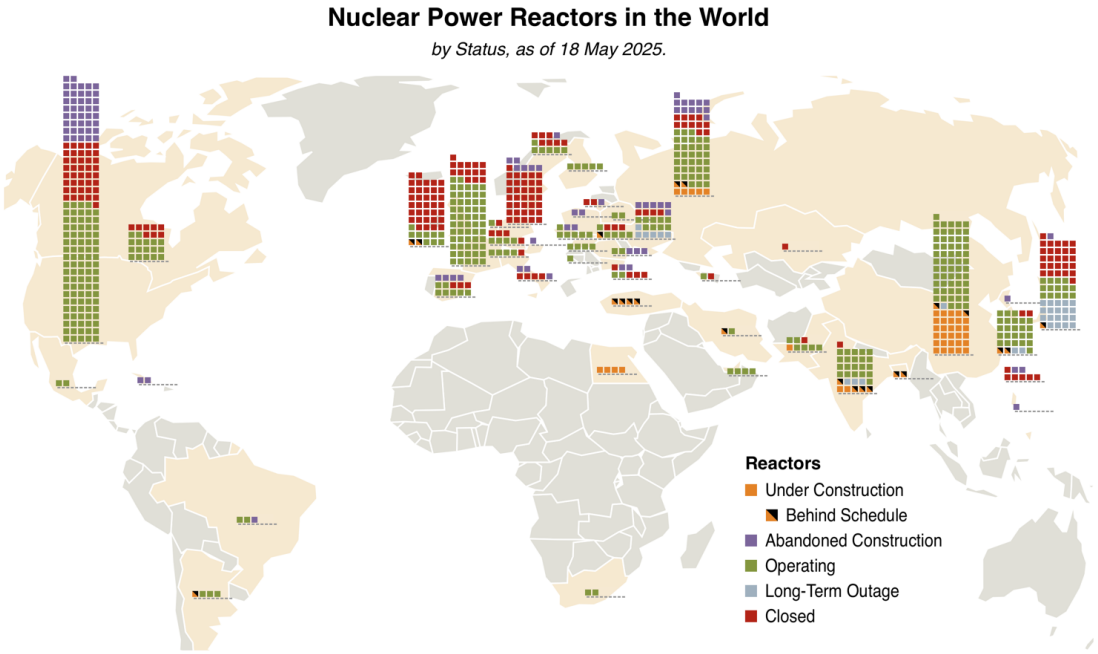

Figure 8.2: Nuclear power reactors in the world [87]. This figure is from May 18, 2025.

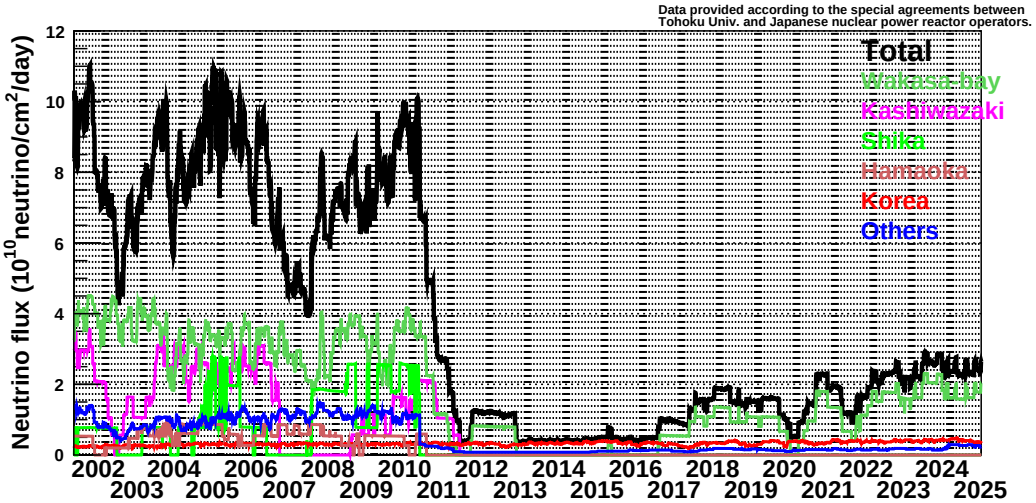

Figure 8.3: Time variation of electron antineutrino flux from reactors

- ^{235}U
  Captures a thermal neutron and undergoes fission:

$$^{235}\mathrm{U} + n \rightarrow \mathrm{A} + \mathrm{B} + 6.1\,\beta^- + 6.1\,\bar{\nu}_e + 202\,[\mathrm{MeV}] + 2.4\,n \tag{8.1}$$

- ^{238}U
  Captures a fast neutron and undergoes fission:

$$^{238}\mathrm{U} + n\,(> 1\,\mathrm{MeV}) \rightarrow \mathrm{C} + \mathrm{D} + 5 \sim 7\,\beta^- + 5 \sim 7\,\bar{\nu}_e + 205\,[\mathrm{MeV}] + x\,n \tag{8.2}$$

  or captures a thermal neutron and, through two successive β-decays, produces ^{239}Pu:

$$^{238}\mathrm{U} + n \rightarrow {}^{239}\mathrm{U} \xrightarrow[T_{1/2}=23.5\,\mathrm{min}]{\beta^-} {}^{239}\mathrm{Np} \xrightarrow[T_{1/2}=2.356\,\mathrm{day}]{\beta^-} {}^{239}\mathrm{Pu} \tag{8.3}$$

- ^{239}Pu
  Captures a thermal neutron and undergoes fission:

$$^{239}\mathrm{Pu} + n \rightarrow \mathrm{E} + \mathrm{F} + 5.6\,\beta^- + 5.6\,\bar{\nu}_e + 210\,[\mathrm{MeV}] + 2.9\,n \tag{8.4}$$

  or after two successive thermal neutron captures, it is converted into ^{241}Pu:

$$\begin{aligned} ^{239}\mathrm{Pu} + n &\rightarrow {}^{240}\mathrm{Pu} \\ ^{240}\mathrm{Pu} + n &\rightarrow {}^{241}\mathrm{Pu} \end{aligned} \tag{8.5}$$

- ^{241}Pu
  Captures a thermal neutron and undergoes fission:

$$^{241}\mathrm{Pu} + n \rightarrow \mathrm{G} + \mathrm{H} + 6.4\,\beta^- + 6.4\,\bar{\nu}_e + 212\,[\mathrm{MeV}] + 2.9\,n \tag{8.6}$$

The reactor antineutrino energy spectra emitted from each isotope have been calculated by Huber [88], Mueller [89], and Vogel [90]. The results are shown in Fig. 8.4. In KamLAND, the reactor antineutrino spectrum is obtained by correcting the Daya Bay spectrum [91] according to the following expression in order to reduce systematic uncertainties:

$$S_i(E_\nu) = S_{\mathrm{DB}}(E_\nu) + \sum_{j \in \mathrm{isotope}} (f_i^j - f_{\mathrm{DB}}^j) S_{i,\mathrm{HM}}^j(E_\nu). \tag{8.7}$$

Here, i denotes the reactor index and j denotes the isotope index. $S_i(E_\nu)$ represents the reactor antineutrino spectrum used in KamLAND, $S_{\mathrm{DB}}(E_\nu)$ is the Daya Bay spectrum, and $S_{i,\mathrm{HM}}^j(E_\nu)$ is the isotope spectrum calculated by Huber and Mueller. The parameters f_i^j and f_{DB}^j are the fission fractions of isotope j in reactor i and in Daya Bay, respectively.

In addition to ^{235}U, ^{238}U, ^{239}Pu, and ^{241}Pu, fission also produces unstable nuclei with half-lives ranging from several hours to several decades. Among them, ^{97}Zr, ^{132}I, and ^{93}Y have relatively short half-lives of a few hors and are therefore considered to decay almost in equilibrium, contributing negligibly to the shape of the reactor antineutrino energy spectrum. On the other hand, the decay of long-lived isotopes, as listed below, can distort

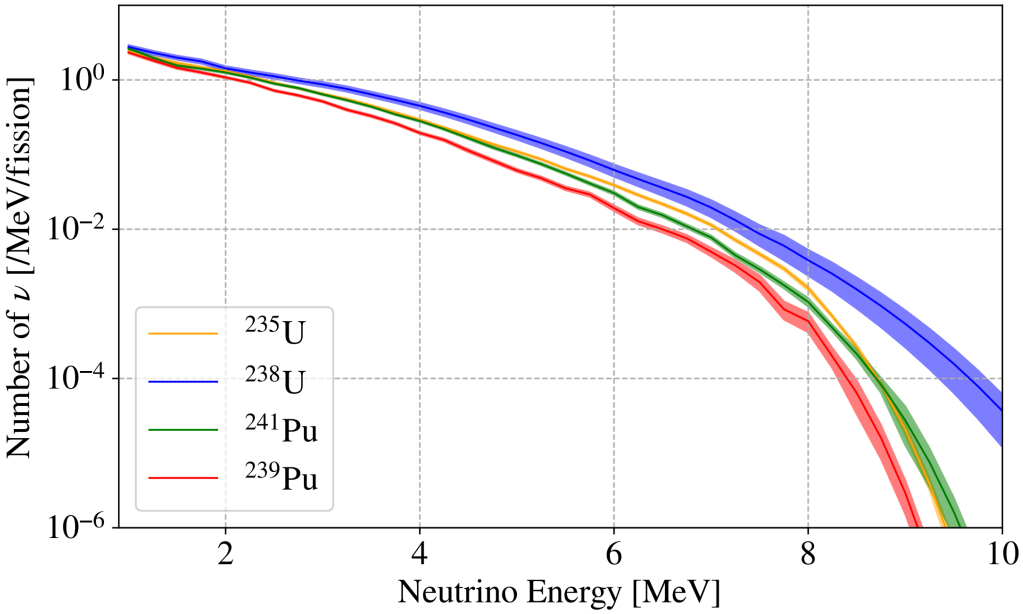

Figure 8.4: Reactor antineutrino spectrum per fission [92]. Originally made by [88, 89, 90].

the spectrum and their contributions are therefore treated as an uncertainty.

$$^{106}\mathrm{Ru} \xrightarrow[T_{1/2}=373.6\,\mathrm{day}]{Q_\beta=0.0394\,\mathrm{MeV}} {}^{106}\mathrm{Rh} \xrightarrow[T_{1/2}=29.8\,\mathrm{sec}]{Q_\beta=3.541\,\mathrm{MeV}} {}^{106}\mathrm{Pd} \tag{8.8}$$

$$^{144}\mathrm{Ce} \xrightarrow[T_{1/2}=284.9\,\mathrm{day}]{Q_\beta=0.3187\,\mathrm{MeV}} {}^{144}\mathrm{Pr} \xrightarrow[T_{1/2}=12.3\,\mathrm{sec}]{Q_\beta=2.9975\,\mathrm{MeV}} {}^{144}\mathrm{Nd} \tag{8.9}$$

$$^{90}\mathrm{Sr} \xrightarrow[T_{1/2}=22.8\,\mathrm{day}]{Q_\beta=0.546\,\mathrm{MeV}} {}^{90}\mathrm{Y} \xrightarrow[T_{1/2}=64.1\,\mathrm{sec}]{Q_\beta=2.282\,\mathrm{MeV}} {}^{90}\mathrm{Zr} \tag{8.10}$$

Tab. 8.1 summarizes the long-lived fission products. Here, E_{max} denotes the maximum energy carried away by reactor antineutrinos through the successive β-decays.

Table 8.1: Long-lived nuclei produced by the fission of ^{235}U、 ^{238}U、 ^{239}Pu、 ^{241}Pu [93]

Fission fragment	Half life	E_{max} [MeV]	Yield [%]			
			^{235}U	^{238}U	^{239}Pu	^{241}Pu
^{97}Zr	16.91 hr	1.922	5.95	5.50	5.30	4.89
^{132}I	2.295 hr	2.104	4.30	5.16	5.40	4.14
^{93}Y	10.18 hr	2.890	6.40	4.97	3.89	3.51
^{106}Ru	373 day	(^{106}Rh) 3.541	0.40	2.55	4.31	6.18
^{144}Ce	285 day	(^{144}Pr) 2.996	5.48	4.50	3.74	4.39
^{90}Sr	28.8 yr	(^{90}Y) 2.279	5.82	2.10	1.57	3.12

8.2.2 Expected Number of Reactor Events

The reactor antineutrino flux is obtained by summing the contributions from each reactor and each isotope, and can be expressed as

$$\frac{d\Phi}{dE_\nu} = \sum_{i\in\text{reactor}} P_{ee}(E_\nu, L_i)\,\frac{1}{4\pi L_i^2}\,\frac{W_i}{\sum_{j\in\text{isotope}} f_i^j e_j}\,S_i(E_\nu), \tag{8.11}$$

where L_i and W_i denote the distance from the i-th reactor to KamLAND and the thermal power of the i-th reactor, respectively. The quantity e_j represents the energy released per fission of isotope j, and $P_{ee}(E_\nu, L_i)$ is the electron antineutrino survival probability. The observable energy spectrum in KamLAND is then expressed as a function of neutrino energy by incorporating the number of target protons N_{proton}, the detection efficiency of the delayed-coincidence selection $\epsilon(E_\nu)$, and the IBD cross section $\sigma(E_\nu)$:

$$\frac{dN}{dE_\nu} = N_{\text{proton}}\,\epsilon(E_\nu)\,\sigma(E_\nu)\int \frac{d\Phi}{dE_\nu}\,dt. \tag{8.12}$$

The conversion from neutrino energy to the positron energy is performed according to [94], as follows:

$$E_\nu \simeq E_e + \Delta + \frac{1}{M}\left[E_e(E_e+\Delta) + y^2\right], \tag{8.13}$$

where $\Delta = M_n - M_p$ and $y^2 = (\Delta^2 - m_e^2)/2$. The spectrum as a function of positron energy, dN/dE_e, is then convolved with a Gaussian function in order to take into account the detector energy resolution σ:

$$\frac{dN}{dE'_e} = \int \frac{dN}{dE_e}\,\frac{1}{\sqrt{2\pi}\sigma}\,\exp\left(-\frac{(E_e - E'_e)^2}{2\sigma^2}\right)dE_e. \tag{8.14}$$

Finally, the expected number of events is obtained by integrating the resulting spectrum over the positron energy.

8.2.3 Reactor Related Uncertainty

The locations of domestic reactors are provided by the Tokyo Electric Power Company (TEPCO). Based on these data, the distances between each reactor and KamLAND are estimated, with an uncertainty of less than 0.1%. In addition, the uncertainty in the reactor neutrino flux arising from the chemical composition of the reactor core is evaluated from TEPCO calculations using a simplified core model, yielding a value of 1.0%.

The thermal power of each reactor is used to normalize the reactor neutrino flux, and thus constitutes another source of uncertainty. For domestic reactors, the thermal power uncertainty is estimated to be 2% per reactor. Since the thermal power of Korean reactors is not publicly available, it is inferred from publicly available electrical power output data, from which the corresponding uncertainty is estimated [92]. For other foreign reactors, the uncertainty is evaluated using data provided by the IAEA [92].

The reactor antineutrino spectra shown in Fig. 8.4 has no experimental measurements above 10 MeV. Therefore, this study adopts the 46.5% uncertainty on the extrapolated antineutrino spectrum estimated in [45], where a polynomial functional form was assumed for the extrapolation. The operational status of domestic reactors is provided on a daily basis, but since fission equilibrium in the reactor core is reached only after about one day, the resulting time-lag effect is estimated to contribute an uncertainty of 0.01%. Finally, as described in Sec. 8.2.1, the presence of long-lived nuclei distorts the reactor neutrino spectrum, and this effect is also taken into account as a source of uncertainty [92].

All reactor-related sources of uncertainty are summarized in Tab. 8.2.

Table 8.2: Summary of the reactor-related systematic uncertainties

	before purification	after purification	post Zen400 start
Distance	$< 0.1\%$	$< 0.1\%$	$< 0.1\%$
– Thermal power –			
Japan	2.0%	2.0%	2.0%
Korea	0.365%	0.474%	3.338%
Taiwan/China	0.071%	0.101%	1.045%
Others	0.042%	0.051%	0.351%
Chemical composition	1.0%	1.0%	1.0%
Long-lived nuclei	1.092%	1.129%	2.044%
Antineutrino spectra	46.5%	46.5%	46.5%
Time lag	0.01%	0.01%	0.01%
Total	46.6%	46.6%	46.7%

8.2.4 Summary of Reactor Neutrino Background

Taking into account the reactor-related systematic uncertainty and the KamNet-related systematic uncertainty described in Sec. 6.5.5, the expected number of reactor neutrino background is estimated to be 1.0 ± 0.6. This value also reflects the signal acceptance of the KamNet cut. In this estimation, the neutrino oscillation parameters are used as $\tan^2\theta_{12} = 0.436^{+0.029}_{-0.025}$, $\Delta m^2 = 7.53^{+0.18}_{-0.18} \times 10^{-5}\,\mathrm{eV}^2$, and $\sin^2\theta_{13} = 0.023^{+0.002}_{-0.002}$ [95].

8.3 Spallation Events

Cosmic-ray muons entering KamLAND induce nuclear spallation of ^{12}C nuclei in the LS, either directly or through secondary particles such as γ rays and pions produced in muon-induced showers. The unstable isotopes created via nuclear spallation subsequently decay, emitting particles that are detected in the KamLAND detector. Some of these spallation products decay with the emission of neutrons, giving rise to delayed-coincidence-like signatures. Tab. 8.3 summarizes the isotopes produced by spallation that undergo β decay accompanied by neutron emission. The contributions from ^{11}Li and ^{12}Be are negligibly small in KamLAND, as their decay modes involving neutron emission are extremely rare.

Table 8.3: Isotopes that emit beta particles or neutrinos [96]

Isotope	Production reaction	Lifetime [ms]	Decay mode	Energy [MeV]	Fraction
^{8}He	^{12}C$(\gamma, 4p)$, ^{12}C$(\pi^-, n3p)$	171.7	β^-	10.7	0.84
			$\beta^- + n$		0.16
^{9}Li	^{12}C$(\gamma, 3p)$, ^{12}C$(\pi^-, n2p)$	257.2	β^-	13.6	0.53
			$\beta^- + n$		0.48
^{11}Li	^{12}C$(\gamma, 2\pi^+p)$, ^{12}C(π^-, π^+p)	12.3	β^-	20.6	0.07
			$\beta^- + xn$		0.92
^{12}Be	^{12}C$(\gamma, 2\pi^+)$, ^{12}C(π^-, π^+)	16.4	β^-	11.7	-
			$\beta^- + n$		-

The numbers of ^{8}He and ^{9}Li events are estimated from the observed data in KamLAND. The selection criteria for these events are essentially identical to those used for standard delayed-coincidence selection, except for the following two points:

- Prompt energy: $0.9 \leq E_p\,[\mathrm{MeV}] \leq 20$
  This range is chosen to cover the expected energy distributions of ^{8}He and ^{9}Li.
- Muon veto criteria: only a 2 ms veto after a muon event is applied.
  Imposing all muon cut would result in insufficient statistics for ^{8}He and ^{9}Li.

Fig. 8.5 shows the prompt energy spectrum of the selected spallation events, together with typical spectra of ^{8}He and ^{9}Li. From this comparison, it is concluded that nearly all of the delayed-coincidence spallation events originate from ^{9}Li.

The number of ^{9}Li events is estimated separately according to the residual charge ΔQ (see Sec. 4.6.1 and Sec. 7.3). For events induced by showering muons with large residual charge, a whole-volume veto within 2 s after the muon in applied. On the other hand, for events induced by non-showering muons with small residual charge, the conventional analysis applied a cylindrical veto of 2 s after the muon and within a distance of $dL < 3$ m from the muon track. Fig. 8.6 shows the time difference between spallation ^{9}Li events and their parent muons, categorized by residual charge and dL. These distributions are confirmed to follow an exponential decay consistent with the ^{9}Li lifetime.

The number of remaining spallation ^{9}Li events after the muon-associated cuts can be estimated as follows. For showering muons, events observed more than 2 s after the muon are considered as background events, and the number of such events is given by

$$N_{\mathrm{shower}} = \int_{2\mathrm{s}}^{\infty} f(t)dt, \tag{8.15}$$

where $f(t)$ is the exponential component of the fitting function shown in Fig. 8.6, and the offset term is excluded as it represents the accidental component. For non-showering

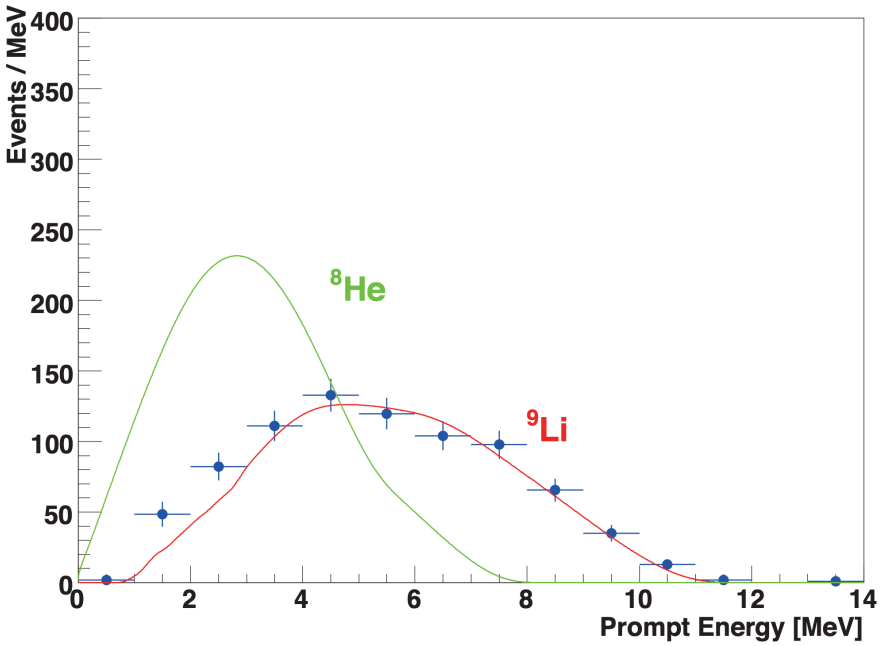

Figure 8.5: Prompt energy spectra of ^{8}He and ^{9}Li events [62]. The original data are taken from [96]. The observed data, shown as blue points, are found to be in good agreement with the ^{9}Li spectrum.

muons, background events consist of those observed more than 2 s after the muon and those with $dL > 3$ m. Considering that the distribution shown in the upper-right panel of Fig. 8.6 corresponds to the events remaining after the application of the cylindrical cut (rejection efficiency = 93.6% [72]), the number of residual events can be expressed as

$$N_{\text{non-shower}} = \int_{2\text{s}}^{\infty} g(t)dt + \int_{0\text{s}}^{\infty} g(t)dt \times \frac{1 - 0.936}{0.936}, \tag{8.16}$$

where $g(t)$ is the exponential component of the fitting function. Subsequently, for the events associated with non-showering muons, the scaling due to the efficiencies of the cylindrical cut and the shower likelihood cut (described in Sec. 7.5) is taken into account. Finally, considering the systematic uncertainty associated with the shower likelihood cut (and a small contribution from the KamNet cut), the expected number of spallation ^{9}Li events is estimated to be 1.9 ± 6.6.

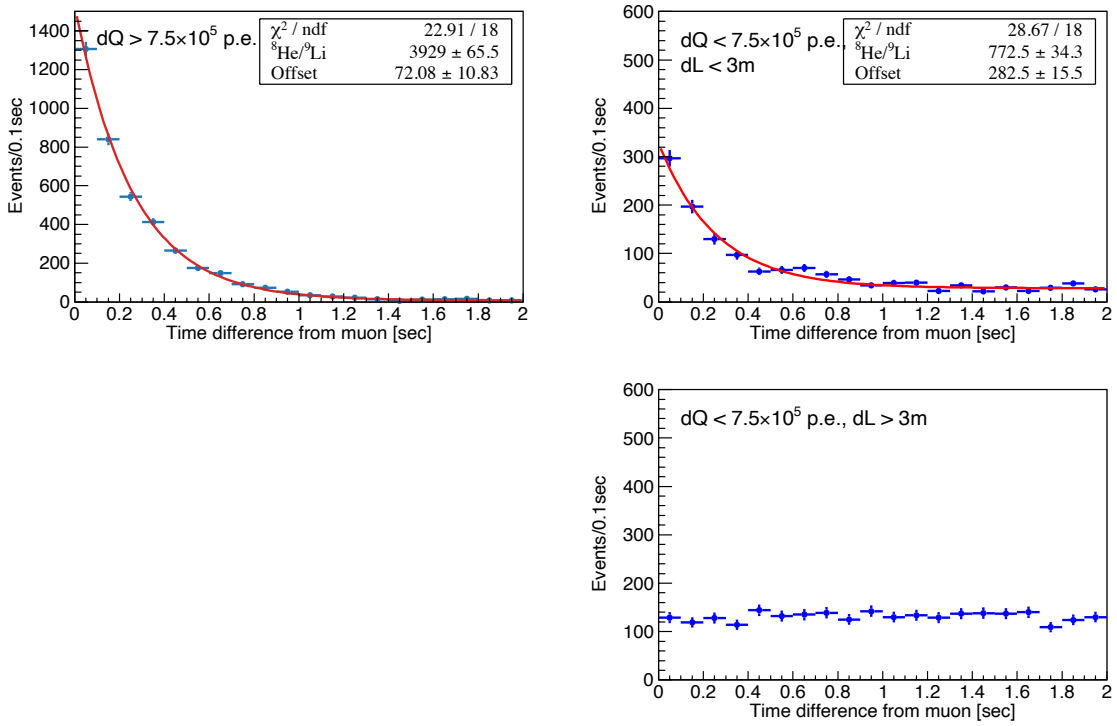

Figure 8.6: Time difference between muon events and spallation ^{8}He/^{9}Li events. The left figure shows spallation events with a large residual charge ($\Delta Q > 7.5 \times 10^5$ p.e.), while the right figures show events with a small residual charge ($\Delta Q < 7.5 \times 10^5$ p.e.). The red line represents an exponential function with a time constant of 257.2 ms, corresponding to the decay lifetime of ^{9}Li.

8.4 Atmospheric Neutrinos

Atmospheric neutrinos are produced when primary cosmic rays interact with atmospheric nuclei such as nitrogen and oxygen. The dominant production channel is the decay of charged pions generated in these interactions,

$$\pi^+ \to \mu^+ + \nu_\mu, \quad \pi^- \to \mu^- + \bar{\nu}_\mu, \tag{8.17}$$

followed by muon decay, which provides an important additional contribution:

$$\mu^+ \to e^+ + \nu_e + \bar{\nu}_\mu, \quad \mu^- \to e^- + \bar{\nu}_e + \nu_\mu. \tag{8.18}$$

Since atmospheric neutrinos arrive from all directions, including from above and through the Earth, their flux exhibits a pronounced dependence on zenith angle. In this study, the estimation of the number of events induced by atmospheric neutrinos is based on the flux calculation reported by Honda et al [97]. Fig. 8.7 shows the all-direction averaged atmospheric neutrino flux at Kamioka site. The dominant source of systematic uncertainty in the expected number of events arises from the uncertainty of the flux itself. This flux uncertainty is energy dependent, and its magnitude is approximately 20%. The main origins of the flux uncertainty include pion and kaon production in hadronic interactions, uncertainties in hadronic interaction cross sections, and the density profile of the atmosphere. Fig. 8.8 presents the uncertainty of each error source for atmospheric neutrino flux and their sum.

Atmospheric neutrinos entering the KamLAND detector interact with protons and carbon nuclei, producing delayed-coincidence-like signatures. These interaction processes are classified into charged-current (CC) and neutral-current (NC) interactions, and the expected number of events from each category is estimated as described below.

8.4.1 Charged Current (CC) Interaction

In charged-current (CC) interactions of atmospheric neutrinos, the neutrino interacts with either a proton or a carbon nucleus mediated by the weak W boson, producing a charged lepton:

$$\begin{aligned}
\bar{\nu}_e + p &\to e^+ + n && (8.19)\\
\bar{\nu}_\mu + p &\to \mu^+ + n && (8.20)\\
\bar{\nu}_\mu + {}^{12}\mathrm{C} &\to \mu^+ + n + {}^{11}\mathrm{B} && (8.21)\\
\nu_\mu + {}^{12}\mathrm{C} &\to \mu^- + n + {}^{11}\mathrm{N} && (8.22)\\
\bar{\nu}_\mu + {}^{12}\mathrm{C} &\to \mu^+ + n + {}^{11}\mathrm{B} + \gamma && (8.23)\\
\bar{\nu}_\mu + {}^{12}\mathrm{C} &\to \mu^+ + n + {}^{7}\mathrm{Li} + \alpha && (8.24)\\
\bar{\nu}_\mu + {}^{12}\mathrm{C} &\to \mu^+ + 2n + {}^{10}\mathrm{B} && (8.25)
\end{aligned}$$

Among these processes, the cross section for neutrino-proton interactions is approximately an order of magnitude larger than that for neutrino-carbon interactions; therefore, the former dominates the total contribution. Fig. 8.9 shows the CC cross section induced by antineutrinos on proton and carbon nuclei. In this study, the estimation of the expected number of events is based on the cross section measurements reported by MiniBooNE experiment [98].

Within atmospheric neutrino CC interactions, the dominant background in the delayed-coincidence analysis arises from processes involving muon decay, as illustrated in the example

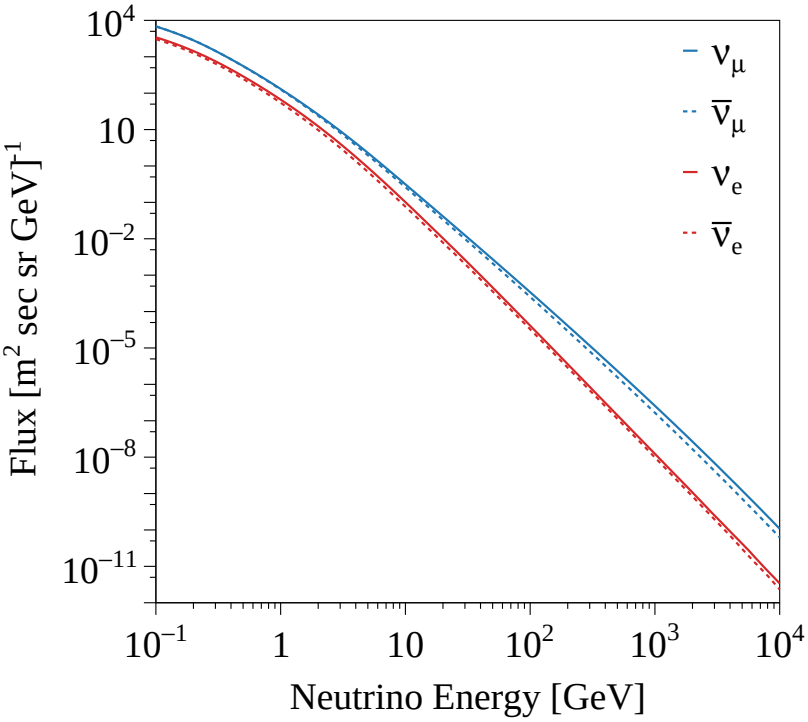

Figure 8.7: All-direction averaged atmospheric neutrino flux at Kamioka site. The data are taken from [97].

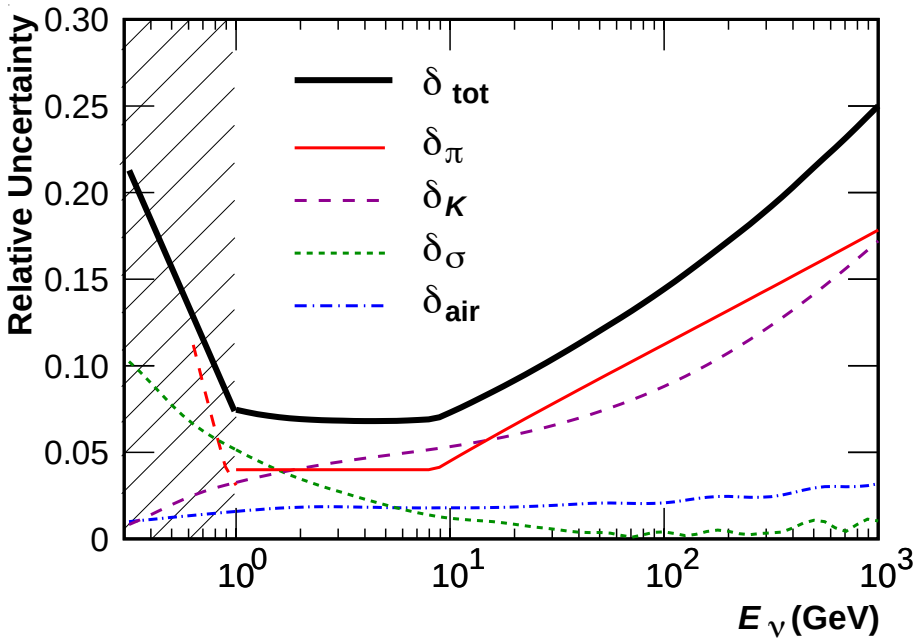

Figure 8.8: Uncertainty of each error source for atmospheric neutrino flux and their sum [97]. δ_π and δ_K represent the uncertainties in pion and kaon production in hadronic interactions, δ_σ denotes the uncertainty in the hadronic interaction cross section, $\delta_{\rm air}$ indicates the uncertainty arising from the atmospheric density profile, and $\delta_{\rm tot}$ is the total uncertainty in the atmospheric neutrino flux. In the energy region below 1 GeV, shown as the shaded area in the figure, the uncertainties are evaluated using a method different from that applied above 1 GeV.

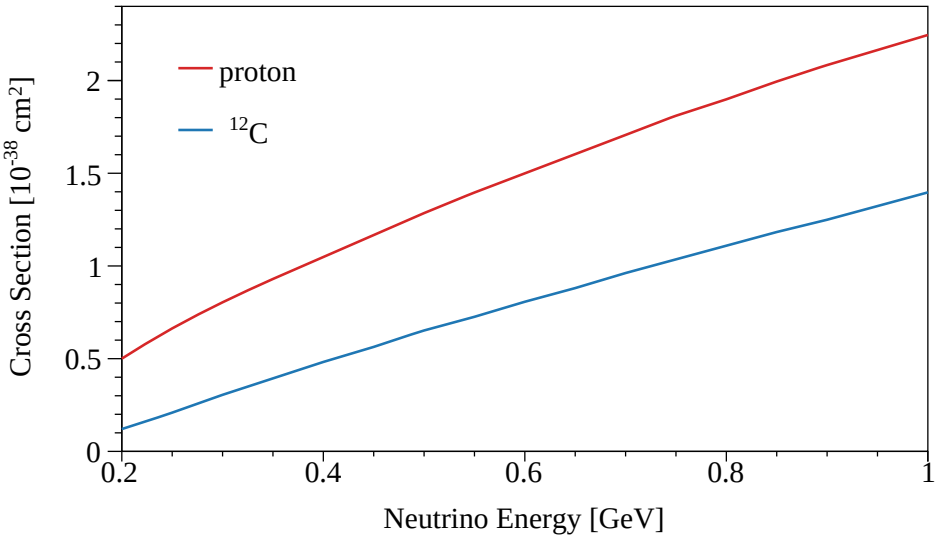

Figure 8.9: Charged-current cross section induced by antineutrinos on proton and carbon. The data are taken from [98].

below:

$$\begin{aligned} \bar{\nu}_\mu + p \rightarrow \quad & \mu^+ \quad + n \\ & \downarrow \quad (\sim 2.2\,\mu\text{sec}) \\ & \mu^+ \quad \rightarrow e^+ + \nu_e + \bar{\nu}_\mu \end{aligned} \tag{8.26}$$

Such backgrounds include prompt events due to the scintillation light from the muon itself, events induced by the positron from muon decay, and events due to neutron capture. These three components form a three-fold coincidence that can mimic delayed-coincidence signals. However, events accompanied by muons can be effectively suppressed by applying a muon veto, with an estimated rejection efficiency of about 78% [99].

8.4.2 Neutral Current (NC) Interaction

In neutral-current (NC) interactions mediated by the weak Z boson, the neutrino flavor remains unchanged before and after the interaction. At KamLAND, the dominant background from atmospheric-neutrino induced NC interactions arises from reactions in which a neutron is knocked out from the nucleus, as illustrated below.

$$\nu(\bar{\nu}) + {}^{12}\text{C} \rightarrow \nu(\bar{\nu}) + n + {}^{11}\text{C}^* \tag{8.27}$$

$$\nu(\bar{\nu}) + {}^{12}\text{C} \rightarrow \nu(\bar{\nu}) + 2n + {}^{10}\text{C} \tag{8.28}$$

Among these processes, the channel in which the final state consists of a neutron and an excited state of ^{11}C gives the largest contribution. In this case, scintillation light from recoil protons produced by the neutron, together with γ rays from the de-excitation of ^{11}C, constitute the prompt signal. The capture γ rays from the thermalized neutron then provide the delayed signal, which together form a delayed-coincidence signature. The cross section of NC interactions with carbon nuclei has not yet been well established. Therefore, in this study, we use the cross sections for neutrino-proton interactions measured at BNL [100] (Fig. 8.10) and the cross sections for neutrino-neutron interactions calculated in [101] on

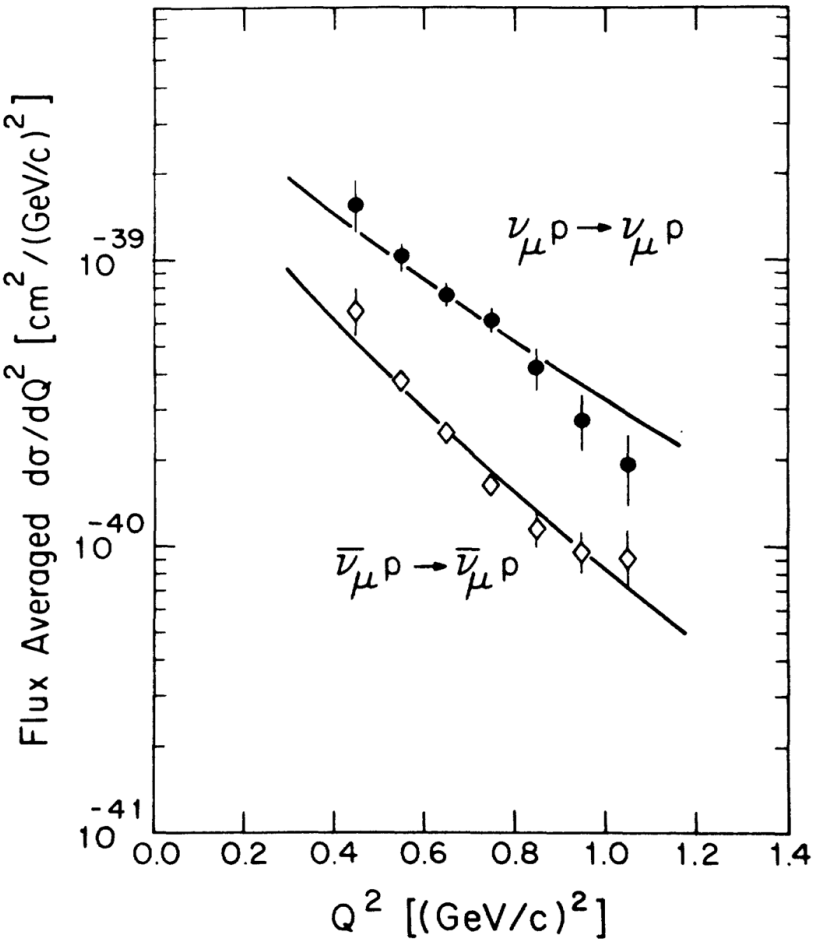

Figure 8.10: Flux-averaged differential cross sections for $\nu_\mu p \to \nu_\mu p$ and $\bar{\nu}_\mu p \to \bar{\nu}_\mu p$ [100]. The data points represent the measured differential cross sections obtained in this experiment, while the solid curves indicate the best-fit results of the fitting function.

the basis of the BNL results. An energy-dependent uncertainty of up to 18% is assigned to these cross sections.

Neutron emission from carbon nuclei can occur either from the P-shell (outer shell) or from the S-shell (inner shell). If the neutron is emitted from the P-shell, the excited $^{11}C^*$ decays by emitting a 2 MeV γ ray. On the other hand, if the neutron is emitted from the S-shell, the de-excitation of $^{11}C^*$ becomes more complicated, as described in [102]:

$$^{11}C^* \to \gamma \tag{8.29}$$
$$^{11}C^* \to {}^{10}B + p + \gamma \tag{8.30}$$
$$^{11}C^* \to {}^{6}Li + p + \alpha \tag{8.31}$$
$$^{11}C^* \to {}^{9}Be + 2p \tag{8.32}$$

For each decay mode, the visible energy is evaluated by converting the particle energies using an energy-scale model that incorporates the nonlinear effects of quenching. In NC interactions, only a small fraction of the atmospheric neutrino energy is transferred to the neutron, resulting in neutron kinetic energies below about 200 MeV. Consequently, the visible-energy spectrum rises gradually toward lower energies.

8.4.3 Summary of Atmospheric Neutrino Background

The atmospheric neutrino background rate in KamLAND has been numerically estimated in [99] with the systematic uncertainty from the atmospheric neutrino flux and cross section. In this study, the rejection efficiency of the KamNet cut (Sec. 6.4) and the associated systematic uncertainty (Sec. 6.5.5) are further taking into account. Fig. 8.11 shows atmospheric neutrino background spectra. The final numbers of atmospheric neutrino CC and NC events are evaluated to be 0.5 ± 0.3 and 10.1 ± 6.2, respectively.

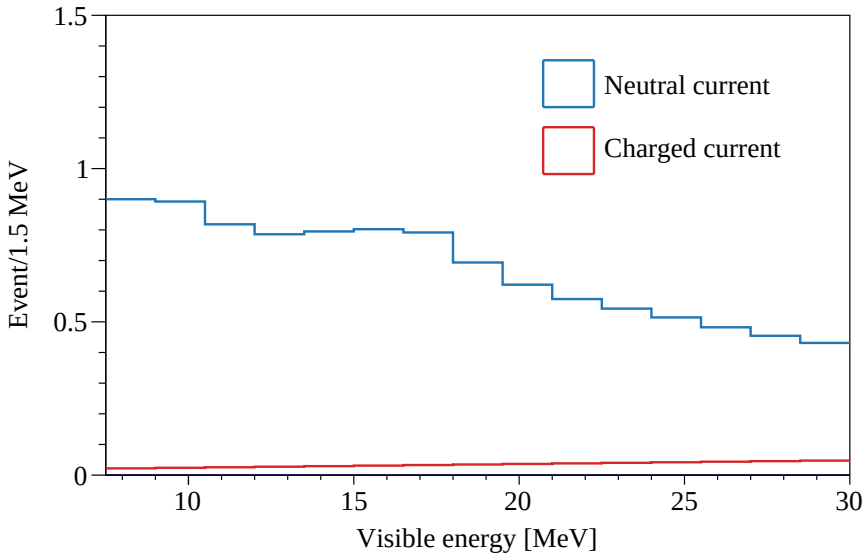

Figure 8.11: Atmospheric neutrino background spectra. Each spectrum is normalized to the expected number of events.

8.5 Fast Neutrons

Cosmic-ray muons arriving at the KamLAND site interact both inside and outside the detector, and the resulting high-energy neutrons produce delayed-coincidence events. Fig. 8.12 illustrates a schematic view of background events induced by fast neutrons. In this example, primary particles such as γ rays, pions, and neutrons generated by hadronic interactions of cosmic-ray muons react with elements such as Si and O in the surrounding rock, thereby producing fast neutrons. These fast neutrons create a prompt signal through recoil of protons or carbon nuclei inside the detector, and after thermalization, they are captured on protons or carbon nuclei, with the emitted γ rays forming the delayed signal. Most fast neutron events are rejected by applying a muon veto using the Cherenkov light in the OD; however, events remain as background if the muon passes through insensitive regions of the OD or does not traverse the OD at all.

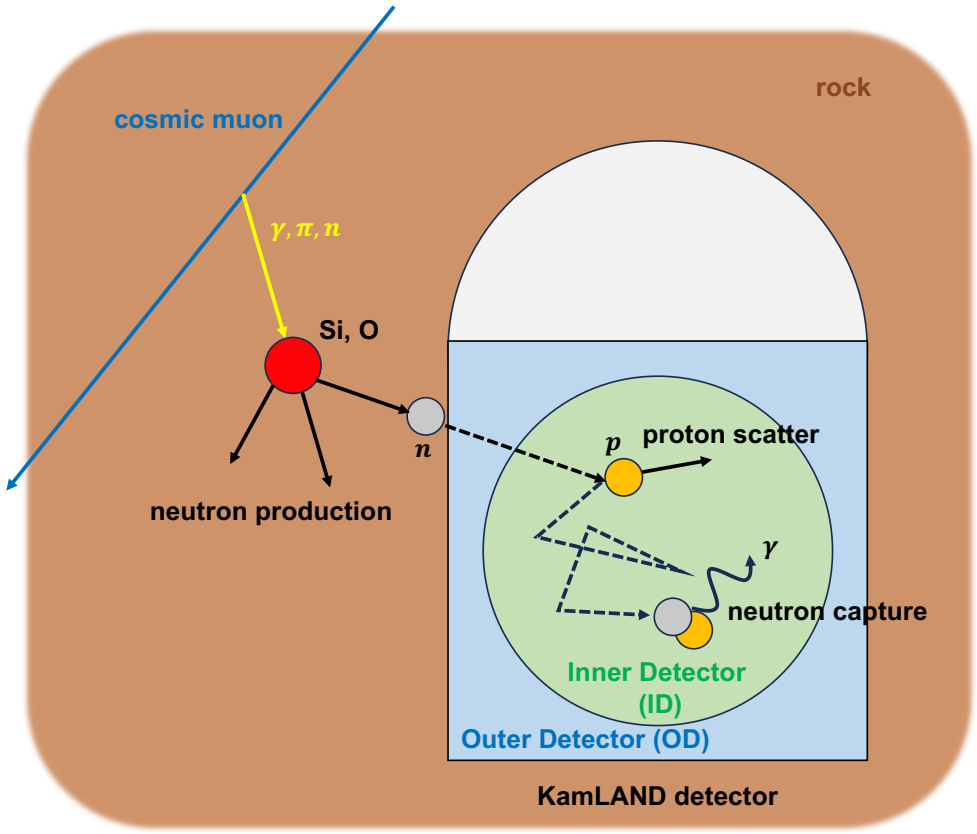

Figure 8.12: Schematic view of the fast neutron background in KamLAND.

In this study, the number of background events induced by fast neutrons is estimated based on [45]. The muon flux arriving at the detector is simulated using the MUon SImulation Code (MUSIC) [103]. MUSIC evaluates the interaction probability of muons by taking into account the topological profile of Mt. Ikenoyama, where KamLAND is located (Fig. 8.13), as well as the composition of the surrounding rock. The resulting muon energy spectrum and angular distribution at the KamLAND site are shown in Fig. 8.14 and Fig. 8.15, respectively.

For the simulation of interactions inside the detector, a KamLAND geometry implemented with Geant4 [74] is employed. Muons are generated from a disk placed above KamLAND according to the energy and angular distributions obtained from MUSIC. In principle, simulating optical photons is required to determine whether muons are tagged by the OD. However, since such photon simulations are computationally very demanding, only

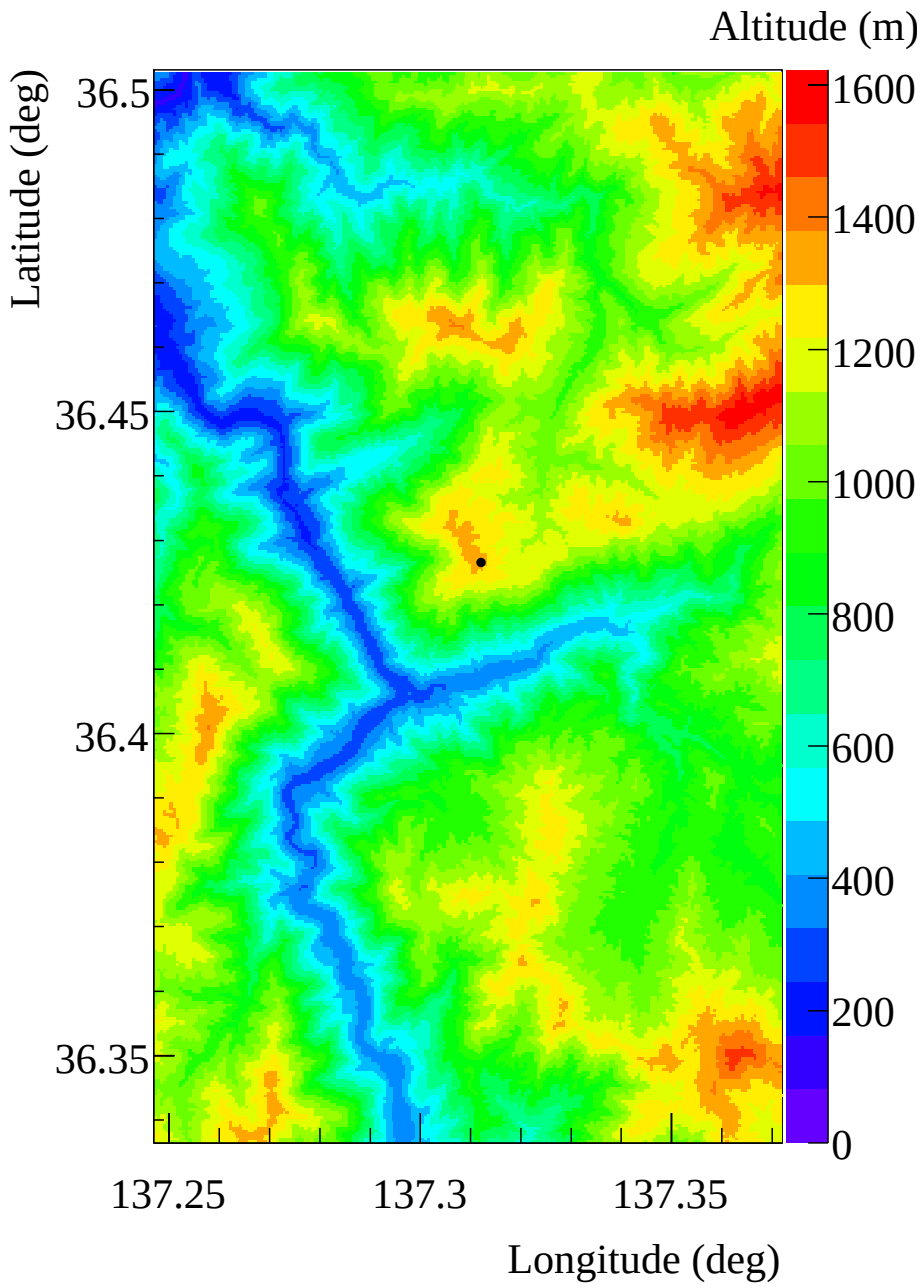

Figure 8.13: Ikenoyama topological profile [104]. This figure is taken from [79]. The black point near the center is the location of KamLAND detector.

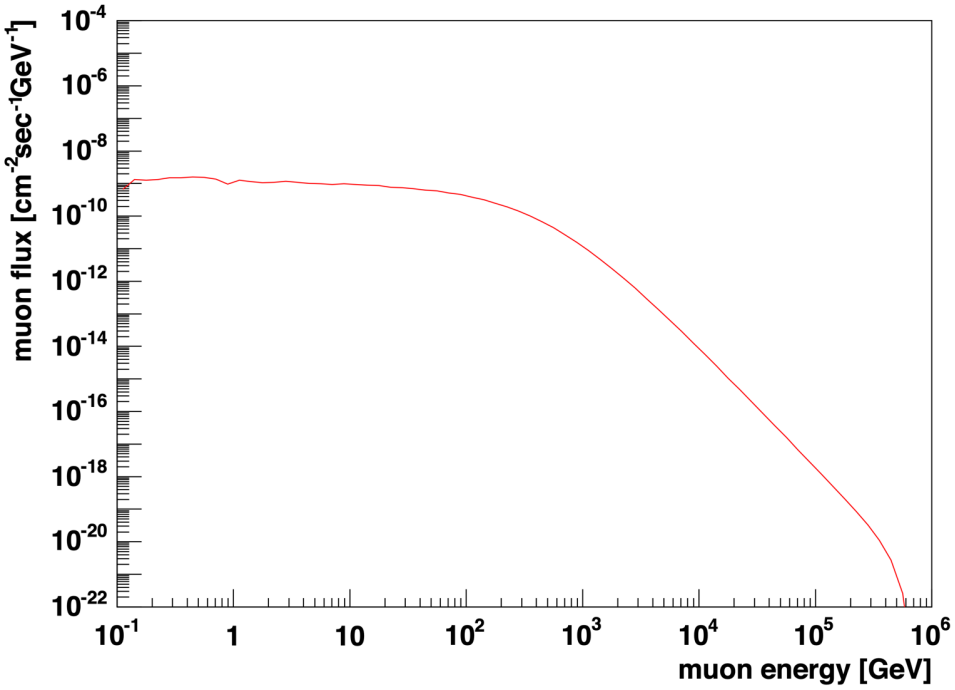

Figure 8.14: Cosmic muon energy distributions at KamLAND site [105].

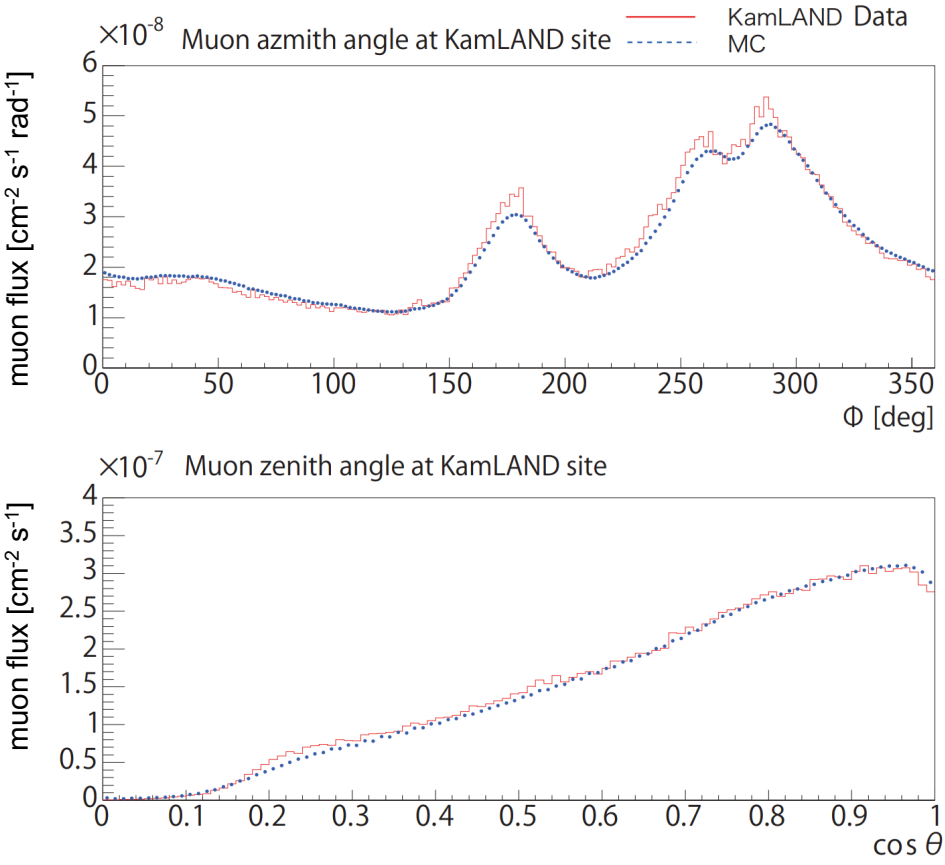

Figure 8.15: Cosmic muon angular distributions at KamLAND site [105].

the track information of charged particles exceeding the Cherenkov threshold in the OD is recorded at this stage. For each event, the deposited energy inside the detector, E_i, is used to calculate the total prompt energy, while the event vertex and time are reconstructed as the weighted averages of the spatial and temporal distributions of the energy deposits. The reconstructed quantities are defined as follows:

$$E_p = \sum_i E_i \tag{8.33}$$

$$\vec{x}_p = \frac{\sum_i E_i \cdot \vec{x}_i}{\sum_i E_i} \tag{8.34}$$

$$T_p = \frac{\sum_i E_i \cdot T_i}{\sum_i E_i} \tag{8.35}$$

Based on these reconstructed parameters, event selection using delayed coincidence is performed. The selection criteria for delayed-coincidence events are almost identical to those described in Sec. 7.4, except that a time-correlation requirement of $\Delta T > 10\,\mu$sec is imposed to suppress contributions from decay electrons. Subsequently, only the fast neutrons identified as delayed-coincidence events are re-simulated. In this re-simulation, only optical photons in the OD are generated in order to determine whether the events can be tagged by the OD.

Fig. 8.16 shows the radial distributions and energy spectra of OD-tagged and OD-untagged events obtained from the fast-neutron simulation, together with the OD-tagged events observed in data. Near the ID boundary (∼650 cm), the vertex reconstruction quality deteriorates, leading to a broader distribution in data; however, within the fiducial volume, the radial distributions in data and simulation are consistent. Assuming that the radial distribution of fast neutrons can be modeled as $f(R) \propto \exp(R/\lambda)$ as a function of the distance R from the detector center, a value of $\lambda = 50.9 \pm 3.0$ cm is obtained. On the other hand, in the energy distribution, noticeable discrepancies between data and simulation are observed, particularly in the low-energy region. This discrepancy originates from the fact that the neutron yield from rock is poorly known. Therefore, a conservative 100% uncertainty is assigned to the expected number of fast-neutron events.

Consequently, incorporating the KamNet rejection efficiency for fast neutrons shown in Tab. 6.8, the expected number of fast neutron background is estimated to be 2.5 ± 2.5.

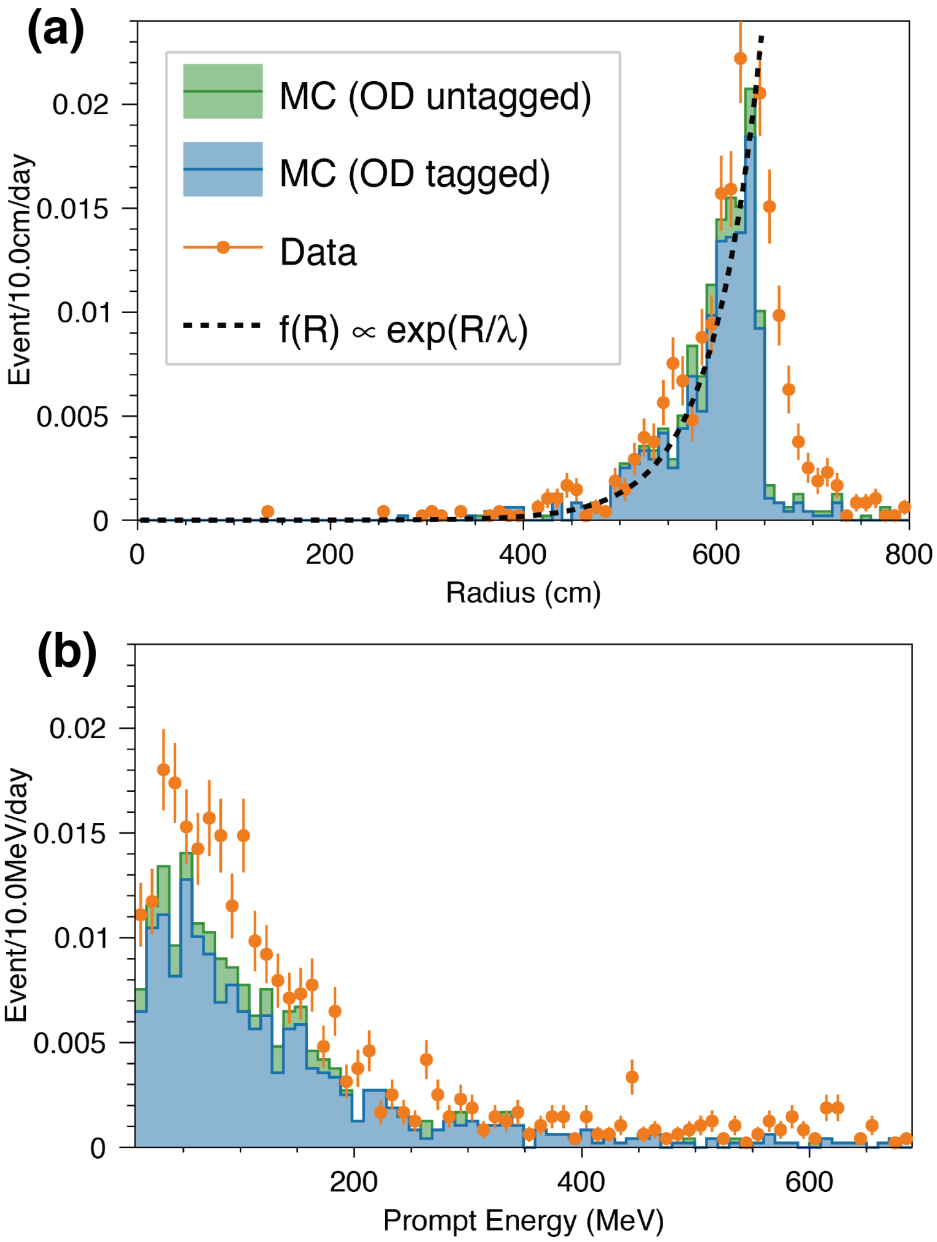

Figure 8.16: Radial distributions and energy spectra of fast neutron events [45]. Events in the radial distribution (a) correspond to the energy region E_p =7.5–30 MeV, while events in the energy spectrum (b) are reconstructed within the 550 cm fiducial volume. The black dashed line indicates the exponential fit function $f(R)$. Simulated OD-tagged (blue) and OD-untagged (green) histograms are shown in stacked form.

8.6 Accidental Background

Two uncorrelated events can sometimes be observed as a delayed coincidence, referred to as an accidental background. In the low-energy region, such coincidences mainly originate from radioactive impurities produced in the balloon, the ID stainless steel tank, and surrounding structures or rock. In particular, ^{208}Tl (2.62 MeV γ) contributes significantly to accidental backgrounds, since its gamma rays can fall within both the prompt and delayed energy regions. In contrast, in the higher-energy region ($E_p > 5$ MeV), prompt events of accidental backgrounds are mainly caused by spallation backgrounds listed in Tab. 7.1, whose decay lifetimes and Q-values are relatively large. The number of accidental backgrounds increases toward the outer balloon; therefore, in this analysis, the fiducial volume is restricted to a radius of 550 cm to suppress their contribution.

The number of accidental background events is estimated from samples collected under the same selection criteria as those used in the delayed coincidence analysis, except for the time correlation requirement, ΔT. To select uncorrelated pairs of prompt and delayed candidates, events observed within the offtime window (0.01–20 s) are used instead of the ontime window (0.5–1000 μs) for the delayed coincidence. Fig. 8.17 shows the prompt energy spectrum of accidental background events, and Fig. 8.18 shows their vertex distribution. Among these events, those with prompt energies above 7.5 MeV and vertices within the 550 cm fiducial volume are counted to obtain the number of events and the corresponding statistical uncertainty. The expected number of accidental background events in the astrophysical neutrino search is then derived by multiplying this number and its uncertainty by the scaling factor of the time windows:

$$\text{scaling factor} = \frac{\text{ontime window}\,(0.5\text{–}1000\,[\mu\text{sec}])}{\text{offtime window}\,(0.01\text{–}20\,[\text{sec}])} = 5 \times 10^{-5}. \tag{8.36}$$

As described in Sec. 6.6, the characteristics of the prompt event of the accidental background are same as those of IBD events. Hence, the same KamNet rejection efficiency and associated systematic uncertainty can be applied to the accidental background. Taking the statistical uncertainty of the offtime window and the KamNet-related systematic uncertainty into account, the expected number of accidental background is estimated to be 0.11 ± 0.02.

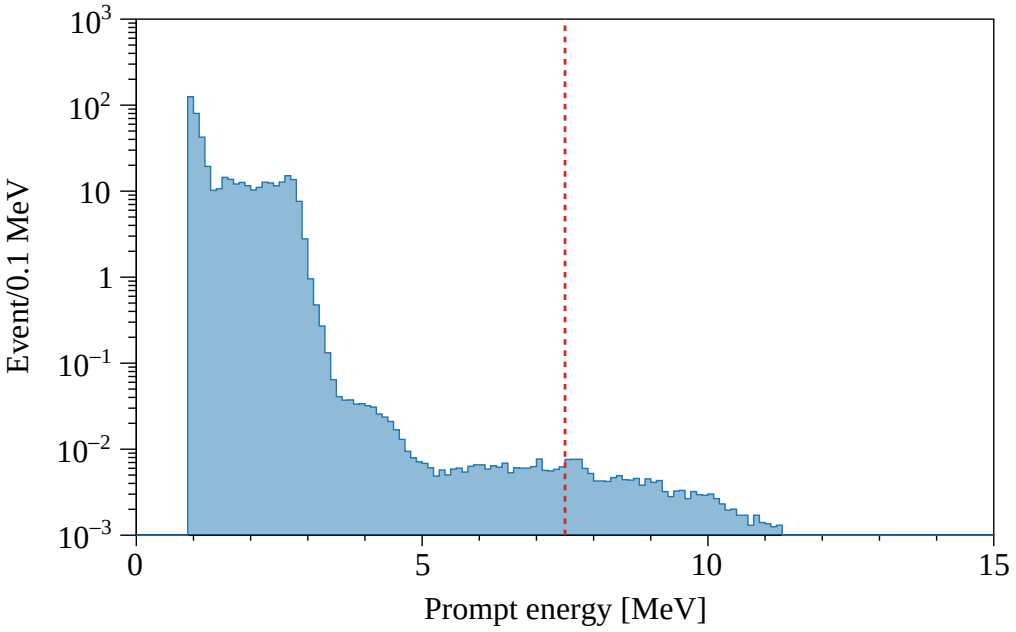

Figure 8.17: Prompt energy spectrum of the accidental background. The red vertical line indicates the energy threshold of 7.5 MeV. The event rate is scaled according to the ontime/offtime window.

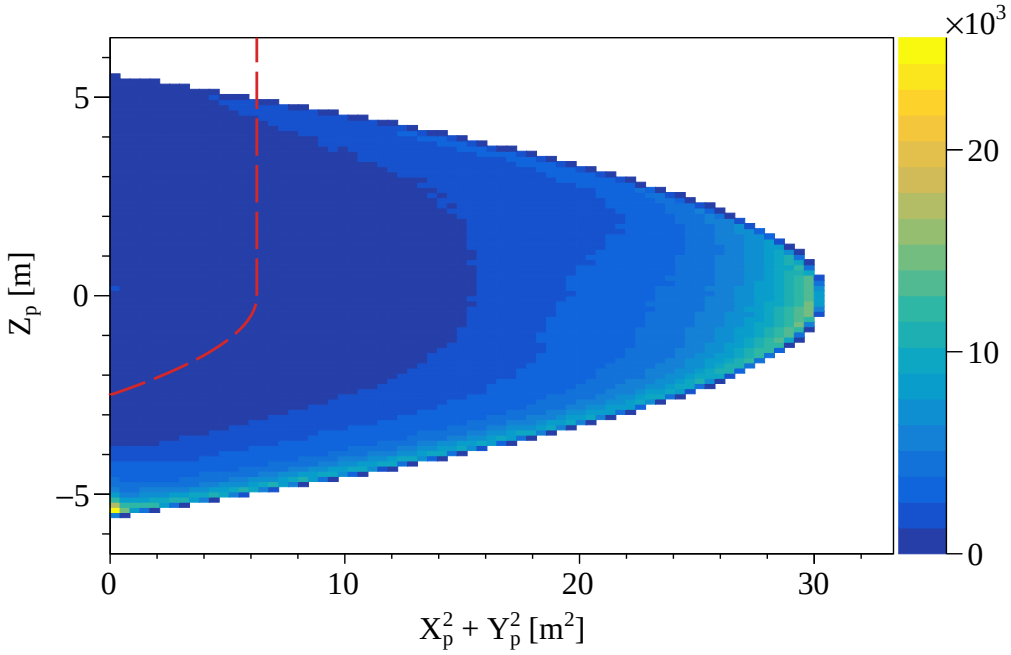

Figure 8.18: Prompt vertex distribution of the accidental background. The red line represents miniballoon region. Event rate is not scaled with offtime window.

8.7 Background Summary

Tab. 8.4 summarizes the expected number of backgrounds in the astrophysical antineutrino search. These values are used as initial inputs and penalty terms in the spectral fitting described in Chap. 9.

Table 8.4: Summary of the expected number of backgrounds

Source	Number of events
Reactor $\bar{\nu}_e$	1.0 ± 0.6
Spallation ^{9}Li	1.9 ± 6.6
Atmospheric neutrino CC	0.5 ± 0.3
Atmospheric neutrino NC	10.1 ± 6.2
Fast neutron	2.5 ± 2.5
Accidental background	0.11 ± 0.02
Total	16.2 ± 9.4

Chapter 9

Analysis and Result

In this chapter, various searches for astrophysical $\bar{\nu}_e$s are performed using the selected six $\bar{\nu}_e$ candidates and the constructed background models. The entire KamLAND dataset is used for the search, with the prompt energy region defined as 7.5–30 MeV and the fiducial volume restricted to within 550 cm from the detector center. The searches for DSNB, PBH neutrinos, and solar antineutrinos are conducted through spectral fitting, while those for model-independent $\bar{\nu}_e$s and neutrinos from light dark matter annihilation are carried out based on the observed and expected numbers of events in each energy bin.

9.1 Diffuse Supernova Neutrino Background

In the astrophysical $\bar{\nu}_e$ search, the data are fitted using the prompt energy spectra and radial distribution of each event component. Since each component has a characteristic energy spectrum, its shape provides essential information for estimating the number of events. In addition, while fast neutrons exhibit a radial distribution that increases toward the detector edge, all other events are spatially uniform. Therefore, the radial distribution is also utilized as discriminating information.

Chi-square formulation for spectrum fitting

As estimated in Chap. 8, the atmospheric neutrino NC provides the largest contribution among all background components. Therefore, a two-dimensional scan is performed over the numbers of astrophysical $\bar{\nu}_e$ signal and atmospheric neutrino NC backgrounds. The χ^2 used in this analysis is defined as follows:

$$\chi^2 = \chi^2_{\text{rate}} + \chi^2_{\text{shape}} + \chi^2_{\text{penalty}} + \chi^2_{\text{BG}}. \tag{9.1}$$

The rate term χ^2_{rate} is expressed as follows:

$$\chi^2_{\text{rate}} = 2\left\{\mu - N_{\text{observed}} + N_{\text{observed}} \ln \frac{N_{\text{observed}}}{\mu}\right\}, \tag{9.2}$$

$$\mu = N_{\text{astro.}\nu} + N_{\text{NC}} + \sum_{i}^{5} N_{\text{BG}i}. \tag{9.3}$$

Here, N_{observed} denotes the number of observed $\bar{\nu}_e$ candidates, $N_{\text{astro.}\nu}$ the number of astrophysical $\bar{\nu}_e$ events, and N_{NC} the number of atmospheric neutrino NC background events. $N_{\text{BG}i}$ represents the numbers of the other background components ($i = 1, 2, ..., 5$), namely reactor neutrinos, spallation ^{9}Li, atmospheric neutrino CC, and accidental backgrounds. The statistical uncertainty σ_{stat} is given by the square root of the total number of expected events.

The shape term $\chi^2_{\rm shape}$, which incorporates the energy and radial distributions, is expressed as follows:

$$\chi^2_{\rm shape} = \sum_{n}^{N_{\rm observed}} \left\{ -2 \ln \left(\frac{\sum_j^7 N_j f_j(R) \cdot g_j(E)}{\sum_j^7 N_j} \right) \right\}. \tag{9.4}$$

Here, $f_j(R)$ and $g_j(E)$ denote the normalized radial and energy distributions, respectively, and j represents the seven event components: the astrophysical $\bar{\nu}_e$ signal, the atmospheric NC background, and the five additional background sources. As described in Sec. 8.5, the $f(R)$ distribution for fast neutrons is modeled as $\propto \exp(R/50.9\,\mathrm{cm})$, while the distributions for the other events are uniform.

The penalty term associated with systematic uncertainties is given by

$$\chi^2_{\rm penalty} = \sum_k \delta_k^2, \tag{9.5}$$

where δ_k corresponds to each component of the detector-related systematic uncertainties described in Sec. 7.7. The penalty term accounting for the uncertainties in the background estimation is defined as

$$\chi^2_{\rm BG} = \sum_i^5 \frac{(N_{{\rm BG}i} - N_{{\rm BG}i}^{\rm expected})^2}{\delta^2_{{\rm BG}i}}, \tag{9.6}$$

in which $N_{{\rm BG}i}^{\rm expected}$ denotes the expected number of events for the i-th background, and $\delta_{{\rm BG}i}$ represents the corresponding uncertainty.

Fit results for the DSNB model (Horiuchi+09)

At first, the DSNB signal is fitted assuming the reference model by Horiuchi+09. Tab. 9.1 summarizes the expected and best-fit numbers of events for each event sources. In this analysis, constraints in the χ^2 are applied to the reactor neutrino, spallation ^{9}Li, and fast neutron backgrounds based on their estimated uncertainties. In contrast, the atmospheric neutrino CC is treated as a free parameter that is anti-correlated with the atmospheric NC background, since it is difficult to distinguish CC events from NC events based solely on the energy and radial distributions. The accidental background is treated as a fixed parameter, as its contribution and uncertainty is small.

Table 9.1: The expected and best-fit numbers of events in the DSNB search. The expected DSNB signal is derived from the prediction by Horiuchi [5].

Source	Expected	Best fit	Fit condition
Reactor $\bar{\nu}_e$	1.0 ± 0.6	1.0	limited
Spallation ^{9}Li	1.9 ± 6.6	2.3	limited
Atmospheric neutrino CC	0.5 ± 0.3	1.6	free
Atmospheric neutrino NC	10.1 ± 6.2	0.0	scan
Fast neutron	2.5 ± 2.5	1.2	limited
Accidental background	0.11 ± 0.02	0.11	fix
DSNB (Horiuchi+09)	1.0	0.0	scan
Total	17.2 ± 9.4	6.2	

Fig. 9.1 shows the two-dimensional scan of the DSNB signal and atmospheric NC background events. The best-fit number of DSNB signal for the Horiuchi+09 model is found to be zero, and the 90% confidence level upper limit is 5.2 events. This range includes the predicted value of 1.0 events, indicating that no significant excess of the signal is observed for this model. On the other hand, although the best-fit value of the atmospheric neutrino NC background is zero, the 1σ uncertainty of the expected number overlaps with the 1σ range of the fit result. Fig. 9.2 shows the prompt energy spectra of the best-fit backgrounds and the DSNB signal at the 90% C.L. upper limit, while Fig. 9.3 shows the corresponding radial distributions.

Fig. 9.4 shows the two-dimensional scan of the DSNB signal and atmospheric neutrino CC events, and Fig. 9.5 shows that of atmospheric neutrino NC and CC events. The 1σ range of the fitted atmospheric CC events is found to include the expected number. In this fit, the best-fit value of the atmospheric CC event is 1.6, and its magnitude is reversed relative to the NC event compared to the expected values. This can be interpreted as follows: the observed energy spectrum favors the atmospheric CC component, and due to the strong anti-correlation among the DSNB signal, atmospheric NC, and CC components, the fitted numbers of the other components are consequently reduced.

Effect of energy-spectrum distortion

If the KamNet selection efficiency depends on energy, it distorts the spectral shapes of the individual event components. Because it is difficult to incorporate this spectral-distortion effect directly into the fit statistic χ^2, a different approach is adopted in this study. Specifically, the 90% C.L. upper limit on the number of DSNB events is conservatively corrected based on the fit results obtained for multiple spectral-distortion patterns.

First, the KamNet efficiency is estimated from simulation in each of the observed-energy ranges 8.5–13 MeV, 13–20 MeV, and 20–30 MeV. Next, several variations are constructed in which the efficiency at each energy range is shifted upward or downward by the systematic uncertainty evaluated in Sec. 6.5.5. The efficiency values including these uncertainties are interpolated with a polynomial to define a set of models describing possible spectral-distortion patterns. Such spectral-distortion models are prepared separately for the signal and background components, and the fits are performed using combinations of these models. Fig. 9.6 shows examples of the spectral distortion applied to the DSNB signal. In total, 20 combinations of spectral-distortion patterns are constructed, and for each combination the $\Delta\chi^2$ distribution for the DSNB signal is obtained. The resulting distributions are shown in Fig. 9.7. From these results, a distribution of the 90% C.L. upper limits is formed and its standard deviation is evaluated. Finally, the nominal 90% C.L. upper limit of 5.2 is shifted in the conservative direction by one standard deviation, yielding a final 90% C.L. upper limit of 5.9 on the DSNB signal.

Comparison of fit results for various DSNB models

Next, spectral fitting searches are performed for various DSNB models introduced in Sec. 2.1.6. The main characteristics of each model are summarized below.

- Totani model

  One of the earliest proposed DSNB models, predicting a large flux. In this analysis, the *constant model*, which assumes a constant supernova rate after $z = 5$, is used.

- Kaplinghat model

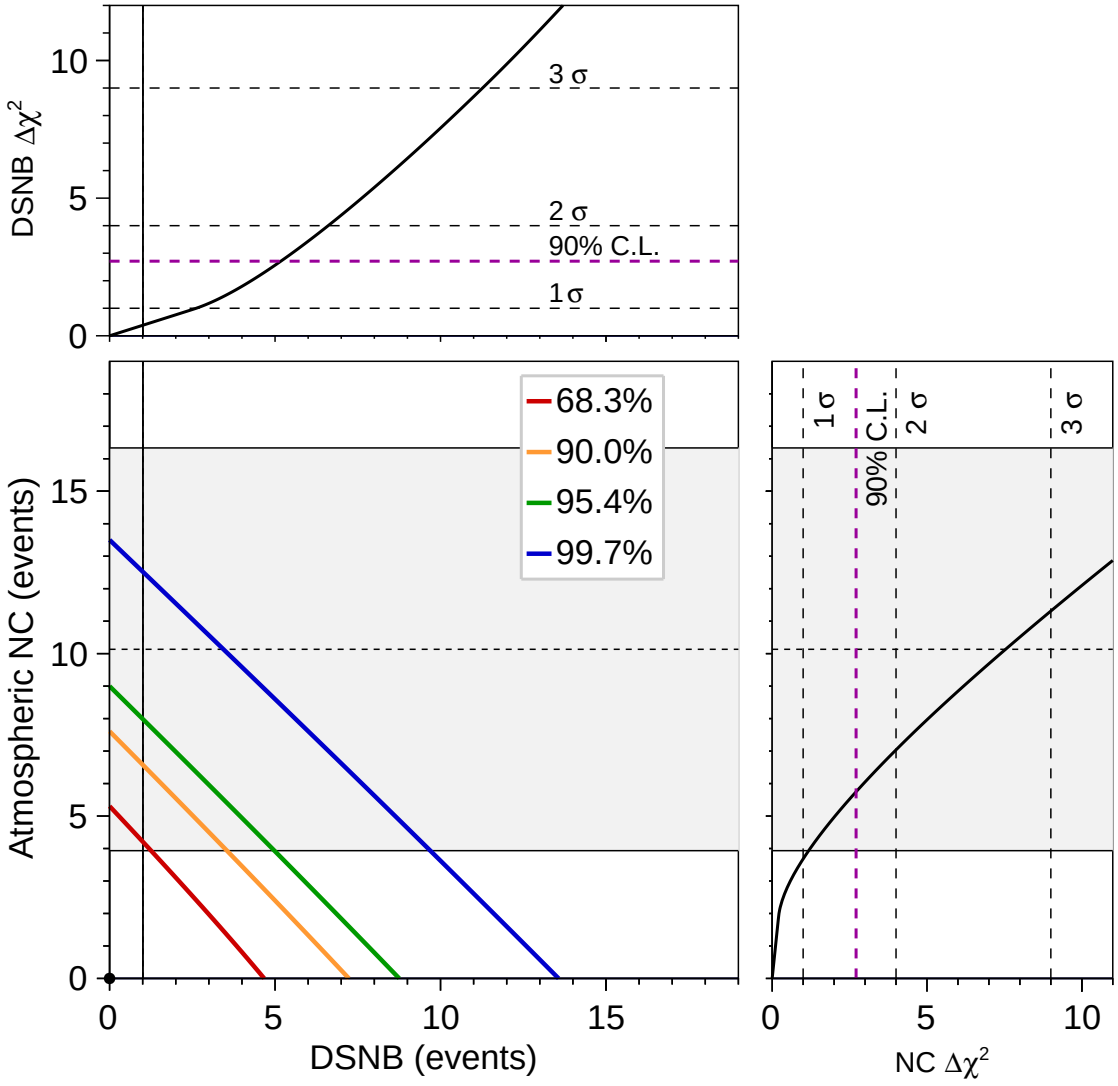

Figure 9.1: Two-dimensional scan of the number of DSNB and atmospheric neutrino NC events. The DSNB model of Horiuchi [5] is adopted. Color contours indicate the 1σ (red), 90% (orange), 2σ (green), and 3σ (blue) confidence regions. The best-fit numbers of DSNB and NC events are both 0.0 (black circle). The horizontally hatched region denotes the expected number of NC events with its 1σ uncertainty, while the vertical line indicates the expected number of DSNB events. The top and right panels show the one-dimensional $\Delta\chi^2$ distributions for the DSNB and NC event components, respectively. The 90% C.L. upper limit on the number of DSNB events is 5.2.

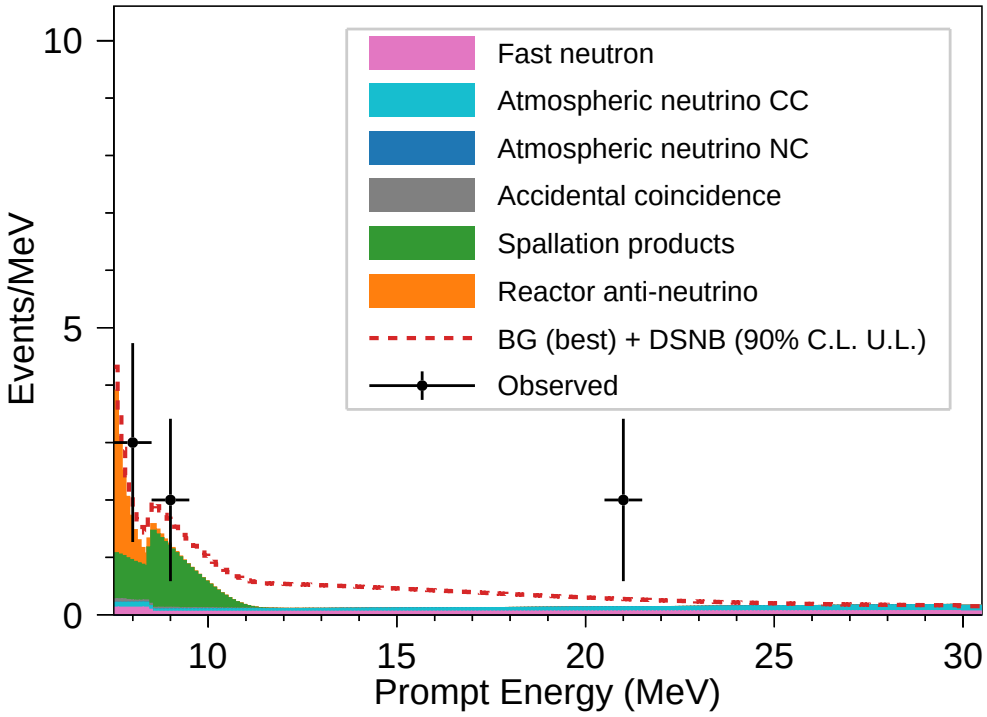

Figure 9.2: Prompt energy spectrum of the best-fit backgrounds and the DSNB signal at the 90% C.L. upper limit. The DSNB model of Horiuchi [5] is adopted. All histograms are stacked.

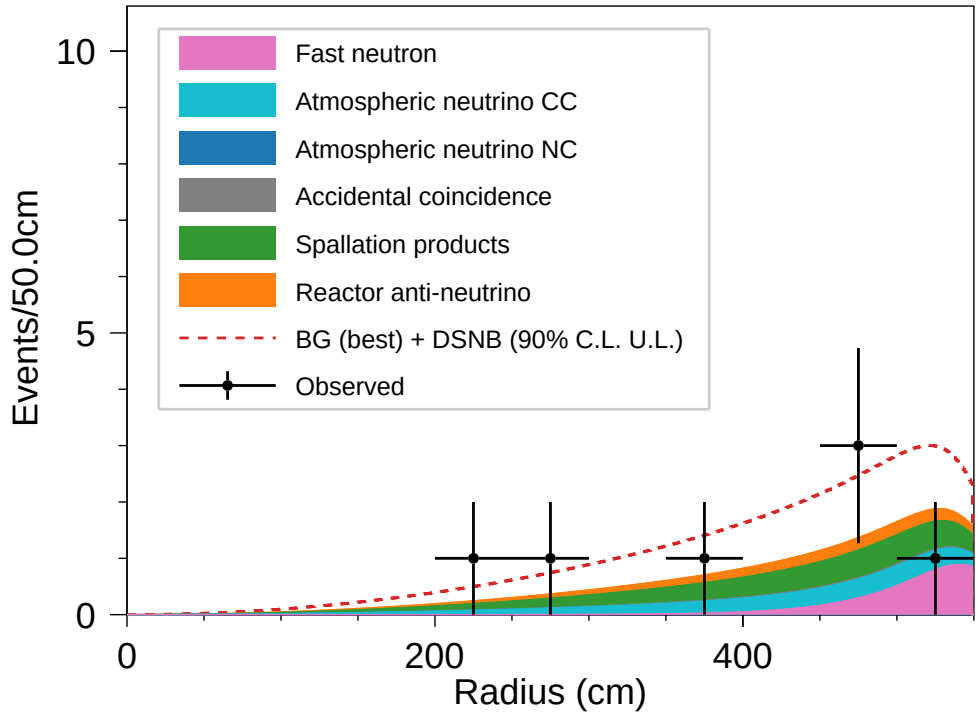

Figure 9.3: Radial distribution of the best-fit backgrounds and the DSNB signal at the 90% C.L. upper limit. The DSNB model of Horiuchi [5] is adopted. All histograms are stacked.

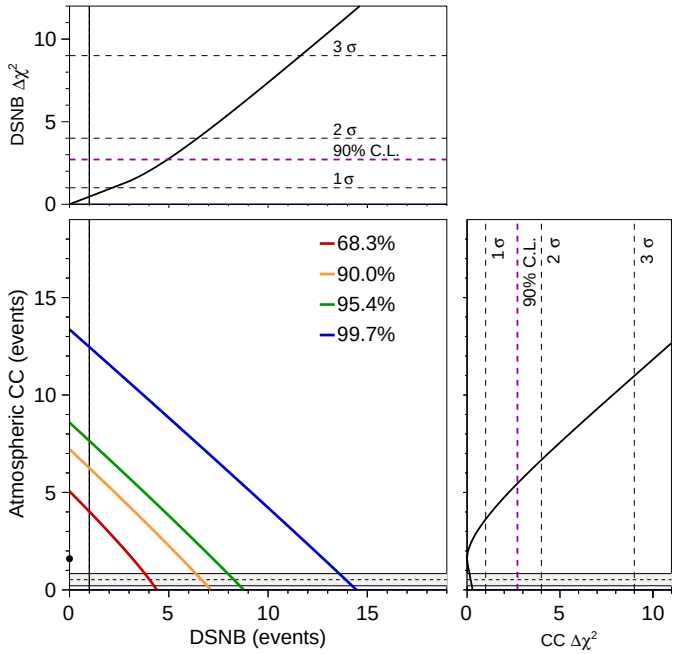

Figure 9.4: Two-dimensional scan of the number of DSNB and atmospheric neutrino CC events. The DSNB model of Horiuchi is adopted. The best-fit numbers of DSNB and CC events are 0.0 and 1.6, respectively (black circle). The horizontally hatched region denotes the expected number of CC events with its 1σ uncertainty, while the vertical line indicates the expected number of DSNB events.

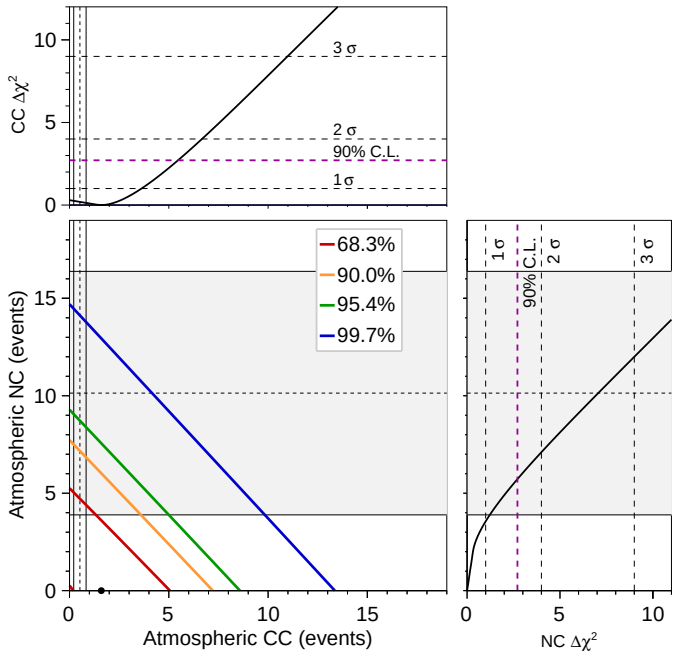

Figure 9.5: Two-dimensional scan of the number of atmospheric neutrino NC and CC events. In this figure, the astrophysical neutrino signal is fixed to zero. The best-fit numbers of atmospheric NC and CC events are 0.0 and 1.6, respectively (black circle). The horizontally hatched region denotes the expected number of NC events with its 1σ uncertainty, while the vertical hatched region indicates the expected number of CC events with its 1σ uncertainty.

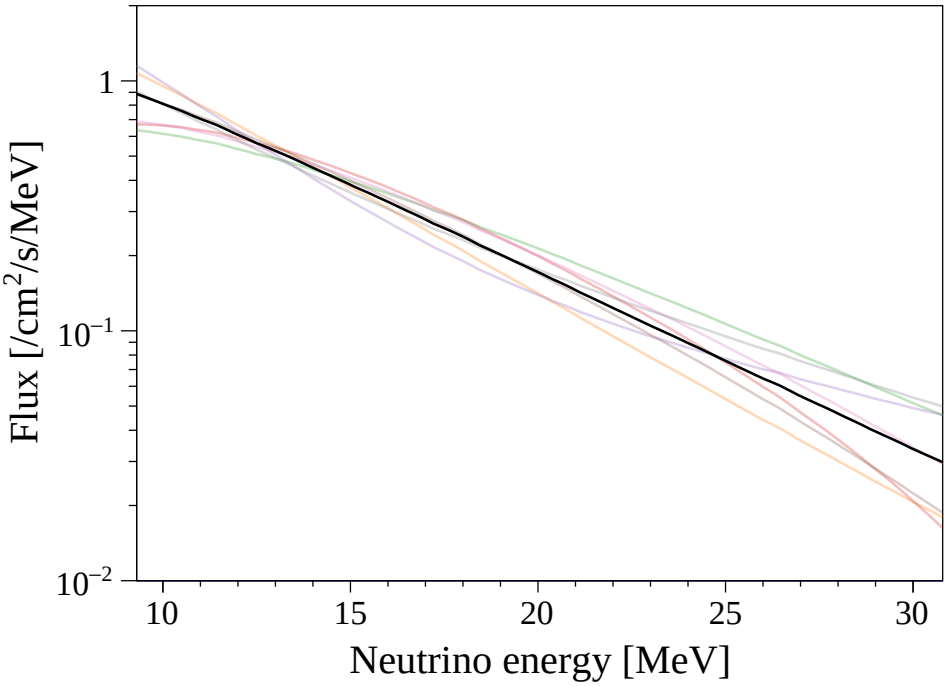

Figure 9.6: Examples of spectral distortion in the DSNB signal. The black line shows the nominal spectrum, while the colored lines indicate the spectral-distortion patterns.

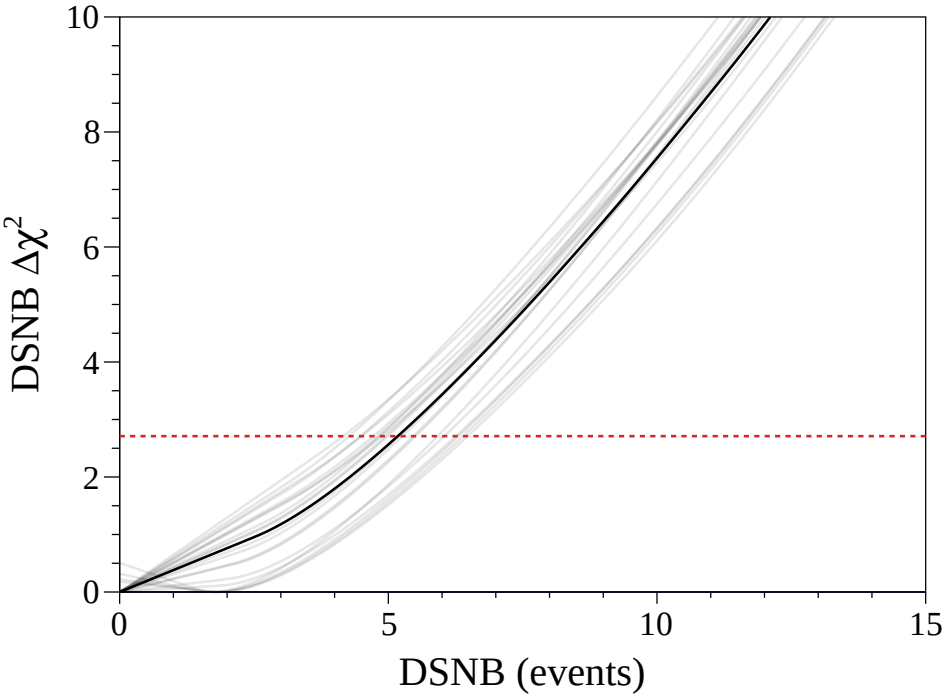

Figure 9.7: $\Delta\chi^2$ distributions of the DSNB signal for various spectral-distortion patterns. The solid black line shows the fit result for the nominal spectrum, while the light-gray lines show the fit results for the distorted spectra. The red horizontal dotted line indicates the 90% confidence level.

The supernova rate is estimated using a metal enrichment rate that is less sensitive to the initial mass function. Along with Totani+95, this model is often regarded as providing an upper-limit estimate of the DSNB flux.

- Ashida model

  This model incorporates the black-hole formation rate and the chemical evolution of galaxies by type. The flux below 10 MeV increases due to contributions form early-type galaxies, while that above 30 MeV is enhanced by black-hole formation. In this analysis, the version adopting the star formation rate by Hopkins and Beacom (HB06) is used.

- Horiuchi model

  The supernova rate is estimated based on the optical measurement of the star formation rate. The model with an effective neutrino temperature of 6 MeV is also adopted as a reference in the SK(-Gd) experiment.

- Nakazato model

  The neutrino emission from core-collapse supernovae is modeled as a function fo the progenitor's initial mass and metallicity. The prediction under the normal mass hierarchy yields one of the smallest DSNB fluxes among the models proposed to date.

The background models and treatment of fit parameters are identical to those described in the analysis of Horiuchi+09. The results of the two-dimensional scans, prompt energy spectra, and radial distributions for each model are described in Appendix A.1. Tab. 9.2 summarizes the best-fit numbers of DSNB signals and their predicted values. For all models, the best-fit number of DSNB signal is 0.0, indicating no significant excess.

The DSNB flux values obtained from the fits, along with the predicted fluxes, are summarized in Tab. 9.3. The predicted flux corresponds to the integral over the neutrino energy range of 8.3–30.8 MeV, which matches the prompt energy range of 7.5–30 MeV. The $+1\sigma$ and 90% C.L. upper-limit flux values are derived from the simple ratio between the event numbers and the corresponding flux. Fig. 9.8 compares the limits on the DSNB flux obtained in this study with the model predictions. The DSNB flux limits obtained for each model in this analysis reach approximately half of the 2022 KamLAND result [45]. This improvement is largely attributed to the enhanced event discrimination provided by the KamNet event selection developed in this study.

Table 9.2: Fitting results and predicted values for the number of DSNB events. The best-fit numbers of DSNB events are shown with 1σ confidence intervals.

DSNB model	Best fit	90% C.L. U.L.	Predicted
Totani+95 (constant)	$0.00^{+3.9}_{-0.0}$	6.0	3.9
Kaplinghat+00	$0.00^{+2.9}_{-0.0}$	5.5	2.6
Ashida+23 (HB06, NH)	$0.00^{+3.5}_{-0.0}$	6.1	1.8
Horiuchi+09 (6 MeV)	$0.00^{+3.6}_{-0.0}$	5.9	1.0
Nakazato+15 (max, IH)	$0.00^{+2.9}_{-0.0}$	5.6	0.5
Nakazato+15 (min, NH)	$0.00^{+2.7}_{-0.0}$	5.3	0.2

Table 9.3: Fitting results and predicted values for the DSNB fluxes (in $\mathrm{cm}^{-2}\,\mathrm{s}^{-1}$). The best-fit values of DSNB fluxes are shown with 1σ confidence intervals.

DSNB model	Best fit	90% C.L. U.L.	Predicted
Totani+95 (constant)	$0.00^{+24.9}_{-0.0}$	38.6	25.0
Kaplinghat+00	$0.00^{+19.8}_{-0.0}$	37.9	17.9
Ashida+23 (HB06, NH)	$0.00^{+24.3}_{-0.0}$	43.0	12.2
Horiuchi+09 (6 MeV)	$0.00^{+23.7}_{-0.0}$	39.1	6.7
Nakazato+15 (max, IH)	$0.00^{+20.7}_{-0.0}$	40.3	3.3
Nakazato+15 (min, NH)	$0.00^{+19.5}_{-0.0}$	38.6	1.4

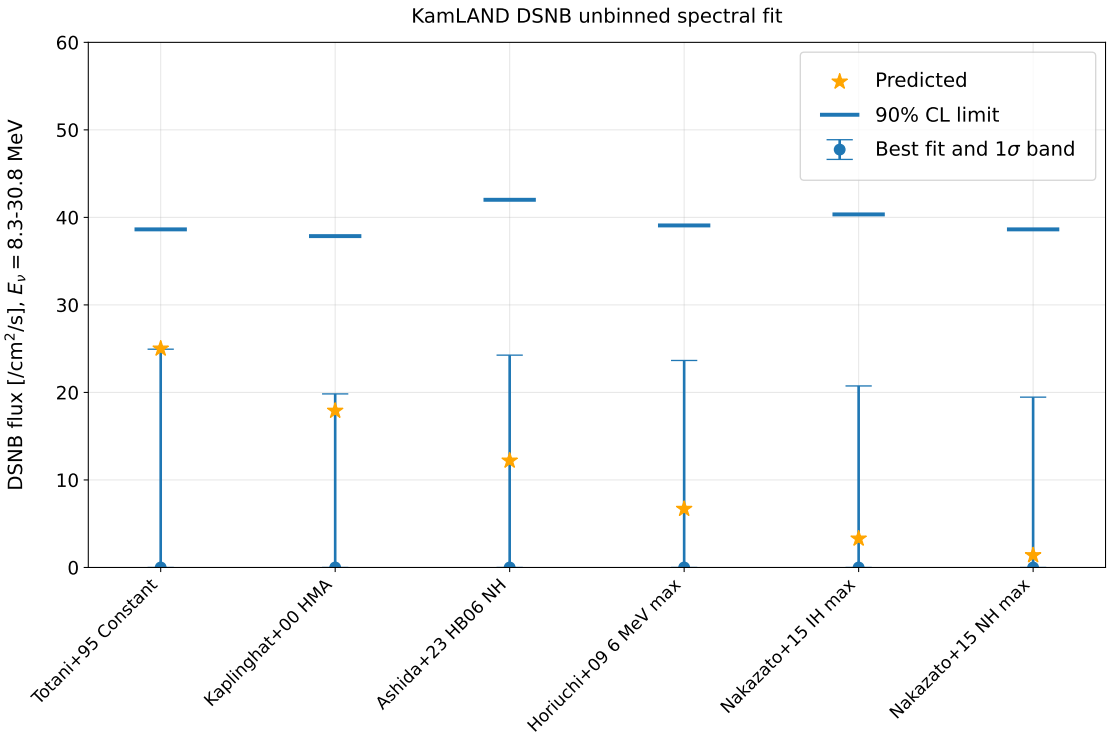

Figure 9.8: Fitting results and predicted values for the DSNB fluxes. The best-fit DSNB fluxes are shown with 1σ confidence interval bands and 90% C.L. upper-limit lines.

9.2 Primordial Black Hole

In the search for neutrinos emitted from PBHs, the same χ^2 function as defined in Eq. 9.1 is used for the fitting, as in the DSNB analysis. In this case, the input astrophysical $\bar{\nu}_e$ signal corresponds to the case where $f_{\mathrm{PBH}} = 1$ (f_{PBH} represents the ratio of the PBH energy density to the dark matter energy density). As described in Sec. 2.4, f_{PBH} is proportional to the total flux; therefore, the ratio of the fitted number of signal events to the expected number of events directly provides the value of f_{PBH} obtained in this analysis. Tab. 9.4 summarizes the expected and best-fit numbers of events for each event source in the case of a PBH mass of 1×10^{15} g. The two-dimensional scan result between the PBH signal and the atmospheric neutrino NC background for this PBH mass is shown in Fig. 9.9, while the fitting result for prompt energy spectrum and radial distribution are presented in Fig. 9.10 and Fig. 9.11, respectively. In this fit, both the atmospheric NC and CC backgrounds yield best-fit values of 0.0 events. This outcome can be attributed to the fact that the neutrino energy spectrum from a PBH with this mass peaks at higher energies. This makes the observed energy distribution more compatible with the PBH neutrino signal than with atmospheric neutrinos.

Table 9.4: The expected and best-fit numbers of events in the PBH neutrino search. The expected PBH neutrino signal is derived assuming a f_{PBH} of 1 and a PBH mass of 1×10^{15} g.

Source	Expected	Best fit	Fit condition
Reactor $\bar{\nu}_e$	1.0 ± 0.6	1.0	limited
Spallation ^{9}Li	1.9 ± 6.6	2.4	limited
Atmospheric neutrino CC	0.5 ± 0.3	0.0	free
Atmospheric neutrino NC	10.1 ± 6.2	0.0	scan
Fast neutron	2.5 ± 2.5	0.9	limited
Accidental background	0.11 ± 0.02	0.11	fix
PBH ν (1×10^{15} g)	416.8	1.7	scan
Total	16.2 ± 9.4 (BG only)	6.1	

The energy spectrum of PBH neutrinos varies significantly with PBH mass. The two-dimensional scan results, prompt energy spectra, and radial distributions for PBH masses other than 1×10^{15} g are presented in Appendix A.2. Tab. 9.5 summarizes the 90% C.L. upper limits on f_{PBH}, derived from the fitted and expected numbers of events for each PBH mass. Here, as in the DSNB search, the effect of energy-spectrum distortion induced by the KamNet selection is taken into account. Fig. 9.12 compares the f_{PBH} limits obtained in this study with those derived from the SK open data [106]. This analysis provides, among the neutrino observations, the most stringent constraints to date on the fraction of dark matter composed of PBHs with masses above 5×10^{15} g.

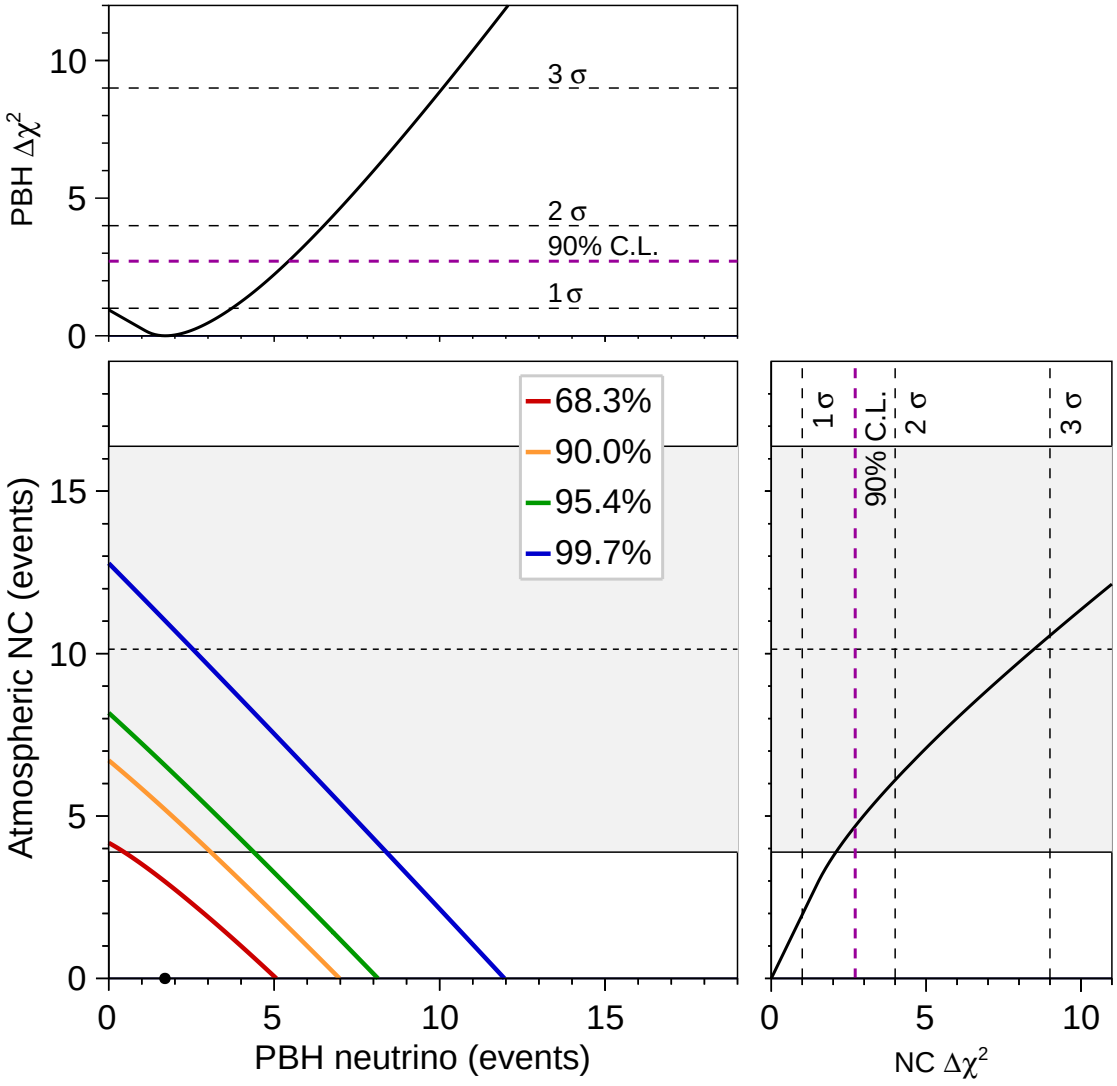

Figure 9.9: Two-dimensional scan of the number of PBH neutrino and atmospheric neutrino NC events. The PBH mass of 1×10^{15} g is adopted. Color contours indicate the 1σ (red), 90% (orange), 2σ (green), and 3σ (blue) confidence regions. The best-fit numbers of PBH neutrino and NC events are 1.7 and 0.0, respectively (black circle). The horizontally hatched region denotes the expected number of NC events with its 1σ uncertainty. The top and right panels show the one-dimensional $\Delta\chi^2$ distributions for the PBH neutrino and NC event components, respectively. The 90% C.L. upper limit on the number of PBH neutrino events is 5.4.

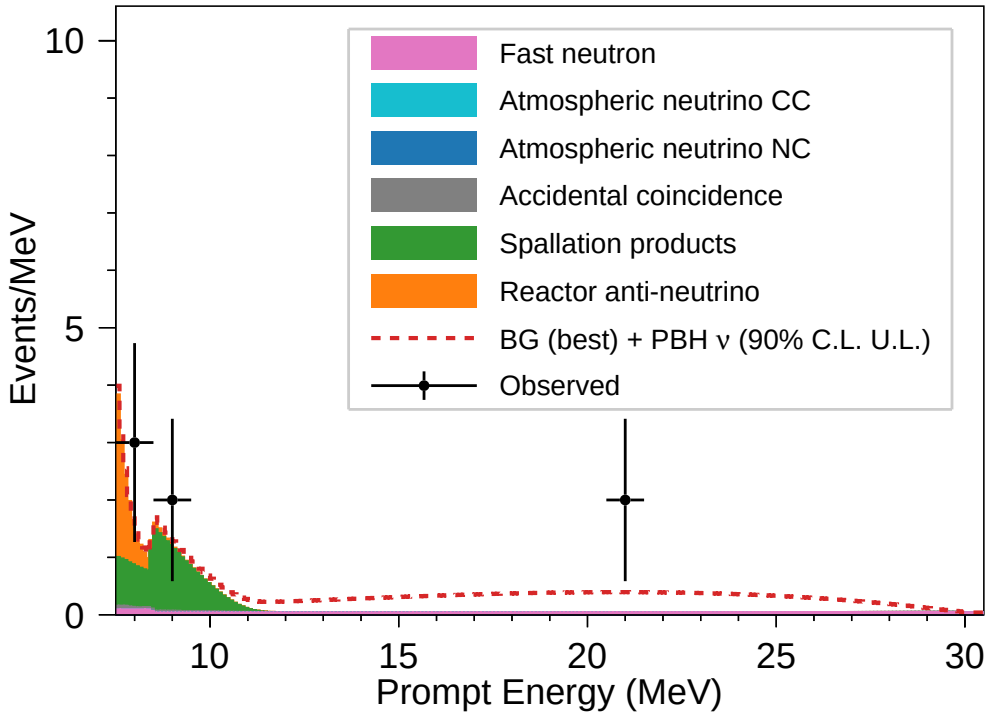

Figure 9.10: Prompt energy spectrum of the best-fit backgrounds and the PBH neutrino signal at the 90% C.L. upper limit. The PBH mass of 1×10^{15} g is adopted. All histograms are stacked.

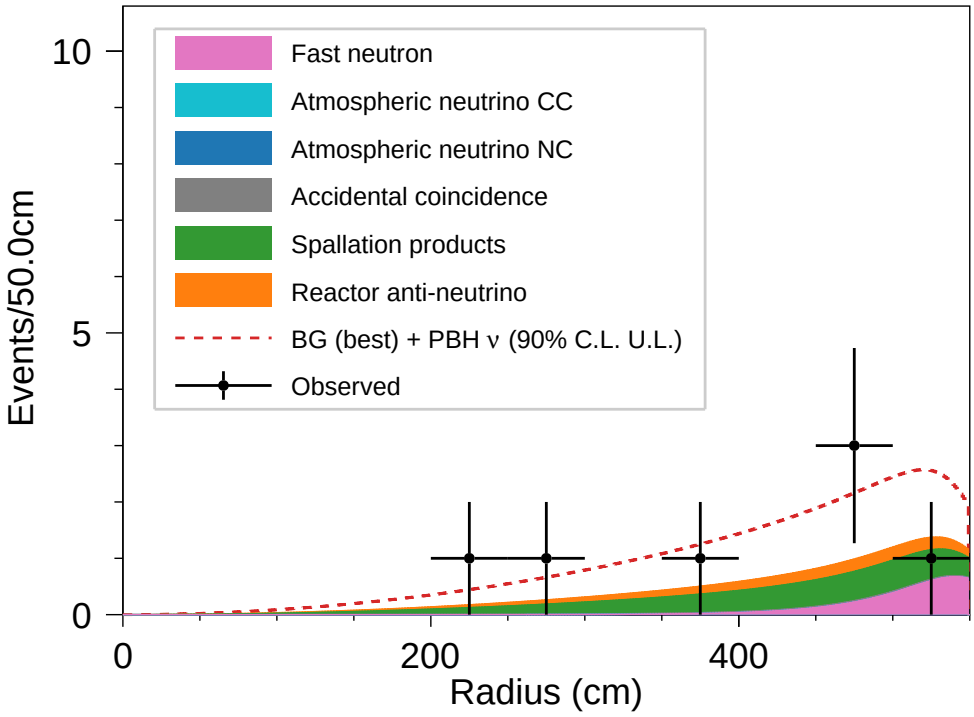

Figure 9.11: Radial distribution of the best-fit backgrounds and the PBH neutrino signal at the 90% C.L. upper limit. The PBH mass of 1×10^{15} g is adopted. All histograms are stacked.

Table 9.5: Fitting results and expected numbers of events in the PBH neutrino search, with the 90% C.L. upper limit on f_{PBH}.

	Number of events			f_{PBH}
PBH mass	Best fit	90% C.L. U.L.	Predicted	90% C.L. U.L.
1×10^{15} g	1.7	5.5	416.8	1.3×10^{-2}
2×10^{15} g	1.7	6.9	178.5	3.8×10^{-2}
3×10^{15} g	0.0	5.4	64.1	8.4×10^{-2}
4×10^{15} g	0.0	3.5	23.1	1.5×10^{-1}
5×10^{15} g	0.0	3.6	8.5	4.3×10^{-1}
6×10^{15} g	0.0	3.9	3.3	(1.2)

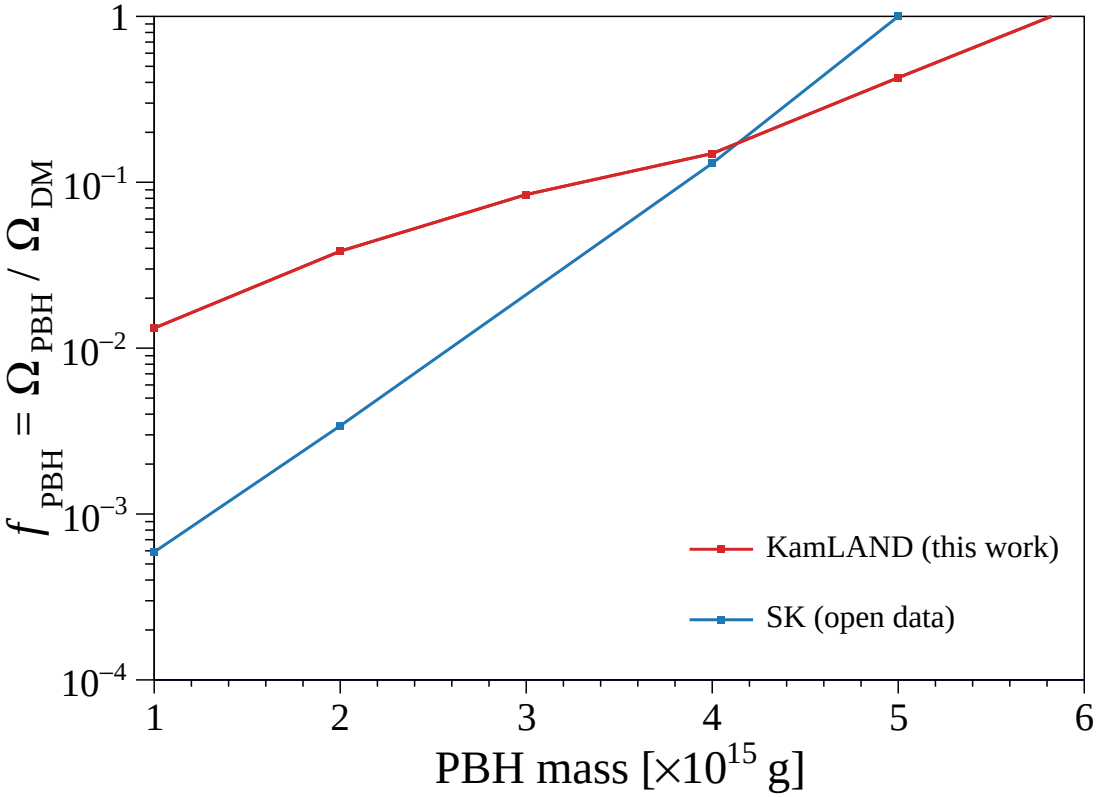

Figure 9.12: The 90% C.L. upper limits on the fraction of PBHs contributing to the dark matter energy density. The SK result is derived using the open data provided in [106], as reported in [41].

9.3 Solar Neutrino Conversion

The search for solar antineutrinos is performed using the same spectral fitting procedure as that applied to the DSNB and PBH neutrino analyses. The astrophysical input assumes the ^{8}B solar neutrino spectrum, where ν_e is converted into $\bar{\nu}_e$ without altering the spectral shape, and the conversion probability is obtained from the fit. Tab. 9.6 summarizes the expected and best-fit numbers of events for the solar antineutrino search. Fig. 9.13 shows the two-dimensional scan result of the solar neutrino conversion probability (CP) and atmospheric neutrino NC background. The best-fit value of the conversion probability is 0.0, and the 90% confidence level upper limit is 4.05×10^{-5}. Fig. 9.14 and Fig. 9.15 present the prompt energy spectrum and radial distribution, respectively, of the best-fit background and the solar antineutrino signal at the 90% C.L. upper limit.

The 90% C.L. upper limit on the conversion probability obtained in this analysis, 4.16×10^{-5} (considering the energy-spectrum distortion effect), is weaker than that from the 2022 KamLAND result [45]. By converting this limit into a constraint on the neutrino magnetic moment using Eq. 2.39, the following result is obtained:

$$\mu < 5.2 \times 10^{-10} \mu_B \left(\frac{10\,\mathrm{kG}}{B_T(0.05 R_\odot)} \right), \tag{9.7}$$

where μ_B is the Bohr magneton, B_T represents the transverse solar magnetic field in the region of neutrino production, and θ_{12} is taken to be 34° [107]. This result provides a weaker constraint than the most stringent limit to date, $0.28 \times 10^{-10} \mu_B$, derived from the Borexino solar neutrino measurement [49].

Table 9.6: The expected and best-fit numbers of events in the solar $\bar{\nu}_e$ search.

Source	Expected	Best fit	Fit condition
Reactor $\bar{\nu}_e$	1.0 ± 0.6	1.0	limited
Spallation ^{9}Li	1.9 ± 6.6	2.3	limited
Atmospheric neutrino CC	0.5 ± 0.3	1.6	free
Atmospheric neutrino NC	10.1 ± 6.2	0.0	scan
Fast neutron	2.5 ± 2.5	1.2	limited
Accidental background	0.11 ± 0.02	0.11	fix
Solar $\bar{\nu}_e$	N/A	0.0	scan
Total	16.2 ± 9.4	6.2	

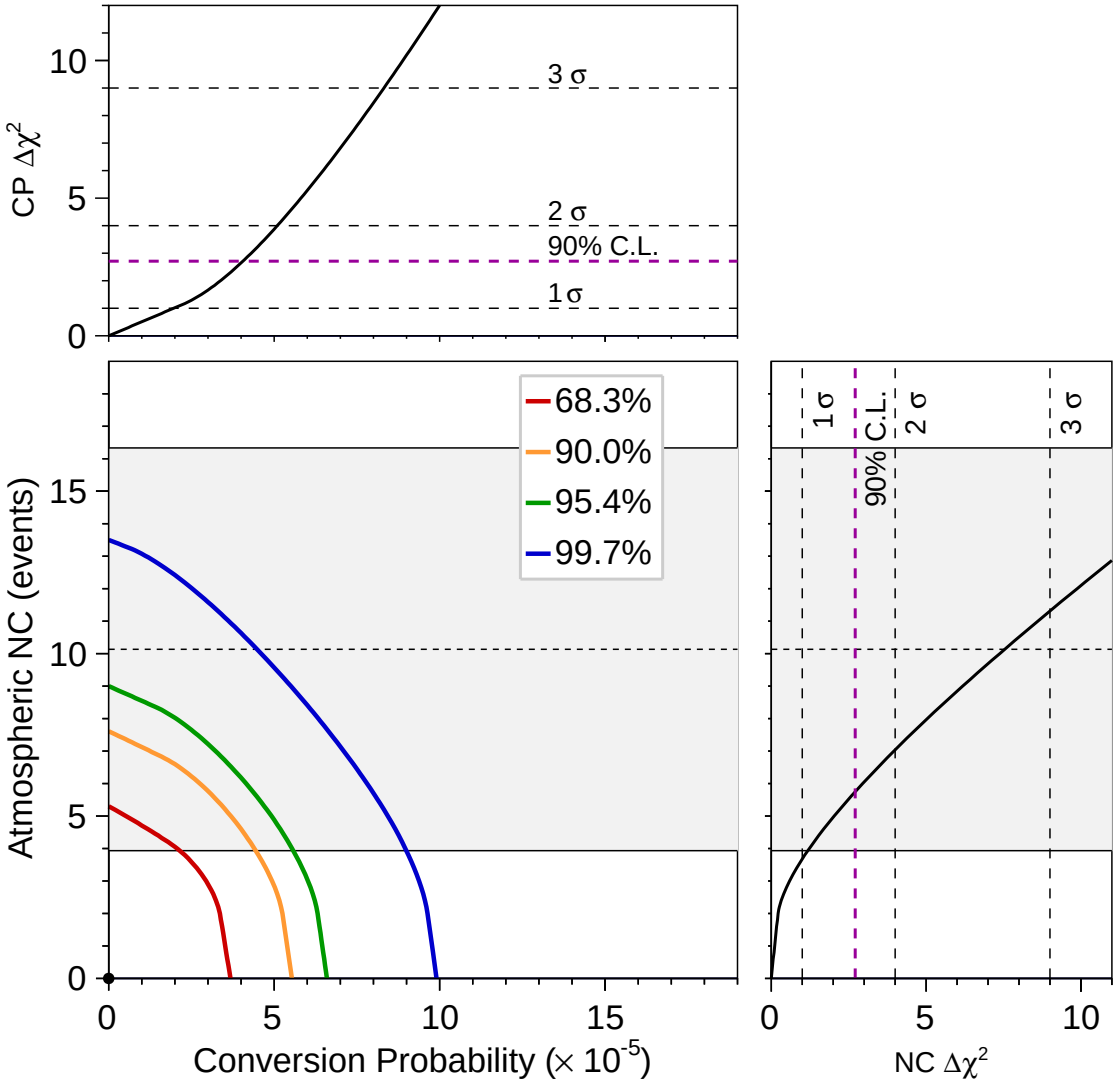

Figure 9.13: Two-dimensional scan of the solar neutrino conversion probability and number of atmospheric neutrino NC events. Color contours indicate the 1σ (red), 90% (orange), 2σ (green), and 3σ (blue) confidence regions. The best-fit value of conversion probability and number of NC events are both 0.0 (black circle). The horizontally hatched region denotes the expected number of NC events with its 1σ uncertainty. The top and right panels show the one-dimensional $\Delta\chi^2$ distributions for the conversion probability and NC event components, respectively. The 90% C.L. upper limit on the solar neutrino conversion probability is 4.05×10^{-5}.

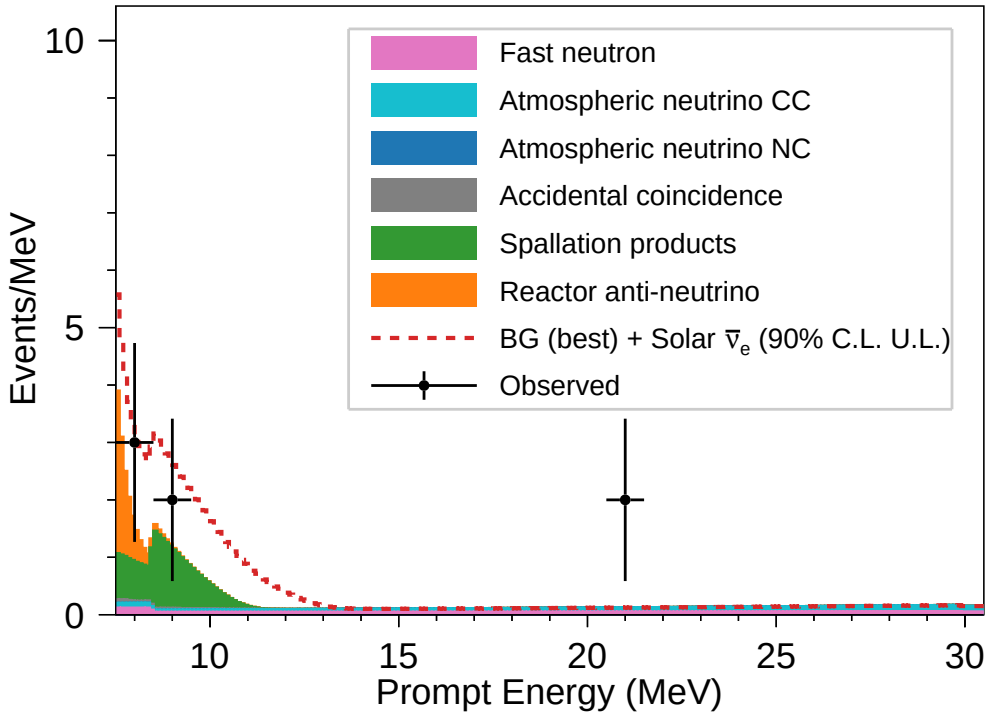

Figure 9.14: Prompt energy spectrum of the best-fit backgrounds and the solar $\bar{\nu}_e$ signal at the 90% C.L. upper limit. All histograms are stacked.

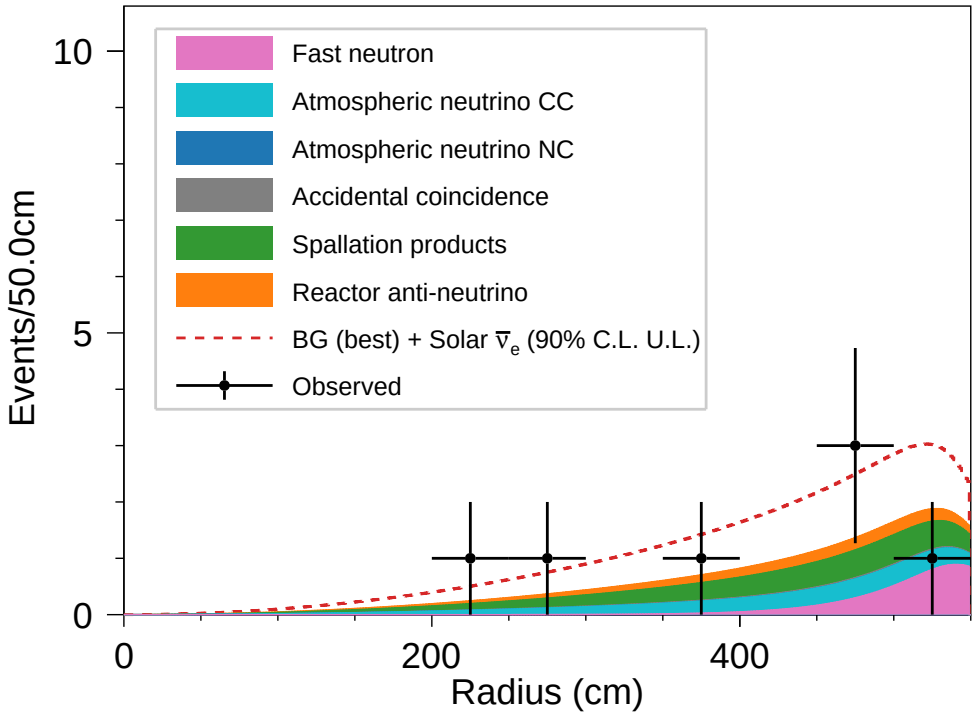

Figure 9.15: Radial distribution of the best-fit backgrounds and the solar $\bar{\nu}_e$ signal at the 90% C.L. upper limit. All histograms are stacked.

9.4 Model Independent Flux

In this section, model-independent limits on the $\bar{\nu}_e$ flux are presented. In this analysis, the astrophysical $\bar{\nu}_e$ signal is assumed to have a monochromatic neutrino energy, and the flux is calculated for each energy bin. The 90% confidence level upper limit on the model-independent $\bar{\nu}_e$ flux is obtained using the following equation:

$$\phi_{90} = \frac{N_{90}}{N_p \cdot \sigma \cdot \epsilon \cdot T}. \tag{9.8}$$

In this expression, N_{90} represents the 90% C.L. upper limit on the number of $\bar{\nu}_e$ events, evaluated using the Feldman and Cousins method [108]. N_p is the number of target protons, σ is the IBD cross section, ϵ is the IBD detection efficiency, and T denotes the detector livetime. Fig. 9.16 shows the upper limits on the $\bar{\nu}_e$ flux obtained in this study, compared with the 2022 KamLAND result, those from other experiments, and the DSNB predictions.

A discussion is given below on the reasons why the limits obtained in this analysis are weaker than the 2022 KamLAND results in some energy bins. After applying the KamNet-based event selection developed in this study, the background events were significantly reduced. However, in these energy bins, no events were observed in either the 2022 analysis or this study. Consequently, in the calculation of N_{90}, the 2022 analysis allowed fewer signal events, resulting in a tighter upper limit.

When the flux is integrated over the neutrino energy range from 8.3 MeV to 18.3 MeV, the total flux is improved from 212.2 $\mathrm{cm^{-2}\,s^{-1}}$ in the 2022 result to 166.3 $\mathrm{cm^{-2}\,s^{-1}}$ in this study. The upper limits on the model-independent $\bar{\nu}_e$ flux are summarized in Tab. 9.7. In conclusion, this study achieves one of the most stringent limit in the world for the neutrino energy range of 8.3–13.3 MeV.

Table 9.7: 90% C.L. upper limits on the model-independent $\bar{\nu}_e$ flux.

Neutrino energy [MeV]	Flux 90% C.L. upper limit [$\mathrm{cm^{-2}\,s^{-1}\,MeV^{-1}}$]
8.3–9.3	55.5
9.3–10.3	38.7
10.3–11.3	12.7
11.3–12.3	12.5
12.3–13.3	10.9
13.3–14.3	9.3
14.3–15.3	8.0
15.3–16.3	7.0
16.3–17.3	6.2
17.3–18.3	5.5

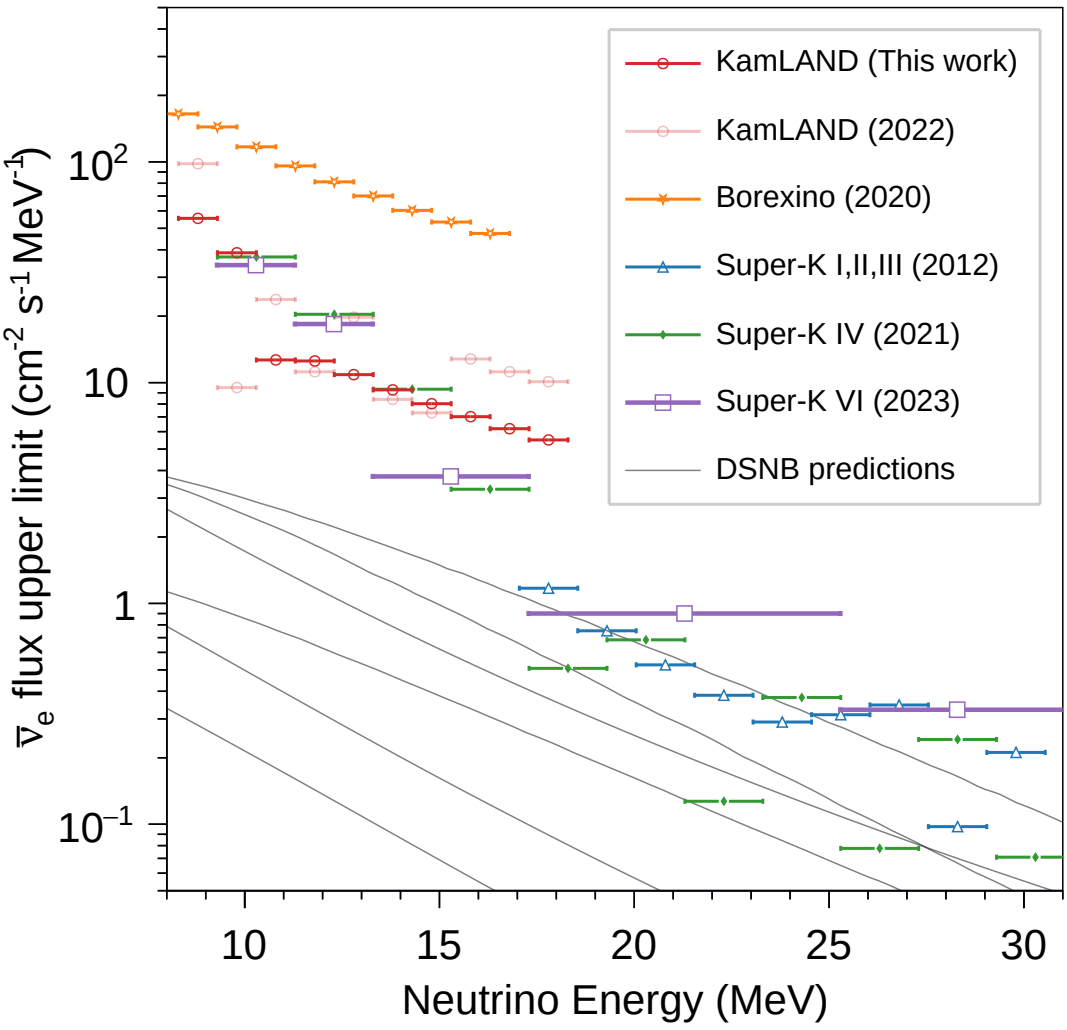

Figure 9.16: The 90% C.L. upper limits on the model-independent $\bar{\nu}_e$ flux. The red points represent the limits obtained in this work, while the lighter red points indicate the limits from the previous KamLAND result (2022) [45]. Other points show the limits reported by Borexino (2020) [48] and Super-Kamiokande during the SK-I, II, III (2012) [106], SK-IV (2021) [28], and SK-VI (2023) [46] periods. The lighter black lines correspond to the DSNB prediction models described in Sec. 2.1.6.

9.5 Dark Matter Annihilation

The upper limits on the $\bar{\nu}_e$ flux can be converted into limits on the dark matter self-annihilation cross section ($\chi\chi \to \nu\nu$). Using Eq. 2.44, the velocity-dependent cross section is expressed as follows:

$$\langle \sigma_A v \rangle_{90}(m_\chi) = \frac{6}{\mathcal{J}_{\rm avg}} \frac{m_\chi^2}{R_{\rm sc}\rho_0^2} \phi_{90}(E_\nu)\delta(E_\nu - m_\chi). \tag{9.9}$$

In this equation, $\mathcal{J}_{\rm avg}$ denotes the angular-averaged intensity over the entire Milky Way, m_χ is the dark matter mass, $R_{\rm sc} = 8.5\,{\rm kpc}$ is the distance from the Sun to the Galactic center, $\rho_0 = 0.3\,{\rm GeV\,cm^{-3}}$ is the local dark matter density, and ϕ_{90} is the upper limit on the $\bar{\nu}_e$ flux. Fig. 9.17 shows the 90% C.L. upper limits on the dark matter annihilation cross section obtained using benchmark values of $\mathcal{J}_{\rm avg} = 1.3$ and 5.0 [36]. This study provides new constraints on the cross section for $m_\chi < 15\,{\rm MeV}$.

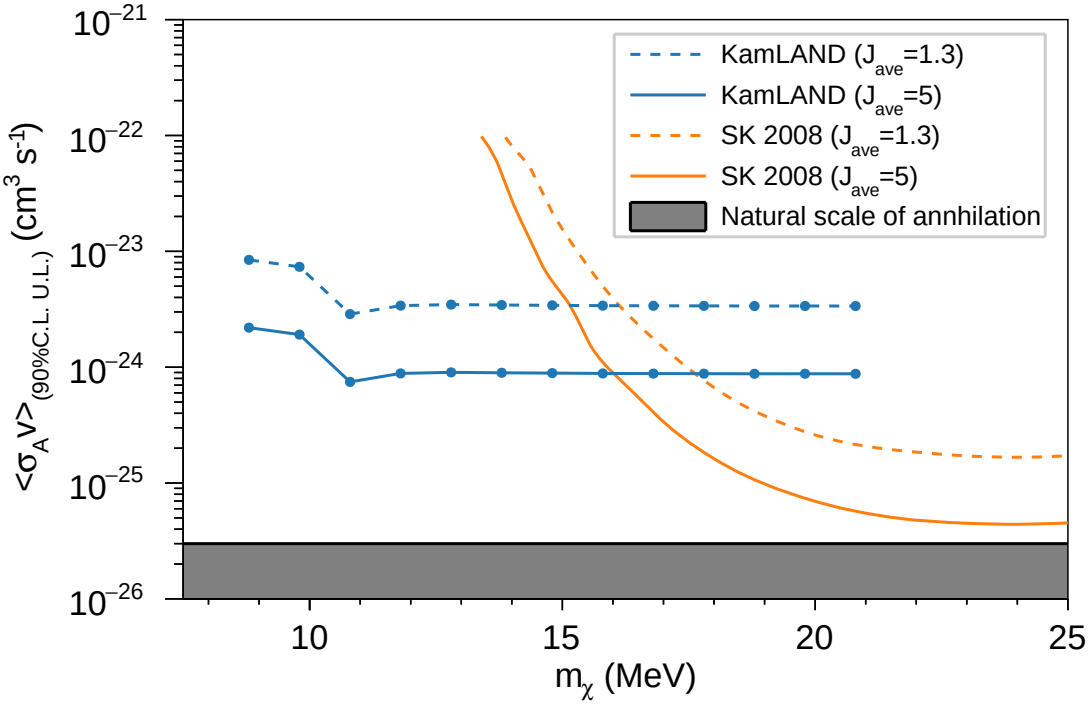

Figure 9.17: The 90% C.L. upper limits on the dark matter self-annihilation cross section. The solid and dashed lines correspond to the benchmark cases of $\mathcal{J}_{\rm avg} = 1.3$ and 5.0, respectively, and the SK results are taken from [36]. The black shaded region indicates the natural scale of the annihilation cross section, $3 \times 10^{-26}\,{\rm cm^3\,s^{-1}}$ [109].

Chapter 10

Conclusion

In this study, a search for astrophysical electron antineutrinos ($\bar{\nu}_e$s) was conducted using the entire KamLAND dataset collected between March 9, 2002, and August 8, 2024. $\bar{\nu}_e$ events were detected through the inverse beta decay (IBD) reaction, with a prompt energy range of 7.5–30 MeV and a fiducial volume within a 550 cm radius from the detector center.

The dominant background events in this search originate from atmospheric neutrinos and fast neutrons, which could not be distinguished from IBD events in previous analyses. In this study, a new method was developed to discriminate between signal and background events by applying a deep neural network to the PMT hit information. The systematic uncertainties associated with the implementation of this new method were also carefully evaluated. Under this improved analysis framework, only seven astrophysical $\bar{\nu}_e$ candidates were selected from the full dataset.

The results of various astrophysical $\bar{\nu}_e$ searches performed using these seven observed events and the background models are summarized as follows:

- Diffuse Supernova Neutrino Background (DSNB):

  No significant excess of signal was observed. The 90% confidence level upper limits on the flux for different models were found to be in the range of 38–43 $\mathrm{cm}^{-2}\,\mathrm{s}^{-1}$, improving the search result by a factor of two compared to the 2022 KamLAND result [45]. With this improvement, KamLAND's DSNB search around 10 MeV has, for the first time, reached a sensitivity comparable to theoretical predictions.

- Neutrinos from Primordial Black Holes (PBHs):

  This work presents the search for PBH-origin neutrinos with KamLAND. Although no significant excess was observed, upper limits on the PBH fraction relative to the dark matter energy density were derived. These limits provide the most stringent constraints among neutrino observations to date for PBHs with masses greater than 5×10^{15} g.

- Model-independent $\bar{\nu}_e$ flux:

  The overall limits improve upon the 2022 results, achieving one of the world's most stringent constraint in the neutrino energy range of 8.3–13.3 MeV.

Additionally, searches for solar antineutrinos and neutrinos from light dark matter annihilation were performed. This study sets upper limits on the ^{8}B solar neutrino conversion probability and the dark matter self-annihilation cross section.

For future improvements, I propose to expand the fiducial volume from 550 cm to 600 cm, which increase the statistics by a factor of approximately 1.3. To realize this, it is crucial to accurately model the fast neutron background increasing near the inner detector edge. This, in turn, requires a better understanding of muon-induced fast neutron production processes, which currently have large uncertainties.

Although no major expansion of the fiducial volume is planned for the next-generation detector KamLAND2, the experiment retains unique advantages for astrophysical $\bar{\nu}_e$ studies. The photon statistics will increase by a factor of five, greatly enhancing the information available for event identification. If the signal acceptance in event identification—currently below 80%—can be improved, a further gain in sensitivity is expected. Moreover, even as the 20-kt liquid scintillator detector JUNO begins accumulating data, KamLAND(2) will continue to maintain superior sensitivity in the lower energy region due to its lower muon-induced background and greater distance from nuclear reactors.

Appendix A

Supplements for the Astrophysical Neutrino Search Result

A.1 DSNB Search

For the DSNB search described in Sec. 9.1, the fit results for various theoretical models are shown in Figs. A.1–A.10.

A.2 PBH Neutrino Search

For the PBH neutrino search described in Sec. 9.2, the fit results for neutrinos emitted from PBHs with different masses are shown in Figs. A.11–A.20.

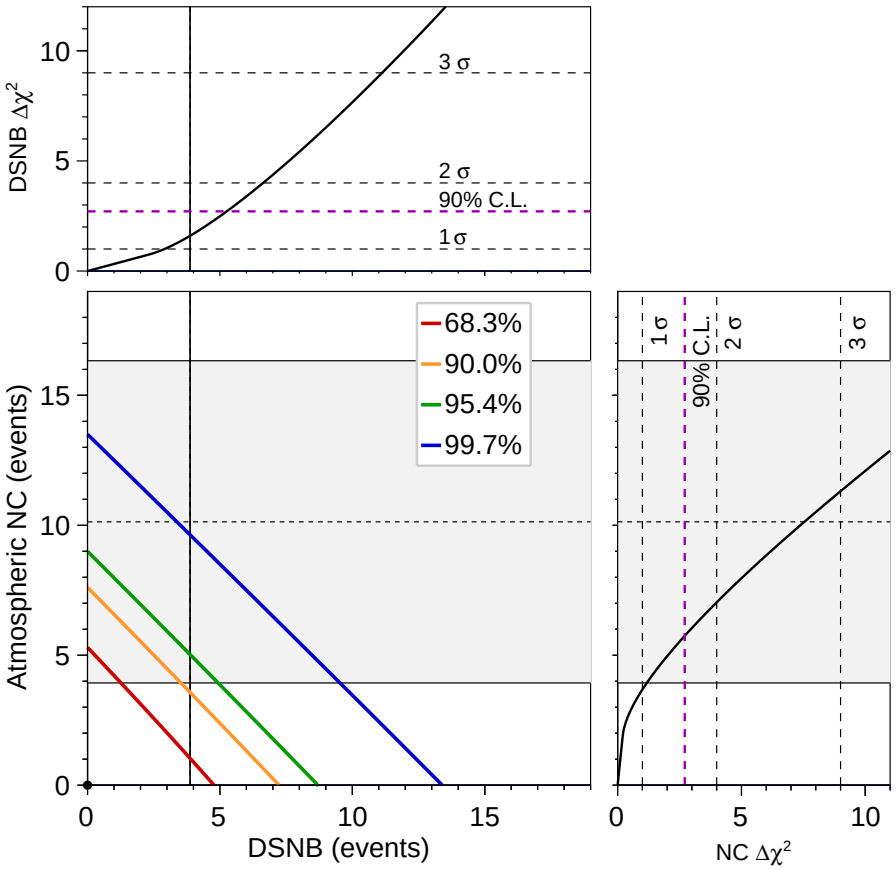

Figure A.1: Two-dimensional scan of the number of DSNB and atmospheric neutrino NC events (Totani+95).

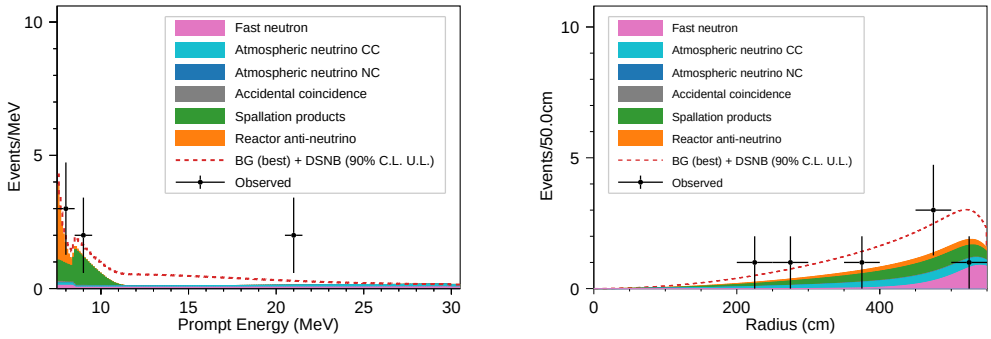

Figure A.2: Prompt energy spectrum and radial distribution of the best-fit backgrounds and the DSNB signal at the 90% C.L. upper limit (Totani+95).

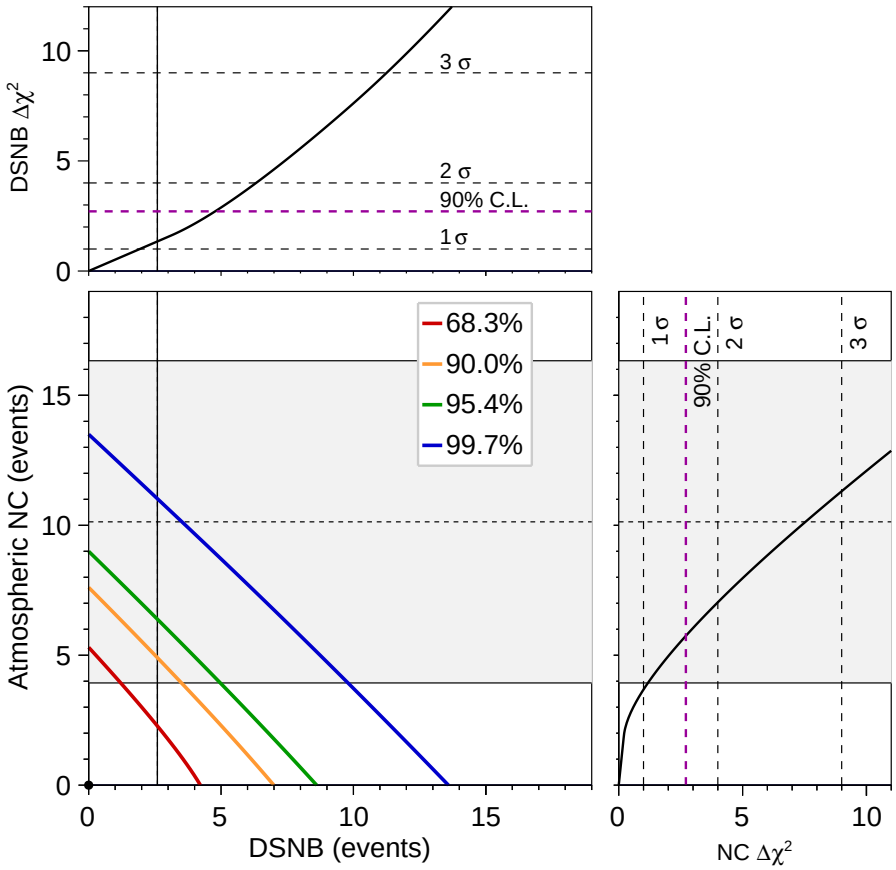

Figure A.3: Two-dimensional scan of the number of DSNB and atmospheric neutrino NC events (Kaplinghat+00).

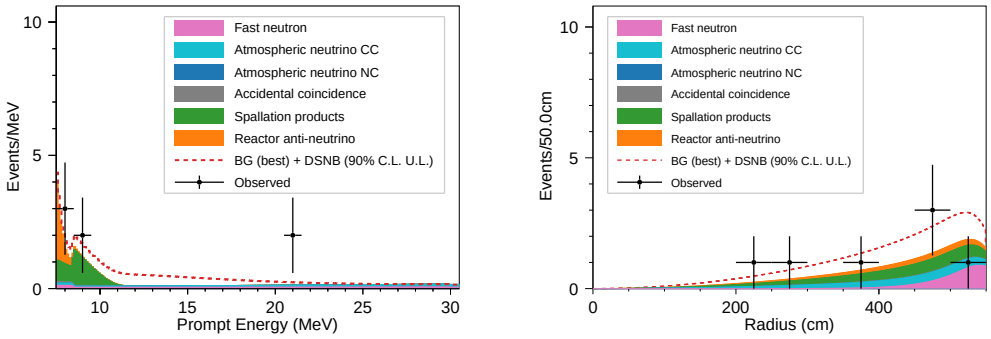

Figure A.4: Prompt energy spectrum and radial distribution of the best-fit backgrounds and the DSNB signal at the 90% C.L. upper limit (Kaplinghat+00).

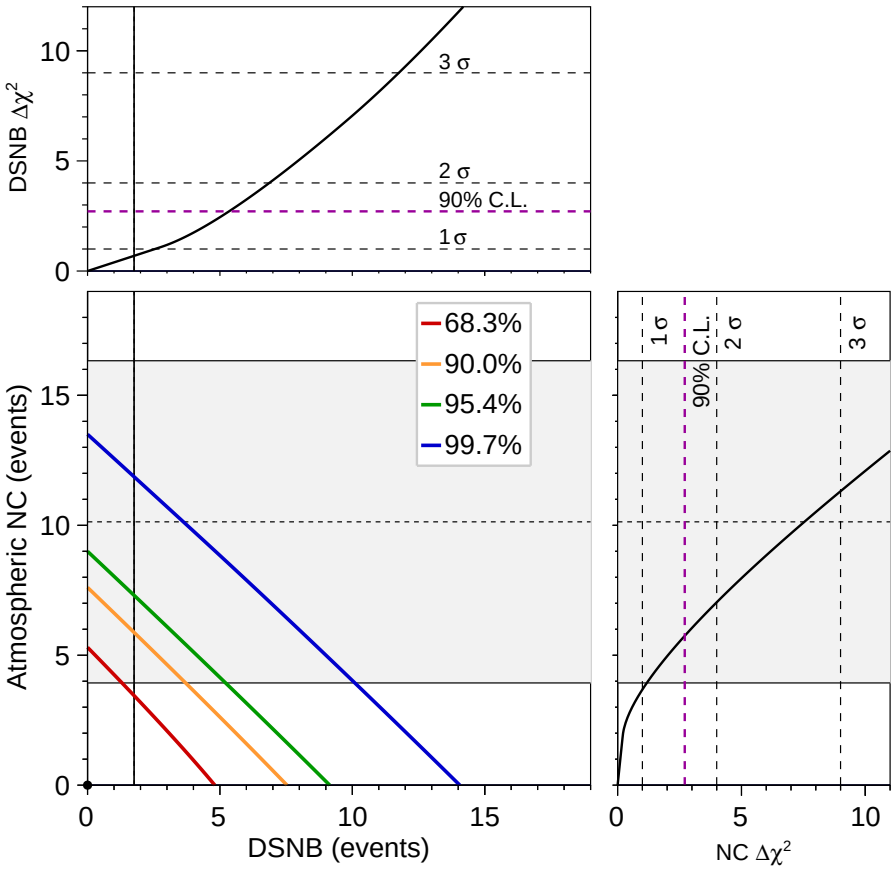

Figure A.5: Two-dimensional scan of the number of DSNB and atmospheric neutrino NC events (Ashida+23).

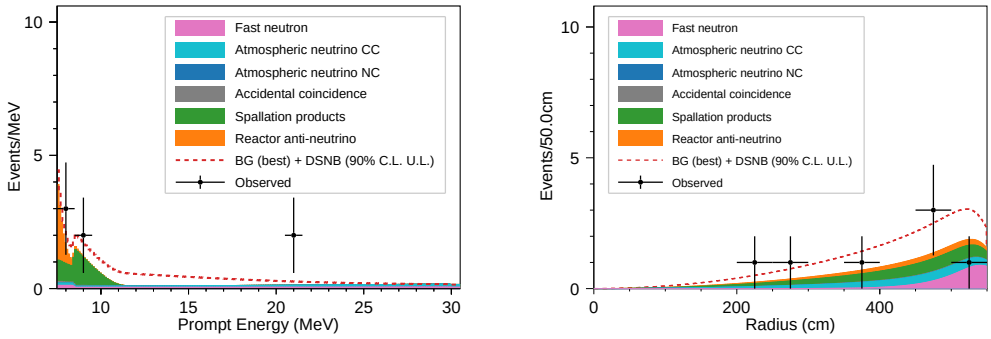

Figure A.6: Prompt energy spectrum and radial distribution of the best-fit backgrounds and the DSNB signal at the 90% C.L. upper limit (Ashida+23).

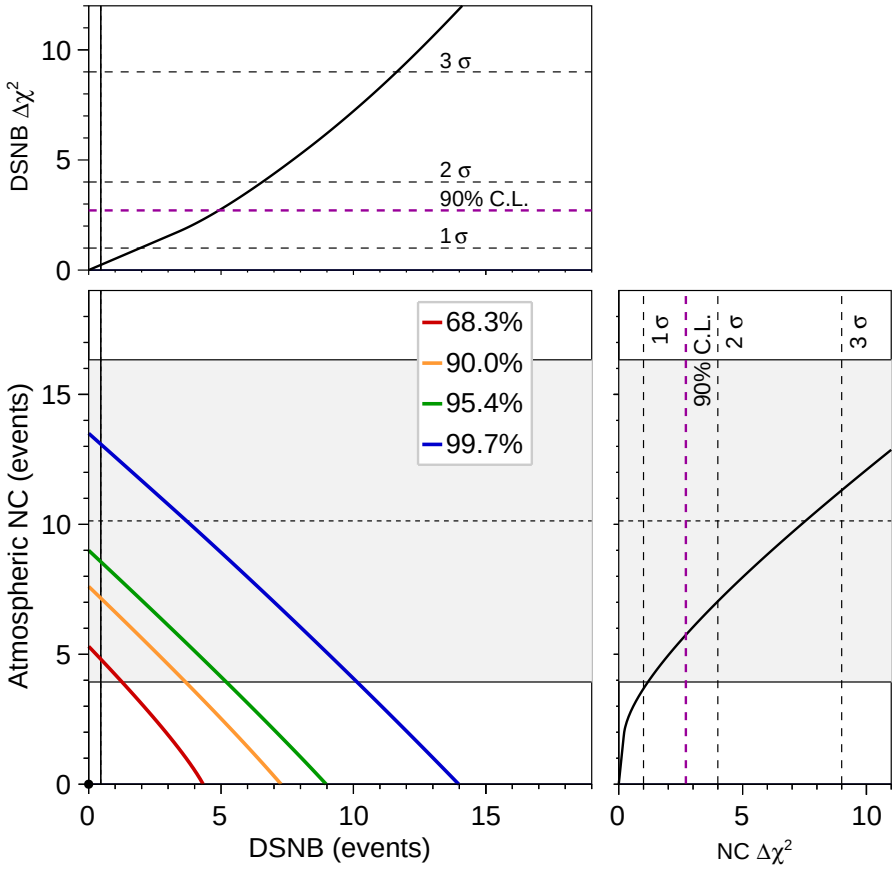

Figure A.7: Two-dimensional scan of the number of DSNB and atmospheric neutrino NC events (Nakazato+15, max, IH).

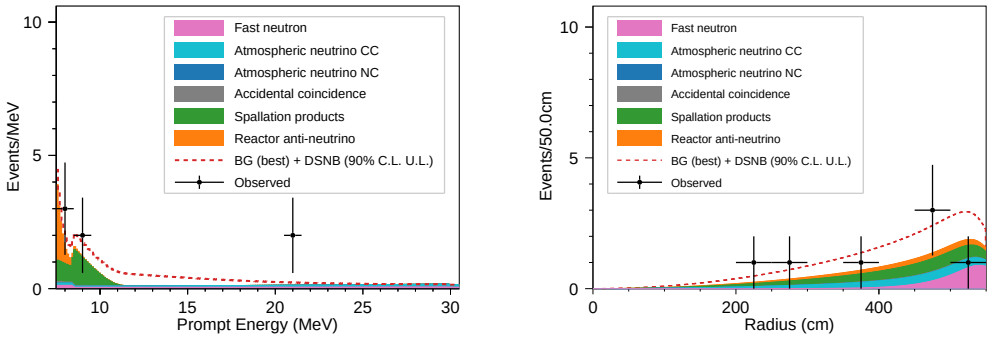

Figure A.8: Prompt energy spectrum and radial distribution of the best-fit backgrounds and the DSNB signal at the 90% C.L. upper limit (Nakazato+15, max, IH).

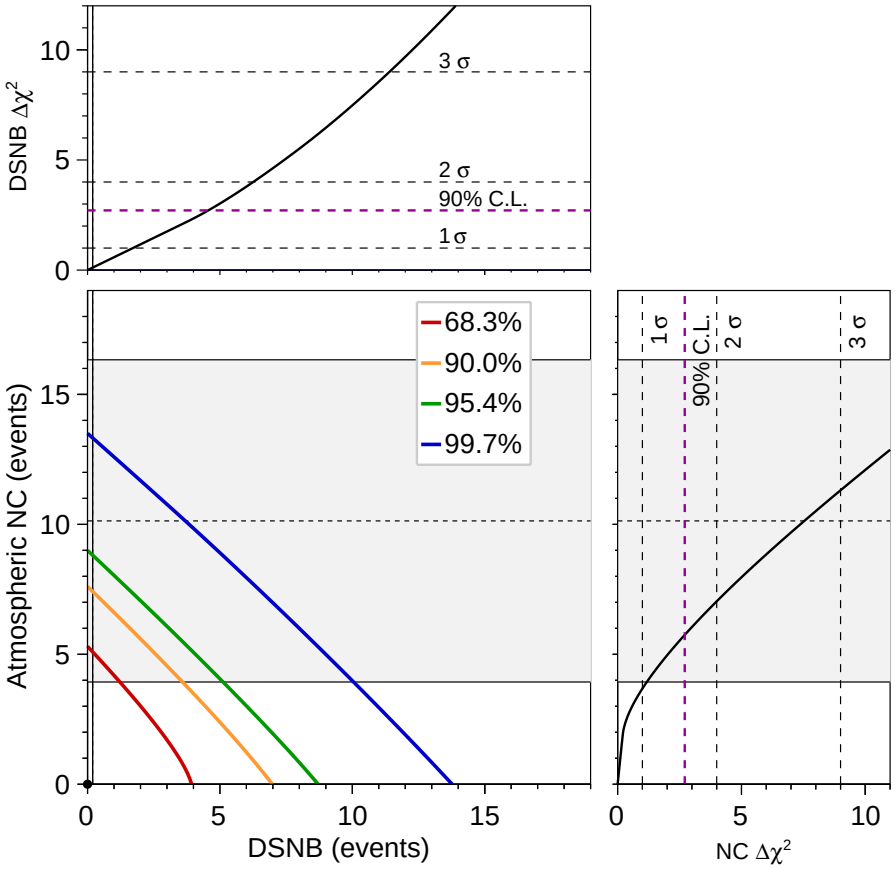

Figure A.9: Two-dimensional scan of the number of DSNB and atmospheric neutrino NC events (Nakazato+15, min, NH).

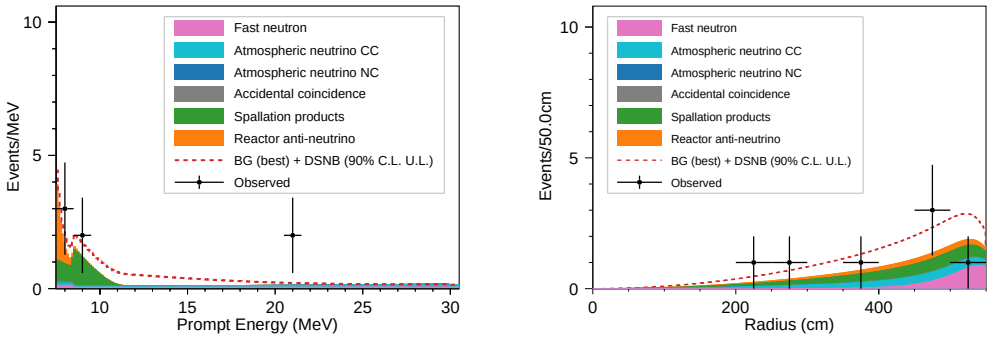

Figure A.10: Prompt energy spectrum and radial distribution of the best-fit backgrounds and the DSNB signal at the 90% C.L. upper limit (Nakazato+15, min, NH).

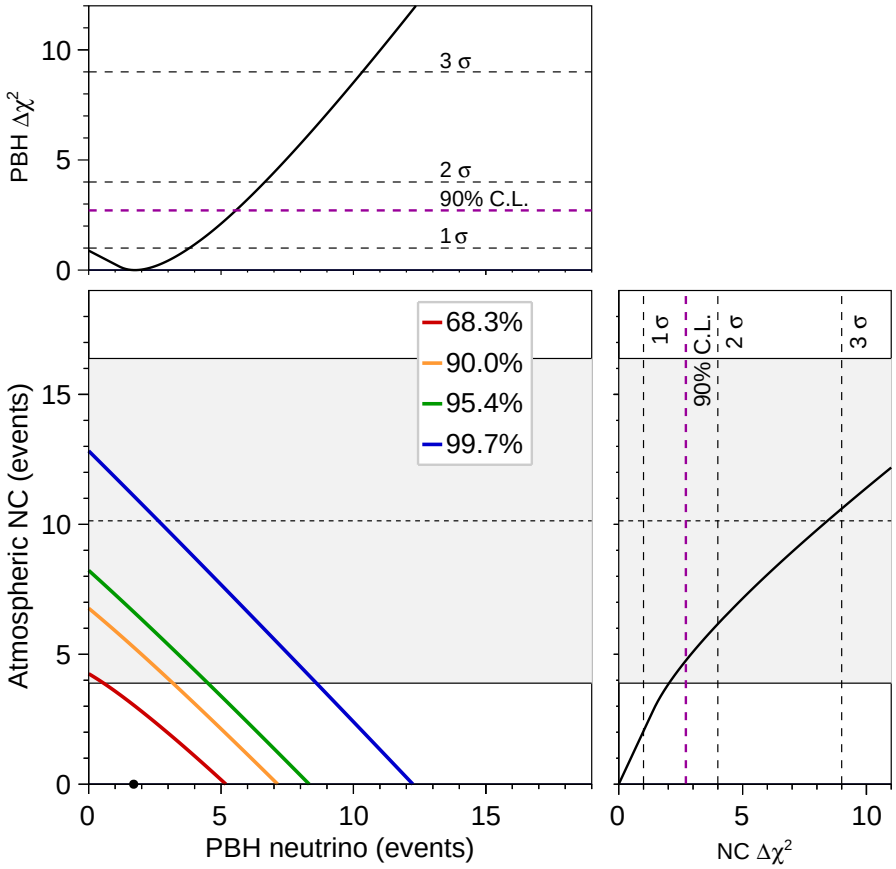

Figure A.11: Two-dimensional scan of the number of PBH neutrino and atmospheric neutrino NC events (PBH mass = 2e15 g).

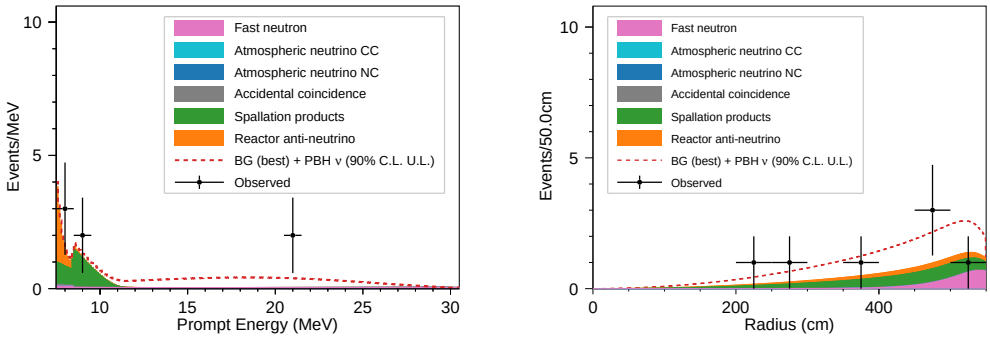

Figure A.12: Prompt energy spectrum and radial distribution of the best-fit backgrounds and the PBH neutrino signal at the 90% C.L. upper limit (PBH mass = 2e15 g).

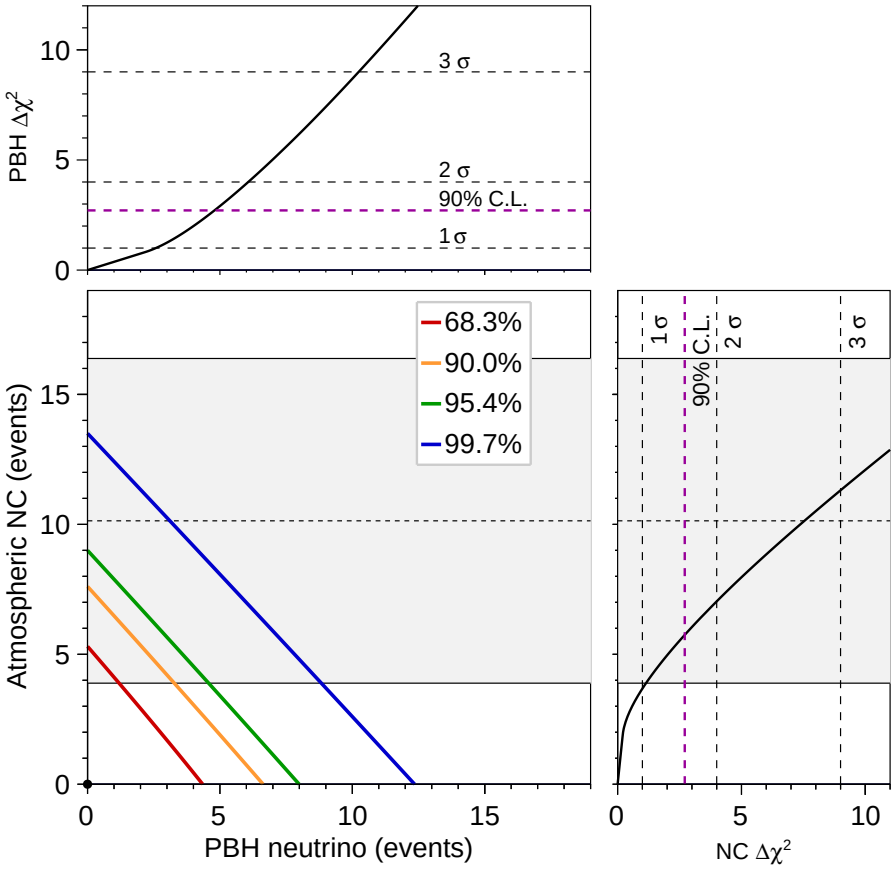

Figure A.13: Two-dimensional scan of the number of PBH neutrino and atmospheric neutrino NC events (PBH mass = 3e15 g).

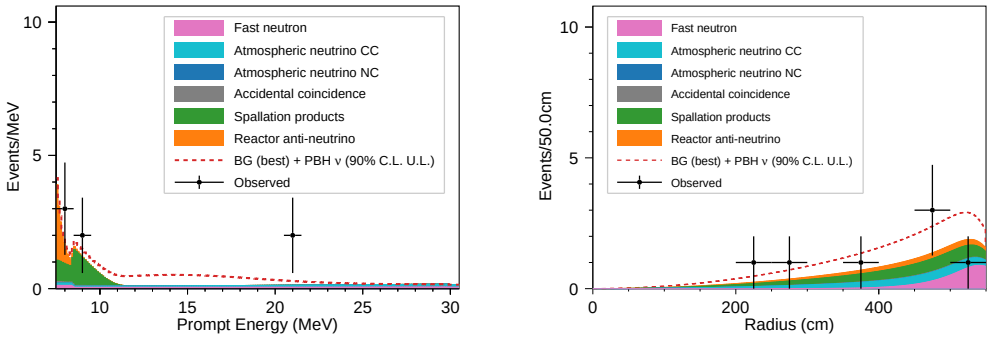

Figure A.14: Prompt energy spectrum and radial distribution of the best-fit backgrounds and the PBH neutrino signal at the 90% C.L. upper limit (PBH mass = 3e15 g).

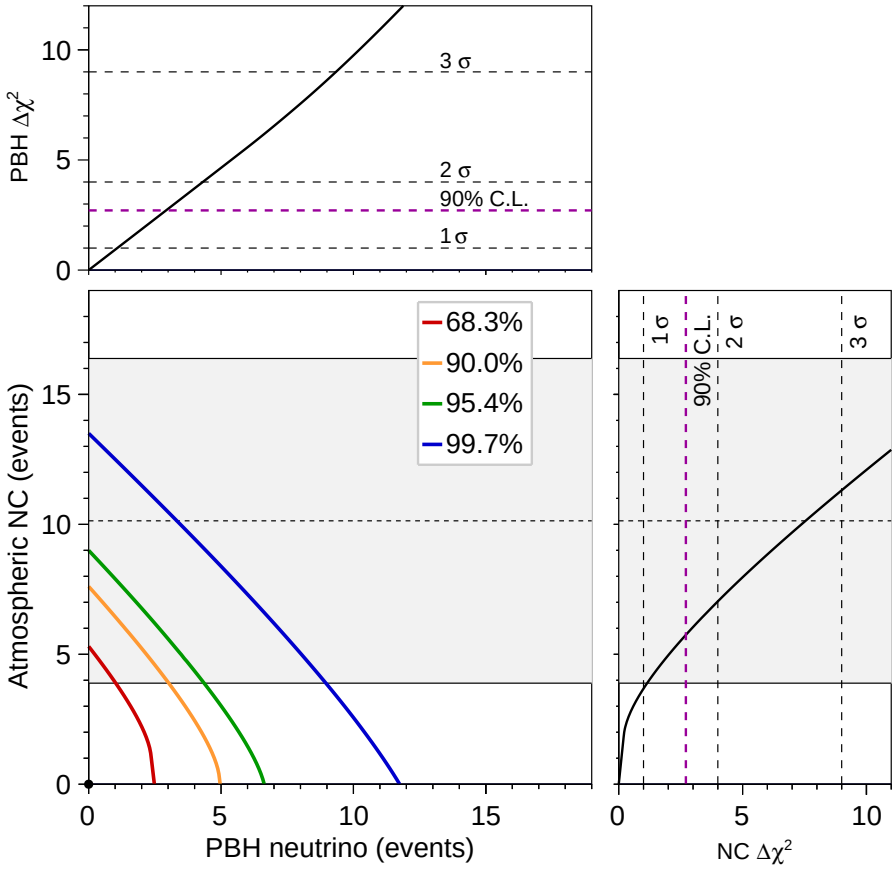

Figure A.15: Two-dimensional scan of the number of PBH neutrino and atmospheric neutrino NC events (PBH mass = 4e15 g).

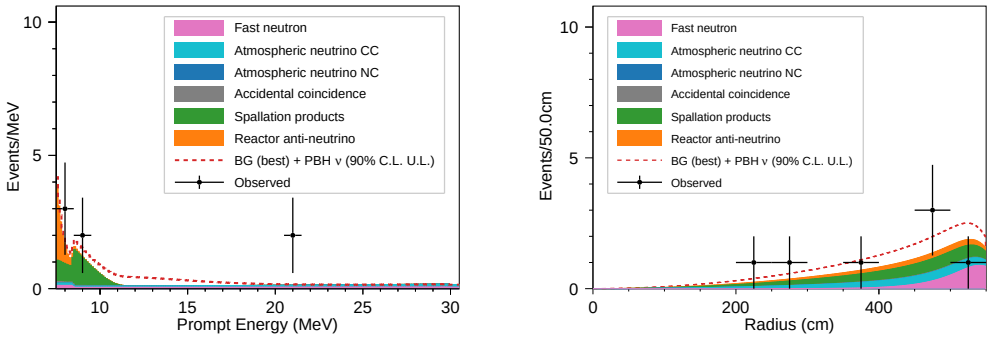

Figure A.16: Prompt energy spectrum and radial distribution of the best-fit backgrounds and the PBH neutrino signal at the 90% C.L. upper limit (PBH mass = 4e15 g).

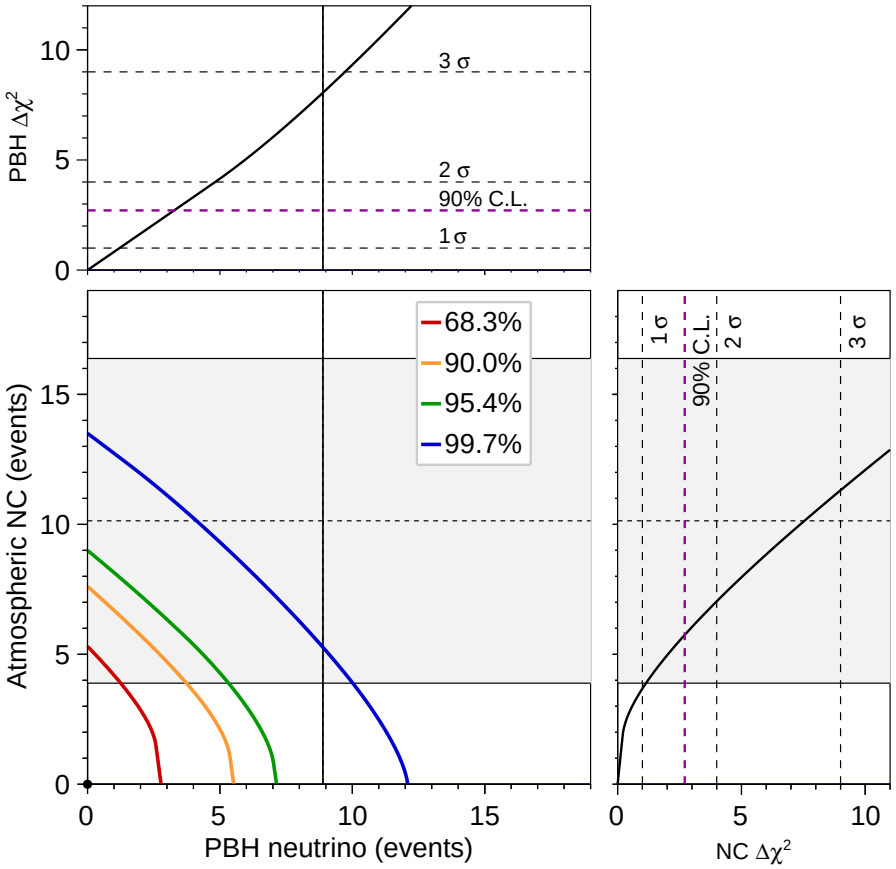

Figure A.17: Two-dimensional scan of the number of PBH neutrino and atmospheric neutrino NC events (PBH mass = 5e15 g).

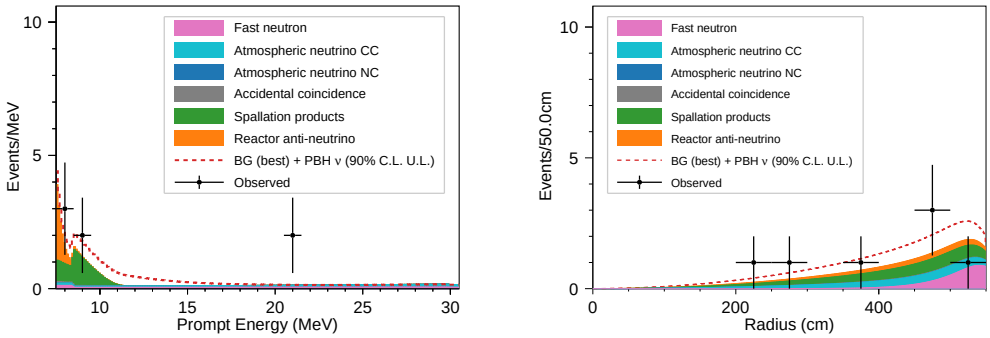

Figure A.18: Prompt energy spectrum and radial distribution of the best-fit backgrounds and the PBH neutrino signal at the 90% C.L. upper limit (PBH mass = 5e15 g).

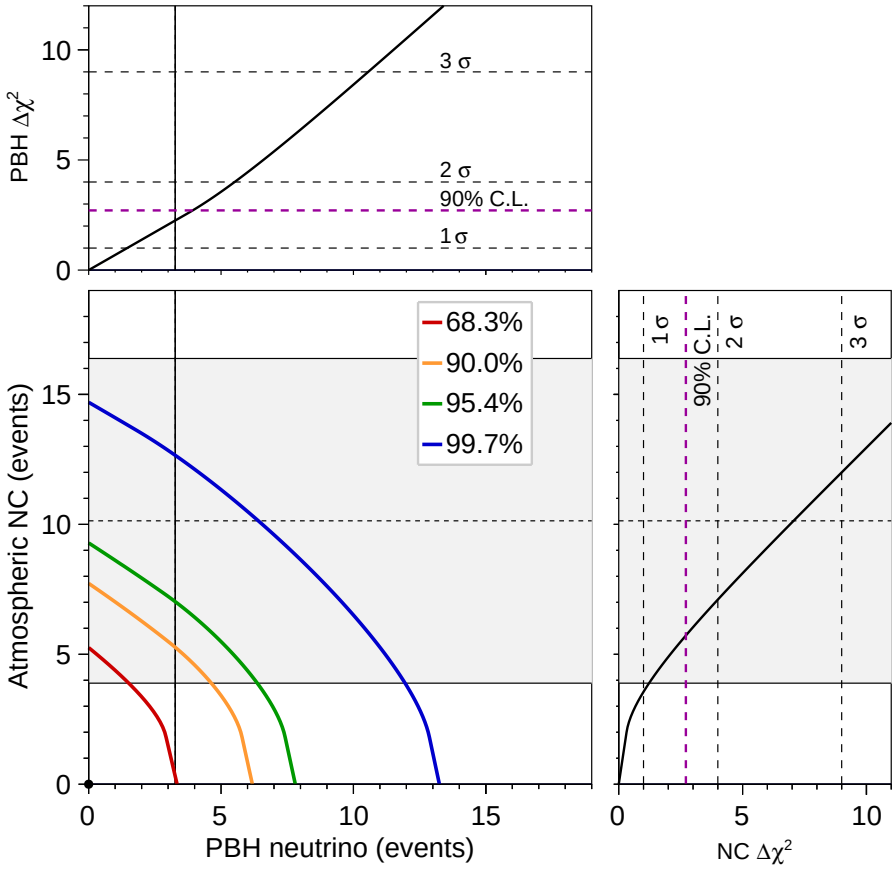

Figure A.19: Two-dimensional scan of the number of PBH neutrino and atmospheric neutrino NC events (PBH mass = 6e15 g).

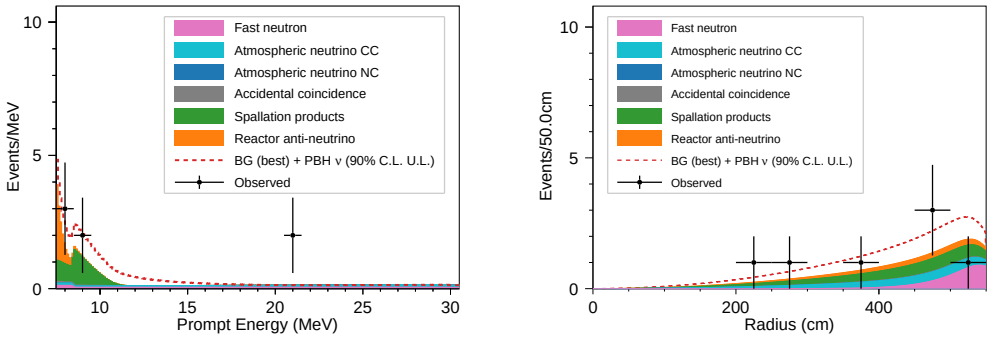

Figure A.20: Prompt energy spectrum and radial distribution of the best-fit backgrounds and the PBH neutrino signal at the 90% C.L. upper limit (PBH mass = 6e15 g).

Bibliography

[1] 山田章一, 超新星, 日本評論社, 2016.

[2] A. Odrzywolek, A. Heger, NEUTRINO SIGNATURES OF DYING MASSIVE STARS: FROM MAIN SEQUENCE TO THE NEUTRON STAR, *Acta Phys. Polon. B* 41 (1) (2010) 1611–1628.

[3] K. Nakazato *et al.*, SUPERNOVA NEUTRINO LIGHT CURVES AND SPECTRA FOR VARIOUS PROGENITOR STARS: FROM CORE COLLAPSE TO PROTO-NEUTRON STAR COOLING, *The Astrophysical Journal Supplement Series* 205 (1) (2013) 2. doi:10.1088/0067-0049/205/1/2.

[4] S. Horiuchi *et al.*, The cosmic core-collapse supernova rate does not match the massive-star formation rate, *The Astrophysical Journal* 738 (2) (2011) 154. doi:10.1088/0004-637X/738/2/154.

[5] S. Horiuchi, J. F. Beacom, E. Dwek, Diffuse supernova neutrino background is detectable in super-kamiokande, *Phys. Rev. D* 79 (2009) 083013. doi:10.1103/PhysRevD.79.083013.

[6] K. Nakazato *et al.*, Spectrum of the supernova relic neutrino background and metallicity evolution of galaxies, *The Astrophysical Journal* 804 (1) (2015) 75. doi:10.1088/0004-637X/804/1/75.

[7] M. Kaplinghat, G. Steigman, T. P. Walker, Supernova relic neutrino background, *Phys. Rev. D* 62 (2000) 043001. doi:10.1103/PhysRevD.62.043001.

[8] Y. Ashida, K. Nakazato, T. Tsujimoto, Diffuse neutrino flux based on the rates of core-collapse supernovae and black hole formation deduced from a novel galactic chemical evolution model, *The Astrophysical Journal* 953 (2) (2023) 151. doi:10.3847/1538-4357/ace3ba.

[9] T. Totani, K. Sato, Spectrum of the relic neutrino background from past supernovae and cosmological models, *Astroparticle Physics* 3 (4) (1995) 367–376. doi:10.1016/0927-6505(95)00015-9.

[10] S. E. Woosley, J. R. Wilson, R. Mayle, Gravitational Collapse and the Cosmic Antineutrino Background, *The Astrophysical Journal* 302 (1986) 19. doi:10.1086/163968.

[11] I. K. Baldry *et al.*, The sloan digital sky survey u-band galaxy survey: luminosity functions and evolution, *Monthly Notices of the Royal Astronomical Society* 358 (2) (2005) 441–456. doi:10.1111/j.1365-2966.2005.08799.x.

[12] D. Schiminovich *et al.*, The galex-vvds measurement of the evolution of the far-ultraviolet luminosity density and the cosmic star formation rate, *The Astrophysical Journal* 619 (1) (2005) L47. doi:10.1086/427077.

[13] S. Arnouts *et al.*, The galex vimos-vlt deep survey* measurement of the evolution of the 1500 Å luminosity function, *The Astrophysical Journal* 619 (1) (2005) L43. doi:10.1086/426733.

[14] Wolf, C. *et al.*, The combo-17 survey: Evolution of the galaxy luminosity function from 25000 galaxies with 0.2 <z< 1.2*, *Astron. Astrophys.* 401 (1) (2003) 73–98. doi:10.1051/0004-6361:20021513.

[15] P. G. Pérez-González *et al.*, Spitzer view on the evolution of star-forming galaxies from z= 0 to z∼3, *The Astrophysical Journal* 630 (1) (2005) 82. doi:10.1086/431894.

[16] R. I. Thompson *et al.*, Star formation history of the hubble ultra deep field: Comparison with the hubble deep field-north, *The Astrophysical Journal* 647 (2) (2006) 787. doi:10.1086/505568.

[17] A. M. Hopkins, J. F. Beacom, On the normalization of the cosmic star formation history, *The Astrophysical Journal* 651 (1) (2006) 142. doi:10.1086/506610.

[18] N. A. Reddy, C. C. Steidel, A steep faint-end slope of the uv luminosity function at z ˜ 2–3: Implications for the global stellar mass density and star formation in low-mass halos*, *The Astrophysical Journal* 692 (1) (2009) 778. doi:10.1088/0004-637X/692/1/778.

[19] James, P. A. *et al.*, The hα galaxy survey* - iv. star formation in the local universe, *Astron. Astrophys.* 482 (2) (2008) 507–516. doi:10.1051/0004-6361:20078560.

[20] E. E. Salpeter, The Luminosity Function and Stellar Evolution., *The Astrophysical Journal* 121 (1955) 161. doi:10.1086/145971.

[21] H. Yüksel, J. F. Beacom, Neutrino spectrum from sn 1987a and from cosmic supernovae, *Phys. Rev. D* 76 (2007) 083007. doi:10.1103/PhysRevD.76.083007.

[22] N. Drory, M. Alvarez, The contribution of star formation and merging to stellar mass buildup in galaxies, *The Astrophysical Journal* 680 (1) (2008) 41. doi:10.1086/588006.

[23] Maiolino, R. *et al.*, Amaze* - i. the evolution of the mass–metallicity relation at z>3, *Astron. Astrophys.* 488 (2) (2008) 463–479. doi:10.1051/0004-6361:200809678.

[24] N. Langer, C. A. Norman, On the collapsar model of long gamma-ray bursts:constraints from cosmic metallicity evolution, *The Astrophysical Journal* 638 (2) (2006) L63. doi:10.1086/500363.

[25] T. Totani, K. Sato, Y. Yoshii, Spectrum of the Supernova Relic Neutrino Background and Evolution of Galaxies, *The Astrophysical Journal* 460 (1996) 303. doi:10.1086/176970.

[26] P. Madau, M. Dickinson, Cosmic star-formation history, *Annual Review of Astronomy and Astrophysics* 52 (2014) 415–486. doi:10.1146/annurev-astro-081811-125615.

[27] Y. Ashida, K. Nakazato, Exploring the fate of stellar core collapse with supernova relic neutrinos, *The Astrophysical Journal* 937 (1) (2022) 30. doi:10.3847/1538-4357/ac8a46.

[28] K. Abe *et al.*, Diffuse supernova neutrino background search at super-kamiokande, *Phys. Rev. D* 104 (2021) 122002. doi:10.1103/PhysRevD.104.122002.

[29] E. G. Adelberger *et al.*, Solar fusion cross sections. ii. the *pp* chain and cno cycles, *Rev. Mod. Phys.* 83 (2011) 195–245. doi:10.1103/RevModPhys.83.195.

[30] A. Serenelli, Alive and well: A short review about standard solar models, *The European Physical Journal A* 52 (2016) 78. doi:10.1140/epja/i2016-16078-1.

[31] K. Fujikawa, R. E. Shrock, Magnetic moment of a massive neutrino and neutrino-spin rotation, *Phys. Rev. Lett.* 45 (1980) 963–966. doi:10.1103/PhysRevLett.45.963.

[32] B. Cañas *et al.*, Updating neutrino magnetic moment constraints, *Physics Letters B* 753 (2016) 191–198. doi:10.1016/j.physletb.2015.12.011.

[33] A. B. Balantekin, P. J. Hatchell, F. Loreti, Matter-enhanced spin-flavor precession of solar neutrinos with transition magnetic moments, *Phys. Rev. D* 41 (1990) 3583–3593. doi:10.1103/PhysRevD.41.3583.

[34] E. Akhmedov, J. Pulido, Solar neutrino oscillations and bounds on neutrino magnetic moment and solar magnetic field, *Physics Letters B* 553 (1) (2003) 7–17. doi:10.1016/S0370-2693(02)03182-9.

[35] Y. Ascasibar *et al.*, Constraints on dark matter and the shape of the milky way dark halo from the 511-kev line, *Monthly Notices of the Royal Astronomical Society* 368 (4) (2006) 1695–1705. doi:10.1111/j.1365-2966.2006.10226.x.

[36] S. Palomares-Ruiz, S. Pascoli, Testing mev dark matter with neutrino detectors, *Phys. Rev. D* 77 (2008) 025025. doi:10.1103/PhysRevD.77.025025.

[37] A. Arbey, J. Auffinger, Blackhawk: a public code for calculating the hawking evaporation spectra of any black hole distribution, *The European Physical Journal C* 79 (8) (2019) 693. doi:10.1140/epjc/s10052-019-7161-1.

[38] A. Arbey, J. Auffinger, Physics beyond the standard model with blackhawk v2.0, *The European Physical Journal C* 81 (10) (2021) 910. doi:10.1140/epjc/s10052-021-09702-8.

[39] T. Sjöstrand *et al.*, An introduction to pythia 8.2, *Computer Physics Communications* 191 (2015) 159–177. doi:10.1016/j.cpc.2015.01.024.

[40] C. Lunardini, Y. F. Perez-Gonzalez, Dirac and majorana neutrino signatures of primordial black holes, *Journal of Cosmology and Astroparticle Physics* 2020 (08) (2020) 014. doi:10.1088/1475-7516/2020/08/014.

[41] S. Wang *et al.*, Constraining primordial black holes as dark matter at juno, *Phys. Rev. D* 103 (2021) 043010. doi:10.1103/PhysRevD.103.043010.

[42] Planck Collaboration *et al.*, Planck 2018 results - vi. cosmological parameters, *Astron. Astrophys.* 641 (2020) A6. doi:10.1051/0004-6361/201833910.

[43] K. C. Y. Ng *et al.*, Resolving small-scale dark matter structures using multisource indirect detection, *Phys. Rev. D* 89 (2014) 083001. doi:10.1103/PhysRevD.89.083001.

[44] S. Obara *et al.*, Search for supernova relic neutrinos at kamland, *Journal of Physics: Conference Series* 2156 (1) (2021) 012138. doi:10.1088/1742-6596/2156/1/012138.

[45] S. Abe *et al.*, Limits on astrophysical antineutrinos with the KamLAND experiment, *The Astrophysical Journal* 925 (1) (2022) 14. doi:10.3847/1538-4357/ac32c1.

[46] M. Harada *et al.*, Search for astrophysical electron antineutrinos in super-kamiokande with 0.01% gadolinium-loaded water, *The Astrophysical Journal Letters* 951 (2) (2023) L27. doi:10.3847/2041-8213/acdc9e.

[47] S. Fukuda *et al.*, The super-kamiokande detector, *Nuclear Instruments and Methods in Physics Research Section A: Accelerators, Spectrometers, Detectors and Associated Equipment* 501 (2) (2003) 418–462. doi:10.1016/S0168-9002(03)00425-X.

[48] M. Agostini *et al.*, Search for low-energy neutrinos from astrophysical sources with borexino, *Astroparticle Physics* 125 (2021) 102509. doi:10.1016/j.astropartphys.2020.102509.

[49] M. Agostini *et al.*, Limiting neutrino magnetic moments with borexino phase-ii solar neutrino data, *Phys. Rev. D* 96 (2017) 091103. doi:10.1103/PhysRevD.96.091103.

[50] L. Hüdepohl *et al.*, Neutrino signal of electron-capture supernovae from core collapse to cooling, *Phys. Rev. Lett.* 104 (2010) 251101. doi:10.1103/PhysRevLett.104.251101.

[51] H. Back *et al.*, Borexino calibrations: hardware, methods, and results, *Journal of Instrumentation* 7 (10) (2012) P10018. doi:10.1088/1748-0221/7/10/P10018.

[52] B. Aharmim *et al.*, Electron antineutrino search at the sudbury neutrino observatory, *Phys. Rev. D* 70 (2004) 093014. doi:10.1103/PhysRevD.70.093014.

[53] J. Boger *et al.*, The sudbury neutrino observatory, *Nuclear Instruments and Methods in Physics Research Section A: Accelerators, Spectrometers, Detectors and Associated Equipment* 449 (1) (2000) 172–207. doi:10.1016/S0168-9002(99)01469-2.

[54] A. Abusleme *et al.*, Prospects for detecting the diffuse supernova neutrino background with juno, *Journal of Cosmology and Astroparticle Physics* 2022 (10) (2022) 033. doi:10.1088/1475-7516/2022/10/033.

[55] K. Abe *et al.*, Hyper-Kamiokande: Neutrino Astrophysics and Status, *PoS* ICRC2025 (2025) 1215. doi:10.22323/1.501.1215.

[56] K. Abe *et al.*, Supernova model discrimination with hyper-kamiokande, *The Astrophysical Journal* 916 (1) (2021) 15. doi:10.3847/1538-4357/abf7c4.

[57] B. Carr *et al.*, Constraints on primordial black holes, *Reports on Progress in Physics* 84 (11) (2021) 116902. doi:10.1088/1361-6633/ac1e31.

[58] S. Enomoto, Neutrino Geophysics and Observation of Geo-Neutrinos at KamLAND, Ph.D. thesis, 東北大学 (2005).

[59] 竹本康浩, CNOサイクル太陽ニュートリノ観測のためのデッドタイムフリー電子回路の開発, Master's thesis, 東北大学 (2009).

[60] 吉田学立, 液体シンチレータでの粒子識別によるα線バックグラウンド除去の研究, Master's thesis, 東北大学 (2011).

[61] O. Tajima, Measurement of Electron Anti-Neutrino Oscillation Parameters with a Large Volume Liquid Scintillator Detector, KamLAND, Ph.D. thesis, 東北大学 (2003).

[62] S. Obara, A Search for Supernova Relic Neutrinos with KamLAND during Reactor-Off Period, Ph.D. thesis, 東北大学 (2018).

[63] B. E. Berger *et al.*, The kamland full-volume calibration system, *Journal of Instrumentation* 4 (04) (2009) P04017. doi:10.1088/1748-0221/4/04/P04017.

[64] H. Yoshida, Limit on Majorana Neutrino Mass with Neutrinoless Double Beta Decay from KamLAND-Zen, Ph.D. thesis, 東北大学 (2014).

[65] S. Hayashida, Search for Neutrinoless Double-Beta Decay with KamLAND-Zen Applying Advanced Spallation Background Reduction, Ph.D. thesis, 東北大学 (2019).

[66] H. Ozaki, High Sensitivity Search for Neutrinoless Double-Beta Decay in KamLAND-Zen with Double Amout of 136Xe, Ph.D. thesis, 東北大学 (2020).

[67] The KamLAND-Zen collaboration *et al.*, The nylon balloon for xenon loaded liquid scintillator in kamland-zen 800 neutrinoless double-beta decay search experiment, *Journal of Instrumentation* 16 (08) (2021) P08023. doi:10.1088/1748-0221/16/08/P08023.

[68] A. Gando *et al.*, Search for majorana neutrinos near the inverted mass hierarchy region with kamland-zen, *Phys. Rev. Lett.* 117 (2016) 082503. doi:10.1103/PhysRevLett.117.082503.

[69] A. Gando *et al.*, Limit on neutrinoless $\beta\beta$ decay of ^{136}Xe from the first phase of kamland-zen and comparison with the positive claim in ^{76}Ge, *Phys. Rev. Lett.* 110 (2013) 062502. doi:10.1103/PhysRevLett.110.062502.

[70] S. Abe *et al.*, Search for Majorana Neutrinos with the Complete KamLAND-Zen Dataset (2024) doi:10.48550/arXiv.2406.11438.

[71] I. Shimizu, An Evidence for Spectral Distortion of Reactor Anti-Neutrinos and A Study of Three Flavor Neutrino Oscillation, Ph.D. thesis, 東北大学 (2004).

[72] H. Watanabe, Comprehensive Study of Anti-neutrino Signals at KamLAND, Ph.D. thesis, 東北大学 (2012).

[73] S. Garrett, Chapter 13 - introductory numerical methods, in: S. Garrett (Ed.), Introduction to Actuarial and Financial Mathematical Methods, Academic Press, San Diego, 2015, pp. 411–463. doi:10.1016/B978-0-12-800156-1.00013-3.

[74] S. Agostinelli *et al.*, Geant4—a simulation toolkit, *Nuclear Instruments and Methods in Physics Research Section A: Accelerators, Spectrometers, Detectors and Associated Equipment* 506 (3) (2003) 250–303. doi:10.1016/S0168-9002(03)01368-8.

[75] A. Li *et al.*, Kamnet: An integrated spatiotemporal deep neural network for rare event searches in kamland-zen, *Phys. Rev. C* 107 (2023) 014323. doi:10.1103/PhysRevC.107.014323.

[76] X. Shi *et al.*, Convolutional lstm network: A machine learning approach for precipitation nowcasting, in: C. Cortes *et al.* (Eds.), Advances in Neural Information Processing Systems, Vol. 28, Curran Associates, Inc., 2015, p. 802.

[77] T. S. Cohen *et al.*, Spherical CNNs (2018) doi:10.48550/arXiv.1801.10130.

[78] S. Abe, First measurement of the strangeness axial coupling constant using neutral current quasi-elastic interactions of atmosphric neutinos at KamLAND, Ph.D. thesis, 東北大学 (2022).

[79] S. Abe *et al.*, Production of radioactive isotopes through cosmic muon spallation in kamland, *Phys. Rev. C* 81 (2010) 025807. doi:10.1103/PhysRevC.81.025807.

[80] T. Hagner *et al.*, Muon-induced production of radioactive isotopes in scintillation detectors, *Astroparticle Physics* 14 (1) (2000) 33–47. doi:10.1016/S0927-6505(00)00103-1.

[81] M. Neuberger, Very long baseline neutrino oscillation analysis at kamland in the korean time-frame, Ph.D. thesis, 東北大学 (2020).

[82] K. Eguchi *et al.*, First results from kamland: Evidence for reactor antineutrino disappearance, *Phys. Rev. Lett.* 90 (2003) 021802. doi:10.1103/PhysRevLett.90.021802.

[83] P. Vogel, J. F. Beacom, Angular distribution of neutron inverse beta decay, $\overline{\nu}_e + \vec{p} \to e^+ + n$, *Phys. Rev. D* 60 (1999) 053003. doi:10.1103/PhysRevD.60.053003.

[84] A. Kurylov, M. J. Ramsey-Musolf, P. Vogel, Radiative corrections to low-energy neutrino reactions, *Phys. Rev. C* 67 (2003) 035502. doi:10.1103/PhysRevC.67.035502.

[85] U. S. Energy Information Administration, Nuclear reactor restarts in Japan have reduced LNG imports for electricity generation.

[86] International Atomic Energy Agency, Operating Experience with Nuclear Power Stations in Member States.

[87] World Nuclear Industry Status Report, World Nuclear Power Reactors 1951–2025.

[88] P. Huber, Determination of antineutrino spectra from nuclear reactors, *Phys. Rev. C* 84 (2011) 024617. doi:10.1103/PhysRevC.84.024617.

[89] T. A. Mueller *et al.*, Improved predictions of reactor antineutrino spectra, *Phys. Rev. C* 83 (2011) 054615. doi:10.1103/PhysRevC.83.054615.

[90] P. Vogel *et al.*, Reactor antineutrino spectra and their application to antineutrino-induced reactions. ii, *Phys. Rev. C* 24 (1981) 1543–1553. doi:10.1103/PhysRevC.24.1543.

[91] F. P. An *et al.*, Improved measurement of the reactor antineutrino flux and spectrum at daya bay*, *Chinese Physics C* 41 (1) (2017) 013002. doi:10.1088/1674-1137/41/1/013002.

[92] N. Kawada, Spectroscopic measurement of geoneutrinos from uranium and thorium with KamLAND, Ph.D. thesis, 東北大学 (2022).

[93] V. I. Kopeikin, L. A. Mikaelyan, V. V. Sinev, Inverse beta decay in a nonequilibrium antineutrino flux from a nuclear reactor, *Physics of Atomic Nuclei* 64 (2001) 849–854. doi:10.1134/1.1378874.

[94] P. Vogel, Analysis of the antineutrino capture on protons, *Phys. Rev. D* 29 (1984) 1918–1922. doi:10.1103/PhysRevD.29.1918.

[95] A. Gando *et al.*, Reactor on-off antineutrino measurement with kamland, *Phys. Rev. D* 88 (2013) 033001. doi:10.1103/PhysRevD.88.033001.

[96] K. Ichimura, Precise measurement of neutrino oscillation parameters with KamLAND, Ph.D. thesis, 東北大学 (2008).

[97] M. Honda *et al.*, Calculation of atmospheric neutrino flux using the interaction model calibrated with atmospheric muon data, *Phys. Rev. D* 75 (2007) 043006. doi:10.1103/PhysRevD.75.043006.

[98] M. S. Athar, S. Ahmad, S. K. Singh, Charged current antineutrino reactions from ^{12}C at miniboone energies, *Phys. Rev. D* 75 (2007) 093003. doi:10.1103/PhysRevD.75.093003.

[99] A. Gando *et al.*, Search for extraterrestrial antineutrino sources with the kamland detector, *The Astrophysical Journal* 745 (2) (2012) 193. doi:10.1088/0004-637X/745/2/193.

[100] L. A. Ahrens *et al.*, Measurement of neutrino-proton and antineutrino-proton elastic scattering, *Phys. Rev. D* 35 (1987) 785–809. doi:10.1103/PhysRevD.35.785.

[101] O. V. Perevozchikov, Search for Electron Antineutrinos From The Sun With KamLAND Detector, Ph.D. thesis, University of Tennessee (2009).

[102] Y. Kamyshkov, E. Kolbe, Signatures of nucleon disappearance in large underground detectors, *Phys. Rev. D* 67 (2003) 076007. doi:10.1103/PhysRevD.67.076007.

[103] P. Antonioli *et al.*, A three-dimensional code for muon propagation through the rock: Music, *Astroparticle Physics* 7 (4) (1997) 357–368. doi:10.1016/S0927-6505(97)00035-2.

[104] Geographical Survey Institute of Japan, Digital Map 50 m Grid (Elevation) (1997) (unpublished).

[105] 嶺川幸江, カムランドによる大気ニュートリノ観測のためのバックグラウンドの研究, Master's thesis, 東北大学 (2008).

[106] K. Bays *et al.*, Supernova relic neutrino search at super-kamiokande, *Phys. Rev. D* 85 (2012) 052007. doi:10.1103/PhysRevD.85.052007.

[107] A. Gando *et al.*, Constraints on θ_{13} from a three-flavor oscillation analysis of reactor antineutrinos at kamland, *Phys. Rev. D* 83 (2011) 052002. doi:10.1103/PhysRevD.83.052002.

[108] G. J. Feldman, R. D. Cousins, Unified approach to the classical statistical analysis of small signals, *Phys. Rev. D* 57 (1998) 3873–3889. doi:10.1103/PhysRevD.57.3873.

[109] G. Steigman, B. Dasgupta, J. F. Beacom, Precise relic wimp abundance and its impact on searches for dark matter annihilation, *Phys. Rev. D* 86 (2012) 023506. doi:10.1103/PhysRevD.86.023506.